NASA
CR
3056
c.1

TECH LIBRARY KAFB, NM
0061787

LOAN COPY: RETU
AFWL TECHNICAL
KIRTLAND AFB,

NASA Contractor Report 3056

The Free Jet as a Simulator of Forward Velocity Effects on Jet Noise

K. K. Ahuja, B. J. Tester,
and H. K. Tanna

CONTRACT NAS3-20050
OCTOBER 1978

NASA

TECH LIBRARY KAFB, NM
0061787

NASA Contractor Report 3056

The Free Jet as a Simulator of Forward Velocity Effects on Jet Noise

K. K. Ahuja, B. J. Tester,
and H. K. Tanna
Lockheed-Georgia Company
Marietta, Georgia

Prepared for
Lewis Research Center
under Contract NAS3-20050

National Aeronautics
and Space Administration

Scientific and Technical
Information Office

1978

FOREWORD

This report was prepared by the Lockheed-Georgia Company, Marietta, Georgia, for the NASA-Lewis Research Center, Cleveland, Ohio, under Contract NAS3-20050, entitled "A Study of the Free Jet as a Simulation Technique for Forward Velocity Effects on Jet Noise."

Dr. Allen Karchmer was the Project Manager for the NASA-Lewis Research Center. Lockheed's Program Manager was Dr. Harry E. Plumblee, Jr., and Dr. H. K. Tanna was the Principal Investigator.

The authors would like to express their sincere acknowledgements to Dr. P. D. Dean for his help in solving some of the experimental problems, Mr. N. Searle and Mr. S. M. Varma for their assistance in conducting the experiments and reducing the data, Mr. D. F. Blakney for developing the computer plots, Mr. J. G. Tibbetts for preparing the transformation charts, Mr. R. H. Burrin for preparing all the figures, and Mrs. Barbara C. Reagan for typing the manuscript .

CONTENTS

Page

SUMMARY 1

1. INTRODUCTION 3

1.1 Inflight Effects on Jet Noise - Current Status 4
1.2 Possible Reasons for Observed Anomalies 4
1.3 Objectives of Present Program 7

2. OUTLINE OF PROPOSED FREE-JET DATA CALIBRATION PROCEDURE 10

2.1 Angle Calibration 12
2.2 Distance Calibration 14
2.3 Amplitude Calibration 18

3. FACILITY AND EXPERIMENTAL SETUP 20

3.1 Anechoic Free-Jet Facility 20
3.1.1 Facility Description 20
3.1.2 Facility Performance 27
3.2 Experimental Setups and Relevant Calibrations for Point Source Tests 31
3.2.1 Point Source 31
3.2.2 Experimental Configurations 38
3.2.3 Experimental Conditions 42
3.2.4 Data Acquisition and Analysis 46
3.3 Internal Noise Source 46
3.4 Test Procedure 48

4. EXPERIMENTAL STUDY OF TRANSMISSION, REFLECTION AND SCATTERING OF SOUND IN A FREE-JET FLIGHT SIMULATION FACILITY AND COMPARISON WITH THEORY 56

4.1 Objectives 56
4.2 Angle Calibration 56
4.2.1 Calculated Time Delays 57
4.2.2 Measured Time Delays 60
4.3 Internal Reflection 73
4.4 Amplitude Calibration Factors 109
4.5 Turbulence Absorption 115
4.6 Turbulence Scattering 121
4.7 Problems at Low Frequencies 136
4.8 Summary 139

CONTENTS (Cont'd)

Page

5. THEORETICAL INVESTIGATION 141

5.1 Jet Noise Calibration Factor 141
5.2 Facility Calibration Factor Based Upon Approximate Solutions to the Lilley Equation 143
5.2.1 Low-Frequency Approximation (Vortex Sheet Model) . . . 144
5.2.2 High-Frequency Approximation (Geometric Acoustics) . . 147
5.3 Numerical Results for Jet Mixing Noise Sources 154
5.3.1 Definition of Parameters for Calculations 154
5.3.2 Calibration Factor Results for Complete Profile 160
5.3.3 Results for Partial Profile 164
5.3.4 Results for Plug Flow Profile 166
5.3.5 Area Ratio Study 169
5.4 Results for Internal Noise Sources 169
5.5 Summary 176

6. TRANSFORMATION CHARTS AND COMPUTATIONAL PROCEDURE 178

6.1 Transformation Charts 179
6.1.1 Free-Jet to Wind-Tunnel Data Transformation 179
6.1.2 Wind-Tunnel to Flight Data Transformation 197
6.2 Computational Procedure 209
6.2.1 General Structure 209
6.2.2 Transformation Options 209
6.2.3 Computer Program Details 212
6.2.4 Input Requirements 219
6.2.5 Sample Case 221

7. VALIDATION OF TRANSFORMATION PROCEDURE 235

7.1 Objectives and Approach 235
7.2 Experimental Program 236
7.2.1 Test Configuration and Data Acquisition 236
7.2.2 Calibration of Jet Operating Conditions 236
7.2.3 Experimental Conditions 240
7.2.4 Comparison Between Measured and Predicted Jet Noise Spectra 242
7.2.5 Inverse Square Law Calibration 242
7.2.6 Background Noise and Data Quality 244
7.3 Experimental Results 250
7.4 Discussion and Conclusions 253

8. EFFECTS OF SIMULATED FORWARD FLIGHT ON JET NOISE, SHOCK NOISE AND INTERNAL NOISE 258
8.1 Objectives 258
8.2 Test Program 258

CONTENTS (Cont'd)

Page

8.3 Experimental Results Without Internal Noise 259
8.3.1 Effect of Source Location Corrections 259
8.3.2 Spectral Results 261
8.3.3 Overall SPL Results 266
8.3.4 Relative Velocity Scaling of Shock-Free Data 268
8.4 Experimental Results With Internal Noise 271
8.4.1 Spectral Results 271
8.4.2 Overall SPL Results 273
8.4.3 Scaling of Internal Noise 281
8.5 Conclusions 290

9. CONCLUSIONS 292

APPENDIX 4A. SNELL'S LAW AND MINIMUM TRAVEL TIME 296

APPENDIX 4B. EXPERIMENTAL DETERMINATION OF AMPLITUDE CALIBRATION FACTOR 298

APPENDIX 4C. SAMPLE CALCULATION OF AMPLITUDE CALIBRATION FACTORS . . . 300

APPENDIX 6A. DISTANCE AND ANGLE CORRECTIONS FOR THE FLIGHT CASE . . . 302

APPENDIX 7A. TRANSFORMATION OF INFLOW MEASUREMENTS TO IWT CONDITIONS . 307

APPENDIX LIST OF SYMBOLS 310

REFERENCES 314

SUMMARY

The work described in this report deals with the overall problem of aircraft forward motion effects on jet engine noise. The three specific objectives are:

(1) To obtain a thorough theoretical and experimental understanding of the effects of the free-jet shear layer on the transmission of sound from a model jet placed within the free jet to the far-field receiver located outside the free-jet flow, and hence, to evaluate the validity and accuracy of the free-jet flight simulation technique for forward velocity effects on jet noise.

(2) To provide transformation charts and a systematic computational procedure for converting measurements obtained from a free-jet simulation to the corresponding results from a wind-tunnel simulation, and, finally, to the flight case.

(3) To experimentally establish the effects of simulated forward flight on engine internal noise source and shock-associated noise from model-scale unheated and heated jets, and hence, to illustrate the role played by these non-jet mixing noise sources in producing the currently observed anomalies between flight data and free-jet simulation data projected to the flight case.

(1) Free-Jet Flight Simulation Technique - The individual components of a theoretical transformation procedure, developed in our previous work, are verified experimentally using a point sound source in the Lockheed anechoic free-jet facility. The five specific (acoustical) aspects examined and/or verified are (i) redirection or refraction (i.e., angle changes), (ii) internal reflection, (iii) transmission (i.e., amplitude changes), (iv) turbulence absorption, and (v) turbulence scattering.

In the theoretical work, the validity of the amplitude calibration factor, derived in our previous work using geometric acoustics, is assessed by detailed comparisons with numerical solutions to the Lilley equation. It is shown that for most practical cases, model-scale jet noise data measured in a free-jet facility can be converted to ideal-wind-tunnel (IWT) conditions using the simple high-frequency amplitude calibration factor with remarkable accuracy.

Following the verification of the important *individual components* of the transformation procedure, the validity of the procedure *in its entirety* is established experimentally using a model jet as the sound source. Detailed measurements are conducted both inside and outside the flow, and both sets of data are compared after transformation to IWT conditions. Good agreement is obtained over a wide range of frequencies, angles and free-jet velocities.

(2) Transformation Charts and Computational Procedure - In order to convert flight simulation data measured in a free-jet facility to the corresponding wind-tunnel data and, finally, to the inflight case, a self-contained transformation procedure is provided in two parts. In the first part, transformation charts are provided, and in the second part, a comprehensive computer program is presented and described in the form of a user's guide.

(3) Flight Effects on Jet Noise, Shock Noise and Internal Noise - The effects of simulated forward motion on various combinations of these three noise sources are examined with experimental data acquired in the Lockheed free-jet facility. It is shown that (i) for the jet mixing noise component, a reduction in noise with forward velocity is obtained at all angles and frequencies for both unheated and heated jets, and (ii) for shock-containing jets in the absence of internal noise, or, for jet mixing noise contaminated with internal noise, forward motion provides a noise reduction in the rear arc and a noise increase in the forward arc, with little change at 90°.

When jet noise is contaminated with internal noise, the resulting relative velocity exponent is reduced at all emission angles. The exact value of the exponent depends upon the degree of contamination. It is illustrated that the existing anomalies between full-scale flight data and model-scale flight simulation data could well be due to the contamination of flight data by internal noise.

1. INTRODUCTION

The noise generated by a jet exhaust has been studied in great detail, since the development of jet engines some thirty years ago. During this period, research programs have been devoted not only to the prediction of jet noise, but also to obtain a fundamental understanding of the generating processes, so that noise reduction efforts can be attempted on the basis of firm scientific principles. For a static jet, it has now become possible to predict the noise field, and in fact, the theory to substantiate and explain these predictions is now available.

In recent years, U. S. Government regulations have made it mandatory to control the noise of aircraft operating from U. S. airports. As a result of these regulations, it is necessary to include aircraft noise as a design constraint in new aircraft projects. When noise is considered as an aircraft design parameter, not only are the characteristics of the basic jet of concern, but the effects of aircraft configuration and operation must also be properly accounted for in noise predictions. In this regard, aircraft forward motion is found to be a significant parameter controlling the generation and radiation of jet noise.

Full-scale flight testing is a direct method for obtaining the required noise levels with no intermediate steps or recourse to theory. However, the cost associated with any comprehensive flight test program is prohibitive, and there are several disadvantages which are difficult to overcome. In recognition of this, a high priority has been placed in recent years on developing the technology that will predict the noise received on the ground from a flying aircraft using static noise measurements. Several ground-based techniques that provide accurate *simulation* of the flight environment on various noise sources have evolved in recent years. The three most promising types of flight simulation facilities are (i) stationary jet in a large-scale wind tunnel, (ii) stationary jet immersed in a larger surrounding jet (a free-jet facility), and (iii) jet mounted at the end of a rotating arm (a spinning rig). In addition, a ground-based moving vehicle (e.g. the Bertin Aerotrain in France) is also being used to study flight effects. Each of these has its own merits as well as facility oriented problems, and significant research activity is in progress to understand and resolve the limitations of such flight simulation facilities.

As a result of the major significance of flight velocity on jet noise, the NASA-Lewis Research Center decided to embark on a study of the problems of understanding the generation, propagation, and measurement of exhaust-generated noise from jets in flight. As a part of this research effort, a one-year contract (NAS3-18540) was awarded to the Lockheed-Georgia Company in 1974. It was intended that this contract serve as a program definition phase with the ultimate goal of providing detailed recommendations for future research on effects of flight on jet noise. During this contract work, various fundamental aspects controlling the generation, propagation, and measurement of noise from a conical jet in forward flight were examined in detail. In particular, the inflight effects on pure turbulent mixing

noise from unheated jets were examined experimentally in the inflight simulation mode. Both acoustic and flow characteristics were determined by testing model-scale nozzles in an anechoic free-jet facility and a wind tunnel, respectively. The findings, together with detailed recommendations for future research, were given in the contract final report (ref. 1.1).

1.1 INFLIGHT EFFECTS ON JET NOISE - CURRENT STATUS

One of the major problems facing the aeroacoustics community is that the effects of aircraft forward motion as observed from simulation experiments do not correspond fully with the flight effects derived from full-scale aircraft flyover tests. The problem is illustrated quantitatively in Figure 1.1, where the flight effects on jet noise from a conical nozzle are expressed in terms of the widely used "relative velocity exponent." A *positive* value of the exponent implies static-to-flight noise *reduction*, whereas a *negative* value implies an *increase* in noise level. In the figure, results from various flight simulation facilities are compared with one another as well as with results from aircraft flight tests. (It should be noted that in deriving the relative velocity exponents, some investigators have chosen to retain the so-called dynamic effect factor, whereas other investigators have removed this factor.) The comparison shows that while there is reasonable agreement at large angles in the rear arc, the flight simulation results at 90° and in the forward arc differ significantly from the results obtained from the Rolls-Royce flight tests and the SNECMA aerotrain experiments. The simulation results show a significant noise reduction with forward velocity at 90° and in the forward arc, whereas the flight tests (except ref. 1.9) show either no change or an increase in noise at these angles. Such discrepancies are difficult to comprehend, especially at 90° to the jet axis, where, in the program definition phase, it was conclusively shown that the reduction in noise (from an unheated jet) can be directly attributed to the changes in jet flow characteristics (source alteration) that occur due to the presence of co-flowing airstream. It is a matter of urgency to reconcile these observed differences, since suppressors which have been optimized in static tests or in flight simulation facilities may fall far short of expectations in actual flight tests.

1.2 POSSIBLE REASONS FOR OBSERVED ANOMALIES

In attempting to resolve the observed anomalies between flight data and simulated flight data obtained from free-jet experiments, several possible explanations can be put forward:

(1) When forward-velocity effects are simulated in a free-jet facility, the sound generated by the primary jet has to propagate through the free-jet shear layer on its way to the far-field microphones placed outside the free-jet flow. During this propagation, the acoustic signatures are subjected to several physical phenomena that occur due to the presence of this

CURVE	REFERENCE NO.	DATA SOURCE
1	1.2	LOCKHEED - FREE-JET SIMULATION (UNHEATED MODEL JET)
2	1.3	NGTE - WIND TUNNEL SIMULATION (UNHEATED MODEL JET)
3	1.4	NGTE - WIND TUNNEL SIMULATION (HEATED MODEL JET)
4	1.5	P&WA - FREE-JET SIMULATION (HEATED MODEL JET)
5	1.6	BOEING - WIND TUNNEL SIMULATION (JT8D ENGINE)
6	1.7	SNECMA - BERTIN AEROTRAIN (J85 ENGINE)
7	1.8	RR - AIRCRAFT FLYOVER TESTS
8	1.9	DOUGLAS - DC-9/JT8D AIRCRAFT FLYOVER TESTS

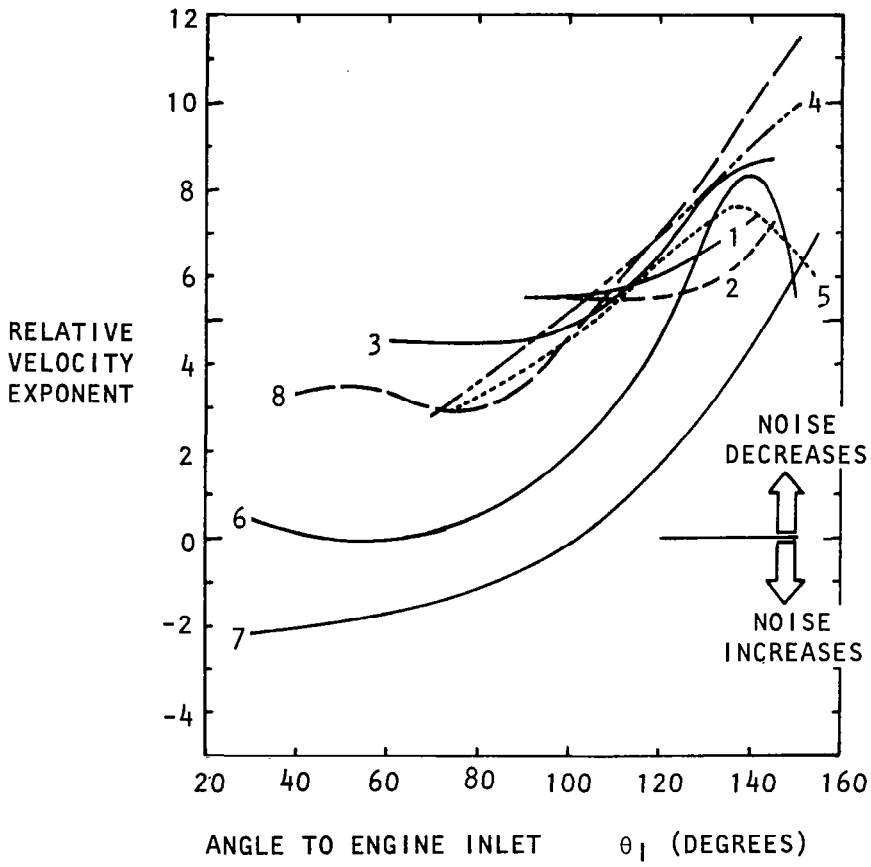

Figure 1.1 Flight effects on jet noise observed from various simulation experiments and flight tests.

outer flow. These include (a) the downstream convection of sound by the free-jet flow, and (b) the reflection, refraction, turbulence scattering and possibly turbulence absorption encountered during the passage through the free-jet shear layer. In order to convert the measured results obtained from free-jet simulation experiments to the corresponding flight case, it is vital to obtain a thorough understanding and accurate quantification of these effects. In principle, it could be argued that the currently observed anomalies between flight data and free-jet data converted to the flight case may be a consequence of a lack of adequate understanding of these effects.

(2) In model scale experiments in a free-jet facility, the primary jet sound field is not contaminated by any significant internal or upstream noise contribution (that is, if the facility has been well designed); therefore, the measured trends and dependencies must be considered to be the true effects of relative velocity on jet mixing noise. On the other hand, it is very difficult to obtain full-scale flight data which can be *guaranteed* to be free from significant contributions from one or more of the other noise sources (for example, the engine-related noise sources like core noise, turbine noise, and lip noise, and the exhaust-related noise like shock noise). The sources other than pure turbulent mixing noise, although slightly lower in magnitude and, therefore, undetected in the static case, can be expected to be either unaffected or amplified in flight. Hence, in the flight case, a possibility exists for the sound field in the forward arc to be dominated by these other noise sources due to the reduced contribution from mixing noise. Indeed, this is the explanation put forward in two recent studies by Von Glahn and Goodykoontz (ref. 1.10) and Stone (ref. 1.11) where the observed discrepancies are attributed to shock-associated noise and core noise, respectively.

(3) Another obvious possibility put forward recently is that, in conducting static-to-flight comparisons of full-scale data, it is necessary to take proper account of source location if the static data and the flight data are acquired at different measurement distances from the nozzle exit plane. It can be argued that, if the published static-to-flight comparisons of full-scale data do not include such source location corrections, the observed effects might be misleading.

(4) In an actual flight test, the jet exhaust noise source is in motion relative to a fixed, ground-based observer, whereas in a flight simulation test, this relative motion between source and observer is lacking. At least according to existing theoretical knowledge, such relative motion is not expected to give rise to the current observation at 90°; i.e., that there is no change in the radiation level at 90° to the jet axis in flight tests. Whether this relative motion does have some peculiar effects, which are not detected theoretically at the present time, needs to be examined experimentally as described in the recommendations given in the final report (ref. 1.1) for the program definition phase.

A relevant theoretical development conducted recently by Dowling (ref. 1.12) must not be overlooked here. In this study, it is shown that, for certain specialized descriptions of sound sources, the effect of source motion is different from that predicted by previous theories, and the source

motion does have a finite (but not necessarily significant) effect on the radiation at 90° to the direction of motion. The question that must be raised is whether the types of sources examined by Dowling can be representative of the types of real sources present in a jet exhaust. Our initial evaluation of this work suggests that, even if the sources examined in this study are found to be realistic, the results will be useful only in conducting static-to-flight comparisons, and the results will not explain the observed discrepancies between flight data and flight-simulation data. However, the study warrants further evaluation in a future program for application to the current problem.

(5) Another explanation which may have some effect on the observed discrepancies can be classified as engine installation and atmospheric propagation effects. In flight-simulation tests, the relative velocity effects are normally evaluated with a clean jet in the absence of any surrounding hardware. In contrast, a full-scale engine in a flight test generates noise in proximity to the complete aircraft structure. In addition, the sound field has to propagate through a complex inhomogeneous environment on its way to the ground-based observer. It is, therefore possible that, if these effects are not properly accounted for, the available flight data may not be strictly valid for accurate static-to-flight comparisons.

(6) Another postulated effect is that the internal noise (especially pure tones) triggers large-scale disturbances in the jet which in turn lead to broadband jet noise amplification. This mechanism has been observed in experiments conducted in Germany (ref. 1.13) and England (ref. 1.14) and has been a subject of much recent interest. The fact that noise from static jets usually scales from model to full engine scale suggests that this broadband noise amplification is not an important practical phenomenon in the static tests. However, its effect in flight has yet to be investigated. Since the turbulence structure is known to be modified by flight, the effect or importance of pure tone acoustic excitation is also likely to be modified by flight.

The explanations for the discrepancy between static and flight data listed above are by no means the only possibilities that can be offered at the present time. The list has, by now, grown quite long. However, they are considered to be the most relevant in the light of existing knowledge.

1.3 OBJECTIVES OF PRESENT PROGRAM

In discussing the role played by the present investigation in understanding and quantifying the effects of forward velocity on jet noise, it is emphasized that the present contract is directed to only the first two possible explanations described above for resolving the anomalies between flight data and free-jet data converted to the flight situation.

To be more specific, the three major objectives of the present investigation are:

(1) To obtain a thorough theoretical and experimental understanding of the effects of the free-jet shear layer on the transmission of sound from a model jet placed within the free jet to the far-field receiver located outside the free-jet flow, and hence, to evaluate the validity and accuracy of the free-jet flight simulation technique for forward velocity effects on jet noise.

(2) To provide transformation charts and a systematic computational procedure for converting measurements obtained from a free-jet simulation to the corresponding results from a wind tunnel simulation, and, finally, to the flight case.

(3) To experimentally establish the effects of simulated forward flight on engine internal noise source and shock-associated noise from model scale unheated and heated jets, and hence, to illustrate the role played by these non-jet mixing noise sources in producing the currently observed anomalies between flight data and free-jet simulation data projected to the flight case.

The work conducted to accomplish these three program objectives is described in Sections 2 through 8 of this report.

The various phenomena associated with flight simulation in a free-jet facility are introduced in Section 2, where a summary of our previous work on transformation of free-jet data to estimated flight data, based essentially on geometric acoustics theory for sound transmission across the free-jet shear layer, is also presented.

The verification of the theoretical calculations for free-jet shear layer effects required some novel and extremely difficult experiments, which are described in Sections 3 and 4. The Lockheed anechoic free-jet facility, and the experimental setup and techniques used for these verification tests are described in Section 3. The results of these experiments (dealing with transmission, internal reflection, turbulence scattering, and turbulence absorption), using experimental point sound sources placed inside the free-jet flow, and comparisons with theory are presented and discussed in Section 4.

The theoretical analysis of the interaction of sound with the mean properties of model-jet and free-jet flows over a wide envelope of model-jet and free-jet operating conditions is described in Section 5, where the validity of the low- and high-frequency asymptotic solutions for the appropriate calibration factors is assessed by detailed comparisons with the numerical solutions to the Lilley equation for flow-acoustic interactions.

The transformation charts and a systematic computational procedure for converting noise data obtained from a free-jet facility to the corresponding wind-tunnel simulation, and finally to the inflight conditions, are given in Section 6.

In order to establish the validity and accuracy of the recommended transformation procedure, a series of experiments using unheated and heated model jets was conducted. For identical test conditions, noise data were acquired both inside and outside the free-jet flow. Both sets of data were converted to ideal wind tunnel conditions using the transformation procedures. The resulting comparisons are presented and discussed in Section 7.

Finally, the effects of forward motion on jet mixing noise, internal noise, and shock noise were examined experimentally in the free-jet simulation facility, for unheated as well as heated model-jet conditions. The results of these experiments, conducted to accomplish the third major objective listed above, are presented in Section 8.

2. OUTLINE OF PROPOSED FREE-JET DATA CALIBRATION PROCEDURE

In the free-jet flight simulation technique, the noise source under examination is placed within the potential core of a larger surrounding jet, and noise data are acquired by placing microphones outside the free-jet flow in an anechoic environment. Although this technique eliminates many of the problems associated with other flight-simulation techniques (e.g., large-scale wind tunnels where the microphones are placed inside the flow, moving sleds, spinning rigs, etc.), it does present some inherent problems, mainly associated with the propagation of sound through the free-jet shear layer. These propagation effects include the downstream convection of sound by the free-jet flow, and the refraction, reflection and scattering of sound encountered during the passage through the free-jet shear layer. In order to convert the measured results obtained from free-jet simulation experiments to the corresponding flight case, it is first necessary to "correct out" the influence of the free-jet shear layer. When this is done, it yields an estimate of the corresponding data that one would obtain in an "ideal wind tunnel (IWT)", where the shear layer between noise source and microphone is not present.

During the past three years or so, several investigators have examined free-jet shear layer effects theoretically and developed transformation or calibration procedures which permit the conversion of free-jet simulation data to the corresponding inflight data. A simple calibration procedure was also derived at Lockheed in the program definition phase (ref. 2.1). However, for the majority of the free-jet shear layer effects, only limited experimental confirmation (ref. 2.2) of the theoretical models has been obtained to date.

The purpose of the present section is to give an outline of the free-jet data calibration procedure derived at Lockheed (ref. 2.1). A detailed experimental study of the free-jet shear layer effects using a point sound source, and comparison of experimental results with theoretical calibration factors will be presented in the subsequent sections of this report.

The present calibration procedure enables the transformation of free-jet data to the corresponding ideal-wind tunnel condition (see Figure 2.1a). The final stage only involves a simple Doppler frequency shift to obtain estimated flyover data from data calculated for the IWT condition and is not considered further here. It is, however, included in the computational procedure for data transformation, which will be presented in Section 6.

The main objective of the *theoretical* program that will be described in Section 5 is to solve the Lilley equation in order to assess the range of validity of our recommended *amplitude* calibration factor which is, in effect, based on a high-frequency or geometric acoustics (GA) solution to the Lilley equation.

In the present section, the recommended calibration procedure is summarized for the case where the microphone polar arc (of radius R_m) outside the free jet is centered on the noise source under test; in general, a further

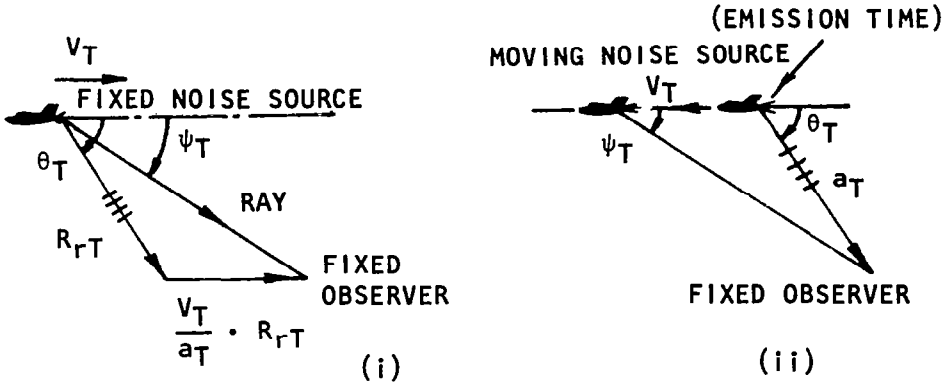

Figure 2.1a Corresponding angles in (i) "ideal wind tunnel" and free-jet potential core, (ii) actual flyover situation.

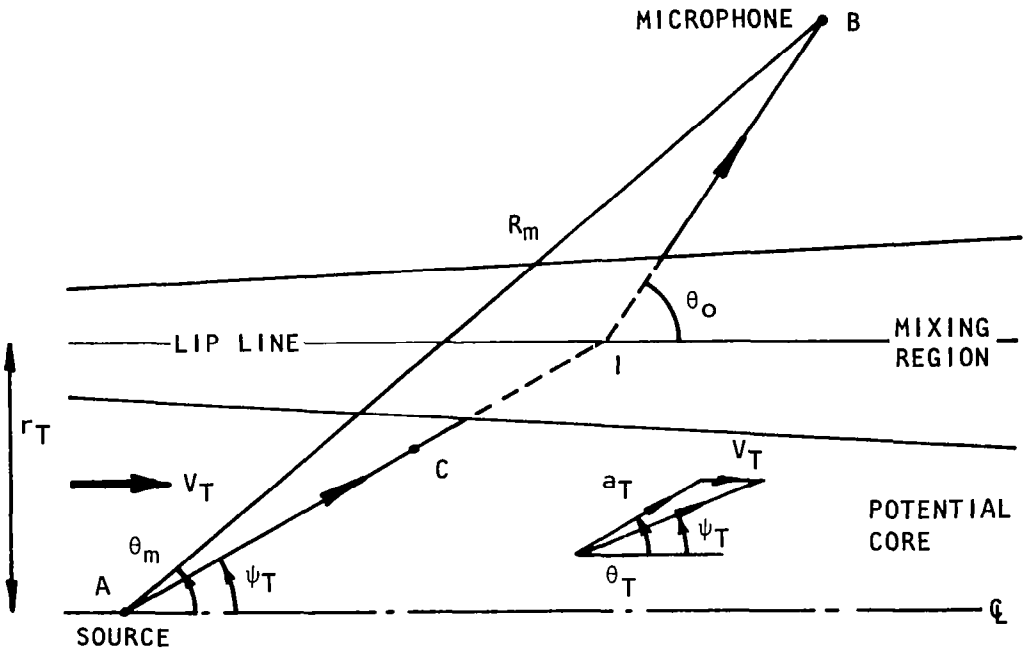

Figure 2.1b The lip-line or vortex-sheet model of sound refraction across the free-jet shear layer.

correction is included to account for true source location relative to the microphone arc origin.

The calibration procedure can be carried out in three steps (see Figure 2.1b):

(i) angle calibration: free-jet microphone angle $\theta_m \rightarrow$ wavenormal angle, θ_T, in free-jet potential core and in ideal wind tunnel;

(ii) distance calibration: free-jet microphone distance $R_m \rightarrow$ wavenormal distance R_{rT};

(iii) amplitude calibration: free-jet sound pressure level at $(R_m, \theta_m) \rightarrow$ ideal wind tunnel sound pressure level at (R_{rT}, θ_T).

The purpose of this calibration procedure is to correct out the influence of the free-jet shear layer (which is, by definition, absent in the ideal wind tunnel and in the flyover cases) and to convert a noise level measured *outside* the free jet, e.g., at point B in Figure 2.1b, to the level that would be measured inside the free jet, e.g., at point C, due to outward-going wavefronts from the source region. The three steps in the calibration procedure are discussed below.

2.1 ANGLE CALIBRATION

The angle calibration is based upon a vortex-sheet or lip-line refraction model. Referring to Figure 2.1b, the outward-going sound ray from the source at A is traced to the microphone position outside the free jet by assuming that Snell's law for parallel flows applies and that the refraction takes place abruptly at the lip line. This is equivalent to the assumption that the mean flow field of the free jet can be replaced by a uniform flow bounded by a cylindrical vortex sheet of the same radius as the jet nozzle. However, the model was not adopted on that basis but upon the results obtained in reference 2.1 for the refraction and axial displacement of ray paths traced through a realistic, spreading shear layer. Those results indicate that the lip-line refraction model should be sufficiently accurate for the purpose of angle and distance corrections. Some recent ray-tracing results are shown in Figure 2.2 to illustrate the validity of the lip-line refraction model. On the other hand, the *amplitude* calibration (described in Section 2.3) is obtained without recourse to the lip-line refraction model and should not be confused with amplitude corrections based on the vortex-sheet model, as used elsewhere (refs. 2.3, 2.4).

According to the lip-line refraction model, the axial distance between the microphone and the source, $R_m \cos\theta_m$ [see Figure 2.1(b)], is equal to the sum of the axial distances travelled by the ray AI inside and the ray IB outside the flow and this yields a relation between the angles θ_m, ψ_T and θ_o:

$$R_m \cos\theta_m = r_T \cot\psi_T + (R_m \sin\theta_m - r_T) \cot\theta_o \qquad (2\text{-}1)$$

(lip-line refraction)

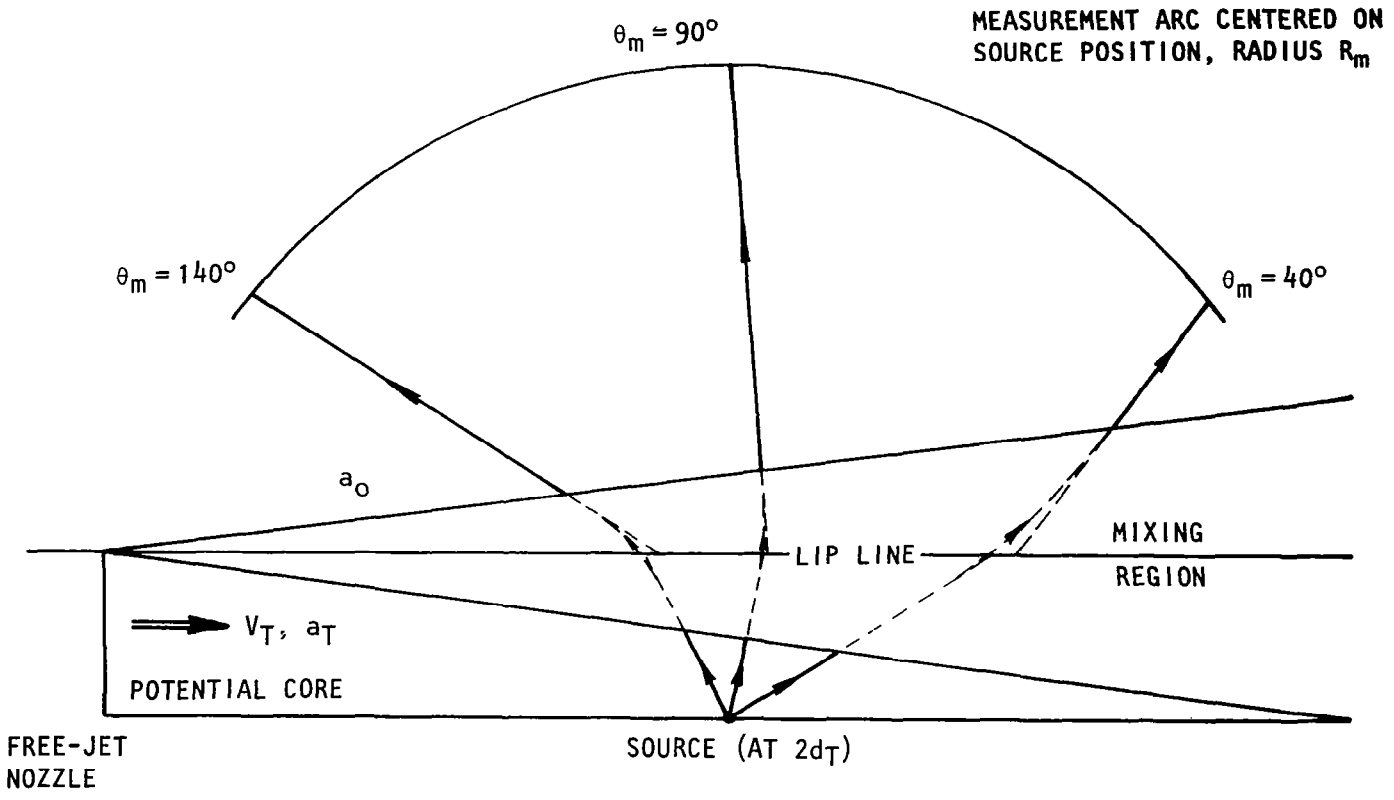

Figure 2.2 Typical ray paths traced through the diverging free-jet shear layer showing small axial displacement effect; $R_m/r_T = 4$, $V_T/a_T = 0.3$, $a_T/a_o = 1$.

The required wavenormal angle θ_T is related to the ray angle ψ_T by

$$\cot\psi_T = (V_T + a_T \cos\theta_T)/a_T \sin\theta_T \tag{2-2}$$

(convection by uniform flow)

(see velocity triangle in Figure 2.1b), and to the refraction angle, θ_o, by Snell's law for axially uniform flows,

$$V_T + a_T/\cos\theta_T = a_o/\cos\theta_o. \tag{2-3}$$

(refraction by stratified flow)

Equations (2-1) through (2-3) can be solved by iteration to yield ψ_T, θ_T and θ_o for a given microphone position (R_m, θ_m), free-jet radius r_T and flow conditions V_T/a_T, a_T/a_o. Typical solutions for θ_T are given in Tables 2.1 for $R_m/r_T = 4$, $a_T/a_o = 1$.

Table 2.1 Variation of wavenormal angle, θ_T, with measurement angle, θ_m, for three free-jet Mach numbers; $R_m/r_T = 4$, $a_T/a_o = 1$.

θ_m \ M_T	0.1	0.2	0.3
40.0	38.6	38.0	38.0
50.0	49.5	49.4	49.7
60.0	60.4	61.0	61.8
70.0	71.0	72.1	73.3
80.0	81.3	82.7	84.2
90.0	91.4	92.8	94.2
100.0	101.3	102.4	103.5
110.0	110.8	111.5	112.0
120.0	120.1	120.1	119.8
130.0	129.2	128.1	126.7
140.0	137.9	135.4	132.7

2.2 DISTANCE CALIBRATION

The distance calibration is also based on the lip-line refraction model, for the reasons discussed earlier. Referring to Figure 2.3, the mean-square

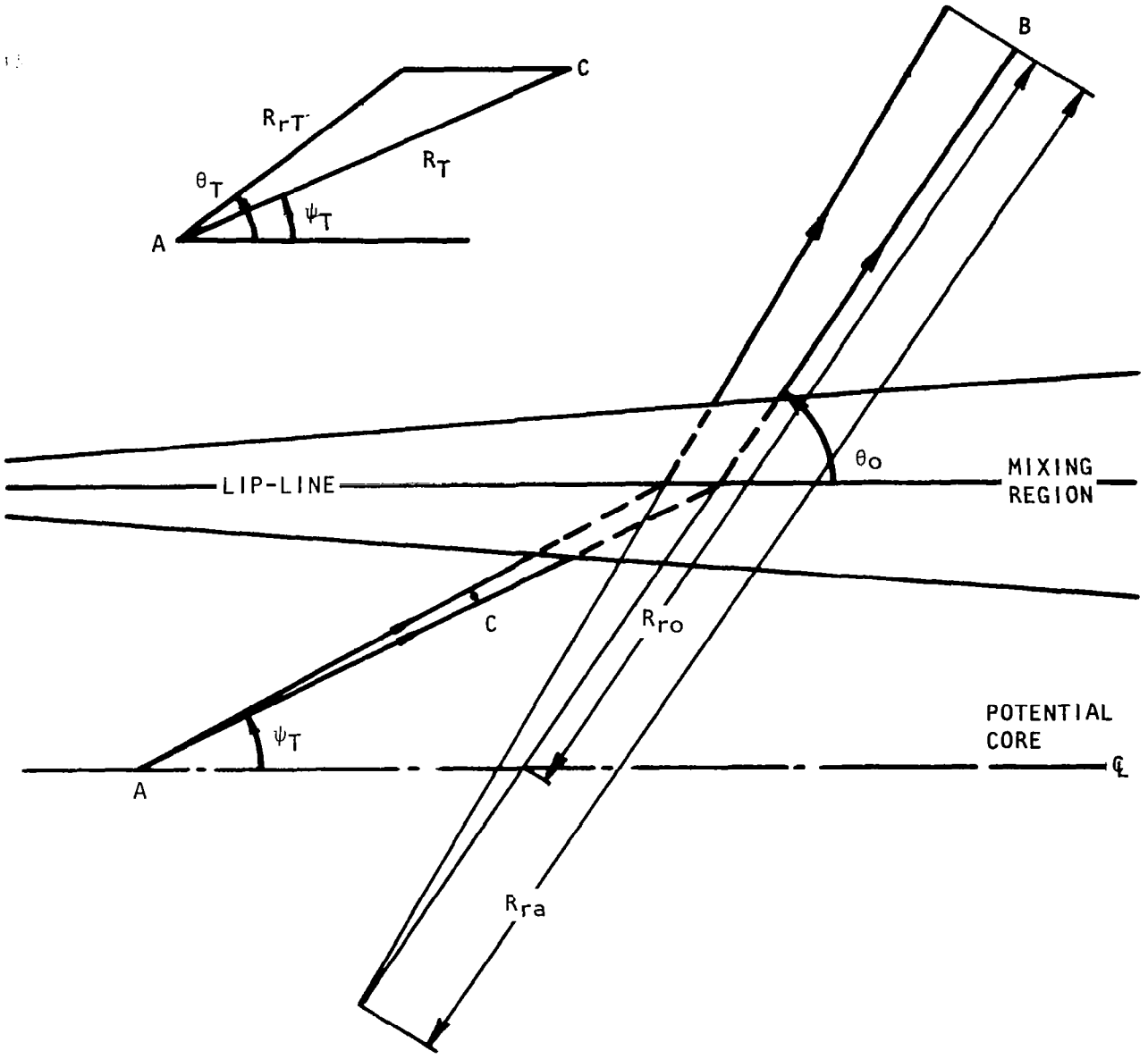

Figure 2.3 Distances used in calibration procedure based on lip-line refraction model.

pressure* outside the flow varies with distance (for a fixed angle θ_o) according to the formula (ref. 2.1)

$$\overline{p^2} \propto (R_{ra}\ R_{ro})^{-1} \tag{2-4}$$

which reduces to R_{ro}^{-2} only when $R_{ro} >> r_T$. The distances R_{ra}, R_{ro} are indicated in Figure 2.3 and can be calculated with expressions from reference (2.1), viz.

$$R_{ro} = R_m \sin\theta_m / \sin\theta_o, \tag{2-5}$$

$$R_{ra} = R_{ro} + (r_T/\sin\theta_o)\ \{(\cot\theta_T/\cot\theta_o)^3\ (a_o/a_T)^2 - 1\} \tag{2-6}$$

where the angles θ_o, θ_T follow from solutions to equations (2-1) through (2-3)

Inside the flow, the mean-square pressure* varies with distance as R_{rT}^{-2} where

$$R_{rT} = R_T/(M_T \cos\psi_T + \sqrt{1 - M_T^2 \sin^2\psi_T}) \tag{2-7}$$

is the distance travelled by the wavefront relative to the uniform flow and R_T is the distance along the ray path (e.g. AC in Figure 2.3).

The amplitude calibration factor, C_F, described in the next section is expressed in terms of a ratio of mean-square pressures*, normalized by the distances defined above, viz.

$$C_F = \frac{R_{rT}^2\ \overline{p^2}_C}{R_{ra}\ R_{ro}\ \overline{p^2}_B} \tag{2-8}$$

Thus the ratio of *measured* mean-square pressures (see Section 4) or the equivalent quantities (involving cross-power spectra) are first normalized by $R_{rT}^2/R_{ra}R_{ro}$ in order to compare an experimentally determined calibration factor, C_{F_m}, with the theoretical calibration factor given below by equation (2-9).

The behavior of the distance factor $R_{ra}R_{ro}/R_{rT}^2$ for $R_{rT} = R_m = 4r_T$ is plotted in Figure 2.4 as a function of θ_m for different values of $M_T (\equiv V_T/a_T)$ with $a_T/a_o = 1$.

Or the power spectral density of the acoustic pressure.

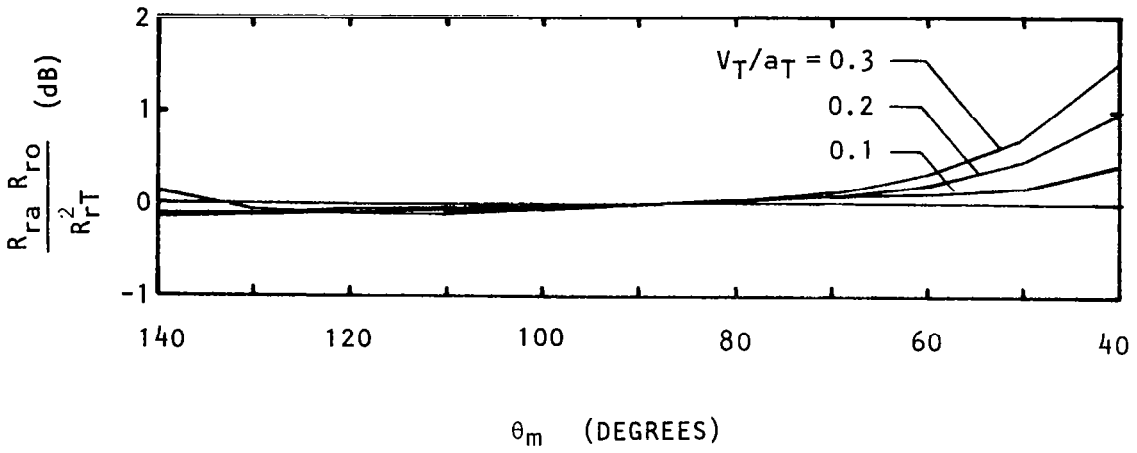

Figure 2.4 Distance factor variation with microphone angle and free-jet Mach number; $R_m/r_T = 4$, $R_{rT} = R_m$, $a_T/a_o = 1$.

2.3 AMPLITUDE CALIBRATION

After the distance corrections have been applied, an amplitude calibration factor converts the (normalized) mean-square pressure outside the free jet, $R_{ra}R_{ro}\overline{p^2}_B$, to the (normalized) mean-square pressure inside the jet, $R_{rT}^2\overline{p^2}_C$, and is given by

$$C_F = \rho_T D_T^4/\rho_o \tag{2-9}$$

where

$$D_T = (1 + V_T\cos\theta_T/a_T)^{-1}. \tag{2-10}$$

This result is based upon the assumption that the free-jet shear layer is sufficiently thick on the wavelength scale for geometric acoustics to apply so that (i) acoustic energy is conserved along the ray tube passing through the points C and B and (ii) the sound pressure at point C is the result of outward-going waves only, since, by definition, reflections are absent in the geometric acoustics limit.

The amplitude and distance calibration factors when combined yield the following simple formula for the SPL at point C:

$$SPL_C = SPL_B + 10\log_{10} C_F + 10\log_{10}\left(\frac{R_{ra}\ R_{ro}}{R_{rT}^2}\right) \tag{2-11}$$

The second term is evaluated in Figure 2.5 for the same condition as used in Figure 2.4.

The theoretical amplitude calibration factor will be compared with experimental results in Section 4 by measuring SPL_B and SPL_C (or the SPL of the sound field which is coherent with that at A) and comparing

$$SPL_C - SPL_B - 10\log_{10}\left(\frac{R_{ra}\ R_{ro}}{R_{rT}^2}\right) \tag{2-12}$$

with the theoretical calibration factor given by equations (2-9) and (2-10).

As a final note, it is emphasized that the simplified data calibration procedure outlined above does not include the effects of turbulence scattering and turbulence absorption, if it exists, in a free-jet flight simulation experiment. The significance of these two effects was examined experimentally during the present program, and the findings are presented and discussed in Section 4 of this report.

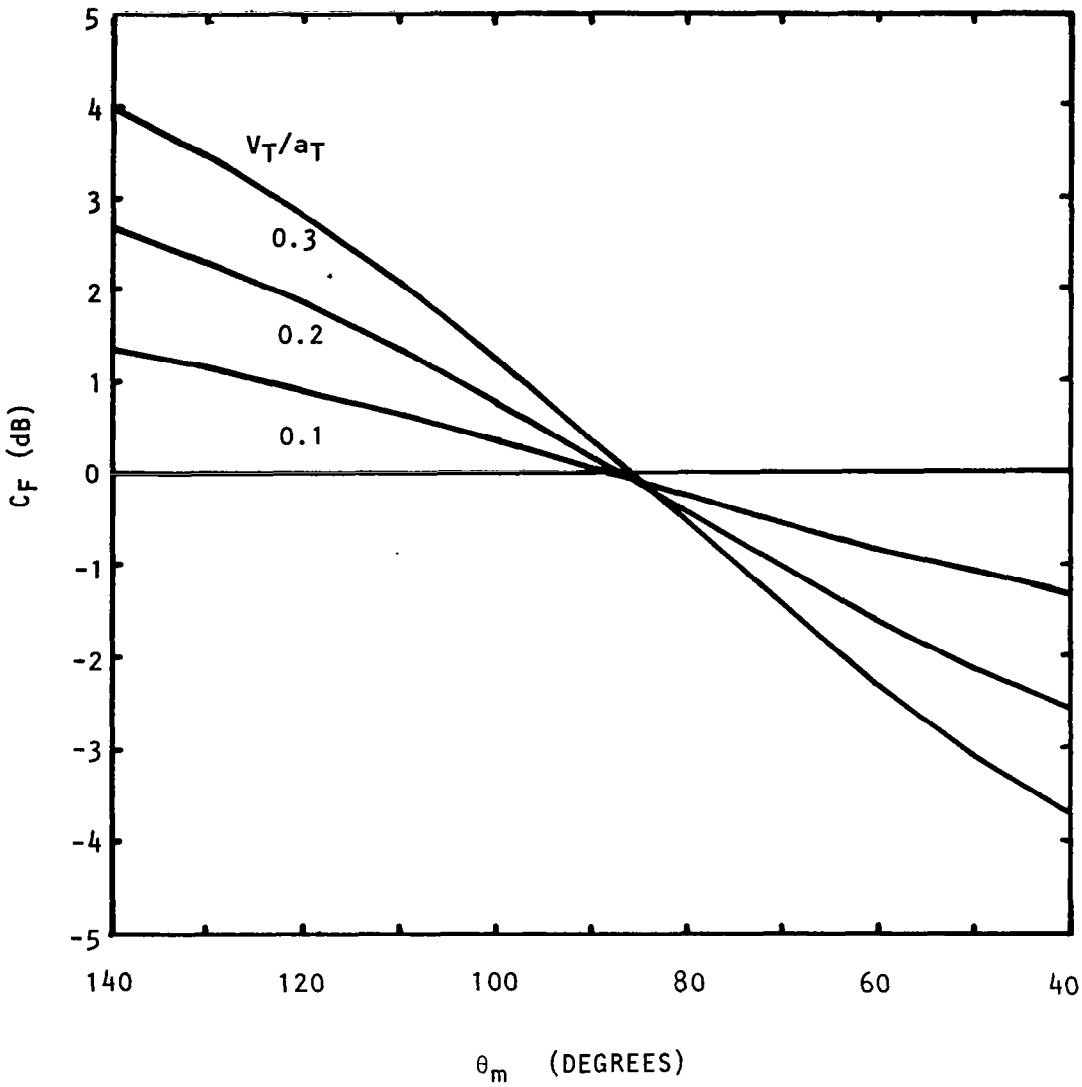

Figure 2.5 Amplitude calibration factor variation with microphone angle and free-jet Mach number; $R_m/r_T = 4$, $a_T/a_o = 1$.

3. FACILITY AND EXPERIMENTAL SETUP

All experiments for this program were conducted in the anechoic free-jet facility located in the Lockheed-Georgia Research Laboratory. The same facility was used in our previous work (ref. 3.1) for studying the effects of forward velocity on jet mixing noise. However, prior to the commencement of experiments for the present program, the facility was modified in two areas. First, the fiberglass wedges in the anechoic chamber surrounding the free-jet test section were replaced by flame-retardant polyurethane foam wedges to obtain improved acoustic performance. The second modification involved the replacement of existing rectangular free-jet nozzle section by a new interchangeable circular free-jet nozzle.

A description of the modified facility and associated performance characteristics is given in Section 3.1 below. Following this, the experimental configurations and relevant calibrations for the point source experiments are described in Section 3.2. In order to examine the effects of forward velocity on internal noise, a noise generator consisting of small intersecting jets was specially designed and tested. The noise source and its acoustic characteristics are described fully in Section 3.3. Finally, the test procedure adopted to set up a typical test condition is given in Section 3.4.

3.1 ANECHOIC FREE-JET FACILITY

3.1.1 Facility Description

The facility is powered by a jet ejector and is capable of providing continuous free-jet velocities up to 95 m/s with a circular test section of diameter 0.71 m. A planview schematic of the complete facility is shown in Figure 3.1. Starting from the left, air is drawn into the intake, through the honeycomb and screens to the contraction, across the anechoic room (test section) to the collector, through the diffuser, the two right-angle corners with turning vanes, and through the duct silencers to the transition section. The exhaust and entrainment flows of the jet ejector (diameter = 8.6 cm) are diffused through the 17.1 m long muffler/diffuser section shown on the right of Figure 3.1.

The basic anechoic room surrounding the free-jet test section is 4.3 m long, 4.3 m wide, and 6.1 m high between wedge tips. The interior is lined with polyurethane foam wedges. The chamber is completely isolated from the rest of the acoustics laboratory since it is mounted on massive springs. A spring-tensioned cable floor, suspended from the walls, provides easy access to the interior of the chamber for instrumentation and hardware changes and for calibration purposes.

Because of the high noise levels generated by the jet ejector, being operated at pressure ratios up to 8 to induce flows through the working section of up to 95 m/s, a significant amount of acoustic treatment has been

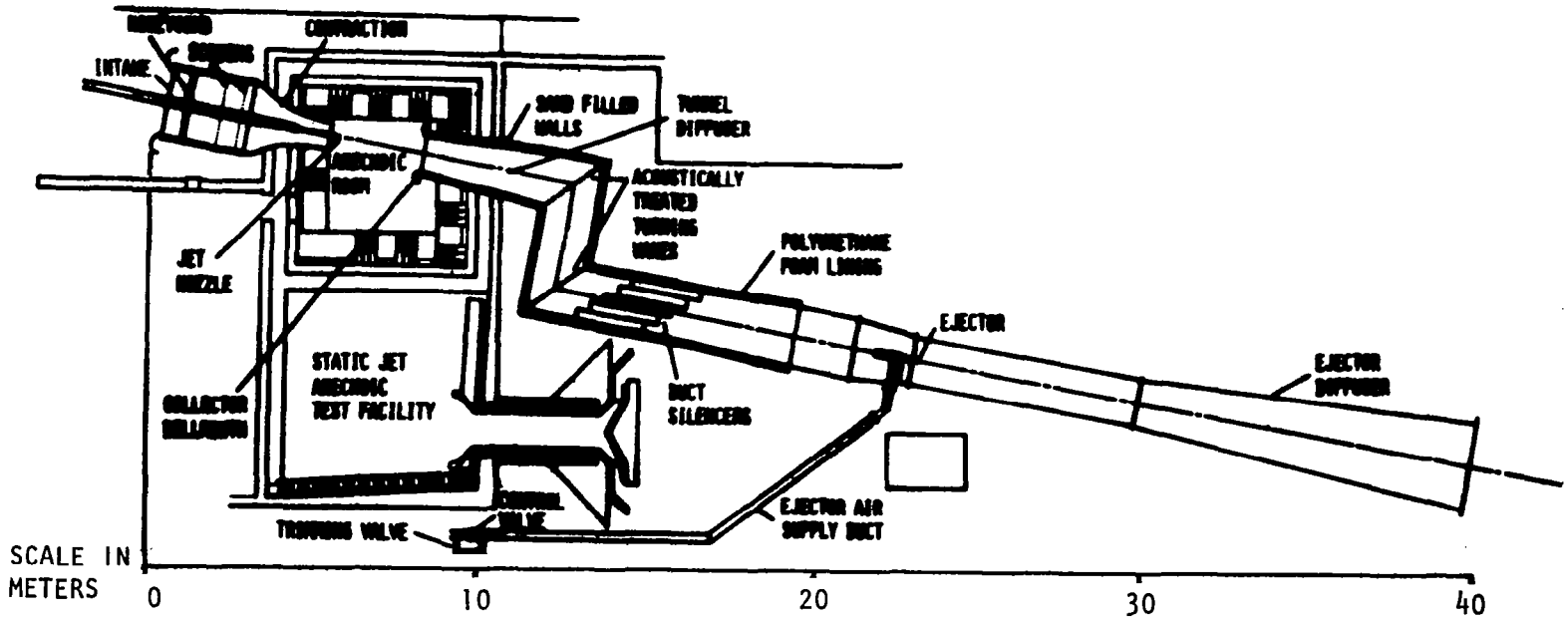

Figure 3.1 Planview schematic of anechoic free-jet facility.

incorporated in the tunnel ducting between the anechoic room and the jet ejector. A detailed description of this treatment is given in reference 3.1.

The free-jet nozzle is 0.71 m in diameter. In order to have an option of utilizing the existing rectangular free-jet nozzle, the round free-jet nozzle has been designed to fit inside the rectangular nozzle section, as shown in Figure 3.2. The inlet diameter of the round nozzle is 1.9 m, and the inner contour has been designed to provide a flat velocity profile at the exit plane. The total length of the nozzle contraction section is 2.44 m. A transition fairing was built - with one end to fit the inlet of the contraction section as shown in Figure 3.3 and the other end to fit the existing rectangular intake (which measures 2.03 m by 2.84 m). Under normal operation, suitable honeycomb flow-straighteners and screens (not shown in Figure 3.3) are fitted in the area between the existing rectangular intake and the transition fairing. This is shown in Figure 3.4, where the model-jet air supply lines are also shown.

The air supply to the jet ejector originates from the main 2.07×10^6 N/m^2 compressor which supplies dry air to all research center facilities. In addition, storage tanks retain approximately 5500 Kgm of air at 2.07×10^6 N/m^2 for higher demands. The ejector air supply ducting and the ejector diffuser section are shown in Figure 3.5.

Model-Jet Air Supply. - For minimum blockage (and therefore minimum flow disturbance) in the working section, the air-supply ducting for the primary jet is installed in the intake/contraction section rather than through a swept pylon mounted on the anechoic room wall. The ducting is designed to avoid any flow separation within the accelerating free-jet flow in the contraction section, a totally welded construction being adopted for this purpose. The ducting is aligned by using a low power laser, placed at the end of the collector/diffuser and aimed along the free-jet centerline, ensuring that the model jet would exhaust axially in the free stream.

For heated jet noise tests, the air is first heated to approximately 1000K by a Marquardt Sudden Expansion (SUE) Propane Burner located outside the laboratory building. The air is then passed through a muffler section followed by an electric after-heater section. The muffler section has been previously shown (ref. 3.1) to be highly effective in minimizing upstream internal noise levels. Downstream of the electric after-heater section, the air passes through approximately 30 meters of 10.2 cm diameter Inconel pipe before finally reaching the model-jet nozzle. To compensate for the heat losses from this long length of pipe, a portion of the pipe (approximately 10 m long and located upstream of free-jet intake) is wrapped with commercially available half-circle electric heating units. In order to provide further heat insulation, all bare pipework and outer surfaces of electric heating units are covered with 7.6 cm thick kaowool blanket. Over the final section of the pipe, just upstream of the model-jet nozzle, the insulation is smoothly tapered to provide a clean free-jet flow.

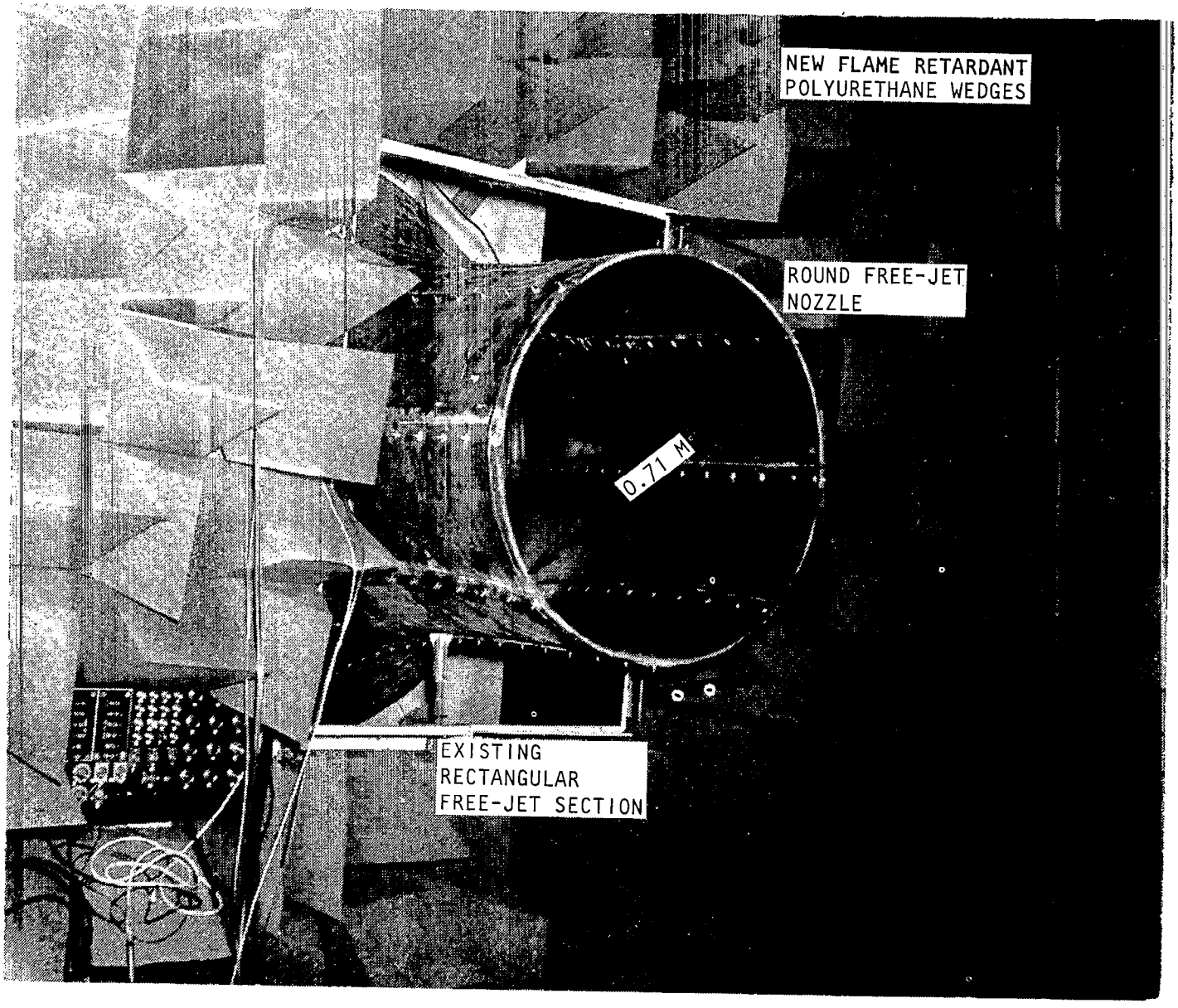

Figure 3.2 Round free-jet nozzle used in the present study.

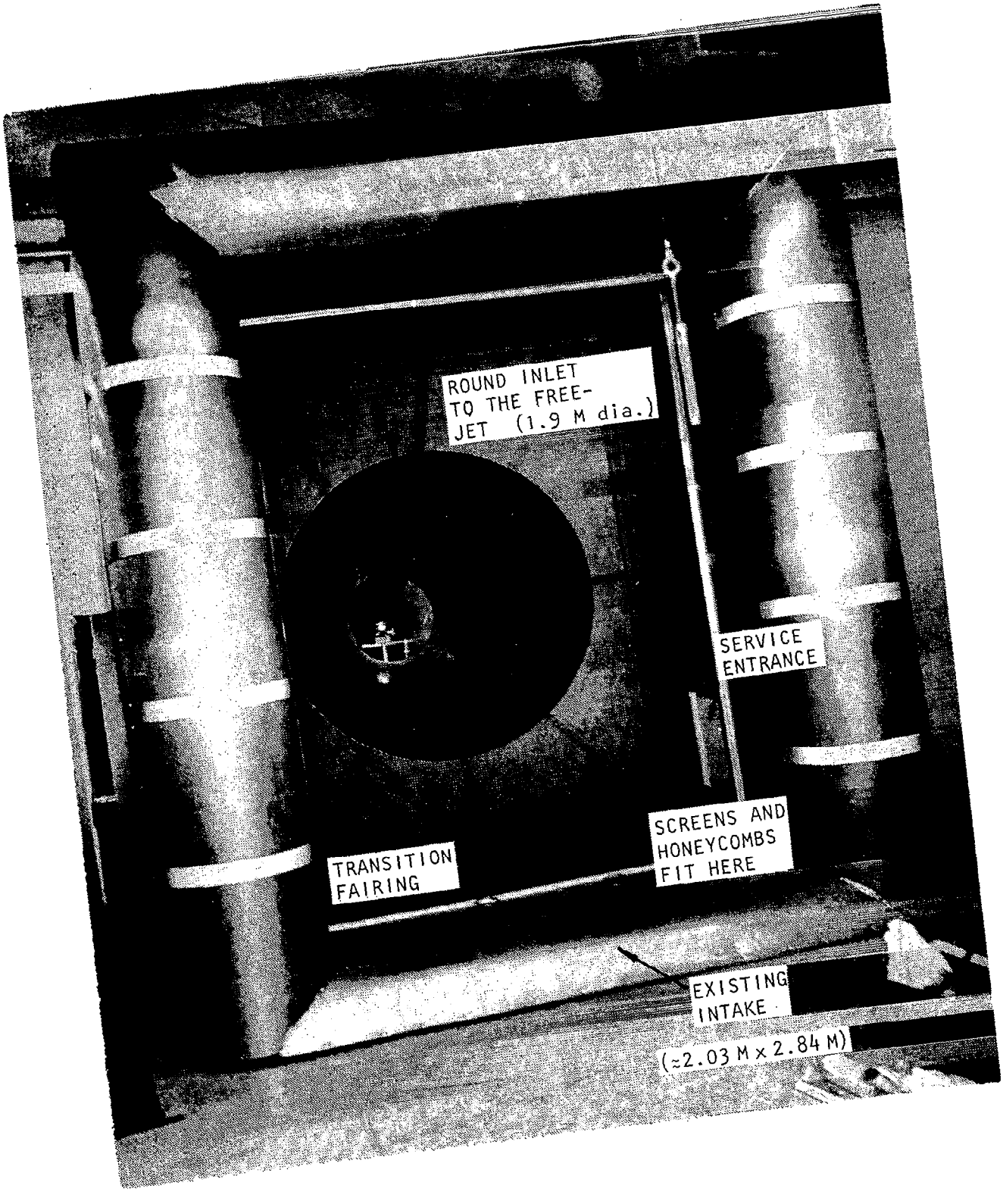

Figure 3.3 Free-jet intake.

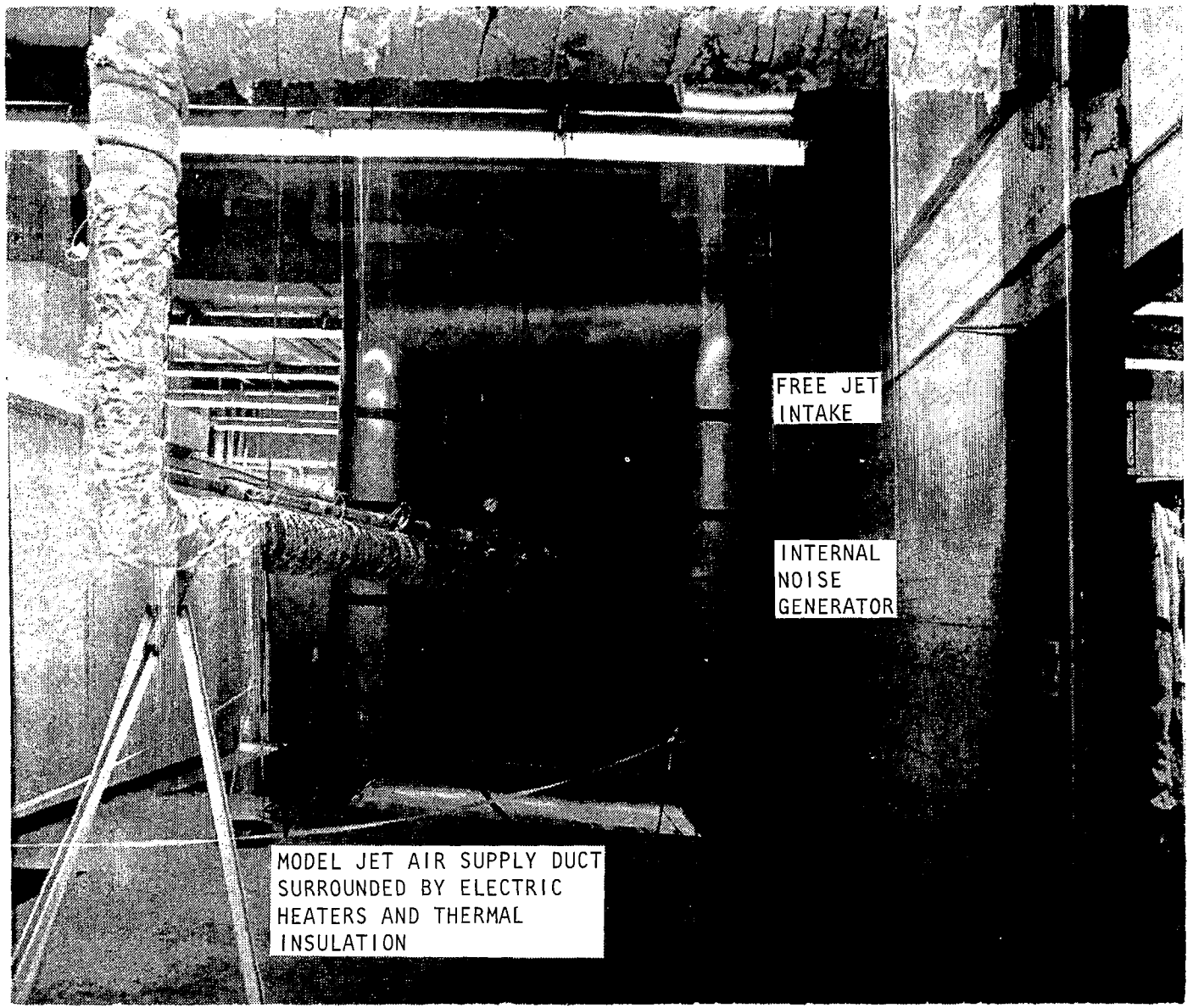

Figure 3.4 Free-jet intake showing model-jet air supply pipework.

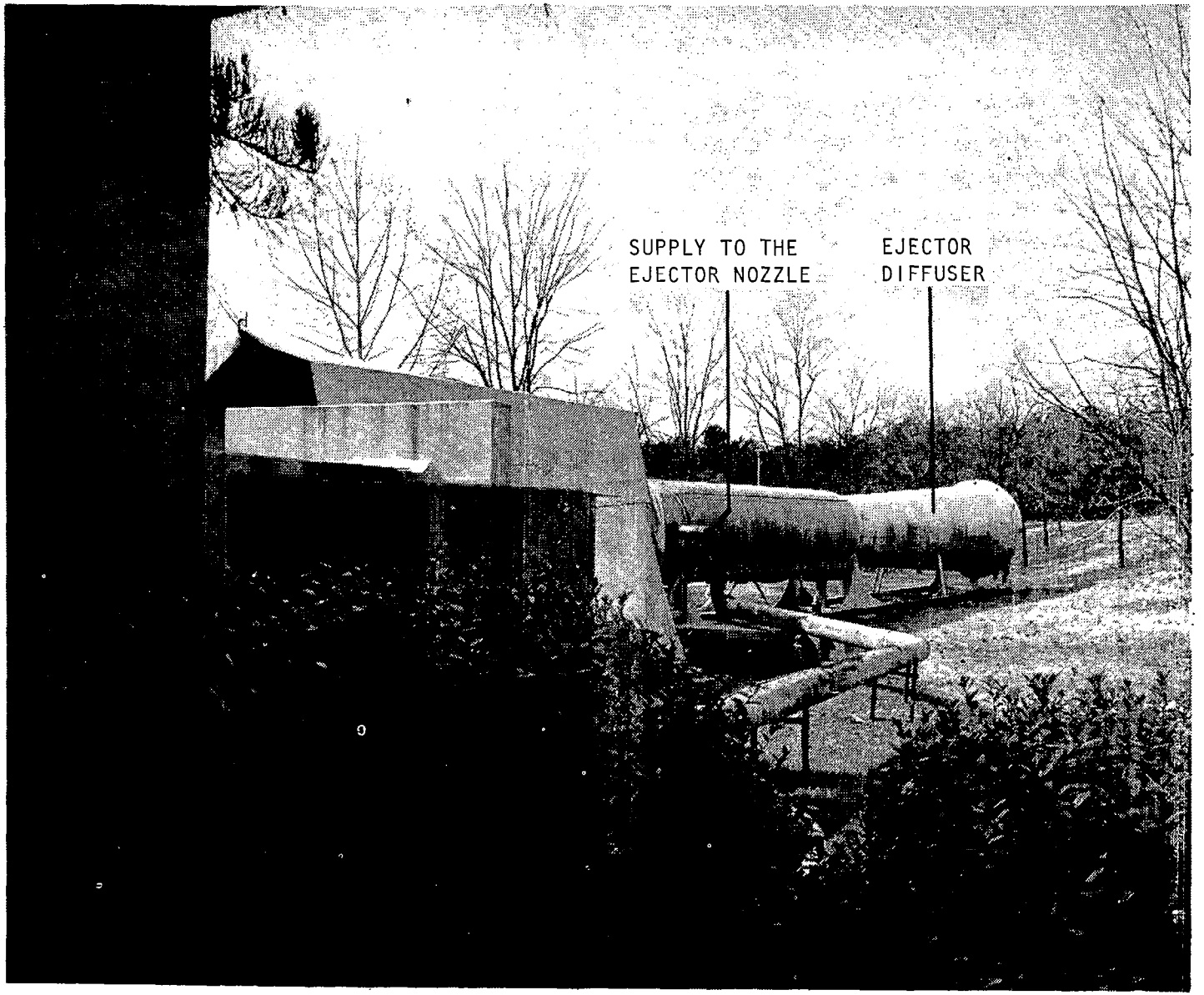

Figure 3.5 Anechoic free-jet facility ejector diffuser and air-supply ducting.

Model-Jet Nozzle. - All jet noise data for the present program were obtained using a specially-designed convergent nozzle of exit diameter 2.54 cm. This nozzle was machined from Inconel 600 bar stock, the external shape being a straight taper from 11.43 cm OD to 2.64 cm OD over a length of 35.56 cm to mate smoothly with the faired 10.16 cm ID air supply pipe, once again to preclude the possibility of flow separation. The nozzle was attached to the pipe with eight countersunk screws around the circumference. A cross-sectional drawing of the nozzle together with a photograph, is shown in Figure 3.6.

3.1.2 Facility Performance

Aerodynamic Performance Evaluation Tests. - Initial tests were performed by using a smoke generator and placing it at various locations within the free-jet intake as well as inside the anechoic chamber. These flow visualization tests established that the free jet was stable throughout its length, and the air-flow circulation velocities in the anechoic room were negligible.

In order to determine the aerodynamic characteristics of the free-jet test section (and hence to obtain basic tunnel calibration), it was necessary to measure the mean velocity profiles at various axial locations downstream of the free-jet nozzle exit plane. The required flow surveys were made by using a specially-built pressure probe rake. This rake could be positioned at any axial station between the free-jet exit plane and the collector bellmouth. The rake itself was made from 1.22 m length of 7 cm × 0.12 cm streamlined steel tube. It was supported by brackets at its extremities and holes were drilled at 2.54 cm intervals along its entire length to accommodate 3.18 mm probes. Sixteen total pressure probes and four static pressure probes were utilized during the test surveys.

Flow surveys were made at the exit plane ($x/d_T = 0$) of the free-jet nozzle and then at $x/d_T = 1$, 2, and 3. The surveys at each axial location were made in four planes passing through the centerline of the free jet and oriented at angles of 0°, 45°, 90° and 135° with respect to the horizontal plane. In addition, piezometer pressures in the settling chamber of the free-jet intake and the room pressures were recorded. The static pressure tappings for the piezometer reading were located at four equally spaced stations around the circumference of the intake contraction.

The flow measurements were made using a portable multi-tube manometer especially built for this purpose. The rake probes were connected in such a way as to display the jet flow profile on the manometer and a photograph was taken for each measurement.

The velocity profile for each measurement was subsequently calculated. In addition, the mean free-jet exit velocity in the potential core was computed by excluding the boundary layer areas of the contraction section.

HP-65 computer programs were written for on-the-spot evaluation of the tunnel conditions from piezometer, temperature and barometric data, and conversely, for obtaining the piezometer differential (with respect to the

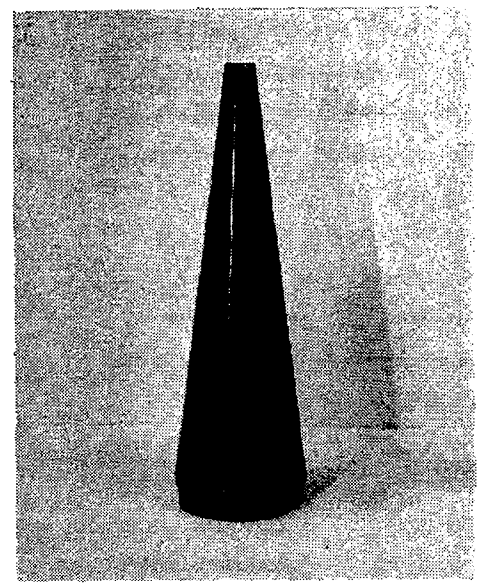

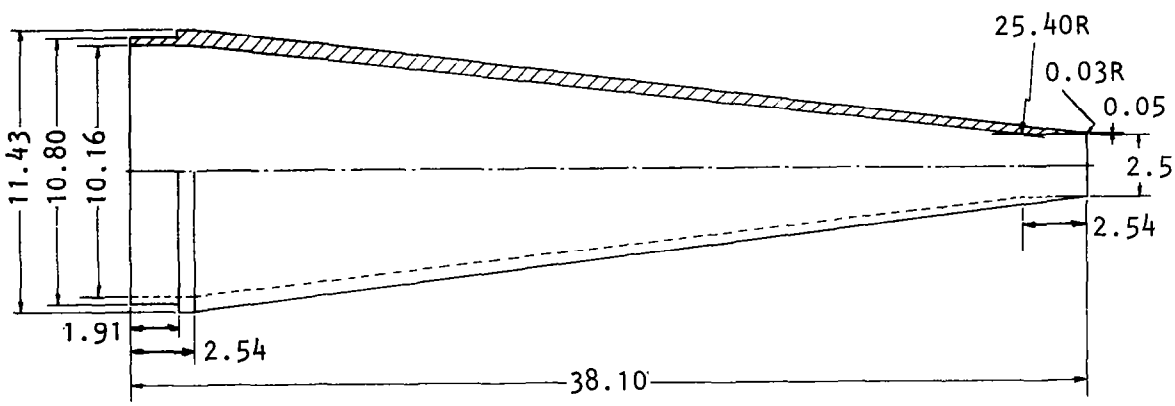

Figure 3.6 2.54 cm diameter model-jet convergent nozzle. (Dimensions in CM)

chamber pressure) for a required tunnel velocity to facilitate test condition setup.

Results of the mean velocity profile survey indicated that the free-jet test section was axisymmetric along its entire length (up to the collector). The overall shapes of the mean velocity profiles of the free jet were similar to those cited in literature for round model jets. Typical mean velocity profiles at various axial locations downstream of the round free-jet nozzle are shown in Figure 3.7.

Acoustic Performance Evaluation Tests. - In our previous work (ref. 3.1) it was found that while the anechoic quality of the facility with fiberglass wedges was acceptable for broadband noise experiments (for example turbulent mixing noise), it presented some reflection problems for discrete-frequency tests. Since the present investigation requires a number of discrete-frequency experiments, it was considered that meaningful results could be obtained only if existing fiberglass wedges are replaced by new wedges which can provide a better anechoic environment for such tests. In view of this, the existing fiberglass wedges were replaced by new polyurethane foam wedges. The material and geometry of these wedges is identical to those used for the wedges in the adjoining large static anechoic facility at Lockheed-Georgia (ref. 3.2). The performance of these wedges has already been proved to be highly superior. In addition, since the new wedges are only 45.72 cm long compared with 91.44 cm length of the old fiberglass wedges, the size of the measurement arena in the anechoic room has increased significantly.

A series of tests were conducted to determine the anechoic quality of the facility with the new wedges and with the new contraction section in place. An audio driver unit placed at two convenient locations near the free-jet exit was used as the point sound source and the "Intensity vs. Distance" plots were obtained with a traversing microphone arrangement. The microphone was traversed along four different directions:

(i) 30° to the downstream jet axis; traverse made in the horizontal plane with the driver placed on the center line of the free jet at a distance of 1 meter from the free-jet exit plane.

(ii) 90° to the downstream jet axis; traverse made in the horizontal plane with the driver placed on the center line of the free jet at a distance of 1 meter from the free-jet exit plane.

(iii) Traverse made in vertical plane with the driver placed at a distance of 1 meter from the free-jet exit plane and 1 meter below its center line; microphone traversed towards the floor of the chamber.

(iv) As (iii) above, but with the microphone traversed towards the ceiling and passing through a diametral plane of the free-jet nozzle.

Measurements of the SPL fall-off as a function of distance were made both for pure-tone noise source and for one-third octave filtered white noise source. Results for each traverse were quite similar for both modes of excitation. Typical results with 1/3-octave excitation are shown in Figure

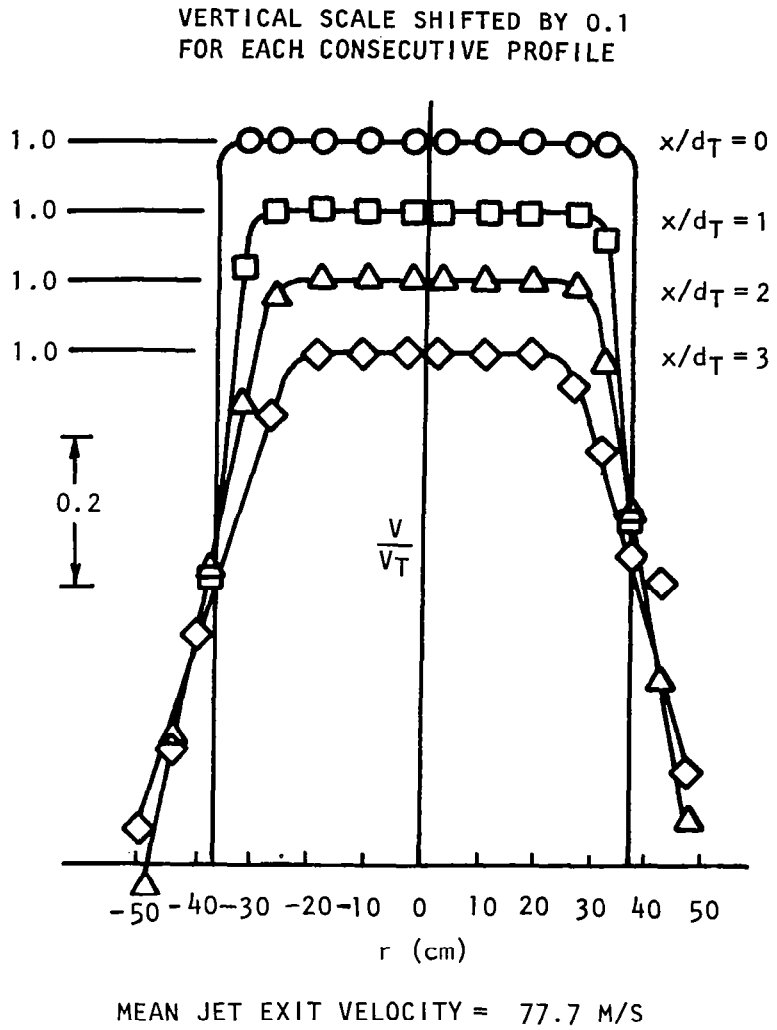

Figure 3.7 Typical mean velocity profiles in the free-jet test section.

3.8. Clearly, the 6 dB fall-off in SPL for each doubling in distance indicates that the anechoic quality of the facility is acceptable down to a frequency of approximately 160 Hz.

It should be noted that for these tests, only the outer surface of the free-jet nozzle was covered with sound-absorbing polyurethane foam. In many cases, the microphone actually traversed in a diametral plane of the nozzle (at a distance of 1 meter from the exit plane), and still provided results which followed an inverse-square law dependence. This shows that the proximity of the nozzle (with a bare interior surface) does not appear to affect the anechoic quality of the chamber for the frequencies of interest.

3.2 EXPERIMENTAL SETUPS AND RELEVANT CALIBRATIONS FOR POINT SOURCE TESTS

3.2.1 Point Source

An experimental point sound source was used to obtain experimental verification of the theoretical free-jet data calibration formulae outlined in Section 2. For these verification tests, the model jet and the associated air supply pipework were not present in the facility. The point source consisted of a commercially available 60-watt acoustic driver unit coupled to a straight tube via an inverse conical horn section. The other end of the tube contained a smooth right-angle bend which terminated into a 0.635 cm diameter opening. The point source is shown schematically in Figure 3.9. The stem of the source was suitably faired to minimize flow separations and associated noise therefrom.

Point Source Directivity Calibration. - A separate calibration test was conducted to determine the directivity of the point source radiation in the absence of any surrounding flow. This test was conducted in the Lockheed anechoic chamber, and the experimental setup is shown in Figure 3.10. Using white noise excitation signal for the driver, 1/3-octave SPL spectra were measured at 15° intervals on a circular arc of radius 0.305 m. The directivity was measured in two orthogonal planes (shown in Figure 3.11) as follows:

Plane #1: perpendicular to the axis of point source stem,
Plane #2: passing through the axis of point source stem.

Typical directivity plots at various frequencies for measurements in plane #1 and plane #2 are shown in Figures 3.12 and 3.13, respectively. The point source is fairly omni-directional over the frequency range considered in these tests.

It is recognized that the directivity of this point source will change when the free-jet flow is turned on. However, this is of no real consequence in the experiments for the present program, as will become apparent in the subsequent parts of this report.

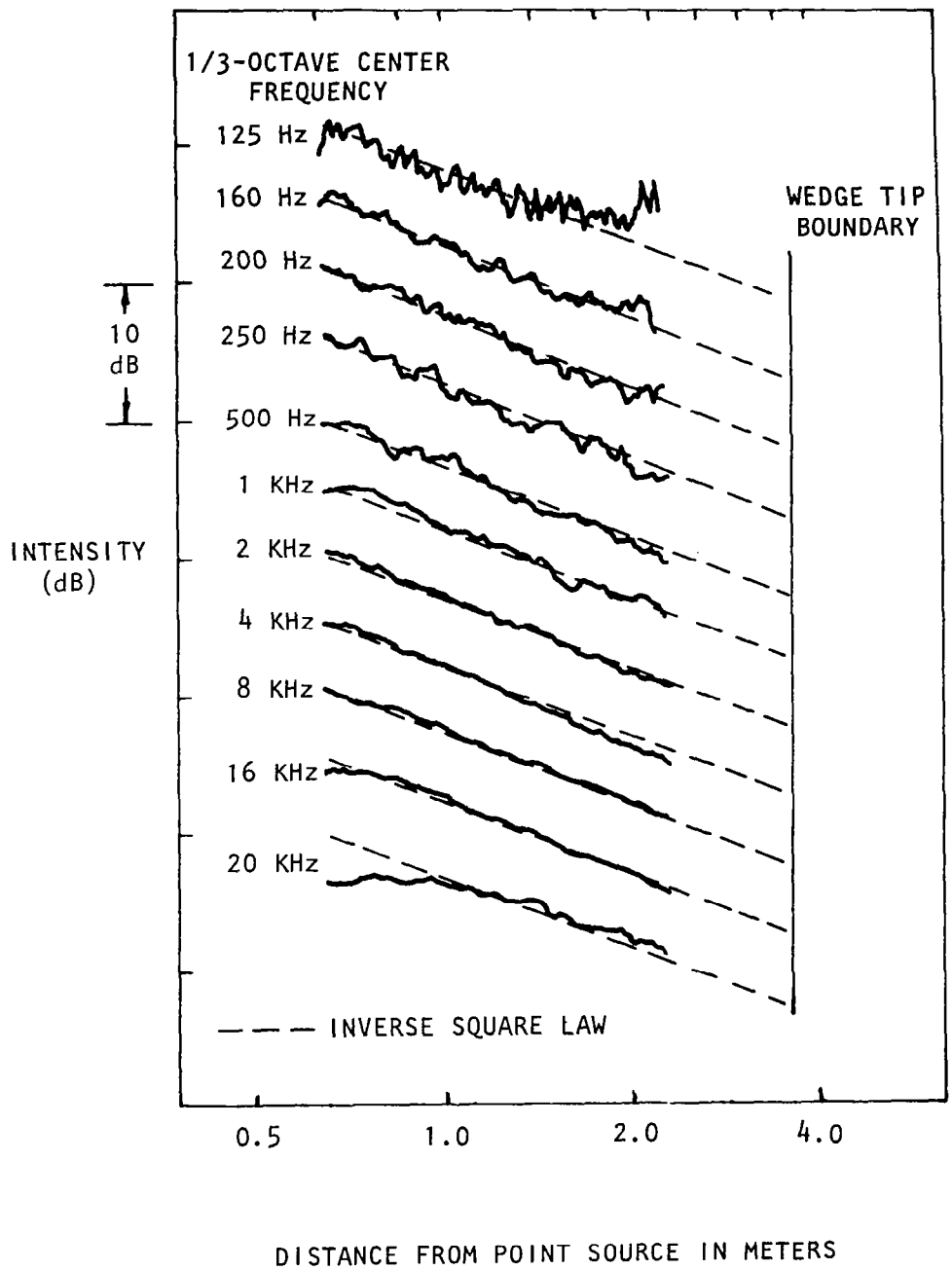

Figure 3.8 Intensity - distance plots with point sound source.

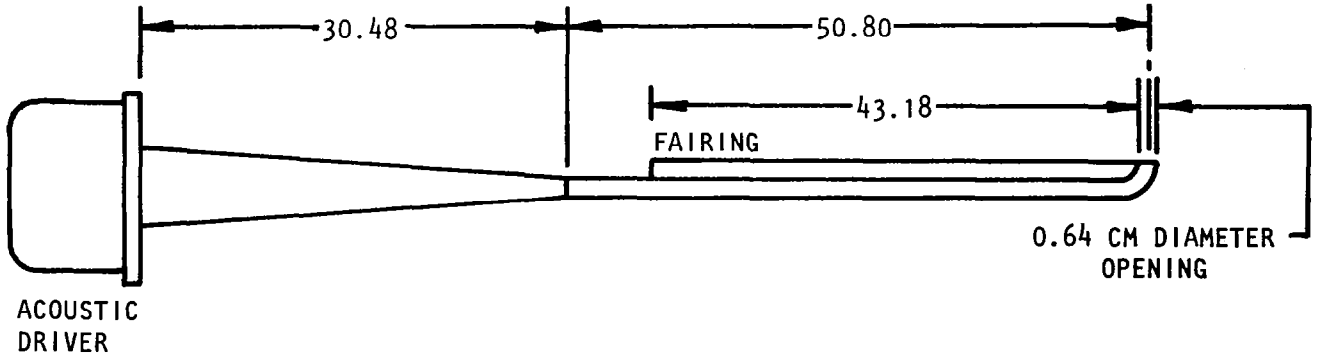

Figure 3.9 Schematic of point sound source.
(Dimensions in CM)

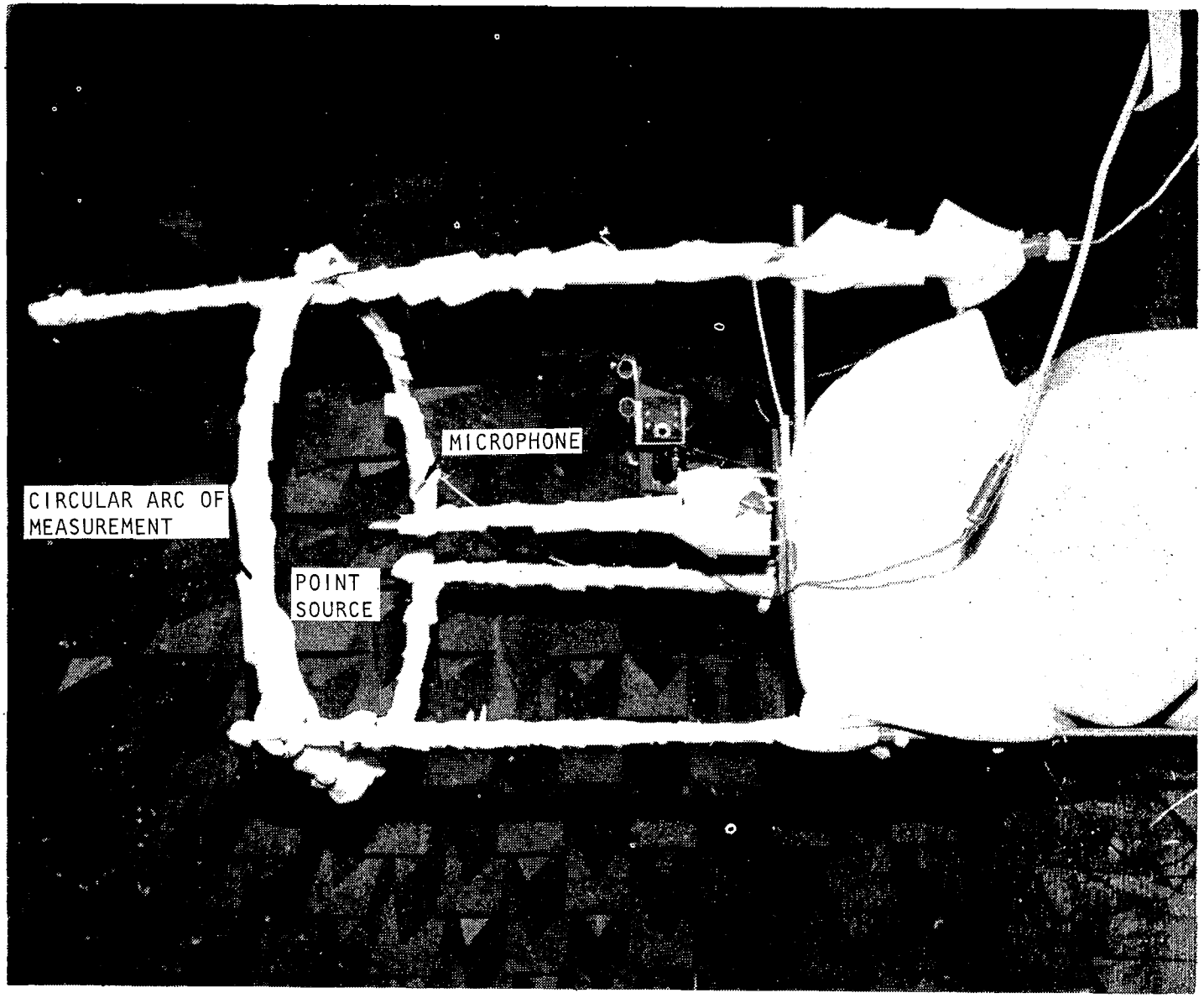

Figure 3.10 Point source directivity calibration setup.

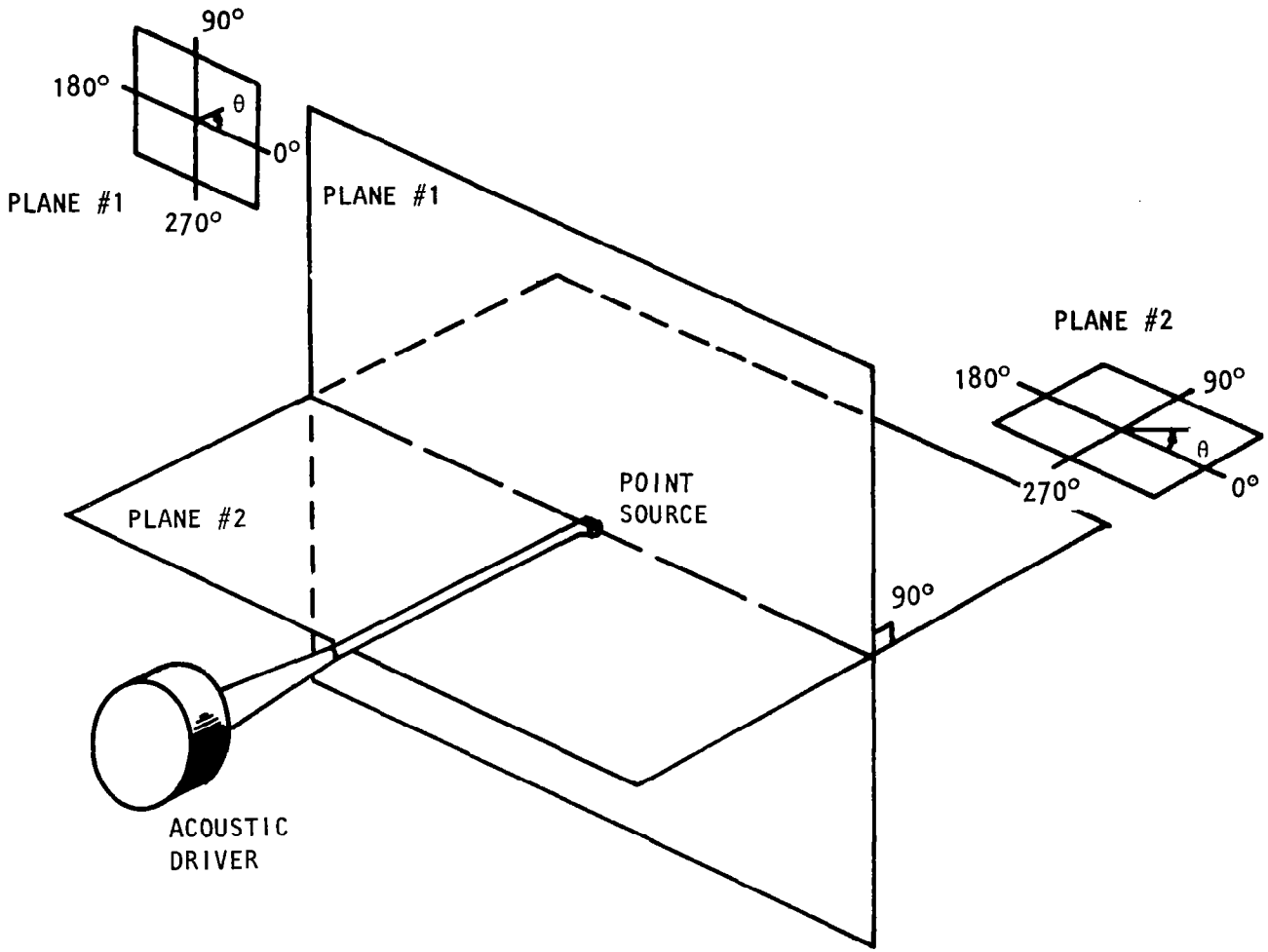

Figure 3.11 Point source directivity measurement planes.

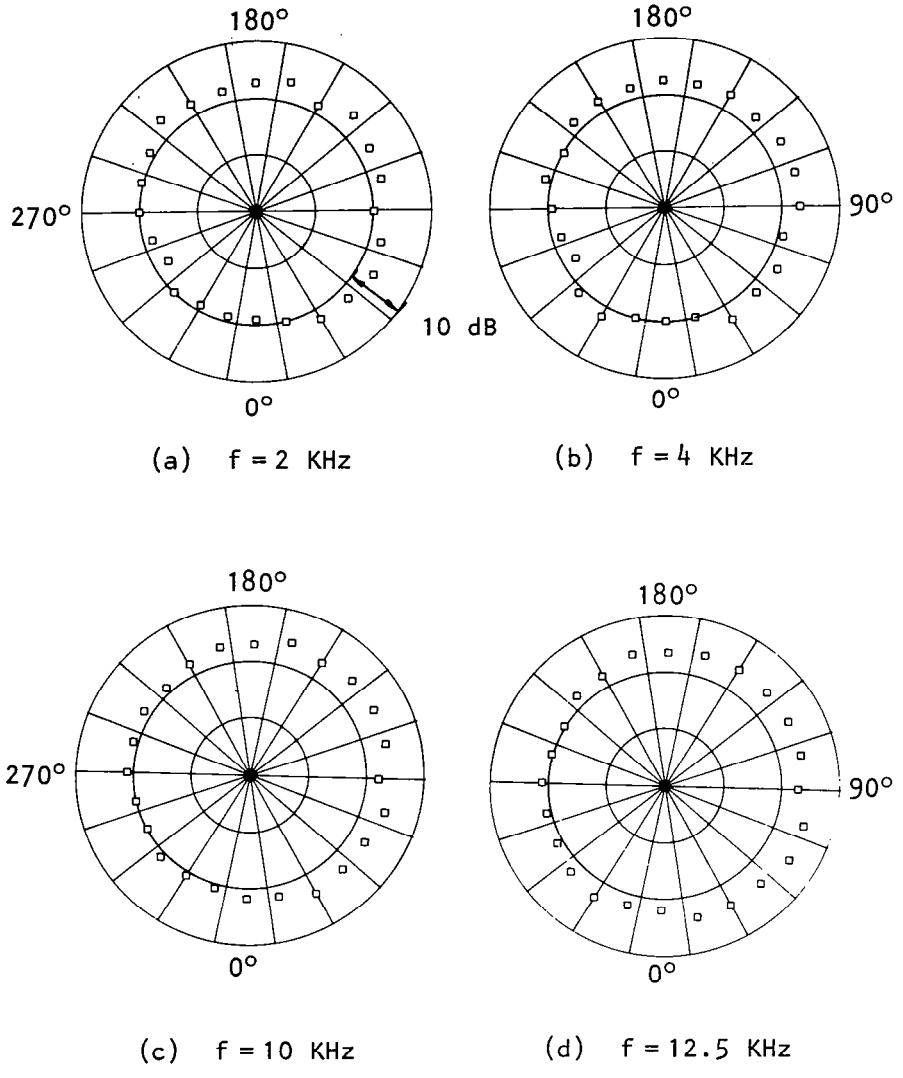

Figure 3.12 Point source directivity in the plane perpendicular to the axis of point source stem (plane #1).

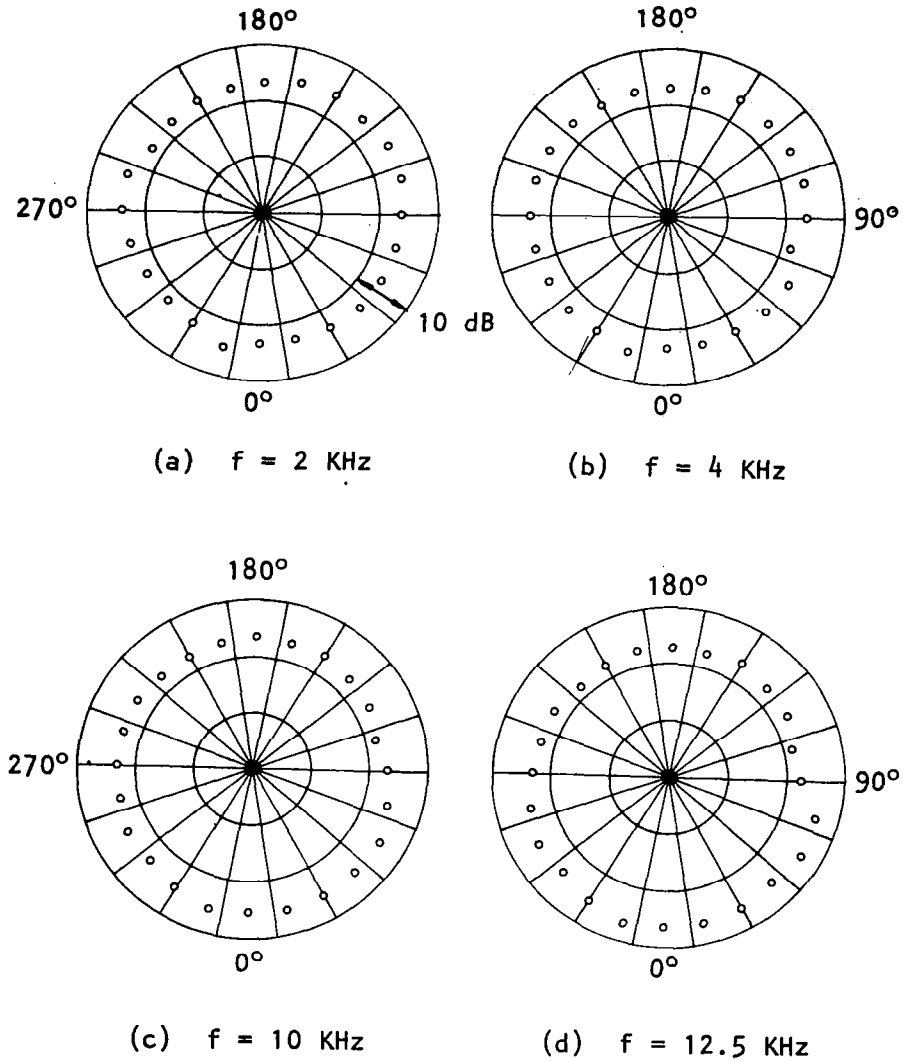

Figure 3.13 Point source directivity in the plane passing through the axis of point source stem (plane #2).

Effect of Vibration on Point Source. - Even though utmost precautions were taken to prevent significant vibrations of the point source stem when the free-jet flow was turned on for the main experimental program, some vibration could still have persisted at higher free-jet velocities. In order to determine the order of magnitude of the effect of these vibrations on the characteristics of point source radiation, a separate test was conducted where artificial vibrations were imposed on the point source stem. This was achieved by attaching the source stem to a motor-cam operated shaker through a 0.635 cm diameter rigid bar, and operating the shaker at various frequencies. Typical results showing the effects of vibrating the point source at a frequency of 10 Hz are presented in Figure 3.14. It was concluded from these tests that the changes in levels and directivity of the point source due to vibration are negligible.

Point Source Mounting. - Due to ease of mounting and better omnidirectionality in plane #2, it was decided to mount the point source such that the microphones used in the main experimental program (to be described later) would be located in plane #2. The point source was, therefore, mounted on one of the walls of the anechoic chamber such that the opening was facing away from the free-jet nozzle exit. This configuration is shown in Figure 3.15 where the point source opening and also a microphone located in the vicinity of the point source are both placed in a horizontal plane passing through the center line of the free jet.

Figure 3.15 also shows various guy wires used to stop the point source or the microphone from vibrating when the free-jet is operating. As will be described later, one microphone was required to be located at the same point as the point source opening. To accomplish this and to make sure that there was no relative movement between the point source opening and the adjacent microphone, the two were attached to each other by a turnbuckle shown in Figure 3.15. The point source and adjacent microphone shown in this figure could be moved as a single unit at various axial locations on the free-jet center line.

3.2.2 Experimental Configurations

The various free-jet shear layer effects examined in the present program can be conveniently separated in three parts for experimental purposes: (i) angle change tests, (ii) transmission and internal reflection tests, and (iii) turbulence scattering tests. Each of these three types of tests required a slightly different experimental configuration and/or data acquisition procedure. The experimental configurations are described below with the help of the geometry defined in Figure 3.16.

Angle Change Tests. - Only two microphones, A and B, were used in these tests. Microphone A was kept fixed touching the point source (as shown photographically in Figure 3.15), and microphone B outside the flow was moved to various values of measured angle θ_m in a polar arc of radius $R_m \doteq 1.53$ m. The cross-correlation function $R_{AB}(\tau)$ between signals at microphones A and B was obtained over a range of θ_m ($\theta_m = 30°$ to $140°$) for several free-jet velocities ($V_T/a_o = 0$ to 0.27) and three axial locations of the point source ($x/d_T = 0.22$, 0.99, and 1.74).

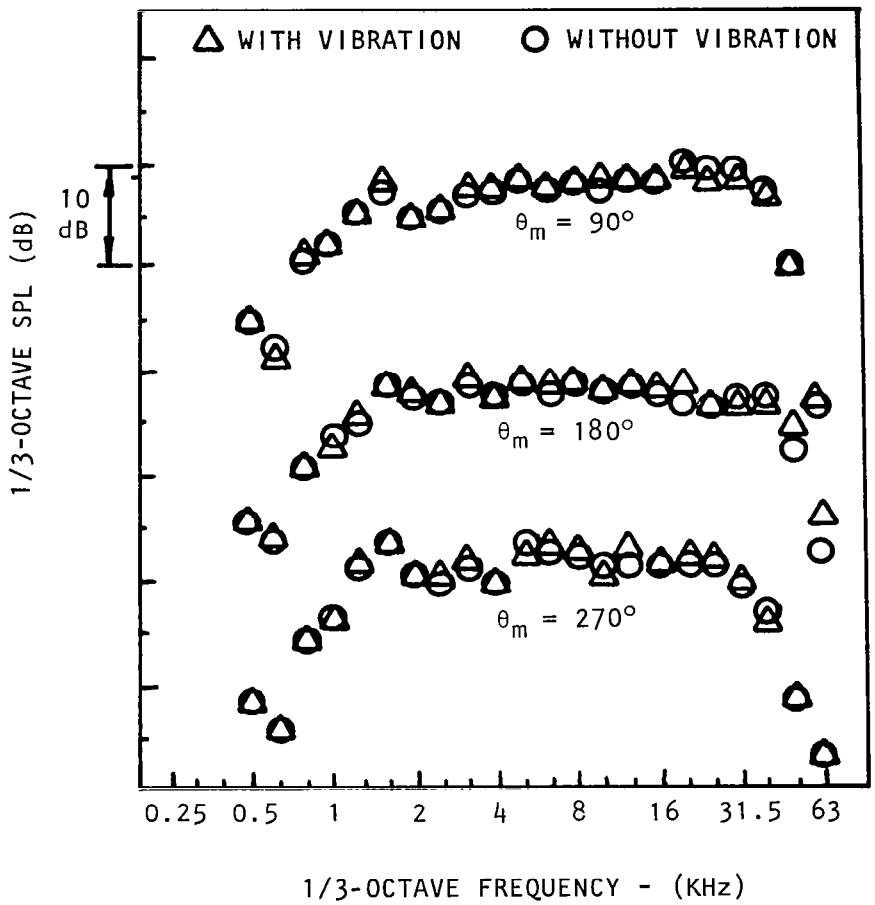

Figure 3.14 1/3-octave SPL spectra from point source with and without vibration.

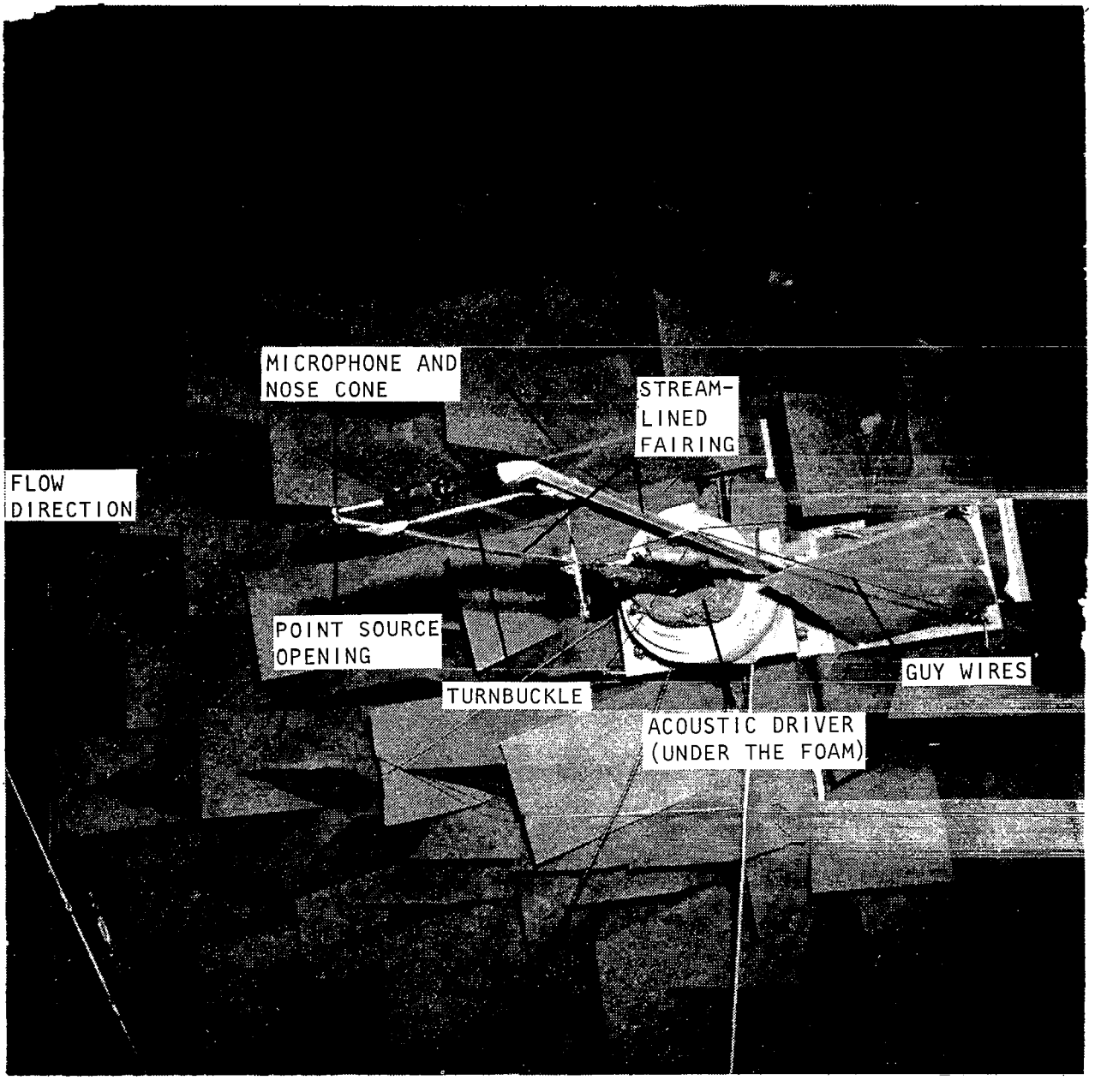

Figure 3.15 Point source and microphone.

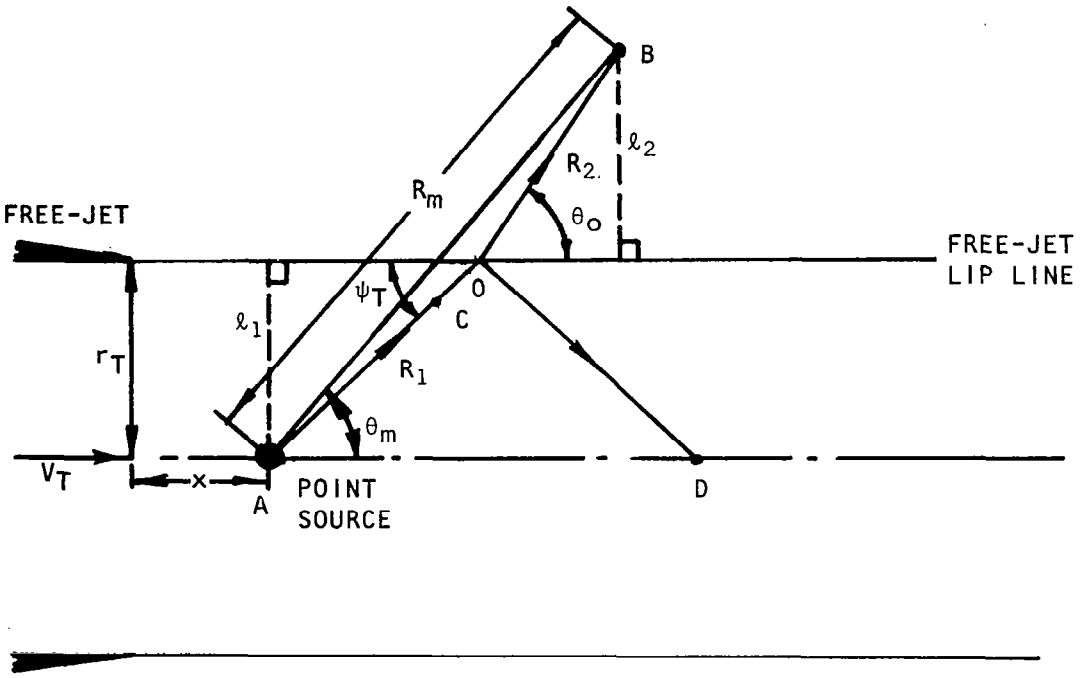

A	REFERENCE MICROPHONE	
AO	INCIDENT RAY	⟶ MICROPHONE C
OB	TRANSMITTED RAY	⟶ MICROPHONE B
OD	REFLECTED RAY	⟶ MICROPHONE D

Figure 3.16 Geometry for transmission, internal reflection and scattering experiments.

Transmission and Internal Reflection Tests. - In this configuration, data were recorded simultaneously at each of the four microphones A, B, C, and D shown in Figure 3.16. For pre-selected values of incident ray angle, ψ_T, the emerging angle θ_o for every test condition (V_T/a_o) was calculated using the vortex-sheet model discussed in Section 2. Microphones C, B and D were then positioned along the incident, transmitted and reflected rays, respectively. Figure 3.17 shows a photographic view of the setup for transmission tests where the point source and microphone A and C are positioned for $\psi_T = 40°$. Microphone B can also be seen mounted on a remotely controlled rotating boom for measurements outside the free-jet flow. Similarly, a typical setup for internal reflection experiments is shown in Figure 3.18 where microphones A and C are positioned along the incident ray with incidence angle $\psi_T = 120°$, and microphone D is located along the corresponding reflected ray in the forward arc. As shown in this figure, several 0.635 cm diameter stiffeners were used to minimize the vibration and/or movement of these microphones in the presence of the free-jet flow.

Turbulence Scattering Tests. - The experimental configuration used to investigate turbulence scattering effects was similar to that used for transmission (amplitude calibration) and internal reflection experiments with the exception that discrete tones were used instead of broadband noise as the source excitation.

For the majority of tests, the point source described in Section 3.2.1 was used. For some additional but limited tests, however, a specially designed 2.54 cm diameter point source was used to increase the signal-to-noise (S/N) ratio. Tests with this noise source were restricted to $\psi_T = 90°$ and $x/d_T = 0.96$ and 2.94. Both discrete tone and white noise excitations were used for this larger noise source. Unlike the smaller point source, this noise source was highly directional, with the major peak along the axis of its opening. For this reason, the opening was pointed towards microphones C and B as shown in Figure 3.19. It should be noted that these additional tests were conducted during a limited time period towards the end of the experimental program. Nevertheless, with the higher signal-to-noise ratio, the tests produced some very useful results on turbulence scattering and turbulence absorption, which are discussed fully in Section 4.

Finally, to end this discussion of point source experimental configurations, it should be noted that throughout the experimental program, 0.635 cm B&K microphones Type 4135 were used. All microphones immersed in the free-jet flow were fitted with B&K nose cones and were aligned axially into the flow.

3.2.3 Experimental Conditions

The transmission, internal reflection and scattering experiments were conducted for three axial locations of the point source, $x/d_T = 0.22$, 0.99, and 2.00. Limited tests were also conducted at $x/d_T = 0.96$ and 2.94 with the larger noise source. Measurements were made for $V_T/a_o = 0$, 0.09, 0.18, and 0.27. Some measurements were also made at two intermediate velocities given by $V_T/a_o = 0.045$ and 0.135. The minimum value of measurement angle θ_m

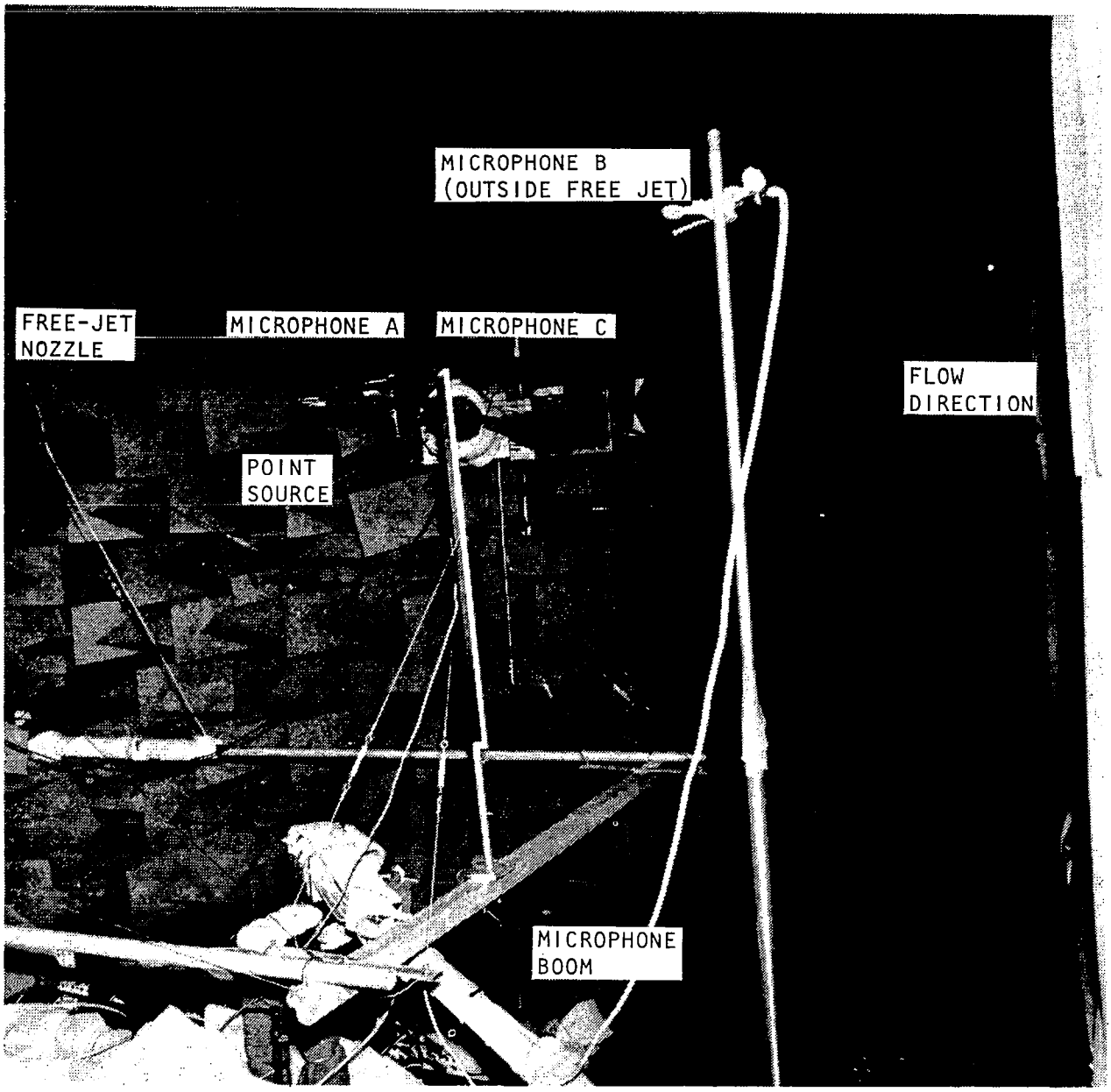

Figure 3.17 Experimental configuration for transmission tests.

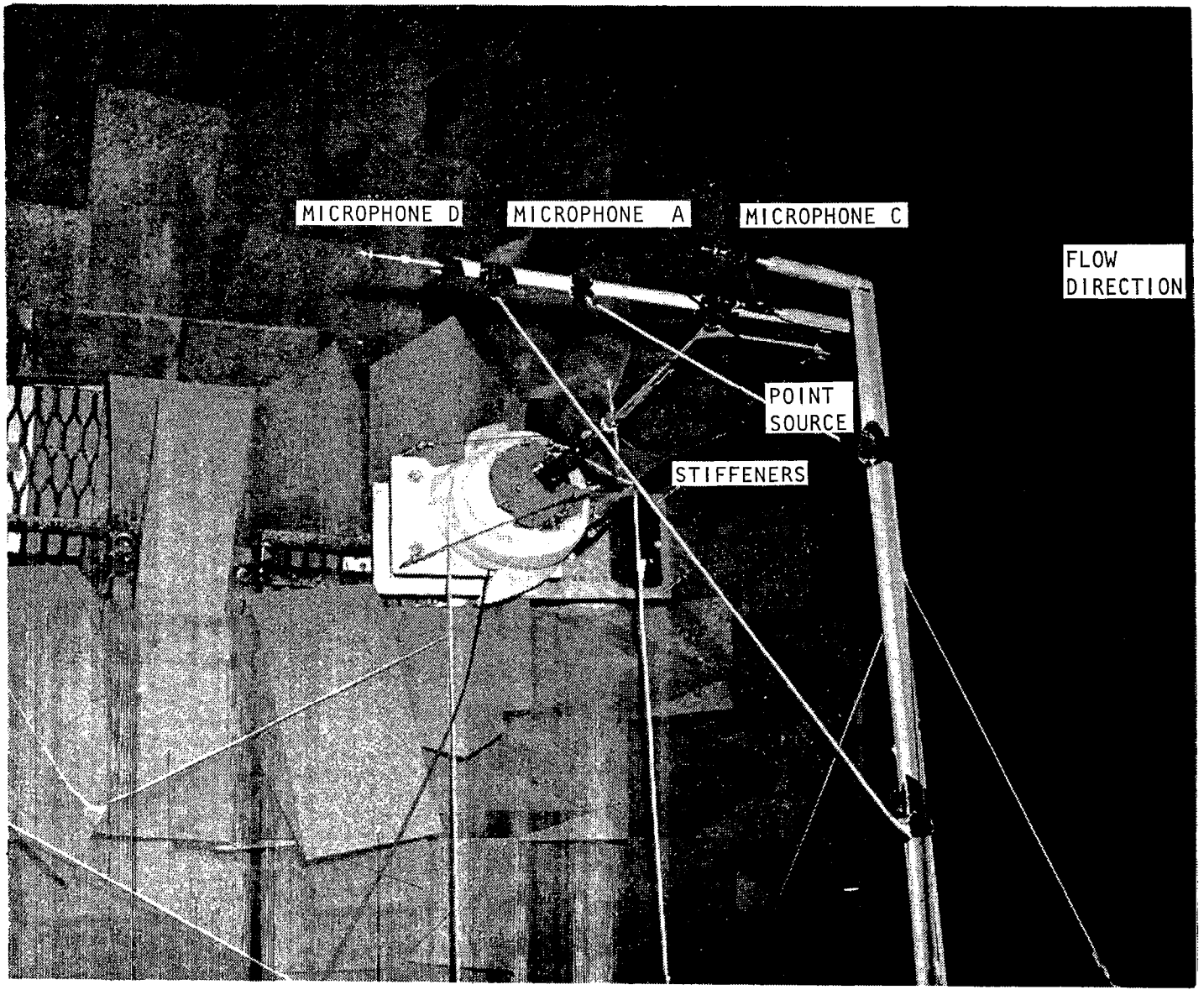

Figure 3.18 Experimental configuration for internal reflection tests.

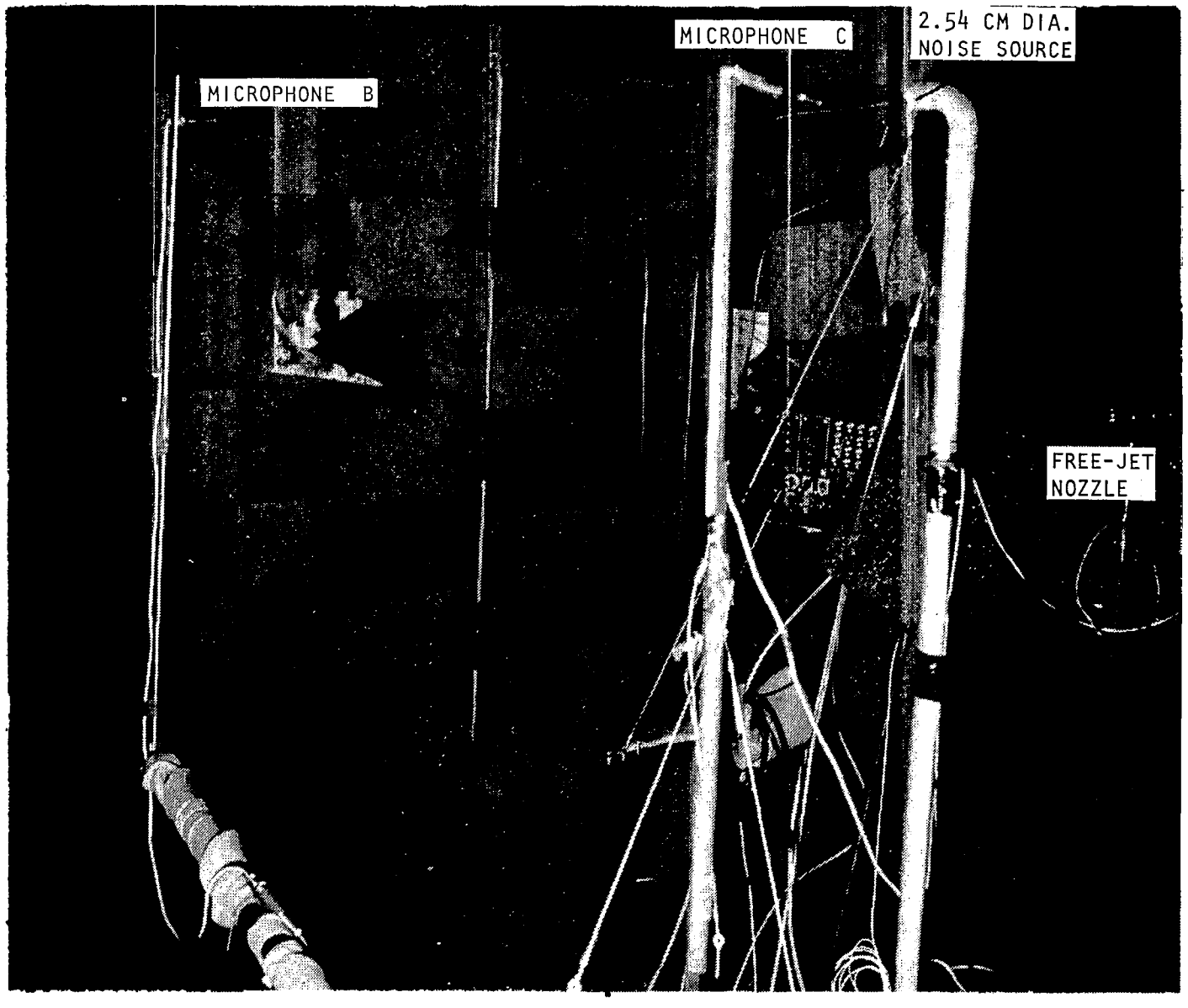

Figure 3.19 Experimental set-up with the larger directional noise source.

was 30° in most cases; the maximum values of θ_m corresponding to the three axial locations, i.e. $x/d_T = 0.22$, 0.99 and 2.00, were 100°, 120°, and 154°, respectively.

The minimum and maximum angles were determined by one or more of three constraints:

(a) line of sight between source and microphone,

(b) proximity of wedges, and

(c) wind noise on microphone signals due to proximity of, or immersion in the free-jet flow.

The majority of the tests were conducted over the frequency range from 300 Hz to at least 10 KHz. Some selected tests (in particular, the scattering tests) were also conducted at frequencies up to 40 KHz.

3.2.4 Data Acquisition and Analysis

The signal received by each microphone was passed through a Krohn-Hite high-pass filter to remove wind noise up to approximately 300 Hz. The filtered signals were recorded on a Honeywell fourteen-channel tape recorder for subsequent detailed analysis using a tape-loop machine and an SD360 Real Time Analyzer. In order to minimize the aliasing errors in the analysis of the data in the frequency domain, suitable anti-aliasing low pass filters were always used. These filters had a roll-off rate of 120 dB/octave and were built into the electronics of the SD360 Real Time Analyzer. The electronics of each channel were phase matched. The reproduce heads of the tape recorder were also adjusted to produce a flat phase response at all frequencies of interest up to 20 KHz. A schematic of the complete data acquisition and analysis system used for point source experiments is shown in Figure 3.20.

3.3 INTERNAL NOISE SOURCE

As mentioned in Section 1, one of the objectives of this program was to illustrate the effects of simulated forward flight on internal noise whose characteristics are roughly representative of core noise encountered in real full-scale engines. To this end, a noise generator which injects broadband sound upstream of the model-jet nozzle exit was required. In the present program, a significant effort was spent in developing such a noise generator. The noise generator had to satisfy at least the following four criteria: (i) the noise levels must be high enough to be detected in the presence of model-jet noise, (ii) the noise level must be controlled independently of the jet velocity (or pressure ratio), and (iii) the noise source must not introduce additional turbulence in the model jet flow.

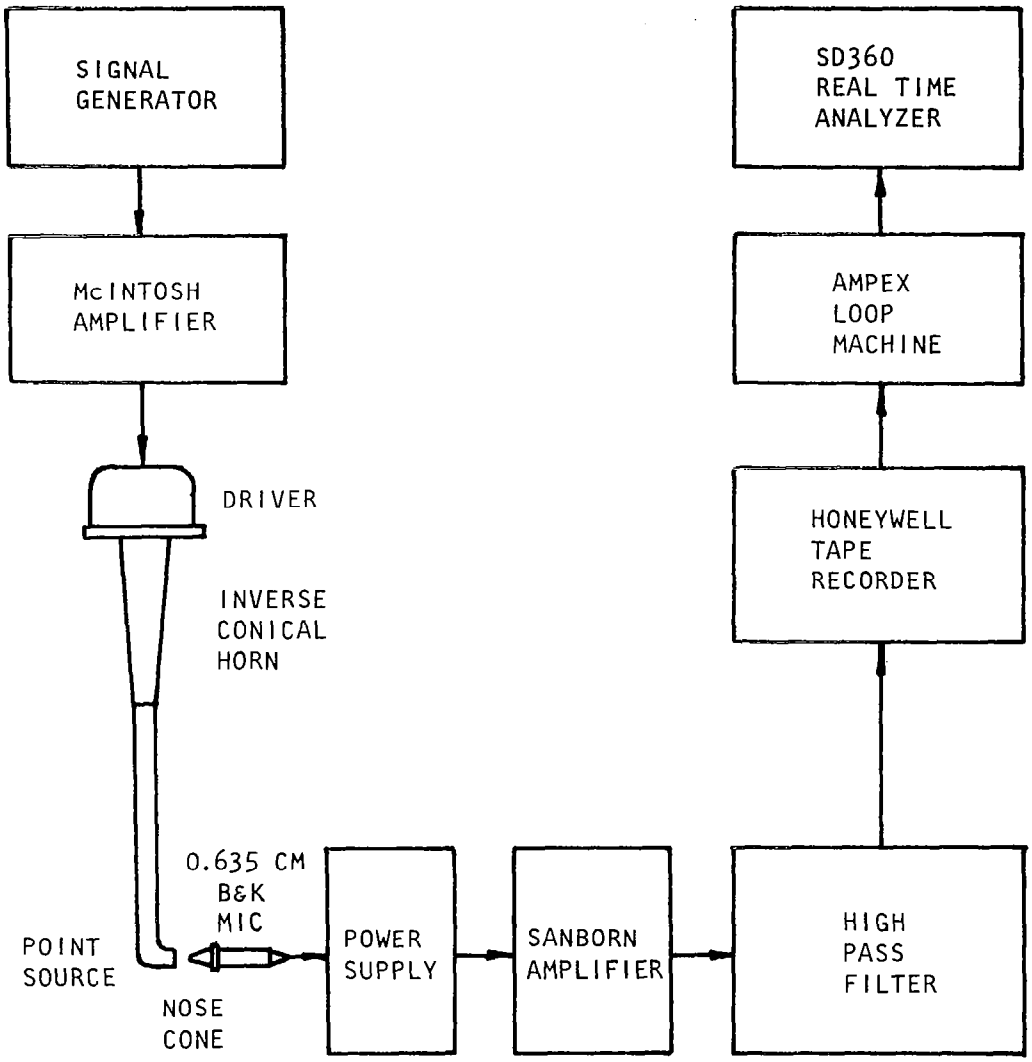

Figure 3.20 Block diagram for data acquisition and analysis system.

(iv) The noise source must withstand a high temperature environment.

Several possible candidates were considered, and a noise generator consisting of small intersecting jets was finally selected and developed for this purpose. A detailed description is given below.

A drawing of the internal noise source is shown in Figure 3.21. The noise generator was mounted on the 10.16 cm pipe upstream of the model-jet nozzle as shown schematically in Figure 3.21 and photographically in Figure 3.22. The noise generator assembly is a small enclosure fitted with four 0.635 cm diameter radial tubes. For each pair of opposing tubes, the centerlines of the two tubes are offset by 0.16 cm. The noise is generated when jets through each tube intersect. The noise levels can be further modified by inserting a 0.635 cm diameter solid rod into the intersecting jets. Each of the tubes can be moved independently in the radial direction and the rod can be moved in the axial direction within the cylindrical enclosure.

Extensive calibration tests were conducted to determine the noise characteristics of the internal noise generator. Noise levels of up to 145 dB were generated inside the pipe but due to unfavorable transmission characteristics of the 2.54 cm model-jet nozzle, the maximum OASPL measured in the anechoic chamber at $R_m/d = 96$ was 95 dB. These noise levels were obtained by operating only two opposite tubes at a reservoir pressure of 17.23×10^5 N/m^2 (250 psig). The reason for using only two tubes was to reduce the (cold) mass flow from these small jets, which was found to reduce the model-jet temperature for heated test conditions (the results for which are discussed in Section 8).

Extensive measurements in the far field were conducted to document the "internal noise" levels relative to "jet mixing noise" levels. These tests were conducted for unheated conditions in an essentially static environment (i.e. free-jet velocity $V_T \doteq 0$). The OASPL directivity results with and without internal noise over a range of model-jet velocities are shown in Figure 3.23. The internal noise dominates over the jet mixing noise at all model-jet velocities considered here. The 1/3-octave spectral comparisons corresponding to the OASPL results of Figure 3.23 are presented in Figures 3.24 and 3.25 for the measurement angles of 90° and 60°, respectively. Two points concerning the far-field noise characteristics of the internal noise generator are worth noting. First, the internal noise is more dominant at lower model-jet velocities than at higher jet velocities. Second, the spectrum of this internal noise is broadband in nature. Both of these features are consistent with the requirements of the present investigation, in which one of the objectives is to examine the effects of simulated forward flight on a noise source which is representative of the core noise component of a full-scale aircraft engine.

3.4 TEST PROCEDURE

The quantities to be measured in setting up the test conditions are defined in the sketch shown in Figure 3.26. In order to set the experiment

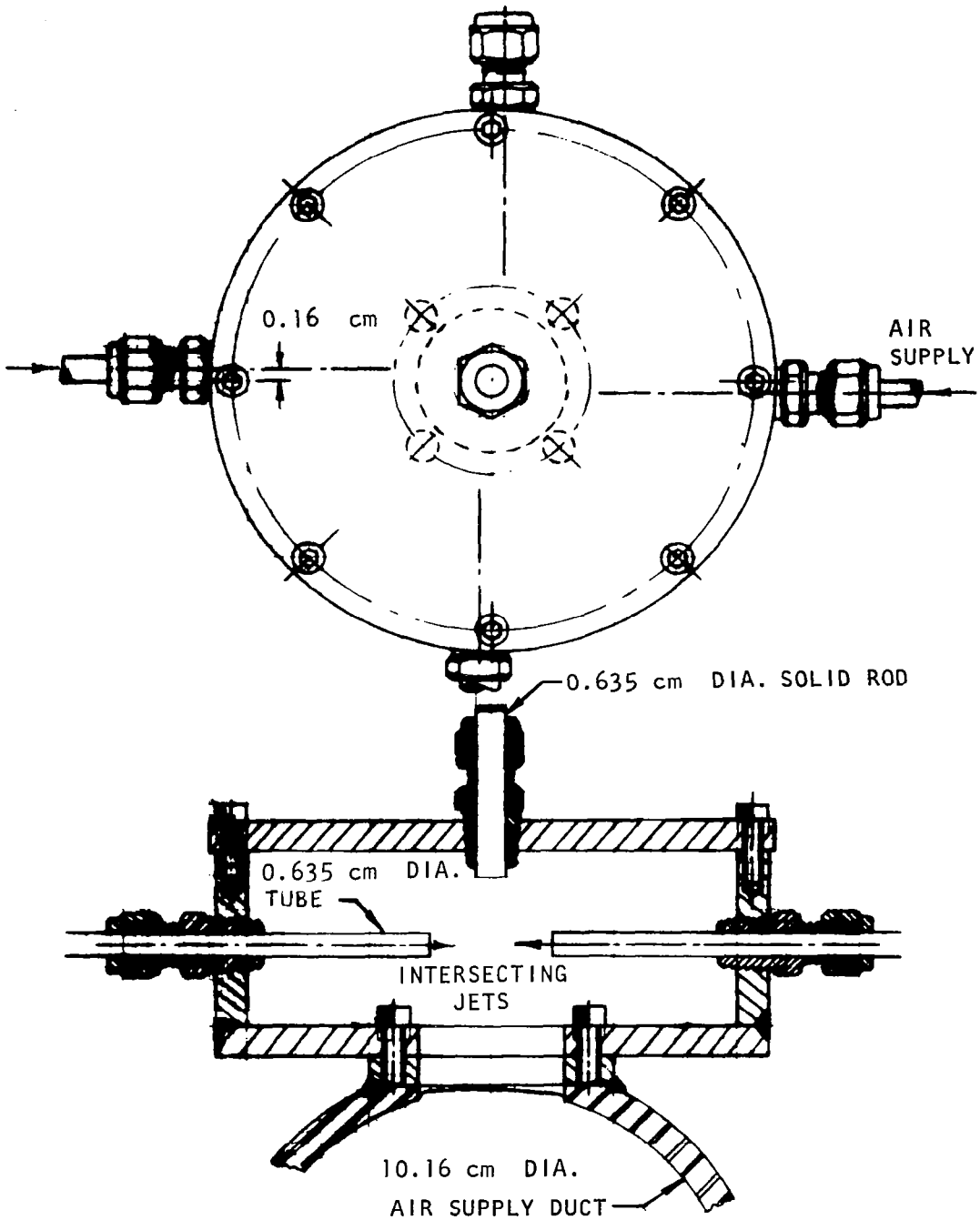

Figure 3.21 Schematic drawing of internal noise generator.

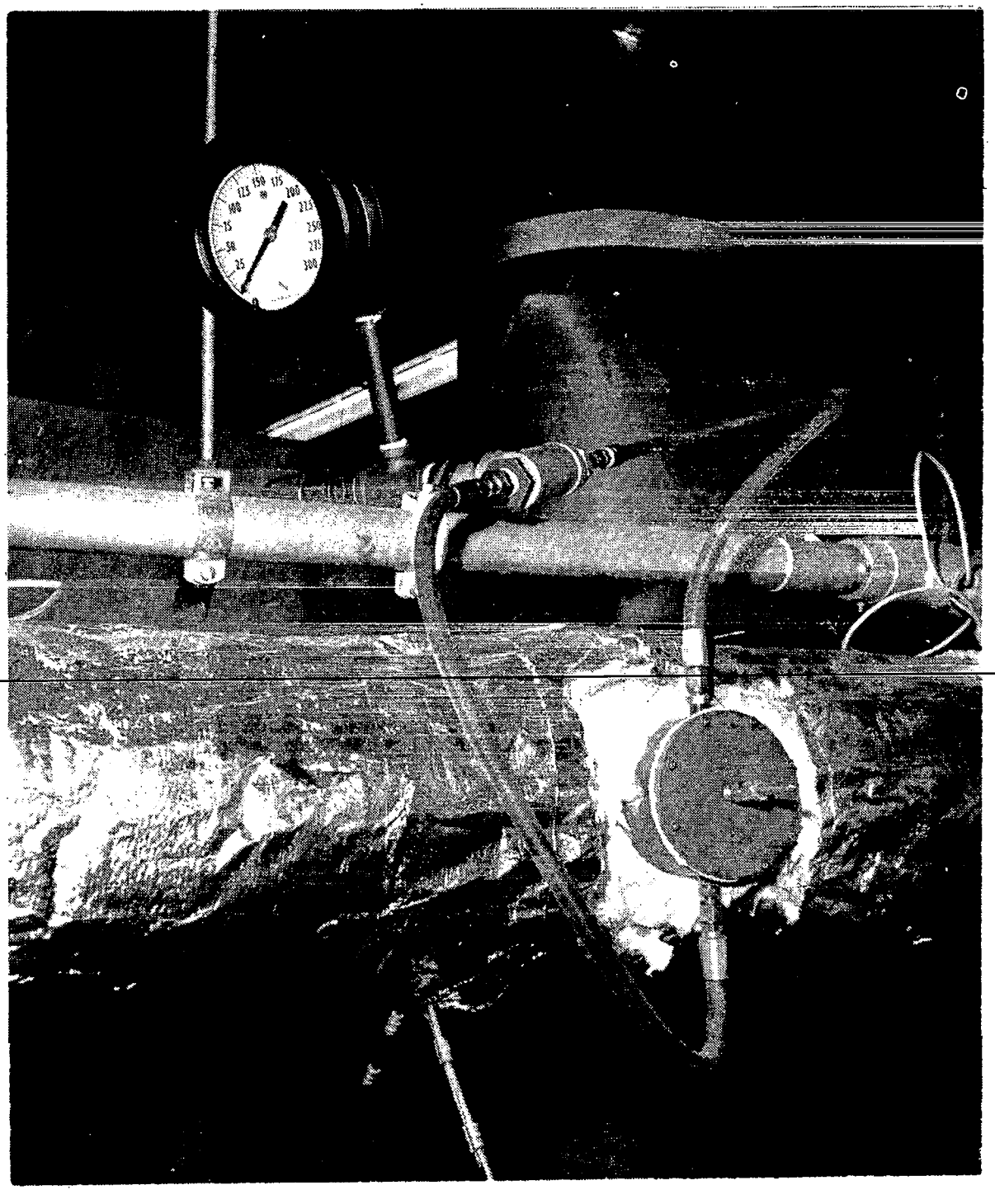

Figure 3.22 Internal noise generator mounted on air supply pipe.

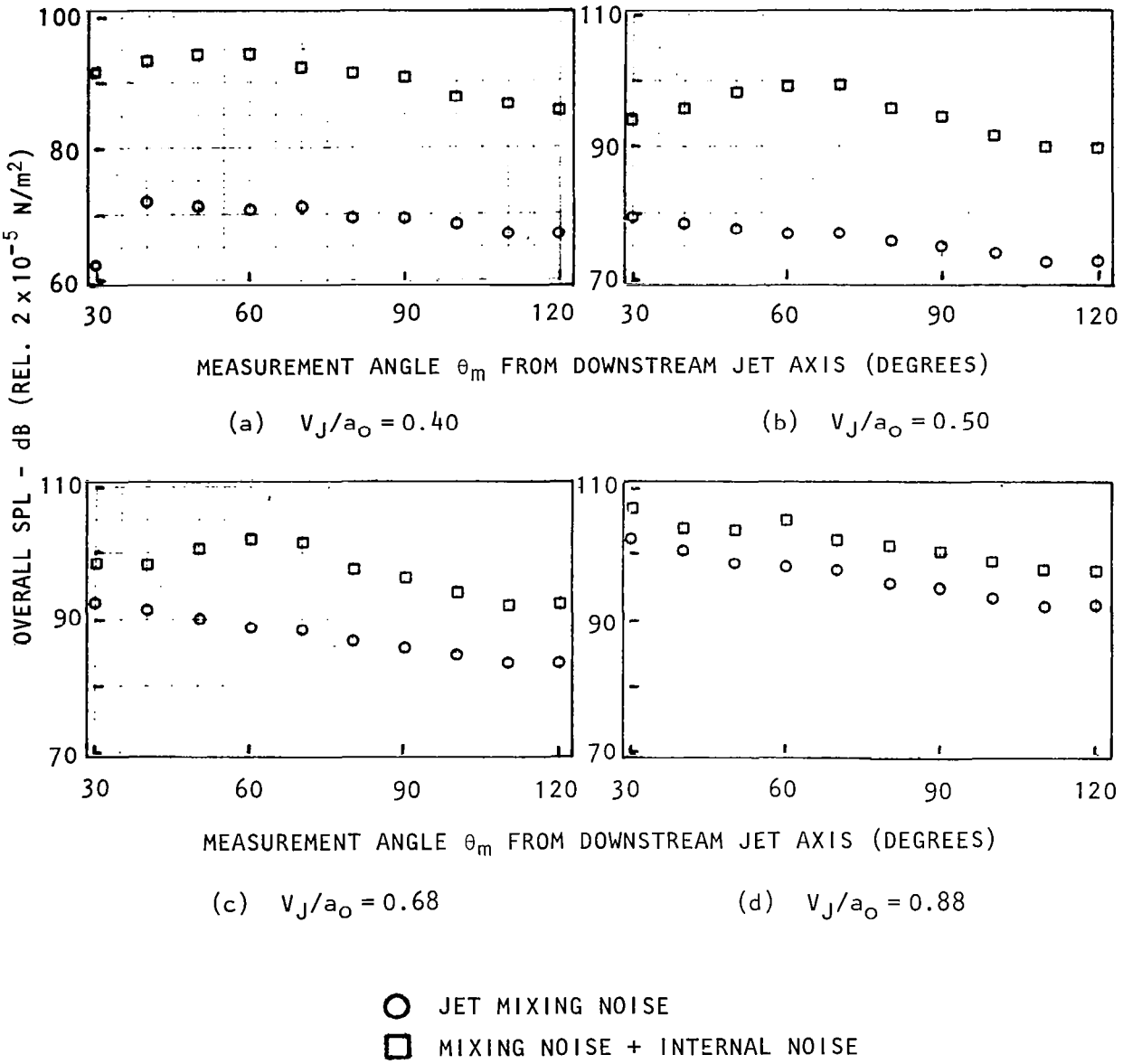

Figure 3.23 Directivity of overall SPL with and without internal noise at various jet velocities: unheated, $V_T/a_o \doteq 0$, $R_m/d = 96$.

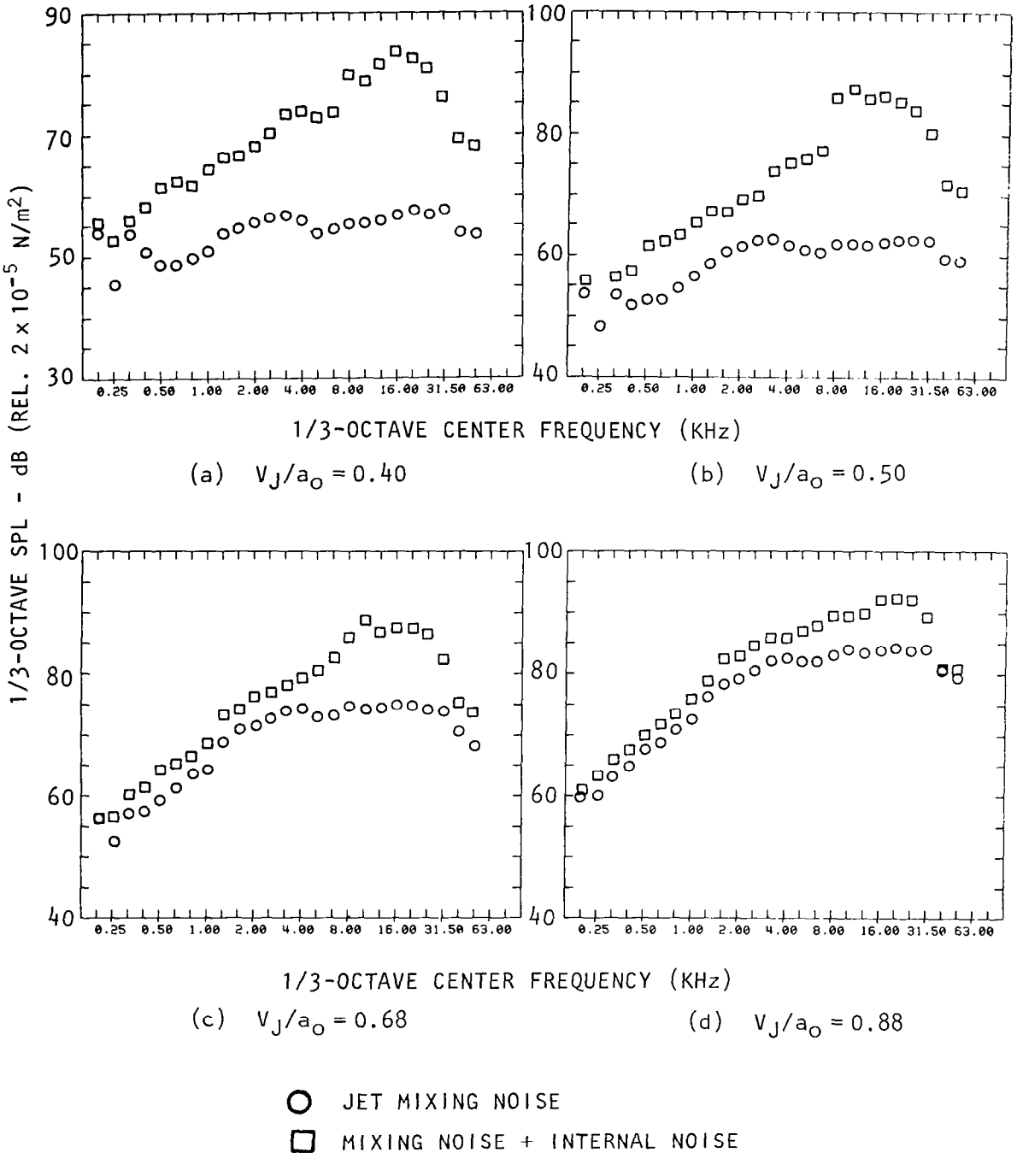

Figure 3.24 1/3-octave SPL spectra at $\theta_m = 90°$ with and without internal noise at various jet velocities: unheated, $V_T/a_o \doteq 0$, $R_m/d = 96$.

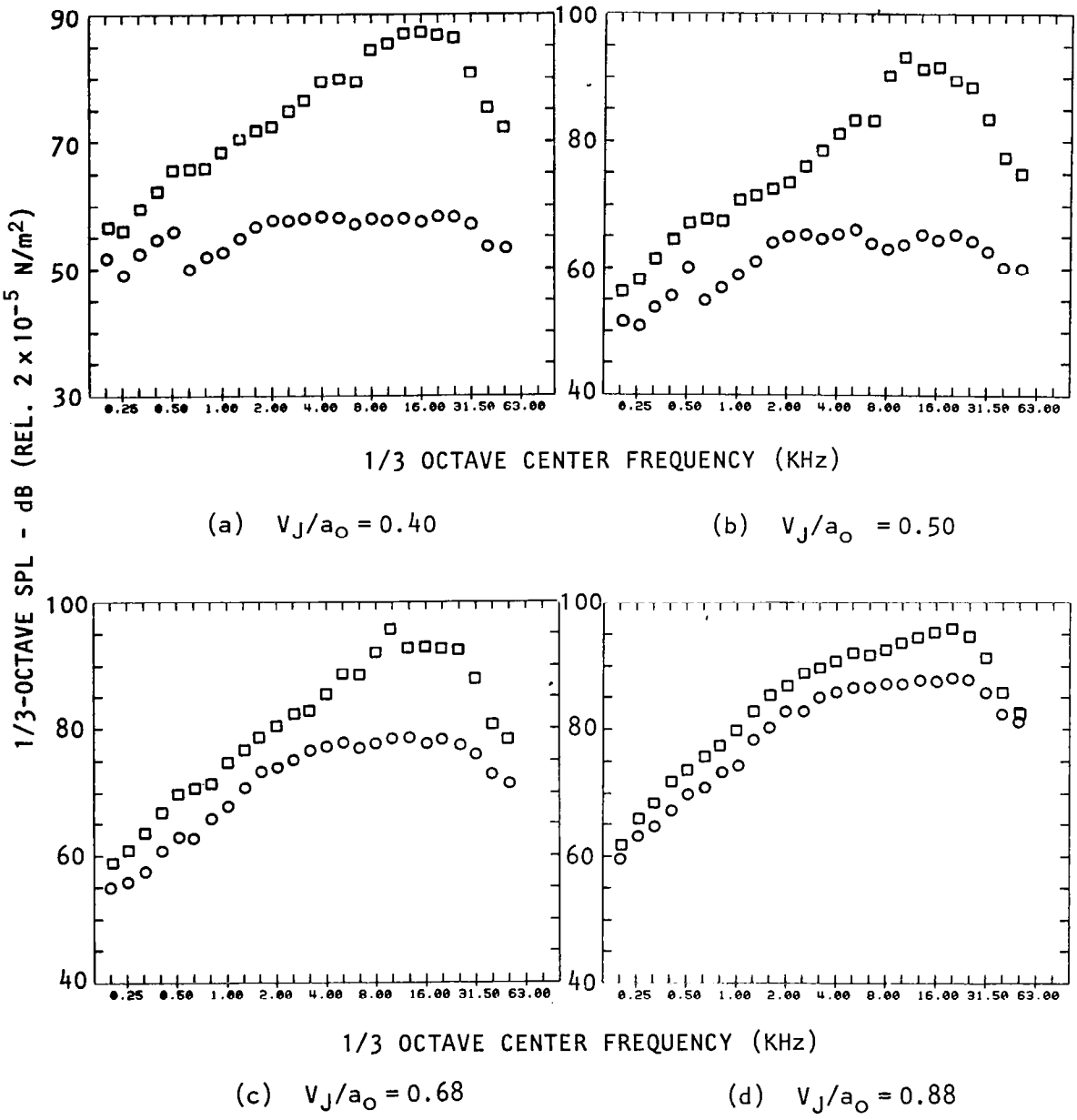

Figure 3.25 1/3-octave SPL spectra at $\theta_m = 60°$ with and without internal noise at various jet velocities: unheated, $V_T/a_o \doteq 0$, $R_m/d = 96$.

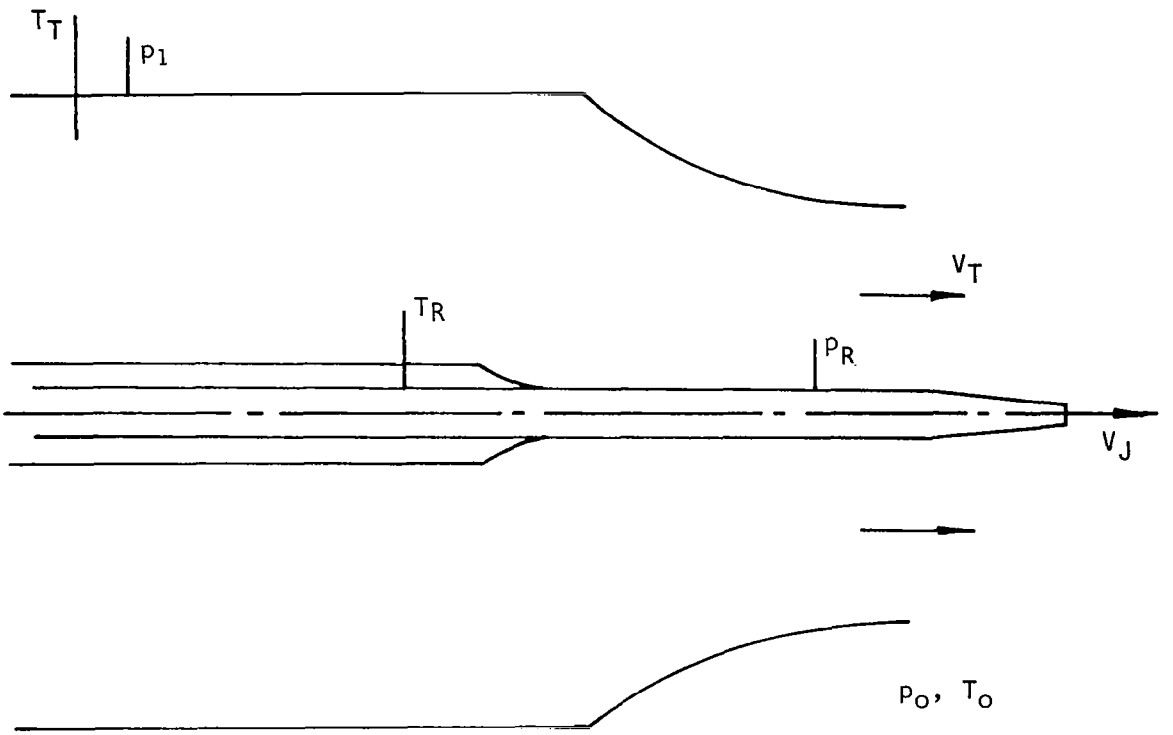

MEASUREMENTS:

T_o	AMBIENT TEMPERATURE IN ANECHOIC ROOM
T_T	TUNNEL INTAKE TEMPERATURE
T_R	UPSTREAM (OR PLENUM) JET TEMPERATURE
p_1	TUNNEL INTAKE STATIC PRESSURE (PIEZOMETER)
p_R	UPSTREAM (OR PLENUM) STATIC PRESSURE
p_o	AMBIENT PRESSURE IN ANECHOIC ROOM

Figure 3.26 Measurements for setting test conditions.

at the desired combination of V_J/a_o and V_T/a_o, the following sequence was adopted:

Free Jet:

1. Specify V_T/a_o
2. Read p_o, T_o and T_T
3. Calculate a_o
4. Calculate V_T
5. Compute $(p_1 - p_o)$ using tunnel calibration computer program on HP-65
6. Set tunnel at $(p_1 - p_o)$ to obtain desired V_T/a_o

Model Jet:

1. Specify V_J/a_o
2. Compute p_R/p_o using isentropic jet flow equations
3. Read p_o
4. Calculate p_R
5. Set jet at p_R to obtain desired V_J/a_o
6. Check if $(p_1 - p_o)$ has altered, and adjust if necessary.

During each test, all pressures and temperatures and chamber humidity were recorded. Subsequent to the test program, these measurements were used to compute the exact jet and tunnel operating conditions, and also to compute the atmospheric absorption corrections for each test condition.

4. EXPERIMENTAL STUDY OF TRANSMISSION, REFLECTION AND SCATTERING OF SOUND IN A FREE-JET FLIGHT SIMULATION FACILITY AND COMPARISON WITH THEORY

4.1 OBJECTIVES

The transformation of jet noise data acquired in a free-jet flight simulation facility to the corresponding inflight conditions can be performed with the *theoretical* but substantially unverified calibration procedure outlined in section 2. The objective of the experiments described in this section was to *verify* (and if necessary modify) each step in that calibration procedure, which is based essentially on a high-frequency or geometric acoustics description of sound transmission across the free-jet shear layer. In order to achieve this objective, a series of experiments was conducted that involved detailed measurements of sound fields both inside and outside the free-jet flow.

The two specific aspects studied in this way were (i) the transmission of sound through the free-jet shear layer, and (ii) the internal reflection of sound by the free-jet shear layer. In addition, the effects of shear-layer *turbulence* on scattering and absorption of sound, emitted by a source immersed in the free-jet flow and received by a microphone located outside the flow, were also examined experimentally.

The point acoustical source and the experimental configurations used for these verification tests were described in Section 3. To determine the transmission characteristics of the free-jet shear layer, the refraction of ray paths across the shear layer (i.e., angle calibration) is examined first, and the results are presented in Section 4.2. The internal reflection effects are discussed in Section 4.3. Measurements inside and outside the free-jet flow along predetermined ray paths are then used to test the validity of the recommended amplitude calibration factors. These results are presented in Section 4.4. Finally, the experimentally observed effects on turbulence absorption and turbulence scattering are given in Sections 4.5 and 4.6, respectively.

4.2 ANGLE CALIBRATION

The first objective of the experimental program was to determine the angle changes, i.e. the refraction of ray paths across the free-jet shear layer, and to compare the results with theoretical values predicted by Snell's law, as outlined in Section 2.1.

Snell's law relates the wavenormal angle, θ_T, on a ray path in the potential core of the free jet to the corresponding angle, θ_O, outside the flow. To determine these angles *directly* would involve an extensive measurement program to obtain the constant phase or wavefront surfaces both inside and outside the free-jet flow, and hence the wavenormal angles. An alternate

approach was, therefore, adopted which indirectly checks the validity of Snell's law. This approach relies on a two-microphone correlation technique to provide a measure of the time taken for an acoustic signal to propagate from a point located in the free-jet potential core to a point outside the flow. The measured time delay can be compared with that calculated directly from a ray path abruptly refracted at the lip line according to Snell's law (the "lip-line refraction model"), i.e. the time delay between the same two points along the straight line ray segments AI and IB in Figure 4.1. If the agreement between measured and calculated time delays is acceptable, then this would be a strong indication that the angle changes across the shear layer obey Snell's law, as assumed in the recommended calibration procedure.

4.2.1 Calculated Time Delays

The calculated time delay, τ_{cv}, based on the lip-line or vortex sheet model, is given by†

$$\tau_{cv} = \frac{(r_T/\sin\theta_T)}{a_T} + \frac{\{(R_m\sin\theta_m - r_T)/\sin\theta_o\}}{a_o} \tag{4-1a}$$

or, equivalently

$$\tau_{cv} = \frac{(r_T/\sin\psi_T)}{V_r} + \frac{\{(R_m\sin\theta_m - r_T)/\sin\theta_o\}}{a_o} \tag{4-1b}$$

where V_r, the ray speed is given by

$$V_r = V_T\cos\psi_T + (a_T^2 - V_T^2\sin^2\psi_T)^{\frac{1}{2}}. \tag{4-1c}$$

The variation of τ_{cv} with θ_m for different free-jet Mach numbers is shown in Figure 4.2 for the case $R_m/r_T = 4$, $a_T/a_o = 1$.

The measured time delays (which are presented in Section 4.2.2) are sometimes found to be slightly, but consistently, different from the minimum value calculated with equation (4-1a), which raises the question of how much error this implies for the predicted emission angle θ_T when calculated according to equations (2-1) through (2-3) of Section 2. To establish the accuracy of the calculated time delay, τ_{cv}, which is based on the approximate lip-line refraction model, the time delay, τ_{cd}, was calculated along the more realistic, curved ray path through a diverging, axisymmetric mixing region. The equations governing this ray path are given by Ugincius (ref. 4.1) and differ from those given in reference 4.2 which are based upon a low Mach number approximation. The same axial mean velocity profiles were used as in reference 4.2, but a transverse (i.e. radial) mean velocity field was included, and also radial and axial mean temperature variations. The mean temperature was calculated by

---

†*This is the minimum travel time, as shown in Appendix 4A.*

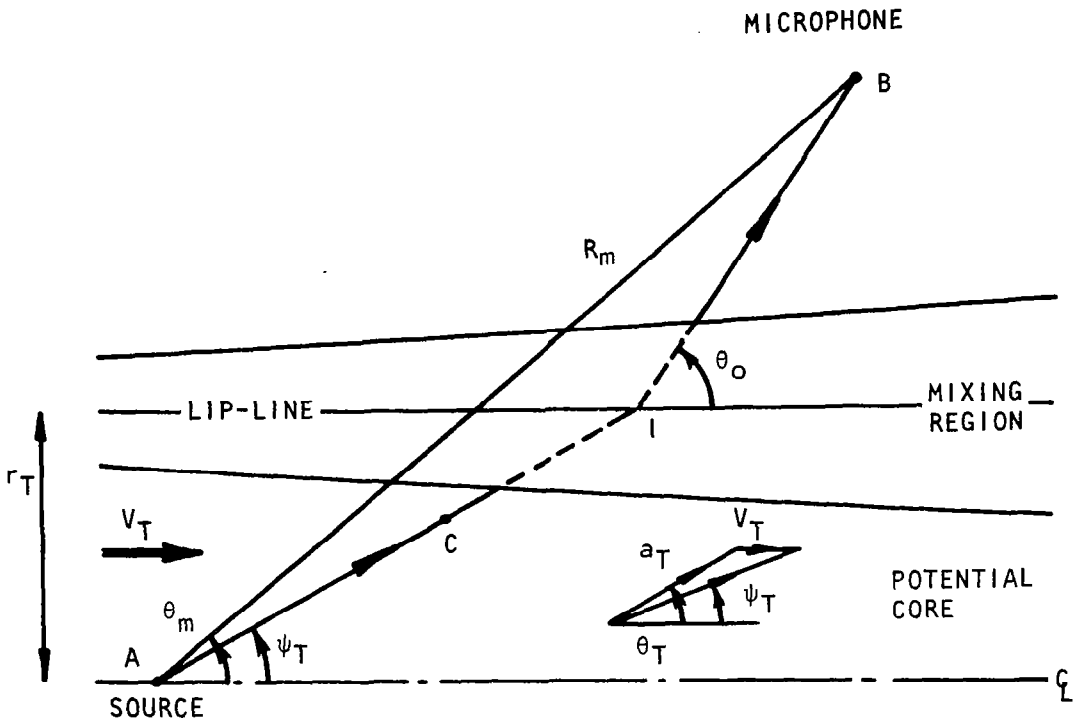

Figure 4.1 The lip-line or vortex-sheet model of sound refraction across the free-jet shear layer.

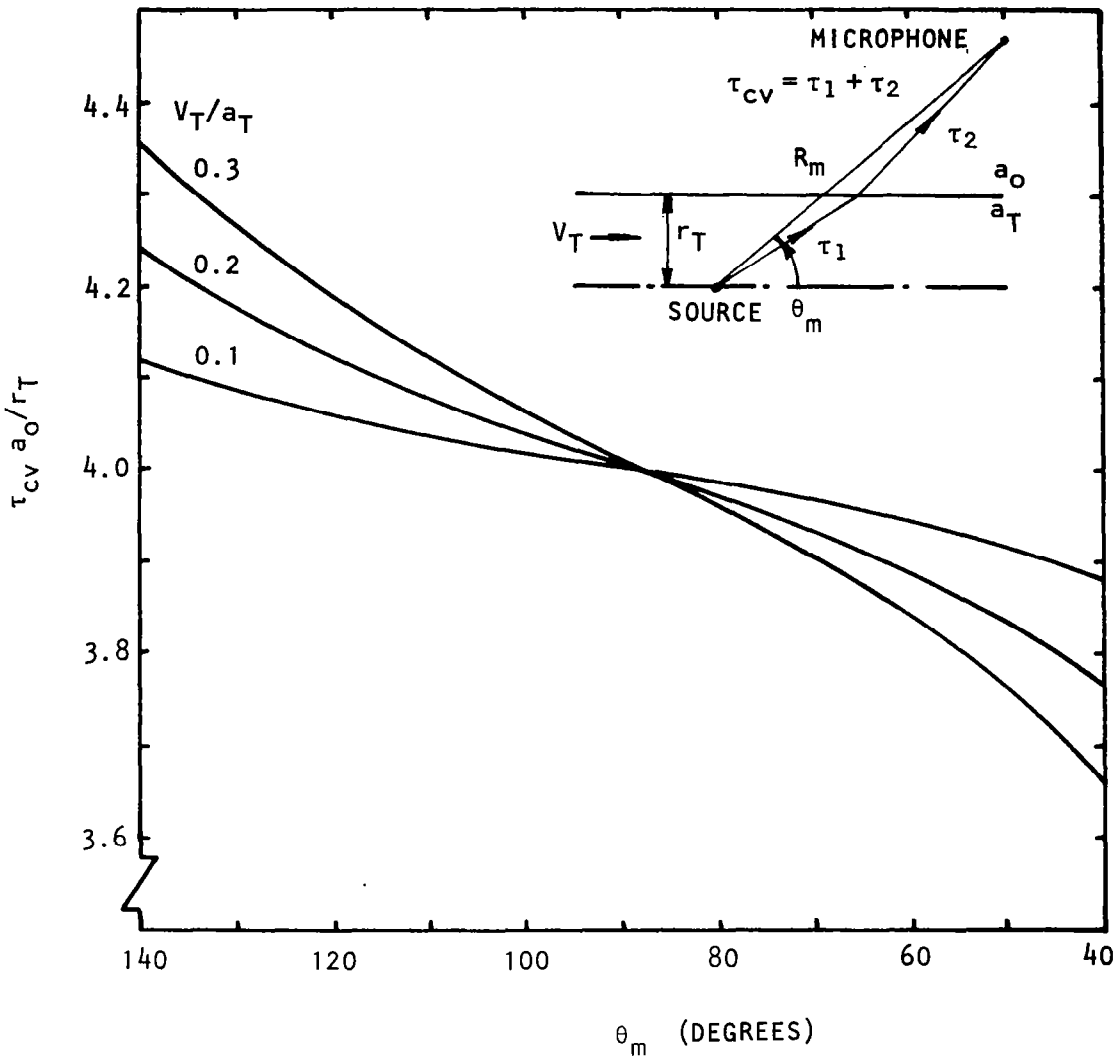

Figure 4.2 Calculated vortex-sheet time delay variation with microphone angle and free-jet Mach number; $R_m/r_T = 4$, $a_T/a_o = 1$.

assuming that the stagnation temperature and velocity profile shapes are identical. Results for the time delay, τ_{cd}, calculated in this way will be compared with measured time delays in Section 4.2.2.

4.2.2 Measured Time Delays

The angle changes across the free-jet shear layer were determined *indirectly* by cross-correlation peak time delay measurements. Referring to Figure 4.1, the outputs from microphone A and B were cross-correlated. When the experimental point source located adjacent to microphone A is excited with broadband noise, the measured cross-correlation function $R_{AB}(\tau)$ exhibits a maximum at some time delay τ_m as illustrated in Figure 4.3. The peak time delay corresponds to the time taken for an acoustic signal to propagate along the ray path from point A to point B.

If the vortex sheet model (i.e., Snell's law) is the correct model, measured peak correlation time delays should be equal to τ_{cv} as given by equation (4-1a). The measured time delays should also follow the trend illustrated in Figure 4.2, i.e., at $\theta_m = 90°$, there should be very little effect of the tunnel Mach number while the peak time delays should *decrease* in the rear arc and *increase* in the forward arc as the tunnel Mach number is increased.

Typical cross-correlation functions $R_{AB}(\tau)$ measured with the experimental point source located at $x/d_T = 1.74$ and with microphone B at $\theta_m = 40°$ and 60° (rear arc), 90° and also 120° and 140° (forward arc) for a range of tunnel velocities $V_T/a_o = 0$, 0.045, 0.090, 0.135, 0.180, 0.225, and 0.270 are shown in Figures 4.4 through 4.8. This demonstrates that, at least qualitatively, the measured time delays follow the behavior calculated from the vortex sheet model (Figure 4.2).

In order to *quantitatively* confirm Snell's law, calculated values of the time delay, τ_{cv}, have been compared in detail with measured time delay data; some typical results are shown in Figures 4.9 and 4.10. Measured time delay data at selected microphone angles ($\theta_m = 40°$, 90° and 140°) are plotted as a function of free-jet Mach number for two axial source positions ($0.21d_T$ and $1.74d_T$). The measured† and calculated time delay values at all microphone angles are given in Tables 4.1 and 4.2 for the point source located at $x/d_T = 0.21$ and 1.74, respectively. It is worth pointing out here that the cross-correlation functions shown in Figures 4.4 through 4.8 and elsewhere in the report are not normalized and that their amplitudes are not important to the present discussion.

In the first case (Figure 4.9, source at $0.21d_T$), measured time delays† agree well with the calculated vortex-sheet prediction (shown as continuous line), there are no consistent deviations and all are well within a 1% error tolerance. In the second case (Figure 4.10, source at $1.74d_T$), which includes the forward arc angle, $\theta_m = 140°$, the vortex sheet model still predicts the time delays quite accurately, but now there is a slight but consistent Mach number and angle dependence deviation. This, if not explained,

---

†*which were measured to an accuracy of 0.01 ms.*

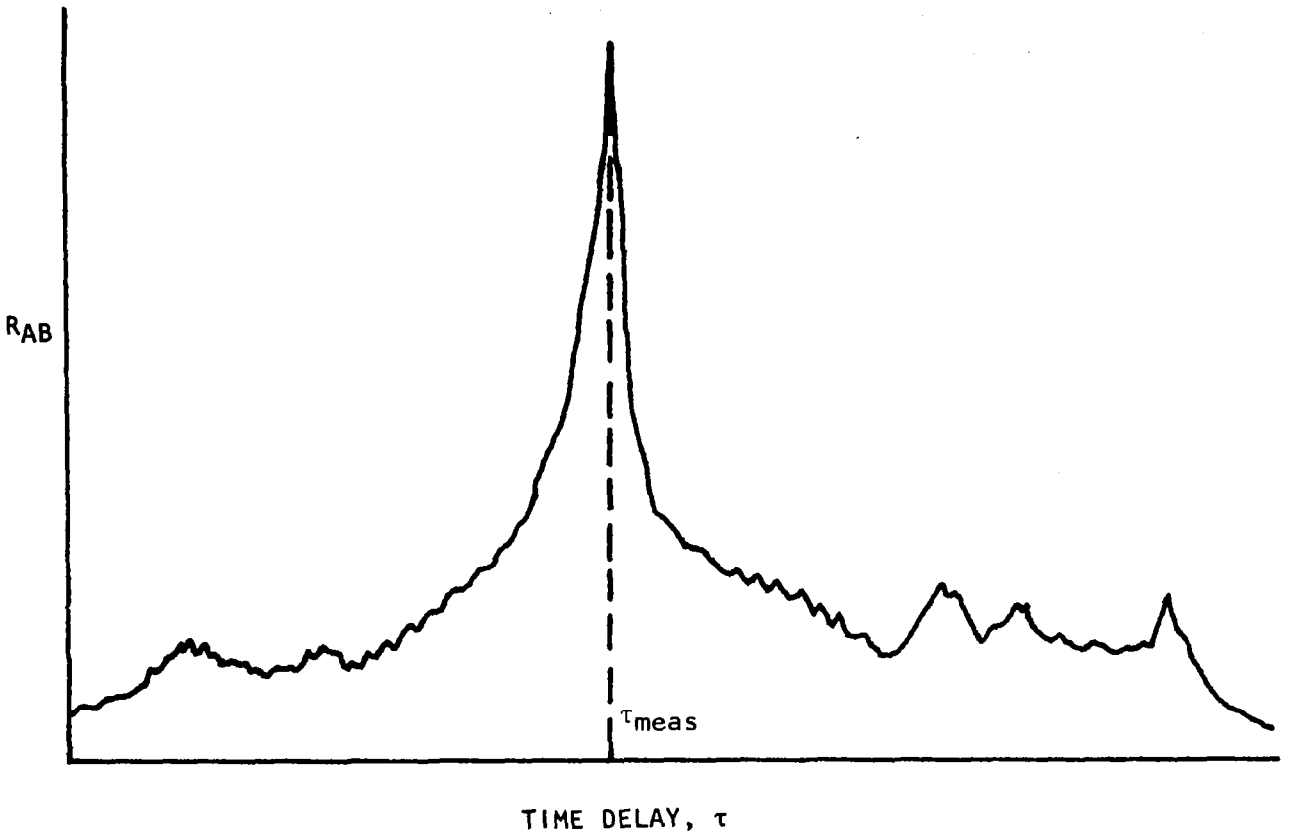

Figure 4.3 Cross-correlation function vs. time delay.

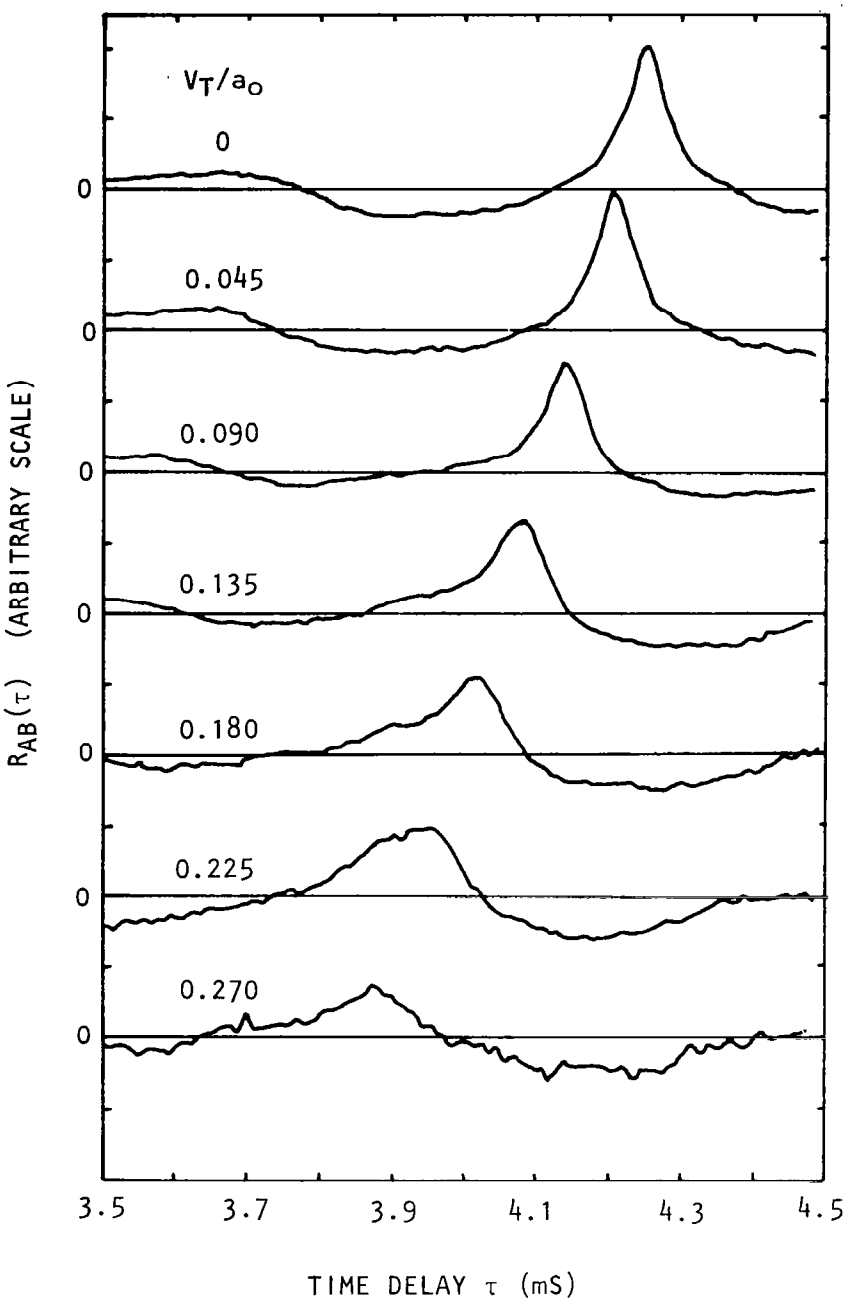

Figure 4.4 Cross-correlation function $R_{AB}(\tau)$ for various free-jet Mach numbers; $\theta_m = 40°$. Point source at $x/d_T = 1.74$.

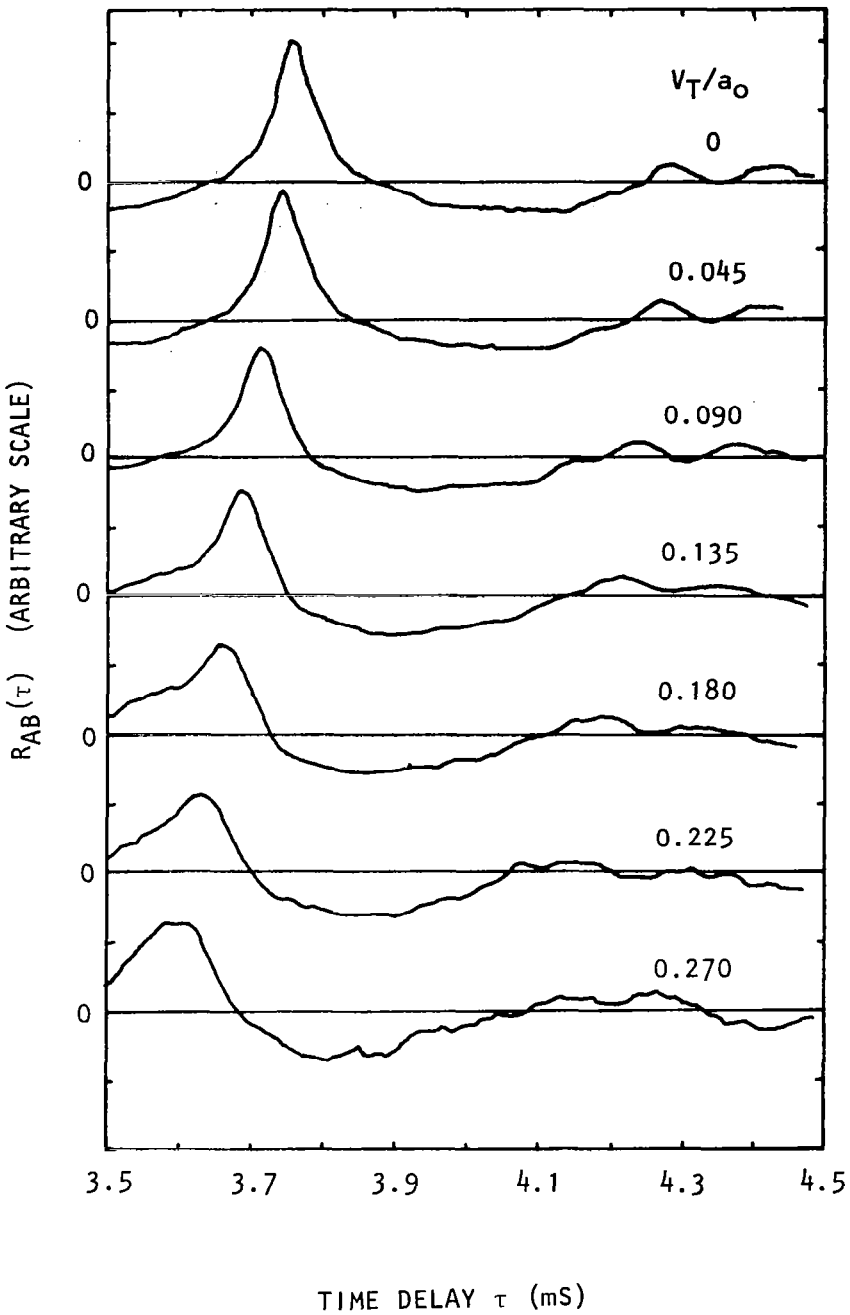

Figure 4.5 Cross-correlation function $R_{AB}(\tau)$ for various free-jet Mach numbers; $\theta_m = 60°$. Point source at $x/d_T = 1.74$.

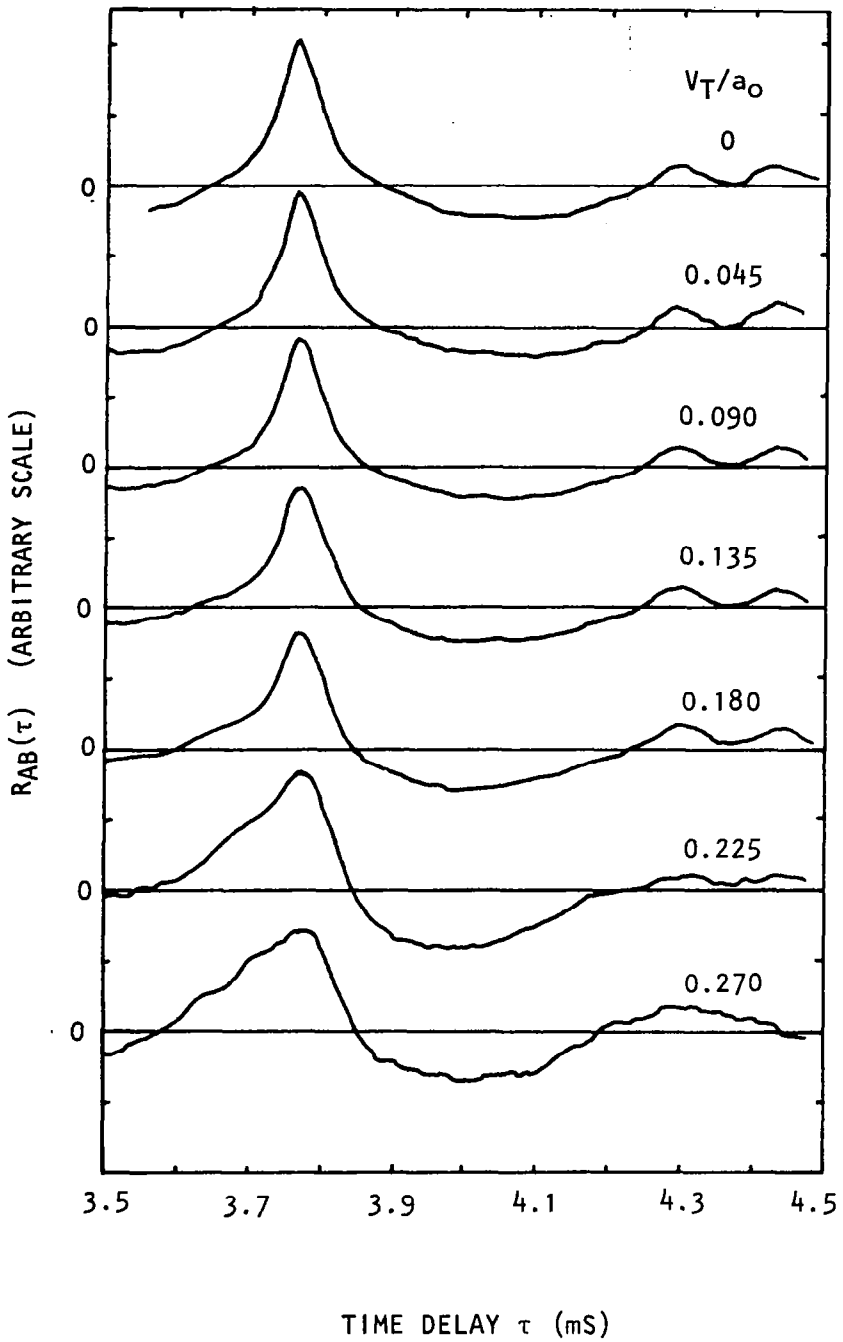

Figure 4.6 Cross-correlation function $R_{AB}(\tau)$ for various free-jet Mach numbers; $\theta_m = 90°$. Point source at $x/d_T = 1.74$.

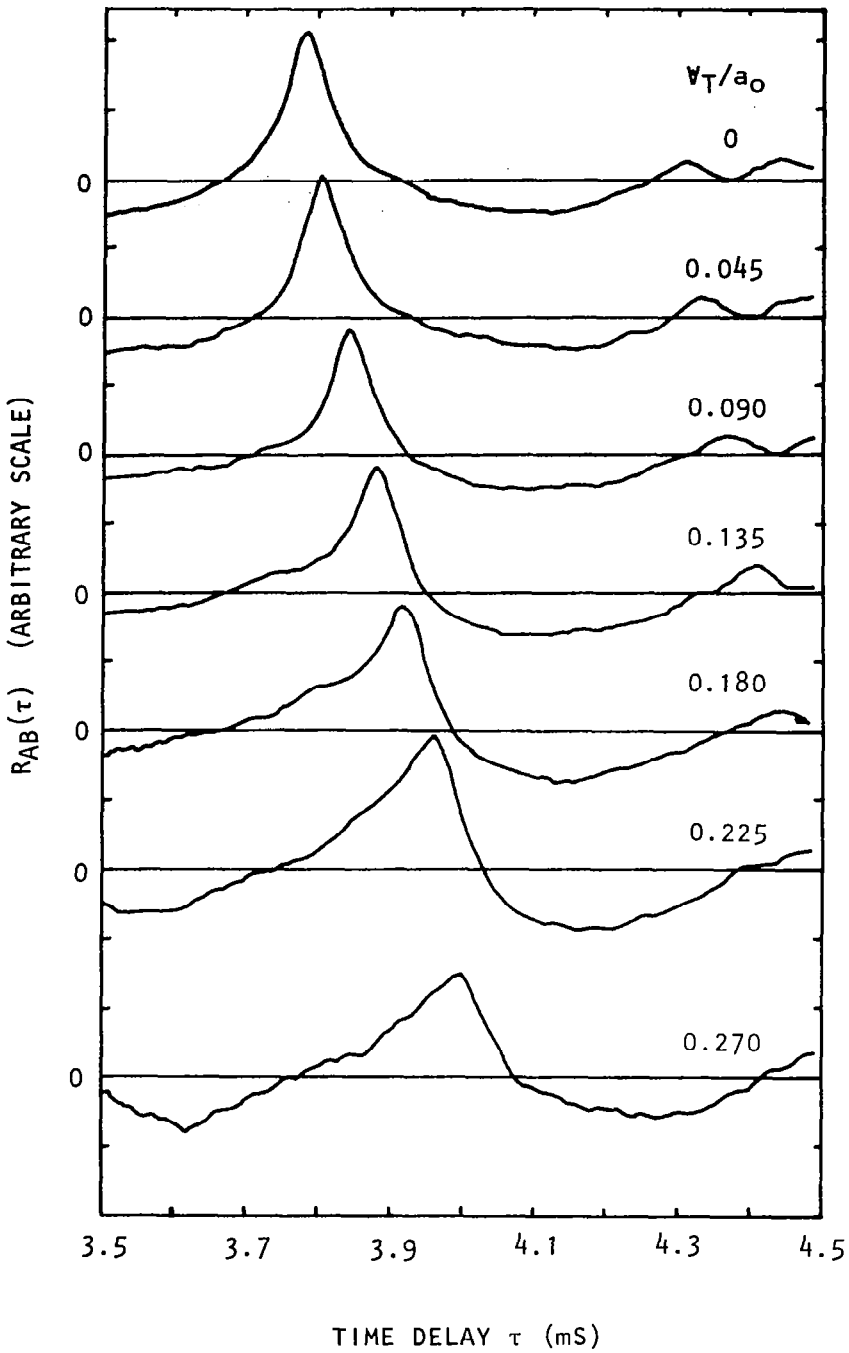

Figure 4.7 Cross-correlation function $R_{AB}(\tau)$ for various free-jet Mach numbers; $\theta_m = 120^o$. Point source at $x/d_T = 1.74$.

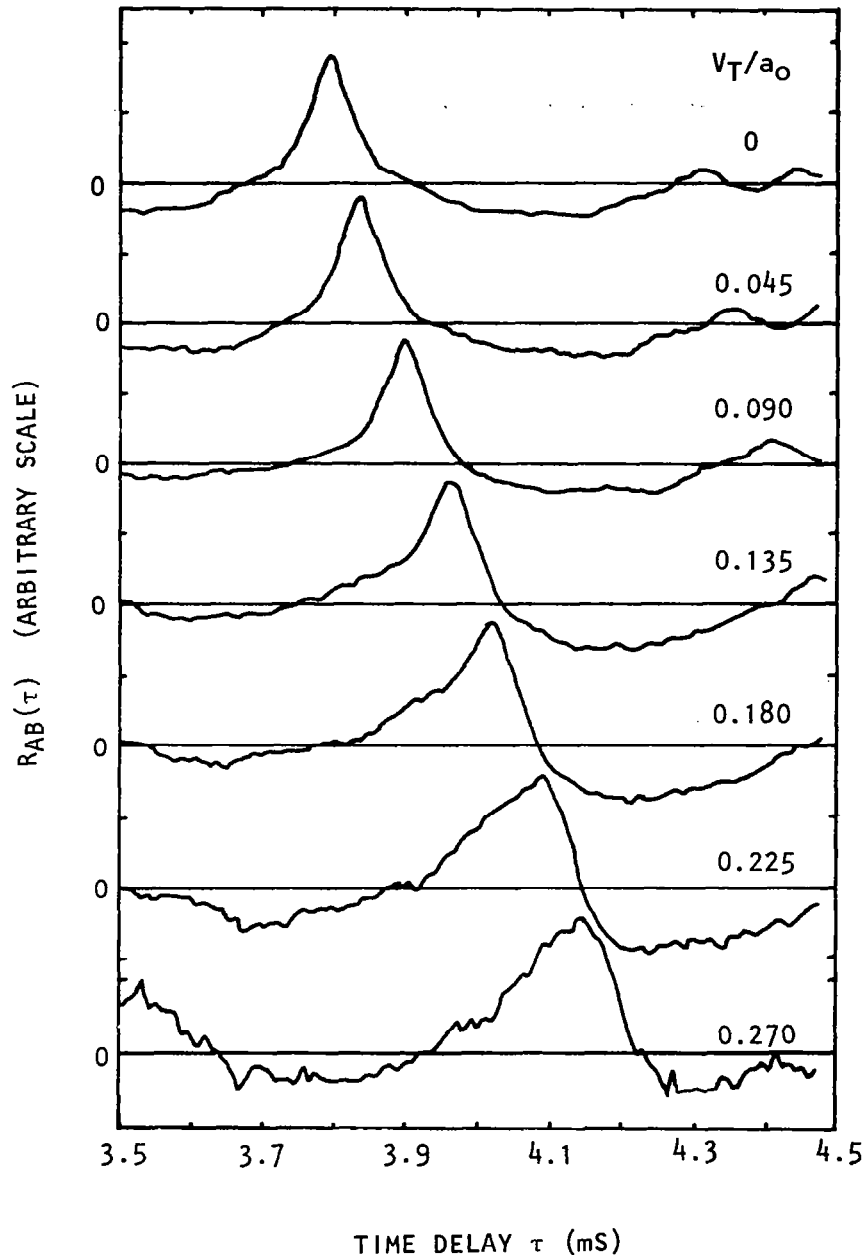

Figure 4.8 Cross-correlation function $R_{AB}(\tau)$ for various free-jet Mach numbers; $\theta_m = 140°$. Point source at $x/d_T = 1.74$.

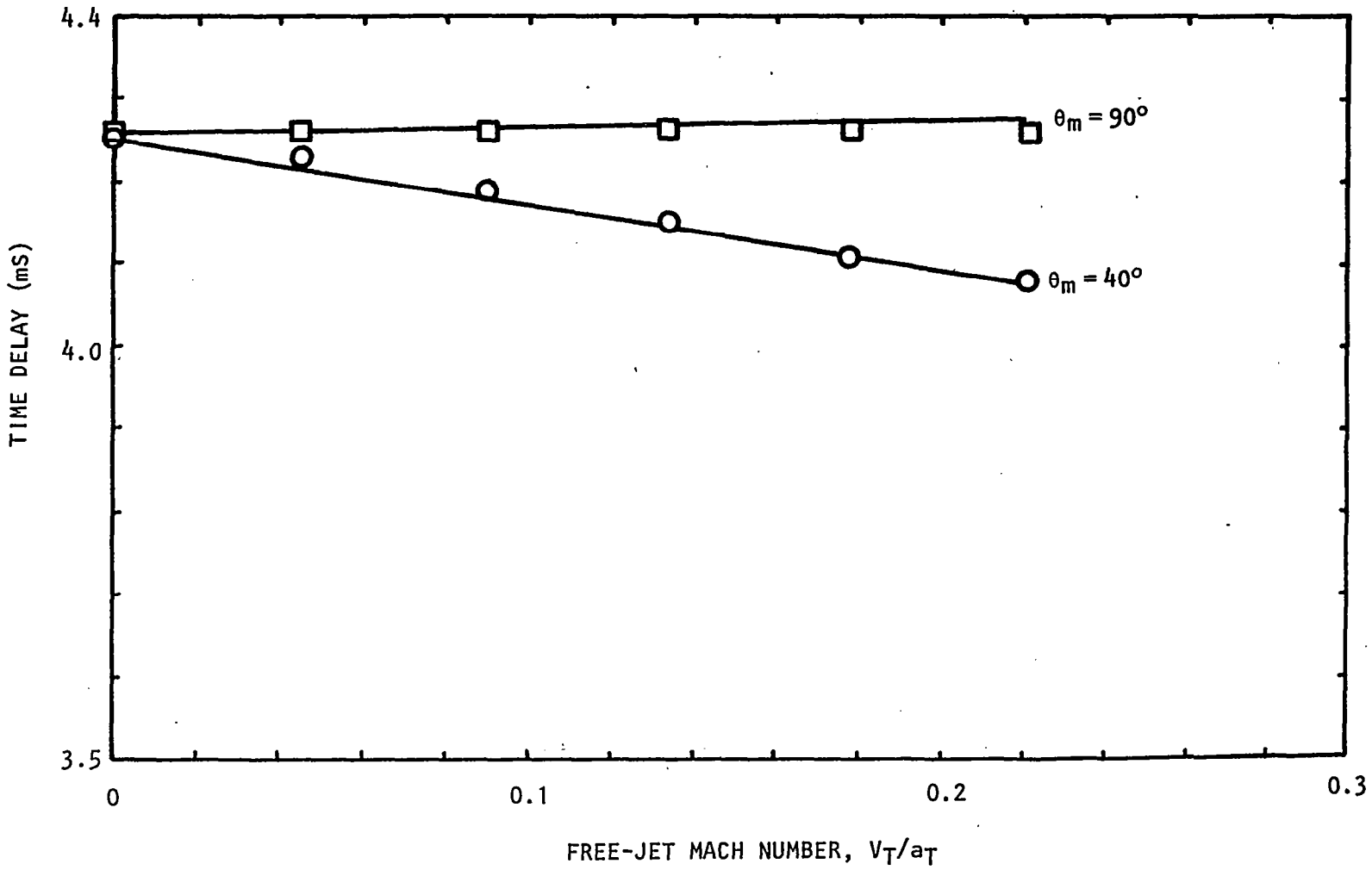

Figure 4.9 Comparison of measured (symbols) peak time delay variation with free-jet Mach number and calculated (——) time delay according to vortex-sheet model. Point source at $x/D_T = 0.21$.

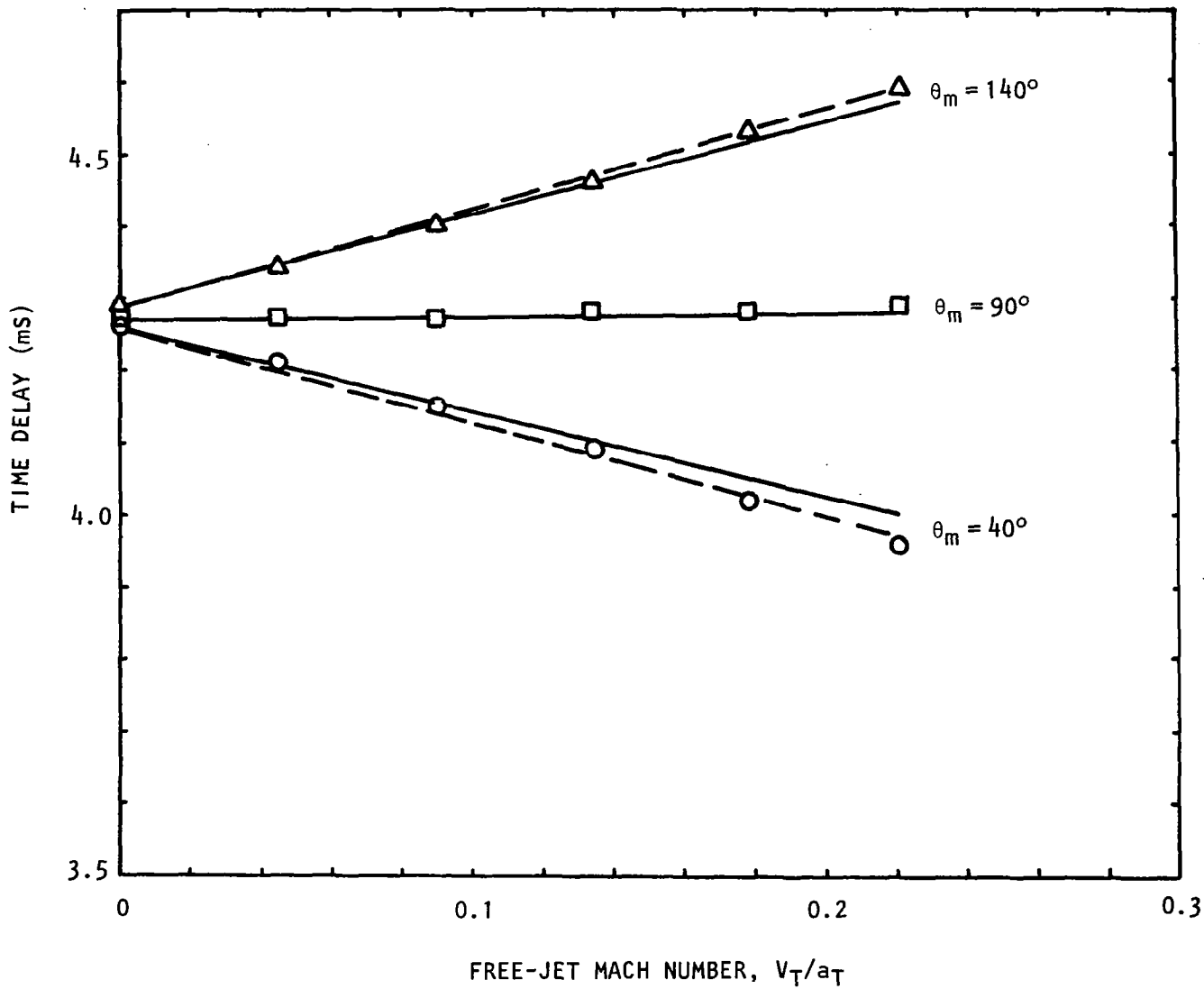

Figure 4.10 Comparison of measured (symbols) peak time delay variation with free-jet Mach number and calculated time delays: —— Vortex-sheet model; --- Diverging flow/ray tracing. Point source at $x/d_T = 1.74$.

Table 4.1 Time delay data for angle change tests; point source at $x/d_T = 0.21$.

Run	θ_m (Degrees)	V_T/a_o (Nominal)	M_T	τ_m (ms)	τ_{cv} (ms)
507	30	0.0	0.0	4.27	--
508	30	0.045	0.04454	4.21	4.190
509	30	0.090	0.08950	4.22	4.110
510	30	0.135	0.13424	4.03	4.033
511	30	0.180	0.17834	3.96	3.960
512	30	0.225	0.22184	3.86	3.889
513	30	0.270	0.26449	3.78	3.824
456	40	0.0	0.0	4.26	--
457	40	0.045	0.04454	4.22	4.206
458	40	0.090	0.08950	4.16	4.152
459	40	0.135	0.13424	4.10	4.100
460	40	0.180	0.17834	4.05	4.050
461	40	0.225	0.22184	3.99	4.003
462	40	0.270	0.26449	3.93	3.959
463	50	0.0	0.0	4.25	--
464	50	0.045	0.04454	4.23	4.212
465	50	0.090	0.08950	4.19	4.175
466	50	0.135	0.13424	4.15	4.139
467	50	0.180	0.17834	4.11	4.106
468	50	0.225	0.22184	4.08	4.074
469	50	0.270	0.26449	3.97	4.044
470	60	0.0	0.0	4.26	--
471	60	0.045	0.04454	4.24	4.232
472	60	0.090	0.08950	4.21	4.207
473	60	0.135	0.13424	4.19	4.183
474	60	0.180	0.17834	4.15	4.161
475	60	0.225	0.22184	4.14	4.140
477	70	0.0	0.0	4.26	--
478	70	0.045	0.04454	4.24	4.240
479	70	0.090	0.08950	4.23	4.233
480	70	0.135	0.13424	4.21	4.210
481	70	0.180	0.17834	4.19	4.190
482	70	0.225	0.22184	4.18	4.180
483	70	0.270	0.26449	4.16	4.159

Table 4.1 Concluded.

Run	θ_m (Degrees)	V_T/a_o (Nominal)	M_T	τ_m (ms)	τ_{cv} (ms)
484	80	0.0	0.0	4.26	--
485	80	0.045	0.04454	4.24	4.252
486	80	0.090	0.08950	4.24	4.246
487	80	0.135	0.13424	4.23	4.240
488	80	0.180	0.17834	4.23	4.235
489	80	0.225	0.22184	4.22	4.231
490	80	0.270	0.26449	4.20	4.228
492	90	0.0	0.0	4.26	--
493	90	0.045	0.04454	4.26	4.261
494	90	0.090	0.08950	4.26	4.263
495	90	0.135	0.13424	4.26	4.267
496	90	0.180	0.17834	4.26	4.271
497	90	0.225	0.22184	4.26	4.275
498	90	0.270	0.26449	4.27	4.281
499	100	0.0	0.0	4.27	--
500	100	0.045	0.04454	4.28	4.280
501	100	0.090	0.08950	4.29	4.290
502	100	0.135	0.13424	4.29	4.299
503	100	0.180	0.17834	4.30	4.310
504	100	0.225	0.22184	4.31	4.322
505	100	0.270	0.26449	4.33	4.335

Table 4.2 Time delay data for angle change tests; point source at $x/d_T = 1.74$.

Run	θ_m (Degrees)	V_T/a_o (Nominal)	M_T	τ_m (ms)	τ_{cv} (ms)
601	20	0.0	0.0	4.26	4.260
602	20	0.045	0.04496	4.15	4.132
603	20	0.090	0.08972	4.00	4.009
594	30	0.0	0.0	4.29	4.290
595	30	0.045	0.04496	4.20	4.209
596	30	0.090	0.08972	4.08	4.130
597	30	0.135	0.13409	3.99	4.053
598	30	0.180	0.17823	3.90	3.979
599	30	0.225	0.22133	3.77	3.909
600	30	0.270	0.26441	3.70	3.843
587	40	0.0	0.0	4.26	4.260
588	40	0.045	0.04496	4.21	4.205
589	40	0.090	0.08972	4.15	4.151
590	40	0.135	0.13409	4.09	4.099
591	40	0.180	0.17823	4.02	4.050
592	40	0.225	0.22133	3.96	4.003
593	40	0.270	0.26441	3.87	3.958
580	50	0.0	0.0	4.26	4.260
581	50	0.045	0.04496	4.22	4.222
582	50	0.090	0.08972	4.17	4.185
583	50	0.135	0.13409	4.13	4.149
584	50	0.180	0.17823	4.08	4.115
585	50	0.225	0.22133	4.03	4.084
586	50	0.270	0.26441	3.98	4.053
573	60	0.0	0.0	4.26	4.260
574	60	0.045	0.04454	4.25	4.234
575	60	0.090	0.08950	4.22	4.209
576	60	0.135	0.13424	4.20	4.185
577	60	0.180	0.17834	4.16	4.163
578	60	0.225	0.22184	4.13	4.142
579	60	0.270	0.26449	4.11	4.122
566	70	0.0	0.0	4.27	4.270
567	70	0.045	0.04454	4.25	0.254
568	70	0.090	0.08950	4.23	4.238
569	70	0.135	0.13424	4.22	4.224
570	70	0.180	0.17834	4.20	4.211
571	70	0.225	0.22184	4.18	4.199
572	70	0.270	0.26449	4.16	4.188

Table 4.2 Concluded.

Run	θ_m (Degrees)	V_T/a_o (Nominal)	M_T	τ_m (ms)	τ_{cv} (ms)
559	80	0.0	0.0	4.27	4.270
560	80	0.045	0.04454	4.26	4.262
561	80	0.090	0.08950	4.25	4.256
562	80	0.135	0.13424	4.24	4.250
563	80	0.180	0.17834	4.23	4.245
564	80	0.225	0.22184	4.22	4.241
565	80	0.270	0.26449	4.21	4.238
545	100	0.0	0.0	4.29	4.290
546	100	0.045	0.04454	4.29	4.279
547	100	0.090	0.08950	4.30	4.288
548	100	0.135	0.13424	4.30	4.310
549	100	0.180	0.17834	4.33	4.310
550	100	0.225	0.22184	4.34	4.323
551	100	0.270	0.26449	4.35	4.336
538	110	0.0	0.0	4.29	4.290
539	110	0.045	0.04454	4.30	4.307
540	110	0.090	0.08950	4.32	4.326
541	110	0.135	0.13424	4.35	4.346
542	110	0.180	0.17834	4.37	4.366
543	110	0.225	0.22184	4.40	4.387
544	110	0.270	0.2649	4.43	4.409
531	120	0.0	0.0	4.29	4.290
532	120	0.045	0.04454	4.31	4.310
533	120	0.090	0.08950	4.35	4.346
534	120	0.135	0.13424	4.38	4.376
535	120	0.180	0.17834	4.42	4.406
536	120	0.225	0.22184	4.46	4.438
537	120	0.270	0.26449	4.45	4.469
613	130	0.0	0.0	4.29	4.290
614	130	0.045	0.04496	4.32	4.329
615	130	0.090	0.08972	4.36	4.370
616	130	0.135	0.13409	4.41	4.412
617	130	0.180	0.17823	4.46	4.454
618	130	0.225	0.22133	4.51	4.496
619	130	0.270	0.26441	4.55	4.539
606	140	0.0	0.0	4.29	4.290
607	140	0.045	0.04496	4.34	4.346
608	140	0.090	0.08972	4.40	4.402
609	140	0.135	0.13409	4.46	4.459
610	140	0.180	0.17823	4.53	4.515
611	140	0.225	0.22133	4.59	4.570

could raise doubts as to whether angle changes across the shear layer were being accurately predicted (by our Snell's law-based calibration procedure recommended in Section 2). It was speculated that these differences could simply be the result of the unrealistic "lip-line refraction" ray path through the shear layer. Time delays were therefore recalculated for *curved* ray paths through a realistic diverging mean flow model of the free-jet shear layer by a ray tracing method as discussed in Section 4.2.1.

It should be emphasized that within the shear layer the ray path is continuously refracted and follows a curved path, not two straight-line segments as sketched in Figure 4.1. The corresponding time delay τ_{cd} or travel time along that ray path is the most accurate prediction we have at this time to compare with the measured time delay, τ_m, through a real turbulent free jet. (Typical ray paths traced through the diverging free-jet shear layer are shown in Figure 2.2.) Time delays along these realistic ray paths were calculated and are compared with the measured results in Figure 4.10 (broken line). The recalculated time delay is *smaller* than the vortex-sheet value in the rear arc ($\theta_m = 40°$) and *larger* in the forward arc ($\theta_m = 140°$). Since the measured data exhibit this same behavior, it is reasonable to suppose that the diverging flow effect is the correct explanation for the deviation between the measured time delays and those predicted by the vortex-sheet model.

To summarize, the measured data agree very well with the theory when the source is located close to the free-jet nozzle exit plane and the ray paths cross the shear layer where it is relatively thin. When the source is located further downstream, the lip-line refraction model under-predicts time delays in the forward arc and over-predicts in the rear arc, but only by a marginal amount. These differences are easily accounted for if realistic, curved ray paths through a diverging, finite thickness shear layer are used in place of the lip-line refraction (or vortex sheet) model as a basis for time delay calculations.

However, as demonstrated in reference 4.2, the *angle* changes predicted by the diverging flow/ray tracing calculations are almost identical to those predicted by the lip-line refraction model. Hence, the measured time delay data have indirectly confirmed the validity of the recommended angle calibration procedure.

4.3 INTERNAL REFLECTION

One of the important objectives of the experimental program was to establish the significance of sound waves *reflected* back inside the free jet (if any) by the shear layer, compared to the free-field or outward-going wave amplitudes *incident* upon the shear layer. If strong reflections *were* detected it would tend to invalidate the geometric acoustic assumptions on which the theoretical amplitude calibration factor is based. The two-microphone correlation technique was again used to detect internal reflections as outlined below. Three 0.635 cm (0.25 inch) microphones suitably fitted with nose cones were positioned at locations A, C and D as indicated in Figure 3.16; each microphone was aligned axially with, and pointing into the flow.

Microphone C was positioned first at some pre-selected value of the incident ray angle, ψ_T. For each ray angle, ψ_T, microphone D was positioned on the centerline of the free jet such that it was on the reflected ray path, i.e. the *first* reflected ray path; multiply reflected rays were assumed to be of secondary importance.

First, consider the cross-correlation of signals from microphones A and D. Since microphone D is placed on the free-jet centerline, any reflected rays from the axisymmetric shear layer would be *focused* there, the time delay for each ray being the same. Therefore, if there is a significant internal reflection, it should be most easily detected through the cross-correlation of signals at microphones A and D; that is, a reasonably strong secondary peak should appear in the correlation function $R_{AD}(\tau)$, at a time delay larger than that of the main peak, which of course corresponds to the *direct* ray path AD.

In order to obtain an indication of where the secondary peak should occur a test was conducted whereby a rigid board was placed along the lip-line to produce a strong reflection and hence a strong secondary peak. (The point source is located at A.) For *zero* flow, the correlograms without and with the reflecting board are shown in Figures 4.11(a) and 4.11(b), respectively. In Figure 4.11(a) only one peak, corresponding to the direct path AD, is seen. In contrast, Figure 4.11(b) shows two peaks: the first peak corresponds to the direct path, and the second peak corresponds to the reflected path. These results also show small amplitude ripples in the correlograms away from the main peak(s) which are characteristic of the noise radiated from the point source used in the present study.

In the real free-jet shear layer case, if significant internal reflections are present, one should expect to see the kind of behavior seen in Figure 4.11(b). As a matter of fact, for cross-correlations between signals at microphones A and C, it is possible that several peaks may occur, where the first (and most dominant) peak corresponds to the direct path AC and the second (or multiple) peak(s) correspond to one or more of the reflected paths.

To clarify the issue, important results are first presented below. This will be followed by presentation of more general results.

A detailed inspection of $R_{AD}(\tau)$ correlograms for various ray angles, ψ_T, and free-jet Mach numbers has not revealed any strong secondary peak or peaks (multiple reflections) for ray angles up to 100°. In the forward arc, for ray angles larger than 100°, there is some indication of internal reflection which becomes more severe as the ray angle is increased (to a maximum of 140° in the present study).

A typical cross-correlation $R_{AD}(\tau)$ is shown in Figure 4.12 for a source position $x/d_T = 0.22$, ray angle $\psi_T = 60°$ and tunnel velocity $V_T/a_o \doteq 0.10$. The R_{AD} scale has been expanded to show as much detail as possible. Also for comparison, the correlograms $R_{AC}(\tau)$ and $R_{AB}(\tau)$ for the same condition as for $R_{AD}(\tau)$ above are shown in Figures 4.13 and 4.14. All three correlograms look similar. The absence of a secondary peak in both R_{AD} and R_{AC} indicates that internal reflection – if present – is not strong enough to be detected by this method.

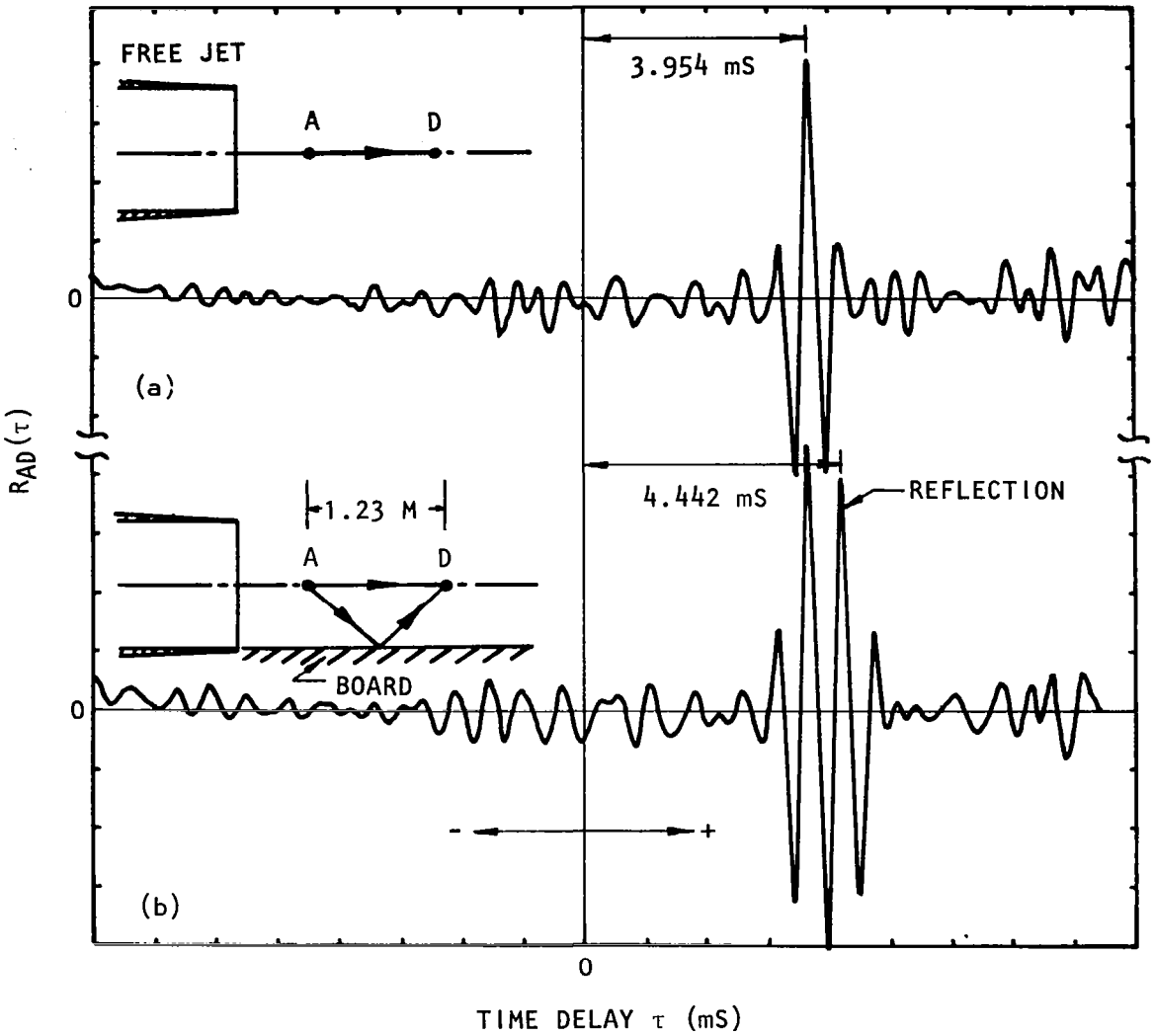

Figure 4.11 Typical cross-correlation functions $R_{AD}(\tau)$ (a) without, and (b) with a hard board placed along the free-jet lip-line; $V_T = 0$.

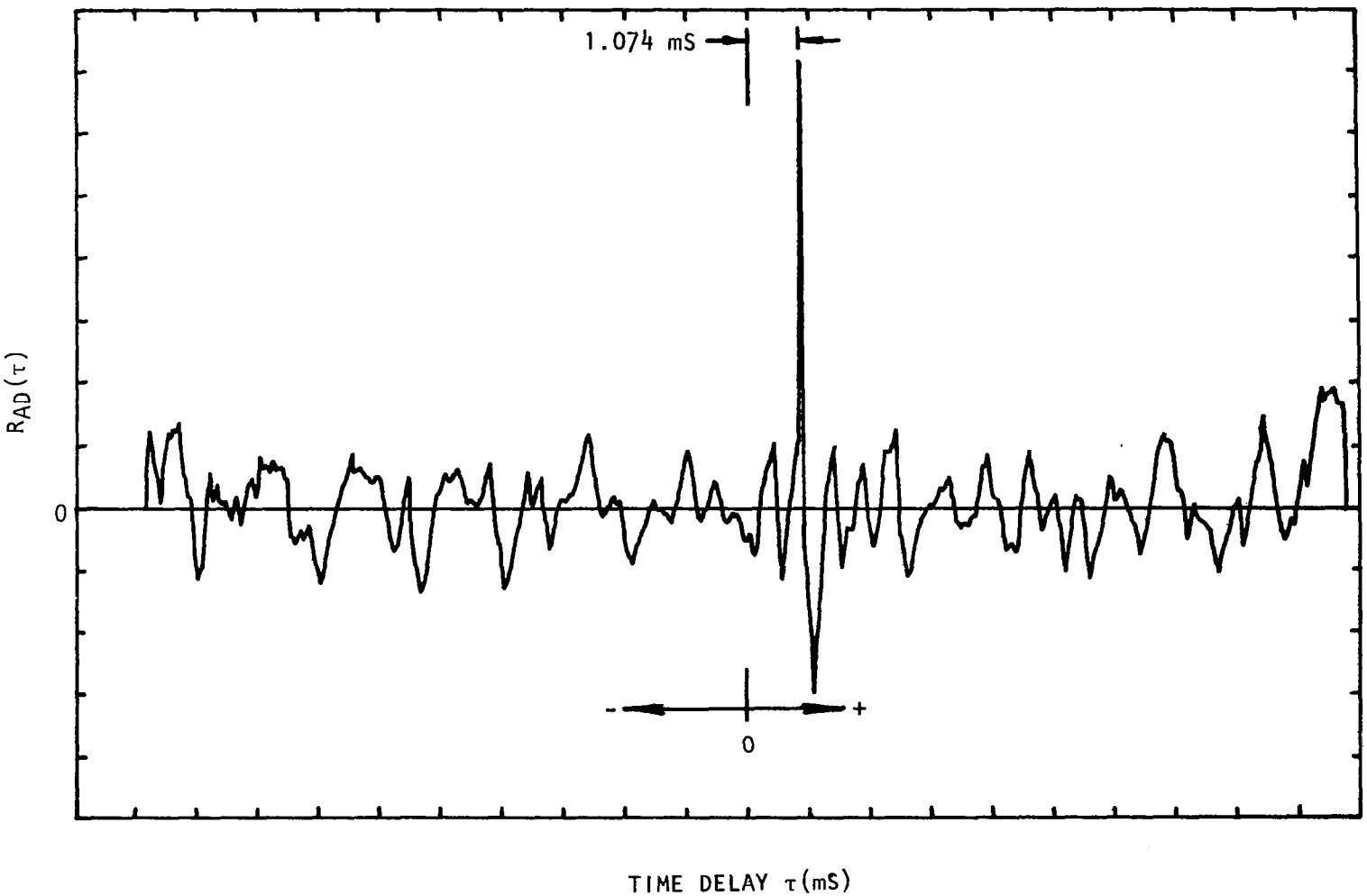

Figure 4.12 Cross-correlation function $R_{AD}(\tau)$; $V_T/a_o \doteq 0.1$, $\psi_T = 60°$. Point source at $x/d_T = 0.22$.

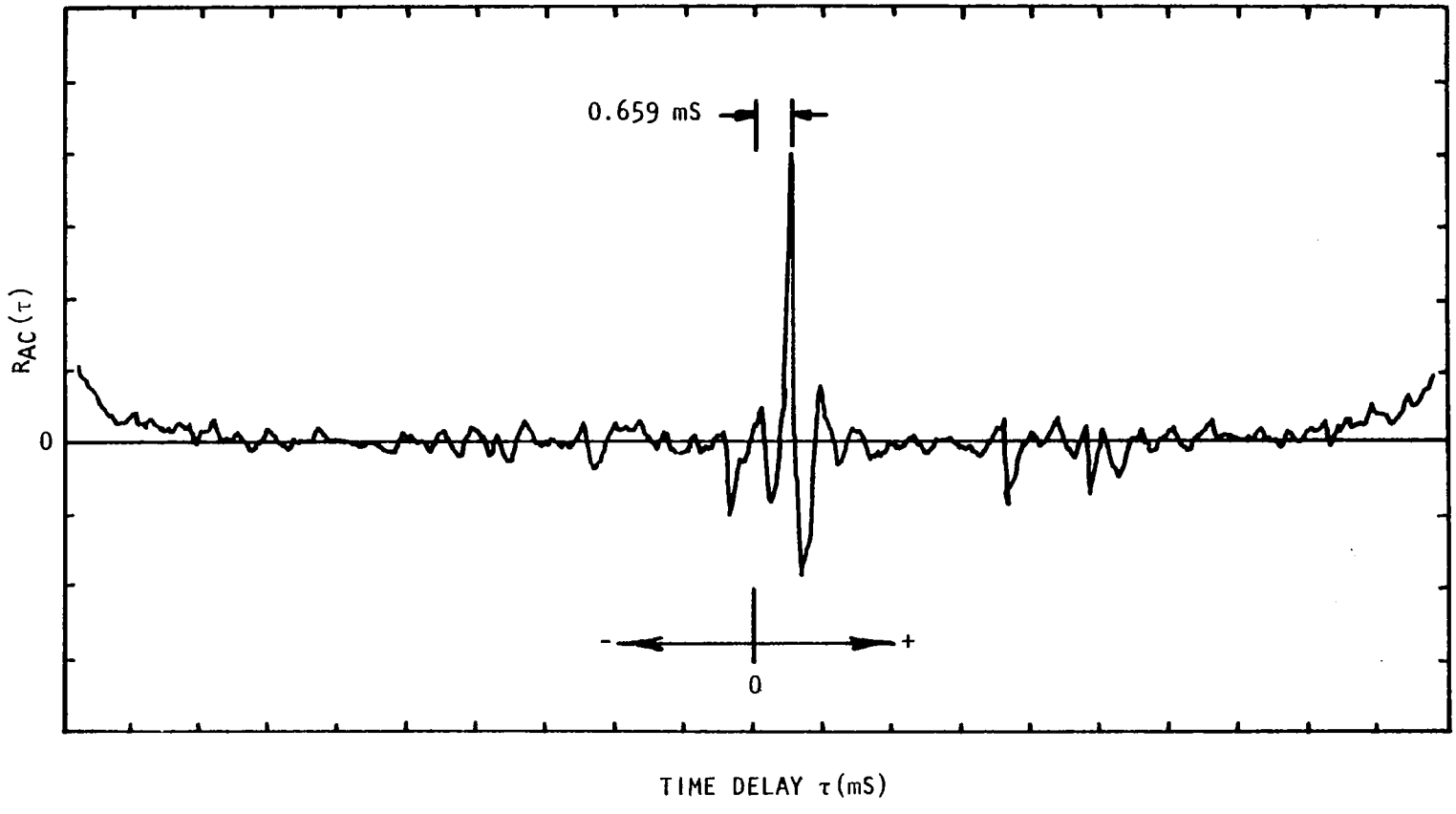

Figure 4.13 Cross-correlation function $R_{AC}(\tau)$; $V_T/a_o \doteq 0.1$, $\psi_T = 60^o$. Point source at $x/d_T = 0.22$.

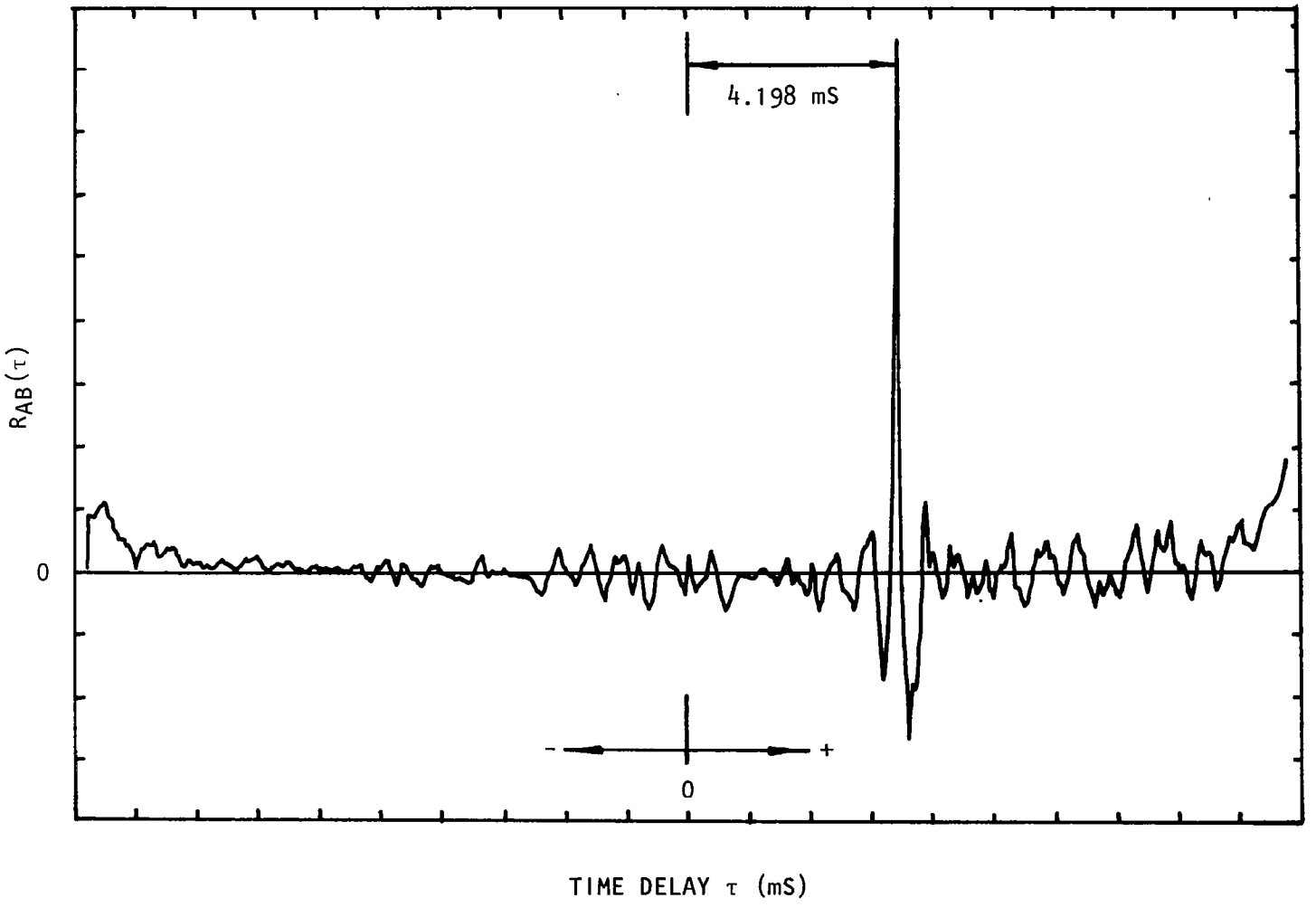

Figure 4.14 Cross-correlation function $R_{AB}(\tau)$; $V_T/a_o \doteq 0.1$, $\psi_T = 60^\circ$. Point source at $x/d_T = 0.22$.

To confirm the absence of any significant reflections by other means, the peak corresponding to the direct path in $R_{AD}(\tau)$ of Figure 4.12 was shifted to zero time delay and the cross-correlation function was then Fourier transformed in order to obtain the zero time delay phase relationship between the signals at A and D. The resulting phase spectrum is shown in Figure 4.15.

The fact that the phase between A and D is almost zero between 1 KHz to about 12 KHz indicates that the only signal (correlated with signal A) which is arriving at microphone D is via the direct path AD. (The main peak in Figure 4.12 occurs at $\tau = 1.074$ ms, which corresponds to the time taken for sound to travel the direct path distance AD.) Had there been internal reflection, the phase would have been different from zero. The fact that the phase $\phi_{AD}(f)$ is far from zero for frequencies below 1 KHz and above 12 KHz is possibly due to low signal-to-noise ratio at these frequencies. The point source, especially in the presence of the flow, was rather inefficient at these frequencies. Minor deviations from zero in the value of the phase were not typical of $\phi_{AD}(f)$ alone. The same order of magnitude of deviation from zero was found in $\phi_{AB}(f)$, where it is known that microphone B located outside the free jet is recording only the direct signal. The peak of $R_{AB}(\tau)$ in Figure 4.14 was also moved to zero time delay and the function was then Fourier transformed to obtain ϕ_{AB}. This is shown in Figure 4.16. Once again, the phase is almost zero between 1 KHz and 12 KHz, which confirms that at B also, the signal is arriving through the direct path alone. The order of magnitude of variation in phase about zero line is similar for both $\phi_{AB}(f)$ and $\phi_{AD}(f)$. Similar results were obtained when the above procedure was performed on $R_{AC}(\tau)$ shown in Figure 4.13. The resultant phase spectrum $\phi_{AC}(f)$ is shown in Figure 4.17. To increase the resolution, frequencies up to 10 KHz only are shown. Once again, the major deviation from zero phase occurs only at lower frequencies (below 1 KHz) showing the absence of reflection at other frequencies. Presence of internal reflection at low frequencies cannot be ruled out completely at this point. This will be discussed later after some more results have been presented.

It was found that the presence or absence of internal reflection could most reliably be detected at lower free-jet velocities and also when the ray angles were large enough such that the distance between the two microphones A and D was not too large. At ray angles (ψ_T) of 30° and 40°, the signal received by microphone D was much too small at higher free-jet velocities. At these velocities, the extraneous noise generated by the interaction between the free-jet flow and the microphone and point source supports was rather high in some instances and was strongly correlated at microphones A, C and D. Some cross-correlation functions were also contaminated by vortex-shedding noise, and thus, even if internal reflection was present it could not be detected due to the oscillatory nature of the correlograms. Most of the conclusions reached are, therefore, based upon results at lower velocities (mostly up to $V_T/a_o = 0.18$). Both contaminated and uncontaminated results are, however, presented here. Typical results are shown in Figure 4.18 through 4.32 for the cross-correlation functions $R_{AD}(\tau)$ and $R_{AC}(\tau)$; corresponding parameter values appear in Table 4.3. Cross-correlation functions $R_{AD}(\tau)$ and some $R_{AC}(\tau)$ are presented. These functions are not normalized and hence they represent a measure of the mean of the product of the rms of the two signals.

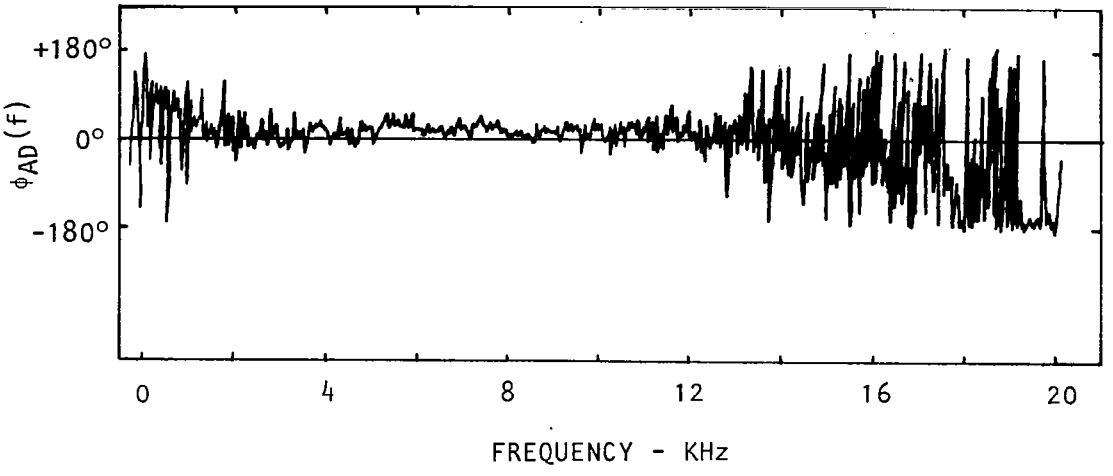

Figure 4.15 Phase spectrum $\phi_{AD}(f)$ obtained by moving peak of $R_{AD}(\tau)$ of figure 4.12 to zero time delay before Fourier transform.

(Analysis bandwidth $\Delta f = 40$ Hz)

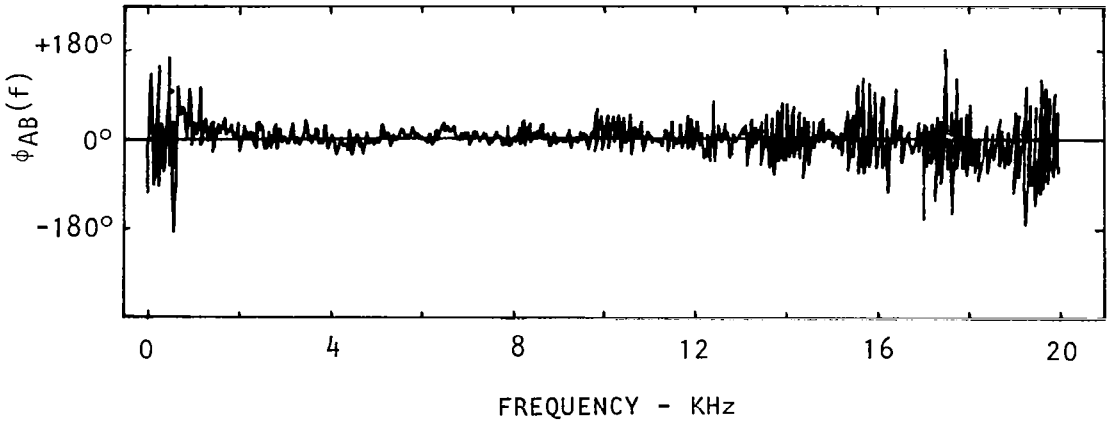

Figure 4.16 Phase spectrum $\phi_{AB}(f)$ obtained by moving peak of $R_{AB}(\tau)$ of figure 4.14 to zero time delay before Fourier transform.

(Analysis bandwidth $\Delta f = 40$ Hz)

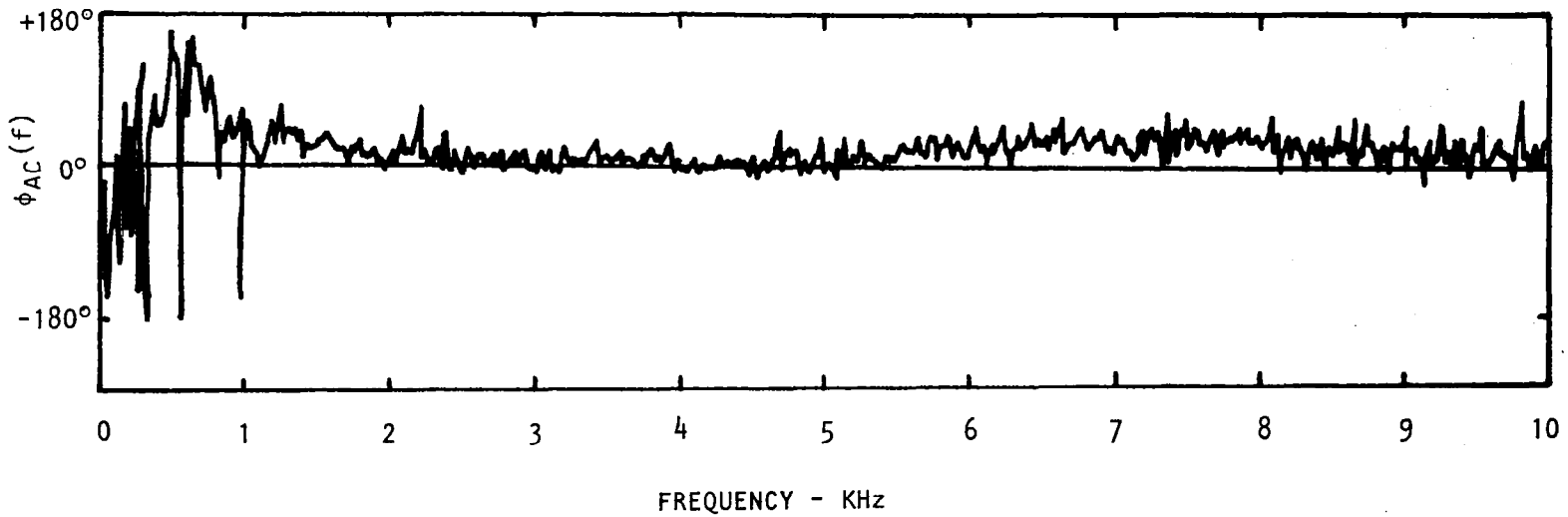

Figure 4.17 Phase spectrum $\phi_{AC}(f)$ obtained by moving peak of $R_{AC}(\tau)$ of figure 4.13 to zero time delay before Fourier transform.

(Analysis bandwidth $\Delta f = 20$ Hz)

Table 4.3 Figures showing correlogram data for internal reflection tests

Figure Number	Correlogram	ψ_T (Degrees)	V_T/a_o (Nominal)	Point Source Location x/d_T	Run #	Calculated Reflection Peak τ_{ref}(ms)	Comments
4.18(a)	$R_{AD}(\tau)$	30	0.0	0.22	822	--	--
4.18(b)			0.090		824	3.831	No reflection
4.18(c)			0.180		826	3.581	Contaminated
4.18(d)			0.270		827	3.389	No sign of direct or reflected peak
4.19(a)	$R_{AD}(\tau)$	40	0.0	0.22	791	--	--
4.19(b)			0.090		793	3.010	No reflection
4.19(c)			0.180		795	2.840	No sign of direct or reflected peak
4.19(d)			0.270		797	2.710	Contaminated
4.20(a)	$R_{AC}(\tau)$	40	0.0	0.22	791	--	--
4.20(b)			0.090		793		No reflection
4.20(c)			0.180		795		Possible reflection
4.20(d)			0.270		797		Contaminated
4.21(a)	$R_{AD}(\tau)$	40	0.0	0.99	1013	--	--
4.21(b)			0.090		1015	3.012	No reflection
4.21(c)			0.180		1017	2.846	No sign of direct or reflected peak
4.21(d)			0.270		1019	2.717	No sign of direct or reflected peak
4.22	$R_{AD}(\tau)$	40	0.090	0.99	1015	3.012	Figure 4.21(b) plotted on enlarged scale (No reflection)

Table 4.3 Continued

Figure Number	Correlogram	ψ_T (Degrees)	V_T/a_o (Nominal)	Point Source Location x/d_T	Run #	Calculated Reflection Peak τ_{ref}(ms)	Comments
4.23(a)	$R_{AD}(\tau)$	60	0.0	0.99	1069	--	--
4.23(b)			0.090		1071	2.291	No reflection
4.23(c)			0.135		1072	2.246	No reflection
4.23(d)			0.270		1073	2.209	No sign of direct or reflected peak, some contamination
4.24(a)	$R_{AD}(\tau)$	100	0.0	0.99	1085	--	--
4.24(b)			0.090		1087	2.133	No reflection
4.24(c)			0.180		1089	2.195	No reflection
4.24(d)			0.270		1091	2.289	Possible reflection
4.25(a)	$R_{AD}(\tau)$	120	0.0	0.99	1115	--	--
4.25(b)			0.090		1117	2.495	No reflection
4.25(c)			0.180		1119	2.636	Possible reflection, some contamination
4.26(a)	$R_{AD}(\tau)$	100	0.0	2.00	1293	--	--
4.26(b)			0.090		1294	2.140	No reflection
4.26(c)			0.180		1295	2.206	No reflection
4.26(d)			0.225		1296	2.251	Possible reflection, some contamination
4.26(e)			0.270		1297	2.300	Possible reflection, some contamination

Table 4.3 Continued

Figure Number	Correlogram	ψ_T (Degrees)	V_T/a_o (Nominal)	Point Source Location x/d_T	Run #	Calculated Reflection Peak τ_{ref}(ms)	Comments
4.27(a)	$R_{AD}(\tau)$	100	0.0	2.00	1293	--	Figures 4.26(a) through (4.26(e) plotted on enlarged scale
4.27(b)			0.090		1294	2.140	No reflection
4.27(c)			0.180		1295	2.206	No reflection
4.27(d)			0.225		1296	2.251	Possible reflection, some contamination
4.27(e)			0.270		1297	2.300	No reflection
4.28(a)	$R_{AD}(\tau)$	110	0.0	2.00	1315	--	--
4.28(b)			0.090		1316	2.277	No reflection
4.28(c)			0.180		1317	2.383	No reflection
4.28(d)			0.225		1318	2.447	No reflection, some contamination
4.28(e)			0.270		1319	2.600	No reflection, some contamination
4.29(a)	$R_{AD}(\tau)$	110	0.0	2.00	1315	--	Figures 4.28(a), 4.28(b) and 4.28(c) plotted on enlarged scale
4.29(b)			0.090		1316	2.277	No reflection
4.29(c)			0.180		1317	2.383	Possible reflection

Table 4.3 Concluded

Figure Number	Correlogram	ψ_T (Degrees)	V_T/a_o (Nominal)	Point Source Location x/d_T	Run #	Calculated Reflection Peak τ_{ref}(ms)	Comments
4.30(a)	$R_{AD}(\tau)$	120	0.0	2.00	1234	--	--
4.30(b)			0.090		1235	2.506	Possible reflection, considerable contamination
4.30(c)			0.180		1236	2.656	No reflection, considerable contamination
4.30(d)			0.225		1237	2.747	No reflection, considerable contamination
4.30(e)			0.270		1238	2.848	Possible reflection, considerable contamination
4.31(a)	$R_{AD}(\tau)$	140	0.0	2.00	1337	--	--
4.31(b)			0.090		1343	3.458	Possible reflection
4.31(c)			0.180		1344	3.759	Strong reflection
4.31(d)			0.225		1345	3.934	Strong reflection
4.31(e)			0.270		1341	4.069	Very strong reflection
4.32(a)	$R_{AC}(\tau)$	140	0.0	2.00	1337		--
4.32(b)			0.090		1343		No reflection
4.32(c)			0.180		1344		No reflection
4.32(d)			0.225		1345		Possible reflection
4.32(e)			0.270		1341		Possible reflection

Some of the cross-correlation functions are shown plotted on two time scales, one much larger than the other. Wherever this occurs it is indicated in the table and also on the appropriate figures. Also, owing to some functional constraints inherent to the equipment used to analyze these results (SD 360), all correlograms do not necessarily have the same vertical scale. Comments (or observations) relevant to each correlogram are also given in Table 4.3. Where possible, the calculated time delay at which reflection peak would have occurred (had internal reflection been dominant) are indicated by τ_{ref}.

After a close inspection of the $R_{AD}(\tau)$ and $R_{AC}(\tau)$ results shown in Figures 4.18 to 4.32, the following conclusions can be drawn.

There is little evidence of significant internal reflection in the rear arc, and possibly up to $\psi_T = 120°$ in the forward arc. In fact, the amplitude calibration results that will be presented in Section 4.4 indirectly show that for angles up to $\psi_T = 120°$, internal reflection is unimportant. A closer analysis of $R_{AD}(\tau)$ at $\psi_T = 30°$ and 40° (Figures 4.18, 4.19 and 4.21) indicates that for higher free-jet Mach numbers, the microphones located on the centerline downstream of the point source receive very little acoustic energy via the direct path or the reflected path. For these same conditions, however, ample energy could be measured along the incident ray, as indicated by the cross-correlations between microphones A and C [see $R_{AC}(\tau)$ in Figure 4.20].

Those correlograms which were not contaminated by other correlated noise sources and which were plotted on enlarged scales also did not reveal a second peak, thus confirming the absence of any significant internal reflection up to free-jet Mach number (M_T) of 0.18 and ray angle (ψ_T) up to 110° [see Figures 4.22, 4.27 and 4.29, which show the correlograms of Figures 4.21(b), 4.26 and 4.28, respectively, on an enlarged scale].

Analysis of the results in the manner shown in Figures 4.15, 4.16 and 4.17 (where the peak corresponding to the direct path was moved to zero time delay and then Fourier transformed to obtain the phase spectrum) was also conducted for some more correlograms. A mean of zero phase was obtained for the majority of the analyzed data that did not show a second peak and contamination in the correlograms. Typical phase spectra $\phi_{AD}(f)$ with the point source located at $x/d_T = 0.99$ are shown in Figure 4.33(a) and 4.33(b), which corresponds to the correlograms $R_{AD}(\tau)$ presented in Figures 4.24(b) and 4.24(c). Once again, it is not possible to isolate the effects at frequencies below 1 KHz: Frequencies up to 300 Hz were filtered before processing (see Section 3.2.4); therefore, no deductions or conclusions can be drawn from phase information up to 300 Hz. For frequencies between 300 Hz and approximately 1 KHz, the phase $\phi_{AD}(f)$ was found to be non-zero even for zero flow, as shown typically in Figure 4.34 which is the phase spectrum of $R_{AD}(\tau)$ shown in Figure 4.23(a) ($\psi_T = 60°$, $x/d_T = 0.99$) with the peak of $R_{AD}(\tau)$ shifted to zero time delay.

Since the point source was not very efficient at low frequencies, the above behavior could be the result of low signal-to-noise ratio at these frequencies.

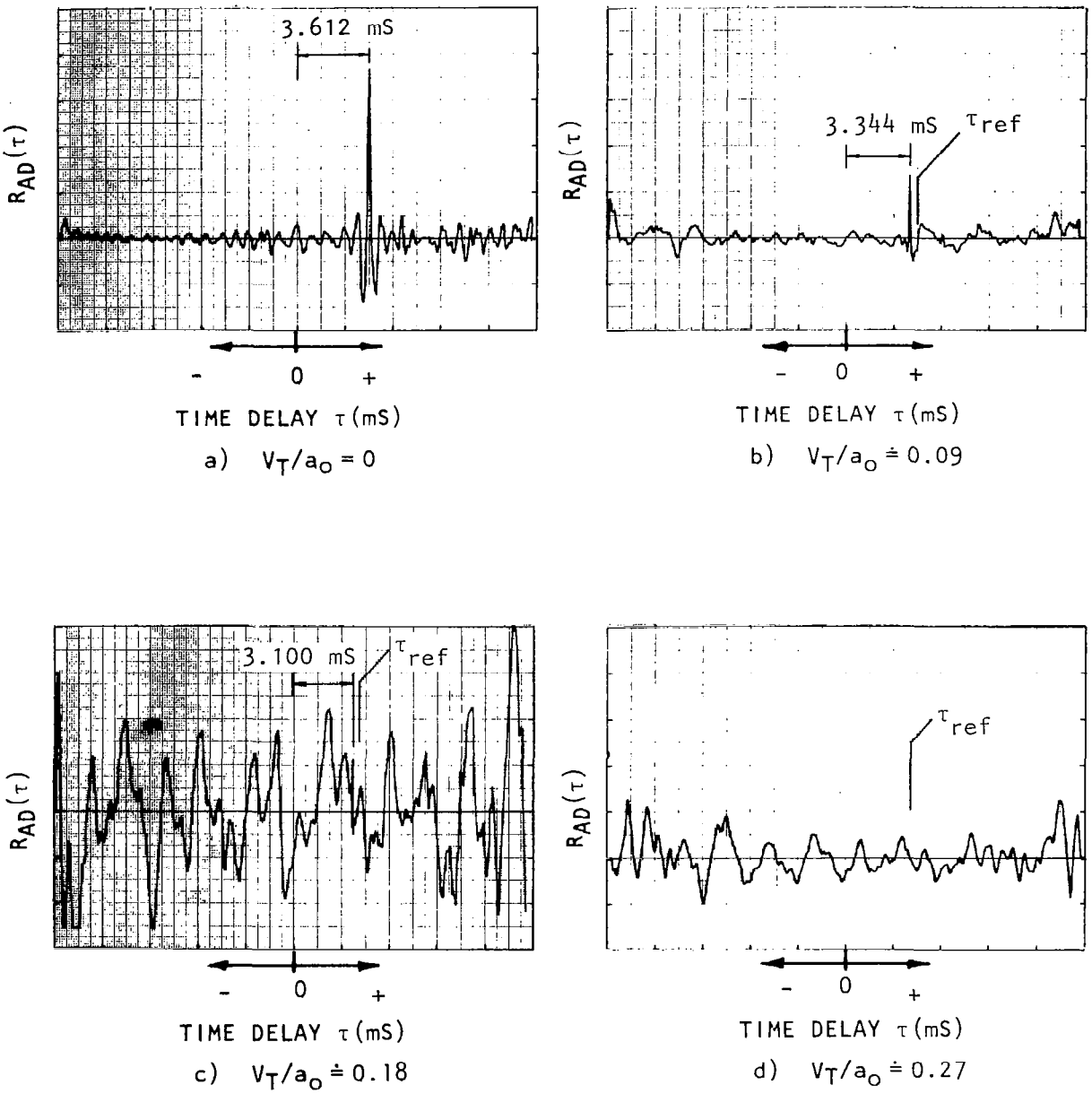

Figure 4.18 Cross-correlation function $R_{AD}(\tau)$: $\psi_T = 30^o$, point source at $x/d_T = 0.22$.

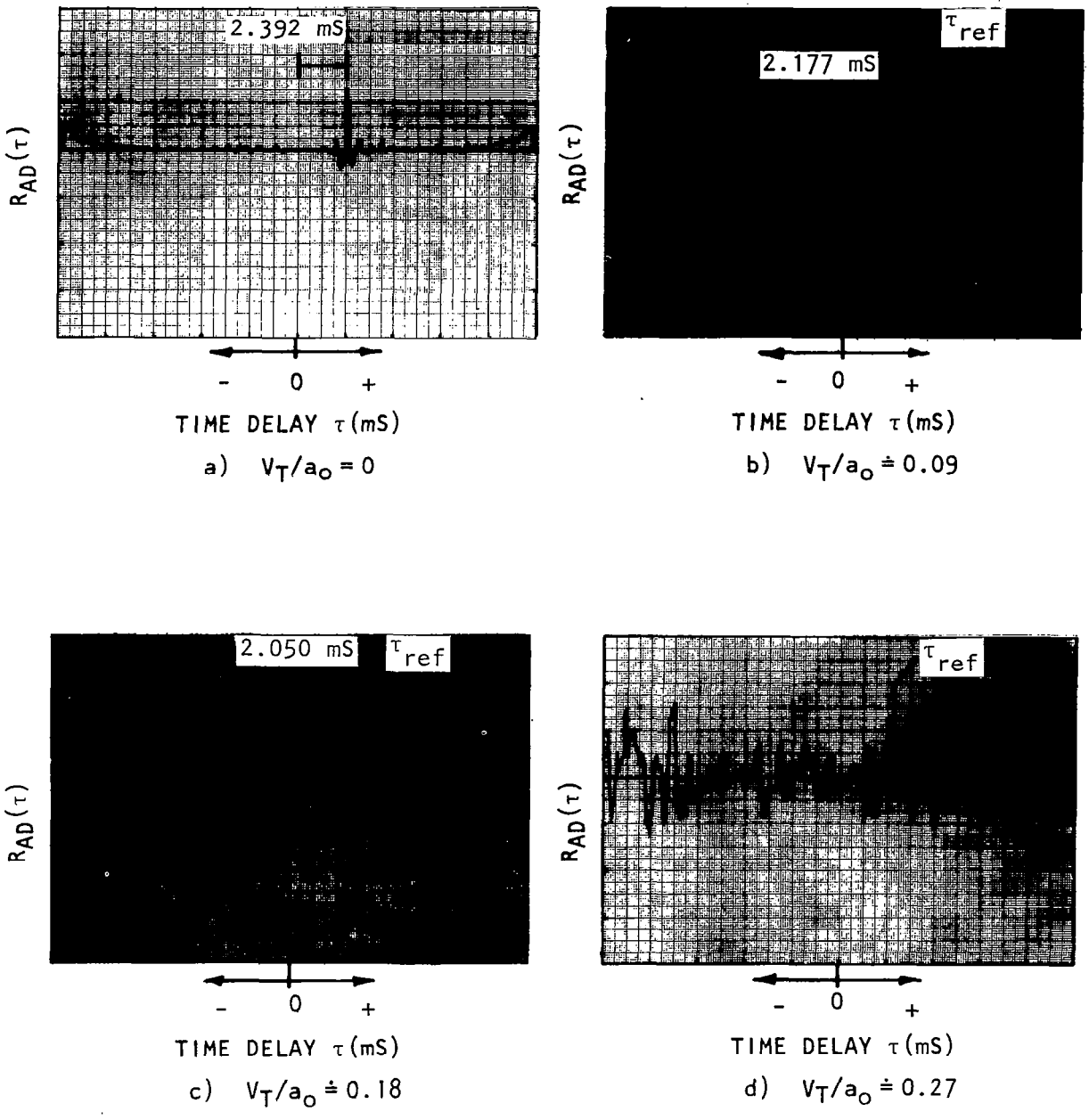

Figure 4.19 Cross-correlation function $R_{AD}(\tau)$: $\psi_T = 40°$, point source at $x/d_T = 0.22$.

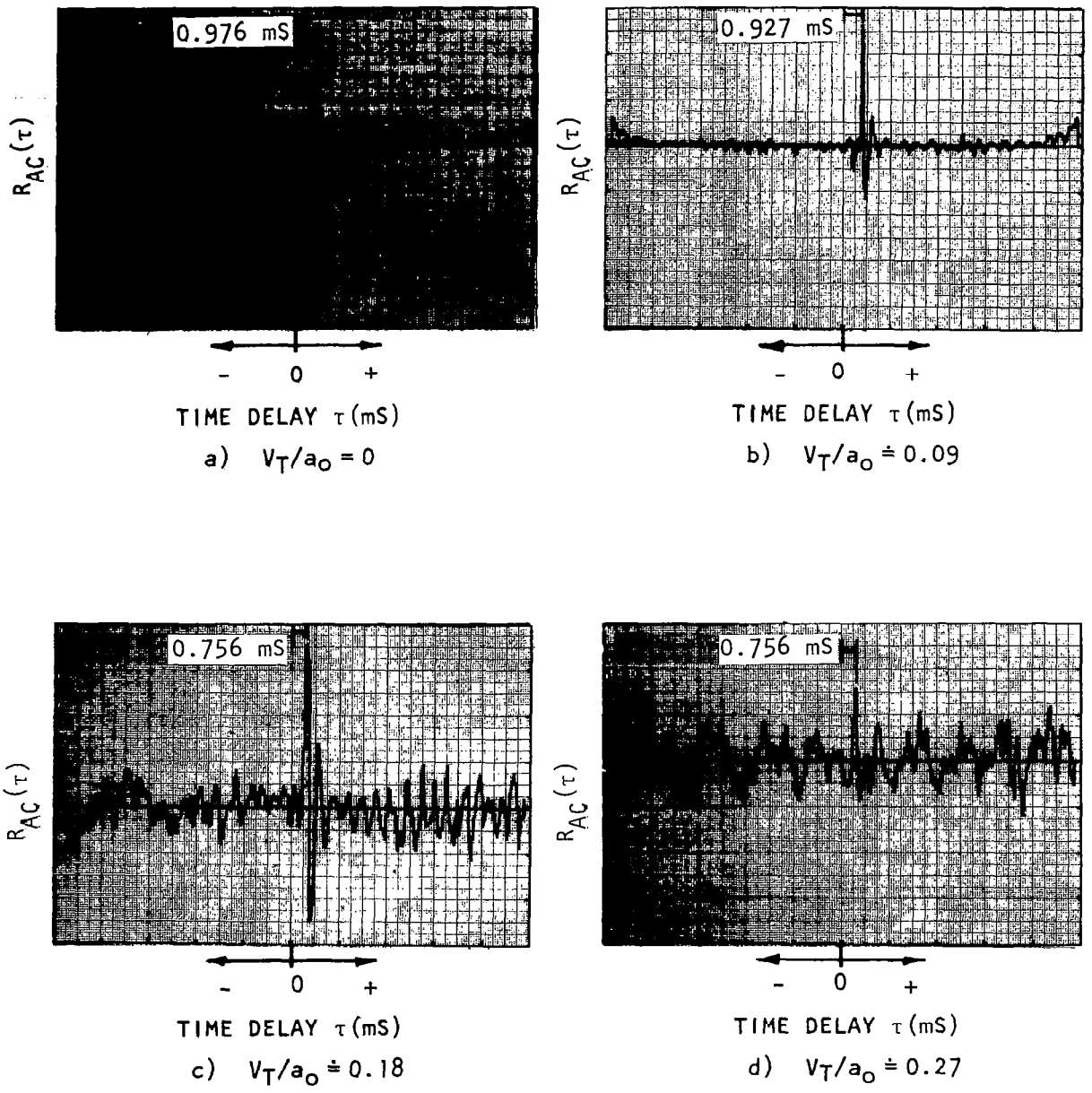

Figure 4.20 Cross-correlation function $R_{AC}(\tau)$: $\psi_T = 40°$, point source at $x/d_T = 0.22$.

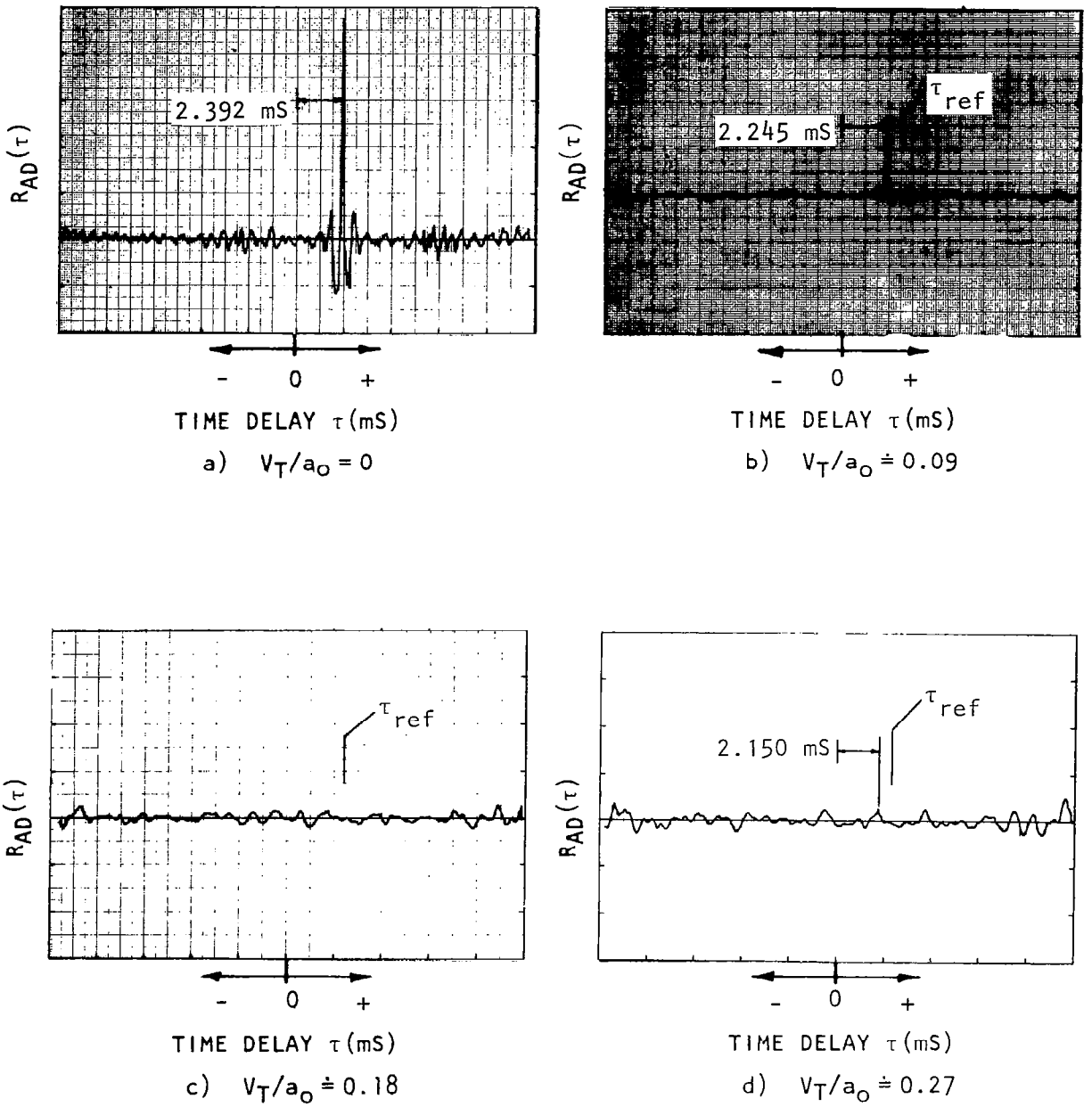

Figure 4.21 Cross-correlation function $R_{AD}(\tau)$: $\psi_T = 40°$, point source at $x/d_T = 0.99$.

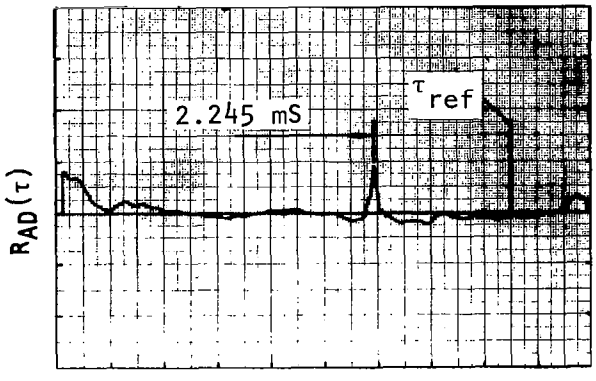

Figure 4.22 Cross-correlation function $R_{AD}(\tau)$: $\psi_T = 40°$, point source at $x/d_T = 0.99$. (Figure 4.21(b) plotted on enlarged scale.) $V_T/a_o = 0.09$

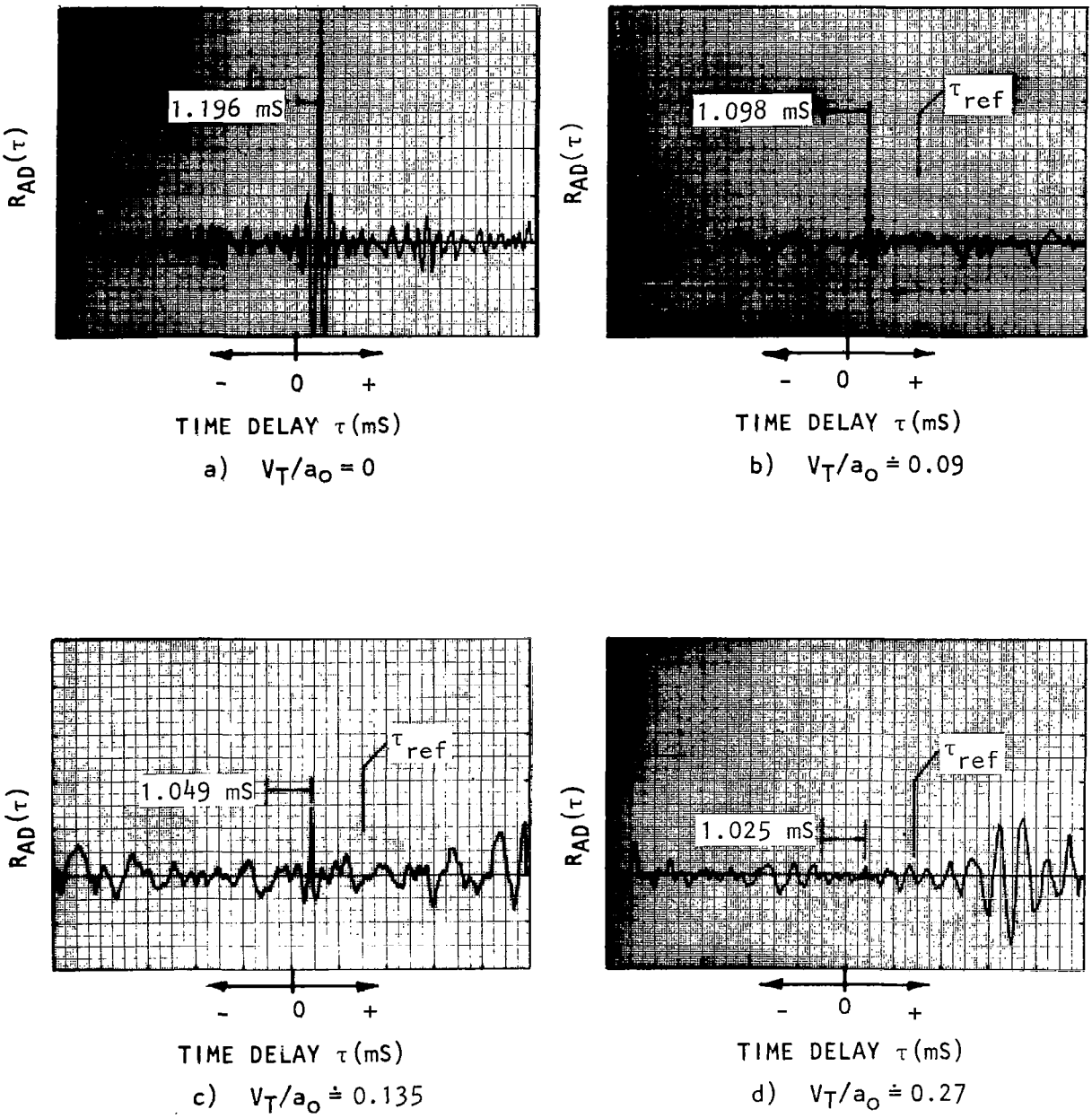

Figure 4.23 Cross-correlation function $R_{AD}(\tau)$: $\psi_T = 60°$, point source at $x/d_T = 0.99$.

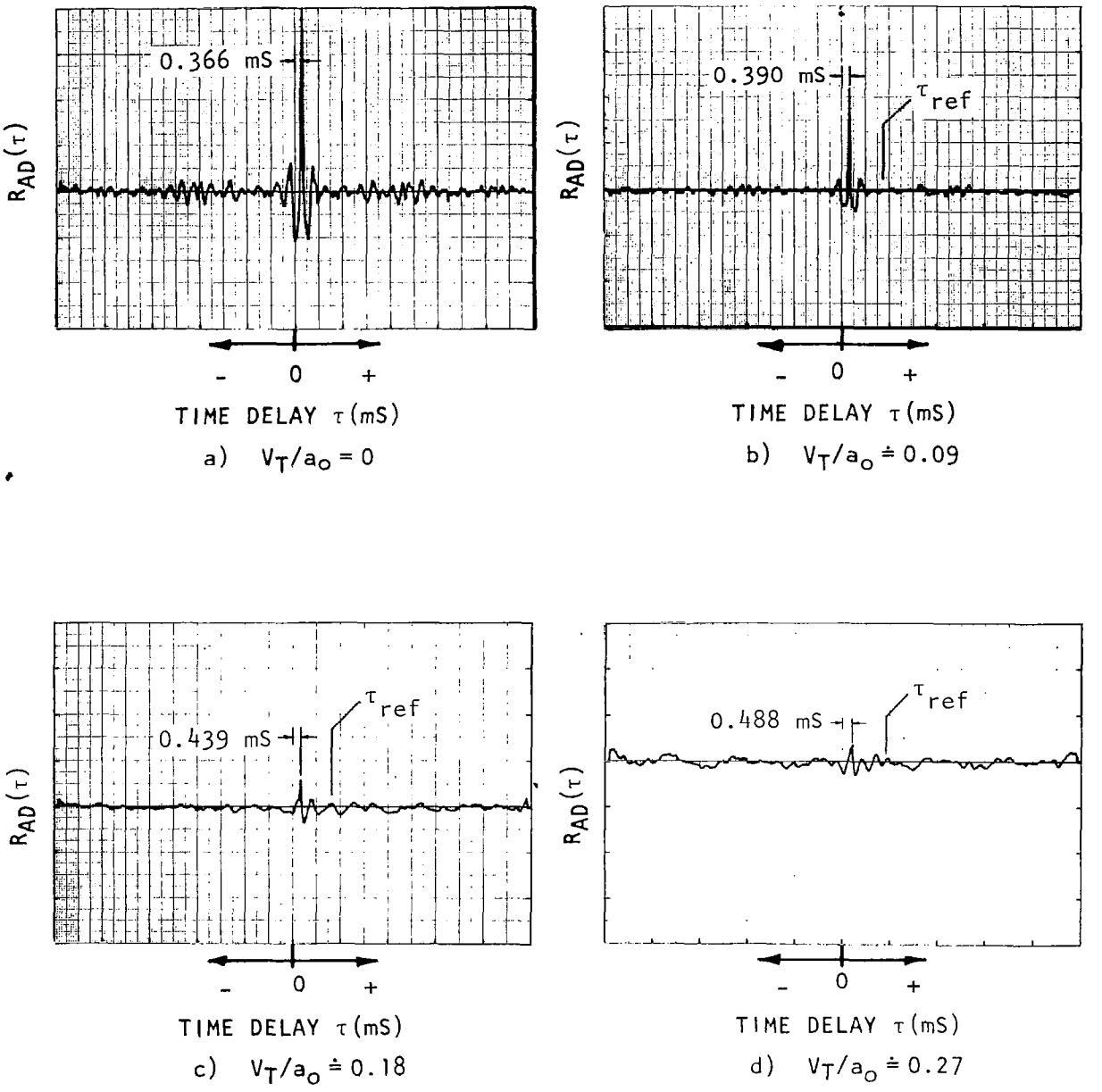

Figure 4.24 Cross-correlation function $R_{AD}(\tau)$: $\psi_T = 100°$, point source at $x/d_T = 0.99$.

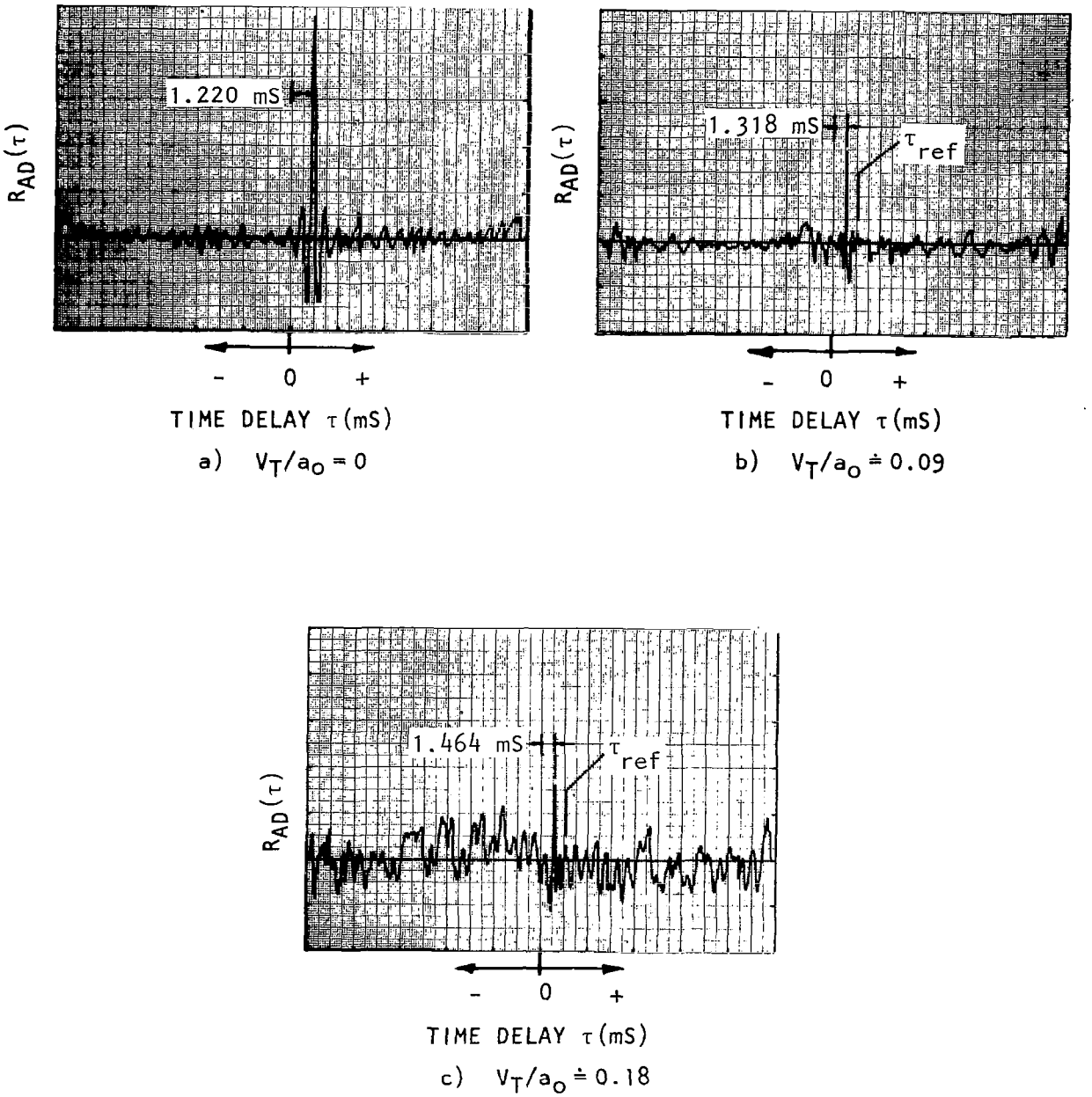

Figure 4.25 Cross-correlation function $R_{AD}(\tau)$: $\psi_T = 120°$, point source at $x/d_T = 0.99$.

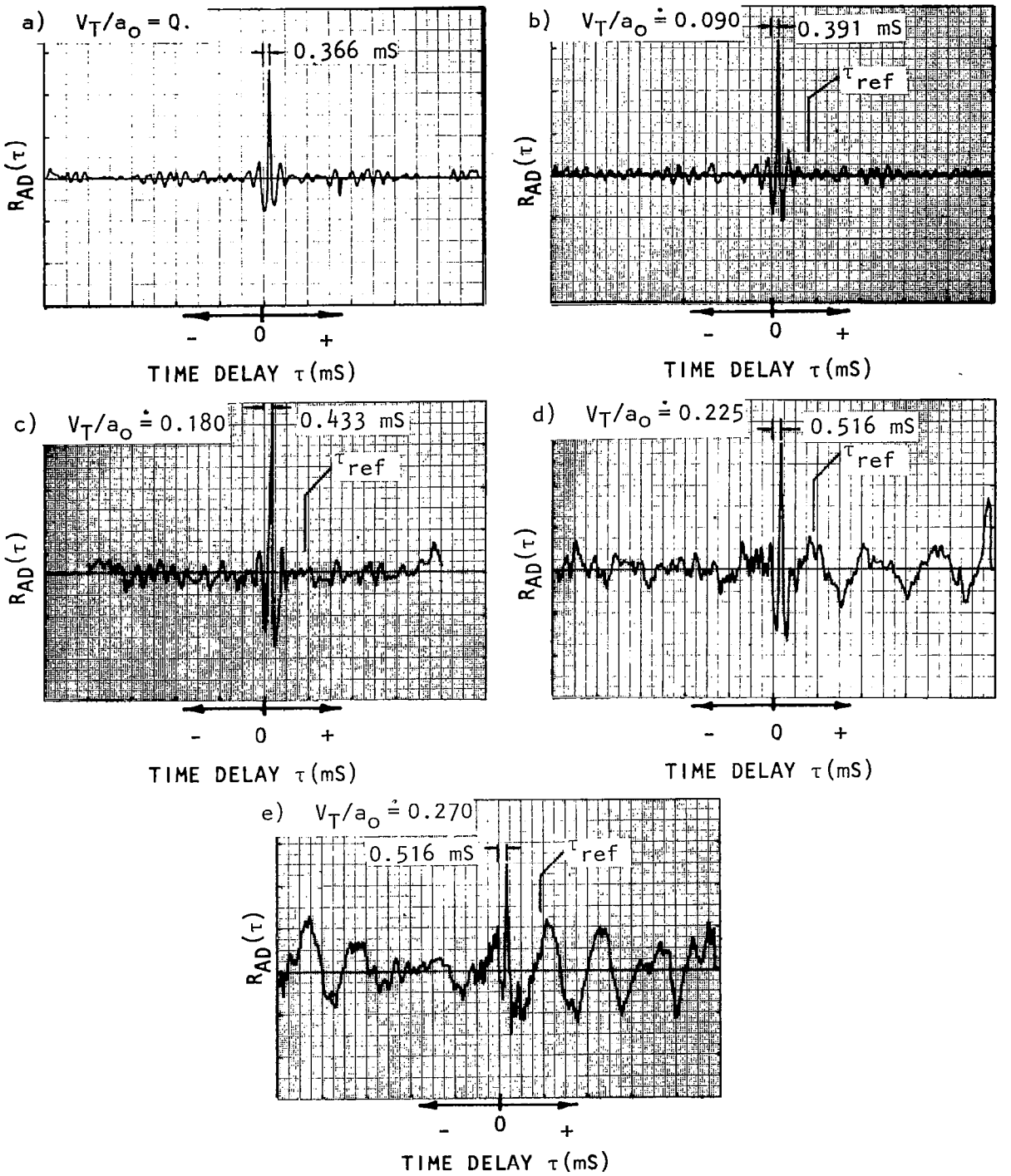

Figure 4.26 Cross-correlation function $R_{AD}(\tau)$: $\psi_T = 100°$, point source at $x/d_T = 2.00$.

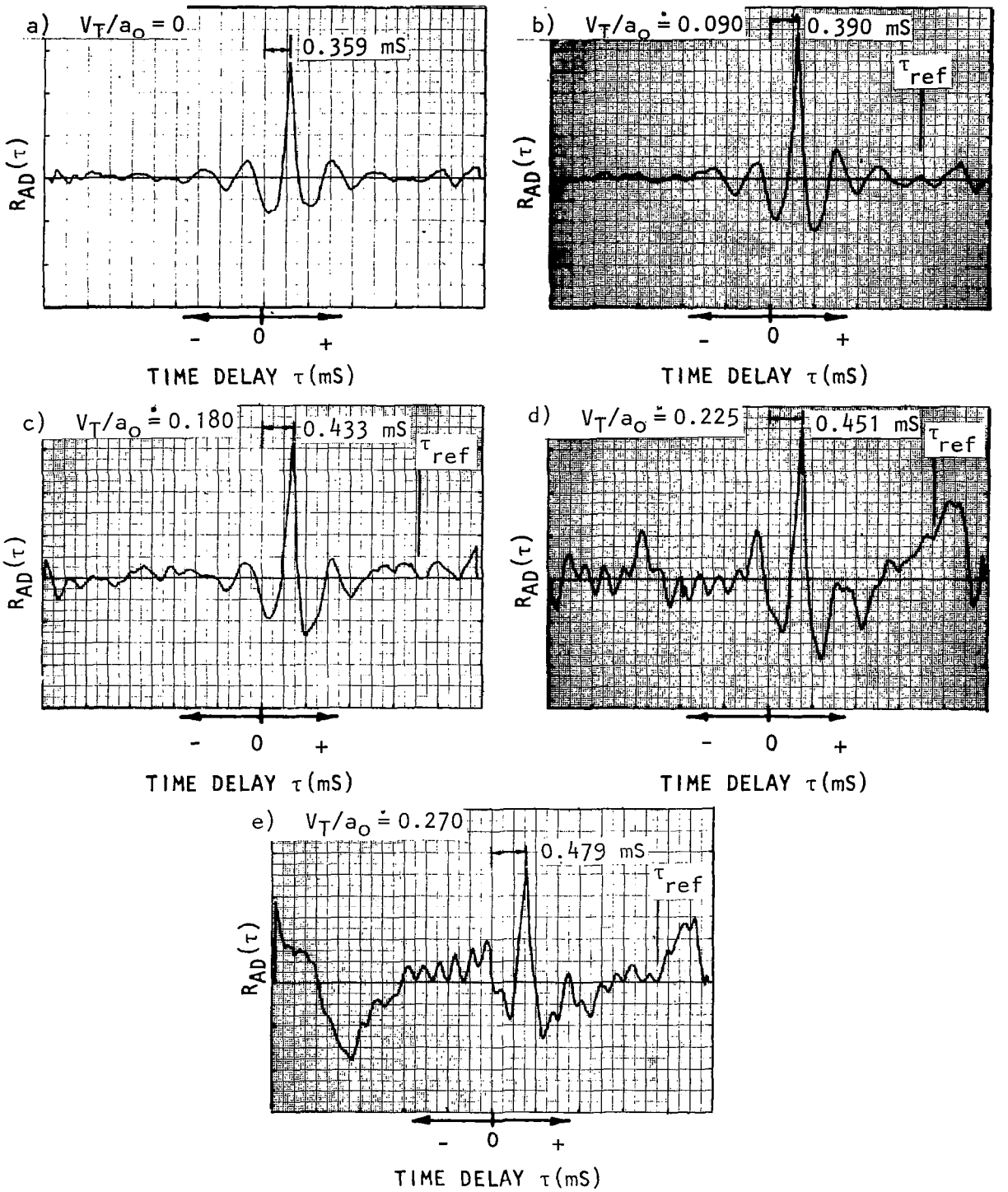

Figure 4.27 Cross-correlation function $R_{AD}(\tau)$: $\psi_T = 100°$, point source at $x/d_T = 2.00$.

(Figure 4.26 plotted on enlarged scale.)

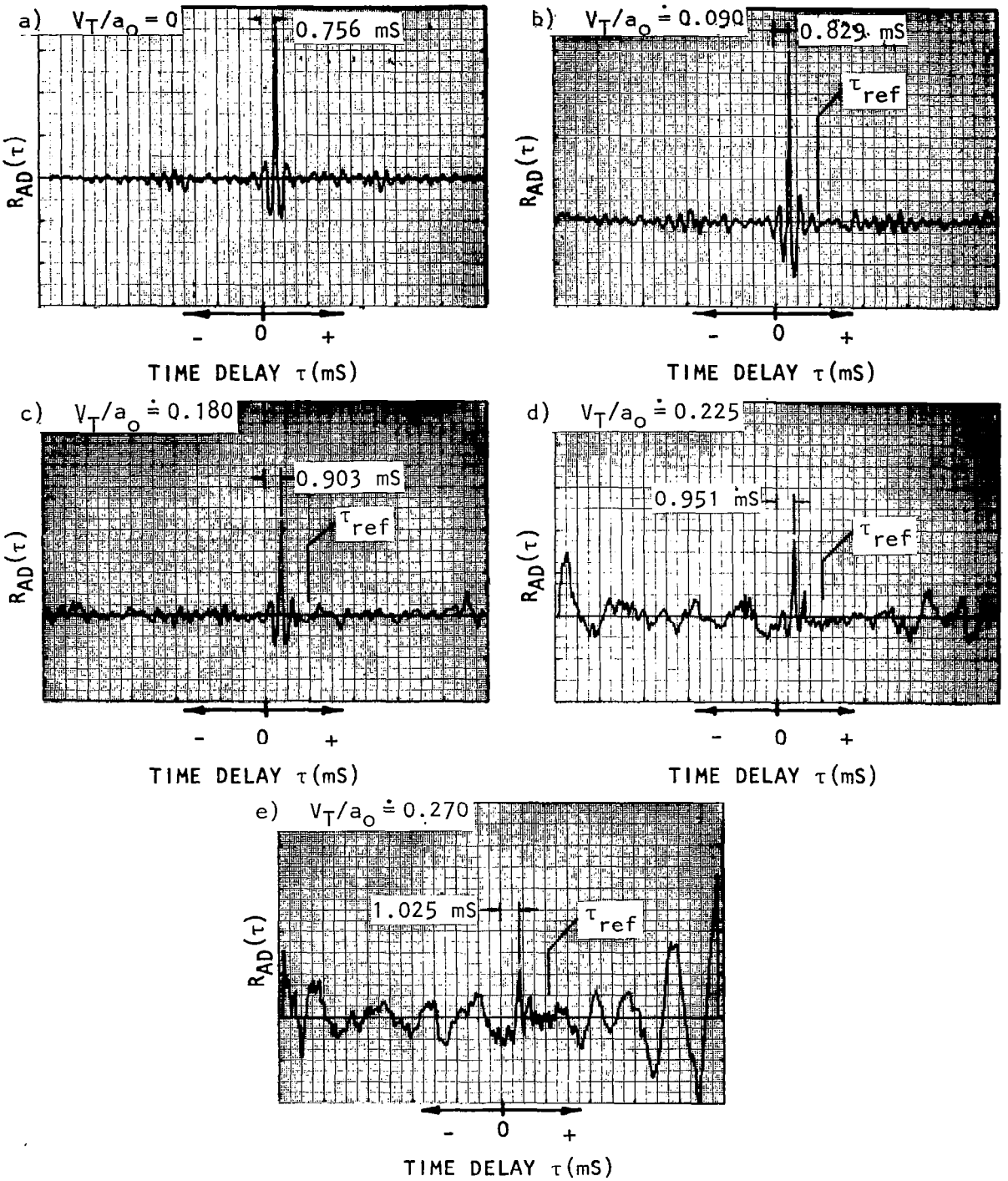

Figure 4.28 Cross-correlation function $R_{AD}(\tau)$: $\psi_T = 110°$, point source at $x/d_T = 2.00$.

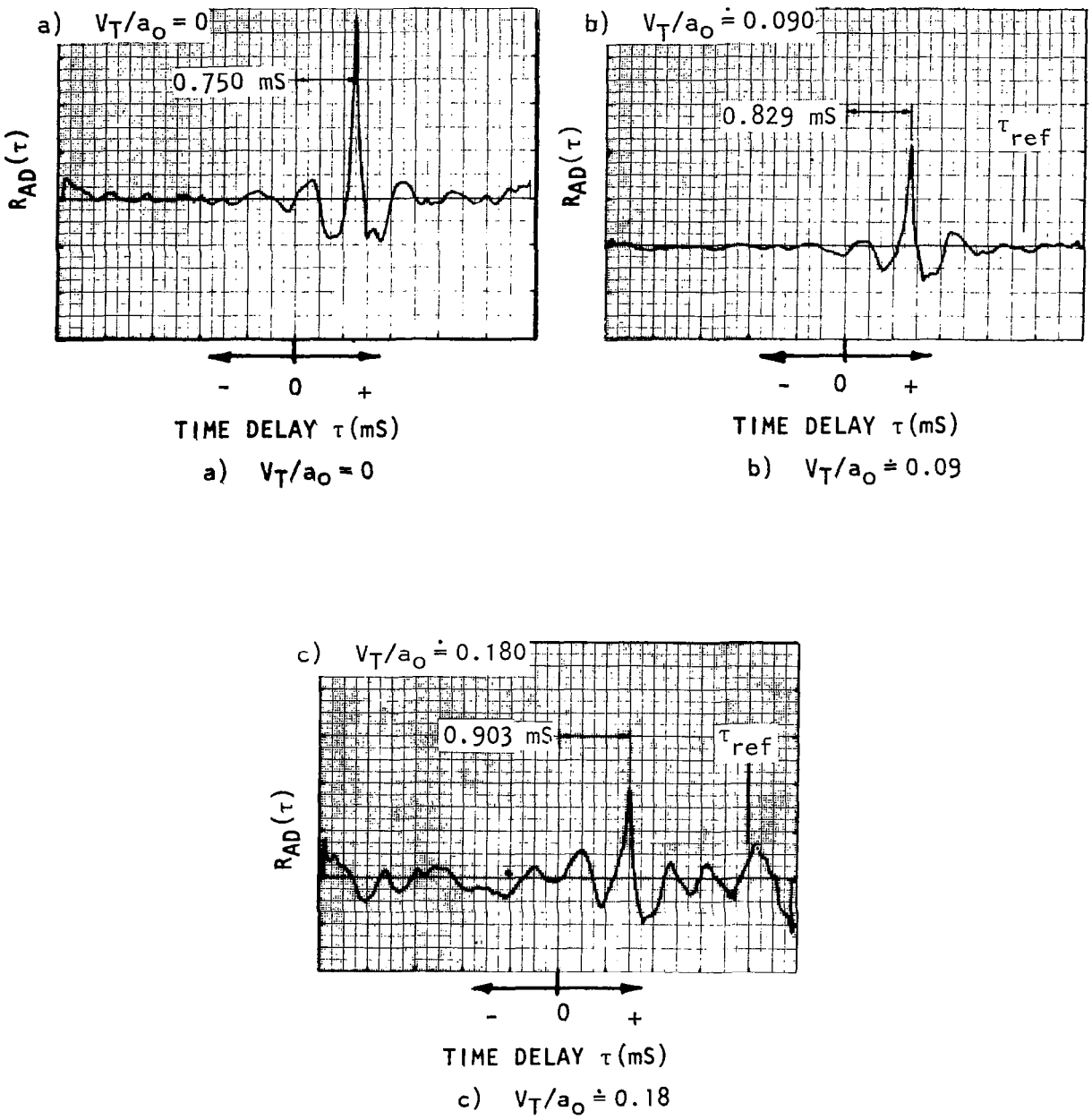

Figure 4.29 Cross-correlation function $R_{AD}(\tau)$: $\psi_T = 110°$, point source at $x/d_T = 2.00$.

(Figure 4.28(a)-4.28(c) plotted on enlarged scale.)

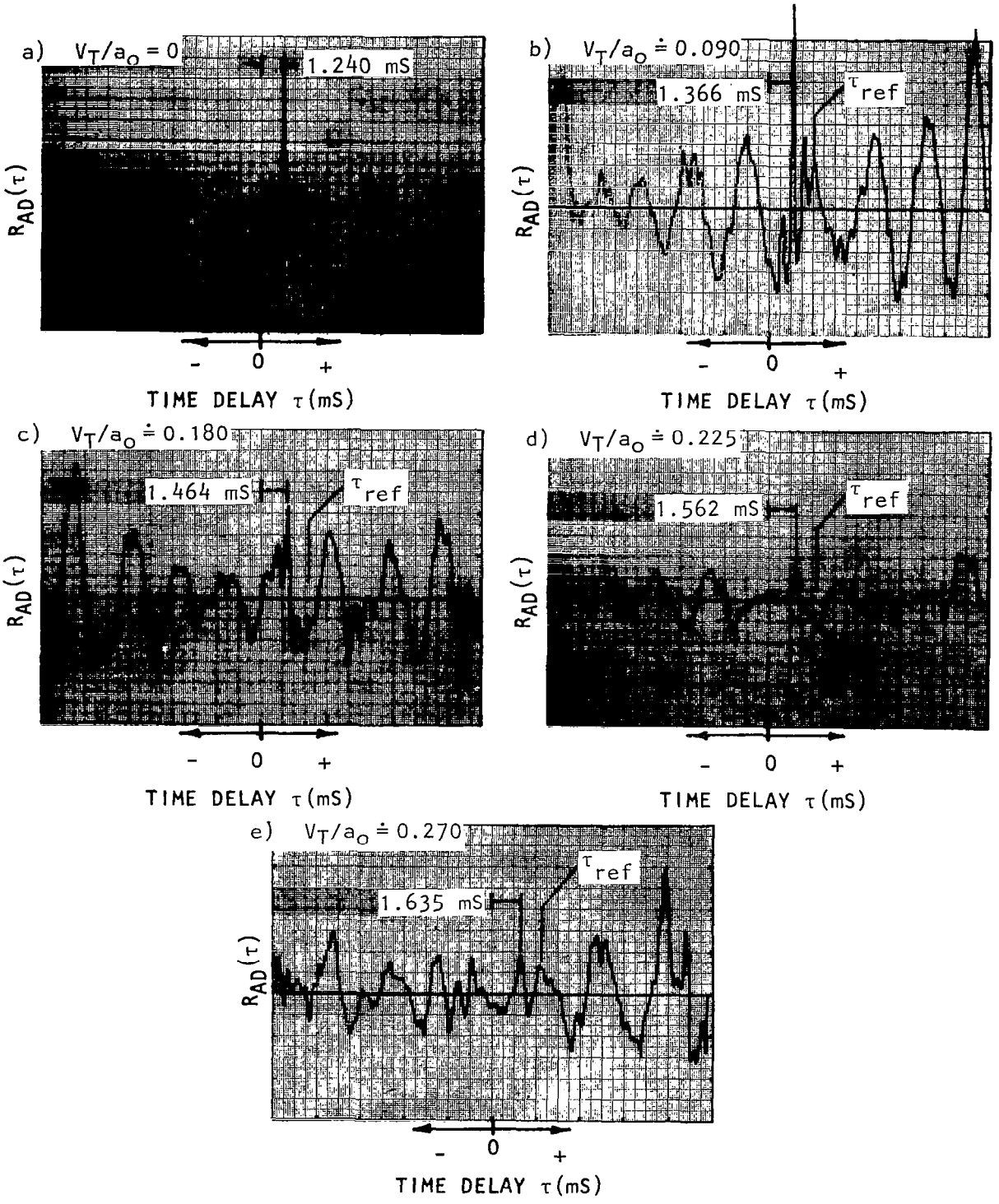

Figure 4.30 Cross-correlation function $R_{AD}(\tau)$: $\psi_T = 120°$, point source at $x/d_T = 2.00$.

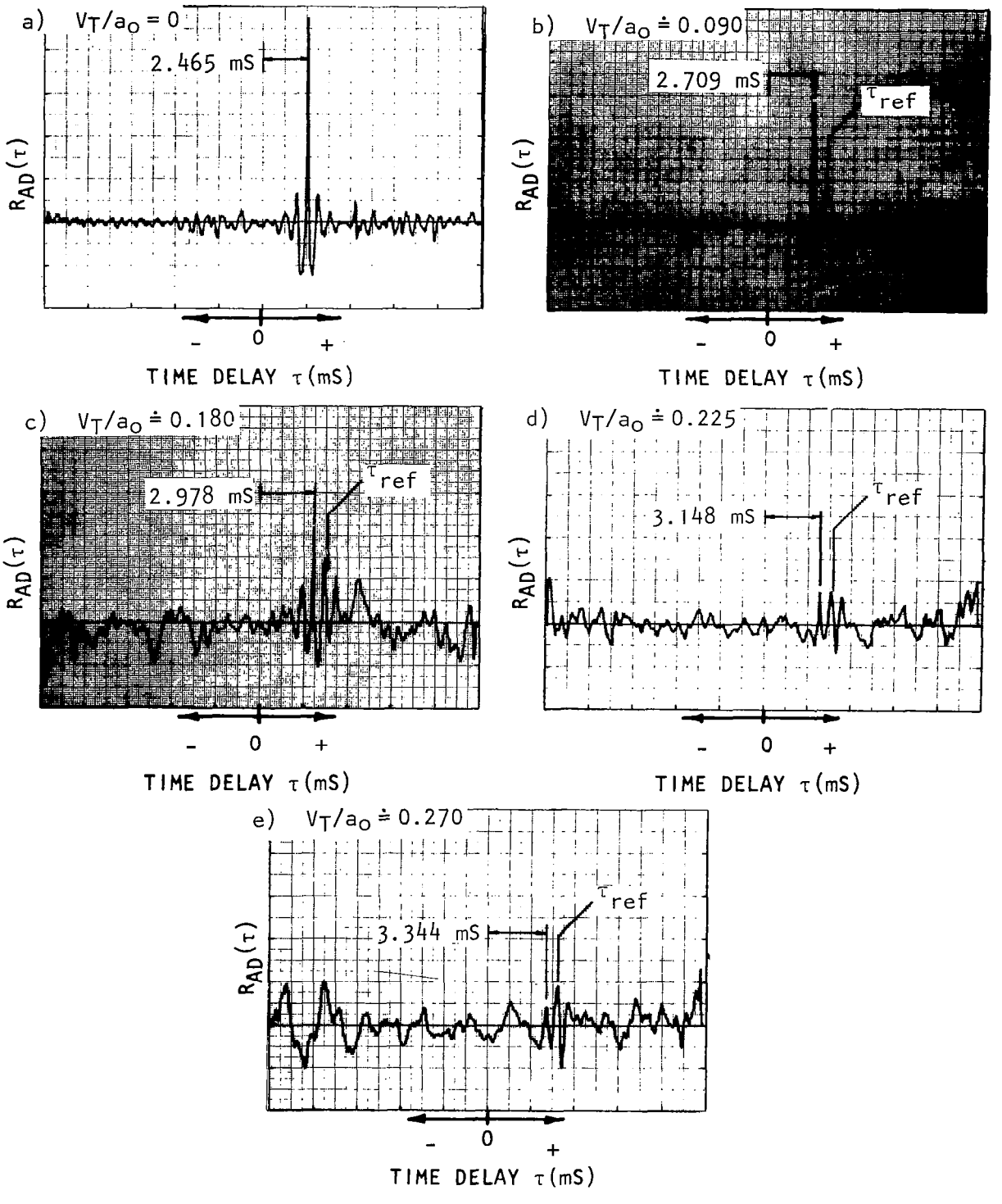

Figure 4.31 Cross-correlation function $R_{AD}(\tau)$: $\psi_T = 140°$, point source at $x/d_T = 2.00$.

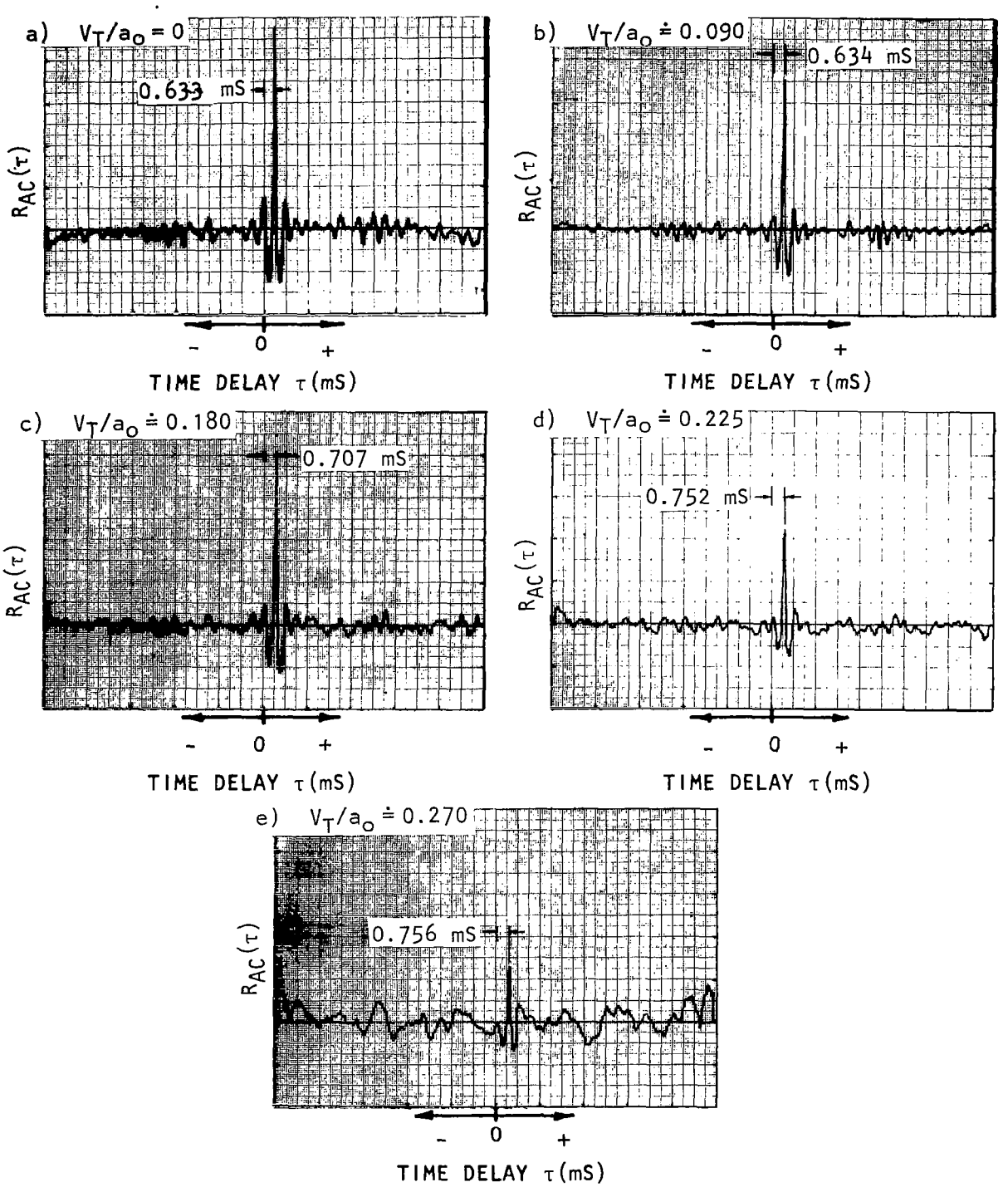

Figure 4.32 Cross-correlation function $R_{AC}(\tau)$: $\psi_T = 140°$, point source at $x/d_T = 2.00$.

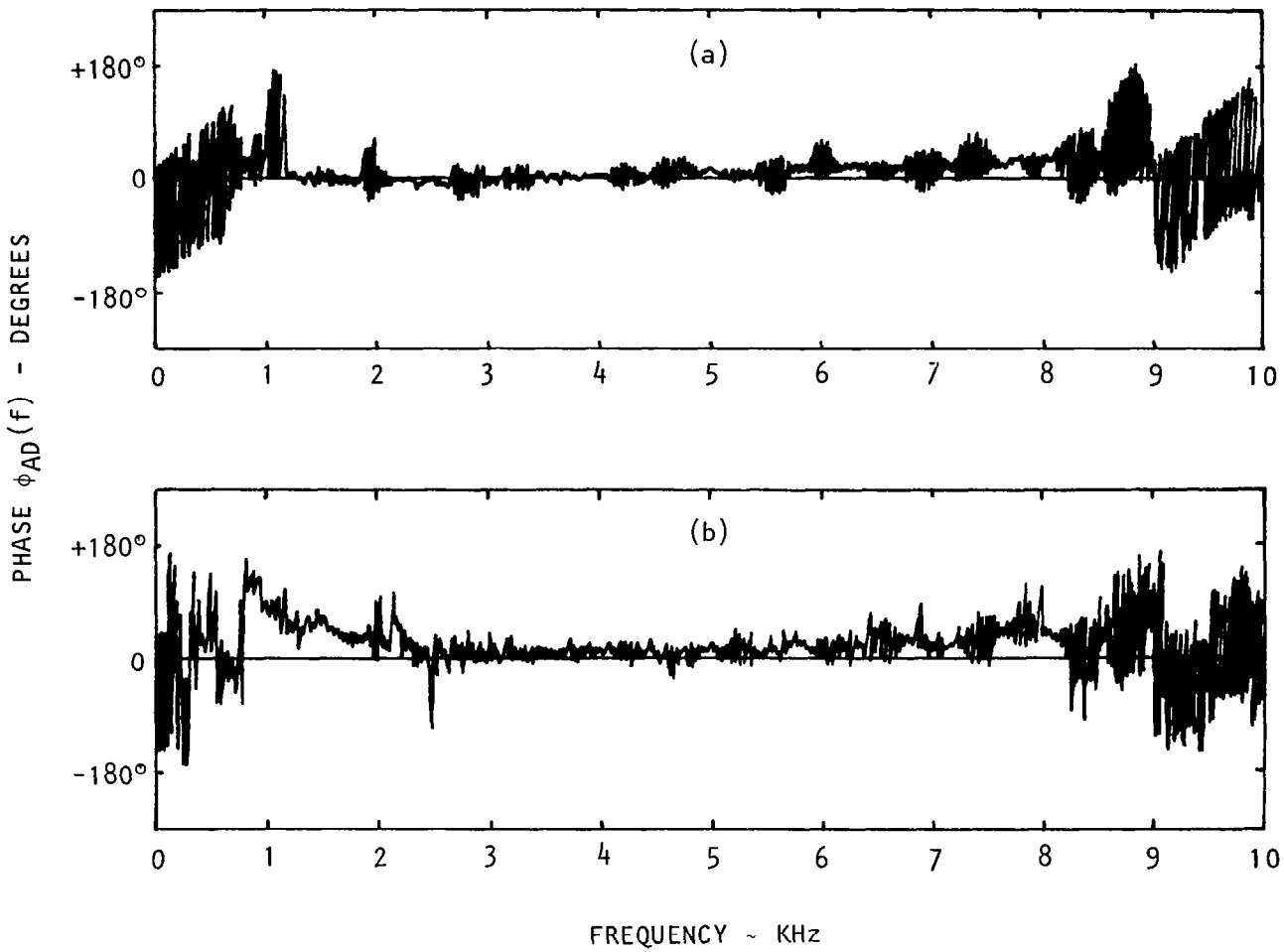

Figure 4.33 Phase spectrum $\phi_{AD}(f)$ obtained by moving peak of $R_{AD}(\tau)$ of Figure 4.24 to zero time delay before Fourier transform; $\psi_T = 100°$; point source at $x/d_T = 0.99$. (a) $V_T/a_o = 0.09$, (b) $V_T/a_o = 0.18$.

(Analysis bandwidth $\Delta f = 20$ Hz)

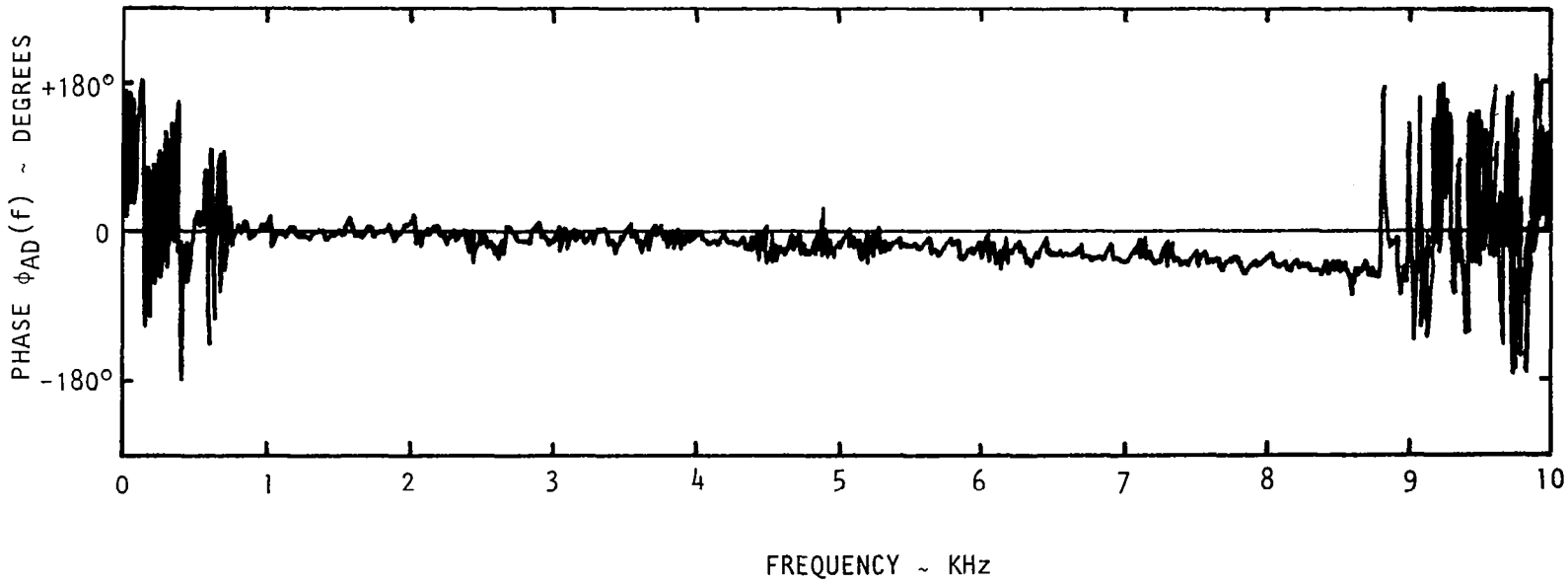

Figure 4.34 Phase spectrum $\phi_{AD}(f)$ obtained by moving peak of $R_{AD}(\tau)$ of Figure 4.23(a) to zero time delay before Fourier transform; $\psi_T = 60$, $V_T/a_o = 0.0$, point source at $x/d_T = 0.99$. (Analysis bandwidth $\Delta f = 20$ Hz)

At the higher frequency end, the last 20% of the phase spectra is not to be relied upon. Aliasing cut-off frequency of 80% of the analysis range was used in obtaining these phase spectra. For this reason all phase spectra presented here show a sudden inconsistent behavior near the highest frequencies analyzed.

Any deviation from zero in phase at other frequencies is caused by the limitation in the time domain resolution [i.e., the time difference between each consecutive point on the correlogram (512 points in all)] of the SD 360 analyzer. Thus, if the peak in the displayed correlogram (to be shifted to zero) does not correspond to the precise physical time delay peak, it will be displayed on the analyzer by the closest time delay available in the machine. This would tend to introduce some error in the phase which will increase with frequency. Such a behavior can be seen in Figure 4.34 (zero flow) where it appears that the zero phase line has been tilted downwards, or in Figure 4.33(a) and 4.33(b) where the zero phase lines are tilted upwards.

Thus, keeping the above restrictions in mind, it can be said that the absence of a second peak in $R_{AD}(\tau)$ together with a nearly zero phase $\phi_{AD}(\tau)$ in the majority of data seen so far demonstrates that there is no significant internal reflection (over the range of angles discussed so far).

For ray angles larger than 100°, there could be some internal reflection and possibly total internal reflection for the largest ray angle tested (i.e. $\psi_T = 140°$) at higher free-jet Mach numbers.

The first case that a second strong peak was detected in $R_{AD}(\tau)$ was for $\psi_T = 110°$ and $V_T/a_o = 0.225$. This is shown in Figure 4.28(d). Evidence of a second peak is also present for $\psi_T = 110°$ and $V_T/a_o = 0.27$ [Figure 4.28(e)] although the correlogram in this case is contaminated with correlated vortex-shedding and flow noise. A similar contamination problem was found for $\psi_T = 120°$ correlograms (Figure 4.30), but data at $\psi_T = 140°$ (Figure 4.31) clearly demonstrate the presence of internal reflection in the forward arc. Correlograms at $\psi_T = 140°$ show that as the free-jet Mach number is increased, the magnitude of the second peak (corresponding to the reflection path) increases, and at the highest Mach number the magnitude of the reflection peak is higher than the magnitude of the direct peak.

The above behavior is consistent with the physical features of the stratified model of the free-jet mean flow field. According to this model, total internal reflection can be expected to occur when the wavenormal or emission angle inside the flow exceeds the limiting emission angle, given by $(\theta_T)_{max} = \cos^{-1}[-a_T/(a_o + V_T)]$. This limiting emission angle is plotted in Figure 4.35 as a function of free-jet Mach number. Also shown in the figure are the values of emission angle (θ_T) corresponding to the values of ray angles $\psi_T = 120°$ and 140° at various Mach numbers. Whenever the actual value of emission angle at a given free-jet Mach number exceeds this limiting emission angle, the incident rays are totally reflected from the shear layer. Thus, as shown in Figure 4.35 (where the circles correspond to the test point Mach numbers), total internal reflection can be expected to occur at $V_T/a_T \gtrsim 0.18$ for $\psi_T = 140°$. It is for this reason that strong reflection peaks were found only for $\psi_T = 140°$ in the present investigation (see Figure 4.31).

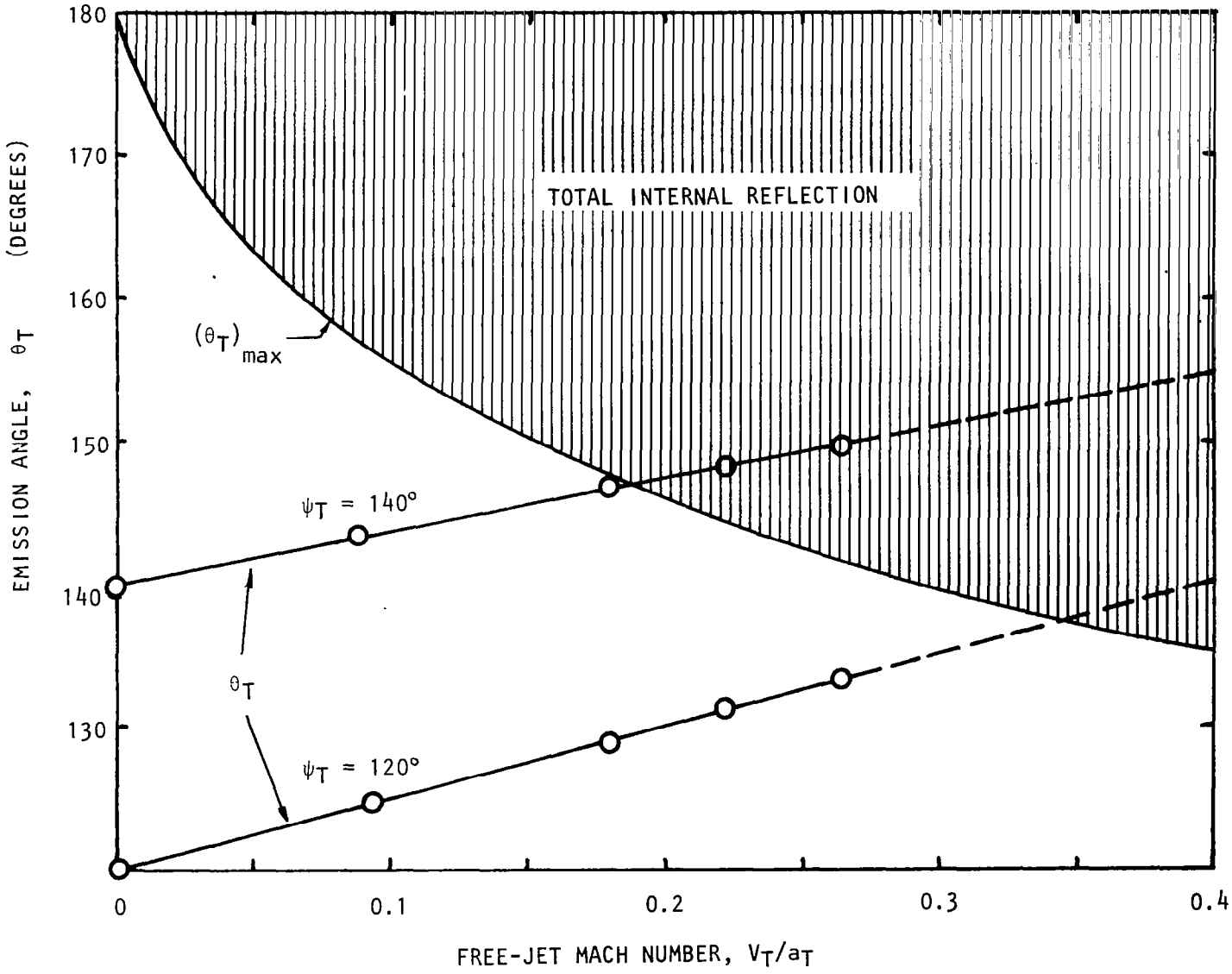

Figure 4.35 Variation of emission angle with free-jet Mach number showing region of total internal reflection.

At other values of ray angle considered here, the corresponding emission angles (at all free-jet Mach numbers) are always smaller than the limiting emission angles, and hence total internal reflection should not be expected to occur.

The reason for the reflection peak to be higher in magnitude than the direct peak could be the focusing effect of the reflected rays at microphone D from all around the periphery of the axisymmetric free-jet shear layer, while there is only one path for the direct ray, namely AD.

With microphone C placed at $\psi_T = 140°$, $R_{AC}(\tau)$ results were also obtained and these are shown in Figure 4.32. If there was internal reflection at microphone C, it would be arriving at microphone C at ray angles smaller than 140°. Based upon Figure 4.35, therefore, microphone C may record total internal reflection only at high free-jet Mach numbers. Figure 4.32 shows little evidence of reflection up to $V_T/a_T \doteq 0.180$ and perhaps some reflection at $V_T/a_T = 0.225$ and 0.27. It is clear, however, that unless there is total internal reflection the direct peak is always dominant.

In order to study the importance of internal reflection, consider the sketch shown in Figure 4.36, where the sound rays emitted by a point source at A are assumed to be totally reflected by the free-jet shear layer. Let $\overline{p_C^2}$ be the mean-square pressure measured at microphone C (placed along the incident ray) due to the incident ray. Similarly, let $\overline{p_D^2}$ be the mean-square pressure measured at microphone D caused by the reflected ray.

Then with a simple model in which the incident *energy* is totally reflected (i.e. the model is partly based on geometric acoustics†), it can be shown that

$$\overline{p_C^2}\ R_T^2 = \overline{p_D^2}\ \tilde{R}_T^2. \tag{4-2}$$

Here ray path distances R_T, $\tilde{R}_T$ can be used since both ray tubes are effectively inside the flow and the factors relating wavenormal and ray path distances cancel out. Values of $10 \log_{10} (\overline{p_C^2}/\overline{p_D^2})$ computed from *measured* data are plotted against free-jet Mach number in Figure 4.37 for a fixed ray angle $\psi_T = 140°$; these are compared with the factor $10 \log_{10}(\tilde{R}_T^2/R_T^2)$ from equation (4-2) in the same figure when total internal reflection occurs, that is, when $V_T/a_T \gtrsim 0.19$. Two measured values are within 3 dB of the calculated factor while the third value differs by just over 6 dB; this may be due to the over-simplified model on which equation (4-2) is based.

Values of $\overline{p_C^2}/\overline{p_D^2}$ were estimated by measuring the ratio of the magnitudes of the "direct peak" in $R_{AC}(\tau)$ (Figure 4.32) and "reflected peak" in $R_{AD}(\tau)$ (Figure 4.31), and equating $\overline{p_C^2}/\overline{p_D^2}$ to the square of this ratio. It can be seen in Figure 4.37 that when total internal reflection does not take place (in this

---

†*Strictly speaking, geometric acoustics cannot be used at and near the the focal point D.*

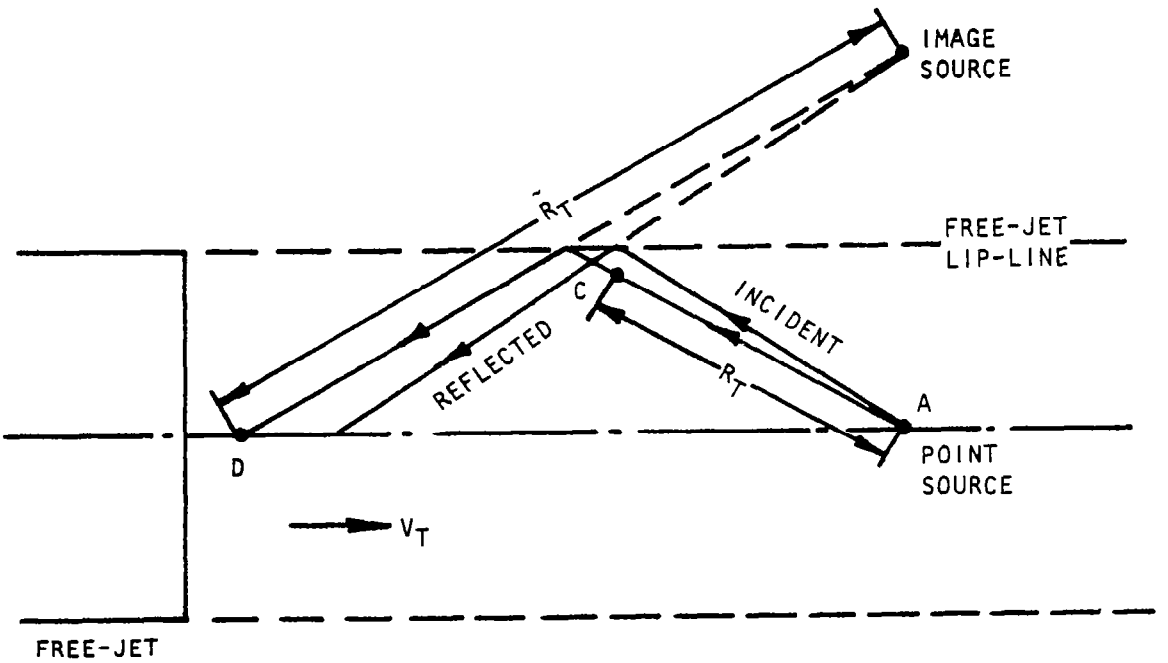

Figure 4.36 Sketch showing total internal reflection in the forward arc.

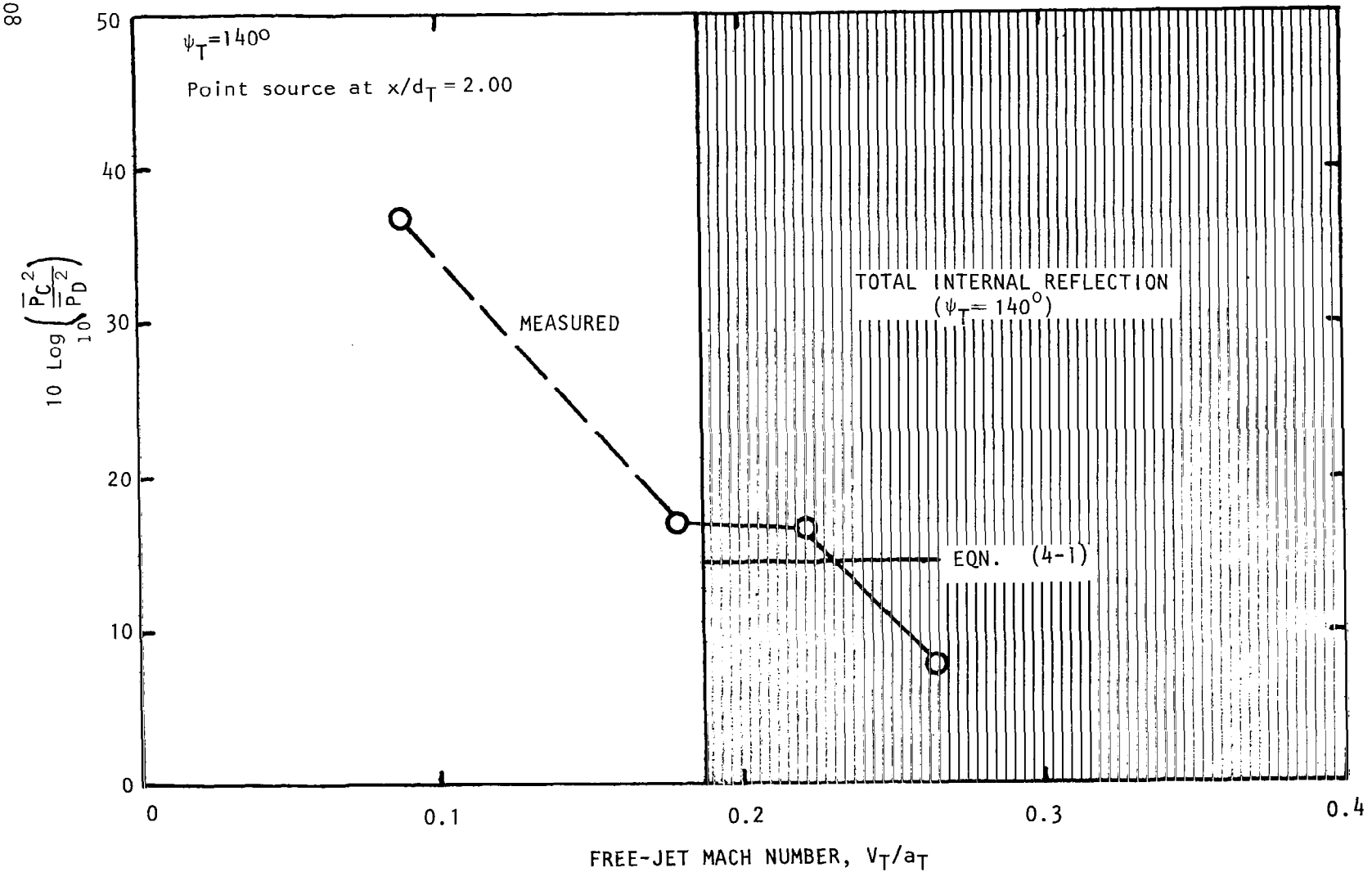

Figure 4.37 Comparison between measurements and theory (total internal reflection).

case when $V_T/a_T \lesssim 0.19$) the mean-square pressure at D is substantially less than the incident value at C. From this and other results we find that internal reflections are insignificant except of course when total internal reflection takes place as illustrated above. Having established that internal reflections are small if not negligible at a large number of flow conditions and angles, the experimental determination of the amplitude calibration factor is considerably simplified, as discussed in the following section.

4.4 AMPLITUDE CALIBRATION FACTORS

The experimental configuration shown in Figure 3.16 was used for these measurements, except that microphone D was not needed for these tests. Microphone A was placed adjacent to the point source. Microphone C was positioned at various ray angles, ψ_T, and for each free-jet Mach number, microphone B was positioned at the corresponding emerging angle, θ_o, calculated from Snell's law. Thus, all measurements used in determining amplitude calibration factors were made on the same ray path, and data were recorded simultaneously at all microphones.

The *measured* calibration factor is defined here as (see Figure 2.3)

$$C_{F_m} = \frac{|G_{AC}(f)|^2}{|G_{AB}(f)|^2} \quad \frac{R_{rT}^2}{R_{ra}\ R_{ro}} \tag{4-3}$$

This differs from the definition of C_{F_m} given by equation (2-8) in that the square of the modulus of the pressure *cross*-power spectral densities $G_{AC}(f)$ and $G_{AB}(f)$ appear in place of the *auto*-power spectral densities or mean-square pressures. This is to ensure that only the component of the pressure signals at points B and C which is *coherent* with the noise signal at A is used to form a measure of the calibration factor (see Appendix 4B). This removes the unwanted contributions to the pressure fluctuations at microphones B and C due to free-jet mixing noise and any other extraneous sources. Naturally when the calibration factor is actually utilized in practice to convert mean-square pressure measurements at microphone position B to flyover data, it is essential that either the data is not significantly contaminated by, for example, free-jet mixing noise or that some appropriate corrections have been applied before calibration of data by the factor C_F.

Measurements of the cross-power spectra between microphones A and B $[G_{AB}(f)]$ and between microphones A and C $[G_{AC}(f)]$ have been obtained for a wide range of ray angles, ψ_T, and free-jet Mach numbers, V_T/a_T, with the experimental point source at three different axial locations $x/d_T = 0.22$, 0.99 and 2.00.

After applying the distance correction (see Section 2.2) to obtain the normalized, squared cross-power spectra amplitudes $R_{rT}^2|G_{AC}(f)|^2$ and $R_{ra}R_{ro}|G_{AB}(f)|^2$, the ratio of these quantities has been formed to yield the

measured calibration factor, C_{F_m}, as defined above. A sample calculation of this factor is given in Appendix 4C.

The measured calibration factor was evaluated as a function of frequency; on the other hand, the theoretical calibration factor

$$C_F = \rho_T \, D_T^4/\rho_o \tag{4-4}$$

where

$$D_T = (1 + V_T \cos\theta_T/a_T)^{-1} \tag{4-5}$$

is frequency independent, having been derived on the basis of high-frequency or geometric acoustics propagation through the free-jet shear layer. Over the range of free-jet flow conditions and angles tested, the measured calibration factor *was* found to be independent of frequency over the range where signal-to-noise ratio was adequate.

In general, this constant value of C_{F_m} agrees well with the theoretical value given by equation (4-4) above. Some comparisons between measured and theoretical amplitude calibration factors are shown as a function of free-jet Mach number in Figures 4.38, 4.39 and 4.40 for various ray angles, ψ_T, and three axial source locations. Data for ray angles lying between $\psi_T = 30°$ and $\psi_T = 140°$ are presented which correspond to a microphone angle range $30° \leq \theta_m \leq 154°$ thus covering the extreme limits of rear arc and forward arc measurement in the present test facility. Most of the deviations between measured and calculated calibration factors fall within the estimated experimental error band.

Typical measured cross-power spectra used to calculate the above amplitude calibration factors are shown in Figure 4.41 for $\psi_T = 90°$ and V_T/a_o (nominal) = 0, 0.090, 0.180 and 0.225 with the point source located at $x/d_T = 2.00$. The two cross-power spectra, $G_{AC}(f)$ and $G_{AB}(f)$, are displayed 10 dB apart in each case to show approximately constant difference as a function of frequency. In fact on applying the appropriate amplitude (and distance) calibration factors to $G_{AB}(f)$, the resultant spectrum is found to agree with spectrum $G_{AC}(f)$ within the accuracy of measurement.

The amplitude calibration factors derived here should strictly be considered valid only for frequencies up to 10 KHz. Beyond 10 KHz, the signal-to-noise ratio was rather low as mentioned earlier. Some results for higher frequencies are, however, available for $\psi_T = 90°$, and these are described in the next section (Section 4.5).

Based upon these and other comparisons, the experimental results substantially confirm the validity of the recommended amplitude calibration factor over a wide range of frequencies.

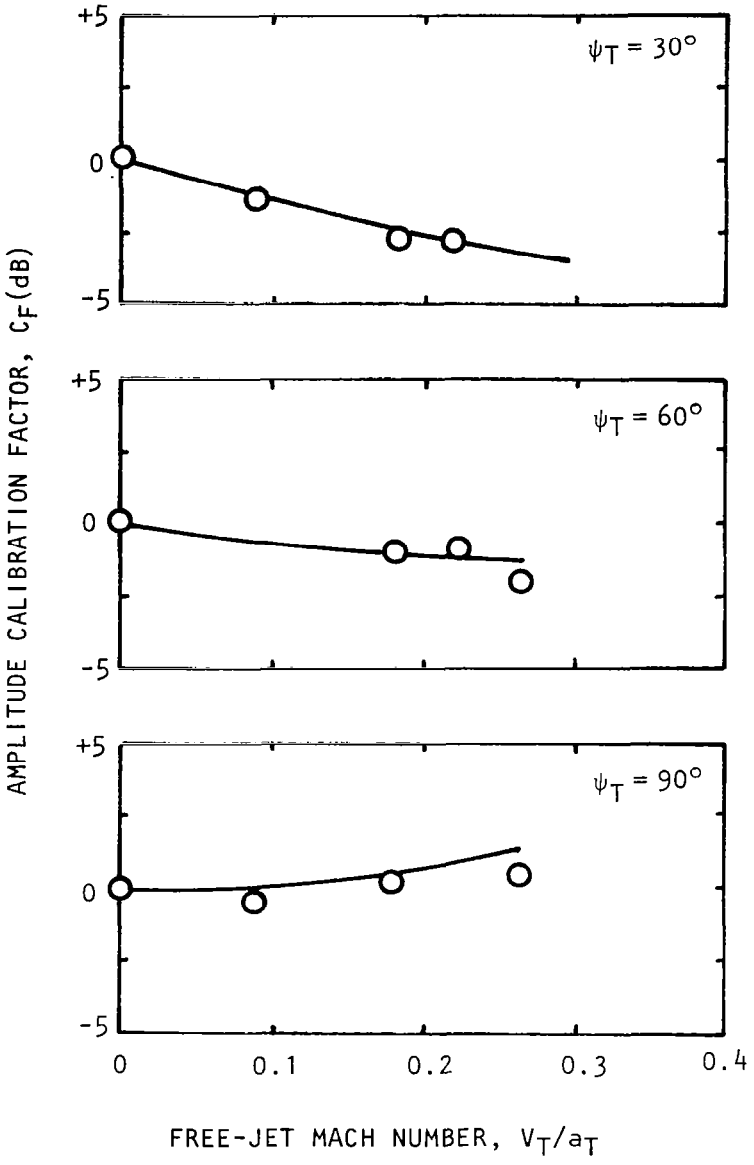

Figure 4.38 Comparison between measured and theoretical amplitude calibration factors; point source at $x/d_T = 0.22$

O , Measurement ; ——— , Theory

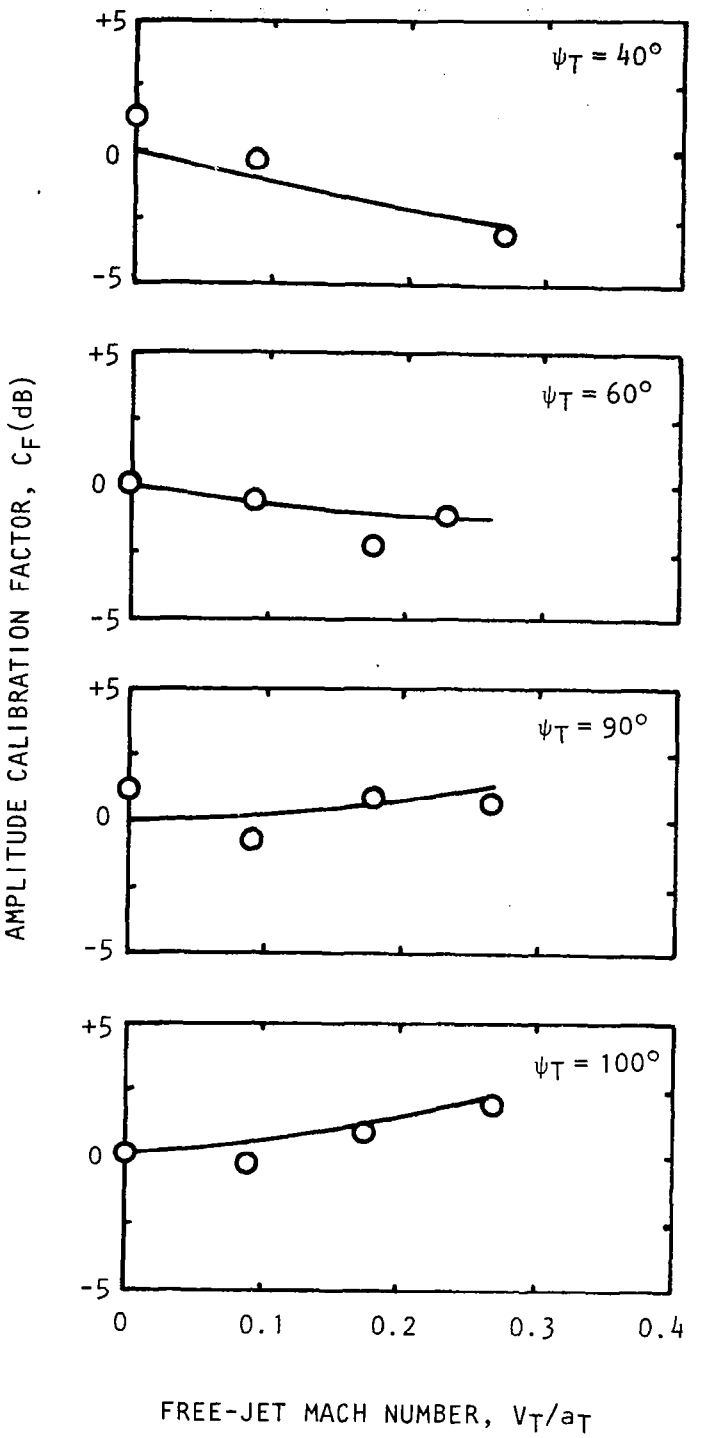

Figure 4.39 Comparison between measured and theoretical amplitude calibration factors; point source at $x/d_T = 0.99$.

○, Measurement; ———, Theory

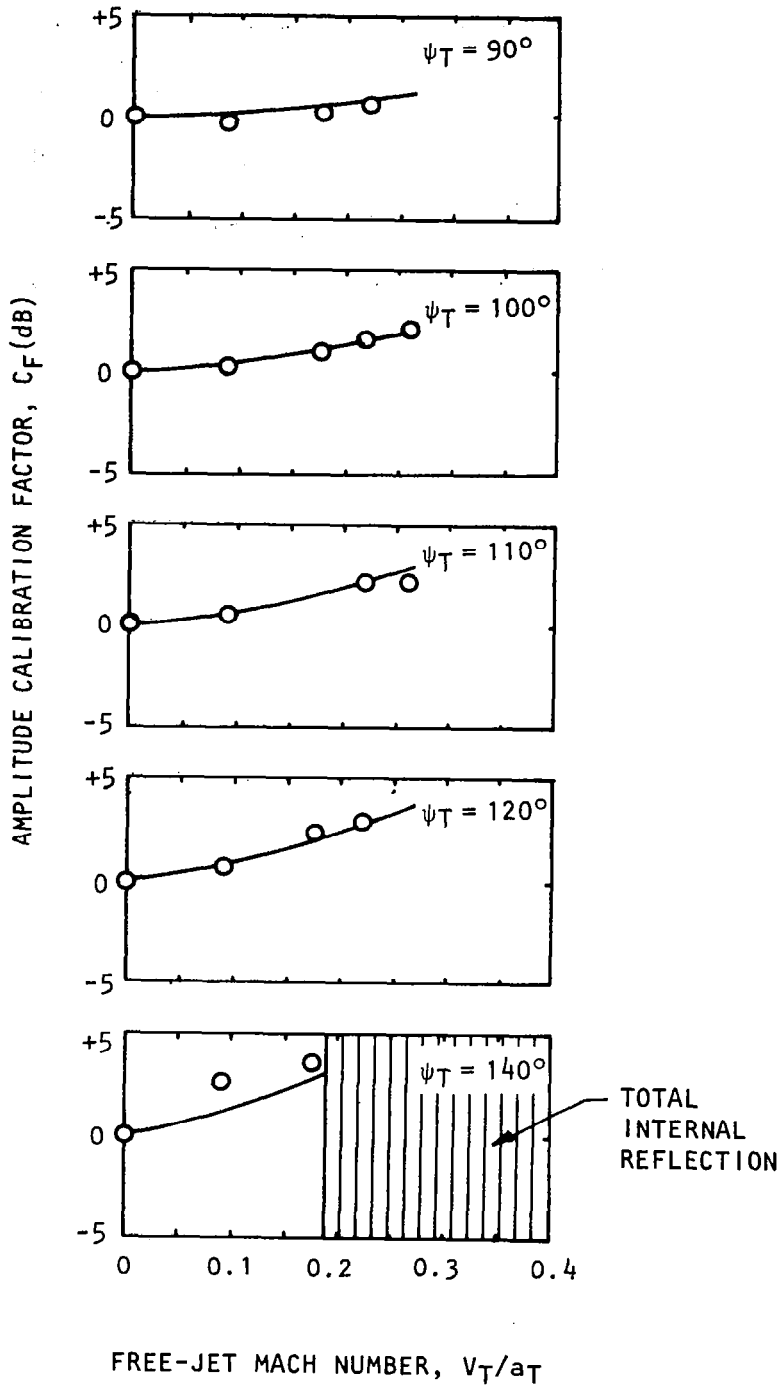

Figure 4.40 Comparison between measured and theoretical amplitude calibration factors; point source at $x/d_T = 2.00$.

O, Measurement; ———, Theory

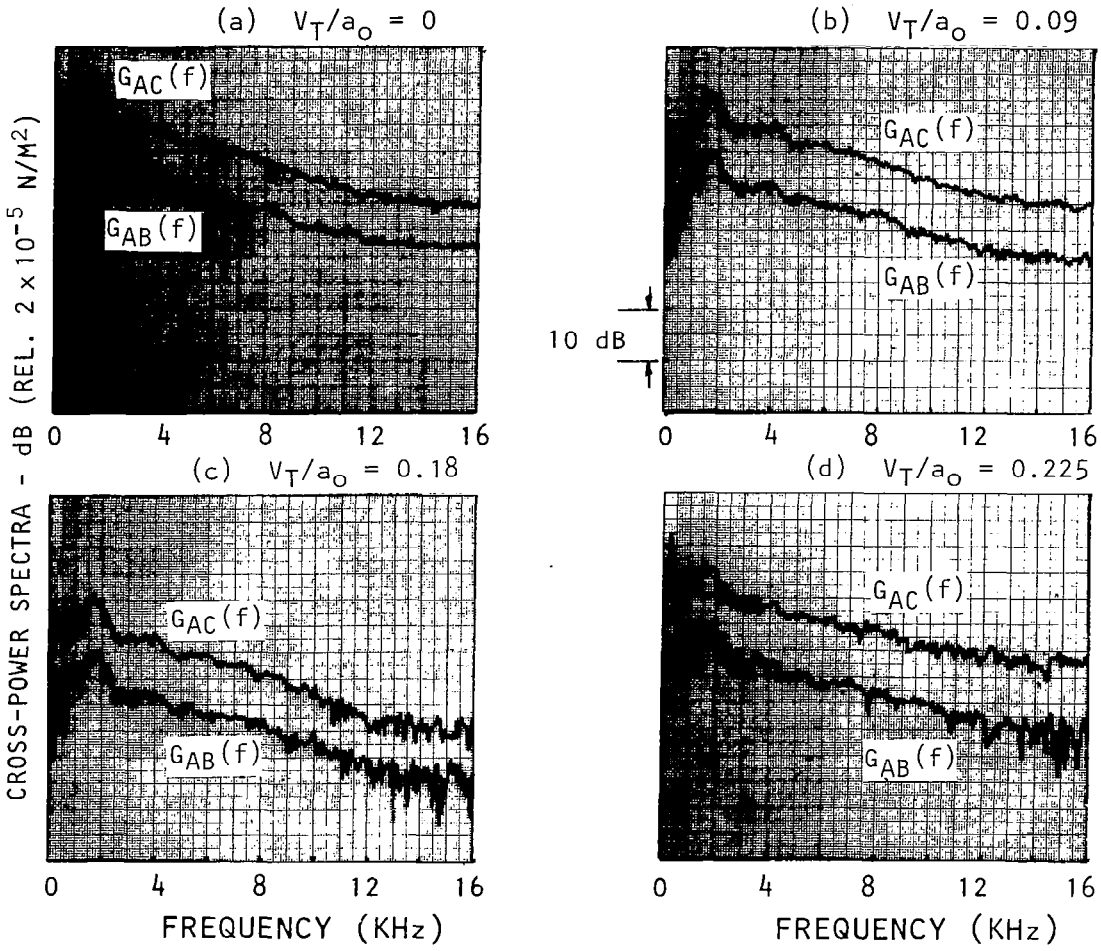

Figure 4.41 Typical cross-power spectra $G_{AC}(f)$ and $G_{AB}(f)$ displayed 10 dB apart. $\psi_T = 90°$, analysis bandwidth $\Delta f = 40$ Hz, point source at $x/d_T = 2.0$

4.5 TURBULENCE ABSORPTION

As described in Section 3.2, a more powerful and directional sound source was used for selected measurements to improve the signal-to-noise ratio at higher frequencies. The noise source, microphone C and microphone B were placed along the $\psi_T = 90°$ ray path for each free-jet Mach number tested. For these tests the auto-power spectra $G_{CC}(f)$ and $G_{BB}(f)$, at microphone C inside the free jet and at microphone B outside the free-jet, were measured. Power spectra at microphone B were scaled to those inside the free jet at the location of microphone C by applying the appropriate theoretical distance (C_R) and amplitude (C_F) calibration factors. Results for free-jet Mach numbers of $V_T/a_o \doteq 0.090$, 0.180, and 0.225 with the source at $x/d_T = 2.94$ are shown in Figures 4.42, 4.43 and 4.44, respectively. In each figure, the power spectral densities $G_{CC}(f)$ and $G_{BB}(f)$ are shown as measured with the point source "ON" and then "OFF" to show the frequency range over which an adequate signal-to-noise (S/N) ratio was obtained. The hatched portions of the figures represent regions with S/N ratio of 10 dB or higher. Comparison is then made between the spectrum measured at microphone C and that measured outside at microphone B corrected to the ideal wind tunnel condition.

The plots on Figures 4.42(c), 4.43(c) and 4.44(c) show once again that, at least up to 10 KHz, the amplitude calibration method recommended here applies accurately, and there is no evidence of sound absorption due to turbulence up to 10 KHz. In fact, what appears to be a possible reduction in noise as observed at microphone B outside the free jet for frequencies higher than 10 KHz is simply the difference in frequency response corrections and atmospheric absorption corrections at the two microphones. (It should be recalled that microphone C was fitted with a nose-cone and was placed parallel to the flow *and at 90° to the ray direction in this case*, while microphone B simply had a B&K microphone grid.) The true magnitude of the frequency response corrections (resulting from this arrangement) is easily determined by comparing the auto-power spectra measured at C and at B for *no flow*, suitably corrected for amplitude and distance calibration factors for zero free-jet velocity. This is shown in Figure 4.45 where the spectrum measured at microphone B is scaled to that measured at microphone C. It is seen that even for zero free-jet flow, microphone B shows a reduction in noise for higher frequencies. This, in fact, is a measure of the correction to be applied at these frequencies when a comparison is to be made between the spectra measured at microphone C and at microphone B. A closer inspection of the difference in $G_{CC}(f)$ and $G_{BB}(f)$ for zero flow in Figure 4.45 and with flow in Figures 4.42(c), 4.43(c) and 4.44(c) in the region of adequate S/N ratio reveals that after these corrections are taken into account, all data at microphone B can be scaled to those at microphone C by applying the amplitude and distance calibration factors outlined in Section 2. When these frequency response corrections for zero free-jet velocity are taken into account, the difference between auto-power spectra $G_{CC}(f)$ and those at B scaled to point C match to within 1 dB – which is the estimated measurement accuracy in these experiments – as shown in Figure 4.46 for f = 5, 10, 15, 20, 25 and 30 KHz. This clearly indicates that turbulence absorption, if present,

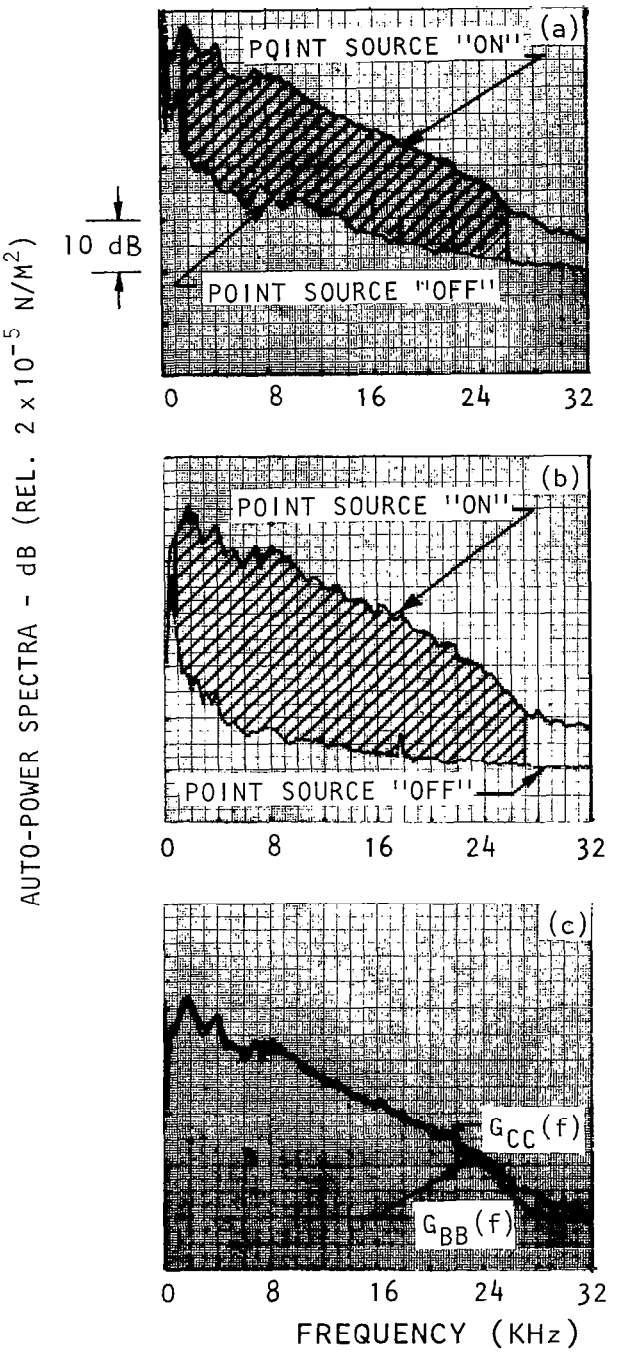

Figure 4.42 Spectra measured at microphone C inside the flow, $G_{CC}(f)$, and at microphone B outside the free jet, $G_{BB}(f)$, with broad band excitation. $\psi_T = 90°$, analysis bandwidth $\Delta f = 40$ Hz, point source at $x/d_T = 2.94$, $V_T/a_o = 0.09$.
(a) $G_{CC}(f)$, (b) $G_{BB}(f)$, (c) $G_{BB}(f)$ transformed to C .

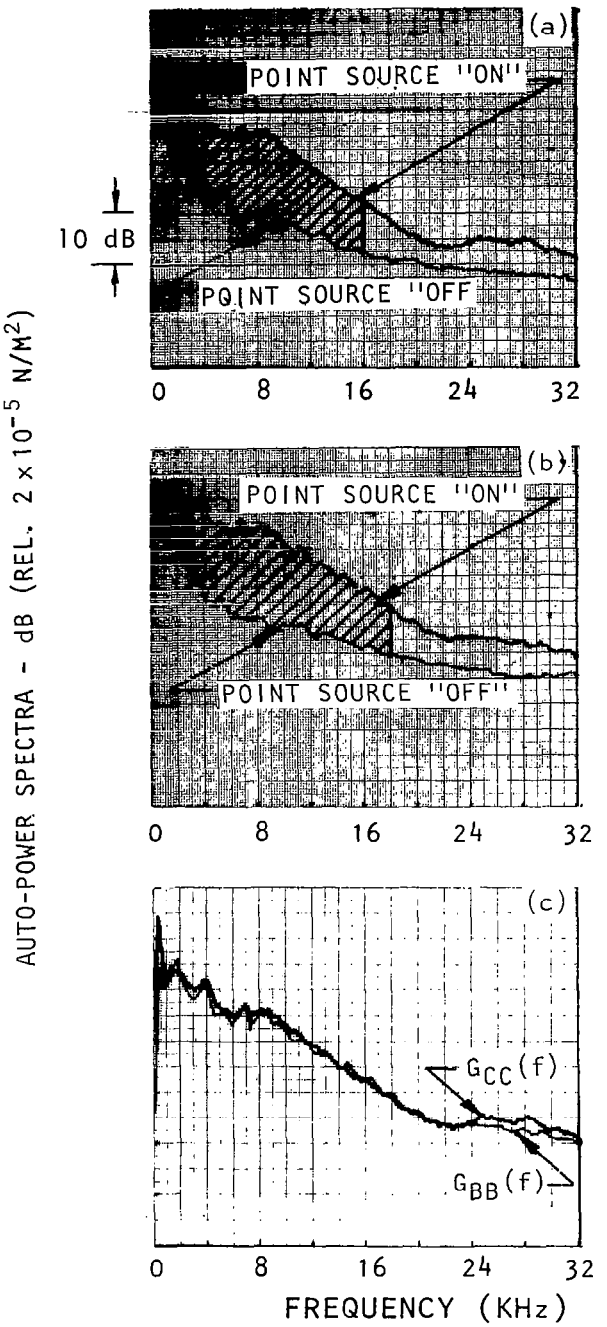

Figure 4.43 Spectra measured at microphone C inside the flow, $G_{CC}(f)$, and at microphone B outside the free jet, $G_{BB}(f)$, with braod band excitation. $\psi_T = 90°$, analysis bandwidth $\Delta f = 40$ Hz, point source at $x/d_T = 2.94$, $V_T/a_o = 0.18$.

(a) $G_{CC}(f)$, (b) $G_{BB}(f)$, (c) $G_{BB}(f)$ transformed to C

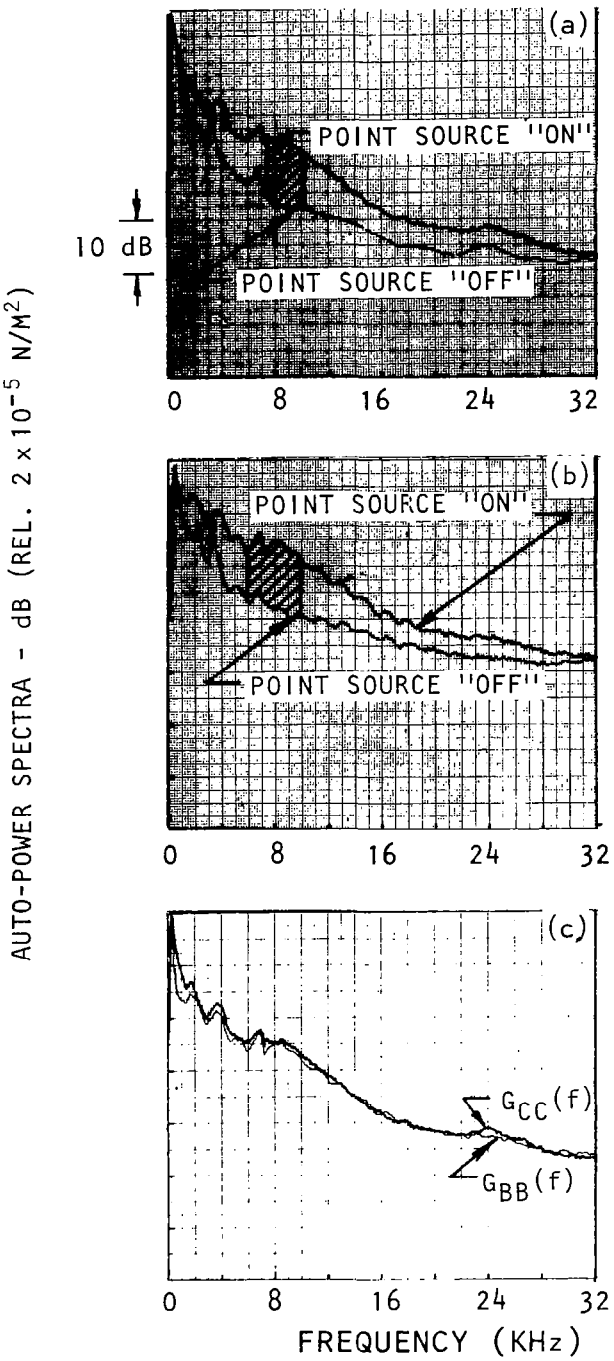

Figure 4.44 Spectra measured at microphone C inside the flow, $G_{CC}(f)$, and at microphone B outside the free jet, $G_{BB}(f)$, with broad band excitation. $\psi_T = 90°$, analysis bandwidth $\Delta f = 40$ Hz, point source at $x/d_T = 2.94$, $V_T/a_o = 0.225$. (a) $G_{CC}(f)$, (b) $G_{BB}(f)$, (c) $G_{BB}(f)$ transformed to C

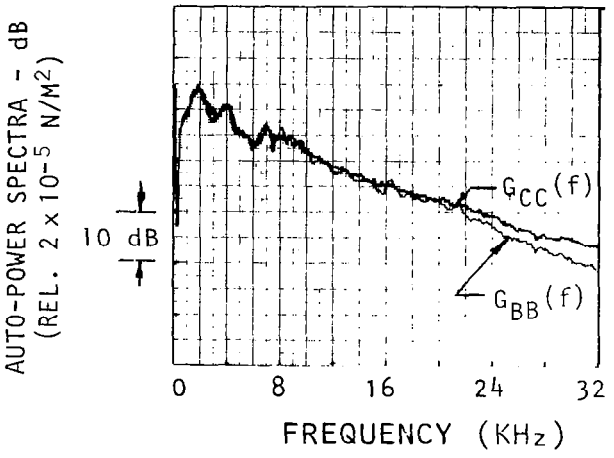

Figure 4.45 Comparison of spectra measured inside and outside the free jet corrected to ideal wind tunnel conditions. $\psi_T = 90°$, analysis bandwidth = 40 Hz, point source at $x/d_T = 2.94$, $V_T/a_o = 0.0$.

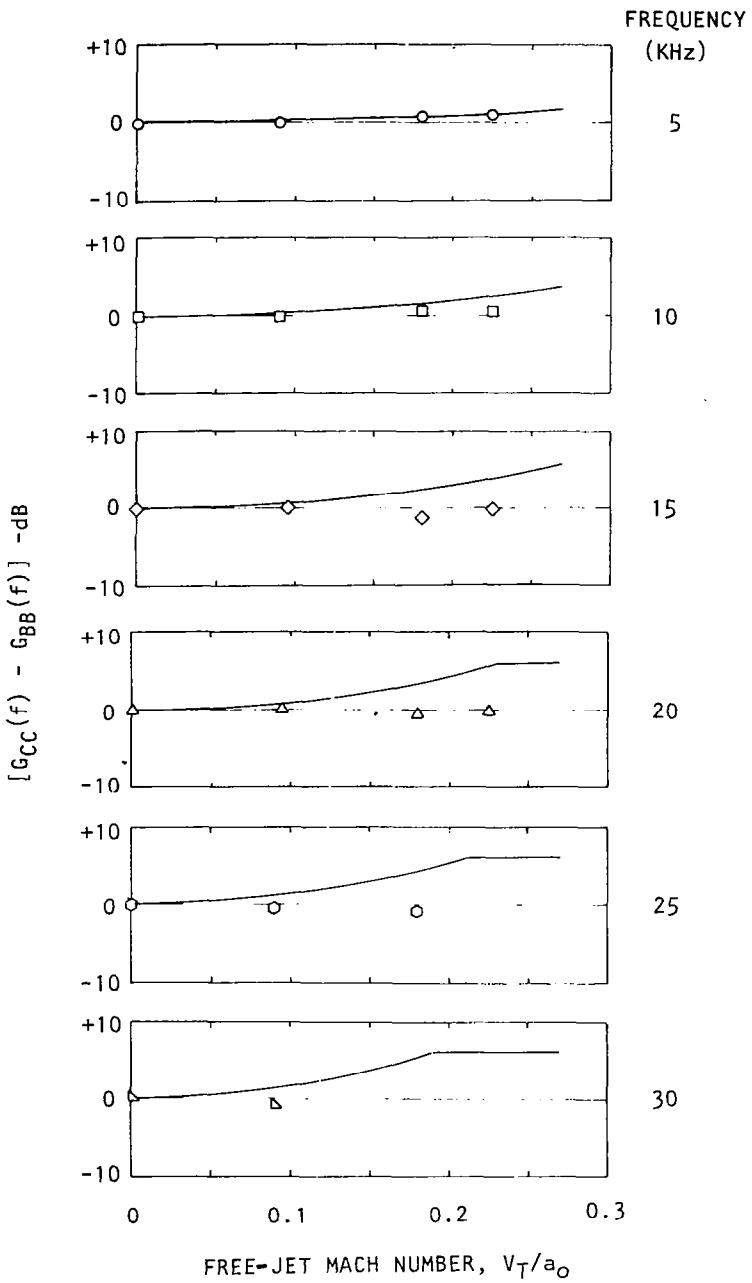

Figure 4.46 Measured corrected SPL-difference (symbols) showing absence of turbulence absorption and comparison with empirical predictions of Reference 4.3(——). $\psi_T = 90°$, point source at $x/d_T = 2.94$.

is not significant over the range of frequencies and test conditions examined here. For the sake of comparison, turbulence absorption levels predicted by empirical methods of reference 4.3 are also plotted on the same figure. It is seen that with the exception of 5 KHz data, where the predicted levels also fall within the measurement accuracy, there is considerable disagreement between the present results and those predicted by reference 4.3. It will be shown in the next section that one could easily detect significant reductions in noise levels across the shear layer, but only if the point source is excited with discrete tones. This is not to be confused with turbulence absorption, but is attributed to scattering effects.

4.6 TURBULENCE SCATTERING

The purpose of this part of the experimental program was to detect any frequency broadening, if present, that may be produced when discrete frequency sound waves propagate through the turbulent free-jet shear layer. The available experimental evidence (ref. 4.4, 4.5) also indicates that such frequency broadening is normally accompanied by a reduction in the sound pressure level of the tone.

The experimental configuration used for investigating scattering effects was similar to that used to determine the amplitude calibration factors (Figure 3.16), with the exception that discrete tones were used instead of broadband noise as the source excitation signal.

Figure 4.47 shows typical auto-power spectra $G_{BB}(f)$ measured at microphone B located outside the free-jet flow. Results for the ray angle $\psi_T = 90°$ and the point source located at $x/d_T = 0.22$ and excited at frequencies $f = 1.024$ KHz plus six harmonics are shown for free-jet Mach numbers $V_T/a_o = 0$, 0.09 and 0.18. This figure shows that at all frequencies up to 10 KHz, the discrete tones do not undergo any noticeable broadening about their peak value. Also, side lobes associated with the scattering phenomenon observed by Candel (ref. 4.4, 4.5) do *not* appear in Figure 4.47 nor in any results of the present experiments. However, it should be pointed out that the analysis bandwidth used here is 20 or 40 Hz whereas in Candel's results a much narrower bandwidth was used. What *appears* to be a possible broadening in the region where the discrete tones merge with the broadband noise is actually due to the spectrum of the flow noise itself. This is demonstrated in Figure 4.48 where $G_{BB}(f)$ for $V_T/a_o = 0.180$ and the same configuration as in Figure 4.47 is plotted with the point source ON and also OFF (i.e. free-jet noise only). Thus, in some cases, what appears to be spectral broadening is actually caused by the flow noise itself. Since the S/N ratio for higher free-jet Mach numbers in these results is considerably reduced, one can deduce very little about scattering effects which generally become more dominant as the free-jet Mach number is increased (ref. 4.4, 4.5). Even when the S/N ratio was adequate, it appeared that much higher values of δ/λ† than those being used were

†*Where λ is the acoustic wavelength and δ is the shear layer thickness given by $\delta \doteq 0.15x$ (here x is the distance from the free-jet nozzle exit plane at which the ray intersects the lip-line.)*

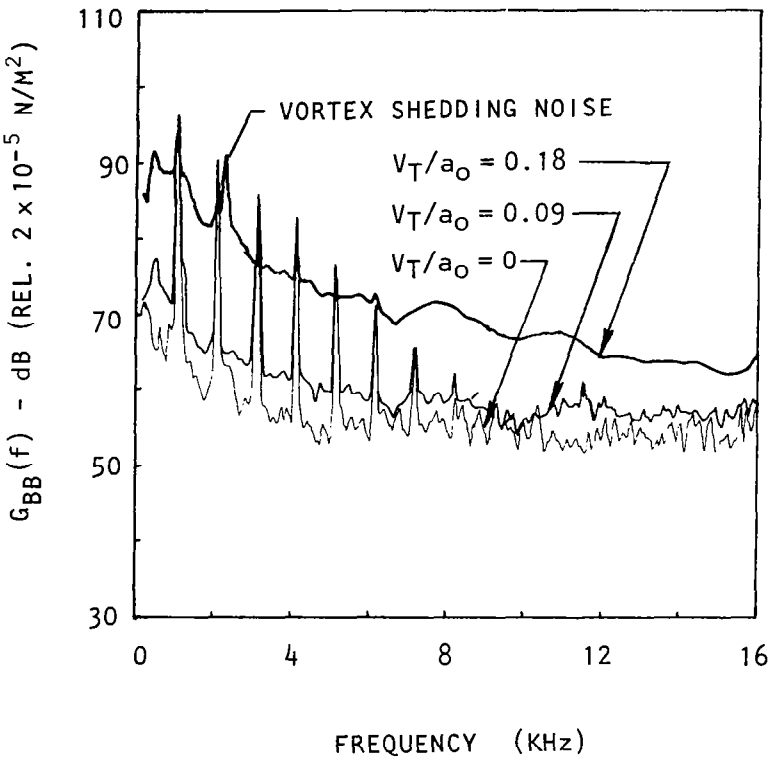

Figure 4.47 Variation of spectra measured at microphone B outside the flow with free-jet Mach number; $\psi_T = 90°$, analysis bandwidth $\Delta_f = 40$ Hz. Point source at $x/d_T = 0.22$; discrete frequency excitation.

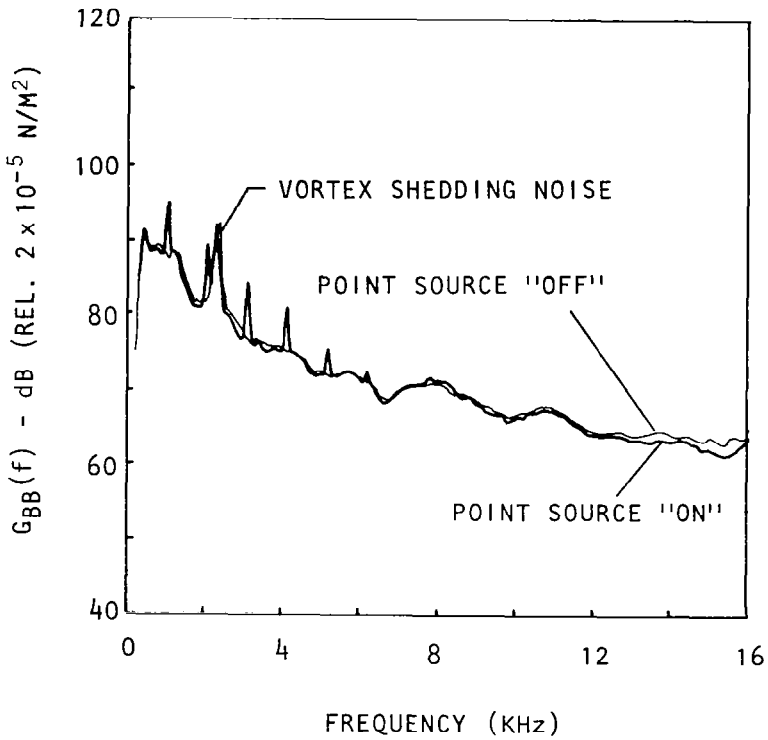

Figure 4.48 Spectra measured at microphone B outside the flow with point source "on" and point source "off"; $V_T/a_o = 0.18$, $\psi_T = 90°$, analysis bandwidth $\Delta_f = 40$ Hz. Point source at $x/d_T = 0.22$.

required to reveal significant turbulence scattering effects. The highest excitation frequency used so far was 15 KHz and the largest axial location for the point source was $x = 2\ d_T$. This provided a maximum ratio of shear layer thickness, δ, to acoustic wavelength, λ, of about 10. Some tests with higher δ/λ and better S/N ratio were thus considered necessary.

It was, therefore, decided to replace the smaller point source by the 2.54 cm larger noise source. This larger source was also used to study turbulence absorption effects, as described in the previous section. The test configurations for those tests and the present tests were similar. This noise source was not omnidirectional, but it provided adequate S/N ratio along the direction of the axis of its opening. Discrete tones at 15 KHz (and a harmonic at 30 KHz) and 19.2 KHz were used for these tests for microphone angle $\theta_m = 90°$, and with the noise source located at $x/d_T = 2.94$.

Auto-power spectra $G_{CC}(f)$ and $G_{BB}(f)$ measured inside and outside the free-jet respectively are presented in Figures 4.49(a) through 4.49(j) with a discrete tone frequency $f = 19.2$ KHz for the above case. This frequency and measurement location provides δ/λ equal to 17.6. These power spectra clearly demonstrate the spectral broadening effect: the shapes of the spectra measured at microphone B are much wider than those measured at microphone C, indicating that this broadening occurs as the sound travels across the shear layer. Wherever possible, the corresponding spectra with the free jet operated alone (i.e. noise source OFF) are also given. The two side lobes in Figure 4.49(f) should not be confused with those *possibly* produced by scattering. These side lobes are seen inside the flow as well [see Figure 4.49(e)] and are caused by the noise source itself. It is interesting to see that these side lobes have also been partly broadened as they cross the free-jet shear layer [compare Figures 4.49(e) and 4.49(f)].

Such an effect also exists at $f \doteq 38.4$ KHz (first harmonic of excitation frequency), as shown in Figure 4.49(c) and 4.49(d). The value of δ/λ corresponding to this frequency was 35.2, but unfortunately, the S/N ratio of this frequency at V_T/a_o larger than 0.09 was very small. The broadening effect at this frequency can, however, still be seen. Figure 4.49(d) shows that for the 38.4 KHz peak, the 10 dB down point is about twice as wide as the 10 dB down point for the 19.2 KHz peak. This indicates that the broadening effect increases with increasing δ/λ.

Similar results were obtained for $f \doteq 15$ KHz ($\delta/\lambda = 13.6$) and $f \doteq 30$ KHz ($\delta/\lambda = 27.2$), and these are shown in Figures 4.50(a) through 4.50(j).

Source of Spectral Broadening. The results described in Section 4.5 demonstrated that if broadband excitation is used, the shear layer turbulence does not appear to produce noticeable changes in either the levels or the spectral shapes of the acoustic signals as they propagate from the potential core of the free jet to the outside. In the work of Candel et al. (ref. 4.4, 4.5), who examined the effects of turbulence scattering on discrete tones, it was found that an increase in velocity produces additional spectral broadening and that the energy at the main carrier frequency is depleted while that in the side bands is progressively increased.

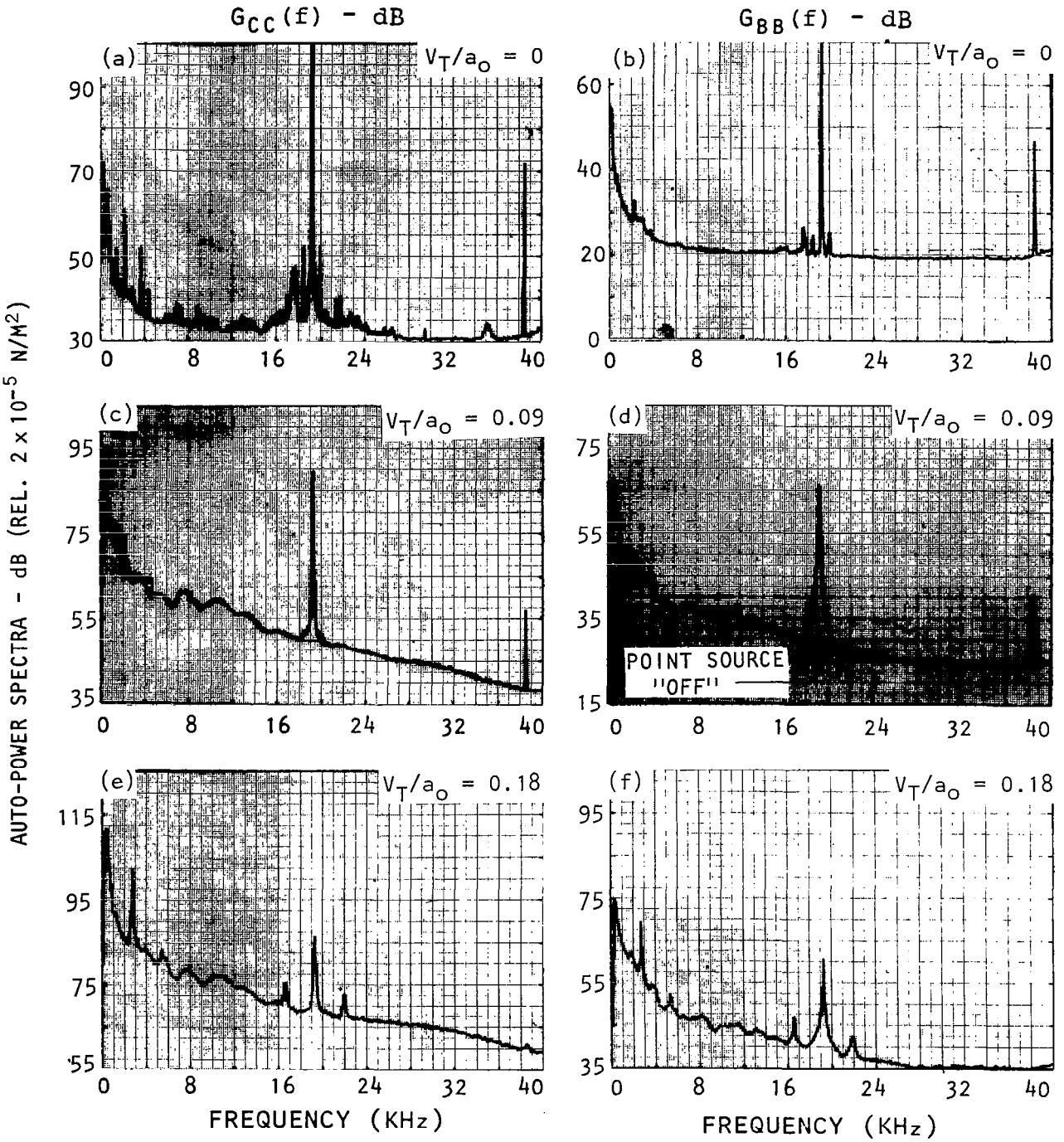

Figure 4.49 Spectra measured at microphone C inside the flow, $G_{CC}(f)$, and at microphone B outside the free jet, $G_{BB}(f)$, with discrete tone excitation. $\psi_T = 90°$, analysis bandwidth $\Delta f = 40$ Hz, point source at $x/d_T = 2.94$.

(Continued on next page)

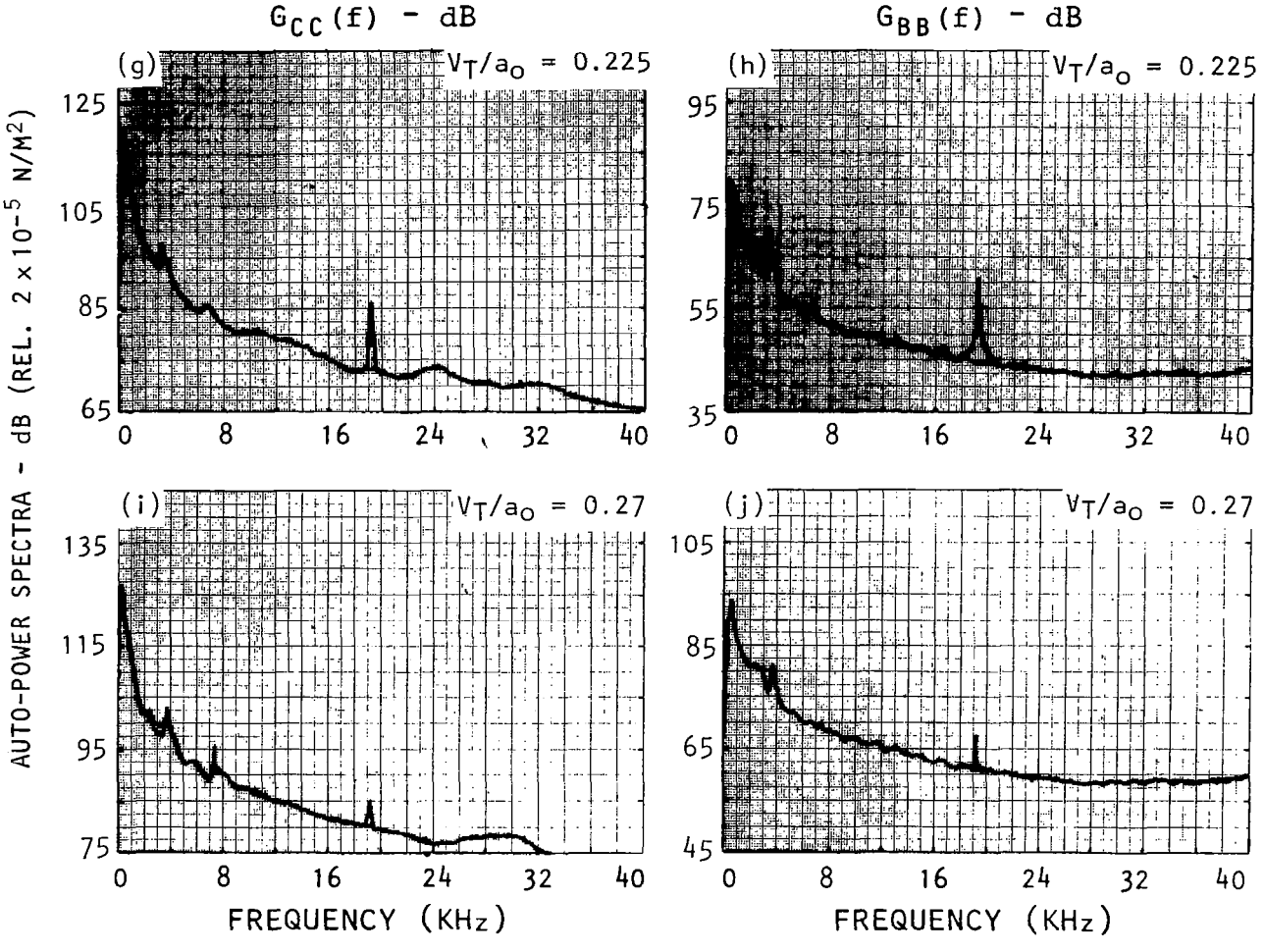

Figure 4.49 Spectra measured at microphone C inside the flow, $G_{CC}(f)$, and at microphone B outside the free jet, $G_{BB}(f)$, with discrete tone excitation. $\psi_T = 90°$, analysis bandwidth $\Delta f = 40$ Hz, point source at $x/d_T = 2.94$

(Concluded)

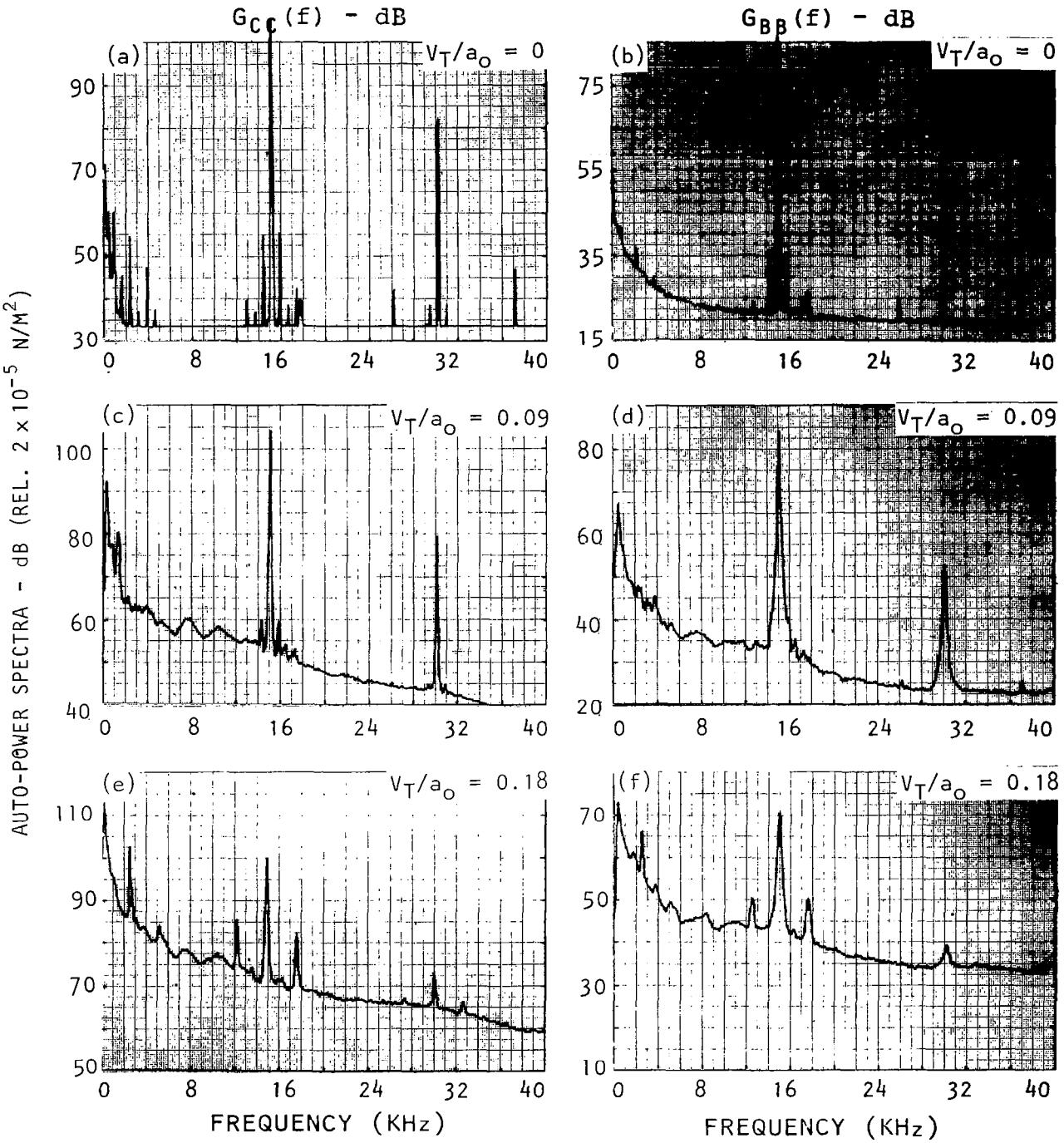

Figure 4.50 Spectra measured at microphone C inside the flow, $G_{CC}(f)$, and at microphone B outside the free jet, $G_{BB}(f)$, with discrete tone excitation. $\psi_T = 90°$, analysis bandwidth $\Delta f = 40$ Hz, point source at $x/d_T = 2.94$.

(Continued on next page)

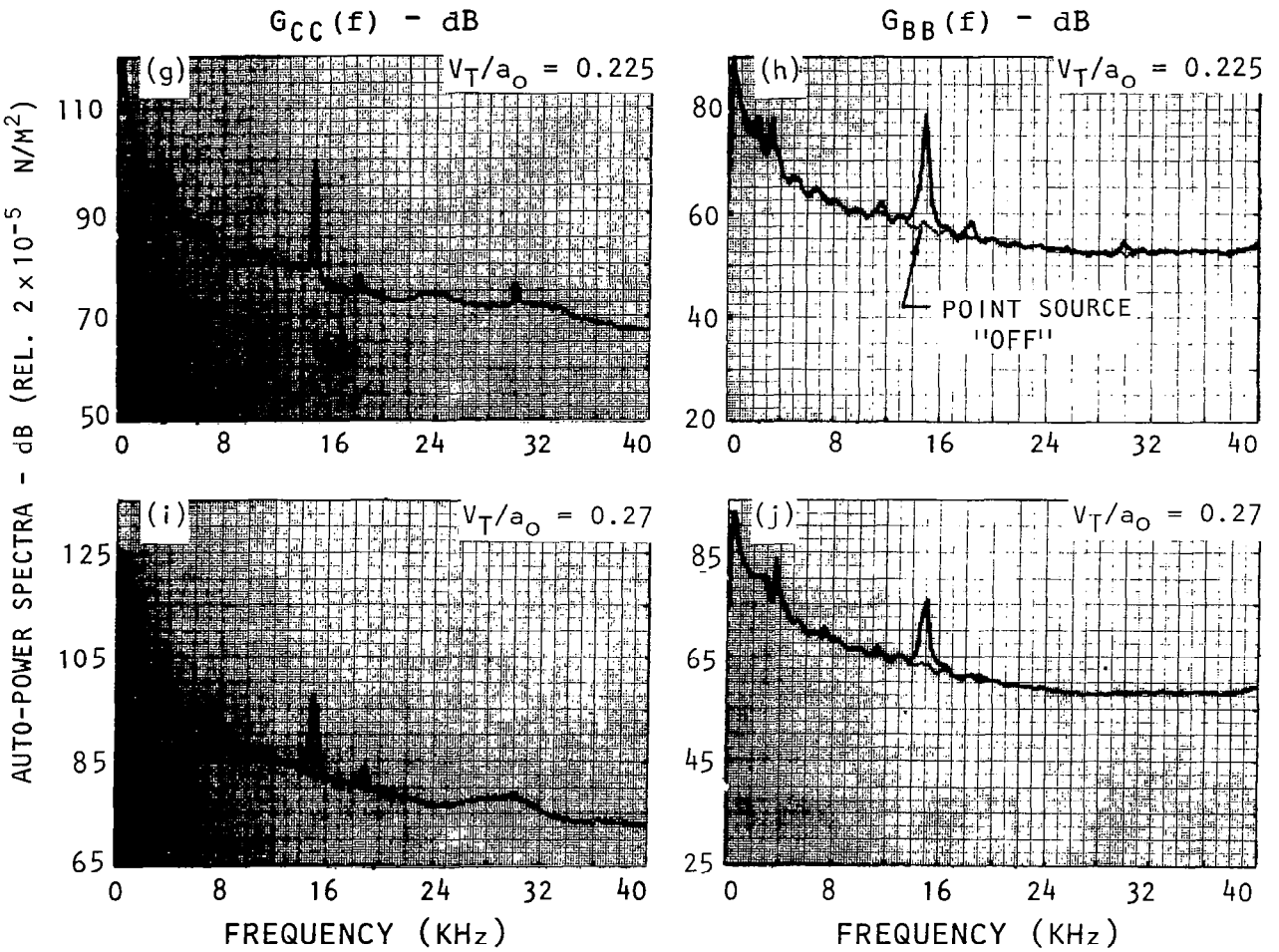

Figure 4.50 Spectra measured at microphone C inside the flow, $G_{CC}(f)$, and at microphone B outside the free jet, $G_{BB}(f)$, with discrete tone excitation. $\psi_T = 90°$, analysis bandwidth $\Delta f = 40$ Hz, point source at $x/d_T = 2.94$.

(Concluded)

In order to study the magnitude of attenuation (or reduction) in the excitation tone level due to turbulence scattering, the measured discrete tone levels inside [i.e. $G_{CC}(f)$] and outside the flow [i.e. $G_{BB}(f)$] were plotted as a function of free-jet Mach number. Using the distance and amplitude calibration factors (C_R and C_F) discussed earlier, the levels measured inside the free-jet at C were scaled to those outside at microphone location B. If the measured values of $G_{BB}(f)$ are lower than these transformed values, the difference is attributed to scattering. Data taken from Figures 4.49 and 4.50 were plotted in this manner in Figure 4.51(a), (b) and (c) for 15 KHz, 20 KHz and 30 KHz, respectively. *(System response corrections were applied in the same way as described in Section 4.5 by comparing $G_{CC}(f)$ and $G_{BB}(f)$ at zero free-jet velocity.)*

Figure 4.51 clearly shows that at these high frequencies, the peak levels of the discrete tones are indeed attenuated (over and above the corrections given by the sum of distance and amplitude calibration factors). This attenuation is indicated by the shaded area in Figure 4.51 and will be denoted by ΔdB_S in the ensuing text. The attenuation (i.e., height of the shaded region) increases both with increasing δ/λ and with increasing free-jet Mach number, V_T/a_T. It should be recalled that the ΔB_S values calculated in the same way from broadband excitation results (described in section 4.5) indicated no attenuation at microphone B located outside the free jet (e.g. see Figures 4.42 through 4.46). The magnitudes of the differences in SPL's inside and outside the flow (corrected to the inside location by amplitude and distance calibration factors) for broadband excitation are plotted in Figure 4.52 as a function of free-jet Mach number for the same frequencies for which discrete tone results are shown in Figure 4.51. A mean value of zero for ΔB_S in Figure 4.52 thus illustrates that the effect of scattering on broadband noise is negligible.

Based upon the spectral broadening results presented above and elsewhere, it is clear that the energy at the center frequency of the discrete tone is distributed over a wider band, and thus, a reduction of the peak level occurs. The broadband data in Figure 4.52 implies that the attenuation at a given frequency is almost exactly compensated by this spectral broadening since only then will a broadband excitation show a zero change. In other words, scattering effects are present for broadband excitation, but the effects average out since the attenuation at any one frequency is augmented by the energy scattered from adjacent frequency bands.

<u>Scattering at Lower Values of δ/λ</u>. The results presented in Figures 4.49 through 4.52 showing scattering effects were all for $\delta/\lambda > 10$. It was found that for smaller values of δ/λ, scattering effects were not so important. Typical results with the 2.54 cm diameter noise source located at $x/d_T = 0.96$ are shown in Figure 4.53 for 19.2 KHz ($\delta/\lambda = 5.8$) discrete tone excitation. Once again, both $G_{CC}(f)$ and $G_{BB}(f)$ are plotted. Unlike the data obtained at $x/d_T = 2.94$ ($\delta/\lambda = 17.6$) for identical configurations, there is little evidence of spectral broadening here. Also, when the data are plotted in the format

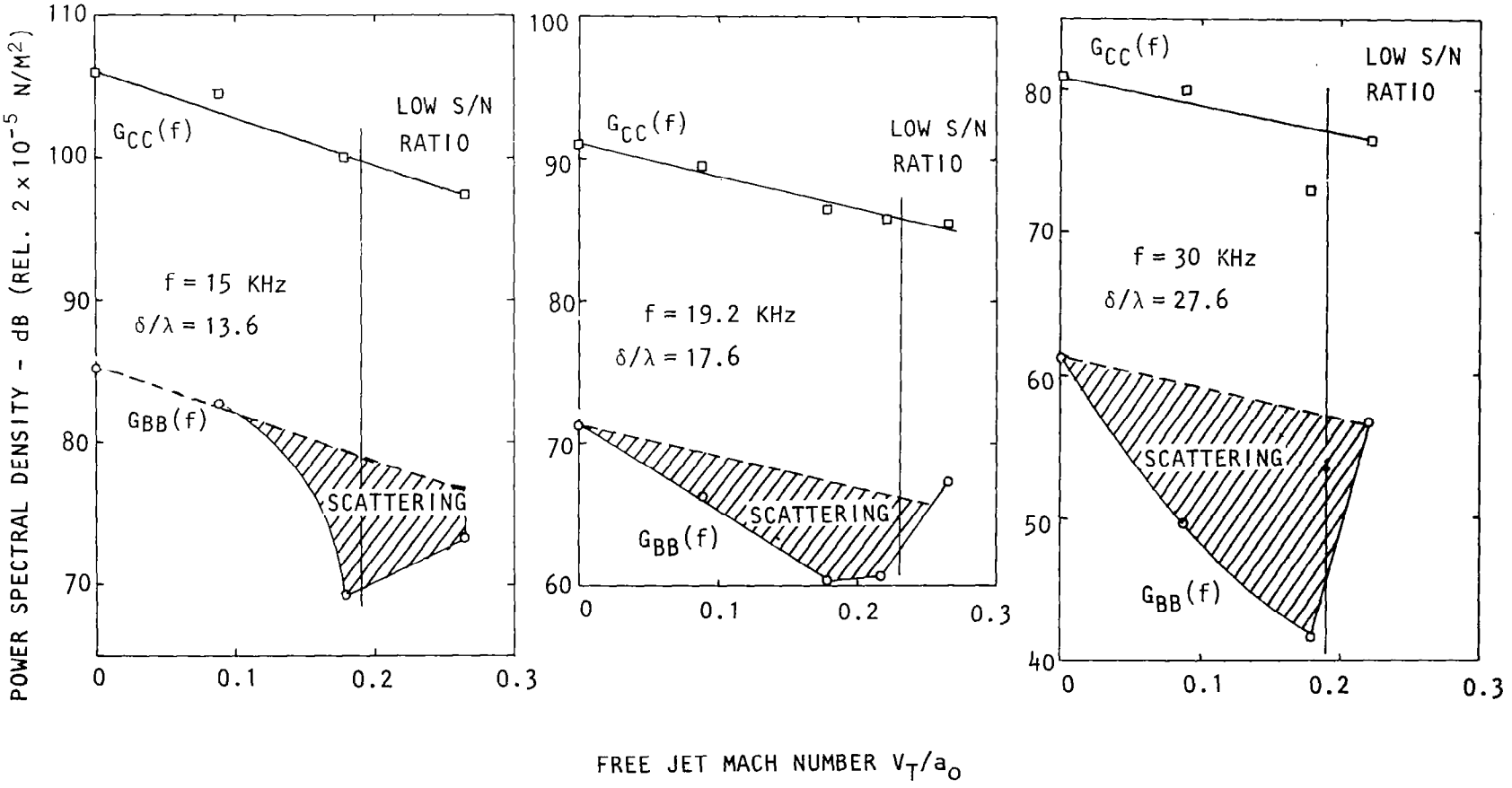

Figure 4.51 Measured SPL's inside the flow (—□—) and outside the flow (—○—) and corrected SPL's at B, $G_{CC}(f) - C_R - C_F$ (- - - - - -), $\theta_m = 90°$, point source at $x/d_T = 2.94$, discrete tone excitation.

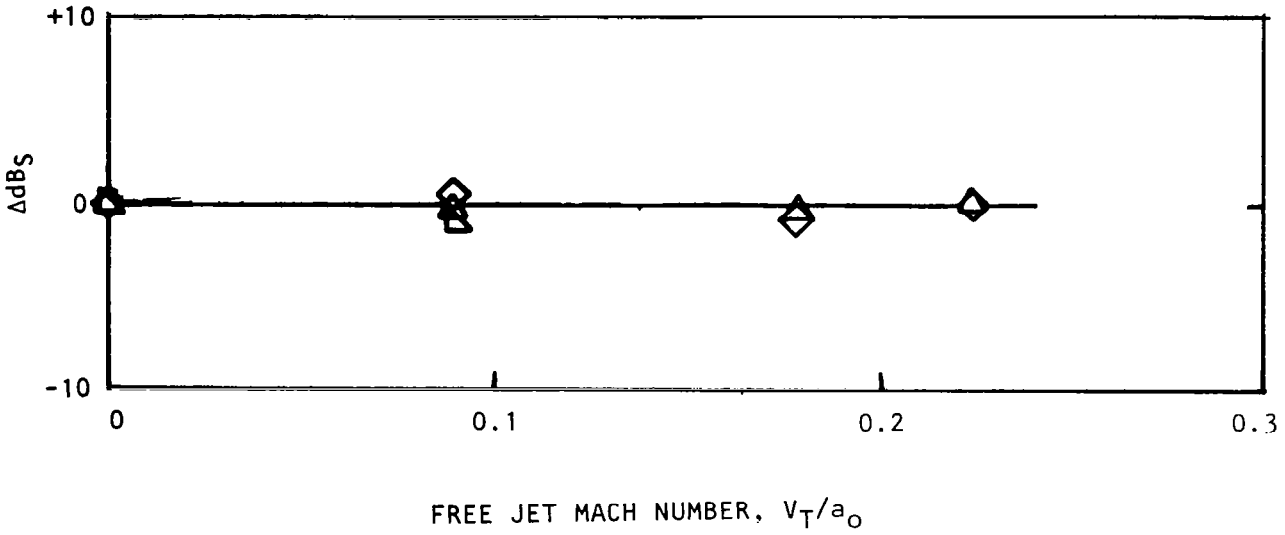

Figure 4.52 Magnitudes of differences in SPL's inside and outside the flow for broadband excitation. ◇ , 15 KHz; △ , 19.2 KHz; ◺ , 30 KHz. Source located at $x/d_T = 2.94$.

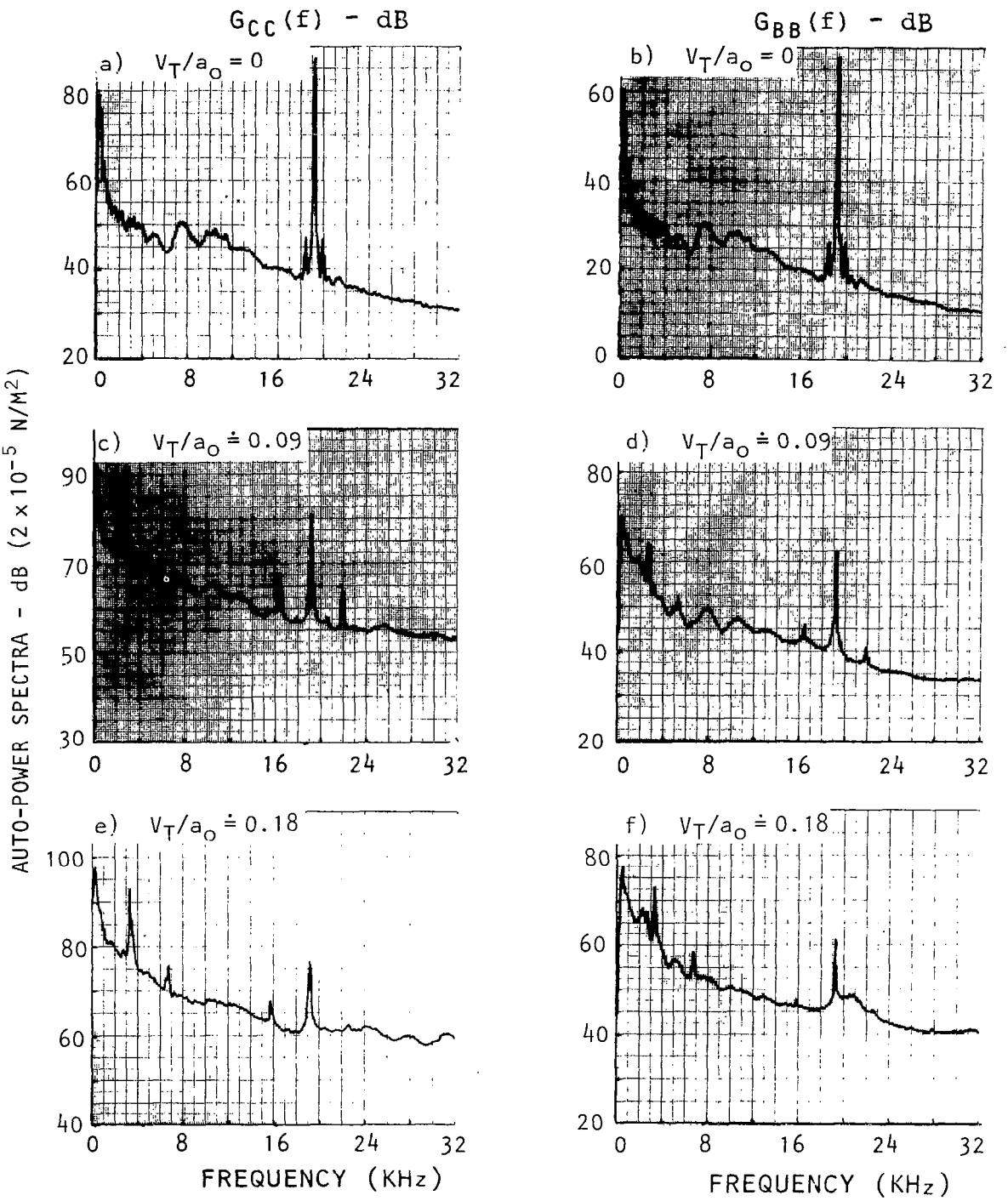

Figure 4.53 Spectra measured at microphone C inside the flow, $G_{CC}(f)$, and at microphone B outside the free jet, $G_{BB}(f)$, with discrete tone excitation. $\psi_T = 90°$, analysis bandwidth $\Delta f = 40$ Hz, point source at $x/d_T = 0.96$.

similar to Figure 4.51, no evidence of scattering is noticed (see Figure 4.54). For free-jet Mach numbers of up to 0.180, the levels at B and C can be fully accounted for by the distance and amplitude calibration factors (thus confirming the absence of turbulence absorption or scattering). For V_T/a_o greater than 0.180, microphone B appears to show an increase in noise.

Although the data obtained by using the small 0.635 cm diameter point source could not be utilized to study the *spectrum broadening effects* owing to low S/N ratio, the data were quite useful to determine the changes in levels of the discrete tone at the excitation frequency along the respective ray paths. In this case, the *cross-power spectra* $G_{AC}(f)$ and $G_{AB}(f)$ were measured, and the difference $G_{AC}(f) - G_{AB}(f)$ was then compared with the value obtained by accounting for the distance and calibration factors. If the measured difference was higher than the predicted value, it was attributed to scattering. Figure 4.55 shows data analyzed in this manner. The data are presented in the order of increasing δ/λ, as shown in Table 4.4.

Table 4.4 Discrete-tone results with increasing δ/λ.

Figure Number	Excitation Frequency f (KHz)	Point Source Location x/d_T	Ray Angle ψ_T	δ/λ
4.55(a)	5.0	0.22	40°	1.3
4.55(b)	5.0	0.99	40°	1.6
4.55(c)	15.0	0.22	60°	2.4
4.55(d)	10.0	0.22	40°	2.6
4.55(e)	10.0	0.99	40°	3.2
4.55(f)	15.0	0.99	40°	4.8
4.55(g)	10.0	2.00	90°	6.2
4.55(h)	15.0	2.00	90°	9.4
4.55(i)	19.2	2.00	90°	12.0

These results clearly demonstrate that it is only when δ/λ approaches a value of 10 that turbulence scattering becomes effective and that peak levels of the discrete tones undergo a reduction on crossing the shear layer. Also, the effect becomes more important at higher Mach numbers.

In an aircraft engine, the majority of noise sources distributed downstream of the nozzle exit are normally broadband in nature. Hence, based upon the scattering results presented in this section, the effects of forward velocity on these broadband sources can be investigated in a free-jet flight simulation facility with minor, if any, complications introduced by turbulence scattering effects. The majority of discrete-frequency or narrow-band noise

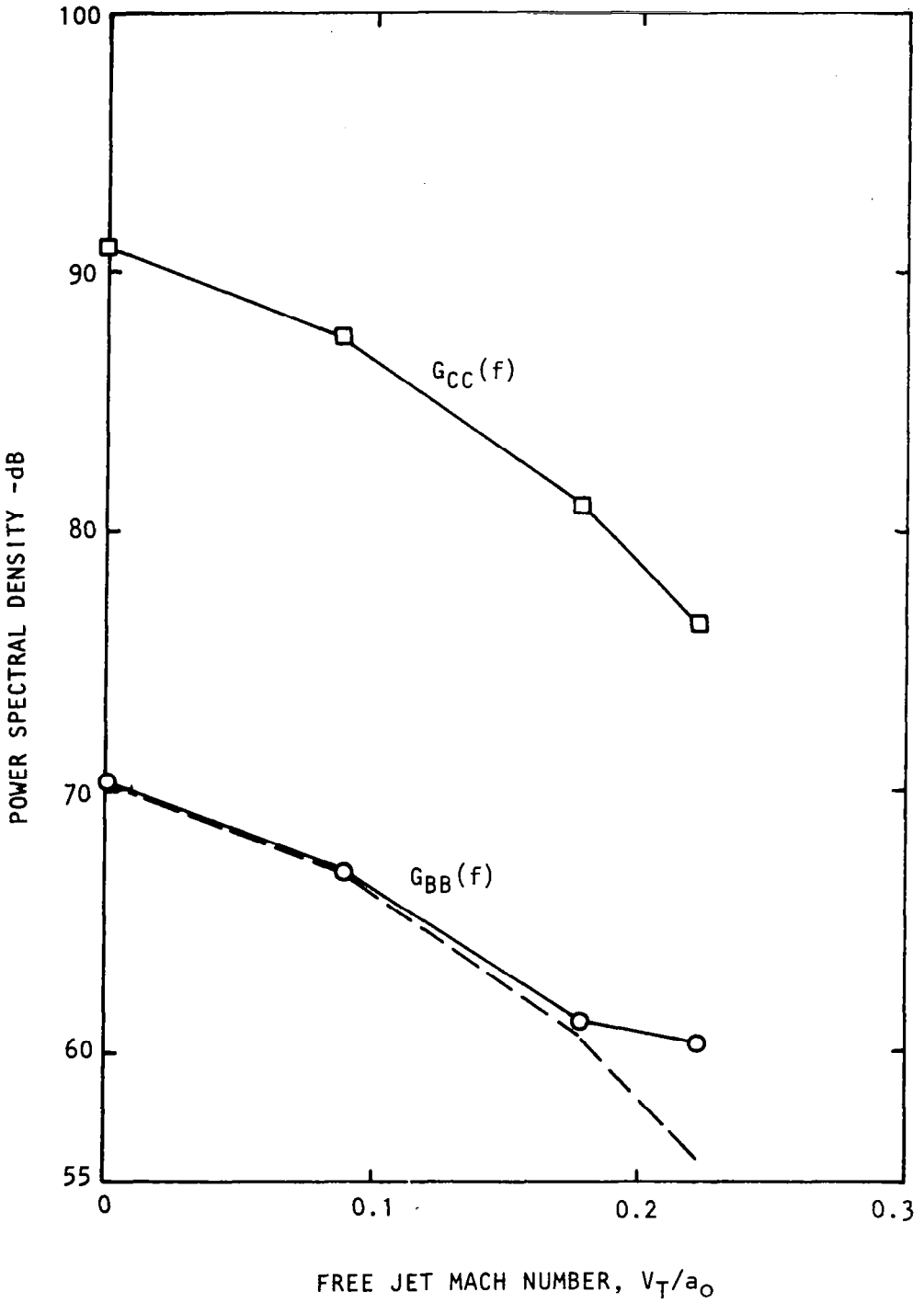

Figure 4.54 Measured SPL's inside the flow (—□—) and outside the flow(—○—) and the corrected SPL's at B, $G_{CC}(f)$ - C_R - C_F(- - -). $\theta_m = 90°$; point source at $x/d_T = 0.96$; discrete tone excitation. $f = 19.2$ KHz ($\delta/\lambda = 5.8$)

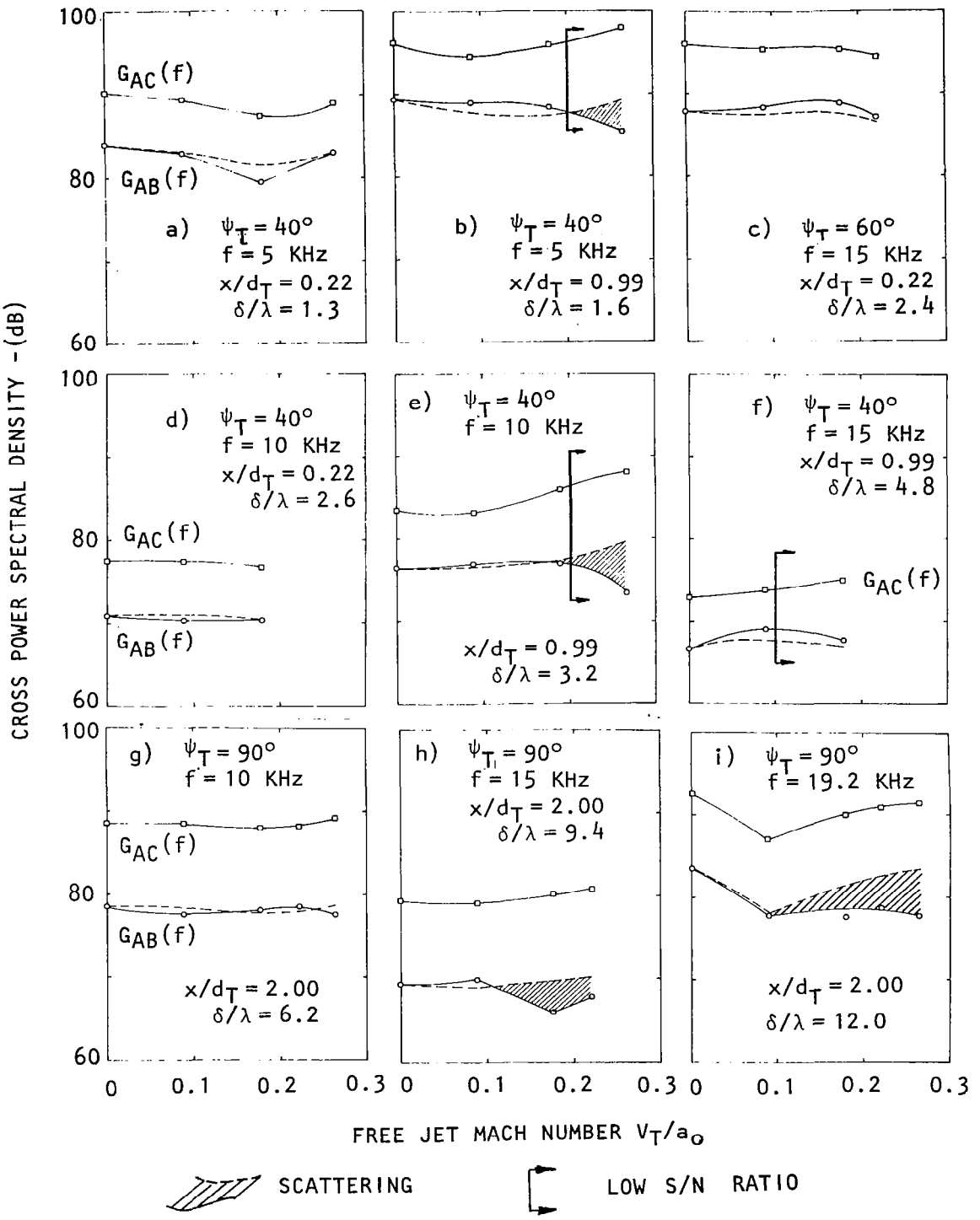

Figure 4.55 Measured cross-power spectral densities $G_{AC}(f)$(—□—), and $G_{AB}(f)$(—O—)and the corrected $G_{AC}(f)$ (– – –) at various ψ_T, x/d_T, f and δ/λ.

sources in an engine are located either inside the engine or quite close to the nozzle exit. In order to investigate flight effects on these discrete-frequency noise sources, it is desirable to keep the values of δ/λ less than approximately 10 in order to minimize scattering effects in a free-jet flight simulation experiment. It is felt that this can be achieved in principle by placing the jet or engine configuration as close to the free-jet nozzle exit plane as possible. It is recommended, however, that a proper scale-optimization study should be conducted prior to free-jet flight simulation experiments for discrete-frequency noise sources from an engine.

4.7 PROBLEMS AT LOW FREQUENCIES

In the majority of results presented in this section so far on transmission, reflection and scattering of sound in a free-jet flight simulation facility, the question about the low-frequency behavior has not been resolved completely, and further study is required. Typical problem areas for low-frequency noise, as determined from some complementary experiments, are summarized below.

Angle Change Tests

The verification of angle changes in the present investigation was conducted by comparing the measured peak time delays in $R_{AB}(\tau)$ with those predicted by Snell's law and the diverging flow model. Broadband point-source excitation was used, and it was assumed at first that the measured peak time delay was constant for all frequencies. In fact, the phase spectra $\phi_{AB}(f)$ obtained by moving the peak of $R_{AB}(\tau)$ to zero time delay before Fourier transform (e.g. see Figure 4.16) confirmed that for the majority of frequency range above 1 KHz, the peak time delay was independent of frequency. This is because in this frequency range, $\phi_{AB}(f)$ was always close to zero. Little could, however, be said with certainty about the frequencies lower than approximately 1 KHz. An experiment was therefore conducted, where the bandwidths of the signals at microphones A and B were varied before the signals were correlated. These measurements were carried out with the experimental point source located at $x/d_T = 1.74$. The five source spectrum bandwidths tested are shown schematically in Figure 4.56. The corresponding cross-correlation functions at various free-jet Mach numbers are shown in Figure 4.57. The measured peak time delays, τ_m, are given in Table 4.5, although clearly in the case of spectrum E1, τ_m is difficult to estimate accurately.

The tabulated values show that for the lowest bandwidth, the peak time delay is smaller than that corresponding to the higher bandwidths. In fact, at each Mach number, the peak time delays for all excitation bandwidths except the 0 - 2 KHz bandwidth agree within the measurement accuracy (± 0.010 ms in this case). These measurements therefore tend to show that low frequency sound may not, after all, follow ray paths as predicted by Snell's law - which has been shown to apply quite accurately to high-frequency sound. Further work , using wave theory, is required to resolve this low frequency behavior.

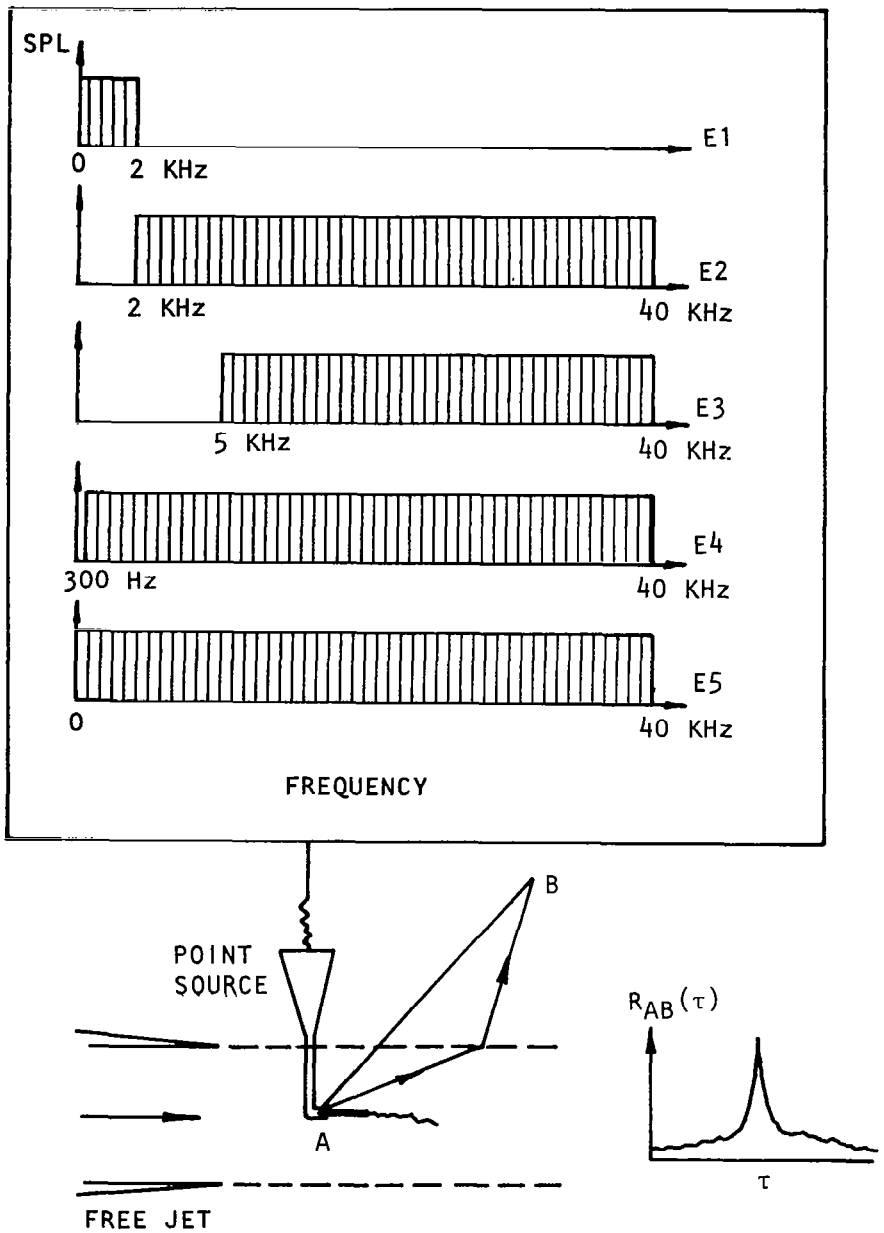

Figure 4.56 Schematic of source spectrum bandwidths tested to measure R_{AB}

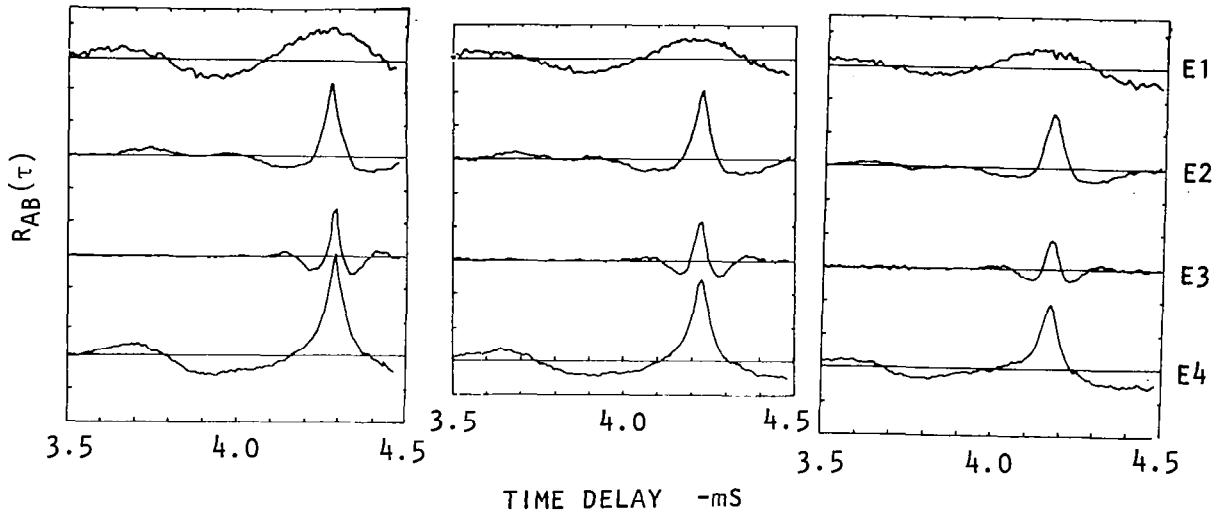

(a) $V_T/a_o = 0$ (b) $V_T/a_o = 0.045$ (c) $V_T/a_o = 0.090$

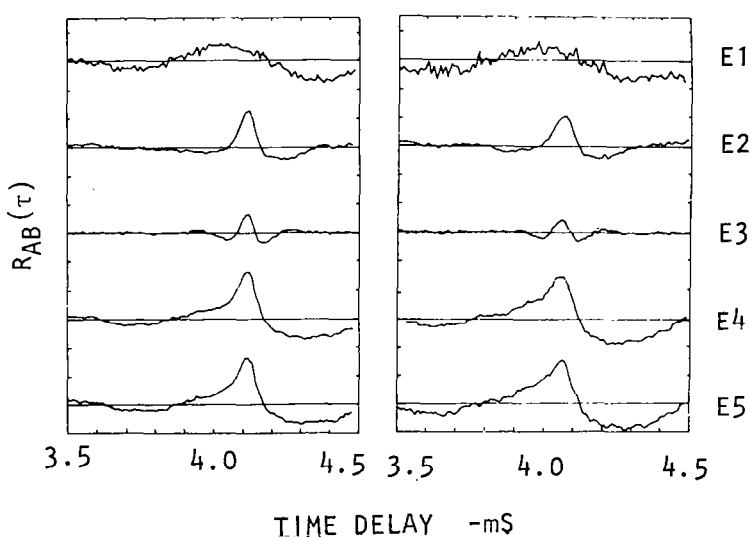

(d) $V_T/a_o = 0.135$ (e) $V_T/a_o = 0.180$

E1 = 0 - 2 KHz , E2 = 2 KHz - 40 KHz, E3 = 5 KHz - 40 KHz,
E4 = 300 Hz - 40 KHz, E5 = 0 - 40 KHz.

Figure 4.57 Cross-correlation functions, $R_{AB}(\tau)$, for various bandwidths of the point source output. $\theta_m = 40^\circ$, point source at $x/d_T = 1.74$.

Table 4.5 Peak time delays (in ms) at various free-jet Mach numbers and point-source bandwidths

Bandwidth \ V_T/a_o	0.0	0.045	0.090	0.135	0.180
0 - 2 KHz, E1	4.290	*4.205	*4.135	*4.020	*4.000
2 KHz - 40 KHz, E2	4.285	4.228	4.173	4.120	4.165
5 KHz - 40 KHz, E3	4.287	4.225	4.174	4.115	4.160
300 Hz - 40 KHz, E4	4.292	4.227	4.170	4.115	4.160
0 - 40 KHz, E5				4.115	4.160

**Rough estimates of "peak" time delay.*

Internal Reflection and Transmission Tests

A clear-cut picture of internal reflection and transmission at low frequencies ($f < 1$ KHz) could not be obtained in this work. Phase spectra $\phi_{AD}(f)$ and $\phi_{AC}(f)$ (for example, see Figures 4.15 and 4.17) could not provide adequate information at these frequencies. This was due to the possibility of some low frequency noise from the free jet itself which could be correlated at microphones A and D or at microphones A and C used to obtain $R_{AD}(\tau)$ and $R_{AC}(\tau)$. Further work is required to explore the internal reflection and transmission effects at low frequencies.

In view of the above remarks, the conclusions given in the next section should be considered valid for frequencies higher than 1 KHz.

4.8 SUMMARY

When a free-jet is used as a wind tunnel to simulate the effects of flight on model noise sources, with microphones placed outside the free-jet (in an anechoic environment), it is necessary *to calibrate out the influence of the free-jet shear layer* on the transmitted sound, since the shear layer is absent in the flight case. Thus, an experimental program using a point sound source was conducted to provide basic information on the physical processes by which sound is transmitted across the axisymmetric, turbulent shear layer of a free jet.

The five important aspects of the transmission process and the conclusions derived from the present work are as follows:

(1) *Redirection or refraction of sound by the mean sheared flow:* An experimental technique used to measure (indirectly) the refraction of waves transmitted across the shear layer confirms that *Snell's law* holds to a good approximation over a wide range of incident wave normal angles and free-jet velocities.

(2) *Internal reflection of sound at the sheared flow:* Internal reflection appears to be insignificant for the majority of data analyzed. Significant reflection was detected only in the *total internal reflection regime* (ray angle $\psi_T = 140°$ and $V_T/a_T > 0.18$ in the present experiments).

(3) *Transmission of sound through the mean sheared flow (coherent transmission):* The relationship between pressure amplitudes *inside* and *outside* the free jet measured on a *common ray path* emanating from a source inside the potential core, behave in a manner consistent with a geometric-acoustics energy-conserving transmission process.

(4) *Transmission of sound through the unsteady sheared flow (turbulence absorption):* The absorption of sound by turbulence in the free-jet shear layer, if present, is insignificant over the ranges of parameters of practical interest.

(5) *Transmission of sound through the unsteady sheared flow (turbulence scattering):* Frequency broadening of transmitted discrete tones is detected only when the ratio of shear layer thickness to sound wavelength, δ/λ, is about 10 or higher. Discrete tones with $\delta/\lambda \lesssim 10$ measured outside the free jet can be transformed to ideal wind tunnel conditions through the use of distance and amplitude calibration factors also used for broadband noise. For broadband noise sources, turbulence scattering effects pose no real problem.

The experimental results thus far confirm the validity of the calibration procedure, outlined in Section 2, and which was recommended as a result of an earlier theoretical investigation conducted at Lockheed-Georgia Company (ref. 4.2).

5. THEORETICAL INVESTIGATION

Previous theoretical approaches (refs. 5.1 through 5.4) to the free-jet facility calibration problem have started from the *assumption* either that the free-jet shear layer is infinitely thin, i.e. a vortex sheet ($\delta_T/\lambda \to 0$), or that it is infinitely thick on a wavelength scale ($\delta_T/\lambda \to \infty$). The latter assumption gives the geometric acoustics (GA) approximation adopted in our previous work (ref. 5.4) and also by Candel et al. (ref. 5.1); more recently the validity of the GA approximation has been assessed by Morfey and Tester (ref. 5.5) and by Amiet (ref. 5.6) with the aid of numerical solutions to the Lilley equation. On the other hand, in earlier work Amiet (ref. 5.2) and Jacques (ref. 5.3) used the vortex sheet model alone.

In terms of sound reflection at the free-jet shear layer, these approximations represent the extremes of zero and maximum reflection. To investigate the effects of finite δ_T/λ, we use *the Lilley equation* (ref. 5.7), which may be written in the form (ref. 5.8)

$$\frac{1}{\bar{a}^2}\frac{\bar{D}^3 p}{Dt^3} - \frac{\bar{D}}{Dt}\nabla^2 p + \frac{1}{\bar{\rho}}\frac{d\bar{\rho}}{dr}\frac{\bar{D}}{Dt}\frac{\partial p}{\partial r} + 2\frac{dV}{dr}\frac{\partial^2 p}{\partial x \partial r} = \bar{\rho} Q \qquad (5\text{-}1)$$

Equation (5-1) describes the propagation of pressure disturbances, p, through a steady axisymmetric parallel shear flow with velocity $[V(r),0,0]$, sound speed $\bar{a}(r)$ and density $\bar{\rho}(r)$ $(\bar{D}/Dt \equiv \partial/\partial t + V\partial/\partial x)$.

In previous applications (refs. 5.8 and 5.9) of equation (5-1) to the effects of acoustic-mean flow interaction on jet mixing noise, the collection of nonlinear terms represented by Q was replaced by an approximate ring source model of the source distribution and exactly the same approach is adopted in the present study as summarized below. A realistic source model is required because it has to be recognized that the influence of the outer free-jet shear layer cannot be strictly decoupled from the source itself; in other words the calibration factor to be applied to the free-jet data will depend in principle on the nature of the source being studied and on its local mean flow field.

5.1 JET NOISE CALIBRATION FACTOR

Of particular concern here is the calibration factor to be applied to turbulent jet mixing noise measurements. Figure 5.1 compares the mean velocity profile *relative to the nozzle* (a) for a primary jet nozzle in forward flight at speed V_T (i.e. in the "ideal wind tunnel") and (b) for the same nozzle in a flight *simulation* free-jet facility. The primary jet exit velocity is V_J in both cases.

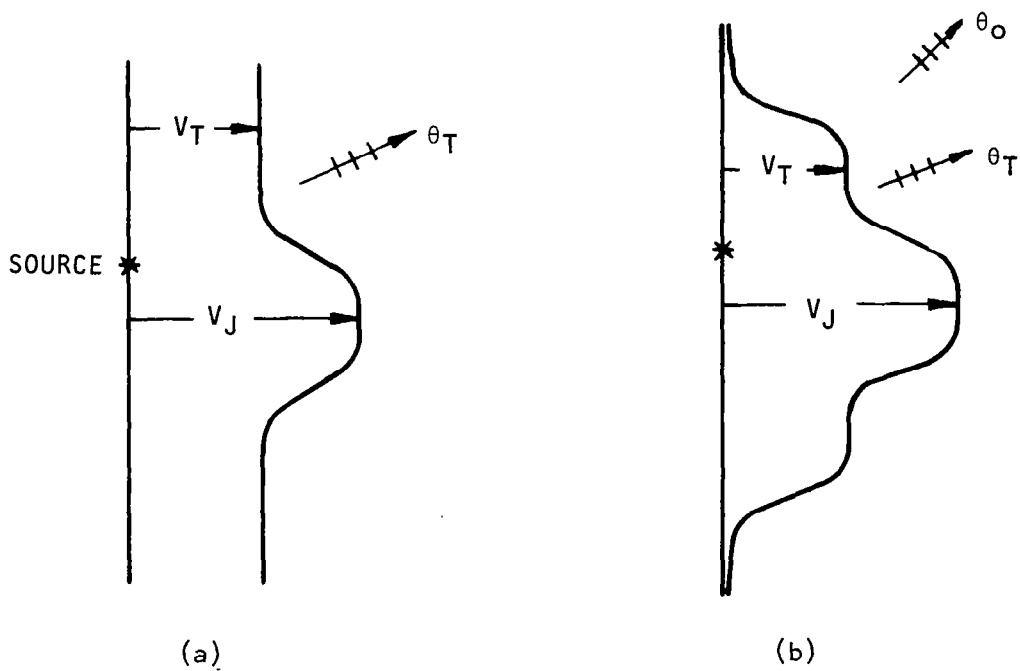

Figure 5.1 Velocity profiles for Lilley equation analysis: (a) ideal wind tunnel, (b) free-jet simulation.

With the aid of simplified but realistic models of the primary jet noise sources and the respective mean flow fields, it is straightforward to obtain from Lilley equation solutions (ref. 5.5) the power spectral densities (PSD) of the far-field acoustic pressure in the two situations represented by Figures 5.1(a) and 5.1(b). Their ratio – which depends in principle on the source model, as well as the frequency and the mean flow description – is referred to as the free-jet calibration factor C_F.

The far-field pressure PSD's are calculated for the same fixed frame frequency and axial wavenumber; this means that the axial phase speed of the radiation is the same in each case, i.e. in Figures 5.1(a) and 5.1(b), viz.

$$\frac{a_o}{\cos\theta_o} = \frac{a_T}{\cos\theta_T} + V_T \qquad (5\text{-}2)$$

(outside free-jet) (in ideal wind tunnel)

where θ_o is the emerging angle in the stationary medium outside the free jet.

The primary jet noise source is modeled as a statistically isotropic multipole ring source (ref. 5.8); statistically isotropic means that when the model source is placed in a uniform medium at rest, its radiated intensity field is omnidirectional. The source strength is also statistically axisymmetric (like the jet turbulence); that is, the source strength PSD and hence the far-field PSD are independent of azimuthal position. By definition, the model ring source is radially compact but here for calculation purposes it is also assumed to be azimuthally compact. This source model was first used in reference 5.8 to study acoustic-mean flow interaction effects on jet mixing noise. Because the mean flow is uniform in the axial direction, source convection and axial noncompactness effects can be accounted for separately and independently of the Lilley equation solutions with an appropriate model for the axial wavenumber-frequency spectrum of the source strength.

In the following sections, results are presented for the calibration factors $C_{Fm}^{(\nu)}$, $C_{Fd}^{(\nu)}$, and $C_{Fq}^{(\nu)}$. The index ν indicates the temporal order of the model source: e.g., $\nu = 1$ (volume-acceleration), 2 (volume-velocity), or 3 (volume-displacement). The subscripts m, d, q indicate the spatial order of the model source; i.e. monopole, dipole, or quadrupole.

5.2 FACILITY CALIBRATION FACTOR BASED UPON APPROXIMATE SOLUTIONS TO THE LILLEY EQUATION

The free-jet calibration factor can be evaluated with closed-form solutions to the Lilley equation in the limiting cases $\delta_T/\lambda \to 0$ and $\delta_T/\lambda \to \infty$; then the solutions and corresponding calibration factors are referred to here as the low-frequency (LF) and high-frequency or geometric acoustics (GA) approximations. The low-frequency case can be pictured as indefinitely large sound wavelengths in a shear layer of non-zero thickness *or* sound

of any wavelength on both sides of a (cylindrical) vortex sheet, sometimes referred to as a plug flow model of the real flow profile. The high-frequency case can be interpreted in a similar fashion. In the former case the more usual vortex sheet picture is normally employed here but when the Lilley equation is solved numerically for a fixed profile – as a function of frequency – the alternative interpretation is required.

Both limiting cases have been solved previously but certain assumptions and simplifications have been utilized which are now removed or avoided in the analysis given below, which yields the low- and high-frequency free-jet calibration factors utilized in sections 5.3 and 5.4.

5.2.1 Low-Frequency Approximation (Vortex Sheet Model)

In the low-frequency limit when the sound wavelength, λ, is large compared with the free-jet shear layer thickness ($k_o\delta_T \to 0$), the Lilley equation yields a simple result for the calibration factor if (a) the source can be represented by a point monopole located in the primary-jet potential core on the jet axis – or off-axis a small distance compared with λ – and if (b) the sound wavelength is also large compared with the primary-jet shear layer thickness ($k_o\delta_J \to 0$) *and* the primary-jet nozzle radius ($k_o r_J \to 0$) as will be the case, in practice, when $k_o\delta_T \to 0$. This simple result will be used to assess the effect of the free-jet mean flow field on sound radiated from *internal* noise sources through the primary-jet nozzle at *low* frequencies. The approach is of course consistent with the vortex sheet or plug flow models utilized by Amiet (ref. 5.2) and Jacques (ref. 5.3), except there the primary jet flow was ignored at the outset. The results given here provide theoretical justification for those models.

The analysis is straightforward for plug flows (see Figure 5.2) and yields the following calibration factors. For the complete profile:

$$C_{Fmo}^{(\nu)} = D_T^6 \left|\frac{W_{o,FJ}}{W_{o,IWT}}\right|^2 \qquad \text{(free-jet + primary jet profiles)} \tag{5-3a}$$

where

$$\begin{aligned} W_{o,FJ} = (j\pi/2)\ [J_o(\kappa_J R_J)\ \{E_o\kappa_T R_J\ H_o^{(2)'}(\kappa_T R_J) \\ - F_o\kappa_T R_J\ H_o^{(1)'}\ (\kappa_T R_J)\} \\ - \kappa_J R_J \frac{\rho_J D_T^2}{\rho_J D_J^2}\ J_n'(\kappa_J R_J)\{E_o H_o^{(2)}(\kappa_T R_J) - F_o H_o^{(1)}(\kappa_T R_J)\}]\ , \end{aligned} \tag{5-3b}$$

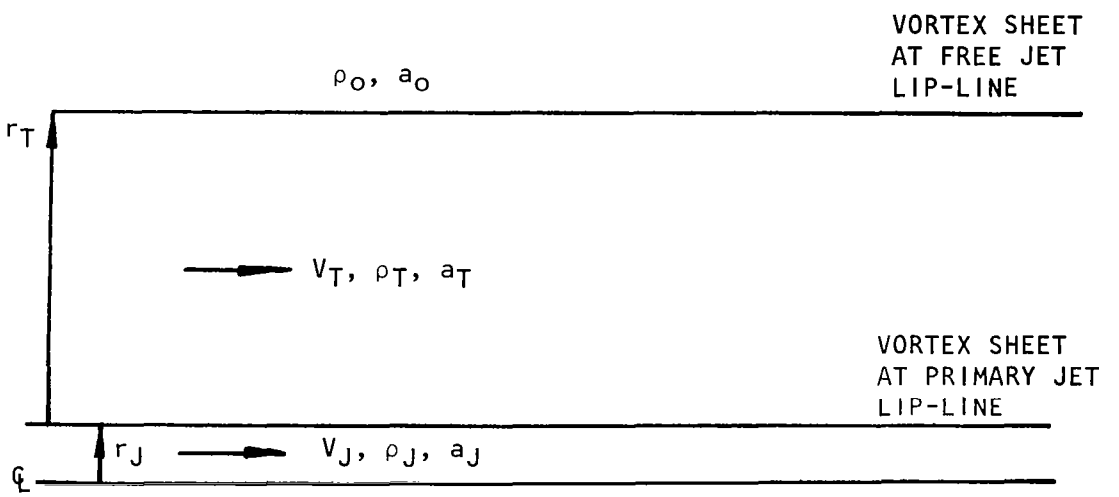

Figure 5.2 Plug flow model of primary-jet and free-jet mean flow fields for low frequency calibration factor.

$$E_o = (j\pi/4)[\kappa_o R_T \; H_o^{(2)'}(\kappa_o R_T) \; H_o^{(1)}(\kappa_T R_T)$$

$$- \frac{\rho_o}{\rho_T D_T^2} \kappa_T R_T \; H_o^{(2)}(\kappa_o R_T) \; H_o^{(1)'}(\kappa_T R_T)], \qquad (5\text{-}3c)$$

$$F_o = (j\pi/4)[\kappa_o R_T \; H_o^{(2)'}(\kappa_o R_T) \; H_o^{(2)}(\kappa_T R_T)$$

$$- \frac{\rho_o}{\rho_T D_T^2} \kappa_T R_T \; H_o^{(2)}(\kappa_o R_T) \; H_o^{(2)'}(\kappa_T R_T)] \qquad (5\text{-}3d)$$

$$W_{o,IWT} = (j\pi/2) \; [J_o(\kappa_J R_J)\kappa_T R_J \; H_o^{(2)'}(\kappa_T R_J)$$

$$- \kappa_J R_J \frac{\rho_T D_T^2}{\rho_J D_J^2} J_o'(\rho_J R_J) \; H_o^{(2)}(\kappa_J R_J)] \qquad (5\text{-}3e)$$

$$\kappa = \left\{ \frac{a_o^2 D^2}{a^2} - \cos^2\theta_o \right\}^{\frac{1}{2}}, \qquad (5\text{-}3f)$$

$$R = k_o r, \qquad k_o = \omega/a_o \qquad (5\text{-}3g)$$

$$D = 1 - V\cos\theta_o/a_o \; . \qquad (5\text{-}3h)$$

The corresponding partial profile calibration factor is given by

$$C_{Fmo,par}^{(\nu)} = D_T^6 \; |W_{o,par}|^2 \qquad \text{(free-jet profile alone)} \qquad (5\text{-}4a)$$

where

$$W_{o,par} = E_o + F_o$$

$$= (j\pi/2) \; [J_o(\kappa_T R_T) \; \kappa_o R_T \; H_o^{(2)'}(\kappa_o R_T)$$

$$- \frac{\rho_o}{\rho_T D_T^2} J_o'(\kappa_T R_T) \; \kappa_T R_T \; H_o^{(2)}(\kappa_o R_T)] \qquad (5\text{-}4b)$$

Note that both calibration factors are independent of the source temporal order (ν) as might be expected when the source is placed within a uniform flow region.

Thus, a low-frequency calibration factor can be calculated with equations (5-3a) - (5-3h) and these take into account the effect of both the primary and free-jet shear layers on low-frequency sound transmission. However, in practice, a further simplification automatically follows. That is, the sound wavelength will normally be large compared with the primary nozzle diameter ($k_o r_J \to 0$) if, as assumed, it is sufficiently large compared with the typical shear layer thicknesses δ_J, δ_T for the vortex sheet profile approximation to be employed in the first place (being valid only in the limit $k_o\delta_J$, $k_o\delta_T \to 0$).

When the limit $k_o r_J \to 0$ *is* applied to equations (5-3b), (5-3e) so that $\kappa_J R_J$, $\kappa_T R_J \to 0$ ($J_o(z) \to 1$, $J_o'(z) \to -z/2$, $z\, H_o^{(2)\prime}(z) \to -\, 2j/z$), then

$$W_{o,FJ} \to E_o + F_o$$

$$W_{o,IWT} \to 1$$

and clearly the calibration factor for the complete profile, $C_{Fmo}^{(\nu)}$ becomes identical with that for the partial profile, $C_{Fmo,par}^{(\nu)}$, given by equations (5-4). Thus, the primary jet flow conditions (V_J, ρ_J, a_J) can be ignored and only the free-jet flow conditions (V_T, ρ_T, a_T) determine the low-frequency calibration factor. Although this factor (given by equations (5-4)) is not as simple as the high frequency one described in the next section, it is still a relatively straightforward expression to evaluate, involving four Bessel functions of order zero with real arguments.

This result justifies the earlier work by Amiet (ref. 5.2) and Jacques (5.3) in which primary-jet profile effects are not considered at all. However, it is emphasized that this low-frequency calibration factor is intended only for low-frequency *internal* noise data calibration, as will be discussed in Section 5.4. For jet mixing noise and, in general, internal noise the high-frequency approximation can be used (as will be shown in Section 5.3) and that factor is derived in the following section.

5.2.2 High-Frequency Approximation (Geometric Acoustics)

The problem of sound transmission across a parallel, cylindrical shear layer at high frequencies has already been solved (refs. 5.10, 5.8, and 5.4) by utilizing (a) Snell's law for parallel sheared flows and (b) the Blokhintsev (ref. 5.11) GA energy conservation law together with the concept of local wavefronts in uniform flows; this approach implies that Lilley's equation is solved in the high-frequency limit. An alternative approach is described here that utilizes Lilley equation solutions directly and thus avoids the concept employed in the earlier derivation of "azimuthally averaged" far-field quantities (which is unattractive from the experimental viewpoint) by describing the source excitation and radiation field in terms of azimuthal modes. In this way nonstatistically axisymmetric noise sources (e.g. internal noise sources generating azimuthal standing waves) can be calibrated. In fact, the analysis below shows that for sufficiently large area ratios the calibration factor is independent of azimuthal mode order

and is equal to the already well established high-frequency or GA calibration factor

$$C_{F_\infty} = \rho_T D_T^4/\rho_o \,. \tag{5-5}$$

Only the "partial profile" is considered in what follows since the analysis applies to any source distribution of arbitrary temporal and spatial order. The analysis starts with defining† the temporal order of the source function Q

$$Q^{(\nu)} = \frac{\bar{D}^\nu S^{(\nu)}}{Dt^\nu} \tag{5-6}$$

and with the Fourier transform of equation (5-1) with respect to x,ϕ and t

$$\frac{1}{r}\frac{d}{dr}\left(r\frac{d\tilde{p}^{(\nu)}}{dr}\right) + \left(-\frac{1}{\bar{\rho}}\frac{d\bar{\rho}}{dr} - \frac{2}{D}\frac{dD}{dr}\right)\frac{d\tilde{p}^{(\nu)}}{dr}$$

$$+\left\{k_o^2\left(\frac{a_o^2 D^2}{\bar{a}^2} - \frac{k_x^2}{k_o^2}\right) - \frac{n^2}{r^2}\right\}\tilde{p}^{(\nu)}$$

$$= -\bar{\rho}\,(j\omega)^{\nu-1}\,D^{\nu-1}\,\tilde{S}^{(\nu)} \tag{5-7}$$

where

$$D(r) = 1 - k_x\,V(r)/\omega, \qquad k_o = \omega/a_o$$

and

$$\tilde{p}^{(\nu)}(k_x,r,n,\omega) = \int_{-\infty}^{\infty} dx \int_{-\pi}^{+\pi} d\phi \int_{-\infty}^{\infty} dt\; p^{(\nu)}(x,r,\phi,t)e^{j(k_x x + n\phi - \omega t)}$$

and similarly for $\tilde{S}^{(\nu)}$.

The solution to equation (5-7) (ref. 5.8) is

$$\tilde{p}^{(\nu)}(k_x,r,n,\omega) = \int_0^\infty dr'\; r'G^{(3)}(r|r')\;(j\omega)^{\nu-3}\;D^{\nu-3}(r')\;\tilde{S}^{(\nu)}(r') \tag{5-8}$$

---

†*This serves to link this approach with our previous work, but it is not essential for the present analysis.*

where $G^{(3)}(r|r')$ is the solution of

$$\frac{d}{dr}\left(\frac{r}{\bar{\rho}\omega^2 D^2}\ \frac{dG^{(3)}(r|r')}{dr}\right)+\frac{rG^{(3)}(r|r')}{\bar{\rho}\omega^2 D^2}\left\{k_o{}^2\kappa^2-\frac{n^2}{r^2}\right\}=\delta(r-r') \tag{5-9}$$

satisfying the finiteness condition at $r=0$ and the radiation condition. In equations (5-8) and (5-9) the dependence of $\tilde{S}^{(\nu)}$ and $G^{(3)}$ on k_x, n and ω has been suppressed for simplicity and here

$$\kappa = \{a_o{}^2D^2/\bar{a}^2 - (k_x/k_o)^2\}^{\frac{1}{2}}. \tag{5-10}$$

The formal solution to equation (5-9) (ref. 5.8) is

$$G^{(3)}(r|r') = \omega^2\ \frac{j\pi}{2}\ p_o(r)\ p_i(r')\left[\frac{2\bar{\rho}(r')\ D^2(r')}{j\pi r' W\{p_i(r'),p_o(r')\}}\right],\quad r\geq r', \tag{5-11}$$

where $p_i(r)$ and $p_o(r)$ are two independent solutions to the *homogeneous* form of equation (5-9); outside the flow $p_o(r)$ must satisfy the radiation condition while $p_i(r)$ must be finite at $r=0$. Thus, in order to solve Lilley's equation, we require an "inner" solution $p_i(r)$ valid over the source region $0\leq r'\leq r'_{max}$, and inner and outer solutions which allow their Wronskian

$$W\{p_i(r),\ p_o(r)\}\equiv p_i(r)\ p_o'(r) - p_i'(r)\ p_o(r)$$

to be determined. However, since the factor in square brackets in equation (5-11) is independent of radial position (see ref. 5.8), it can be evaluated outside the flow where $p_o(r)$ is known and thus only $p_i(r)$ is required.

In what follows, the required solutions and final results are presented for both the "ideal wind tunnel" and free-jet conditions illustrated respectively in Figure 5.1(a) and 5.1(b) (except that the primary-jet profile and its source distribution are replaced here by an effective source distribution, Q.).

The outer solutions satisfying the radiation condition are, without approximation,

$$p_o(r) = (\rho_T D_T{}^2)^{\frac{1}{2}}\ H_n^{(2)}(k_o\kappa_T r),\qquad 0\leq r\leq\infty \qquad \text{(IWT)} \tag{5-12a}$$

$$p_o(r) = \rho_o{}^{\frac{1}{2}}\ H_n^{(2)}(k_o\kappa_o r),\ r_{To}\leq r\leq\infty \qquad \text{(FJ)} \tag{5-12b}$$

where r_{To} is the outer radius of the flow (see Figure 5.3). The inner solution is the same in both cases

$$p_i(r) = (\rho_T D_T{}^2)^{\frac{1}{2}}\ J_n\ (k_o\kappa_T r),\qquad 0\leq r\leq\infty \tag{5-13a}$$

$$0\leq r\leq r_{Ti} \tag{5-13b}$$

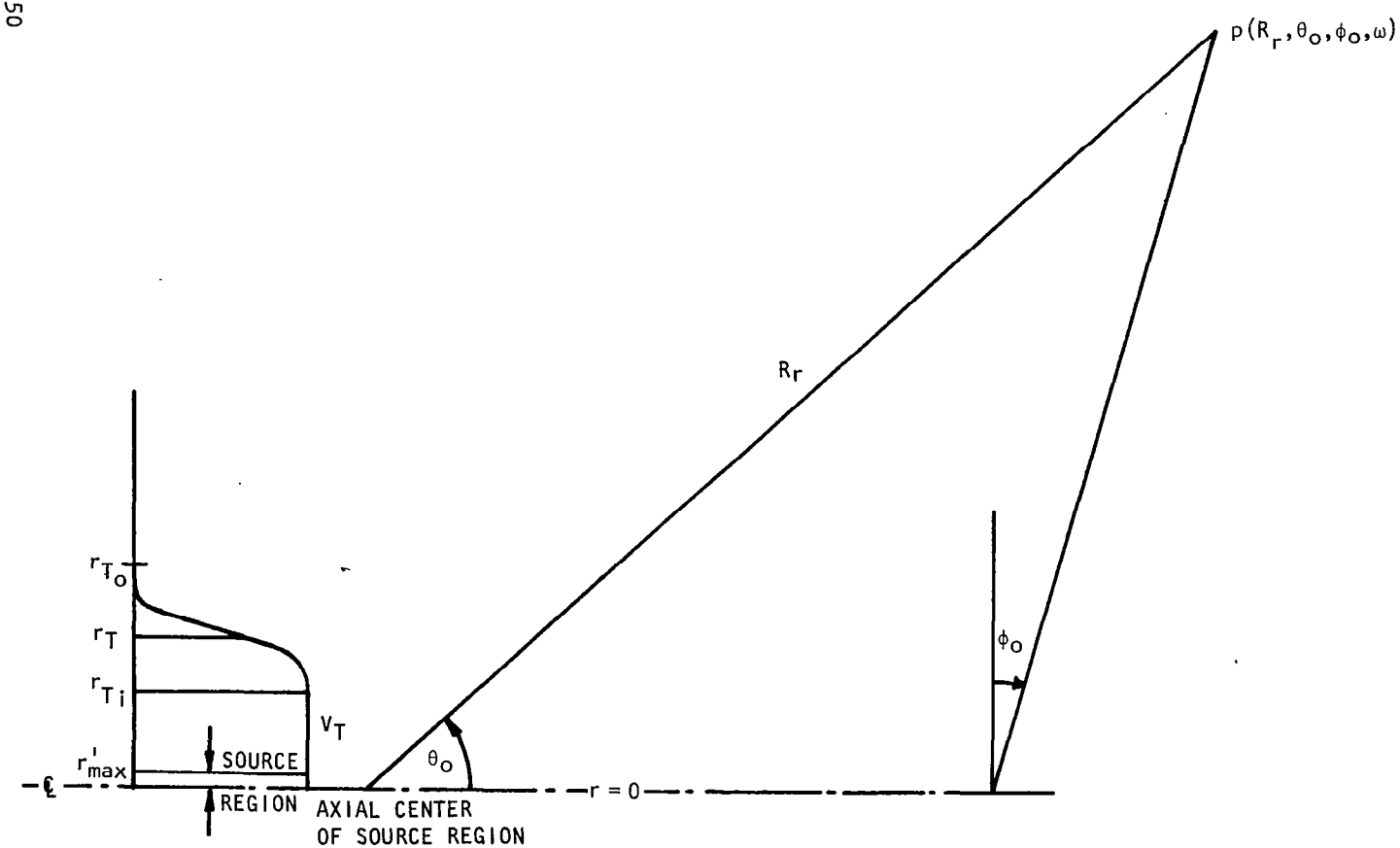

Figure 5.3 Definition sketch for high-frequency (GA) Lilley equation solutions.

and thus the Green function, from equation (5-11) can be written as

$$G^{(3)}(r|r') = \omega^2 \frac{j\pi}{2} (\rho_T D_T^2)^{\frac{1}{2}} H_n^{(2)}(k_o\kappa_T r)\ C^{(3)}(r')\quad (r \geq r') \tag{5-14a}$$

$$= \omega^2 \frac{j\pi}{2}\ \rho_o^{\frac{1}{2}}\ H_n^{(2)}\ (k_o\kappa_o r)\ C^{(3)}(r')\quad (r \geq r') \tag{5-14b}$$

where

$$C^{(3)}(r') = (\rho_T D_T^2)^{\frac{1}{2}}\ J_n(k_o\kappa_T r')\left[\frac{2\bar{\rho}D^2}{j\pi r W\{p_i, p_o\}}\right]\quad 0 \leq r' \leq \infty \tag{5-15a}$$

$$0 \leq r' \leq r_{Ti} \tag{5-15b}$$

To evaluate the Wronskian and hence the factor in square brackets in equation (5-15), we use a WKB *approximate* solution to the homogeneous equation (5-9) (valid in the limit $\delta_T/\lambda \to \infty$)

$$p_i(r) = (\bar{\rho}D^2)^{\frac{1}{2}} \left(\frac{2}{\pi k_o \kappa r}\right)^{\frac{1}{2}} \cos[k_o \int_o^r \kappa(s)ds - \frac{n\pi}{2} - \frac{\pi}{4}]\quad (r_{Ti} \leq r \leq \infty); \tag{5-16}$$

this solution has been obtained by also neglecting the term n^2/r^2 in equation (5-9). The maximum value of this term is $O(n_{max}^2/r_{Ti}^2)$ where n_{max}, according to reference 5.8, is given by

$$n_{max} \sim k_o\kappa_T\ r'_{max} \tag{5-17}$$

and r'_{max} is the maximum effective radial dimension of the source region; here r'_{max} can be interpreted as being of order r_J, the primary nozzle radius. Hence, we compare the leading term $k_o^2\kappa_T^2$ with the neglected term $k_o^2\kappa_T^2 r'^2_{max}/r_{Ti}^2 = k_o\kappa_T^2 r_J^2/r_{Ti}^2$ and find that provided the area ratio $(r_T/r_J)^2$ is large and the source region is not too close to the end of the potential core ($r_{Ti}/r_T \sim 1$), then equation (5-16) should be a good approximation to the exact Lilley equation solution.

With this approximate solution, we obtain (evaluating the Wronskian "at infinity")

$$\left[\frac{2\bar{\rho}D^2}{j\pi r W\{p_i, p_o\}}\right] = 1 \tag{5-18a}$$

$$= \exp[jk_o\ \{\kappa_o r_{To} - \int_o^{r_{To}} \kappa(s)ds\}] \tag{5-18b}$$

and hence equations (5-15a,b) become

$$C^{(3)}(r') = (\rho_T D_T^2)^{\frac{1}{2}} J_n(k_o \kappa_T r') \tag{5-19a}$$

$$= (\rho_T D_T^2)^{\frac{1}{2}} J_n(k_o \kappa_T r') \exp\left[jk_o\{\kappa_o r_{To} - \int_o^{r_{To}} \kappa(s)ds \right] \tag{5-19b}$$

The Green functions are therefore determined and the solutions to Lilley's transformed equation are

$$\tilde{p}^{(\nu)}(r) = \omega^2 \frac{j\pi}{2} (j\omega)^{\nu-3} \cdot \rho_T D_T^2 \cdot H_n^{(2)}(k_o \kappa_T r)$$

$$\int_o^{\infty} r'dr' \; J_n(k_o \kappa_T r') D^{\nu-3}(r') \; \tilde{S}^{(\nu)}(r') \tag{5-20a}$$

$$\tilde{p}^{(\nu)}(r) = \omega^2 \frac{j\pi}{2} (j\omega)^{\nu-3} \rho_o^{\frac{1}{2}} (\rho_T D_T^2)^{\frac{1}{2}} H_n^{(2)} (k_o \kappa_o r)$$

$$\exp\left[jk_o\{\kappa_o \; r_{To} - \int_o^{r_{To}} \kappa(s)ds \right] \int_o^{\infty} r'dr' \; J_n(k_o \kappa_T r') D^{\nu-3}(r') \tilde{S}^{(\nu)}(r') \tag{5-20b}$$

When these expressions are inverted with respect to k_x and n in the far-field ($R_r >> r_T$) both are very similar in form:

$$p^{(\nu)}(R_{rT}, \theta_T, \phi_o, \omega) = - \omega^2 (j\omega)^{\nu-3} \frac{e^{-j\omega R_{rT}/a_T}}{4\pi R_{rT}}$$

$$\times \sum_{n=-\infty}^{\infty} \left[A_{nIWT}^{(\nu)} \right]_{k_x = \frac{\omega \cos\theta_T}{a_T + V_T \cos\theta_T}} \cdot e^{-jn\phi_o} \tag{5-21a}$$

$$p^{(\nu)}(R_r, \theta_o, \phi_o, \omega) = -\omega^2 (j\omega)^{\nu-3} \frac{e^{-j\omega R_r/a_o}}{4\pi R_r}$$

$$\times \sum_{n=-}^{\infty} \left[A_{nFJ}^{(\nu)} \right]_{k_x = \omega \cos\theta_o/a_o} \cdot e^{-jn\phi_o} \tag{5-21b}$$

but have differing azimuthal mode amplitudes given by

$$A_{nIWT}^{(\nu)} = \frac{\rho_T D_T^2 \; D_T^{\nu-3}}{(1 + V_T \cos\theta_T / a_T)} \cdot e^{jn\pi/2} \cdot \int_0^\infty r dr \; J_n(k_o \kappa_T r) \tilde{S}^{(\nu)}(k_x, r, n, \omega) \qquad (5\text{-}22a)$$

$$A_{nFJ}^{(\nu)} = \rho_o^{\frac{1}{2}} (\rho_T D_T^2)^{\frac{1}{2}} \; D_T^{\nu-3} \; e^{jn\pi/2} \int_0^\infty r dr \; J_n(k_o \kappa_T r) \tilde{S}^{(\nu)}(k_x, r, n, \omega)$$

$$\times \exp[jk_o\{\kappa_o r_{To} - \int_0^{r_{To}} \kappa(s) ds\}] \qquad (5\text{-}22b)$$

The power spectral density of the far-field pressure is proportional to the square of the *modulus* of the Fourier coefficients given by equations (5-21a), (5-21b); hence phase differences that are independent of azimuthal mode order can be ignored. It follows that the amplitude of any given azimuthal radiation mode in the ideal wind tunnel will be the same as that in the free-jet facility for a given source distribution at a fixed frequency, ω, if

(a) $R_{rT} = R_r$ (equal wavenormal distance)

(b) $\dfrac{\cos\theta_T}{a_T + V_T \cos\theta_T} = \dfrac{\cos\theta_o}{a_o}$ (equal axial wavenumber)

and (c) the free-jet radiated mode *amplitude* is multiplied by $(\rho_T D_T^2/\rho_o)^{\frac{1}{2}}$.

Condition (a) is a *far-field* result which can be improved on by analyzing the geometry of ray-tube spreading in the near-field along the lines suggested by Schubert (ref. 5.10) (details are given in Ref. 5.4); this yields the finite distance corrections of Section 2.2. Condition (b) is analogous to Snell's law and determines the radiation angle in the free-jet facility, θ_o, at which data can be obtained on the radiation emitted at wavenormal angle θ_T in the ideal wind tunnel (or, equivalently, at the emission time angle θ_T in the flyover case). Again, ray tracing allows this far-field result to be interpreted in the near-field as the emerging ray angle rather than the source-observer angle, as described in Section 2.1. Both conditions (a) and (b) emerge from the general case when numerical Lilley equation solutions are obtained in place of the high-frequency closed-form solutions derived above. Condition (c), however, leads directly from those approximate solutions and is identical to the previously obtained high-frequency calibration factor. However, it is not confined to radiation from centerline sources nor to azimuthally-averaged far-field quantities alone but can be applied to any azimuthal mode or to any nonaxisymmetric radiation field, provided of course that the area ratio is reasonably large (say >100) – which will be the case

in general — and that the source region is not too close to the end of the free-jet potential core.

5.3 NUMERICAL RESULTS FOR JET MIXING NOISE SOURCES

In this section, numerical results for C_F, the free-jet facility amplitude calibration factor, are presented and compared with the low- and high-frequency approximations derived in the previous section.

5.3.1 Definition of Parameters for Calculations

In order to introduce a degree of realism into the numerical calculations, *a standard case has been chosen* which corresponds to the *original* Lockheed-Georgia facility (ref. 5.4). This is shown in Figure 5.4; the key dimensions are $d_T = 1.016$ m (equivalent), $x_n = 0.305$ m, and $d_J = 5.08$ cm. The free-jet velocity V_T has been taken as the maximum value used in reference 5.4, namely $V_T/a_o = 0.2$. Since departures from GA are expected principally at low frequencies, and jet noise frequencies scale on velocity, a relatively low primary-jet velocity has been chosen for the standard case, $V_J/a_o = 0.5$. The mean flow field is taken either as isothermal throughout or heated to a static temperature ratio $T_J/T_o = 3$.

For purposes of modeling isothermal, primary-jet mixing noise sources, a source model of major interest is the statistically isotropic quadrupole ring source (ref. 5.8) of volume displacement ($\nu = 3$) or volume acceleration ($\nu = 1$) type. Dipole and/or monopole order sources arise when modeling hot jet mixing noise. Values of C_F obtained with the different source models will be distinguished as $C_{Fm}^{(\nu)}$, $C_{Fd}^{(\nu)}$, and $C_{Fq}^{(\nu)}$, where subscripts m, d, q denote monopole, dipole, and quadrupole ring sources, respectively. The superscript (ν) denotes the temporal source order.

Details of the mean velocity and mean temperature distributions are given below, together with the source locations assumed and a specification of the model source functions.

Radial Source Location and Primary-Jet Velocity and Temperature Profiles. The radius of the ring source is chosen (except where otherwise stated) to correspond to the radius at which $(V - V_T)/V_{CL} - V_T) = \phi_{rel}$ equals 0.6, V_{CL} being the centerline velocity.

The radial profile of the primary-jet velocity, V(r), relative to the surrounding uniform flow of the free-jet potential core, is determined by the Strouhal number $fd_J/V_J = S$. Four values of S are used in the present study, namely 0.1, 0.315, 1, 3.15 to cover the jet noise spectrum. For the two higher Strouhal numbers (S = 1, 3.15), an error function profile is used (ref. 5.12), viz.

$$\frac{V(r) - V_T}{V_J - V_T} = \phi_{rel} = \frac{1}{2}\left[1 - \mathrm{erf}\left\{\sqrt{\pi}\left(\frac{r - r_J}{\delta_J}\right) - .297\right\}\right] \qquad (5\text{-}23)$$

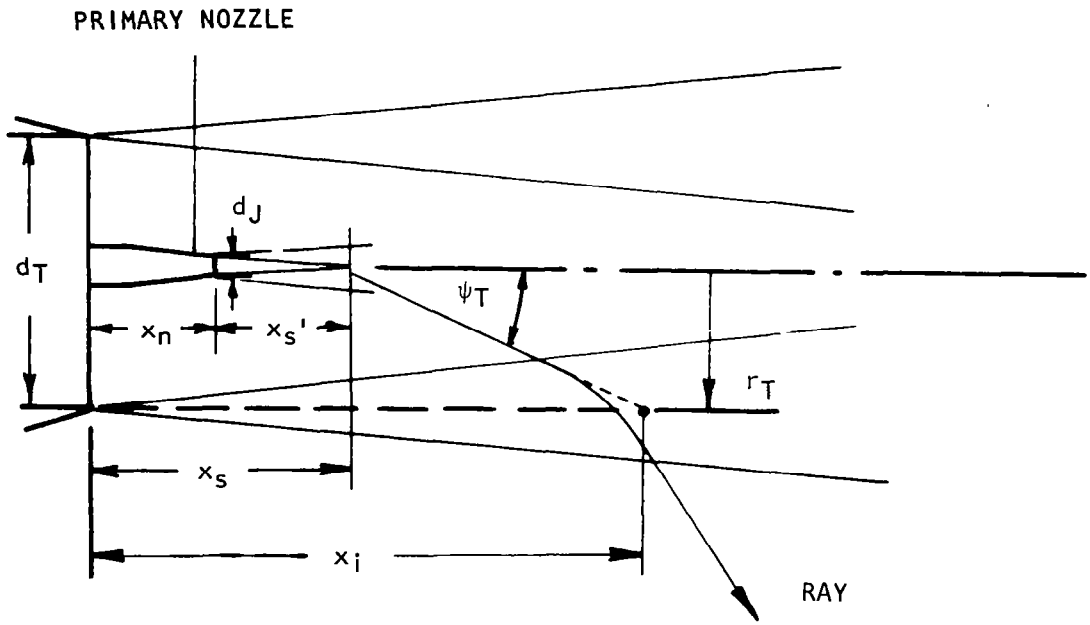

Figure 5.4 Free-jet facility for jet noise measurement under simulated flight conditions.

with $\delta_J/d_J = 0.53$, 0.26, respectively. These profiles correspond to axial locations $x_s'/d_J = 4$, 2 in accordance with the source location data of Grosche (ref. 5.13) and Laufer et al. (ref. 5.14).

For the two lower Strouhal numbers ($S = 0.1$, 0.315), the assumed profile is

$$\frac{V(r) - V_T}{V_{CL} - V_T} = \phi_{rel} = \exp -(r/Cd_J)^2 \tag{5-24}$$

with $C = 1.21$ and 0.780, respectively, corresponding to axial source locations $x_s'/d_J = 13$, 7.

The temperature† variation through the jet shear layer, $T(r)$, is calculated by assuming that the stagnation temperature, T_{st}, follows the same profile as the mean velocity profile. Thus,

$$\frac{T_{st} - T_{T,st}}{T_{cL,st} - T_{T,st}} = \phi_{rel} \tag{5-25}$$

from which it follows that

$$\frac{T}{T_o} = \frac{T_T}{T_o} + \phi_{rel} \left\{ \frac{T_{cL}}{T_o} - \frac{T_T}{T_o} + \frac{\gamma - 1}{2} \left(\frac{V_{cL}}{a_o} - \frac{V_T}{a_o} \right)^2 \right\} (1 - \phi_{rel}) \tag{5-26}$$

The ratio of specific heats, γ, is taken to be a constant for these calculations ($=1.4$) and T_T/T_o is set equal to unity.

<u>Axial Decay of Primary-Jet Centerline Velocity and Temperature</u>. The axial velocity decay along the jet centerline is specified by

$$\frac{V_{cL} - V_T}{V_J - V_T} = A_V(S), \tag{5-27}$$

with $A_V(S)$ values given in Table 5.1.

---

†*The fluid is assumed to be a perfect gas of constant specific heat ratio and $\bar{\rho}(r)$, $\bar{a}(r)$ are determined from $T(r)$.*

Table 5.1 Values of $A_V(S)$, $A_T(S)$

S	$A_V(S)$	$A_T(S)$
0.1	0.5	0.35
0.315	0.9	0.70
1.0	1.0	1.0
3.15	1.0	1.0

The axial temperature variation along the jet centerline is specified by

$$\frac{T_{cL,st} - T_{T,st}}{T_{J,st} - T_{T,st}} = A_T(S), \tag{5-28}$$

with $A_T(S)$ values given in Table 5.1.

Axial Source Location Relative to Free-Jet Exit Plane. The axial source location indicated in Figure 5.4 is specified by

$$x_s/d_T = x_n/d_T + B(S)\ d_J/d_T = 0.3 + 0.05\ B(S) \tag{5-29}$$

with B(S) values given in Table 5.2.

Table 5.2 Values of B(S)

S	B(S)
0.1	13
0.315	7
1.0	4
3.15	2

The quantity B(S) represents the axial source location x_s'/d_J relative to the primary-jet nozzle exit; the values in Table 5.2 are based on the far-field source imaging measurement referenced above.

Definition of Free-Jet Velocity Profile. The mean velocity profile in the outer jet shear layer is determined as a function of axial position (x) by assuming the standard error-function profile – given by equation (5-23) – with

$$\delta_T = \sqrt{\pi}\,\frac{x}{\sigma_T} \doteq 0.13\ x \tag{5-30}$$

and a spreading parameter $\sigma_T = 13.5$. Free-jet profiles beyond the end of the potential core are of no interest for flight simulation.

The choice of axial location for the free-jet profile is determined (except where stated otherwise) by the position, x_i, at which the incident ray meets the lip line (see Figure 5.4) which is given by

$$x_i/d_T = x_s/d_T + 0.5\ (1 - d_J/d_T)\ \cot\psi_T. \tag{5-31}$$

Lilley Equation Source Functions. Monopole, dipole, and quadrupole sources of volume *displacement* type ($\nu = 3$) have been assumed for the source function, Q, in Lilley's equation (equation 5-1) to obtain numerical solutions and hence values for the calibration factors, $C_{Fm}^{(3)}$, $C_{Fd}^{(3)}$, and $C_{Fq}^{(3)}$. These displacement source functions take the form

$$Q^{(3)} = \frac{\bar{D}^3}{Dt^3}\ (S_m^{(3)})$$ monopole (proposed additional source† (ref. 5.15) for hot jet mixing noise) (5-32a)

$$= \frac{\bar{D}^3}{Dt^3}\ (M_\alpha\ S_d^{(3)})$$ dipole (proposed additional source† (refs. 5.8, 5.9, 5.15) for hot jet mixing noise) (5-32b)

$$= \frac{\bar{D}^3}{Dt^3}\ (M_{\alpha\beta}\ S_{q\alpha\beta}^{(3)})$$ quadrupole [proposed isothermal jet mixing noise source (refs. 5.8, 5.9, 5.15)] (5-32c)

where

$$(\alpha,\beta) = (x,r,\phi)$$

and the dipole and quadrupole operators, M_α, $M_{\alpha\beta}$ are given by

$$M_\alpha = \left(\frac{\partial}{\partial x} \quad \frac{1}{r}\frac{\partial}{\partial r}\,r \quad \frac{1}{r}\frac{\partial}{\partial \phi}\right), \tag{5-33}$$

†*But see comments at end of Section 5.3.4.*

$$M_{\alpha\beta} = \begin{array}{c} \\ (x) \\ (r) \\ (\phi) \end{array} \begin{array}{c} \begin{array}{ccc} (x) & (r) & (\phi) \end{array} \\ \begin{bmatrix} \frac{\partial^2}{\partial x^2} & \frac{1}{r}\frac{\partial^2 r}{\partial x \partial r} & \frac{\partial^2}{\partial x \partial \phi}\frac{1}{r} \\ \frac{1}{r}\frac{\partial^2 r}{\partial r \partial x} & \frac{1}{r}\frac{\partial^2}{\partial r^2} r & \frac{1}{r^2}\frac{\partial^2 r}{\partial r \partial \phi} \\ \frac{\partial^2}{\partial x \partial \phi}\frac{1}{r} & \frac{1}{r^2}\frac{\partial^2 r}{\partial r \partial \phi} & \frac{\partial^2}{\partial \phi^2}\frac{1}{r^2} - \frac{1}{r}\frac{\partial}{\partial r} \end{bmatrix} \end{array} \tag{5-34}$$

The above source functions had been developed at Lockheed from Lilley's original formulation because analysis appeared to show that a form of Lilley's *original* source function (ref. 5.9, Appendix 3A) did *not* lead to the required mean velocity dependence (V_J^8) for isothermal mixing noise at low velocities (refs. 5.8, 5.9). More recent work at Lockheed (unpublished) suggests, however, that the original right-hand side of Lilley's equation (ref. 5.7) does in fact give rise to the correct V_J dependence. Thus, the following source functions have also been utilized in the calibration factor calculations and are denoted here by $\nu = 1$ although these are not strictly of the volume *acceleration* type alone (except for the monopole source).

$$Q^{(1)} = \frac{\bar{D}}{Dt}\left(S_m^{(1)}\right) \qquad \text{monopole} \tag{5-35a}$$

$$= \frac{\bar{D}}{Dt}\left(M_\alpha S_{d\alpha}^{(1)}\right) - 2\frac{dV}{dr}\frac{\partial}{\partial x}\left(S_{dr}^{(1)}\right) \tag{5-35b}$$

(first term is an acceleration dipole; proposed additional source for hot jet mixing noise)

$$= \frac{\bar{D}}{Dt}\left(M_{\alpha\beta} S_{q\alpha\beta}^{(1)}\right)$$

$$- 2\frac{dV}{dr}\frac{\partial}{\partial x}\left\{\frac{\partial}{\partial x}\left(S_{qxr}^{(1)}\right) + \frac{1}{r}\frac{\partial}{\partial r}\left(r\, S_{qrr}^{(1)}\right) + \frac{1}{r}\frac{\partial\left(S_{qx\phi}^{(1)}\right)}{\partial \phi} - \frac{S_{q\phi\phi}^{(1)}}{r}\right\}^2 \tag{5-35c}$$

(first term is an acceleration quadrupole; proposed isothermal jet mixing noise source)

The second and third source functions given above lead respectively to correct scaling laws for hot and isothermal jet mixing noise at low velocities. The distinction between volume displacement and acceleration sources is unimportant except when modeling supersonic jet mixing noise. Furthermore, the results described below show that the calibration factor is for all practical

purposes independent of temporal order† and thus a choice does not have to be made between the two alternative source models for the purposes of calibrating mixing noise data acquired in a free-jet facility.

5.3.2 Calibration Factor Results for Complete Profile

Free-jet calibration factors for the volume displacement quadrupole source model, positioned as described above, in an isothermal‡ jet are shown in Figure 5.5 as a function of primary jet Strouhal number S. Between $S = 0.1$ and $S = 3.15$, there is virtually no variation with Strouhal number, and the $C_{Fq}^{(3)}$ values obtained by solving the Lilley equation numerically are in close agreement with the high-frequency or GA calibration factor, $C_{F\infty}$, derived in section 5.2.2 (which is of course independent of frequency). Figures 5.6 and 5.7 show equivalent results for volume displacement dipole and monopole ring sources, and again there is close agreement with the asymptotic high-frequency calibration factor, $C_{F\infty}$.

The effect of primary-jet temperature on these results is almost negligible and general trends are exactly the same. To emphasize the close agreement with the GA calibration factor $C_{F\infty}$, numerical results for $C_F^{(3)}$ at a temperature ratio, $T_J/T_O = 3$, for two angles are given in Table 5.3 together with the ratio, Δ(dB), of the numerical and GA calibration factors. The actual centerline static temperature ratios at Strouhal numbers $S = 0.1$, 0.315 are $T_{CL}/T_O = 1.7$ and 2.4. (At the two highest Strouhal numbers T_{CL}/T_O is equal to T_J/T_O.) Table 5.3 shows that, as in the isothermal case, the deviation of $C_F^{(3)}$ from $C_{F\infty}$ is less than 1/2 dB and the maximum deviation for the dipole and quadrupole sources is even smaller ($\lesssim$0.3 dB).

The numerical calibration factors are even less affected by a change of source type, i.e. from the displacement type ($\nu = 3$) to the type labelled $\nu = 1$ in Section 5.3.1. At the high temperature condition described above, the change is less than 0.01 dB (which is less than the expected error in the numerical solutions) except at low Strouhal numbers for the quadrupole source where it reaches 0.03 dB.

This result will almost certainly be understood (from inspection of the governing equations) to indicate that there *is* no effect of ν for monopole and dipole sources and only a minor one for the quadrupole source. Thus, for all practical purposes, the superscript ν can be omitted from the calibration factor notation, i.e. $C_{Fm,d,q}^{(\nu)} \rightarrow C_{Fm,d,q}$.

---

†*Strictly not of temporal order but of the alternative source functions* $Q^{(3)}$, $Q^{(1)}$ *defined above.*

‡*In these isothermal calculations* $\bar{\rho}(r)$ *and* $\bar{a}(r)$ *are uniform and equal to the ambient values* ρ_O, a_O.

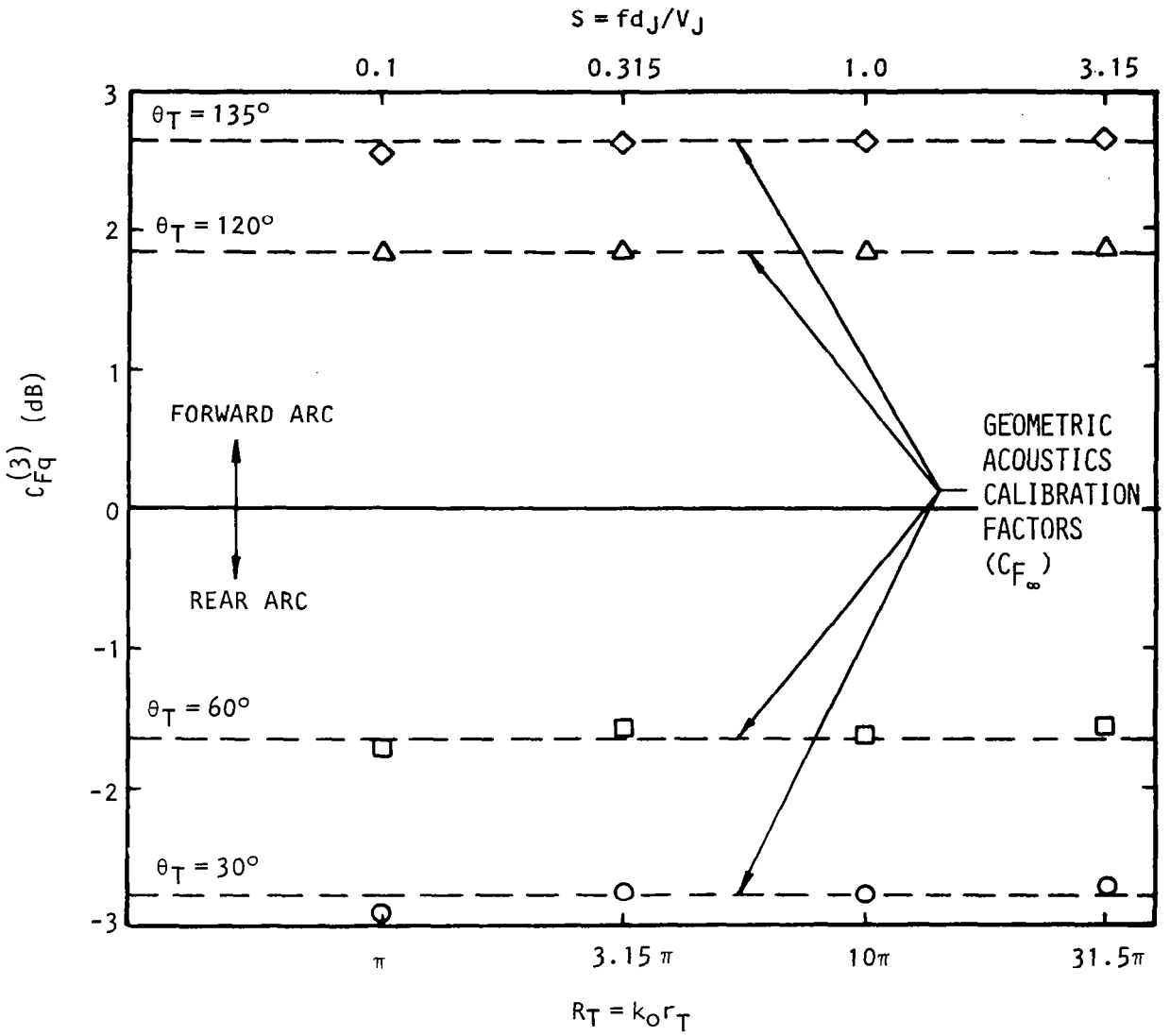

Figure 5.5 Lilley equation calibration factors for a volume displacement *quadrupole* ring source. ($\phi_{rel,s} = 0.6$, $V_T/a_o = 0.2$, $V_J/a_o = 0.5$) High-frequency approximation (GA) shown as broken line at each angle.

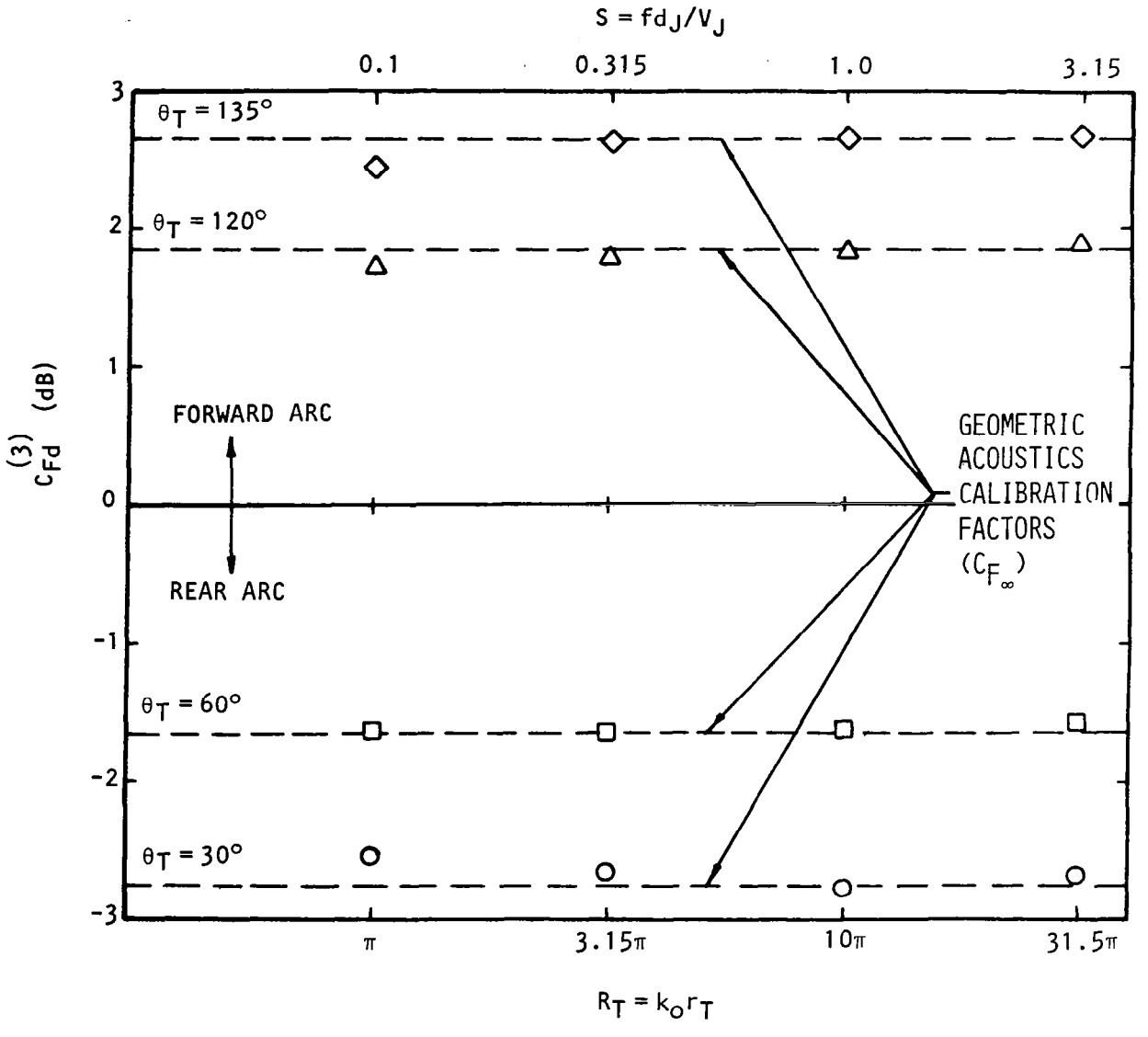

Figure 5.6 Lilley equation calibration factors for a volume displacement *dipole* ring source. ($\phi_{rel,s} = 0.6$, $V_T/a_o = 0.2$, $V_J/a_o = 0.5$.) High-frequency approximation (GA) shown as broken line at each angle.

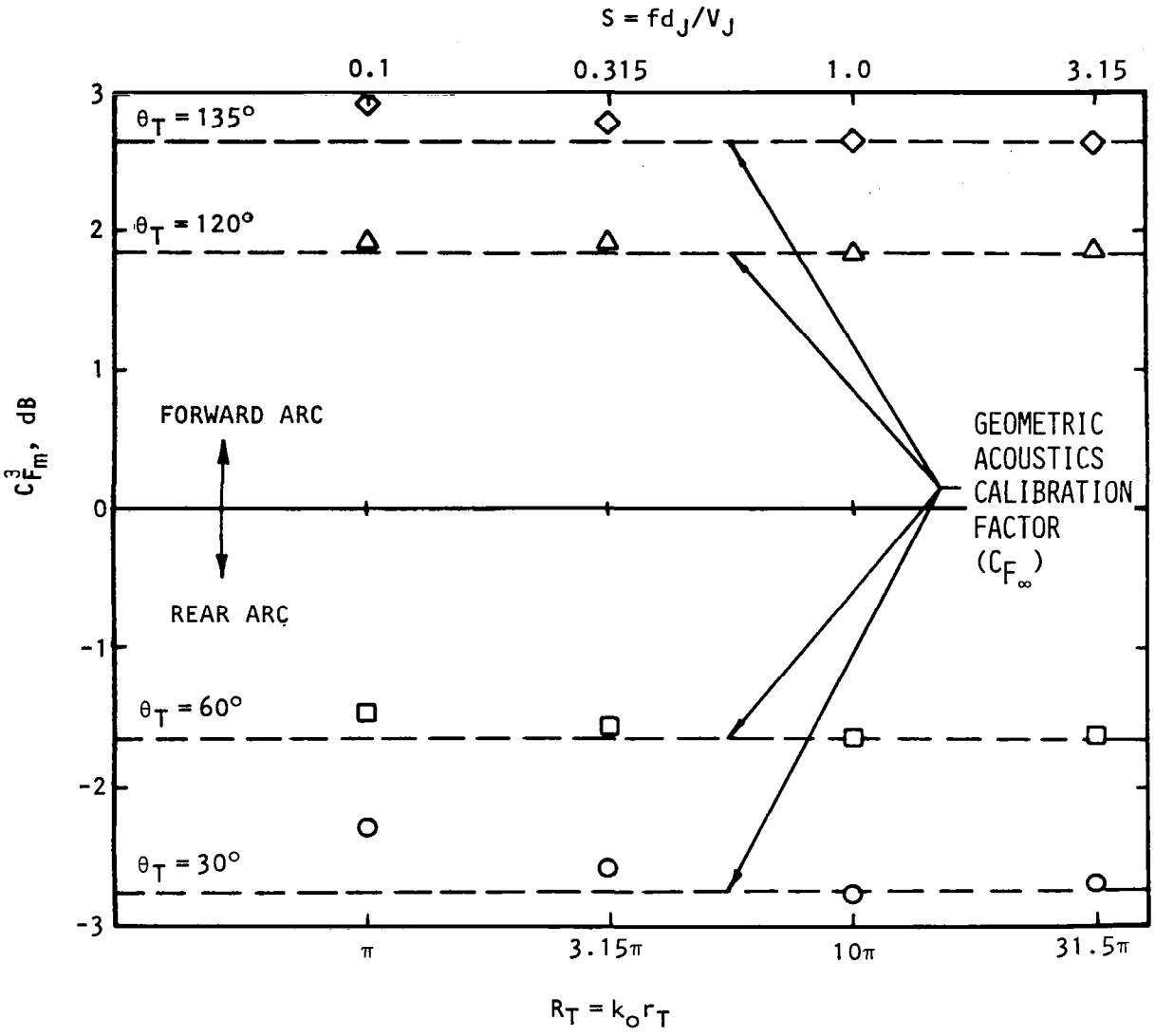

Figure 5.7 Lilley equation calibration factors for a volume displacement *monopole* ring source. ($\phi_{rel,s} = 0.6$, $V_T/a_o = 0.2$, $V_J/a_o = 0.5$.) High-frequency approximation (GA) shown as broken line at each angle.

Table 5.3 Monopole, dipole and quadrupole volume displacement calibration factors, in dB, calculated from Lilley's equation for $T_J/T_O = 3$ ($\phi_{rel,s} = 0.6$, $V_T/a_O = 0.2$, $V_J/a_O = 0.5$) and deviation, Δ(dB), from C_{F_∞}

(a) $\theta_T = 30°$ (C_{F_∞}: -2.77 dB)

S	$C_{Fm}^{(3)}$	Δ	$C_{Fd}^{(3)}$	Δ	$C_{Fq}^{(3)}$	Δ
0.1	-2.28	0.49	-2.46	0.31	-2.82	-0.05
0.315	-2.61	0.16	-2.69	0.08	-2.77	0.00
1.0	-2.77	0.00	-2.77	0.00	-2.78	-0.01
3.15	-2.69	0.08	-2.70	0.07	-2.70	0.07

(b) $\theta_T = 135°$ (C_{F_∞}: 2.65 dB)

S	$C_{Fm}^{(3)}$	Δ	$C_{Fd}^{(3)}$	Δ	$C_{Fq}^{(3)}$	Δ
0.1	2.92	0.27	2.53	-0.12	2.58	-0.07
0.315	2.70	0.05	2.64	-0.01	2.65	0.00
1.0	2.75	0.10	2.73	0.08	2.71	0.06
3.15	2.79	0.14	2.76	0.11	2.73	0.08

5.3.3 Results for Partial Profile (Free-Jet Profile Only)

A possible cause of deviations from geometric acoustics, in the situation of Figure 5.4 is the multiple reflection process which occurs, in principle, between the two shear layers. To determine whether in practice this process is significant, the calculations of Figures 5.5 through 5.7 have been repeated with the primary-jet relative flow field suppressed, leaving only the free-jet flow surrounding the source (equivalent to $V_J = V_T$ in Figure 5.1). This situation is referred to as the "partial" profile, in contrast to the complete profile of Section 5.3.2.

Results for the monopole source are shown in Figure 5.8. Comparison of Figures 5.7 and 5.8 reveals that the calibration factors are virtually identical with and without the primary jet flow field. The same is found for the dipole and quadrupole ring source models. We conclude that re-reflection from the primary-jet mean flow field is insignificant, for the typical parameter values on which the present study is based.

It remains to explain the deviations from geometric acoustics exhibited in Figure 5.8 and why these decrease so rapidly with increasing Strouhal

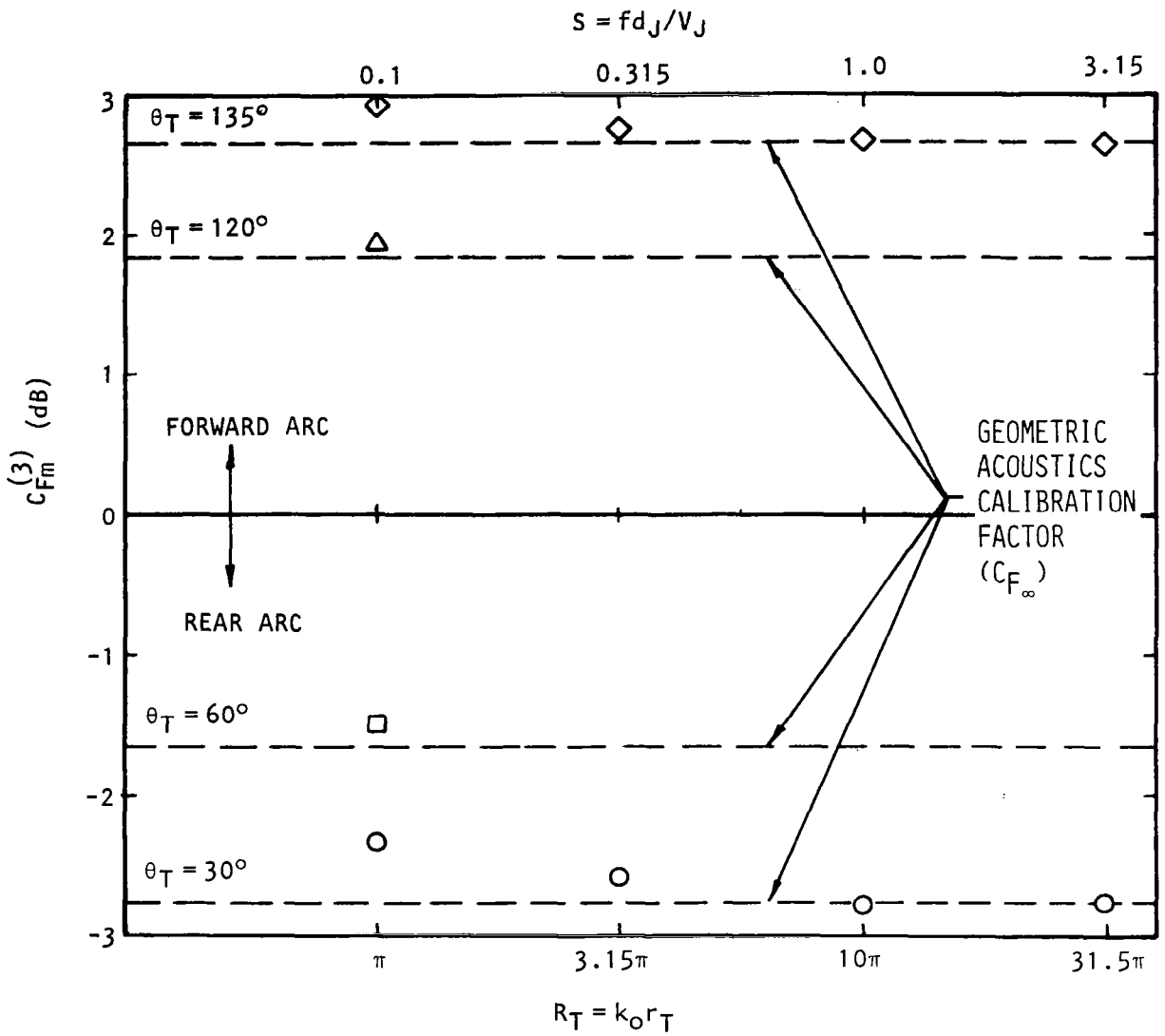

Figure 5.8 Partial profile Lilley equation calibration factors for a volume displacement monopole ring source. ($\phi_{rel,s} = 0.6$, $V_T/a_o = 0.2$, $V_J = V_T$) High-frequency approximation (GA) shown as broken line at each angle.

number, when in some cases – particularly at 135° – the shear layer at the incident ray location is still quite thin on a wavelength scale. Specifically, at $\theta_T = 135°$, the value of $k_o\delta_T$ ranges from 0.503 ($S = 0.1$) to 1.56 ($S = 3.15$).

One possible reason is that the source is a ring source of radius r_s and values of $k_o r_s$ in these calculations range from 0.27 (at $S = 0.1$) to 5.0 (at $S = 3.15$). Even at $S = 0.1$, therefore, we might expect some mitigation of the interference effects associated with reflection from the outer shear layer. However, the effect of $k_o r_s$ turns out to be insignificant at the two lower Strouhal numbers as shown in Table 5.4. At the higher Strouhal numbers the reverse is true: interference effects have been increased apparently by setting $r_s = 0$, causing a 0.24 dB change at $S = 1.0$ and a smaller change of 0.1 dB at $S = 3.15$.

Table 5.4 Effect of finite source radius on monopole calibration factor, $C_{Fm}^{(3)}$, at $\theta_T = 135°$. (Flow conditions as in Figure 5.8.) $C_{F_\infty} = 2.65$ dB.

S	$k_o r_s \neq 0$	$k_o r_s = 0$	Difference
0.1	2.92	2.94	0.02
0.315	2.78	2.82	0.04
1.0	2.68	2.44	-0.24
3.15	2.64	2.54	-0.10

5.3.4 Results for Plug Flow Profile

The smallness of $k_o\delta_T(x_i)$ at $\theta_T = 135°$ raises the question of whether the vortex sheet approximation, $k_o\delta_T \to 0$, would correctly reproduce the calibration factor in this case. A comparison of Lilley equation results for the finite and zero thickness (plug flow) shear layers was therefore carried out for the same situation as Figure 5.8, with the one modification that the monopole source was located on the jet axis. The zero shear layer thickness Lilley equation solutions are of course in closed form and are referred to as the low-frequency approximation in Section 5.2.1; for the partial profile the low-frequency calibration factor is given by equation (5-4).

Some results of the comparison are shown in Figure 5.9 plotted against the frequency parameter $k_o r_T$. The results for finite $k_o\delta_T$ at $S = 0.1$ agree quite closely with the plug flow or low-frequency approximation, showing that at these low $k_o\delta_T$ values the free-jet calibration factor could be estimated as if $k_o\delta_T \to 0$. The same is true at the next Strouhal number, $S = 0.315$; results for the two higher Strouhal numbers are not shown in Figure 5.9 but are given in Table 5.5. These results must be interpreted bearing in mind the oscillatory nature of the calibration factor which is clearly demonstrated in Figure 5.9; the oscillations are an interference effect caused by

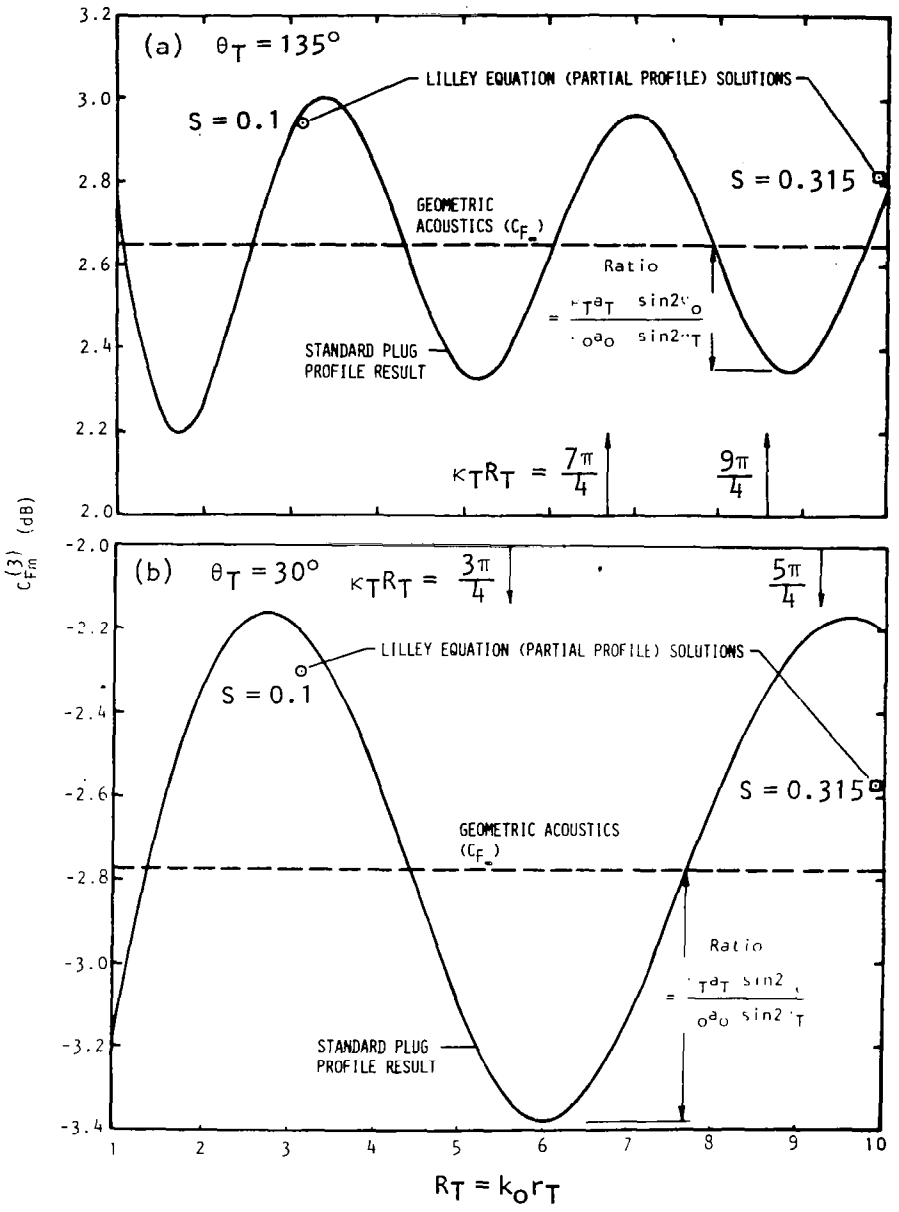

Figure 5.9 Comparison of C_F values from three different approximations to the free-jet shear layer. The solid line refers to the plug flow model ($k_o\delta_T \to 0$), the broken line to the GA model ($k_o\delta_T \to \infty$). The symbols refer to full numerical solutions of the Lilley equation for $S = 0.1$, 0.315 at the same $k_o\delta_T$ values used previously (i.e. 0.503, 0.806 at 135°; 1.60, 4.31 at 30°). Source: volume displacement monopole located *on the jet axis*. $V_T/a_o = 0.2$; $V_J = V_T$ (i.e. partial profile calculation).

Table 5.5 Effect of finite shear layer thickness on monopole calibration factor, $C_{Fm}^{(3)}$, at $\theta_T = 135°$ (Flow conditions as in Figure 5.8.) $C_{F\infty}$: 2.65 dB.

		$k_o\delta_T = 0$	
S	$k_o r_s \neq 0$	$k_o r_s = 0$	$k_o\delta_T$, $k_o r_s = 0$
0.1	2.92	2.94	2.96
0.315	2.78	2.82	2.73
1.0	2.68	2.44	2.35
3.15	2.64	2.54	2.76

reflections from the free-jet shear layer. This frequency dependence was first illustrated with calculations performed at Lockheed-Georgia and published in reference 5.16; subsequently Amiet (ref. 5.6) published further Lilley equation solutions, confirming this result for centerline source models ($r_s = 0$).

From Figure 5.9 and Table 5.5, it can be seen that the deviation from the high-frequency calibration factor, $C_{F\infty}$, is almost solely due to back reaction effects (caused by reflections) at the two lower Strouhal numbers, since the finite and zero thickness shear layer results are almost the same irrespective of source radius. Whereas at the two higher Strouhal numbers, the interference effect is suppressed partly because $k_o r_s \neq 0$, and partly because the reflections are weaker at higher frequencies.

Thus, to summarize, as the frequency (or Strouhal number) is increased, the deviation from $C_{F\infty}$ is caused first by thin shear layer reflections (i.e. thin on the wavelength scale); then the deviation is gradually suppressed through non-zero source radius effects and finally the reflections and deviations diminish as the shear layer thickness becomes large on the wavelength scale.

It remains to consider then how the *maximum* deviation from $C_{F\infty}$, which is clearly determined by the low-frequency calibration factor, C_{Fmo}, varies with the free-jet flow conditions. It should be emphasized that C_{Fmo} is a low-frequency approximation in the sense that $k_o\delta_T \to 0$, but $k_o r_T$ or more precisely $k_o r_T \kappa_T$ can take any value. However, if $k_o r_T$ is sufficiently *large*, a simple expression is obtained for C_{Fmo} (as described in Appendix 2 of ref. 5.5), which shows that C_{Fmo} oscillates either side of $C_{F\infty}$, the maximum deviation in either direction being a factor $\rho_T a_T \sin 2\theta_o / \rho_o a_o \sin 2\theta_T$. Thus, as $\theta_T \to 0$, or as $\theta_o \to \pi$ (forward-arc simulation limit), large oscillations in the calibration factor are expected as a function of frequency. However, it is shown in Appendix 2 of ref. 5.5 that if an appropriate *frequency-average* is carried out the calibration factor for all three source models (monopole, dipole and quadrupole) is *identical* to the high-frequency value so that for a broadband source it becomes reasonable to use the GA calibration factor, $C_{F\infty}$, provided

the measured bandwidth covers a range $\Delta(\kappa_T R_T)$ of $\pi/2$ or more. It is reminded that the calibration factor variation with frequency has been considered in detail for the *monopole* source model, mainly because this apparently caused the largest deviation from the GA calibration factor. However, it has now been established (ref. 5.15) – from a careful analysis of the Lockheed (static) mixing noise data (ref. 5.17) – that only the dipole and quadrupole source models are required as a basis for a jet mixing noise prediction scheme. The calibration factors for those source models exhibit similar or even smaller deviations from $C_{F\infty}$ than for the monopole source as indicated in Figures 5.5 through 5.7. Thus, the monopole deviation factor $\rho_T a_T \sin 2\theta_o / \rho_o a_o \sin 2\theta_T$ may be used to ascertain the *maximum* deviation expected from $C_{F\infty}$, but in practice the calibration factor is unlikely to differ significantly from $C_{F\infty}$ for broadband noise sources.

5.3.5 Area Ratio Study

As a final application of the Lilley equation approach, the dependence of C_F on the free-jet/primary-jet area ratio has been investigated. A single combination of angle and Strouhal number ($\theta_T = 30°$, $S = 0.1$) was chosen for this purpose, and the variation of d_T/d_J was carried out holding $k_o \delta_T$ constant at 1.62 (the value used previously for the standard case $d_T/d_J = 20$). The combination ($\theta_T = 30°$, $S = 0.1$) was chosen as being the one which gave the largest departures from GA in Figures 5.5 through 5.7. The ring source radius and primary jet profile were maintained constant, as described in Section 5.3.1.

Results for the three different source models (monopole, dipole and quadrupole) are plotted in Figure 5.10 *versus* area ratio $(d_T/d_J)^2$. It is clear that for realistic area ratios (values much below 400 are unsuitable for simulating effects of flight on low frequency jet noise, as discussed in reference 5.5), the simple GA or high-frequency calibration factor of Section 5.2.2 comes very close to the full numerical results, despite the low value of S. A plug flow/centerline source model, on the other hand, would show exaggerated free-jet acoustic interference effects at high Strouhal numbers (because of the unrealistic source radius and vanishing shear layer thickness) but at low Strouhal numbers it would yield a good indication of the *maximum* expected deviation of $C_F/C_{F\infty}$ from unity.

The low frequency asymptotes shown in Figure 5.10 are derived in Appendix 3 of reference 5.5 and were first given in reference 5.16; recently the same type of result has been derived by Dash (ref. 5.18), as applied to radiation from the *primary* jet in an ideal wind tunnel.

5.4 RESULTS FOR INTERNAL NOISE SOURCES

The calibration factor results presented in the previous section for jet mixing noise exhibit almost insignificant deviations from the GA asymptote for Strouhal numbers at and above $S = 0.1$ and area ratios above 400. *Lower* values of the Strouhal number and/or area ratio (and hence frequency) were not considered in detail since practical considerations such as an adequate

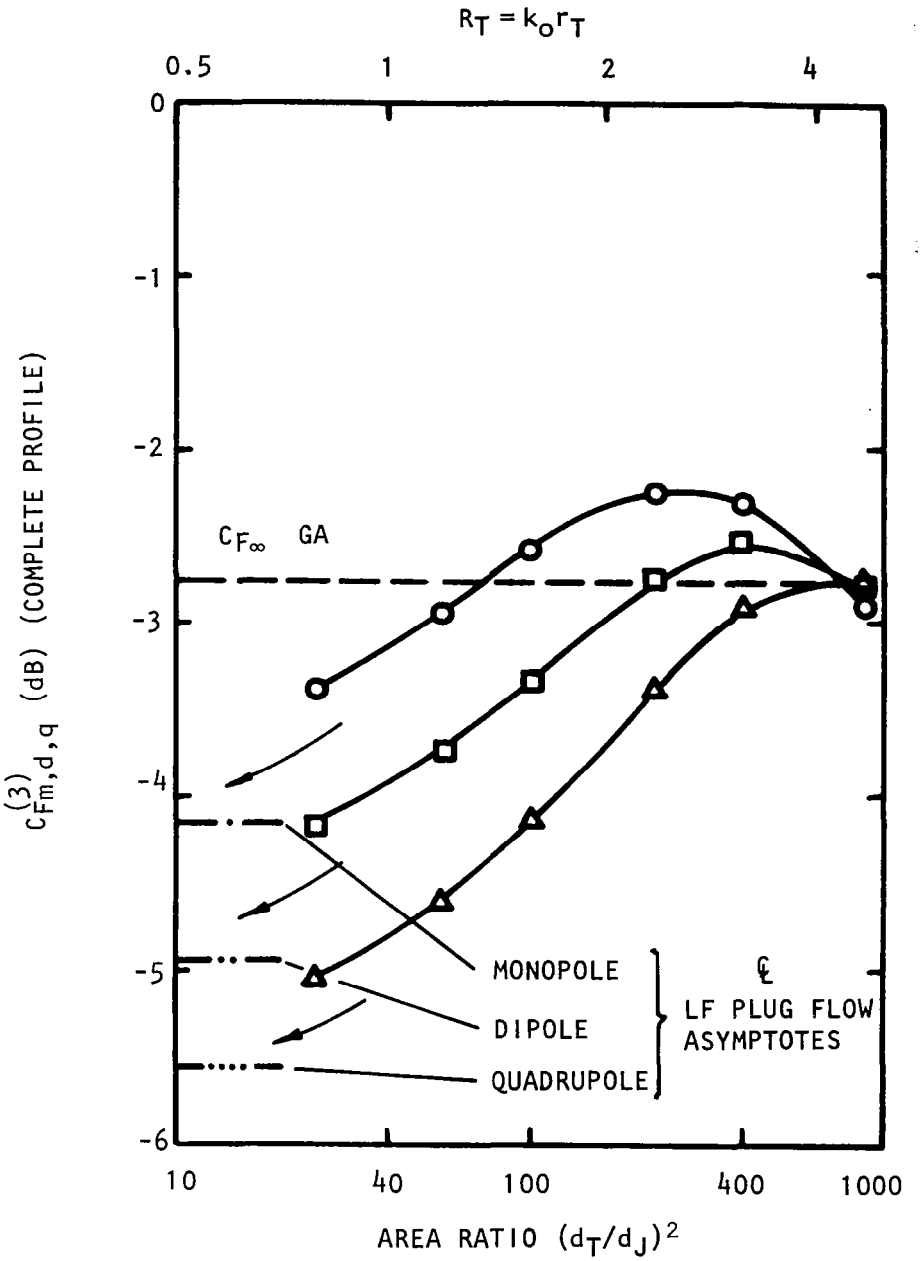

Figure 5.10 Area ratio dependence of Lilley equation calibration factor for the volume displacement monopole, dipole and quadrupole source models at $\theta_T = 30°$, $S = 0.1$ ($\phi_{rel,s} = 0.6$, $V_T/a_o = 0.2$, $V_J/a_o = 0.5$) ○, Monopole; □, dipole; △, quadrupole.

primary jet-to-free jet signal-to-noise ratio limit S and $(d_T/d_J)^2$ to those values, as discussed in reference 5.5.

Internal noise sources on the other hand can, in principle, be independent of jet exit conditions; hence, frequencies lower than that radiated from the primary jet at $S = 0.1$ ($d_T/\lambda = 1$ with $V_J/a_o = 0.5$) may occur in free-jet tests at a level well above the free-jet "background" noise level. Thus, we consider here the transmission of low-frequency sound from the nozzle exit plane across the primary and free-jet shear layers.

Ideally, a theoretical model of this process should include the primary and free-jet nozzle surfaces or some approximation to them (such as semi-infinite unflanged pipes). Internal noise radiation through a cylindrical vortex sheet issuing from a semi-infinite pipe has been successfully analyzed by Munt (ref. 5.19) but extension of that work to the *coannular* nozzle problem has not been completed. The presence of the nozzle or pipe undoubtedly has some influence on the radiated sound field, particularly in the forward arc, but it is argued here that a reasonable indication of transmission effects (i.e. effects on the calibration factor) can be obtained from a model which does *not* include any solid boundaries.

In the absence of solid boundaries, the *surface* source distribution over the nozzle exit plane (generated by the internal noise sources) has to be replaced by a volume source distribution. A point monopole source located on the jet axis is used here on the grounds that, at these low frequencies ($k_o r_J \ll 1$, since $k_o r_T \leq \pi$) the actual surface source distribution would be uniform at low frequencies (below the first cut-on frequency, $k_o r_J < 1.84$).

With this model for internal noise radiation from the primary nozzle exit plane, and the low-frequency restriction, the analytic calibration factor derived in Section 5.2.1 can be utilized. There it is shown that when $k_o r_J \ll 1$ the vortex sheet or plug flow model yields the expected result that the calibration factor is independent of primary-jet flow conditions. In other words, as in the mixing noise study, the "partial profile" (free-jet profile alone) can be used to evaluate the calibration factor.

Before describing that, a selection of results are shown in Figures 5.11 and 5.12 to demonstrate the validity of the vortex sheet model, upon which the low-frequency calibration factor is based. Taking the partial profile, the Lilley equation calibration factor for a particular free-jet shear layer thickness, $\delta_T/r_T = 1/2$ (i.e. the thickness at about 2 diameters downstream of the nozzle exit plane) is compared with the low-frequency approximation at frequency $k_o r_T = \pi/4$ in Figure 5.11 and $k_o r_T = 3\pi/4$ in Figure 5.12; hence, $k_o \delta_T = \pi/8$ and $3\pi/8$, respectively. The two calibration factors agree almost perfectly, showing again that if $k_o \delta \leq 1$ the vortex sheet flow model is a good approximation for a study of transmission effects [see Figure 5.9(a) where $k_o \delta_T = 0.5$, 0.8 at $S = 0.1$, 0.315 and 5.9(b) where $k_o \delta_T = 1.6$ at $S = 0.1$]. Note, however, that even at a free-jet velocity of $V_T/a_o = 0.3$ in Figure 5.11, the low-frequency and numeric calibration factors differ by only 1 dB from the GA asymptote. This deviation from the GA asymptote, first considered in the previous section, is now considered in more detail.

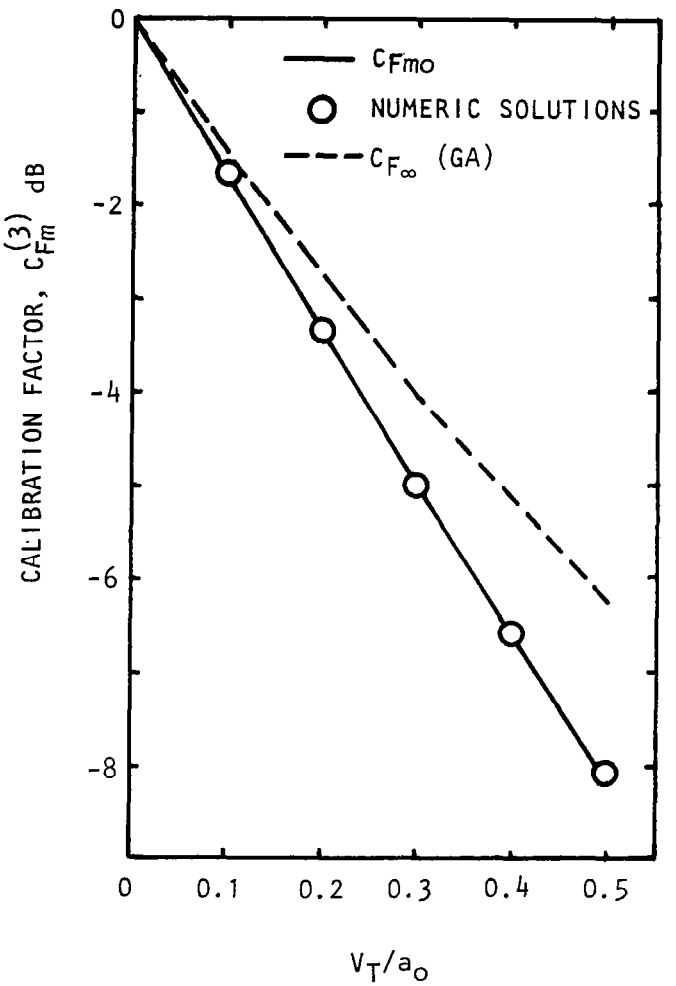

Figure 5.11 Comparison of low-frequency (solid line), numeric (symbol) and high-frequency (broken line) C_F values from Lilley equation solutions at low frequency; partial profile ($V_J = V_T$), volume displacement monopole source on jet axis. ($\theta_T = 30°$, $k_o r_T = \pi/4$, $k_o \delta_T = \pi/8$.)

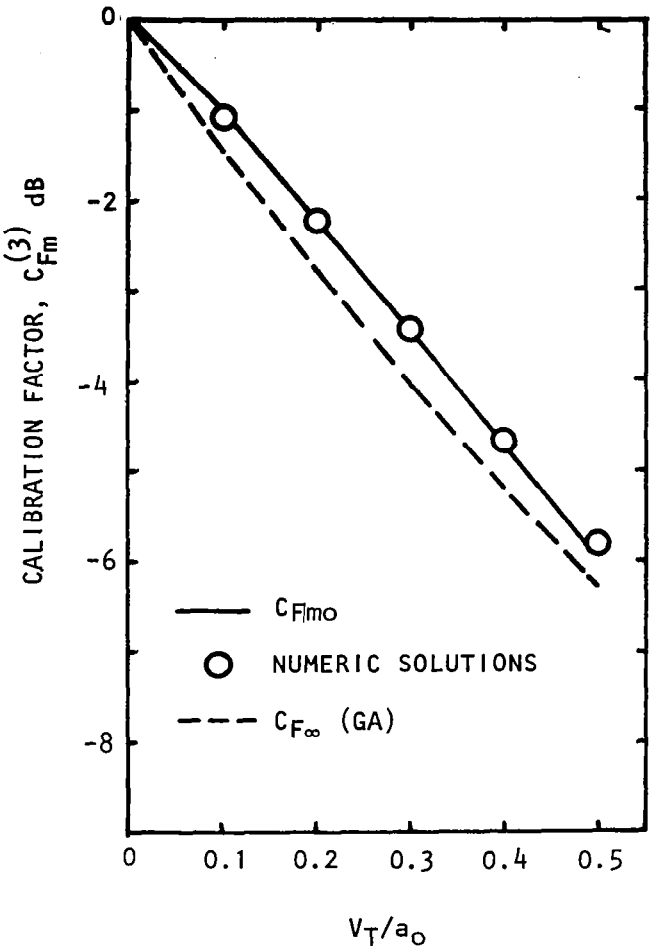

Figure 5.12 Comparison of low-frequency (solid line), numeric (symbol) and high-frequency (broken line) C_F values from Lilley equation solutions at low frequency; partial profile ($V_J = V_T$) volume displacement monopole source on jet axis. ($\theta_T = 30^o$, $k_o r_T = 3\pi/4$, $k_o \delta_T = 3\pi/8$.)

As long as the absence of solid boundaries in this partial profile - vortex sheet model does not prove to be a gross approximation, we argue that the resulting low-frequency calibration factor simply provides three rules for the calibration of low-frequency sound $k_o\delta_T \leq 1$ (internal noise, large-scale structure radiation, etc.). First, we can deduce an estimate for the frequency parameter $k_o r_T$, above which the calibration factor is an oscillatory function of frequency having a dB-mean given by the GA asymptote as illustrated in Figure 5.9. This estimate is defined by setting the normalized transverse wavenumber equal to unity

$$\kappa_T R_T = 1$$

or

$$k_o r_T = \kappa_T^{-1} = \{a_o^2 \frac{D_T^2}{a_T^2} - \cos^2\theta_o\}^{-\frac{1}{2}}$$

$$= (a_T + V_T \cos\theta_T)/(a_o \sin\theta_T)$$

$$\omega r_T/a_T = (1 + M_T \cos\theta_T)/\sin\theta_T \tag{5-36}$$

Thus, if $\omega r_T/a_T \geq (1 + M_T\cos\theta_T)/\sin\theta_T$ and $k_o\delta_T \leq 1$, the calibration factor will in general deviate from $C_{F\infty}$ but the deviation in dB is small and approximately given by (see Appendix 2 of reference 5.5)

$$\Delta(\text{dB}) = 10 \log_{10} \frac{\rho_T a_T \sin 2\theta_o}{\rho_o a_o \sin 2\theta_T} \tag{5-37}$$

the second rule deduced from the low-frequency calibration factor.

If $\omega r_T/a_T < (1 + M_T\cos\theta_T)/\sin\theta_T$, then the calibration factor lies somewhere between $C_{F\infty}$ (dB) $\pm\Delta$(dB) and a second low-frequency limit, attained when $k_o r_T \to 0$ and that is simply given by (Appendix 3 of reference 5.5).

$$C_{F_{mo}} = D_T^6. \tag{5-38}$$

$$k_o r_T \to 0$$

Unlike the high-frequency limit, there is no density ratio effect. This low-frequency limit is not reached in Figure 5.9; Figure 5.13 demonstrates the transition between it and the oscillatory high-frequency behavior.

In most practical situations the free-jet diameter will be sufficiently large on the wavelength scale for this low-frequency limit to be irrelevant, and even if the ray paths indicate that $k_o\delta_T \leq 1$, the oscillatory deviations from $C_{F\infty}$ [given approximately by equation (5-37)] will be almost always less than or equal to 1/2 dB.

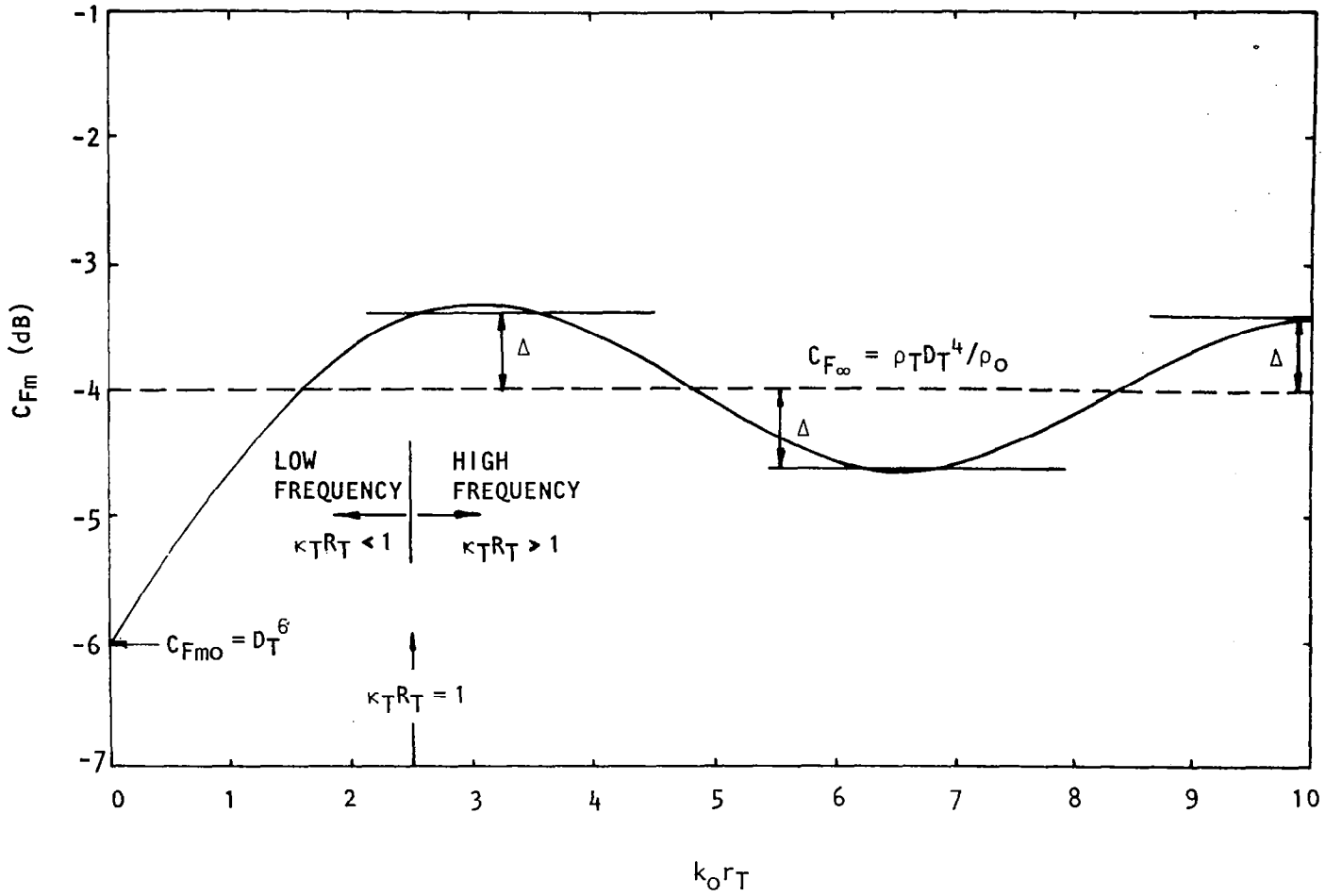

Figure 5.13 Variation of LF ($k_o\delta_T \to 0$) monopole calibration factors C_{Fmo} with frequency ($k_o r_T$) showing onset of oscillatory behavior about high-frequency mean ($k_o\delta_T \to \infty$); Δ is maximum deviation predicted by equation (5-37). ($\Delta = 0.62$ dB, $\theta_T = 30°$, $V_T/a_o = 0.3$, $V_J = V_T$.)

5.5 SUMMARY

The theoretical investigation described in this section has concentrated on the amplitude calibration factor, C_F, since this plays a key role in the free jet-to-ideal wind tunnel data transformation procedure described in sections 2 and 6. In that transformation, the high-frequency or geometric acoustics (GA) calibration factor

$$C_{F_\infty} = \rho_T D_T^4/\rho_O$$

is used, which can be obtained from analytic solutions to the *Lilley equation* when the typical free-jet shear layer thickness is large compared with the wavelength of sound; the derivation is given in Section 5.2.2. The main task of the work described in this section has been to *solve the Lilley equation numerically* in order to assess the validity of C_{F_∞} using realistic models of the primary-jet and free-jet mean flow fields and of the noise source itself (Section 5.3.1), particularly for jet mixing noise.

A set of basic numerical results for C_F are presented in Section 5.3.2 which shows that over the frequency range considered the ratio of C_F to C_{F_∞} for the monopole ring source falls within an "error" band of ±1/2 dB and moreover the magnitude of the dipole and quadrupole calibration factor deviations are similar if not even less significant. This strongly suggests that any higher-order multipole source models that might be required to model internal noise or shock-associated noise will also have these negligible deviations of C_F from C_{F_∞}. Theoretical results for the three different types of noise source are summarized under separate headings below.

Jet Mixing Noise

The measurement of jet mixing noise in a free-jet flight simulation facility is subject to a low-frequency cutoff due either to acoustic or to aerodynamic interference effects as described in reference 5.5. That is, either the free-jet background noise is too high, giving rise to inadequate signal-to-noise ratio or, at some distance downstream of the primary-jet exit plane in the low Strouhal number source region, the primary-jet and free-jet turbulent regions begin to merge, thus further modifying the turbulence structure and noise characteristics of the primary jet. The basic results given in Section 5.3.2 have been calculated at and above this cutoff Strouhal number so that for jet *mixing* noise lower Strouhal numbers need not be considered. These numberical results show that isothermal (quadrupole source) or heated (quadrupole and dipole sources) jet mixing noise data from a free-jet facility can be calibrated using the simple high-frequency factor C_{F_∞} with a remarkable degree of accuracy, at any frequency above the low-frequency cutoff defined above.

Internal Noise

Provided that the primary-jet and free-jet nozzle *surfaces* do not significantly influence the calibration factor, then over the frequency

range covered by the basic results of Section 5.3.2 and irrespective of the multipole distribution required to model the internal noise excitation at the exit plane, the high-frequency calibration factor C_{F_∞} can be used with acceptable accuracy. If narrow band analysis is involved so that the C_F deviations that oscillate with frequency about C_{F_∞} are not averaged out, the *maximum* deviation or "error" band about C_{F_∞} can be estimated with the formula given by equation (5-37).

At lower frequencies not covered by the basic results of Section 5.3.2 (internal noise is not, in principle, subject to the low-frequency cutoff associated with jet mixing noise), the low-frequency monopole calibration factor defined by equation (5-4) can be used which requires the evaluation of four Bessel functions. The transition between low and high frequencies in this case is defined by equation (5-36). However, these low frequencies are unlikely to occur in practice (typically $\lambda > \pi d_T$) when testing model-scale noise sources in a free-jet facility. For this reason the high-frequency calibration factor is also recommended for internal noise data calibration, bearing in mind its low-frequency cutoff determined by equation (5-36).

Shock-Associated Noise

This noise source has not been considered in the theoretical investigation but again we can appeal (i) to the basic numerical results referred to above for multipole sources and (ii) to the fact that shock-associated noise occurs at high jet velocities (i.e. high frequencies) in order to conclude, tentatively, that no significant deviations from C_{F_∞} are to be expected in practice. However, if low-frequency shock-associated noise is to be considered, the transition to low frequency defined by equation (5-36) can be used in this case also, to determine the frequency above which C_{F_∞} can be used with confidence, allowing only the maximum deviations estimated from equation (5-37).

6. TRANSFORMATION CHARTS AND COMPUTATIONAL PROCEDURE

The purpose of this section is to describe our recommended calibration or transformation procedure. The procedure can be used to transform flight simulation data measured in a free-jet facility to the corresponding data that one would obtain from a wind-tunnel simulation, and finally, in a flight situation. Every effort is made to present this procedure in a manner such that it can be used by any user with little or no reference to the work described in other sections of this report, or for that matter, by any user who has little or no knowledge of the underlying acoustic phenomena. In other words, the content of the present section is meant to stand on its own.

The data transformation procedure is presented here in two parts. In the first part (Section 6.1), the various concepts on which the transformation procedure is based are introduced briefly. This provides a basic breakdown of the various components of the procedure. Transformation charts corresponding to these components are given in terms of nondimensional or normalized parameters for general application. In the second part (Section 6.2), a comprehensive computer program is presented and described in detail in the form of a user's guide.

The transformation charts provide the order of magnitude of the various effects, i.e. the various steps or components of the transformation procedure. Although these charts can in principle be used to transform free-jet data to wind-tunnel conditions and then to flight conditions, in practice, this route will be very tedious and time-consuming. Instead, it is recommended that the computational procedure be used to conduct the data transformation.

The following five points must be noted before using the transformation charts and/or procedures described in this section:

(1) The transformation procedure works in terms of *lossless* data throughout. That is, the measured free-jet data that form the input to the procedure should be lossless (i.e., atmospheric attenuation corrections must be applied to the measured levels prior to data transformation), and the estimated wind-tunnel data or flight data, which is the output from the procedure, will also be lossless in nature. The computer program does not include atmospheric attenuation effects or ground reflection effects.

(2) All angles are expressed relative to the jet *exhaust* (or free-jet/wind-tunnel flow direction, if appropriate) and not relative to the jet inlet.

(3) For simplicity, the transformation charts are given for the special case where the free-jet flow temperature and the temperature of the ambient medium surrounding the free jet are equal (i.e. $T_T = T_O$). This implies that the corresponding sound speeds and the densities are also equal (i.e. $a_T = a_O$ and $\rho_T = \rho_O$). For most practical applications, the effect of this minor assumption will be insignificant. In the computational procedure, however, this assumption has been removed for the sake of completeness.

(4) The estimated wind-tunnel data and/or flight data are computed at the specified *polar arc radius* and not *sideline distance*. If it is required to express the transformed data at some desired *sideline distance* from the nozzle, certain parts of the computer program need to be modified.

(5) The transformation procedure does not include any size scaling requirements. That is, the measured free-jet data and the transformed wind-tunnel or flight data refer to the same nozzle size. Once again, if it is necessary to transform *model-scale* free-jet data to *full-scale* flight data, the appropriate scaling laws need to be incorporated in the computer program.

6.1 TRANSFORMATION CHARTS

6.1.1 Free-Jet to Wind-Tunnel Data Transformation

In the free-jet flight simulation experiments, noise data are normally acquired at several measurement (or microphone) angles θ_m on a measurement arc of radius R_m centered at the nozzle exit. The corresponding wind-tunnel data need to be expressed as a function of the emission angle θ_T at some specified emission radius R†. Thus, the transformation of free-jet data to wind-tunnel data first of all requires a relationship between measurement angle θ_m and emission angle θ_T. This is referred to as the "angle correction." In addition, two other correction or calibration factors are required in the transformation: one is called the "amplitude correction" (C_F) and the other is called the "distance correction" (C_R). Using these correction factors, the wind-tunnel SPL's corresponding to the free-jet SPL can be expressed as

$$SPL_{WT}(R,\theta_T) = SPL_{FJ}(R_m,\theta_m) + 10 \log_{10} C_F + 10 \log_{10} C_R \ . \qquad (6\text{-}1)$$

Before presenting the relationships and the transformation charts for each of these three calibration factors, it is important to discuss certain angular *limits* beyond which data in a free-jet flight simulation experiment cannot be acquired.

<u>Angular Limits in Free-Jet Experiments</u>

(1) In free-jet flight simulation experiments, the microphones are placed outside the flow. For a source located on the centerline of the free jet, the minimum measurement angle, $(\theta_m)_{min}$, is determined by the ratio (r_T/R_m) of the free-jet nozzle radius to the microphone arc radius. From Figure 6.1, this minimum angle, *based on nondiverging free-jet flow*, is given by

$$(\theta_m)_{min} = \sin^{-1} (r_T/R_m) \ . \qquad (6\text{-}2)$$

---

†*In other sections of this report, the emission radius (or distance) is denoted by R_{rT}. Throughout the present section, it is denoted by R for simplicity.*

For measurement angles smaller than $(\theta_m)_{min}$, the microphone becomes embedded in the flow. The variation of $(\theta_m)_{min}$ with r_T/R_m is given in Chart 1. In reality, the free-jet flow spreads with downstream distance, and the actual value of $(\theta_m)_{min}$ would be larger than that given by equation (6-2) for the non-diverging case.

(2) Another constraint on the microphone position (R_m, θ_m) in the rear arc is governed by the so-called "cone of silence" effect. In the far field $(R_m/r_T \to \infty)$, this cone of silence angle is given by

$$\theta_c = (\theta_m)_{min} = \cos^{-1}\left(\frac{a_o}{a_T + V_T}\right) \cdot \tag{6-3}$$

According to the simplified model shown in Figure 6.2, sound waves emitted inside the flow in the downstream direction (i.e., emission angle $\theta_T = 0°$) always emerge outside the flow at angle θ_c given by the above equation. The variation of $(\theta_m)_{min}$ (for $R_m/r_T \to \infty$ and $a_T = a_o$) with free-jet Mach number M_T according to this cone of silence effect is shown in Chart 2.

(3) For sound radiated in the forward arc, the maximum emission angle inside the flow is given by

$$(\theta_T)_{max} = \cos^{-1}\left(\frac{-a_T}{a_o + V_T}\right) \cdot \tag{6-4}$$

For emission angles greater than this limit, total internal reflection at the free-jet lip line occurs, and sound cannot escape outside the flow. The variation of $(\theta_T)_{max}$ with free-jet Mach number M_T is given in Chart 3 for $a_T = a_o$.

Turbulent Mixing Noise Source Location

One of the miscellaneous charts that needs to be considered in the data transformation is the variation of the jet mixing noise source location with frequency. If the microphones in a free-jet flight simulation experiment are located at large measurement distances (i.e. large values of R_m/d where d is the primary-jet nozzle diameter) from the model-jet nozzle, these source location corrections are not important. On the other hand, for small values of measurement distances (typical values of R_m/d used in practice vary from 50 to 100), the actual jet mixing noise source locations can be important, especially at the lower frequencies where it is known that the dominant sound sources are located quite far downstream of the nozzle exit plane.

For static jets, the variation of source location with frequency [derived from published experimental results (ref. 6.1)] is given by the following set of relationships:

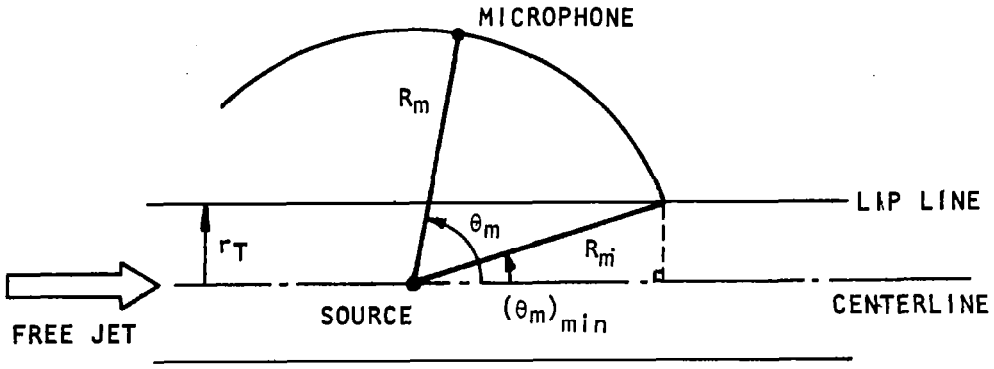

Figure 6.1 Minimum measurement angle dictated by test geometry.

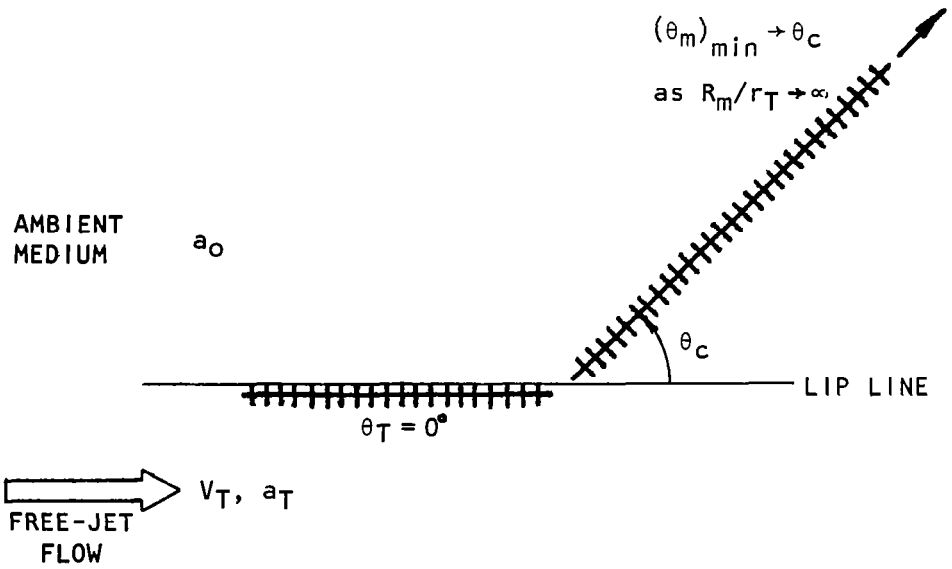

Figure 6.2 Minimum measurement angle dictated by cone of silence effect.

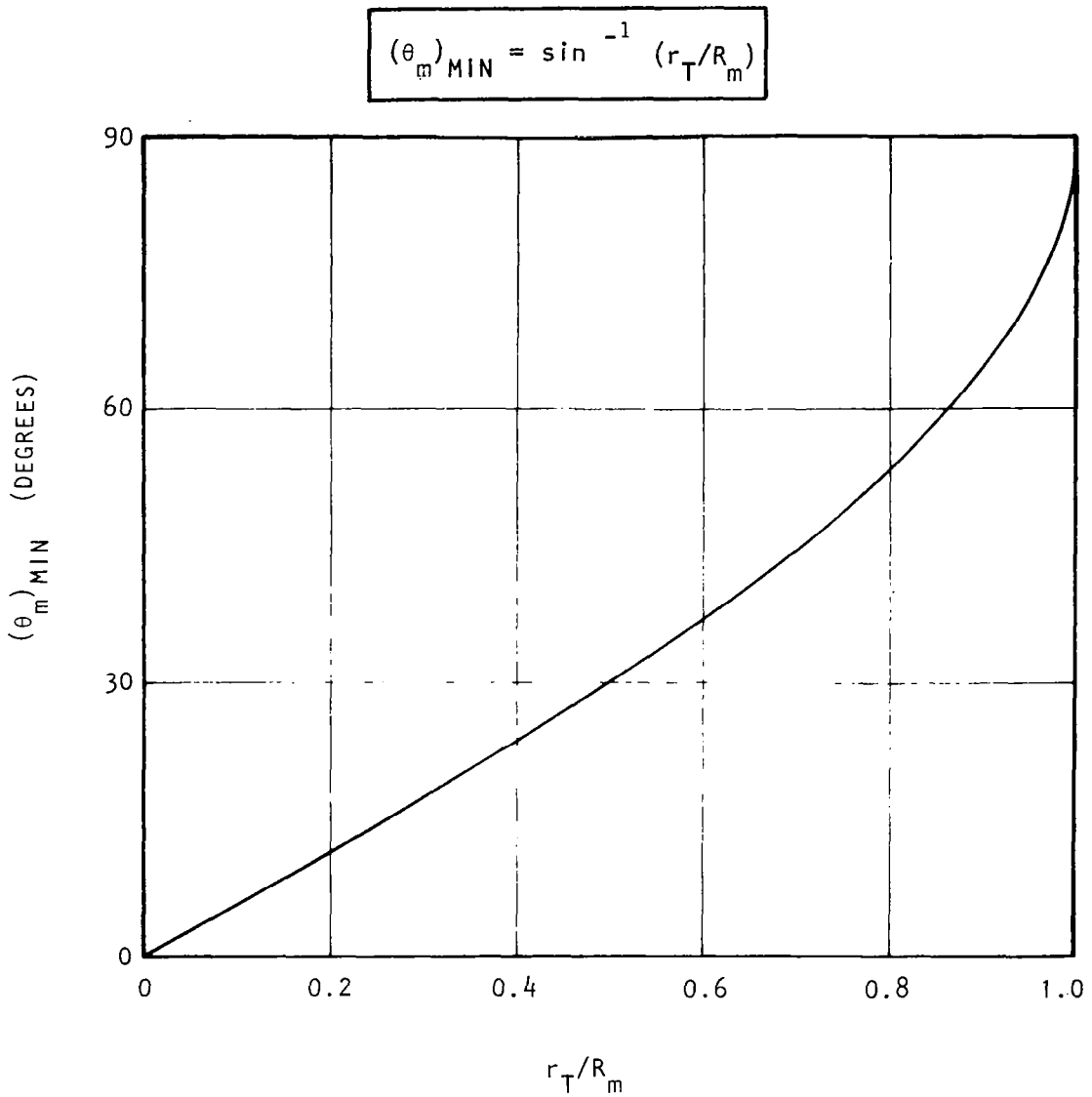

Chart 1 Variation of minimum measurement angle with r_T/R_m.

$$(\theta_m)_{MIN} = \cos^{-1}\{1/(1+M_T)\}$$

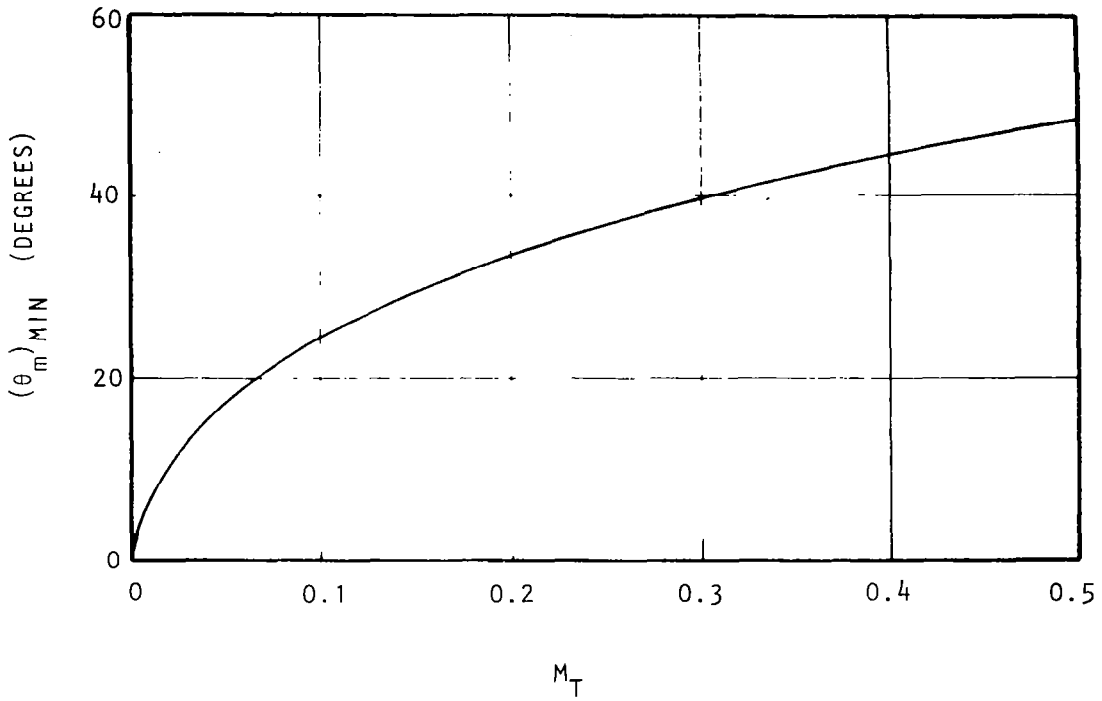

Chart 2 Variation of minimum measurement angle with free-jet Mach number M_T.

$$(\theta_T)_{MAX} = \cos^{-1}\{-1/(1+M_T)\}$$

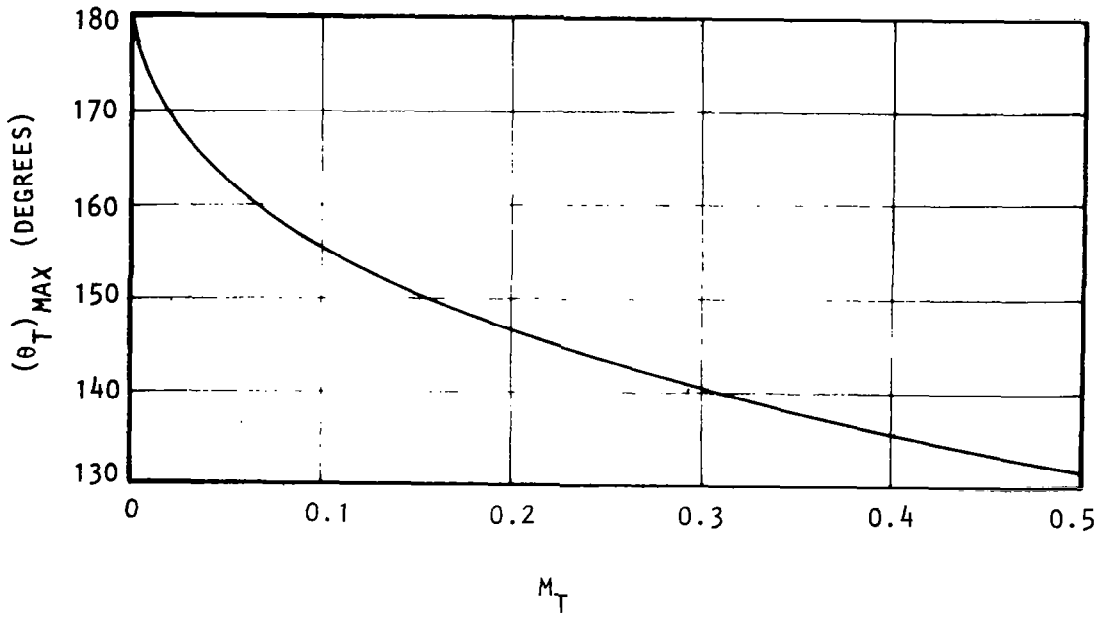

Chart 3 Variation of maximum emission angle with free-jet Mach number M_T.

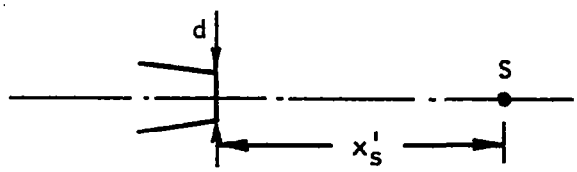

$$x_s'/d = (0.057\ S_m + 0.021\ S_m^2)^{-\frac{1}{2}} \tag{6-5}$$

where

$$S_m = SD_m \tag{6-6}$$

$$S = fd/V_J \tag{6-7}$$

$$D_m = \{(1 - M_c\cos\theta_T)^2 + \alpha^2 M_c^2\}^{\frac{1}{2}} \tag{6-8}$$

$$M_c = 0.67\ V_J/a_o \quad \text{and} \quad \alpha = 0.3. \tag{6-9}$$

The variation of x_s'/d with modified Strouhal number S_m is presented in Chart 4. These source location relationships are strictly valid only for a static jet. For a jet immersed in a co-flowing stream, although it is known that the jet potential core stretches with forward velocity, no experimental results are available which accurately quantify the changes in source locations with forward motion. In view of this missing experimental information, it is recommended that the source locations given in Chart 4 be applied to static as well as all practical forward velocity conditions. Although the changes in source locations due to jet stretching can be estimated and incorporated in the above relationships, it is felt that this modification is of secondary importance for all practical cases (i.e., R_m/d of the order of 50 to 100).

Angle Correction

The various angles involved in the transformation of free-jet data to corresponding wind-tunnel conditions are defined in Figure 6.3. The acoustic signal emitted by the source at emission angle (or wavenormal angle) θ_T inside the flow is convected downstream by the free-jet flow as shown by the velocity triangle. The resulting ray (which makes a ray angle ψ_T relative to the flow direction) intersects the lip line at point I, where it is refracted away from the flow direction. The emerging angle or the wavenormal angle outside the flow (which is identical to the ray angle in ambient medium) is denoted by θ_o. Finally, the measurement angle θ_m is simply the angle between the source-to-observer line and the flow direction.

The ray angle ψ_T is related to the emission angle θ_T by

$$\tan\psi_T = \frac{a_T \sin\theta_T}{V_T + a_T\cos\theta_T}\ . \tag{6-10}$$

(convection by uniform flow)

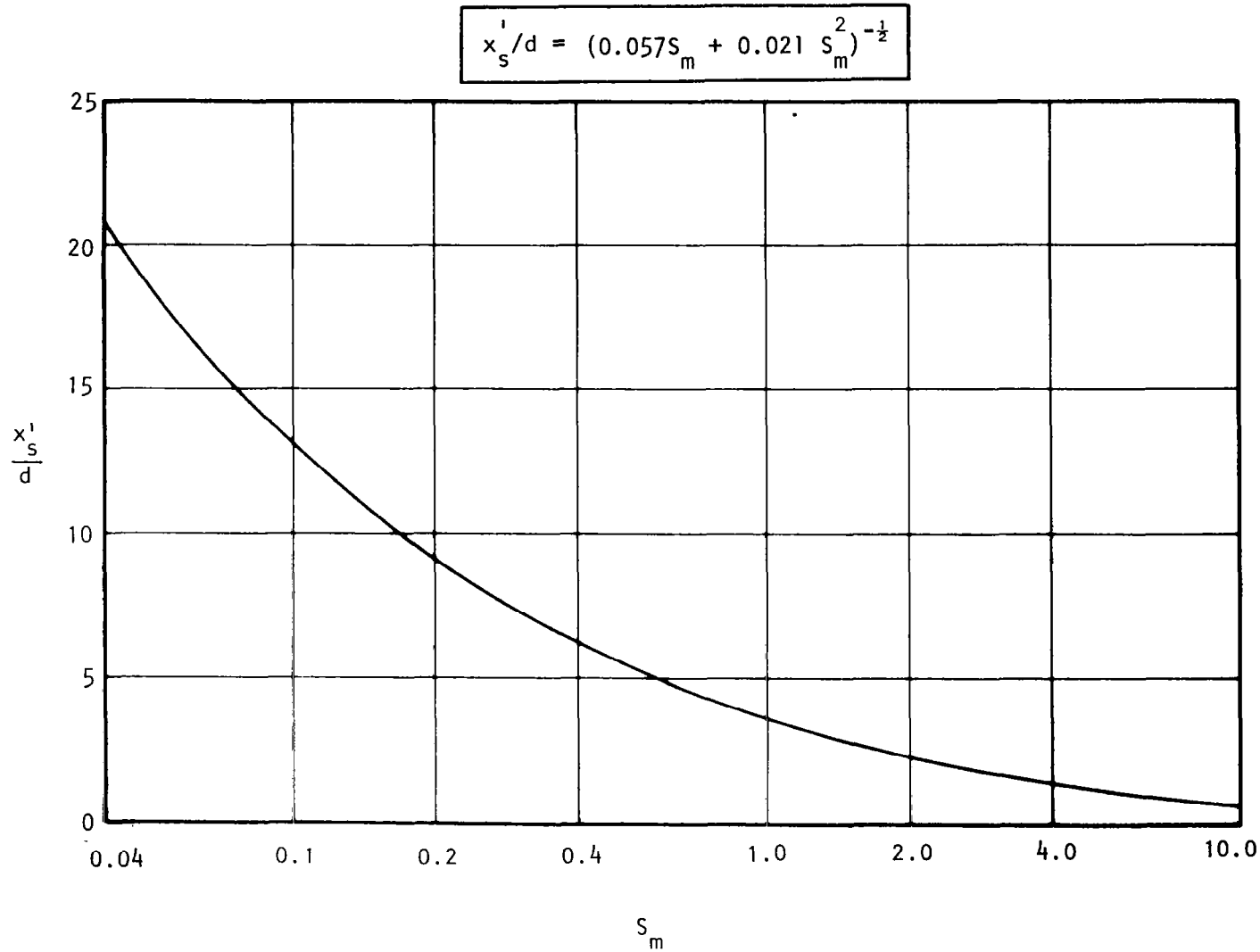

Chart 4 Variation of jet mixing noise source location x_s'/d with modified Strouhal number S_m.

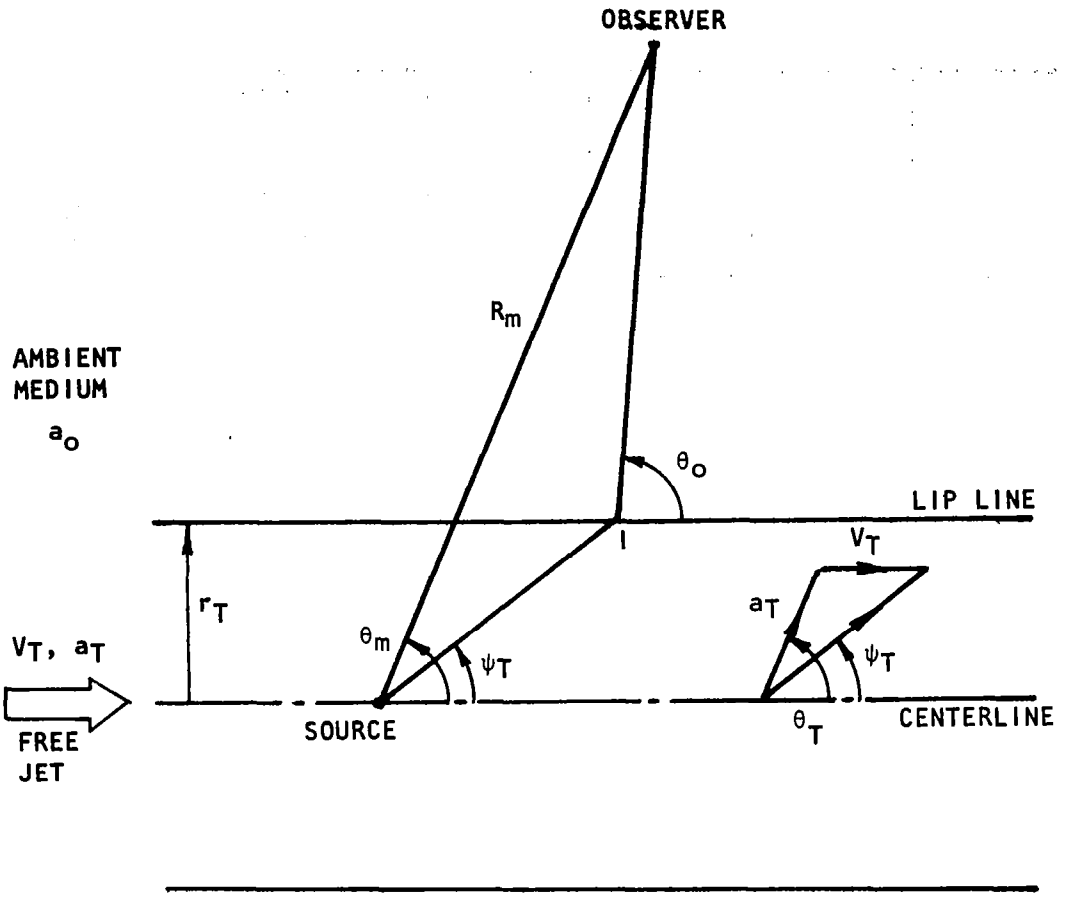

Figure 6.3 Geometry showing various angles according to the lip-line model of sound refraction.

The variation of ψ_T with θ_T at various free-jet Mach numbers $M_T(=V_T/a_T)$ is presented in Chart 5.

The emerging angle θ_o is related to the emission angle θ_T by

$$\cos\theta_o = \frac{(a_o/a_T)\ \cos\theta_T}{1 + (V_T/a_T)\ \cos\theta_T} \ . \tag{6-11}$$

(Snell's law)

The variation of θ_o with θ_T at various free-jet Mach numbers is given in Chart 6.

Finally, the third relationship required in the angle transformation is given by the lip line refraction geometry (see Figure 6.3) as

$$\cos\theta_m = (r_T/R_m)\ \cot\psi_T + (\sin\theta_m - r_T/R_m)\ \cot\theta_o \ . \tag{6-12}$$

(lip-line refraction)

For a given free-jet Mach number M_T, free-jet nozzle radius r_T, and measurement radius R_m, equations (6-10) through (6-12) can be solved to yield θ_m in terms of θ_T, or, conversely, to yield θ_T in terms of θ_m. Of course, it is this transformation between θ_m and θ_T that is of direct interest in the free-jet to wind-tunnel data transformation. The variation of θ_m with θ_T at various values of r_T/R_m for five values of free-jet Mach number (from 0.1 to 0.5) is given in Charts 7 through 11 (assuming $a_T = a_o$). It should be noted that in each of these five charts, the curves are terminated at $(\theta_T)_{max}$ discussed above and given by equation (6-4) or Chart 3.

Amplitude Correction

The amplitude correction (or calibration) factor C_F based on geometric acoustics is given by

$$C_F = \rho_T\ D_T^4/\rho_o \tag{6-13}$$

where

$$D_T = (1 + V_T\cos\theta_T/a_T)^{-1} \tag{6-14}$$

is the Doppler factor. The variation of amplitude correction in decibels with emission angle θ_T is given in Chart 12 for various free-jet Mach numbers M_T $(=V_T/a_T)$. Here again, the chart is presented for the case where $\rho_T = \rho_o$, and the curves are terminated at $(\theta_T)_{max}$ values given in Chart 3.

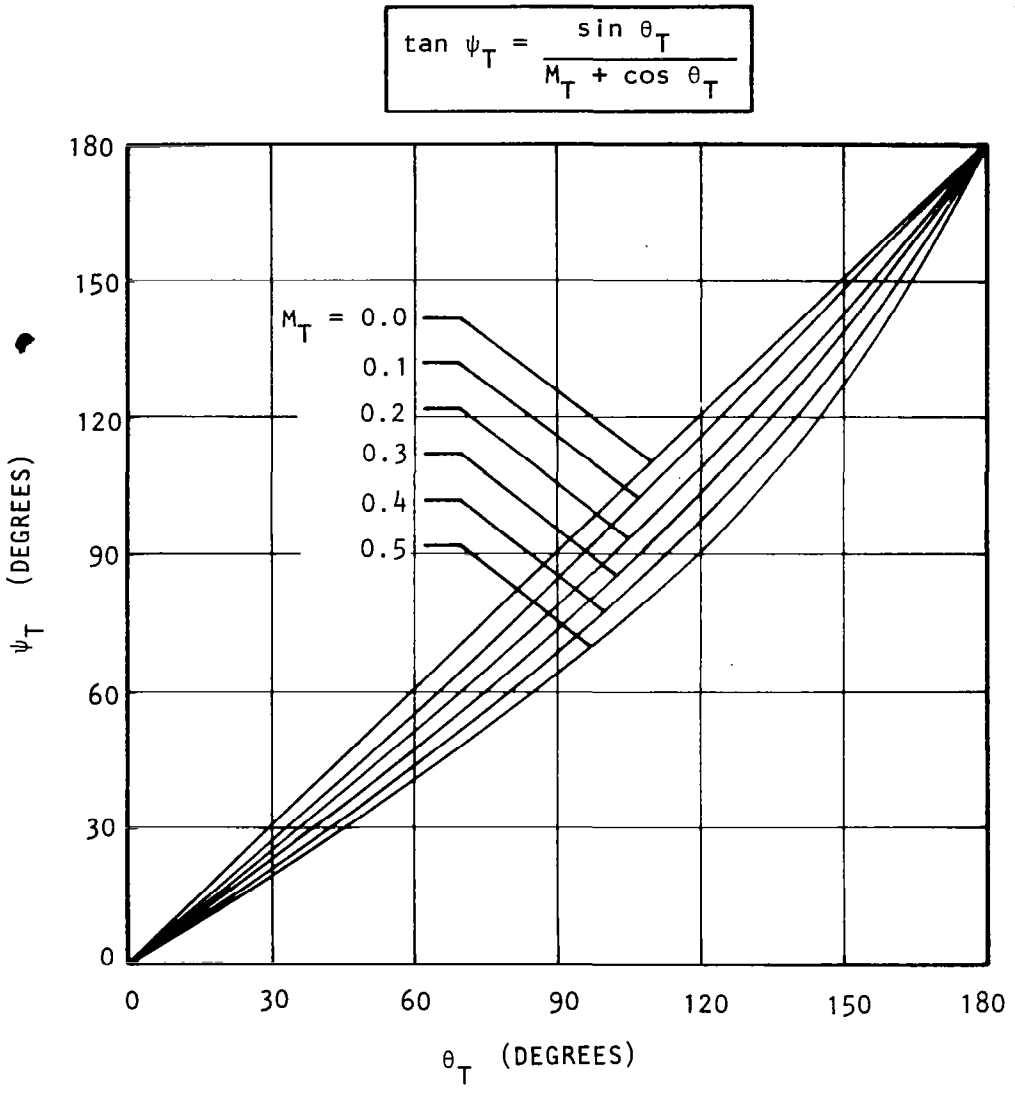

Chart 5 Variation of ray angle ψ_T with emission angle θ_T at various free-jet Mach numbers M_T.

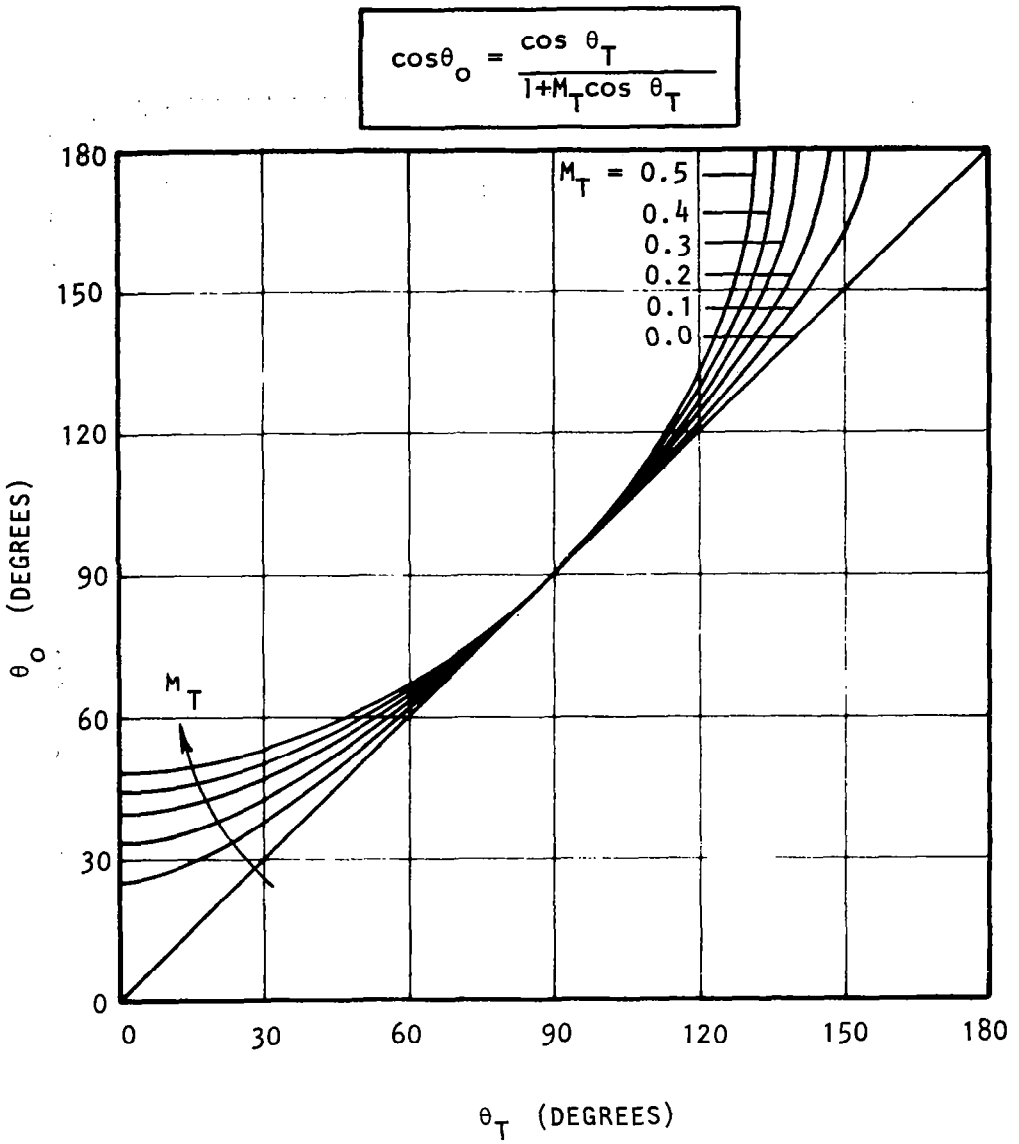

Chart 6 Variation of emerging angle θ_o with emission angle θ_T at various free-jet Mach numbers M_T.

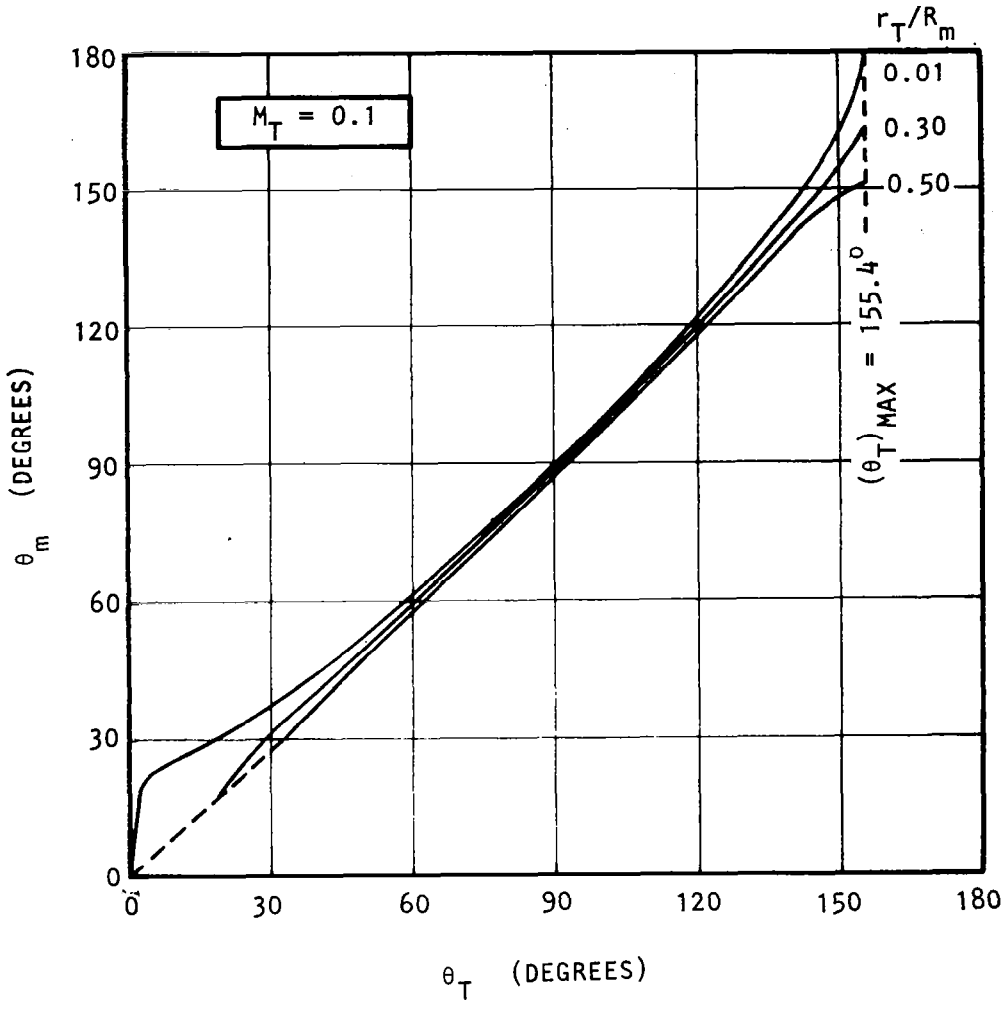

Chart 7 Variation of measurement angle θ_m with emission angle θ_T at various values of r_T/R_m . Free-jet Mach number M_T=0.1.

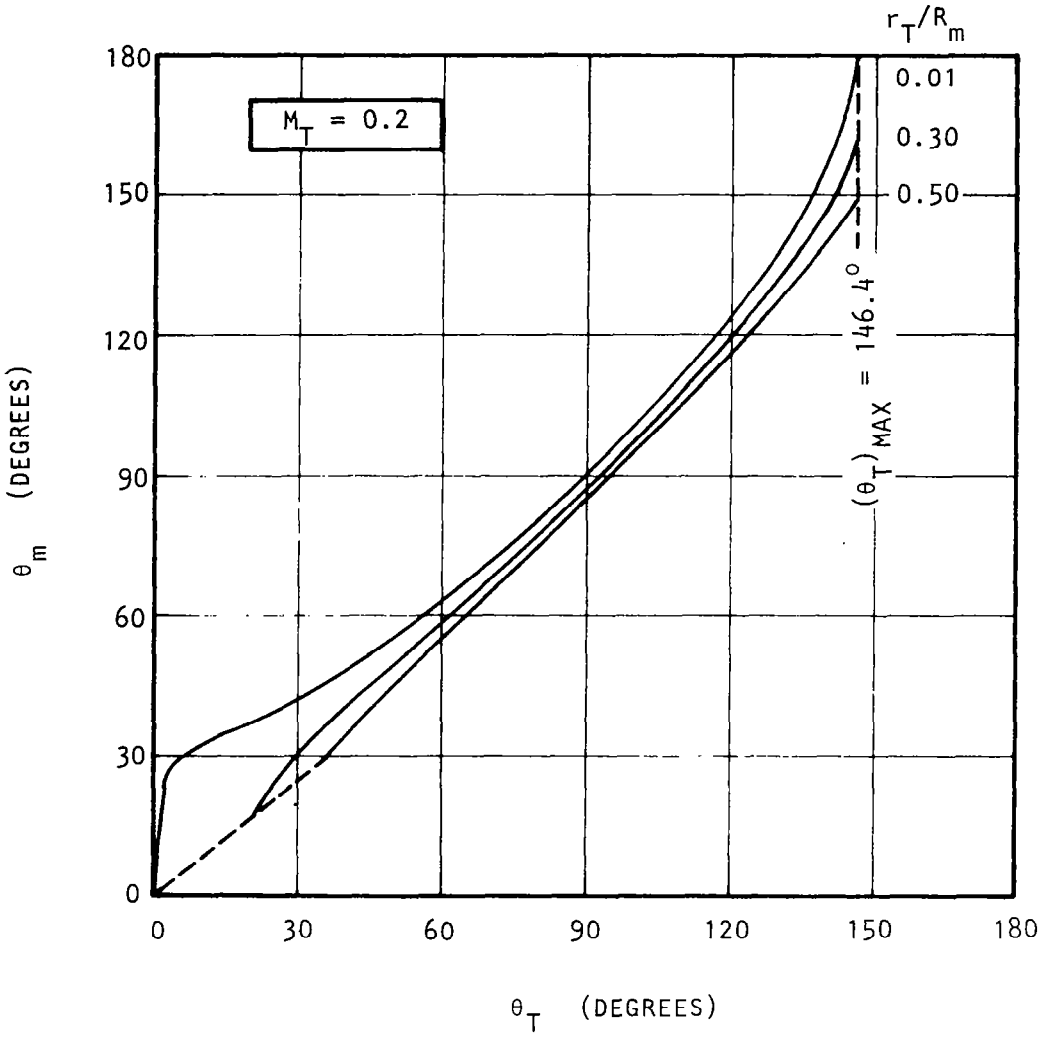

Chart 8 Variation of measurement angle θ_m with emission angle θ_T at various values of r_T/R_m. Free-jet Mach number M_T=0.2.

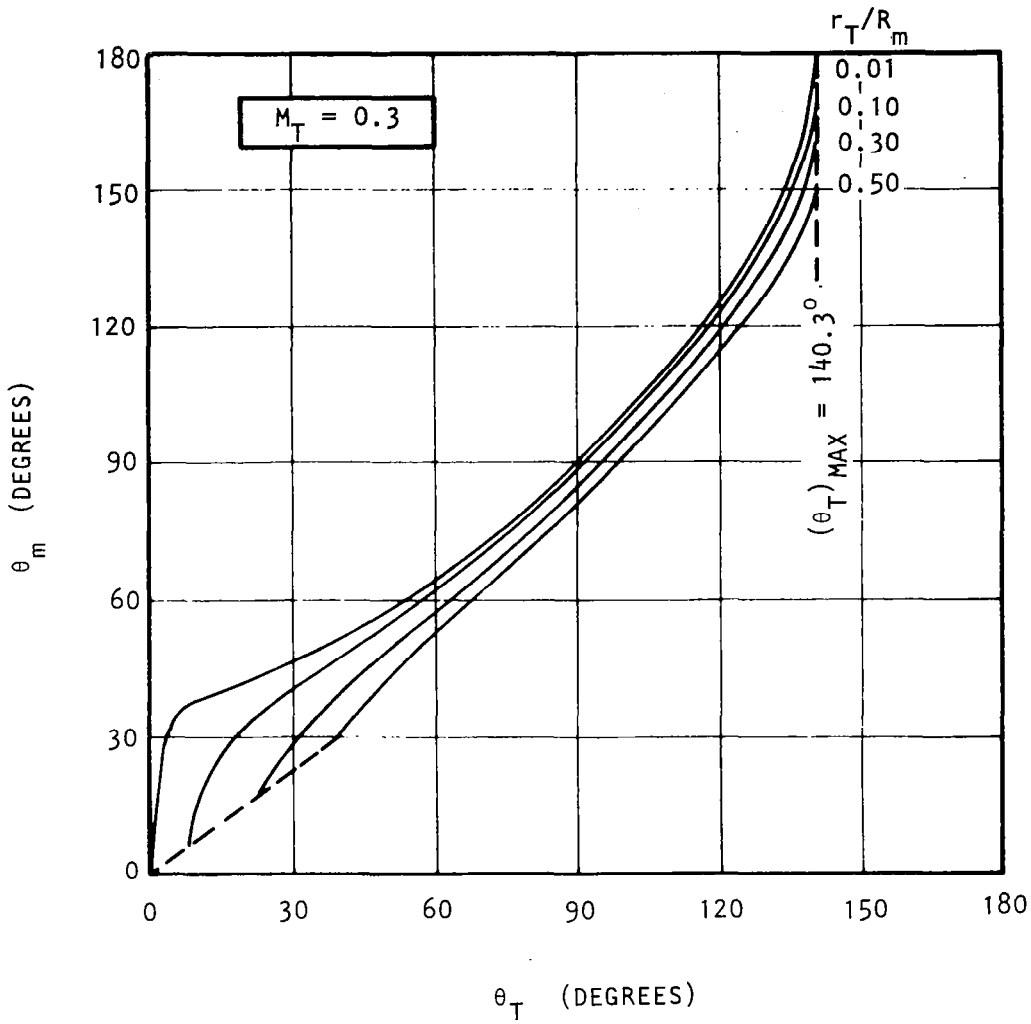

Chart 9 Variation of measurement angle θ_m with emission angle θ_T at various values of r_T/R_m. Free-jet Mach number M_T=0.3.

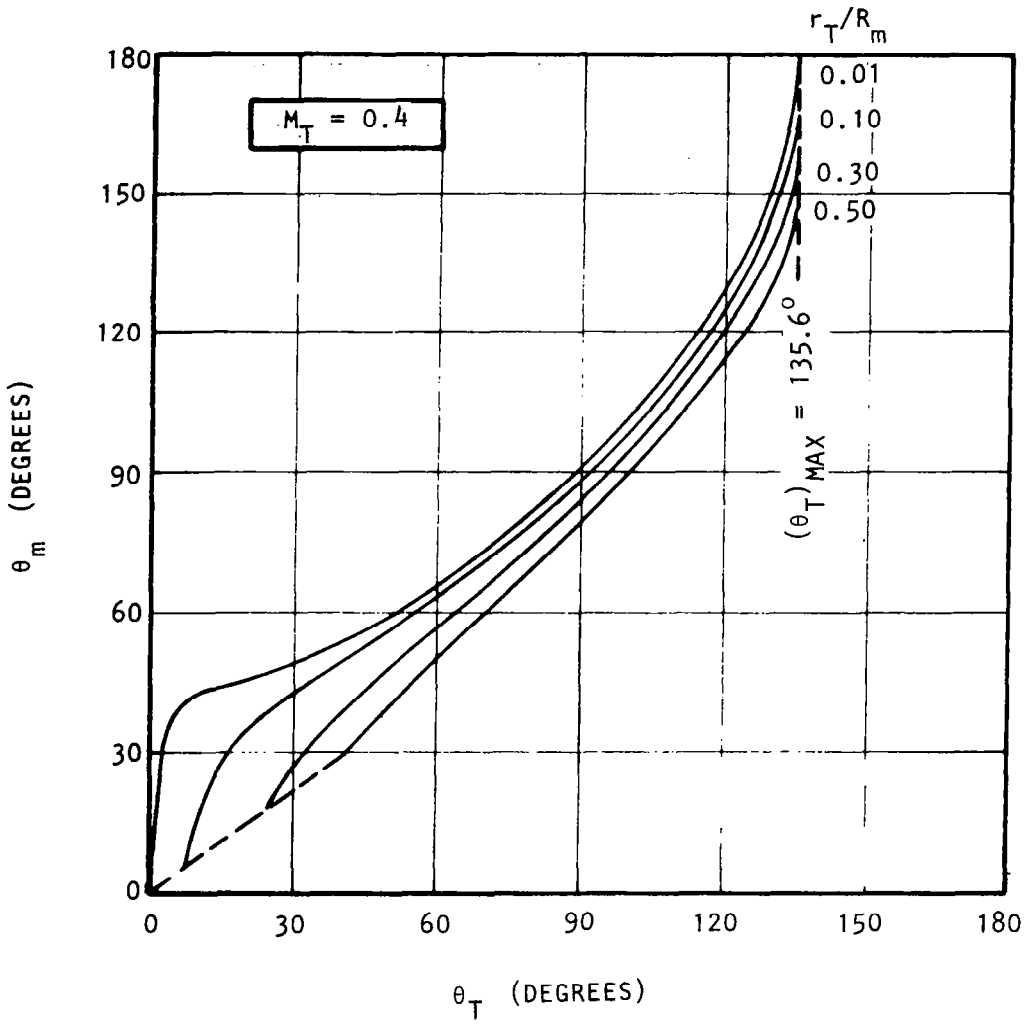

Chart 10 Variation of measurement angle θ_m with emission angle θ_T at various values of r_T/R_m . Free-jet Mach number M_T=0.4.

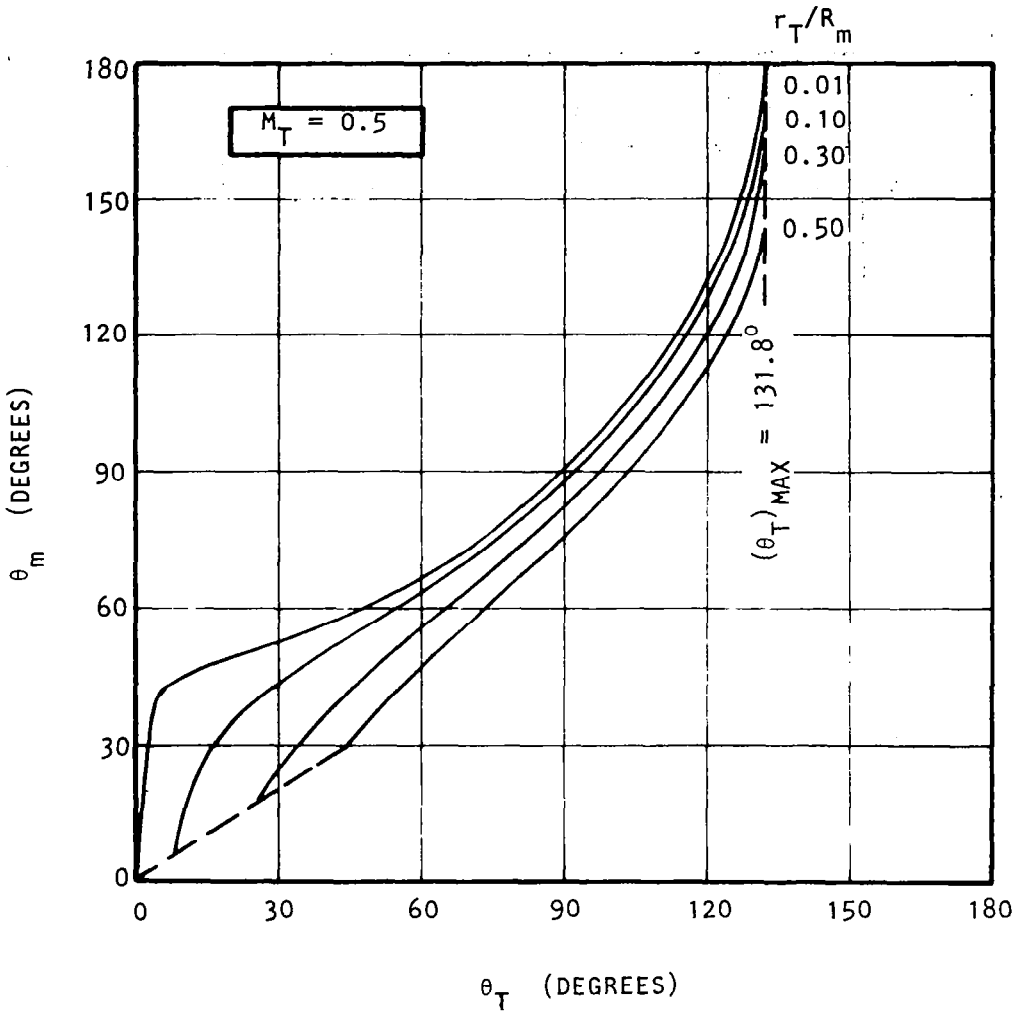

Chart 11 Variation of measurement angle θ_m with emission angle θ_T at various values of r_T/R_m . Free-jet Mach number M_T=0.5.

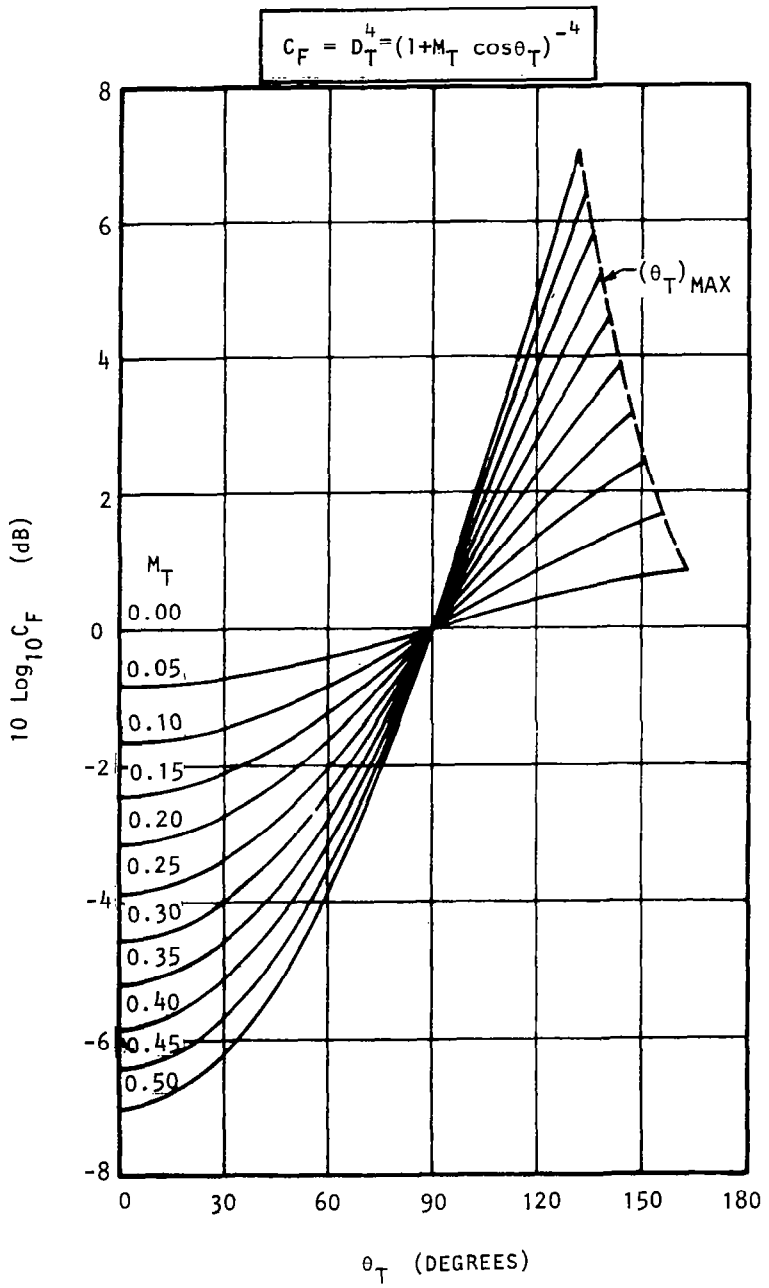

Chart 12 Variation of amplitude calibration factor C_F with emission angle θ_T at various free-jet Mach numbers M_T.

Distance Correction

The distance correction factor C_R is given by

$$C_R = R_{ro}R_{ra}/R^2 \tag{6-15}$$

where

$$R_{ro} = R_m \sin\theta_m / \sin\theta_o \,, \tag{6-16}$$

$$R_{ra} = R_{ro} + (r_T/\sin\theta_o)\ \{(\cot\theta_T/\cot\theta_o)^3\ (a_o/a_T)^2 - 1\}, \tag{6-17}$$

and where the angles θ_T, θ_m and θ_o are related by equations (6-10) through (6-12). The distance calibration factor is therefore a function of five parameters: θ_T, M_T, r_T, R_m and R.

The distance calibration factor in decibels is plotted against the emission angle θ_T in Charts 13 through 17 for five values of free-jet Mach number. The variables r_T and R_m are included in the charts in the form of ratio r_T/R_m. As done previously for other charts, a_T is assumed to be equal to a_o in the present charts also. It should be noted that these five charts are computed for the case where the fifth parameter, i.e. the emission (or prediction) distance R, is equal to r_T (i.e. $R/r_T = 1$). Therefore, for any other desired value of the distance R (i.e. $R \neq r_T$) where the wind-tunnel data are to be predicted, the final distance calibration factor should actually be obtained by using the following relationship:

$$\begin{array}{l}\text{Final distance}\\ \text{calibration factor}\\ \text{for } R/r_T \neq 1\end{array} = \begin{array}{l}\text{Distance calibration}\\ \text{factor from charts}\\ \text{for } R/r_T = 1\end{array} - 20 \log_{10} (R/r_T). \tag{6-18}$$

6.1.2 Wind-Tunnel to Flight Data Transformation

Doppler Frequency Shift

In the wind-tunnel simulation, there is no relative motion between the nozzle and the observer, whereas in the flight case, the nozzle is moving relative to a fixed observer. The transformation of wind-tunnel data to the corresponding flight case therefore requires a Doppler frequency shift. This is the only correction that is required to transform SPL spectra measured in proportional bandwidths (as is the case in one-third octave band SPL spectra). The Doppler frequency shift is given by

$$\frac{f_{flight}}{f_{wind\text{-}tunnel}} = D_T = (1 + M_T\cos\theta_T)^{-1} . \tag{6-19}$$

The variation of flight-to-wind-tunnel frequency ratio with emission angle θ_T at various tunnel Mach numbers is given in Chart 18.

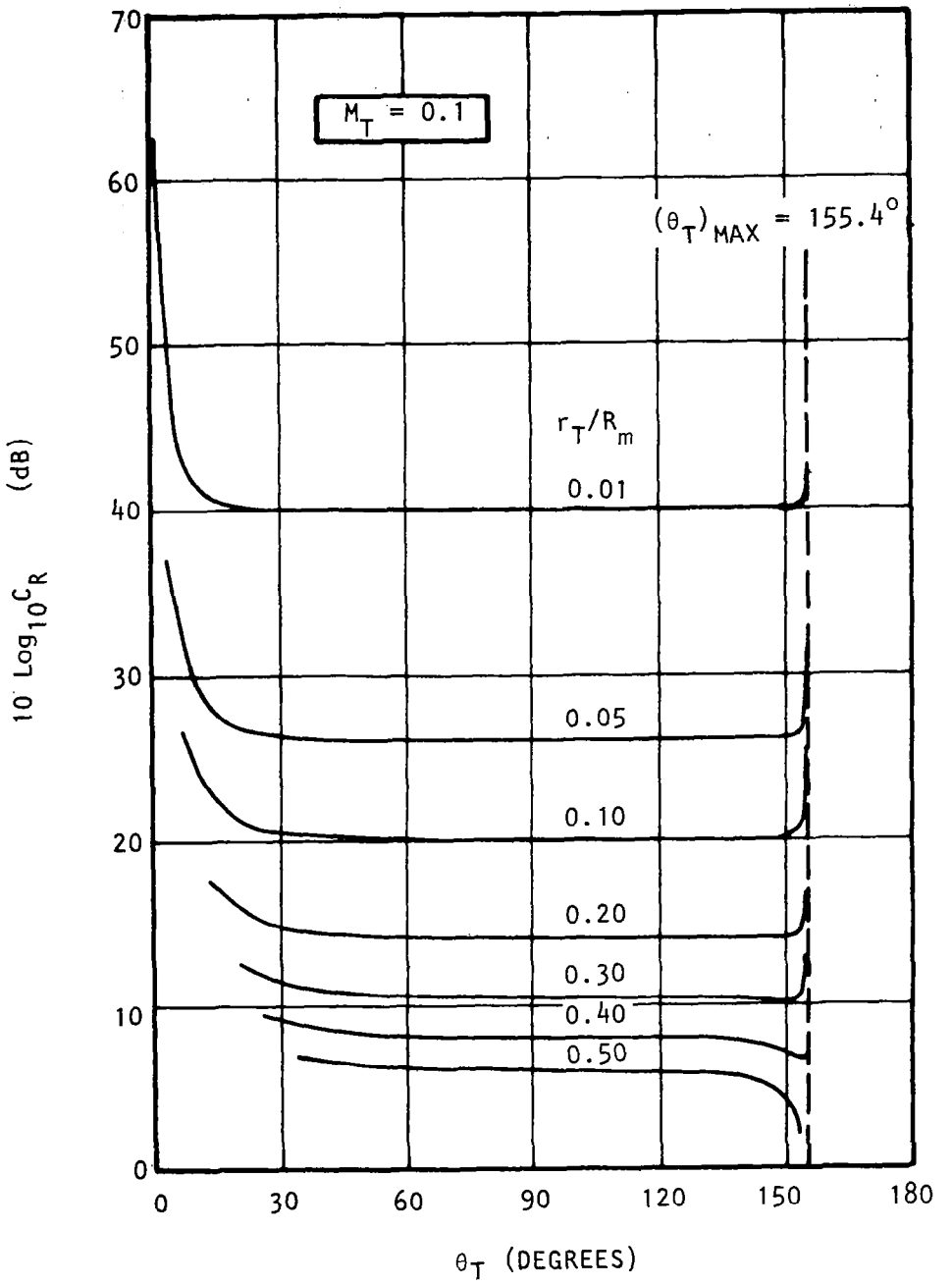

Chart 13 Variation of distance calibration factor C_R with emission angle θ_T at various values of r_T/R_m. Free-jet Mach number M_T=0.1 ; prediction distance $R=r_T$.

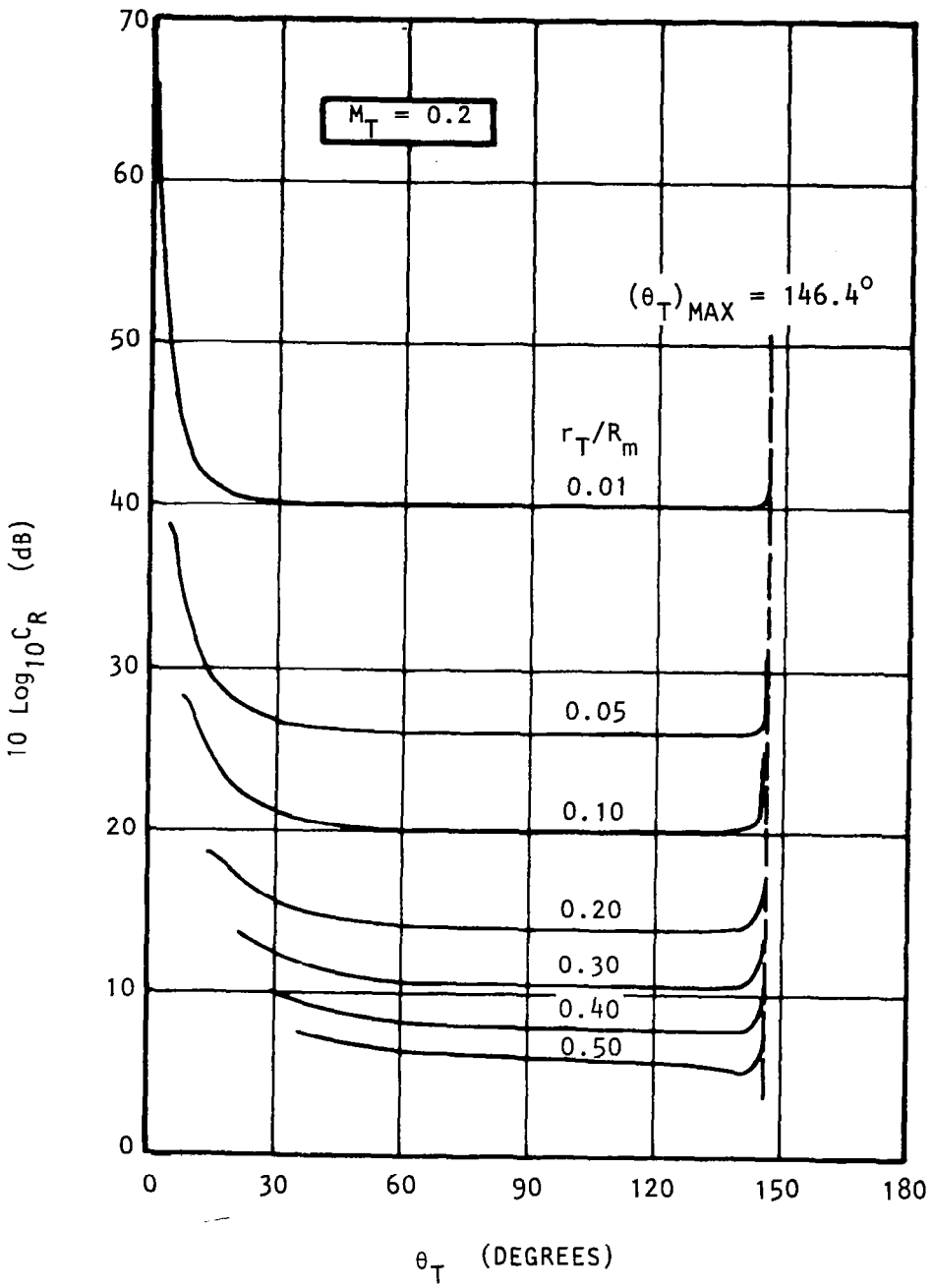

Chart 14 Variation of distance calibration factor C_R with emission angle θ_T at various values of r_T/R_m. Free-jet Mach number M_T=0.2 ; prediction distance $R=r_T$.

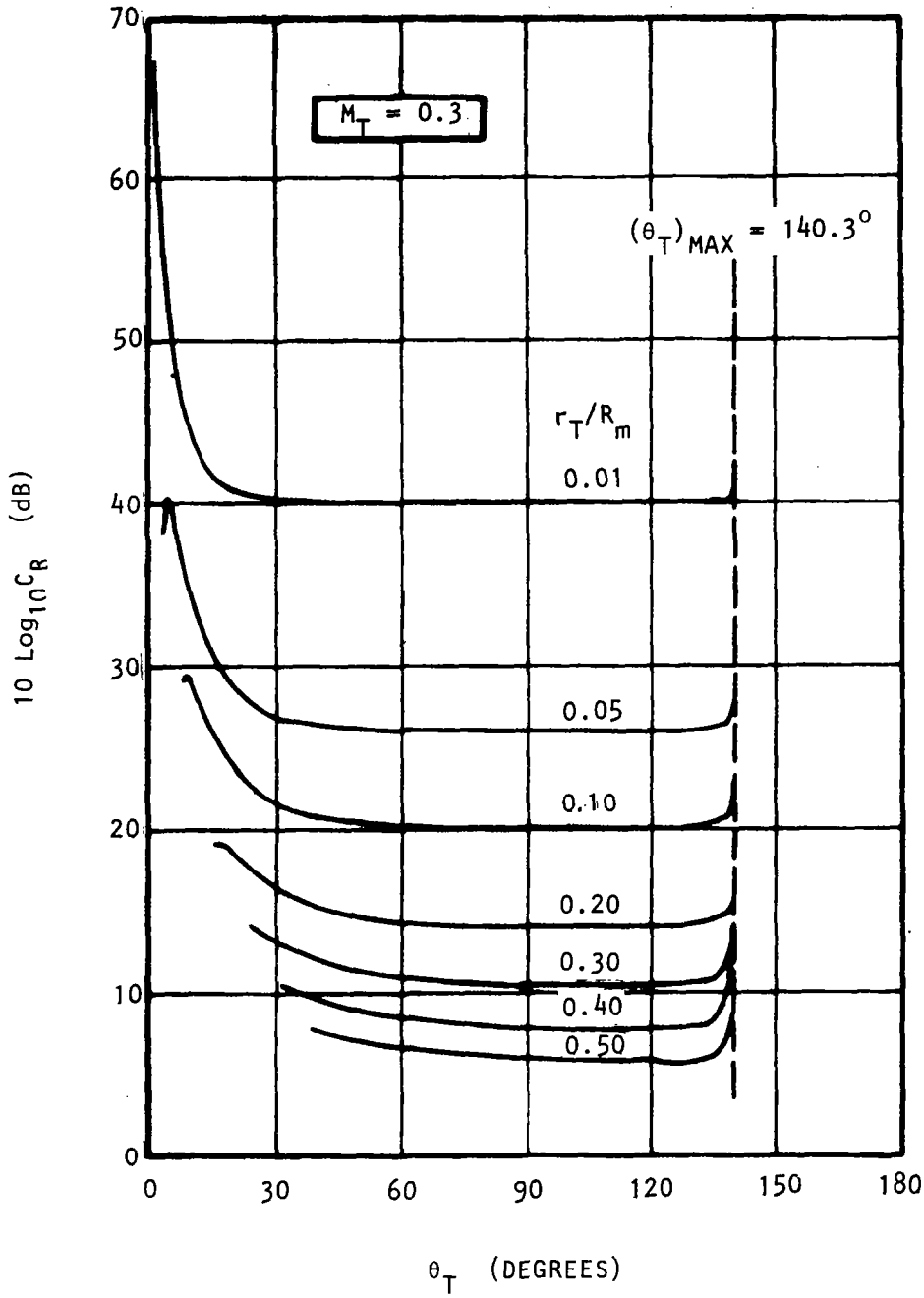

Chart 15 Variation of distance calibration factor C_R with emission angle θ_T at various values of r_T/R_m. Free-jet Mach number M_T=0.3 ; prediction distance $R=r_T$.

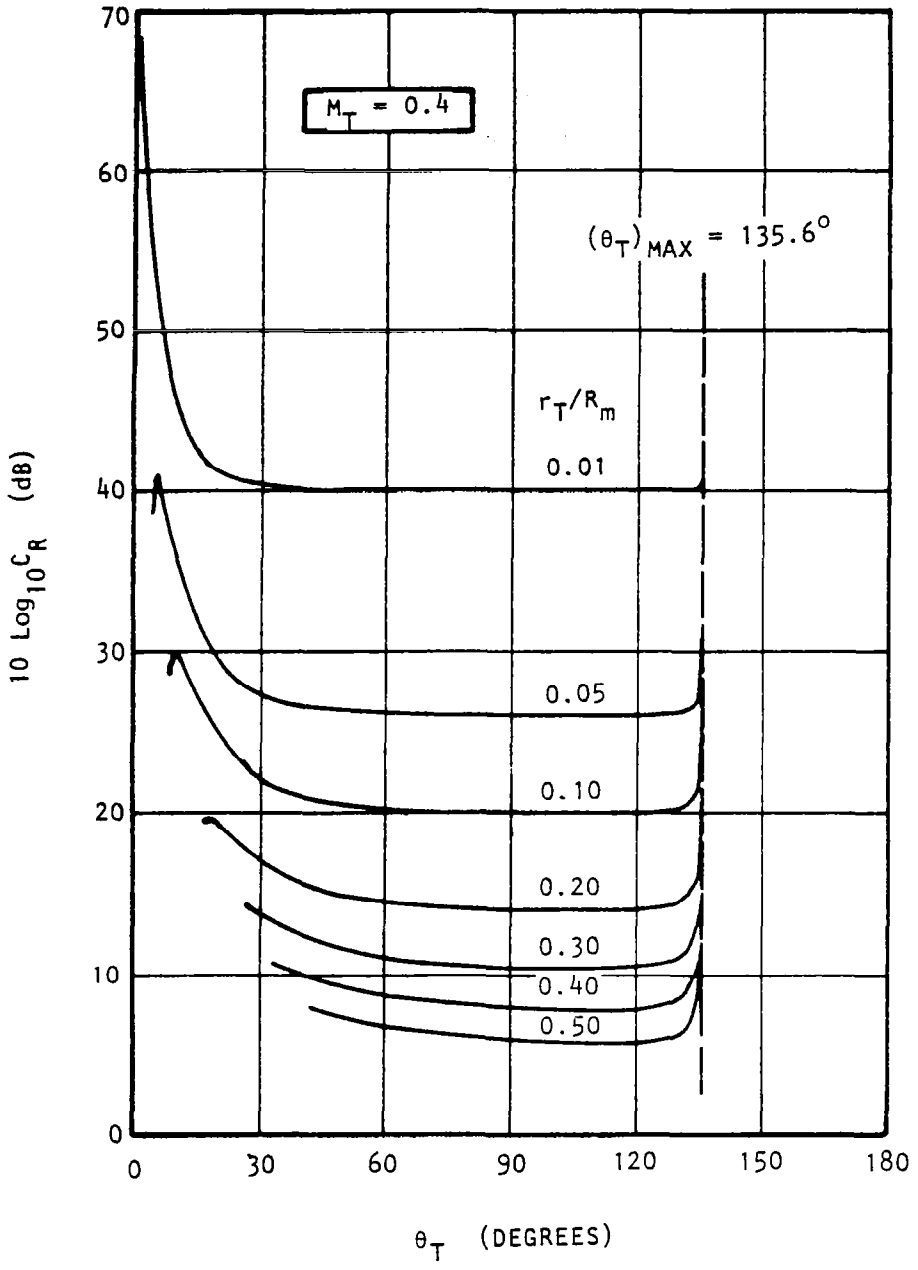

Chart 16 Variation of distance calibration factor C_R with emission angle θ_T at various values of r_T/R_m . Free-jet Mach number $M_T = 0.4$; prediction distance $R = r_T$.

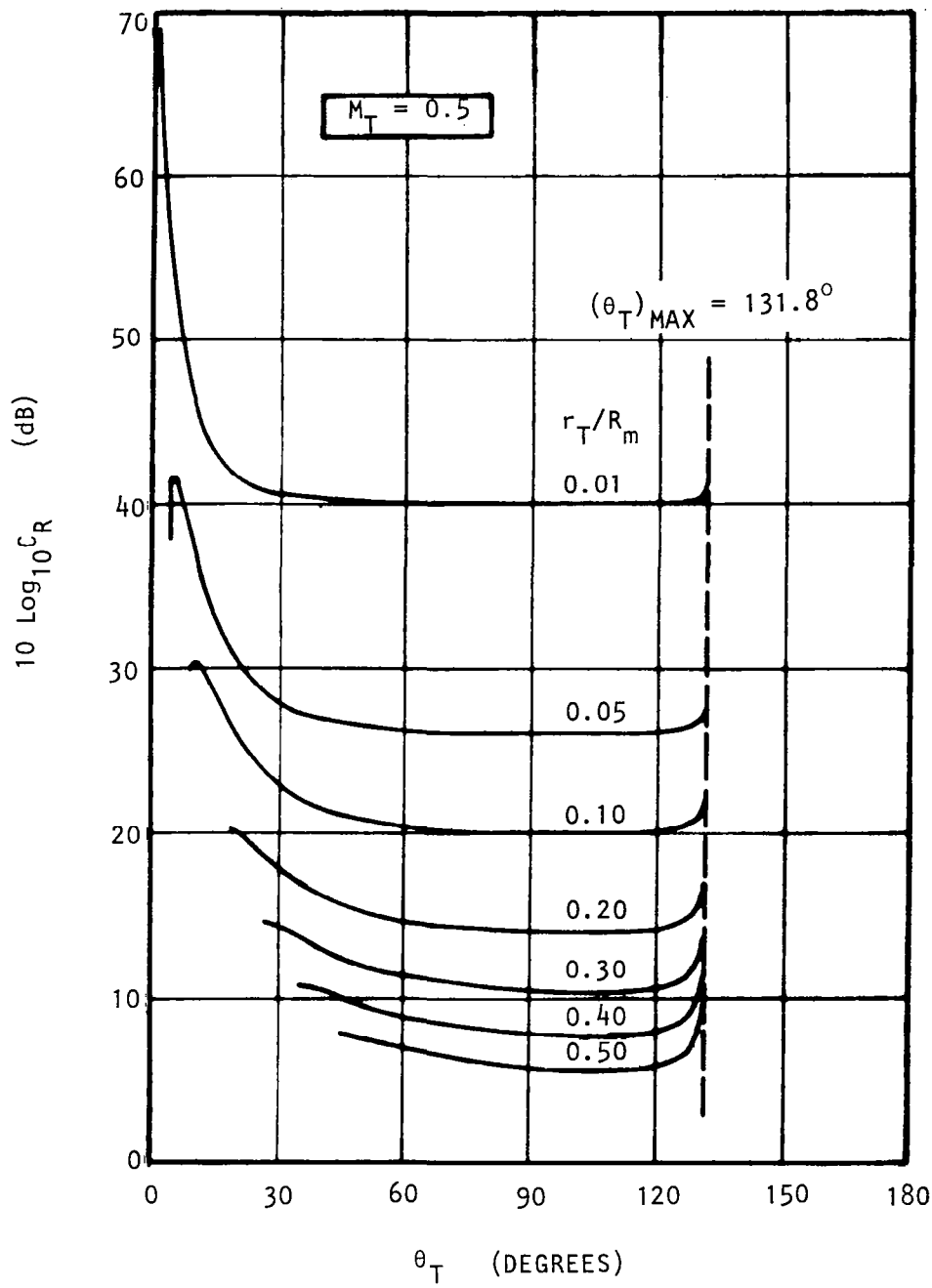

Chart 17 Variation of distance calibration factor C_R with emission angle θ_T at various values of r_T/R_m. Free-jet Mach number $M_T = 0.5$; prediction distance $R=r_T$.

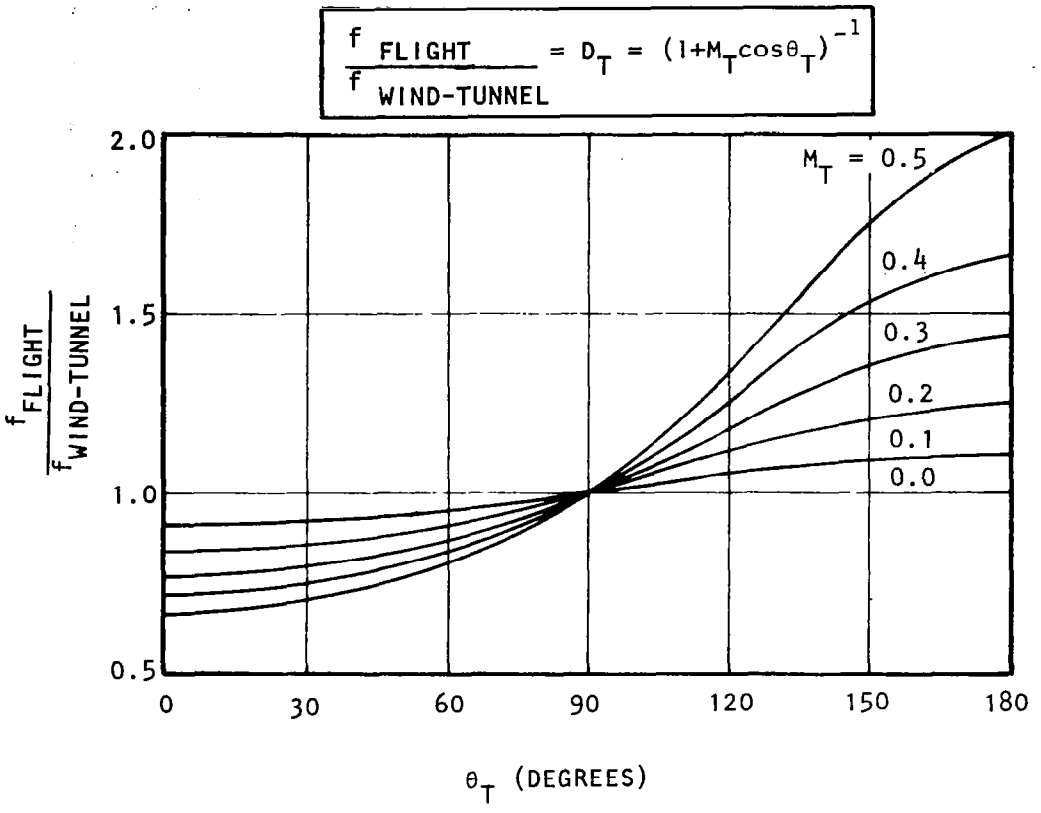

Chart 18 Variation of flight-to-wind-tunnel frequency ratio with emission angle θ_T at various tunnel Mach numbers M_T.

Miscellaneous Charts for the Flight Case

(1) In an actual aircraft flyover test, the sound emitted by the engine when the aircraft is located at emission-time location (R_θ, θ_T) relative to the fixed observer will be received by the observer when the aircraft has moved to location (R_ψ, ψ_T), as shown in Figure 6.4. The emission angle θ_T (i.e. source-to-observer angle at emission time) and the reception angle ψ_T (i.e. source-to-observer angle at reception time) are related by

$$\tan\psi_T = \frac{\sin\theta_T}{M_A + \cos\theta_T}, \tag{6-20}$$

and the variation of ψ_T with θ_T at various flight Mach numbers (M_A) is shown in Chart 19.

(2) With reference to the same flight geometry (Figure 6.4), the source-to-observer distances R_ψ and R_θ, at reception time and emission time, respectively, are related by

$$R_\psi/R_\theta = (1 + M_A^2 + 2M_A \cos\theta_T)^{\frac{1}{2}} . \tag{6-21}$$

The variation of this distance ratio with emission angle θ_T for various values of M_A is given in Chart 20.

(3) The comparison between actual flight data and flight simulation data transformed to the flight case is normally conducted at constant emission angles (θ_T) and some constant observer distance R. In the case of the aircraft flyover noise test, the measured pressure-time history shown in Figure 6.5(a) can first of all be transformed to a directivity plot as shown in Figure 6.5(b), i.e. SPL against ψ_T. Using the angle transformation discussed under item (1) above, the next step is to display the directivity in the form of SPL vs. emission angle θ_T, as illustrated in Figure 6.5(c). This completes the angle transformation. However, the actual noise levels in Figure 6.5(c) refer to different values of the emission-time distance R_θ. A distance correction is therefore required to obtain the results at constant observer distance R (for varying θ_T).

The parameter that is normally recorded in any flight test program is the normal distance H between the observer and the aircraft flight path. The relationship between R_θ and H is given from Figure 6.6 as

$$R_\theta = H/\sin\theta_T . \tag{6-22}$$

Hence to display the results at constant R, the following correction is required:

$$SPL(R,\theta_T) = SPL(R_\theta,\theta_T) - 20 \log_{10} (R/R_\theta) \tag{6-23}$$

where

$$R/R_\theta = R \sin\theta_T/H . \tag{6-24}$$

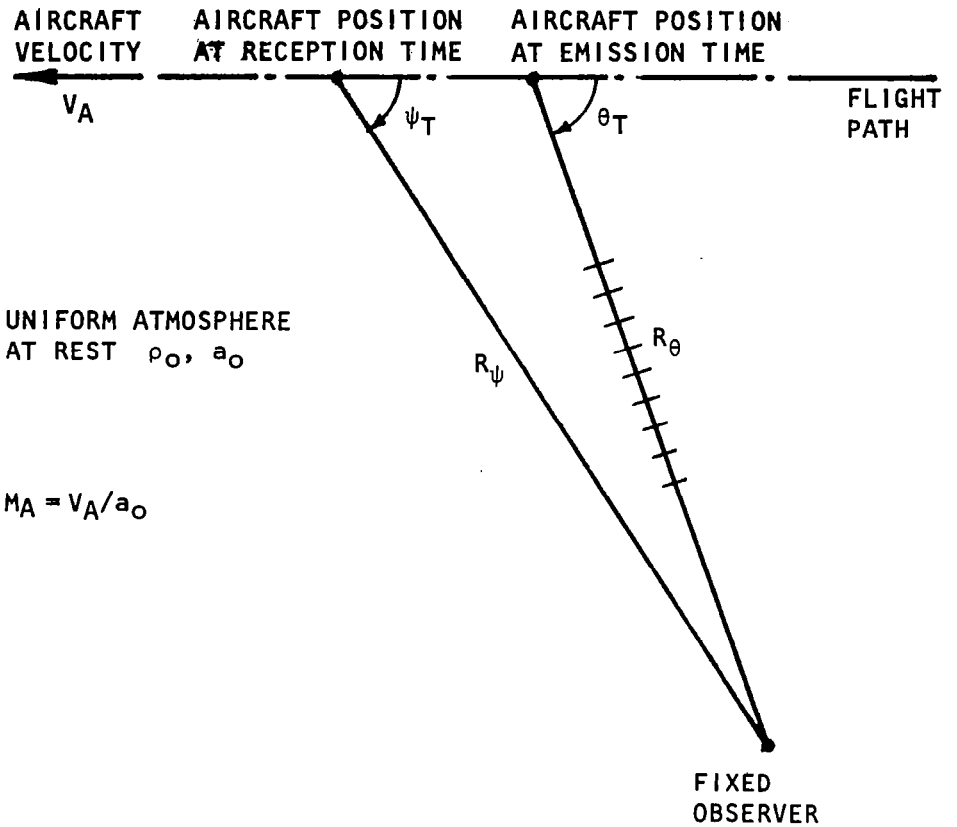

Figure 6.4 Aircraft flyover situation.

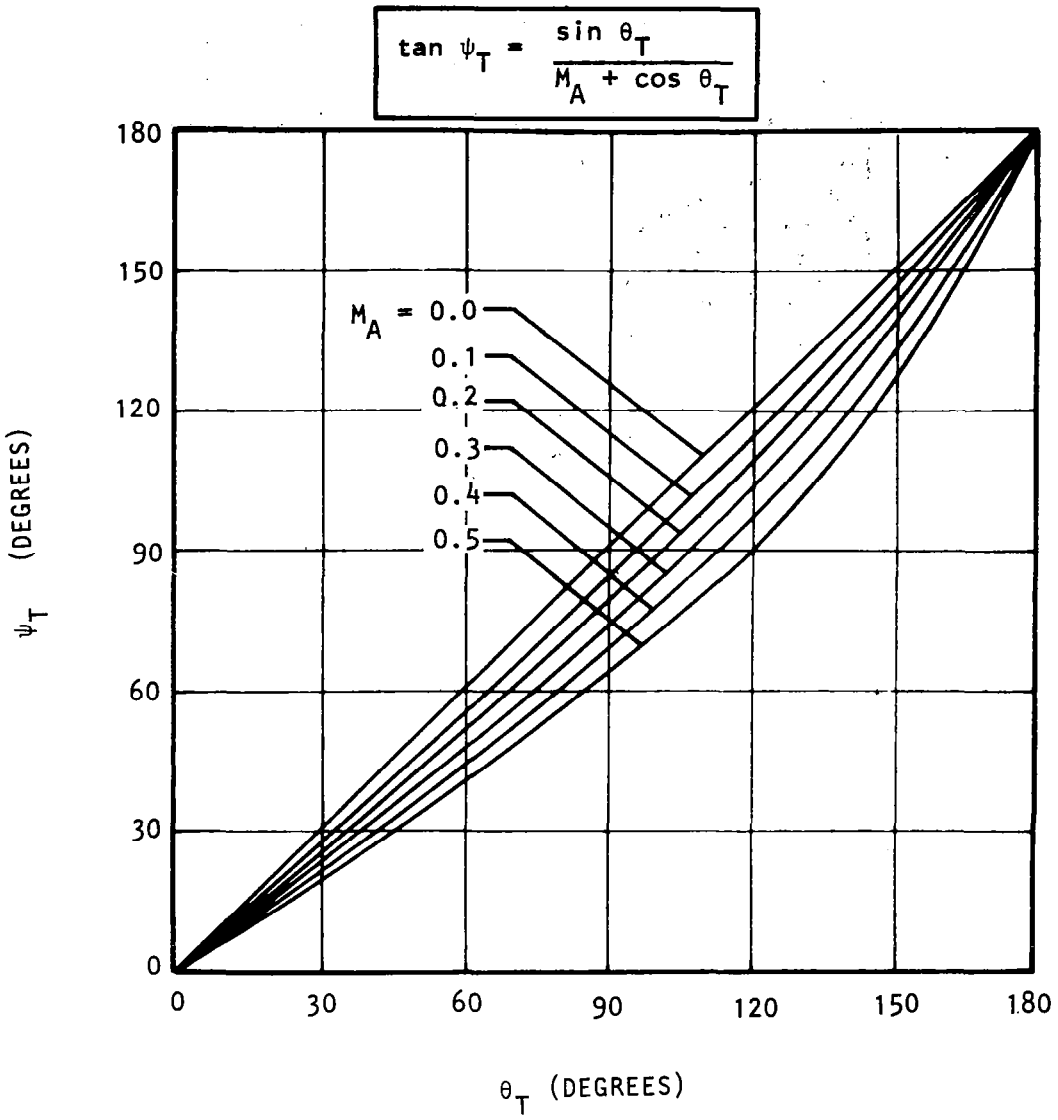

Chart 19 Variation of angle ψ_T at reception-time with angle θ_T at emission-time for various flight Mach numbers M_A.

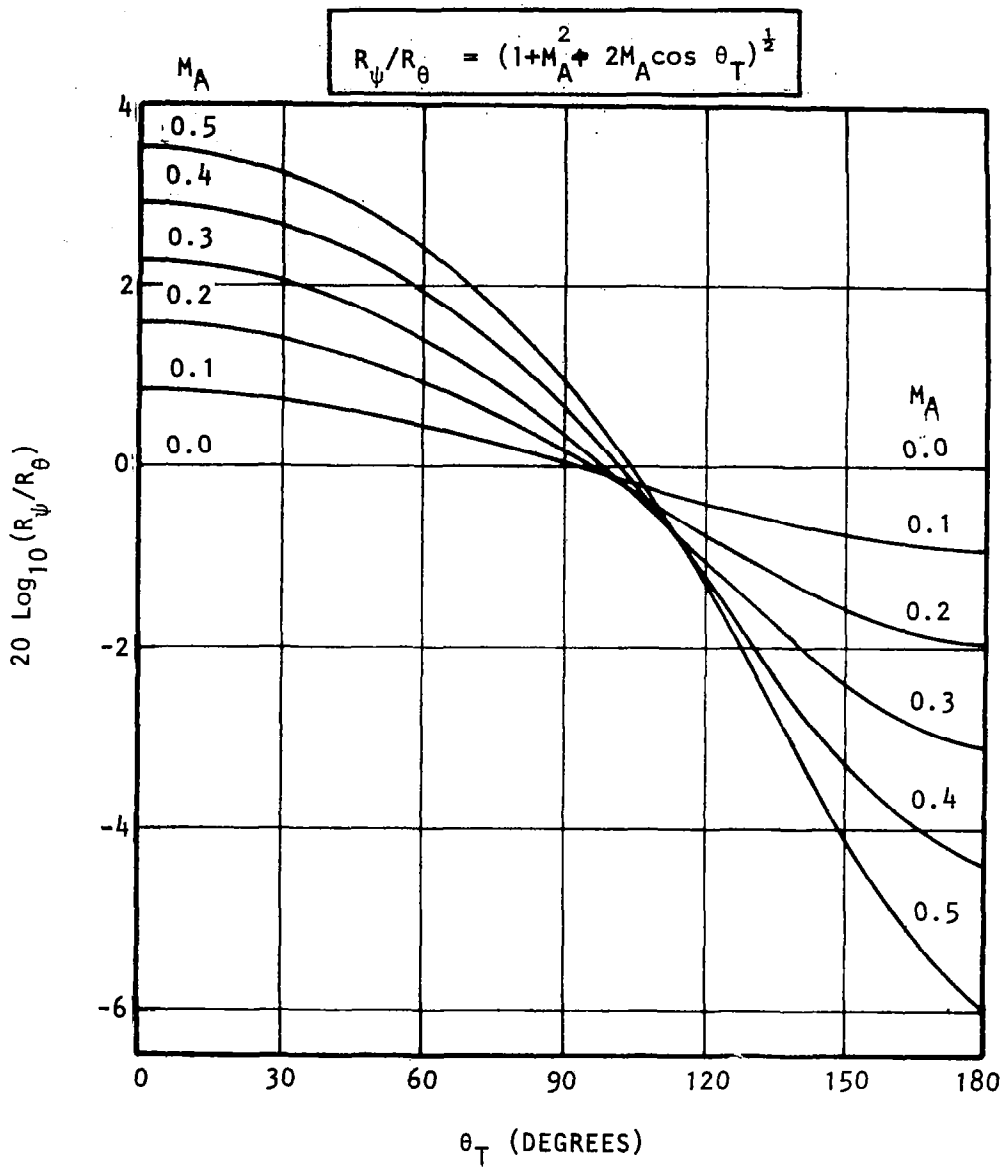

Chart 20 Variation of reception-time-to-emission-time distance ratio R_ψ/R_θ with emission angle θ_T at various flight Mach numbers M_A.

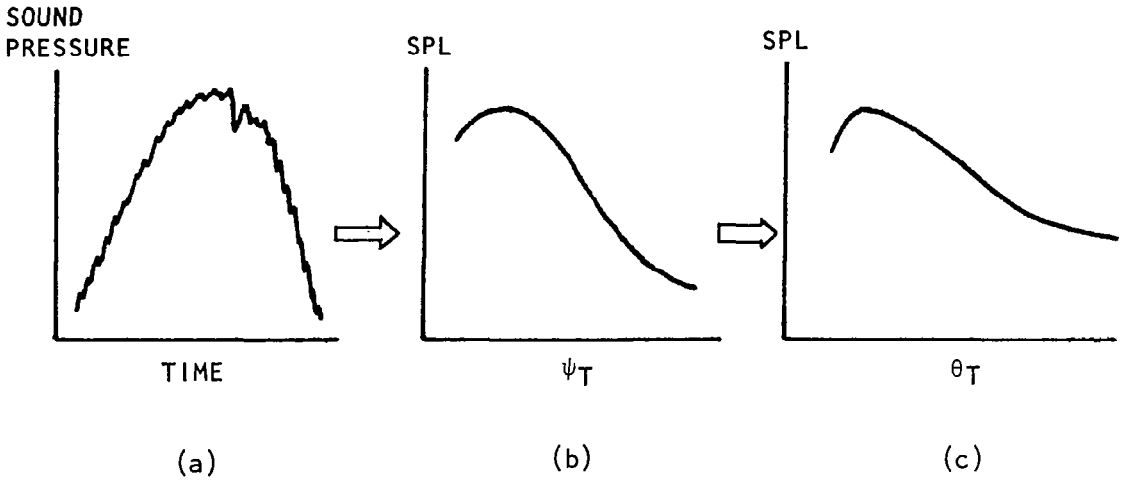

Figure 6.5 Aircraft flyover noise data processing.

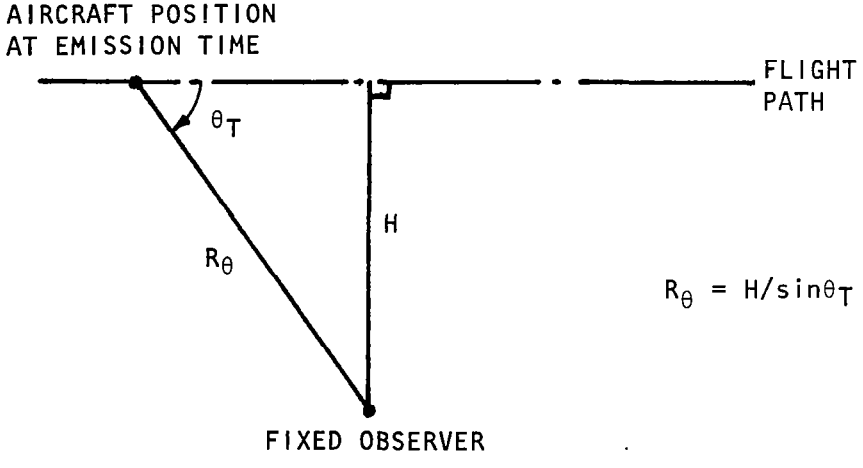

Figure 6.6 Aircraft flight case showing distances R_θ and H.

This distance correction in decibels is shown in Chart 21, where its variation with emission angle θ_T is calculated for various values of ratio R/H.

6.2 COMPUTATIONAL PROCEDURE

The purpose of this subsection is to describe the computer program developed to transform or convert noise data obtained in a free-jet flight simulation experiment to the corresponding wind-tunnel situation, and finally to the corresponding flight condition.

6.2.1 General Structure

The overall structure of the computational procedure is shown in the form of a flow chart in Figure 6.7. In essence, there are three parts to the transformation procedure as follows.

(1) In the first part, the program takes the measured free-jet data as input, and computes the corresponding wind-tunnel data. The free-jet data are specified at measurement locations (R_m,θ_m) relative to the nozzle exit, and the wind-tunnel data are computed at desired emission angles θ_T and desired emission (or prediction) radius R *relative to the source position*. The transformation of $SPL_{FJ}(R_m,\theta_m)$ to $SPL_{WT}(R,\theta_T)$ requires angle, amplitude, distance, and source location corrections. In addition, an interpolation of free-jet data is required to predict wind-tunnel data at specified values of θ_T.

(2) In the second part, a Doppler frequency shift is applied to the wind-tunnel spectra to obtain the flight spectra $SPL_F(R,\theta_T)$. In order to express the flight SPL's in conventional one-third octave bands (i.e. for conventional 1/3-octave band center frequencies), this part of the transformation also requires an interpolation.

(3) In the final part, the Doppler shifted wind-tunnel spectra are transformed to the flight condition. It is desirable to express the flight data at specified values of emission angles θ_{Tn} and prediction distance R_n, where the subscript "n" signifies that these parameters are *referenced to the nozzle exit*. Thus, the transformation of $SPL_F(R,\theta_T)$ obtained in step (2) above to $SPL_F(R_n,\theta_{Tn})$ requires certain angle and distance correction (as discussed in Appendix 6A), and this is followed by an interpolation to obtain flight data at specified values of θ_{Tn}.

6.2.2 Transformation Options

The computer program has been designed to provide three main options and two source location options. These options are defined below, and the user can select and specify any of these options.

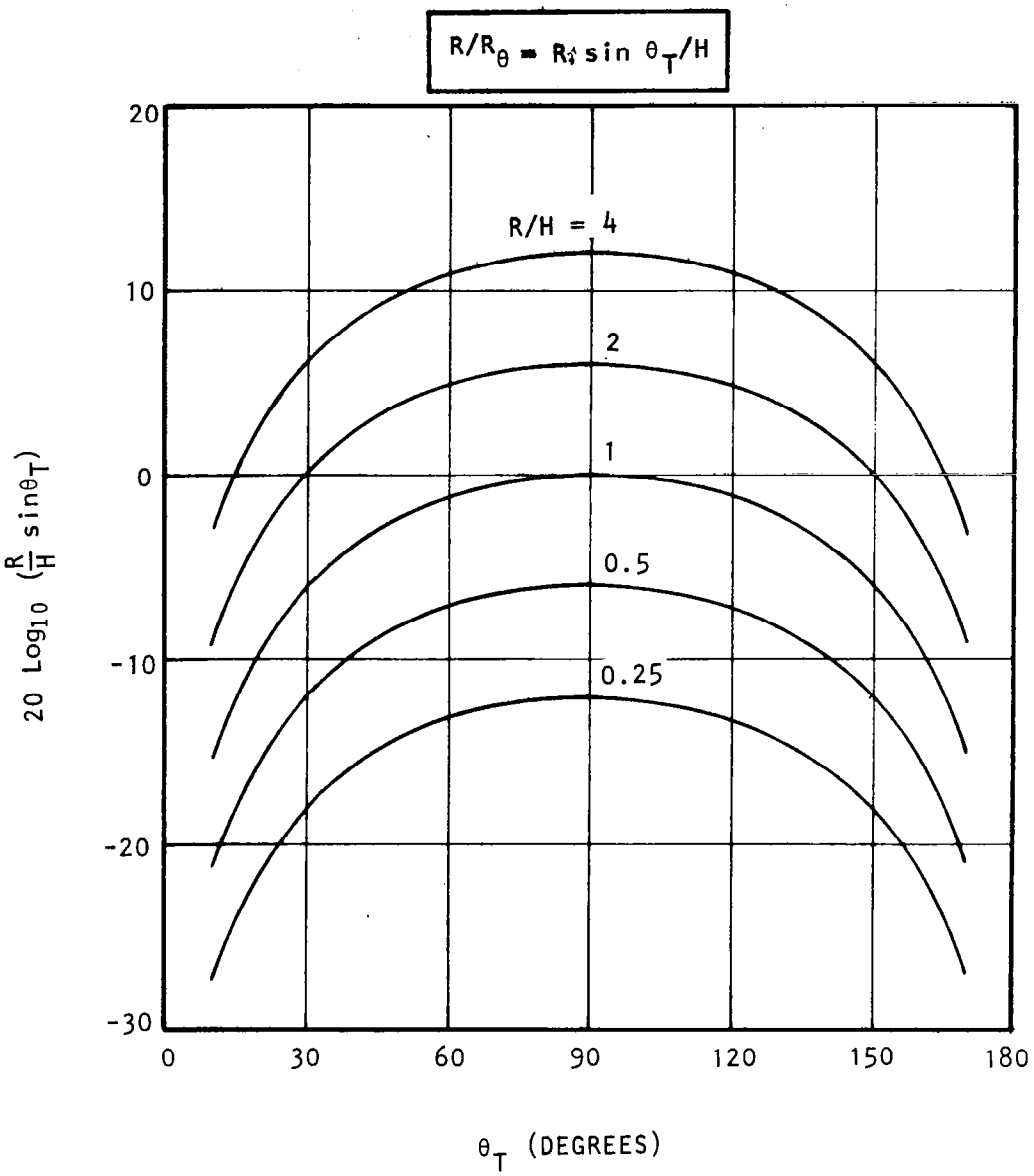

Chart 21 Variation of distance correction (for aircraft flyover noise measurements) with emission angle θ_T at various values of R/H.

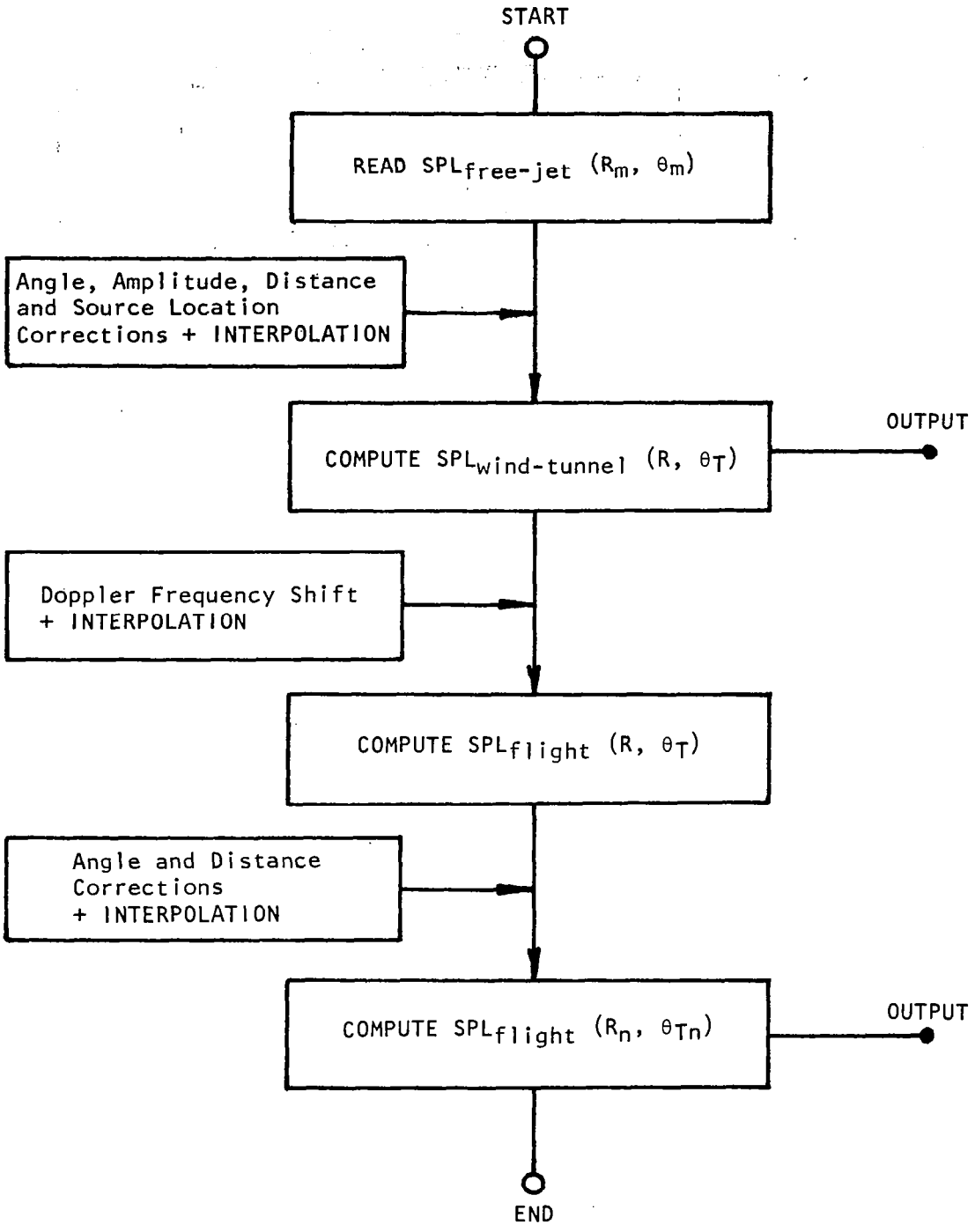

Figure 6.7 General structure of computational procedure.

Main Options (OPNO):

OPNO = 1:

$$SPL_{FJ}(R_m,\theta_m) \rightarrow SPL_{WT}(R,\theta_T)$$

Print $SPL_{WT}(R,\theta_T)$

OPNO = 2:

$$SPL_{FJ}(R_m,\theta_m) \rightarrow SPL_{WT}(R,\theta_T) \rightarrow SPL_F(R_n,\theta_{Tn})$$

Print $SPL_F(R_n,\theta_{Tn})$

OPNO = 3:

$$SPL_{FJ}(R_m,\theta_m) \rightarrow SPL_{WT}(R,\theta_T) \rightarrow SPL_F(R_n,\theta_{Tn})$$

Print $SPL_{WT}(R,\theta_T)$ and $SPL_F(R_n,\theta_{Tn})$

Source Location Options (SLOP):

SLOP = 0: Transformation *without* source location corrections.

SLOP = 1: Transformation *with* source location corrections.

In practice it is recommended that the transformation of jet mixing data be conducted with SLOP = 1. For cases where the sound is emitted (effectively) in the vicinity of the nozzle exit, the data can be transformed with SLOP = 0.

6.2.3 Computer Program Details

The steps used in the computer program are outlined in a logical order below. The equations used in various steps are identified by numbers placed alongside the steps. The corresponding equations are listed in the second half of this subsection. This information is provided for the sake of completeness, and unless one wants to modify the program, one can proceed straight to Section 6.2.4.

Program Steps

Read	TITLE, OPNO, SLOP	
Read	number of third-octave frequency bands (NFREQ), number of measurement angles θ_m (NTHEM), and number of emission angles θ_T (NTHET)	
Read	d, r_T	
Read	R_m	
Read	measurement angles θ_m (THEM)	
Read	third-octave center frequencies f (F)	
Read	R	
Read	R_n (only if OPNO = 2 or 3)	
Read	emission angles θ_T (THET)	
Calculate	$\bar{R}$, $\bar{R}_m$, $\bar{R}_n$	(6-25)
Start	main program loop	
Read	V_J, V_T, T_o, T_T	
Calculate	a_o, a_T, a_o/a_T, ρ_T/ρ_o	
Calculate	V_J/a_o, V_T/a_o, V_T/a_T	
Calculate	$(\theta_T)_{max}$	(6-26)
Write	title page including input parameters and initial computed parameters	
Read	free-jet measured data $SPL_{FJ}(R_m;\ \theta_m,\ f)$	
Prepare	a new page for printing $SPL_{WT}(R;\ \theta_T,\ f)$	

DO	for all f	
Calculate	S	(6-27)
DO	for all θ_T	
Calculate	$\cot\psi_T$	(6-28)
Calculate	$\cos\theta_o$, $\sin\theta_o$, $\cot\theta_o$	(6-29)
Calculate	C_F in dB	(6-30)
Calculate	D_m, S_m, x_s'/d	(6-31)
Calculate	$\overline{x_s^T}$	(6-32)
Calculate	$\bar{x}_\ell$, $\bar{\ell}$	(6-33)
Calculate	$\bar{R}_{ro}$, $\bar{R}_{ra}$	(6-34)
Calculate	θ_{ml}	(6-35)
Calculate	C_R in dB	(6-36)
Calculate	SPL_{FJ} (θ_{ml}) by interpolation	(6-37)
Calculate	$SPL_{WT}(\theta_T)$	(6-38)
Write	f, $SPL_{WT}(\theta_T,f)$ for all θ_T	
Calculate	$OASPL_{WT}$ for all θ_T	
Write	$OASPL_{WT}$ for all θ_T	
DO	for all θ_T	
Calculate	D_T	(6-39)
Calculate	$\log_{10}(f_f)$ for all f	(6-40)
DO	for all f	
Calculate	$\log_{10}(f)$	
Calculate	$SPL_F(f_c)$ (where $f_c \equiv f$) by interpolation	(6-41)

Prepare	a new page for printing $SPL_F(R_n;\theta_{Tn}, f)$	
DO	for all f	
Calculate	S	(6-42)
DO	for all θ_T	
Calculate	D_m, S_m, x_s'/d, $\overline{x_s'}$	(6-43)
Calculate	$\overline{x_s'}/\bar{R}_n$	
Calculate	θ_{Tn} corresponding to θ_T	(6-44)†
Calculate	$\overline{SO}^2$	(6-45)†
Calculate	C_{R_n} in dB	(6-46)†
Calculate	$SPL_F(R_n,\theta_{Tn})$	(6-47)†
Arrange	θ_{Tn} values in monotonically increasing order	
DO	for all θ_T	
Calculate	SPL_F (θ_{Tn}) (where $\theta_{Tn} \equiv \theta_T$) by interpolation	(6-48)
Write	f, $SPL_F(\theta_{Tn}, f)$ for all θ_{Tn} $(\equiv\theta_T)$	
Calculate	$OASPL_F$ for all $\theta_{Tn}(\equiv\theta_T)$	
Write	$OASPL_F$ for all $\theta_{Tn}(\equiv\theta_T)$	
GO TO	the beginning of main program loop	

†*See Appendix 6A.*

Equations Used

$$\bar{R} = R/r_T, \ \bar{R}_m = R_m/r_T, \ \bar{R}_n = R_n/r_T \tag{6-25}$$

$$(\theta_T)_{max} = \cos^{-1} \{-a_T/(a_o + V_T)\} \tag{6-26}$$

$$S = fd/V_J \tag{6-27}$$

$$\cot\psi_T = \{\cos\theta_T + (V_T/a_T)\}/\sin\theta_T \tag{6-28}$$

$$\left.\begin{aligned} \cos\theta_o &= \frac{(a_o/a_T)\ \cos\theta_T}{1 + (V_T/a_T)\ \cos\theta_T} \\ \sin\theta_o &= (1 - \cos^2\theta_o)^{\frac{1}{2}} \\ \cot\theta_o &= \cos\theta_o/\sin\theta_o \end{aligned}\right\} \tag{6-29}$$

$$C_F(dB) = 10 \log_{10} \frac{\rho_T/\rho_o}{\{1 + (V_T/a_T)\cos\theta_T\}^4} \tag{6-30}$$

$$\left.\begin{aligned} D_m &= \{(1 - M_c\cos\theta_T)^2 + \alpha^2 M_c{}^2\}^{\frac{1}{2}} \\ &\quad \text{where} \quad M_c = 0.67\ V_J/a_o, \ \alpha = 0.3 \\ S_m &= S\ D_m \\ x_s'/d &= (0.057\ S_m + 0.021\ S_m{}^2)^{-\frac{1}{2}} \end{aligned}\right\} \tag{6-31}$$

$$\overline{x_s'} = (x_s'/d)\ (d/r_T) \tag{6-32}$$

$$\left.\begin{aligned} \overline{x_\ell} &= \overline{x_s'} + \cot\psi_T \\ \bar{\ell} &= \overline{x_\ell} - \cot\theta_o \end{aligned}\right\} \tag{6-33}$$

$$\left.\begin{aligned}
\bar{R}_{ro} &= (\bar{R}_m^2 - \bar{\ell}^2 \sin^2\theta_o)^{\frac{1}{2}} - \bar{\ell} \cos\theta_o \\
\bar{R}_{ra} &= \bar{R}_{ro} + \left(\frac{1}{\sin\theta_o}\right)\left[\left\{\frac{\sin\theta_o}{\{(a_o/a_T)^2 \ (1 - M_T\cos\theta_o)^2 - \cos^2\theta_o\}^{\frac{1}{2}}}\right\}^3 \left(\frac{a_o}{a_T}\right)^2 - 1\right]
\end{aligned}\right\} \quad (6\text{-}34)$$

$$\theta_{ml} = \cos^{-1}\left[\frac{(\bar{R}_m^2 + \bar{\ell}^2 - \bar{R}_{ro}^2)}{2\,\bar{\ell}\,\bar{R}_m}\right] \quad (6\text{-}35)$$

$$C_R(dB) = 10 \log_{10} (\bar{R}_{ro}\ \bar{R}_{ra}/\bar{R}^2) \quad (6\text{-}36)$$

$$\left.\begin{aligned}
SPL_{FJ}(\theta_{ml}) &= SPL_{FJ}(\theta_{mi}) + h\left[SPL_{FJ}(\theta_{mi+1}) - SPL_{FJ}(\theta_{mi})\right] \\
&\text{where} \quad \theta_{mi} \le \theta_{ml} \le \theta_{mi+1} \\
&\text{and} \quad h = \left(\frac{\theta_{ml} - \theta_{mi}}{\theta_{mi+1} - \theta_{mi}}\right)
\end{aligned}\right\} \quad (6\text{-}37)$$

$$SPL_{WT}(\theta_T) = SPL_{FJ}(\theta_{ml}) + C_F(dB) + C_R(dB) \quad (6\text{-}38)$$

$$D_T = (1 + M_T\cos\theta_T)^{-1} \quad (6\text{-}39)$$

$$\log_{10} (f_f) = \log_{10} (f\ D_T) \quad (6\text{-}40)$$

$$\left.\begin{aligned}
SPL_F(f_c) &= SPL_{WT}(f_{fi}) + h\left[SPL_{WT}(f_{fi+1}) - SPL_{WT}(f_{fi})\right] \\
&\text{where} \quad f_{fi} \le f_c \le f_{fi+1} \\
&\text{and} \quad h = \left(\frac{\log f_c - \log f_{fi}}{\log f_{fi+1} - \log f_{fi}}\right)
\end{aligned}\right\} \quad (6\text{-}41)$$

$$S = fd/V_J \quad (6\text{-}42)$$

$$\left.\begin{aligned} D_m &= \{(1 - M_c\cos\theta_T)^2 + \alpha^2 M_c^2\}^{\frac{1}{2}} \\ &\quad \text{where} \quad M_c = 0.67\ V_J/a_o,\ \alpha = 0.3 \\ S_m &= S\ D_m \\ x_s'/d &= (0.057\ S_m + 0.021\ S_m^2)^{-\frac{1}{2}} \end{aligned}\right\} \tag{6-43}$$

$$\left.\begin{aligned} &\text{(a)} \quad \text{For} \quad \overline{x_s'}/\bar{R}_n < 1, \\ &\qquad \theta_{Tn} = \theta_T - \sin^{-1}\ (\overline{x_s'}\ \sin\theta_T/\bar{R}_n) \quad \text{for all } \theta_T \\ &\text{(b)} \quad \text{For} \quad \overline{x_s'}/\bar{R}_n = 1, \quad \theta_T \leq 90^\circ \quad \text{is not allowed, and} \\ &\qquad \theta_{Tn} = \theta_T - (180^\circ - \theta_T) \quad \text{for} \quad \theta_T > 90^\circ \\ &\text{(c)} \quad \text{For} \quad \overline{x_s'}/\bar{R}_n > 1, \quad \theta_T \leq \{180^\circ - \sin^{-1}\ (\bar{R}_n/\overline{x_s'})\} \quad \text{is not allowed, and} \\ &\qquad \begin{cases} \theta_{Tn2} = \theta_T - \sin^{-1}\ (\overline{x_s'}\ \sin\theta_T/\bar{R}_n) \\ \theta_{Tn1} = 2\theta_T - 180^\circ - \theta_{Tn2} \end{cases} \\ &\qquad \text{for} \quad \theta_T > \{180^\circ - \sin^{-1}\ (\overline{R_n}/\overline{x_s'})\}. \ \text{That is, there are two} \\ &\qquad \text{values of } \theta_{Tn} \text{ corresponding to one value of } \theta_T. \end{aligned}\right\} \tag{6-44}^\dagger$$

$$\overline{SO}^2 = \bar{R}_n^2 + \overline{x_s'}^2 + 2\bar{R}_n\ \overline{x_s'}\ \cos\theta_{Tn} \tag{6-45}^\dagger$$

$$C_{R_n}\ (\text{dB}) = 10\ \log_{10}\ (\bar{R}^2/\overline{SO}^2) \tag{6-46}^\dagger$$

$$SPL_F(R_n,\theta_{Tn}) = SPL_F(R,\theta_T) + C_{R_n}\ (\text{dB}) \tag{6-47}^\dagger$$

---

†*See Appendix 6A.*

$$
\left.
\begin{aligned}
& SPL_F(\theta_{Tn}) = SPL_F(\theta_{Tni}) + h\left[SPL_F(\theta_{Tni+1}) - SPL_F(\theta_{Tni})\right] \\
& \quad \text{where} \quad \theta_{Tni} \le \theta_{Tn} \le \theta_{Tni+1} \\
& \quad \text{and} \quad h = \left(\frac{\theta_{Tn} - \theta_{Tni}}{\theta_{Tni+1} - \theta_{Tni}}\right)
\end{aligned}
\right\} \qquad (6\text{-}48)
$$

Program Listing

A complete listing of the computer program is given in Figure 6.8. Several comment statements have been included to facilitate easy identification of various parts of the transformation procedure.

6.2.4 Input Requirements

The input parameters and their format, required to run the data transformation program, are described below.

TITLE
12A6

TITLE - Any title desired by the user to appear on output; two lines maximum.

OPNO	SLOP
I2	I2

OPNO - Main option number.
SLOP - Source location option number.

NFREQ	NTHEM	NTHET
I2	I2	I2

NFREQ - Number of one-third octave bands for which measured free-jet data are available; the *same number* of frequencies is used to compute the wind-tunnel data or the flight data (NFREQ $\le$ 36).

NTHEM - Number of measurement angles (θ_m) at which free-jet data are available (NTHEM $\le$ 18).

NTHET - Number of emission angles (θ_T) at which the wind-tunnel or flight data are to be computed (NTHET $\le$ 18).

DJ	RT
F10.2	F10.2

DJ - Model-jet nozzle diameter (d) in centimeters.
RT - Free-jet nozzle radius (r_T) in meters.

RM
F10.2

RM - Microphone or measurement arc radius (R_m) in meters at which free-jet data are available.

THEM(I), I = 1, NTHEM

F10.2	F10.2	F10.2					F10.2

THEM - Microphone or measurement angles (θ_m) in degrees at which free-jet data are available ($\theta_m = 0°$ or 180° not allowed).

F(J), J = 1, NFREQ

F10.2	F10.2	F10.2					F10.2

F - Third-octave center frequencies (f) in Hz for which measured free-jet data are available; the wind-tunnel or the flight data are computed at the *same set of center frequencies*.

R
F10.2

R - Emission or prediction distance (R) in meters, *relative to source position*, at which the *wind-tunnel* data are to be computed.

RN
F10.2

RN - Emission or prediction distance (R_n) in meters, *relative to nozzle exit*, at which the *flight* data are to be computed. This parameter is not required if OPNO=1 is selected.

THET(K), K = 1, NTHET

F10.2	F10.2	F10.2					F10.2

THET - Emission angles (θ_T) in degrees at which the wind-tunnel or the flight data are to be computed. It should be noted that only one set of emission angles is input to the program. That is, the wind-tunnel data will be computed at the specified values of θ_T *relative to source position*, and the flight data will be computed automatically at the *same values* of θ_{Tn} *relative to nozzle exit*. ($\theta_T = 0°$ not allowed.)

This completes the basic input requirements. The following input should be provided for *every* test point:

VJ	VT	TO	TT
F10.2	F10.2	F10.2	F10.2

VJ - Model-jet exit velocity (V_J) in meters per second. ($V_J = 0$ not allowed.)

VT - Free-jet or tunnel velocity (V_T) in meters per second.

TO - Temperature (T_O) in °C of ambient medium surrounding the the free jet.

TT - Free-jet or tunnel flow temperature (T_T) in °C.

{SPLFJ(I,J), J = 1, NFREQ}, I = 1, NTHEM

F6.1	F6.1	F6.1									F6.1

SPLFJ - Third-octave SPL data in dB acquired in the free-jet simulation experiment; three lines maximum for each θ_m.

At the end of the input for the *last* test point, put a card with a negative number (e.g. -5.0) in columns 1 through 10. This will end the program execution.

6.2.5 Sample Case

The input data for a sample case with OPNO = 3 and SLOP = 1 are shown in Figure 6.9, and the corresponding output is presented in Figure 6.10 (three pages). The input data, when examined in conjunction with the description presented in Section 6.2.4, is self-explanatory.

The first page of the output shows the title selected by the user, and an indication of whether the source location corrections have been applied or not is also given. Following this, the output consists of a list of various input parameters and several computed parameters. At the bottom of this first page, several failure codes and the corresponding explanations are listed. These failure codes form a very important part of the computational procedure, and they have been provided specifically to prevent premature termination of the program execution. In the absence of these failure codes, the program execution would terminate whenever the frequency range or the angular range of the data to be interpolated (in one or more of the three interpolation steps) does not cover the frequency or angle at which the interpolation is to be conducted. With this failure codes provision, however, the program indicates the nature of the problem (whenever it occurs), and proceeds to the next frequency or angle until a valid computation of wind-tunnel SPL or flight SPL is obtained. In this manner, the program scans through all frequencies and all angles and provides a matrix of transformed data, with correct answers where possible and failure codes where a problem is encountered.

The second page of the output gives the third-octave SPL spectra and OASPL's for data transformed to ideal-wind-tunnel conditions. The printout on this page is suppressed if OPNO = 2 is selected.

Finally, if OPNO = 2 or 3 is specified in the input data, the program gives a listing (on a separate page) of the third-octave SPL spectra and OASPL's corresponding to the flight condition.

```
C     ***************************************************************
C     *                                                             *
C     *   THIS COMPUTER PROGRAM TRANSFORMS NOISE DATA MEASURED IN A *
C     *   FREE-JET FLIGHT SIMULATION FACILITY TO THE IDEAL WIND-TUNNEL *
C     *   SITUATION, AND FINALLY, TO THE FLIGHT SITUATION.          *
C     *                                                             *
C     *   SPLFJ = MEASURED SPL DATA FROM FREE-JET FLIGHT            *
C     *           SIMULATION EXPERIMENT (INPUT)                     *
C     *   SPLWT = COMPUTED SPL DATA FOR IDEAL WIND-TUNNEL CASE (OUTPUT)*
C     *   SPLF  = COMPUTED SPL DATA FOR FLIGHT CASE (OUTPUT)        *
C     *                                                             *
C     *   PROGRAM OPTIONS--                                         *
C     *                                                             *
C     *        OPNO = OPTION NUMBER                                 *
C     *             OPNO = 1  TRANSFORM SPLFJ TO SPLWT,             *
C     *                       AND PRINT SPLWT                       *
C     *             OPNO = 2  TRANSFORM SPLFJ TO SPLWT TO SPLF,     *
C     *                       AND PRINT SPLF                        *
C     *             OPNO = 3  TRANSFORM SPLFJ TO SPLWT TO SPLF,     *
C     *                       AND PRINT SPLWT AND SPLF              *
C     *        SLOP = SOURCE LOCATION OPTION                        *
C     *             SLOP = 0  TRANSFORMATION WITHOUT SOURCE         *
C     *                       LOCATION CORRECTIONS                  *
C     *             SLOP = 1  TRANSFORMATION WITH SOURCE            *
C     *                       LOCATION CORRECTIONS                  *
C     *                                                             *
C     ***************************************************************
C
      DIMENSION TITLE(24),THEM(18),F(36),THET(18),SPLFJ(18,36),
     2 TTN(18),SPLF(18,36),SPLWT(18,36),SUM(18),THETN(18),SPL(18,36)
C
      REAL MT,MC,LBAR,LOGFF(36),LF
      INTEGER OPNO,SLOP
C
C *****  READ INPUT PARAMETERS  *****
C
      READ(5,100) TITLE
      READ(5,102) OPNO,SLOP
      READ(5,102) NFREQ,NTHEM,NTHET
      READ(5,104) DJ,RT
      READ(5,104) RM
      READ(5,104) (THEM(I),I=1,NTHEM)
      READ(5,104) (F(J),J=1,NFREQ)
      READ(5,104) R
      IF(OPNO.NE.1) READ(5,104) RN
      READ(5,104) (THET(K),K=1,NTHET)
C
C *****  INPUT FORMAT STATEMENTS  *****
C
  100 FORMAT(12A6)
  102 FORMAT(3I2)
  104 FORMAT(8F10.2)
  106 FORMAT(12F6.1)
C
```

Figure 6.8 Computer program listing.

```
      D=DJ/100.
      RBAR=R/RT
      RMBAR=RM/RT
      IF(OPNO.NE.1) RNBAR=RN/RT
C
C *****  START MAIN PROGRAM LOOP -- READ MODEL-JET  *****
C *****  AND FREE-JET OPERATING CONDITIONS          *****
C
 1000 READ(5,104) VJ,VT,TO,TT
C
      IF(VJ.LE.0.0) GO TO 900
C
      AO=20.04*SQRT(TO+273.)
      AT=20.04*SQRT(TT+273.)
      AOAT=AO/AT
      RHOR=(TO+273.)/(TT+273.)
      VJAO=VJ/AO
      MT=VT/AO
      VTAT=VT/AT
      THETMX=57.29577951*ACOS(-AT/(AO+VT))
C
C *****  WRITE TITLE PAGE INCLUDING INPUT PARAMETERS  *****
C *****  AND INITIAL COMPUTED PARAMETERS              *****
C
      WRITE(6,200) TITLE
      IF(SLOP.EQ.0) WRITE(6,202)
      IF(SLOP.EQ.1) WRITE(6,204)
      WRITE(6,205) DJ,RT
      WRITE(6,206) RM,R
      IF(OPNO.NE.1) WRITE(6,208) RN
      WRITE(6,209) VJ,VT
      WRITE(6,210) TO,TT
      WRITE(6,212) (THEM(I),I=1,NTHEM)
      WRITE(6,213) AO,AT,RHOR
      WRITE(6,214) VJAO,MT
      WRITE(6,216)
      WRITE(6,217)
C
C *****  READ FREE-JET SPL DATA  *****
C
      DO 10 I=1,NTHEM
      READ(5,106) (SPLFJ(I,J),J=1,NFREQ)
   10 CONTINUE
C
      IF(OPNO.EQ.2) GO TO 12
C
      WRITE(6,200) TITLE
      WRITE(6,218) (THET(K),K=1,NTHET)
      WRITE(6,220)
C
C *****  INITIALIZE WORKING MATRIX FOR COMPUTATION  *****
C *****  OF WIND-TUNNEL OASPL                       *****
C
      DO 50 K=1,NTHET
```

Figure 6.8 Continued.

```
   50 SUM(K)=0.0
C
C *****  TRANSFORMATION TO IDEAL WIND-TUNNEL CASE  *****
C
   12 DO 60 J=1,NFREQ
      S=F(J)*D/VJ
      DO 80 K=1,NTHET
      IF(THET(K).LE.THETMX) GO TO 31
      SPLWT(K,J)=0.5
      GO TO 80
   31 CTHET=COS(THET(K)/57.29577951)
      STHET=SIN(THET(K)/57.29577951)
      COTPST=(CTHET+VTAT)/STHET
      COSTH0=(A0AT*CTHET)/(1.0+VTAT*CTHET)
      SINTH0=SQRT(1.0-COSTH0*COSTH0)
      COTTH0=COSTH0/SINTH0
      CF=-40.0*ALOG10(1.0+VTAT*CTHET)+10.0*ALOG10(RHOR)
      ALP=0.3
      MC=0.67*VJA0
      DM=SQRT((1.0-MC*CTHET)**2+ALP*ALP*MC*MC)
      SM=S*DM
      XSPD=0.0
      IF(SLOP.EQ.1) XSPD=1.0/SQRT(0.057*SM+0.021*SM*SM)
      XSPBAR=XSPD*(D/RT)
      XLBAR=XSPBAR+COTPST
      LBAR=XLBAR-COTTH0
      RROBAR=SQRT(RMBAR*RMBAR-LBAR*LBAR*SINTH0*SINTH0)-LBAR*COSTH0
      RRABAR=RROBAR+(1.0/SINTH0)*((((SINTH0/SQRT(((1.0-MT*COSTH0)**2)
     2 *A0AT*A0AT-COSTH0*COSTH0))**3)*A0AT*A0AT)-1.0)
      THEMI=57.29577951*ACOS((RMBAR*RMBAR+LBAR*LBAR-RROBAR*RROBAR)/
     2 (2.0*LBAR*RMBAR))
      CR=10.*ALOG10(RROBAR*RRABAR/(RBAR*RBAR))
      IF(THEMI.GE.THEM(1).AND.THEMI.LE.THEM(NTHEM)) GO TO 32
      SPLWT(K,J)=0.1
      GO TO 80
   32 NTM=NTHEM-1
      DO 34 I=1,NTM
      IF(THEMI.LE.THEM(I+1)) GO TO 36
      GO TO 34
   36 SPLWT(K,J)=SPLFJ(I,J)+((THEMI-THEM(I))/(THEM(I+1)-THEM(I)))*
     2 (SPLFJ(I+1,J)-SPLFJ(I,J))
      GO TO 38
   34 CONTINUE
   38 CONTINUE
      SPLWT(K,J)=SPLWT(K,J)+CF+CR
      IF(SPLWT(K,J).LT.1.0) SPLWT(K,J)=1.0
      IF(OPNO.NE.2) SUM(K)=SUM(K)+10.**(SPLWT(K,J)/10.)
   80 CONTINUE
      IF(OPNO.NE.2) WRITE(6,222) F(J),(SPLWT(K,J),K=1,NTHET)
   60 CONTINUE
      IF(OPNO.EQ.2) GO TO 92
      DO 90 K=1,NTHET
   90 IF(SUM(K).GT.0.0) SUM(K)=10.*ALOG10(SUM(K))
      WRITE(6,224) (SUM(K),K=1,NTHET)
```

Figure 6.8 Continued.

```
   92 CONTINUE
C
      IF(OPNO.EQ.1) GO TO 1000
C
C *****  APPLICATION OF DOPPLER FREQUENCY SHIFT  *****
C *****  TO WIND-TUNNEL DATA                     *****
C
      DO 160 K=1,NTHET
      IF(THET(K).LE.THETMX) GO TO 161
      DO 163 J=1,NFREQ
  163 SPLF(K,J)=0.5
      GO TO 160
  161 DT=1.0/(1.0+MT*COS(THET(K)/57.29577951))
      DO 180 JJ=1,NFREQ
      LOGFF(JJ)=ALOG10(F(JJ)*DT)
  180 CONTINUE
      DO 182 J=1,NFREQ
      LF=ALOG10(F(J))
      IF(LF.GE.LOGFF(1).AND.LF.LE.LOGFF(NFREQ)) GO TO 150
      SPLF(K,J)=0.2
      GO TO 182
  150 NF=NFREQ-1
      DO 156 JJ=1,NF
      IF(LF.LE.LOGFF(JJ+1)) GO TO 154
      GO TO 156
  154 IF(SPLWT(K,JJ).GE.1.0.AND.SPLWT(K,JJ+1).GE.1.0) GO TO 155
      SPLF(K,J)=0.3
      GO TO 182
  155 SPLF(K,J)=SPLWT(K,JJ)+((LF-LOGFF(JJ))/(LOGFF(JJ+1)-LOGFF(JJ)))*
     2 (SPLWT(K,JJ+1)-SPLWT(K,JJ))
      GO TO 182
  156 CONTINUE
  182 CONTINUE
  160 CONTINUE
C
      WRITE(6,200) TITLE
      WRITE(6,230) (THET(K),K=1,NTHET)
      WRITE(6,220)
C
C *****  RE-INITIALIZE WORKING MATRIX FOR COMPUTATION OF  *****
C *****  FLIGHT  OASPL                                    *****
C
      DO 258 K=1,NTHET
  258 SUM(K)=0.0
C
C *****  TRANSFORMATION TO FLIGHT CASE  *****
C
      DO 260 J=1,NFREQ
      S=F(J)*D/VJ
C
C ***  COMPUTATION OF NOZZLE EMISSION ANGLES CORRESPONDING TO  ***
C ***  SOURCE EMISSION ANGLES                                  ***
C
      NTT=0
```

Figure 6.8 Continued.

```
      DO 280 K=1,NTHET
      DM=SQRT((1.0-MC*COS(THET(K)/57.29577951))**2+ALP*ALP*MC*MC)
      SM=S*DM
      XSPD=0.0
      IF(SLOP.EQ.1) XSPD=1.0/SQRT(0.057*SM+0.021*SM*SM)
      XSPBAR=XSPD*D/RT
      CHECK=XSPBAR/RNBAR
      N2=0
      IF(CHECK.GE.1.0) GO TO 272
      NTT=NTT+1
      TTN(NTT)=THET(K)-57.29577951*ASIN(CHECK*SIN(THET(K)/
     2 57.29577951))
      GO TO 278
  272 IF(CHECK.GT.1.0) GO TO 274
      IF(THET(K).LE.90.0) GO TO 280
      NTT=NTT+1
      TTN(NTT)=THET(K)-(180.-THET(K))
      GO TO 278
  274 CK2=180.-57.29577951*ASIN(RNBAR/XSPBAR)
      IF(THET(K).LE.CK2) GO TO 280
      NTT=NTT+1
      TTN(NTT)=THET(K)-57.29577951*ASIN(CHECK*SIN(THET(K)/
     2 57.29577951))
      NTT=NTT+1
      TTN(NTT)=2.0*THET(K)-180.-TTN(NTT-1)
      N2=1
  278 CONTINUE
      SOBR21=RNBAR*RNBAR+XSPBAR*XSPBAR+2.0*RNBAR*XSPBAR*COS(TTN(NTT)/
     2 57.29577951)
      IF(N2.EQ.1) SOBR22=RNBAR*RNBAR+XSPBAR*XSPBAR+2.0*RNBAR*XSPBAR*
     2 COS(TTN(NTT-1)/57.29577951)
      CRN1=10.*ALOG10(RBAR*RBAR/SOBR21)
      IF(N2.EQ.1) CRN2=10.*ALOG10(RBAR*RBAR/SOBR22)
      SPL(NTT,J)=SPLF(K,J)
      IF(N2.EQ.1) SPL(NTT-1,J)=SPLF(K,J)
      IF(SPLF(K,J).GE.1.0) SPL(NTT,J)=SPLF(K,J)+CRN1
      IF(N2.EQ.1.AND.SPLF(K,J).GE.1.0) SPL(NTT-1,J)=SPLF(K,J)+CRN2
  280 CONTINUE
C
C ***  ARRANGEMENT OF NOZZLE EMISSION ANGLES IN MONOTONICALLY  ***
C ***  INCREASING ORDER                                        ***
C
      NN=NTT
      NKX=NTT-1
      DO 290 N=1,NKX
      XMIN=TTN(1)
      NI=1
C
      DO 288 I=2,NN
      IF(TTN(I).GT.XMIN) GO TO 288
      XMIN=TTN(I)
      NI=I
  288 CONTINUE
C
```

Figure 6.8 Continued.

```
      THETN(N)=TTN(NI)
      SPLF(N,J)=SPL(NI,J)
      NN=NN-1
C
      DO 286 I=1,NN
      IF(I.GE.NI) GO TO 285
      GO TO 286
  285 TTN(I)=TTN(I+1)
      SPL(I,J)=SPL(I+1,J)
  286 CONTINUE
C
      IF(NN.GT.1) GO TO 290
      THETN(NTT)=TTN(1)
      SPLF(NTT,J)=SPL(1,J)
  290 CONTINUE
C
C ***  INTERPOLATION TO OBTAIN FLIGHT SPL  ***
C
      DO 262 K=1,NTHET
      IF(THET(K).LE.THETMX) GO TO 263
      SPL(K,J)=0.5
      GO TO 262
  263 IF(THET(K).GE.THETN(1).AND.THET(K).LE.THETN(NTT)) GO TO 264
      SPL(K,J)=0.4
      GO TO 262
  264 DO 266 KK=1,NKX
      IF(THET(K).LE.THETN(KK+1)) GO TO 268
      GO TO 266
  268 IF(SPLF(KK,J).GE.1.0.AND.SPLF(KK+1,J).GE.1.0) GO TO 269
      SPL(K,J)=0.6
      GO TO 262
  269 SPL(K,J)=SPLF(KK,J)+((THET(K)-THETN(KK))/(THETN(KK+1)-THETN(KK)))
     2 *(SPLF(KK+1,J)-SPLF(KK,J))
      SUM(K)=SUM(K)+10.**(SPL(K,J)/10.)
      GO TO 262
  266 CONTINUE
  262 CONTINUE
      DO 267 K=1,NTHET
      SPLF(K,J)=SPL(K,J)
  267 CONTINUE
      WRITE(6,222) F(J),(SPLF(K,J),K=1,NTHET)
  260 CONTINUE
      DO 670 K=1,NTHET
      IF(SUM(K).GT.0.0) SUM(K)=10.*ALOG10(SUM(K))
  670 CONTINUE
      WRITE(6,224) (SUM(K),K=1,NTHET)
C
      GO TO 1000
C
C *****  OUTPUT FORMAT STATEMENTS  *****
C
  200 FORMAT('1',5X,12A6,/,5X,12A6)
  202 FORMAT(//,5X,'TRANSFORMATION WITHOUT SOURCE LOCATION CORRECTIONS')
  204 FORMAT(//,5X,'TRANSFORMATION WITH SOURCE LOCATION CORRECTIONS')
```

Figure 6.8 Continued.

```
205 FORMAT(//,5X,'INPUT PARAMETERS:',//,8X,'MODEL-JET NOZZLE DIAMETER'
   2 ,5X,'DJ =',F6.3,' CM',/,8X,'FREE-JET NOZZLE RADIUS',8X,'RT =',
   3 F6.3,' M')
206 FORMAT(/,8X,'MEASUREMENT DISTANCE FROM NOZZLE EXIT PLANE FOR',
   2 ' FREE-JET DATA',9X,'RM =',F6.3,' M',/,8X,'EMISSION DISTANCE',
   3 ' FROM SOURCE LOCATION FOR IDEAL WIND-TUNNEL DATA',6X,'R =',
   4 F6.3,' M')
208 FORMAT(8X,'EMISSION DISTANCE FROM NOZZLE EXIT PLANE FOR FLIGHT',
   2 ' DATA',14X,'RN =',F6.3,' M')
209 FORMAT(/,8X,'JET VELOCITY',8X,'VJ =',F7.2,' M/S',/,8X,
   2 'TUNNEL VELOCITY',5X,'VT =',F7.2,' M/S')
210 FORMAT(/,8X,'AMBIENT TEMPERATURE',3X,'T0 =',F5.1,' DEG C',/,
   2 8X,'TUNNEL TEMPERATURE',4X,'TT =',F5.1,' DEG C')
212 FORMAT(/,8X,'MEASUREMENT ANGLES (RELATIVE TO JET EXHAUST) ',
   2 'REFERENCED TO NOZZLE EXIT PLANE FOR FREE-JET DATA,',/,8X,
   3 'THEM(I),I=1,NTHEM (DEGREES) :',/,8X,18F6.1)
213 FORMAT(//,5X,'COMPUTED PARAMETERS:',//,8X,
   2 'SPEED OF SOUND IN AMBIENT MEDIUM SURROUNDING FREE-JET FLOW',
   3 4X,'A0 =',F7.2,' M/S',/,8X,'SPEED OF SOUND INSIDE FREE-JET',
   4 ' FLOW',27X,'AT =',F7.2,' M/S',/,8X,'DENSITY RATIO (FREE-JET/',
   5 'AMBIENT)',28X,'RHOR =',F6.3)
214 FORMAT(/,8X,'JET VELOCITY/AMBIENT SOUND SPEED',8X,'VJ/A0 =',
   2 F6.3,/,8X,'TUNNEL VELOCITY/AMBIENT SOUND SPEED',5X,'VT/A0 =',
   3 F6.3)
216 FORMAT(//,5X,'FAILURE CODES:',//,8X,'SPL=0.1  IN TRANSFORM',
   2 'ING FREE-JET DATA TO WIND-TUNNEL DATA, THE MEASUREMENT ANGLE ',
   3 'CORRESPONDING TO DESIRED',/,17X,'EMISSION ANGLE FELL OUTSIDE',
   4 ' THE RANGE OF MEASUREMENT ANGLES FOR FREE-JET DATA.',/,8X,
   5 'SPL=0.2  IN TRANSFORMING WIND-TUNNEL DATA TO FLIGHT DATA, THE',
   6 ' DESIRED OBSERVED FREQUENCY FELL OUTSIDE THE',/,17X,'RANGE OF',
   7 ' DOPPLER SHIFTED FREQUENCIES AVAILABLE FROM WIND-TUNNEL DATA.',
   8 /,8X,'SPL=0.3  IN COMPUTING SPL UNDER FLIGHT CONDITIONS FOR',
   9 ' SPECIFIED VALUES OF FREQUENCY AND EMISSION ANGLE, THE',/,17X,
   1 'INTERPOLATION FAILED SINCE ONE OR BOTH VALUES OF WIND-TUNNEL',
   2 ', DOPPLER-CORRECTED SPL WAS 0.1,0.2,OR 0.5.')
217 FORMAT(8X,'SPL=0.4  IN TRANSFORMING WIND-TUNNEL DATA TO FLIGHT',
   2 ' DATA, THE DESIRED NOZZLE EMISSION ANGLE FELL OUTSIDE',/,17X,
   3 'THE RANGE OF NOZZLE EMISSION ANGLES CORRESPONDING TO SOURCE',
   4 ' EMISSION ANGLES FOR WIND-TUNNEL DATA.',/,8X,'SPL=0.5  IN',
   5 ' TRANSFORMING FREE-JET DATA TO WIND-TUNNEL DATA, THE DESIRED',
   6 ' EMISSION ANGLE EXCEEDED THE MAXIMUM',/,17X,'VALUE, BEYOND',
   7 ' WHICH TOTAL INTERNAL REFLECTION IN THE FREE-JET OCCURS.',/,8X,
   8 'SPL=0.6  IN TRANSFORMING WIND-TUNNEL DATA TO FLIGHT DATA, THE',
   9 ' INTERPOLATION FAILED SINCE ONE OR BOTH VALUES',/,17X,
   1 'OF WIND-TUNNEL, DOPPLER-CORRECTED SPL WAS 0.3,0.4,OR 0.5.',/,
   2 8X,'SPL=1.0  ANY SPL WHICH IS ACTUALLY COMPUTED TO BE LESS',
   3 ' THAN 1.0 DB IS SET EQUAL TO 1.0 DB.')
218 FORMAT(//,26X,'*** IDEAL WIND-TUNNEL SPL (DB) ***',///,10X,
   2 'EMISSION ANGLE (RELATIVE TO JET EXHAUST) REFERENCED TO',
   3 ' SOURCE POSITION (DEGREES)',//,10X,18F6.1)
220 FORMAT(5X,'FREQ',/,5X,'(HZ)')
222 FORMAT(3X,F7.0,18F6.1)
224 FORMAT(/,4X,'OASPL',1X,18F6.1)
230 FORMAT(//,26X,'*** FLIGHT  SPL (DB) ***',///,10X,
```

Figure 6.8 Continued.

```
      2 'EMISSION ANGLE (RELATIVE TO JET EXHAUST) REFERENCED',
      3 ' TO NOZZLE EXIT POSITION (DEGREES)',//,10X,18F6.1)
C
  900 STOP
      END
```

Figure 6.8 Concluded.

```
1          SAMPLE CASE  -  TRANSFORMATION OF JET MIXING NOISE DATA
2          MEASURED IN LOCKHEED ANECHOIC FREE-JET FLIGHT SIMULATION FACILITY
3     0301
4     271015
5     2.54       0.3556
6     2.438
7     30.        40.        50.        60.        70.        80.        90.        100.
8     110.       120.
9     200.       250.       315.       400.       500.       630.       800.       1000.
10    1250.      1600.      2000.      2500.      3150.      4000.      5000.      6300.
11    8000.      10000.     12500.     16000.     20000.     25000.     31500.     40000.
12    50000.     63000.     80000.
13    2.54
14    2.54
15    20.        30.        40.        50.        60.        70.        80.        90.
16    100.       110.       120.       130.       140.       150.       160.
17    299.8      30.72      22.        21.6
18    68.6  67.6  71.1  73.3  76.0  79.0  78.9  83.2  84.1  89.1  90.9  91.6
19    91.6  92.6  92.3  90.3  89.0  88.1  89.0  88.4  83.7  84.2  81.4  81.0
20    78.7  78.4  75.0
21    61.5  63.5  65.0  68.4  70.7  74.4  76.6  79.2  82.2  84.3  86.1  87.7
22    88.3  88.7  89.7  89.7  89.4  89.3  89.5  89.1  88.5  87.9  86.3  81.8
23    78.5  78.9  75.1
24    61.7  60.5  62.0  65.6  68.3  70.3  72.2  74.4  77.4  80.3  83.0  84.6
25    84.7  86.5  86.6  87.1  87.4  87.6  88.1  87.3  87.3  86.6  85.2  84.4
26    82.2  81.4  77.4
27    58.9  61.1  62.6  65.0  66.7  68.7  71.7  73.7  76.6  78.9  81.5  82.7
28    82.6  84.4  85.9  85.2  85.6  85.9  86.7  86.6  86.7  86.8  85.2  80.6
29    77.1  76.7  74.4
30    58.0  60.0  61.5  64.1  65.8  68.0  69.6  72.9  75.1  78.6  79.1  80.5
31    81.3  81.9  82.5  83.7  84.0  83.4  84.5  84.1  83.8  84.2  83.2  82.7
32    80.2  81.9  77.2
33    57.6  58.7  61.2  63.6  65.5  67.6  68.8  71.0  74.9  77.9  78.5  80.0
34    80.4  80.7  81.6  81.8  82.6  82.7  83.6  82.3  83.1  82.7  81.9  80.4
35    77.8  77.0  74.6
36    56.7  59.0  61.3  64.7  65.6  67.6  68.8  70.7  74.7  76.5  78.3  79.2
37    80.6  81.1  81.0  81.5  82.2  82.5  83.0  82.9  83.1  82.2  82.7  80.4
38    79.2  78.3  75.5
39    57.7  57.6  59.1  62.5  62.8  64.7  67.7  69.5  72.7  74.3  76.3  77.2
40    79.1  79.8  79.2  79.5  78.9  79.9  80.9  79.9  80.8  79.1  77.6  73.6
41    71.5  70.2  66.0
42    57.6  55.5  58.8  60.4  63.4  65.1  66.3  69.5  72.2  74.4  76.1  76.4
43    77.8  77.6  77.5  77.3  79.0  81.0  80.7  79.6  82.6  81.7  80.3  76.6
44    75.2  76.7  74.0
45    59.0  55.9  57.1  60.4  63.4  65.3  67.5  68.2  69.5  74.2  75.9  76.7
46    77.0  78.4  77.2  77.7  78.7  79.8  81.2  81.0  82.4  81.4  81.2  78.9
47    77.7  78.9  75.9
48    -5.0
```

Figure 6.9 Input data for sample case.

```
     SAMPLE CASE  -  TRANSFORMATION OF JET MIXING NOISE DATA
    MEASURED IN LOCKHEED ANECHOIC FREE-JET FLIGHT SIMULATION FACILITY

TRANSFORMATION WITH SOURCE LOCATION CORRECTIONS

INPUT PARAMETERS:

   MODEL-JET NOZZLE DIAMETER      DJ = 2.540 CM
   FREE-JET NOZZLE RADIUS         RT =  .356 M

   MEASUREMENT DISTANCE FROM NOZZLE EXIT PLANE FOR FREE-JET DATA          RM = 2.438 M
   EMISSION DISTANCE FROM SOURCE LOCATION FOR IDEAL WIND-TUNNEL DATA       R = 2.540 M
   EMISSION DISTANCE FROM NOZZLE EXIT PLANE FOR FLIGHT DATA               RN = 2.540 M

   JET VELOCITY          VJ = 299.80 M/S
   TUNNEL VELOCITY       VT =  30.72 M/S

   AMBIENT TEMPERATURE    TO = 22.0 DEG C
   TUNNEL TEMPERATURE     TT = 21.6 DEG C

   MEASUREMENT ANGLES (RELATIVE TO JET EXHAUST) REFERENCED TO NOZZLE EXIT PLANE FOR FREE-JET DATA,
   THEM(I),I=1,NTHEM (DEGREES) :
     30.0  40.0  50.0  60.0  70.0  80.0  90.0 100.0 110.0 120.0

COMPUTED PARAMETERS:

   SPEED OF SOUND IN AMBIENT MEDIUM SURROUNDING FREE-JET FLOW     AO = 344.20 M/S
   SPEED OF SOUND INSIDE FREE-JET FLOW                            AT = 343.96 M/S
   DENSITY RATIO (FREE-JET/AMBIENT)                             RHOR = 1.001

   JET VELOCITY/AMBIENT SOUND SPEED        VJ/AO =  .871
   TUNNEL VELOCITY/AMBIENT SOUND SPEED     VT/AO =  .089

FAILURE CODES:

   SPL=0.1  IN TRANSFORMING FREE-JET DATA TO WIND-TUNNEL DATA, THE MEASUREMENT ANGLE CORRESPONDING TO DESIRED
            EMISSION ANGLE FELL OUTSIDE THE RANGE OF MEASUREMENT ANGLES FOR FREE-JET DATA.
   SPL=0.2  IN TRANSFORMING WIND-TUNNEL DATA TO FLIGHT DATA, THE DESIRED OBSERVED FREQUENCY FELL OUTSIDE THE
            RANGE OF DOPPLER SHIFTED FREQUENCIES AVAILABLE FROM WIND-TUNNEL DATA.
   SPL=0.3  IN COMPUTING SPL UNDER FLIGHT CONDITIONS FOR SPECIFIED VALUES OF FREQUENCY AND EMISSION ANGLE, THE
            INTERPOLATION FAILED SINCE ONE OR BOTH VALUES OF WIND-TUNNEL, DOPPLER-CORRECTED SPL WAS 0.1,0.2,OR 0.5.
   SPL=0.4  IN TRANSFORMING WIND-TUNNEL DATA TO FLIGHT DATA, THE DESIRED NOZZLE EMISSION ANGLE FELL OUTSIDE
            THE RANGE OF NOZZLE EMISSION ANGLES CORRESPONDING TO SOURCE EMISSION ANGLES FOR WIND-TUNNEL DATA.
   SPL=0.5  IN TRANSFORMING FREE-JET DATA TO WIND-TUNNEL DATA, THE DESIRED EMISSION ANGLE EXCEEDED THE MAXIMUM
            VALUE, BEYOND WHICH TOTAL INTERNAL REFLECTION IN THE FREE-JET OCCURS.
   SPL=0.6  IN TRANSFORMING WIND-TUNNEL DATA TO FLIGHT DATA, THE INTERPOLATION FAILED SINCE ONE OR BOTH VALUES
            OF WIND-TUNNEL, DOPPLER-CORRECTED SPL WAS 0.3,0.4,OR 0.5.
   SPL=1.0  ANY SPL WHICH IS ACTUALLY COMPUTED TO BE LESS THAN 1.0 DB IS SET EQUAL TO 1.0 DB.
```

Figure 6.10 Output from sample case.

SAMPLE CASE - TRANSFORMATION OF JET MIXING NOISE DATA
MEASURED IN LOCKHEED ANECHOIC FREE-JET FLIGHT SIMULATION FACILITY

*** IDEAL WIND-TUNNEL SPL (DB) ***

EMISSION ANGLE (RELATIVE TO JET EXHAUST) REFERENCED TO SOURCE POSITION (DEGREES)

FREQ (HZ)	20.0	30.0	40.0	50.0	60.0	70.0	80.0	90.0	100.0	110.0	120.0	130.0	140.0	150.0	160.0
200.	.1	.1	.1	62.7	57.9	59.0	57.4	57.1	57.4	57.7	59.0	60.9	.1	.1	.5
250.	.1	.1	.1	61.9	59.5	58.2	59.4	59.0	58.8	59.0	57.3	.1	.1	.1	.5
315.	.1	.1	.1	63.8	60.8	60.1	60.8	60.7	61.2	60.5	60.1	.1	.1	.1	.5
400.	.1	.1	.1	66.2	64.0	63.3	63.2	63.2	64.4	63.5	61.6	.1	.1	.1	.5
500.	.1	.1	71.9	68.1	66.4	65.4	64.9	65.0	65.6	63.5	64.5	.1	.1	.1	.5
630.	.1	.1	74.7	71.4	68.4	67.3	67.0	67.1	67.6	65.3	66.2	.1	.1	.1	.5
800.	.1	.1	75.2	73.3	70.1	70.2	68.7	68.3	68.8	68.0	67.7	.1	.1	.1	.5
1000.	.1	.1	78.7	75.5	72.3	72.2	71.8	70.5	70.5	70.0	69.9	.1	.1	.1	.5
1250.	.1	.1	80.5	78.2	75.4	74.9	74.2	74.4	74.2	73.0	71.7	.1	.1	.1	.5
1600.	.1	.1	83.7	80.3	78.1	77.5	77.6	77.1	75.8	74.8	75.1	.1	.1	.1	.5
2000.	.1	.1	85.3	82.4	80.7	79.4	78.1	78.0	77.5	76.6	76.7	.1	.1	.1	.5
2500.	.1	.1	86.5	83.9	82.1	80.6	79.5	79.3	78.3	77.1	77.3	.1	.1	.1	.5
3150.	.1	.1	86.9	84.1	82.0	80.8	80.1	80.1	79.8	78.7	77.9	.1	.1	.1	.5
4000.	.1	90.6	87.3	85.4	83.8	81.9	80.5	80.5	80.4	78.7	78.9	.1	.1	.1	.5
5000.	.1	90.3	88.1	85.6	84.7	82.8	81.3	80.9	79.9	78.4	77.9	.1	.1	.1	.5
6300.	.1	88.5	88.0	86.0	84.4	83.2	81.8	81.2	80.2	78.2	78.2	.1	.1	.1	.5
8000.	.1	87.4	87.7	86.1	84.7	83.5	82.4	82.0	79.9	79.3	79.3	.1	.1	.1	.5
10000.	.1	86.7	87.6	86.3	85.0	83.1	82.2	82.2	80.6	81.0	80.5	.1	.1	.1	.5
12500.	.1	87.6	87.8	86.7	85.7	84.1	83.2	82.8	81.4	81.0	81.7	.1	.1	.1	.5
16000.	.1	87.1	87.4	86.0	85.5	83.7	82.1	82.4	80.5	79.9	81.4	.1	.1	.1	.5
20000.	.1	83.4	86.9	85.9	85.6	83.4	82.6	82.7	81.2	82.6	82.9	.1	.1	.1	.5
25000.	.1	83.7	86.3	85.2	85.6	83.7	82.3	81.9	79.6	81.6	81.9	.1	.1	.1	.5
31500.	.1	81.4	84.7	83.8	84.0	82.6	81.5	82.2	78.3	80.2	81.7	.1	.1	.1	.5
40000.	.1	79.9	80.7	83.0	79.7	81.5	80.1	80.0	74.5	76.5	79.4	.1	.1	.1	.5
50000.	.1	77.3	77.7	80.7	76.2	79.0	77.5	78.6	72.4	75.1	.1	.1	.1	.1	.5
63000.	.1	77.3	77.9	79.8	75.7	80.5	77.0	77.8	71.1	76.5	.1	.1	.1	.1	.5
80000.	.1	73.8	74.1	75.9	73.3	76.1	74.3	75.0	66.9	73.7	.1	.1	.1	.1	.5
OASPL	.0	97.7	98.7	97.1	95.9	94.7	93.4	93.4	91.6	91.7	91.8	60.9	.0	.0	.0

Figure 6.10 Continued.

SAMPLE CASE - TRANSFORMATION OF JET MIXING NOISE DATA
MEASURED IN LOCKHELD ANECHOIC FREE-JET FLIGHT SIMULATION FACILITY

*** FLIGHT SPL (DB) ***

EMIS ION ANGLE (RELATIVE TO JET EXHAUST) REFERENCED TO NOZZLE EXIT POSITION (DEGREES)

FREQ (HZ)	20.0	30.0	40.0	50.0	60.0	70.0	80.0	90.0	100.0	110.0	120.0	130.0	140.0	150.0	160.0
200.	.6	.6	56.4	56.9	56.0	56.0	.6	.6	.6	.6	.6	.6	.6	.6	.5
250.	.6	.6	58.5	57.0	57.7	58.0	58.1	58.4	58.5	.6	.6	.6	.6	.6	.5
315.	.6	.6	61.1	59.3	59.4	59.9	60.3	60.6	60.2	.6	.6	.6	.6	.6	.5
400.	.6	.6	64.3	62.7	62.3	62.5	62.9	63.8	63.0	61.7	.6	.6	.6	.6	.5
500.	.6	.6	67.1	65.2	64.5	64.3	64.6	65.2	63.7	64.3	.6	.6	.6	.6	.5
630.	.6	.6	70.4	67.4	66.7	66.5	66.8	67.4	65.4	66.1	.6	.6	.6	.6	.5
800.	.6	.6	72.9	69.7	69.6	68.4	68.0	68.5	68.0	67.8	.6	.6	.6	.6	.5
1000.	.6	.6	75.7	72.6	71.9	71.6	70.5	70.4	70.0	69.8	.6	.6	.6	.6	.5
1250.	.6	.6	78.5	75.8	74.7	74.1	74.2	74.1	73.2	72.1	.6	.6	.6	.6	.5
1600.	.6	.6	81.3	78.7	77.5	77.3	77.1	76.2	75.2	74.8	.6	.6	.6	.6	.5
2000.	.6	.6	83.4	81.1	79.6	78.4	77.9	77.6	77.0	76.6	.6	.6	.6	.6	.5
2500.	.6	.6	84.7	82.4	80.8	79.7	79.2	78.7	77.8	77.3	.6	.6	.6	.6	.5
3150.	.6	.6	85.3	83.0	81.3	80.3	80.0	79.9	79.3	78.4	.6	.6	.6	.6	.5
4000.	.6	89.0	86.2	84.4	82.8	81.2	80.4	80.4	79.8	78.9	.6	.6	.6	.6	.5
5000.	.6	88.7	86.8	84.9	83.7	82.1	81.0	80.5	79.5	78.5	.6	.6	.6	.6	.5
6300.	.6	87.6	86.9	85.2	83.8	82.6	81.6	80.9	79.7	78.3	.6	.6	.6	.6	.5
8000.	.6	86.8	86.9	85.5	84.2	83.0	82.2	81.4	79.8	79.2	.6	.6	.6	.6	.5
10 00.	.6	86.7	87.1	85.8	84.5	82.9	82.2	81.8	80.6	80.8	.6	.6	.6	.6	.5
12500.	.6	87.1	87.2	86.1	85.1	83.7	83.0	82.5	81.3	81.2	.6	.6	.6	.6	.5
16000.	.6	85.7	86.8	85.7	85.0	83.3	82.1	82.1	80.5	80.3	.6	.6	.6	.6	.5
20000.	.6	83.6	86.3	85.5	85.1	83.2	82.6	82.5	81.3	82.3	.6	.6	.6	.6	.5
25000.	.6	83.0	85.5	84.8	85.0	83.3	82.2	81.7	80.0	81.8	.6	.6	.6	.6	.5
31500.	.6	80.9	83.4	83.4	83.1	82.3	81.5	81.8	78.6	80.6	.6	.6	.6	.6	.5
40000.	.6	78.9	79.9	81.9	79.1	81.0	79.9	79.6	74.9	77.2	.6	.6	.6	.6	.5
50000.	.6	77.2	77.8	80.0	76.3	79.0	77.5	78.2	72.8	.6	.6	.6	.6	.6	.5
63000.	.6	76.1	76.9	78.6	75.6	79.7	76.9	77.4	71.5	.6	.6	.6	.6	.6	.5
80000.	.6	.6	.6	.6	.6	.6	.6	74.7	67.5	.6	.6	.6	.6	.6	.5
OASPL	.0	96.7	97.6	96.3	95.2	94.1	93.3	93.1	91.4	91.4	.0	.0	.0	.0	.0

Figure 6.10 Concluded.

7. VALIDATION OF TRANSFORMATION PROCEDURE

7.1 OBJECTIVES AND APPROACH

An outline of the recommended calibration procedure which permits the transformation of free-jet data to ideal wind tunnel conditions was presented in Section 2. Following this, the point source experiments, which were specifically planned and conducted to verify various *individual aspects* of the calibration procedure (e.g. angle changes, amplitude calibration factor, etc.), were described in Section 4. The purpose of the work described in the present section is to obtain a validation of the transformation procedure as a *complete package*. The point source is replaced by a model jet exhaust for this purpose. The method used to obtain this validation is described below.

Jet noise experiments were conducted first with the free-jet facility used in the conventional manner, with the microphones placed entirely outside the free-jet flow. Subsequently, the facility was used as a wind tunnel for which the measurements were conducted inside the potential core of the free jet. The test matrices for both sets of experiments were kept identical.

The free-jet data were transformed to the IWT conditions using the computational procedure described in Section 6. One-third octave band SPL's over the frequency range from 200 Hz to 50 KHz were obtained for emission angles $\theta_T = 30°$ to 120°. Similarly, the wind tunnel data were transformed to IWT conditions using the procedure described in Appendix 7A. In this case also, the third-octave SPL spectra were obtained from 200 Hz to 50 KHz for the same range of emission angles (i.e. $\theta_T = 30°$ to 120°). Both sets of transformed data were referenced to a common emission distance of 100 d (where d is the model-jet nozzle diameter), and the corresponding spectra were compared on an absolute basis.

The data were obtained for both unheated and heated jets operated at subcritical as well as supercritical pressure ratios. Some results were also obtained where the jet noise was purposely "contaminated" with noise generated by an internal noise source located upstream of the jet exit.

The experimental program was actually planned to satisfy two objectives: *First*, to check the validity of the transformation procedure (which is the subject of the present section), and *second*, to study the effects of forward velocity on jet mixing noise, shock-associated noise and internal noise (which is the subject of the following section). Since the experimental setups and relevant configurations required to accomplish these two objectives were the same, they are described in the present section.

The comparison of data measured inside and outside the free jet, corrected to ideal wind-tunnel conditions, is presented and discussed in Section 7.3. The results relevant to the second objective mentioned above are presented separately in Section 8.

7.2 EXPERIMENTAL PROGRAM

7.2.1 Test Configuration and Data Acquisition

The test configuration used for the present experiments is shown schematically in Figure 7.1. The 2.54 cm diameter model-jet nozzle was mounted along the centerline of the free jet. The protrusion of the model-jet nozzle exit plane (beyond the free-jet nozzle exit plane) was 36 model-jet diameters. This was found to be the optimum location of the model-jet exit plane, within the constraints of the chamber geometry. It permitted the measurement of far-field noise over the angular range from $\theta_m = 30°$ to 120° relative to the jet exhaust. For measurements outside the free-jet flow, the microphones were placed at 10° intervals on an arc of radius $R_m = 96$ d.

For measurements inside the potential core of the free jet, a multiple microphone arrangement is neither desirable nor practical. Hence, a microphone traverse arrangement was used. The microphone was traversed parallel to the centerline of the jet (along line AB of Figure 7.1) at a distance of 8 model-jet diameters from the centerline.

Photographic views showing the free jet, model jet, and microphone arrangement are presented in Figure 7.2 (*fixed microphones for measurements outside the free jet*) and Figure 7.3 (*traversing microphone for measurement inside the free jet*). Each microphone used here was a 0.635 cm B&K microphone Type 4135 fitted with a FET cathode-follower Type 2619. All microphones outside the free jet were fitted with B&K windscreens Type UA 0237. The in-flow microphone was fitted with 0.635 cm B&K nose cone type UA 0385. One-third octave SPL's were obtained on a General Radio analyzer, and the levels were recorded on incremental digital tape recorder for subsequent detailed analysis using a data reduction program. This program incorporated the microphone frequency response corrections and the atmospheric absorption corrections. In the case of the inflow microphone, far-field corrections (obtained from B&K) for the nose cone were also applied as appropriate. The results were then displayed in the form of one-third octave band sound pressure levels over the frequency range from 200 Hz to 50 KHz together with the overall sound pressure levels for subsequent analysis.

7.2.2 Calibration of Jet Operating Conditions

The pipe supplying the 2.54 cm model jet had a diameter of 10.16 cm which provided an area contraction ratio of 16. A static pressure tapping in the 10.16 cm diameter pipe was used as an indication of the reservoir or total pressure of the jet. In order to ensure that this did not introduce significant errors in the flow calculation, a pitot tube was placed at the center of the nozzle exit. A comparison between the static pressure reading in the 10.16 cm diameter pipe and the pitot tube reading indicated that the error introduced by measuring the static pressure instead of the total pressure in the upstream pipe was insignificant.

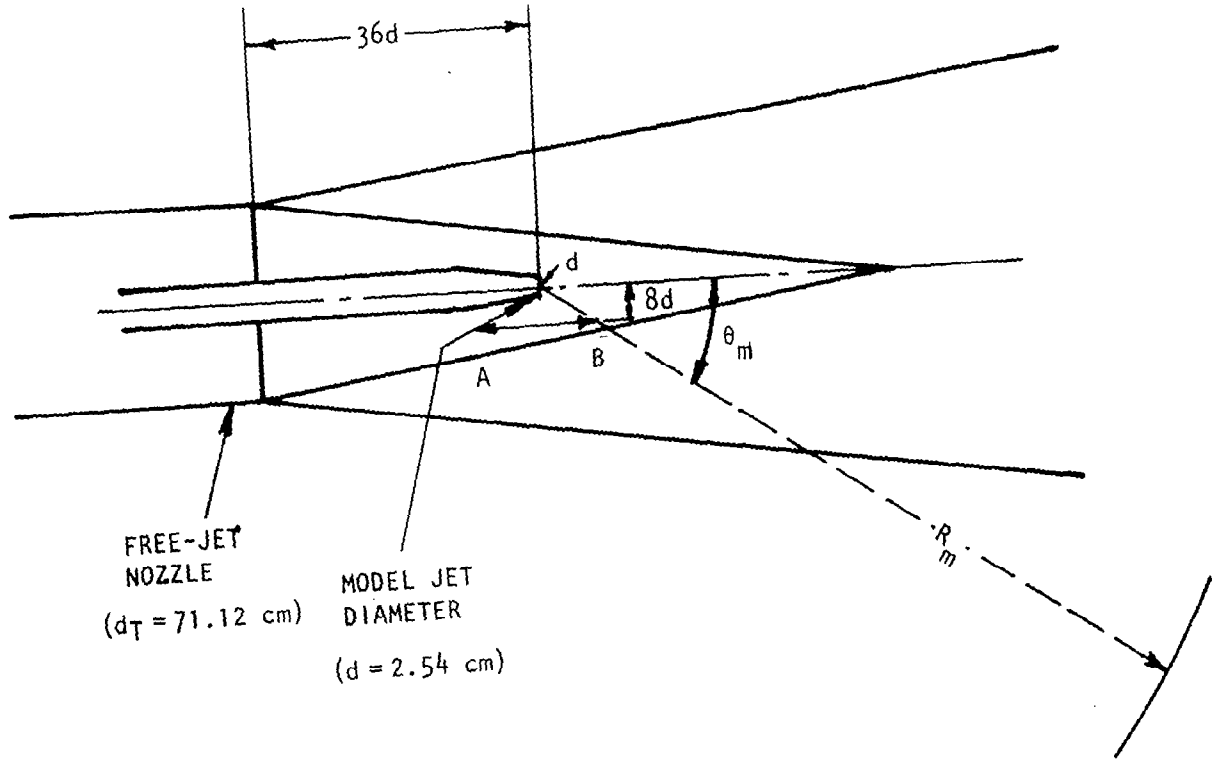

Figure 7.1 Schematic of the free jet and the model jet

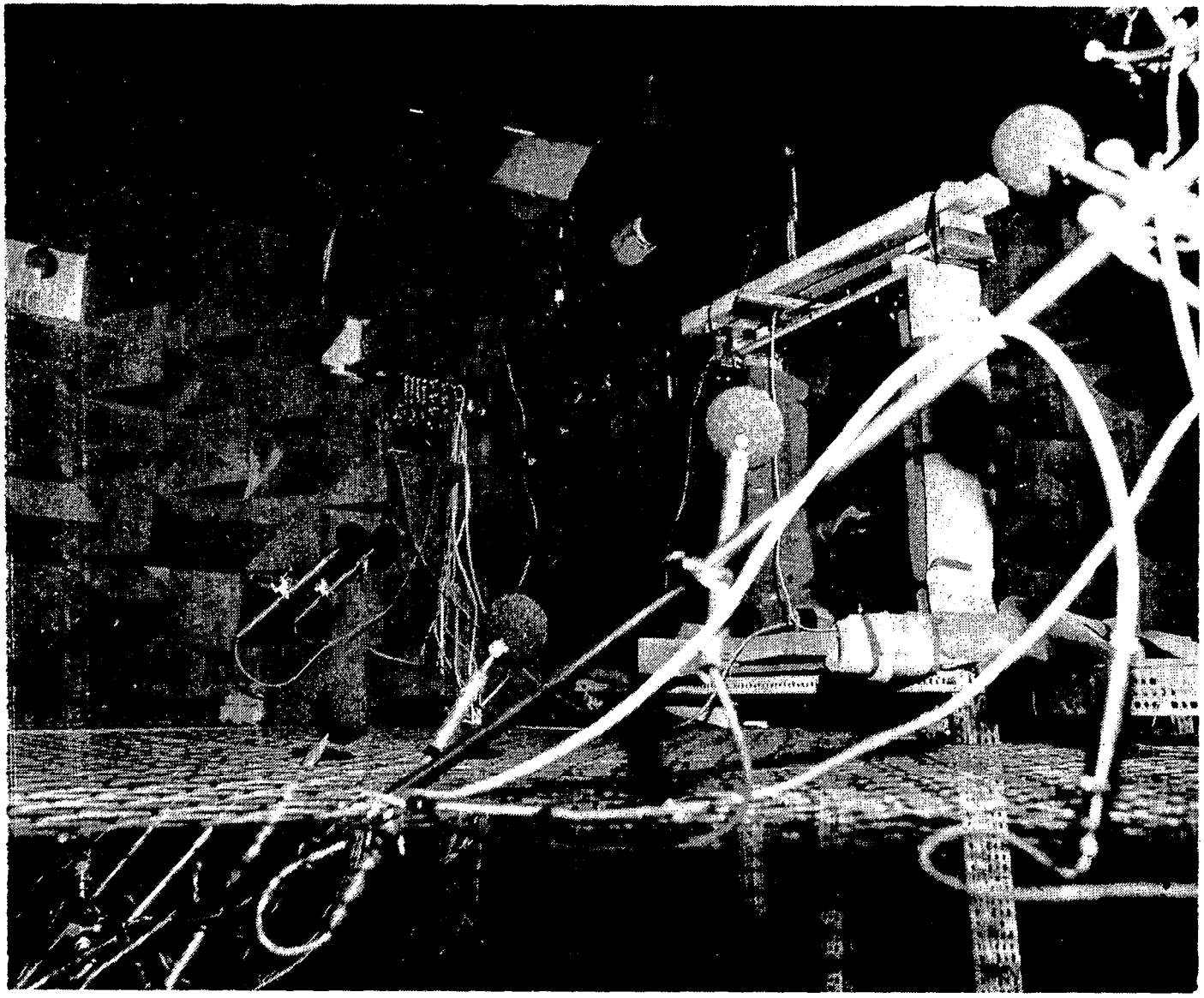

Figure 7.2 Free jet, model jet and microphone configuration

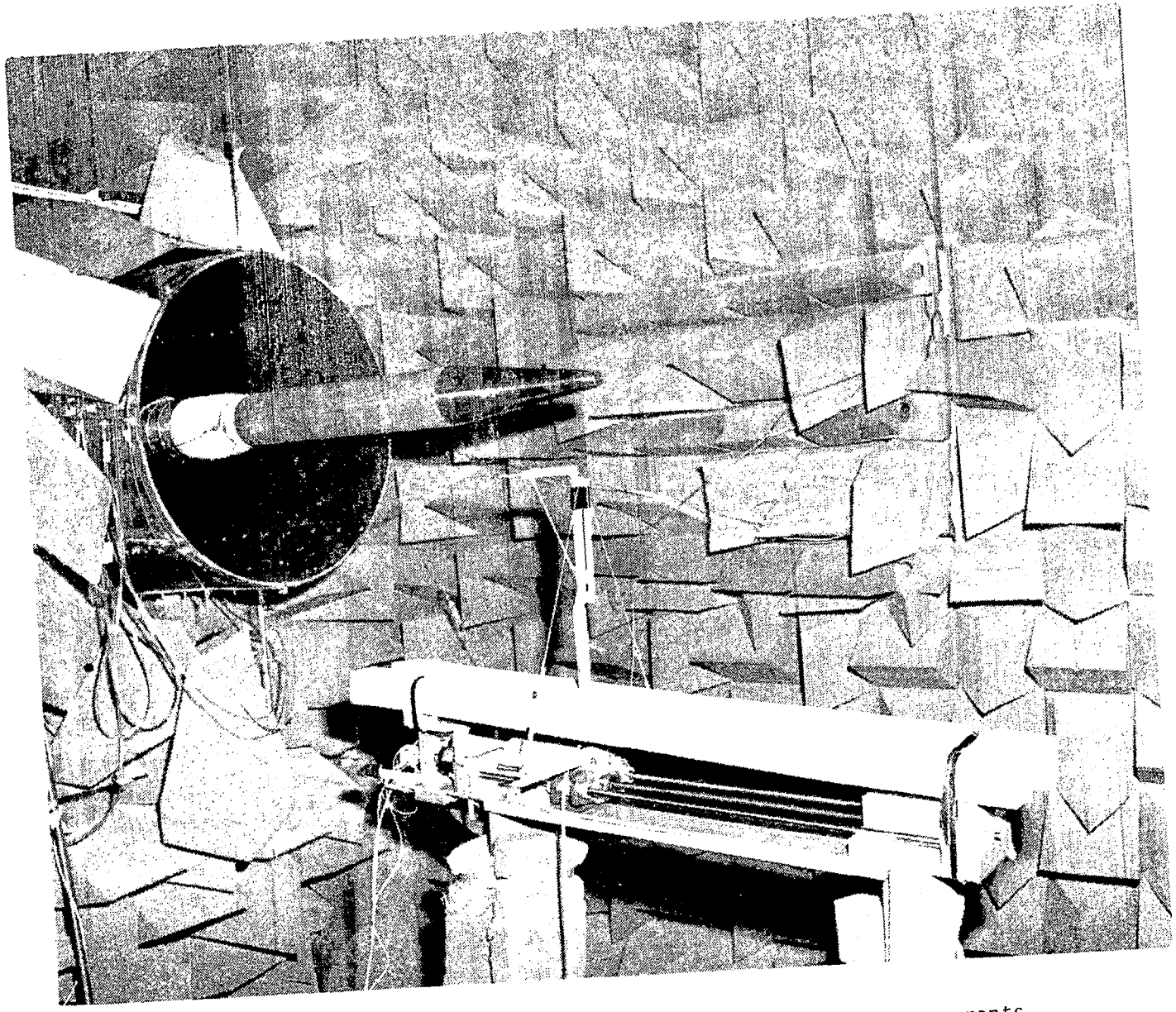

Figure 7.3 Microphone traverse arrangement for the inflow measurements

Similarly a calibration for total temperature of the jet was made by comparing the temperature measured by a thermocouple located upstream of the pipe and one placed at the jet exit center. Due to heat losses from the last 1 m of uninsulated pipe, an average difference of 22°C was noted between the two temperature readings for heated jet conditions. This difference was accounted for in calculating the flow parameters.

7.2.3 Experimental Conditions

The experimental program was carefully planned to yield results at (1) constant jet efflux velocity (V_J/a_o) with varying free-jet velocity (V_T/a_o), and (2) constant free-jet velocity with varying primary-jet velocity. The nominal values of the free-jet (or tunnel) velocity were: V_T/a_o = minimum, 0.09, 0.18 and 0.26.

The minimum tunnel velocity, V_{TO}, is defined as the tunnel velocity which is provided by the ejector action of the primary jet in the absence of any additional velocity supplied by the facility ejector itself. Its magnitude, therefore, increases as V_J/a_o increases.

Unheated Jet. For each tunnel velocity the unheated model jet was operated at the conditions given in Table 7.1.

Table 7.1 Operating Conditions for Unheated Jet

Pressure Ratio p_R/p_o	Jet Exit Velocity Ratio V_J/a_o	Comments
1.4	0.68	Subcritical
1.8	0.88	Subcritical
2.1	0.98	Supercritical
2.5	1.07	Supercritical
3.0	1.17	Supercritical

Heated Jet. For heated tests, the model jet was operated at nominal stagnation temperature of 870K. The pressure ratios and the jet exit velocity ratios are given in Table 7.2.

Table 7.2 Operating conditions for heated jet.

Pressure Ratio P_R/P_o	Jet Exit Velocity Ratio V_J/a_o	Comments
1.107	0.68	Subcritical
1.193	0.88	Subcritical
1.428	1.25	Subcritical
1.965	1.68	Supercritical
2.318	1.85	Supercritical
2.810	2.02	Supercritical
3.567	2.20	Supercritical

Tests With Internal Noise. Due to the limitations in noise levels generated by the internal noise source (see Section 3.3), the jet noise tests in the *presence* of internal noise (as opposed to jet noise tests with *no* internal noise) were conducted only for lower jet velocities. Tables 7.3 and 7.4 give the nominal unheated and heated jet operating conditions, respectively, at which the flight effects on jet noise were examined in the presence of internal noise. The heated jet, in this case, could not be maintained at 870K due to the mixing between the heated air from the primary jet reservoir and the unheated air from the internal noise generator (intersecting jets). An average temperature of 533K was attained at the jet exit plane with the internal noise source operating.

Table 7.3 Operating conditions for unheated jet with internal noise source.

Pressure Ratio P_R/P_o	Jet Exit Velocity Ratio V_J/a_o	Comments
Minimum	0.40	Model-jet exhaust flow only due to flow from internal noise source
1.2	0.50	
1.4	0.68	
1.8	0.88	

Table 7.4 Operating conditions for heated jet with internal noise source

Pressure Ratio P_R/P_o	Jet Exit Velocity Ratio V_J/a_o	Comments
Minimum	0.69	Model-jet exhaust flow only due to flow from internal noise source
1.362	0.88	
1.4	0.93	
1.8	1.32	

7.2.4 Comparison Between Measured and Predicted Jet Noise Spectra

In order to ensure that the noise radiated from the present model jet is true jet mixing noise and free from unwanted upstream noise sources, if any, the measured spectra were compared with those predicted by the current Lockheed jet noise prediction computer program. A typical comparison for $V_J/a_o = 0.89$ and $\theta_m = 90°$ is shown in Figure 7.4(a) for $R_m/d = 72$. The agreement is within measurement accuracy.

Since, for all measurements inside the free-jet flow, the microphone is only 8 nozzle diameters from the jet centerline, it was decided to compare the measured spectra at small distances from the jet with those predicted by the Lockheed method. A comparison for the measurement distance of $R_m = 2.75$ d is shown in Figure 7.4(b) for $\theta_m = 90°$ and $V_J/a_o = 0.89$. The measured levels for frequencies beyond 1.5 KHz agree very well with those predicted, thus indicating the dominance of true jet mixing noise. The reason for the discrepancy at lower frequencies could be two-fold. First, the microphone could actually be in the near field at these frequencies. Second, the ejector action of the model jet induces a certain amount of free-jet flow. The microphone located within the free-jet (as in this case) will thus be affected by the flow noise which is normally low-frequency noise. For all in-flow measurements, the low frequency parts of the spectra will be contaminated (and in fact dominated) by the flow noise. This is discussed further in Section 7.2.6.

7.2.5 Inverse Square Law Calibration

Since the transformation methods in essence utilize the inverse square law, calibration tests were conducted by measuring the jet noise spectra at $\theta_m = 90°$ for microphones located sequentially at $R_m/d = 2.75$, 6, 9, 12, 18, 24, 36, and 72. The normal practice in jet noise calibration tests is to compare the variation of measured noise levels with distance with the $1/R^2$ law where R is taken to be the distance between the center of the nozzle exit plane and

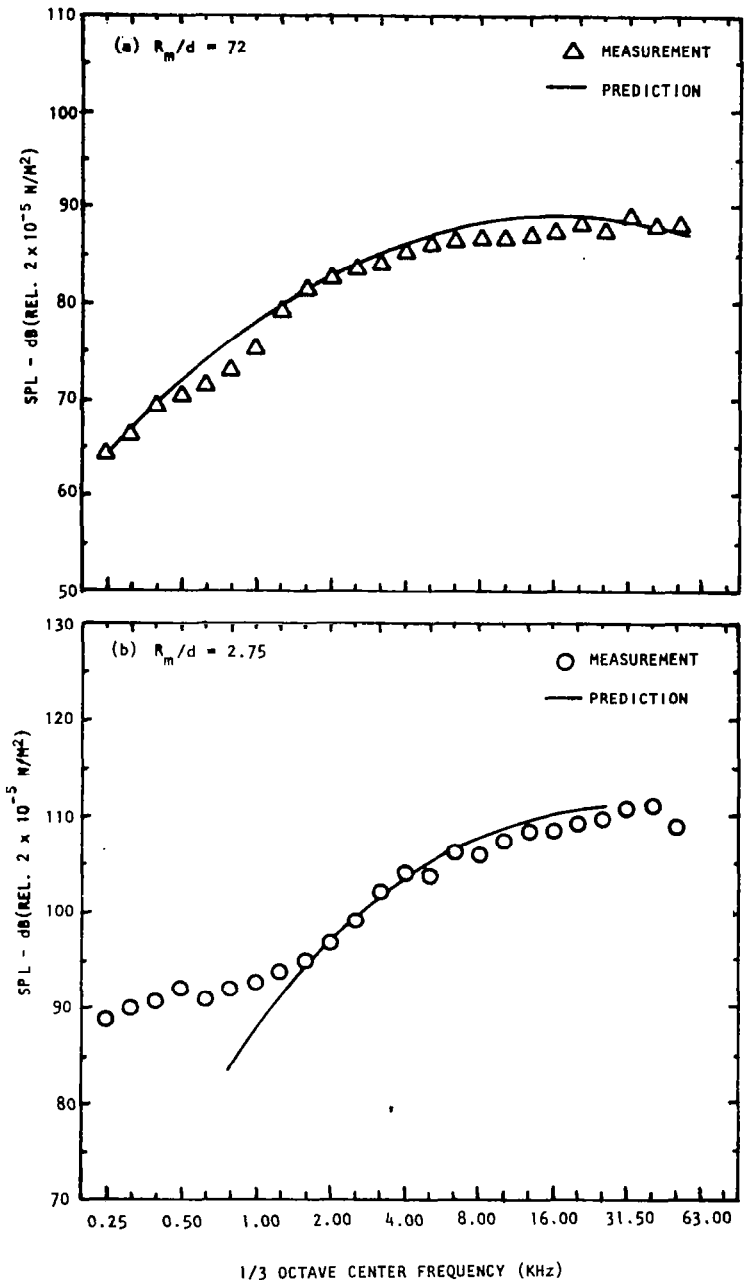

Figure 7.4 Comparison of jet noise spectra measured in the free-jet facility with those predicted by Lockheed prediction program. $\theta_m = 90°$, $V_J/a_o = 0.89$ (unheated), $V_T/a_o \doteq 0$.

the microphone location. On this basis, one inherently assumes that the jet noise sources are located at the nozzle exit plane. However, a true $1/R^2$ comparison would be one where the actual source location is taken into account. Thus, for example, for $R_m = 2.75$ d, the distance from a high-frequency source of jet noise will be smaller than that from a low-frequency source of noise which is located farther downstream of the jet exit (than the high-frequency source). However, Lockheed's jet noise prediction program takes proper account of the true source locations. A more meaningful comparison can be achieved if these true source locations are introduced in the comparison. Figure 7.5 shows the following set of data plotted against R_m/d:

(a) Measured data at various measurement locations for various frequencies

(b) Ordinary $1/R^2$ law, i.e. $1/R_m^2$ law in this case

(c) True $1/R^2$ law where the sound pressure levels have been predicted by the Lockheed program taking account of the true distance between the microphone and the source at each particular frequency, as well as the directivity at the true radiation angle ($\neq 90°$).

Figure 7.5 clearly demonstrates that what appears to be a deviation from an ordinary $1/R^2$ law is primarily due to a lack of accounting for those real effects. The results indicate that we can utilize an inverse square law up to about 3 nozzle diameters, provided the source location effects are correctly accounted for, at least for the frequency range for which this test was conducted.

We consider these results to be quite significant as they have demonstrated that the microphone side-line distance of 8 nozzle diameters within the free jet (see Figure 7.1) is an adequate distance for our purpose.

It should be noted that (the absolute values of) some of the measured SPL's are lower than those predicted by a true $1/R^2$ law. Even if these differences are genuine deviations from a true $1/R^2$ law, they do not pose a major problem in our present objective for two reasons. First, the magnitudes of these deviations are quite small. Second, our validation of the transformation procedure (i.e. the comparison between free-jet data and wind tunnel data after both are transformed to the IWT conditions) will first be conducted for the *zero free-jet velocity* case. This will provide a measure of the deviation, if any, from the true $1/R^2$ law. These deviations will then be used during the assessment of the validity of the transformation procedure at *other free-jet velocities*.

7.2.6 Background Noise and Data Quality,

Model Jet and Free Jet Operated Separately. The quality of data that will be presented in the subsequent parts of this report will be primarily determined by the background noise levels. For microphones outside the free-jet flow, the background noise consists of the noise generated by the free jet

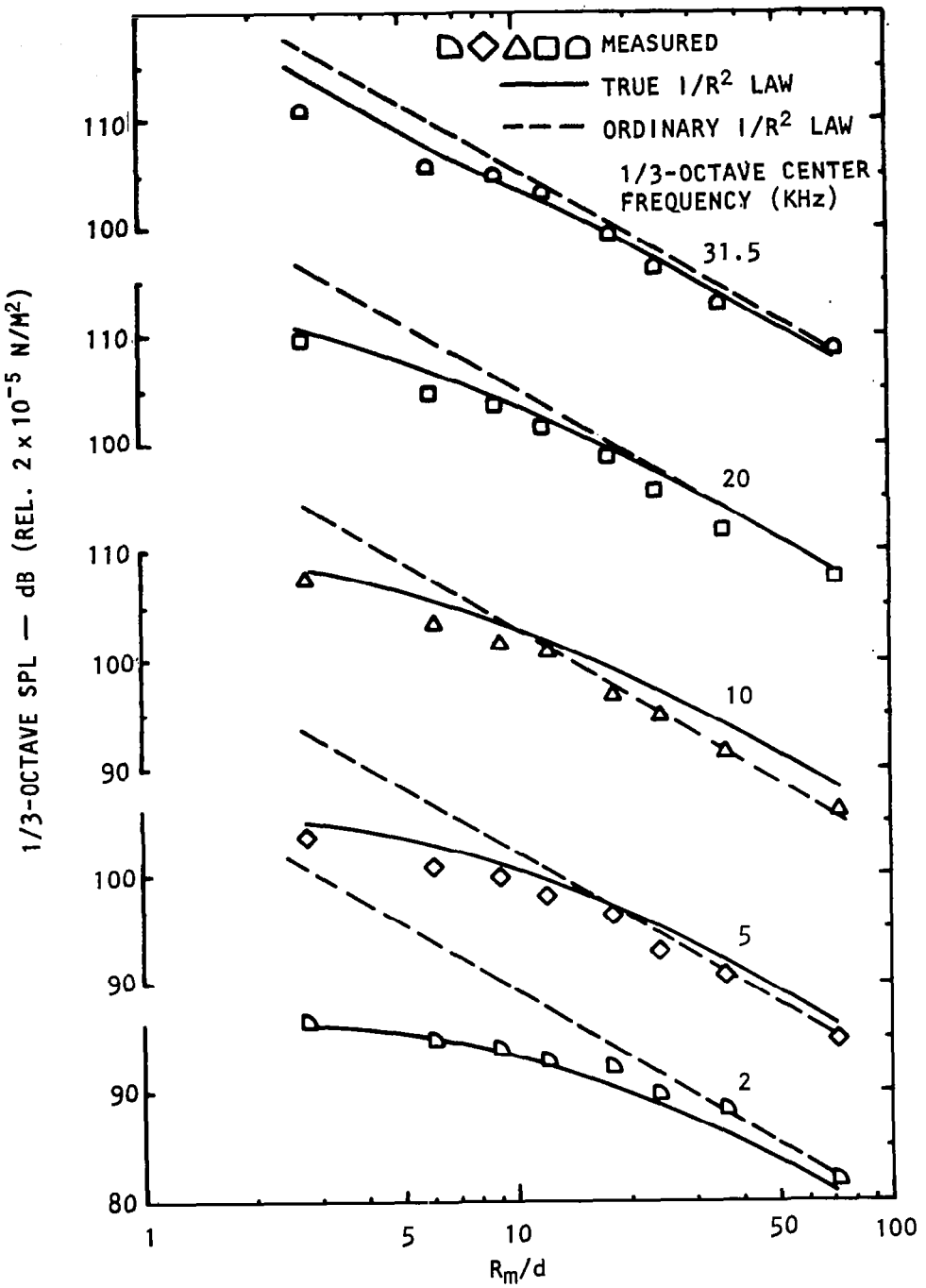

Figure 7.5 Inverse square law calibration of measured jet noise in the free-jet facility. $\theta_m = 90°$, $V_J/a_o = 0.89$ (unheated), $V_T/a_o \doteq 0$.

itself. For inflow measurements, however, the total background noise contains additional noise generated by turbulent pressure fluctuations over the microphone. In order to assess the contamination of jet noise by the background noise, the noise levels from unheated and heated model jets operated alone (i.e. without free-jet flow) are compared with the noise levels from the free jet operated alone at various tunnel velocities. The SPL spectra measured outside the free jet are shown in Figure 7.6(a) (unheated jet) and Figure 7.6 (b) (heated jet). During these measurements the inflow microphone was not present. The comparison of model-jet noise and free-jet noise presented in these figures clearly indicates that significant contamination of model-jet noise by the free-jet noise (i.e. background noise) can be expected to occur at combinations of low V_J/a_o and high V_T/a_o. The background noise levels are particularly high at low frequencies.

Similar results were obtained for SPL's measured by the inflow microphone. Typical results at $\theta_m = 90°$ are shown in Figure 7.7(a) for the unheated jet and Figure 7.7(b) for the heated jet. *The data presented in Figures 7.7(a) and 7.7(b) do not include the free-field frequency response corrections for the microphone nose cone and have been extrapolated to* $R_m/d = 96$. Since the microphone was placed inside the free-jet flow, the background noise levels are much higher than the background noise levels measured by the microphone located outside the free-jet flow (compare Figure 7.7 with Figure 7.6). In particular, the low-frequency noise is much higher at the two highest free-jet velocities, $V_T/a_o = 0.18$ and 0.26. A comparison of the results in Figure 7.7(a) and Figure 7.7(b) shows that for a fixed V_J/a_o, the heated jet is quieter than the unheated jet, at least over the range of V_J/a_o considered here (i.e. $V_J/a_o \geq 0.68$). Since the background noise is essentially independent of the model-jet temperature, the limitations imposed by the background noise (in subsequent results) will be more severe for the heated jet noise tests than for the unheated tests (at the same jet velocity V_J).

Model Jet and Free-Jet Operated Simultaneously. The background noise problem has so far been assessed by examining the noise levels from the free jet and the model jet in isolation. When these two jets are operated simultaneously, the background noise limitation can be expected to be even more severe. This is due to the fact that while the background noise remains essentially unaltered in the presence of the primary jet, the noise from the model jet decreases in level due to the relative velocity effect when the free-jet flow is turned on.

To summarize, for all measurements conducted inside the free jet, only the high-frequency parts of the spectra will be dominated by the model jet noise; the low-frequency noise will be contaminated and in some cases masked by the background noise. An example is shown in Figure 7.8(a) which represents the worst case (i.e. highest free-jet velocity, $V_T/a_o \doteq 0.26$). In this figure, the spectra measured inside the flow at $\theta_m = 90°$ are presented for various jet velocities. A similar, but not as severe, contamination also exists for all measurements conducted outside the free-jet flow. A typical result for the unheated jet at $\theta_m = 90°$ and $R_m/d = 96$ is shown in Figure 7.8(b). The low frequencies up to 1 KHz are dominated by the free-jet noise whereas

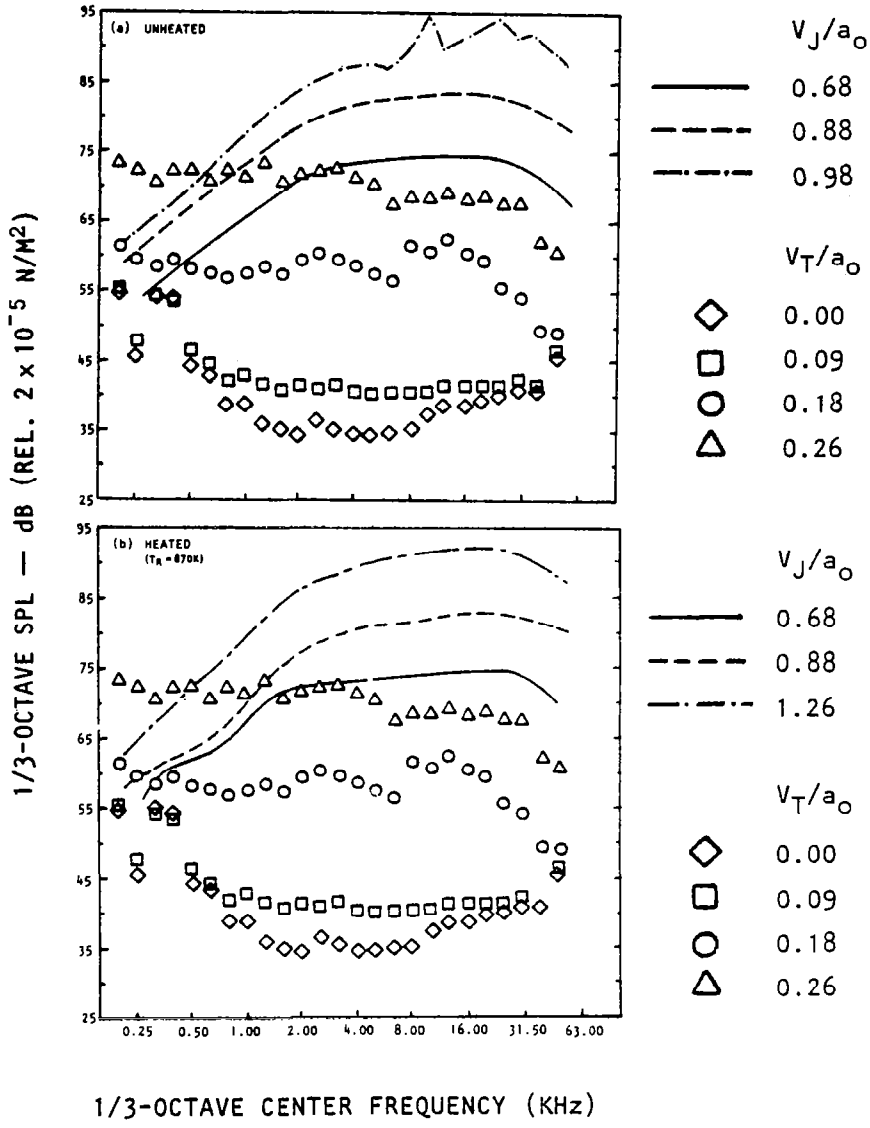

Figure 7.6 Spectra measured outside the free jet ($\theta_m = 90°$, $R_m/d = 96$) with free jet operated alone ($V_J/a_o = 0$, symbols) and model jet operated alone ($V_T/a_o = 0$, curves).

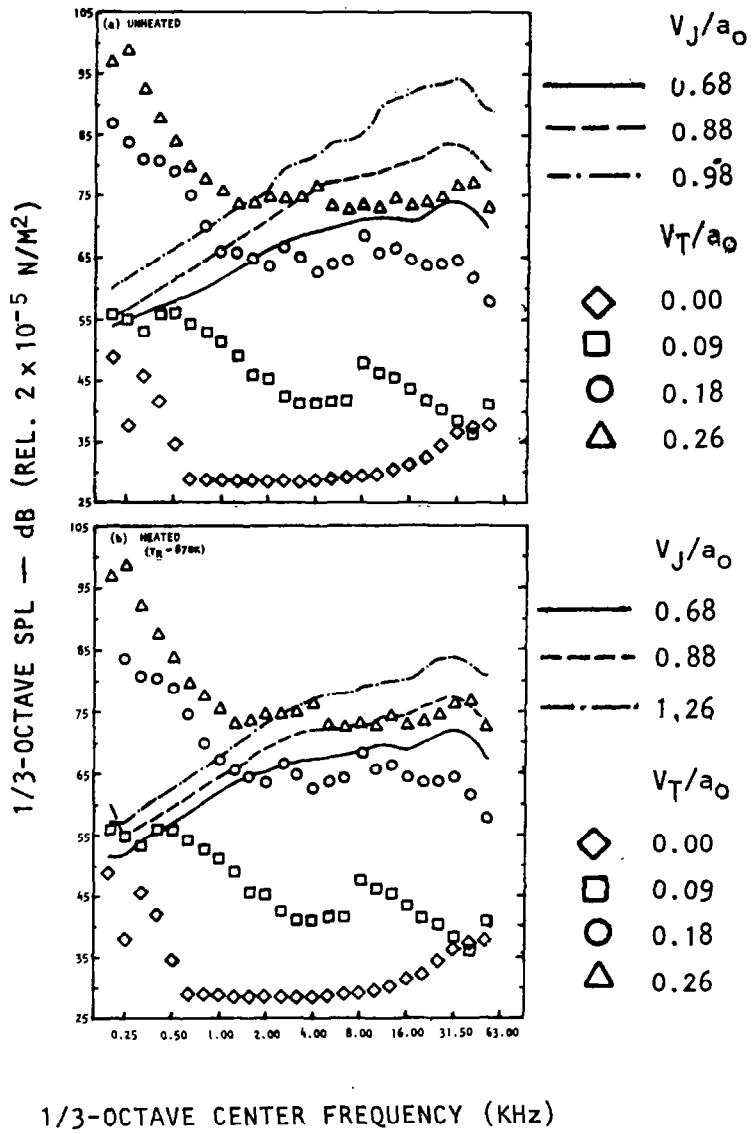

Figure 7.7 Spectra measured inside the free jet ($\theta_m = 90°$) with free jet operated alone ($V_J/a_o = 0$, symbols) and model jet operated alone ($V_T/a_o = 0$, curves). (Data scaled to $R_m/d = 96$ but not corrected for nose cone free-field frequency response.)

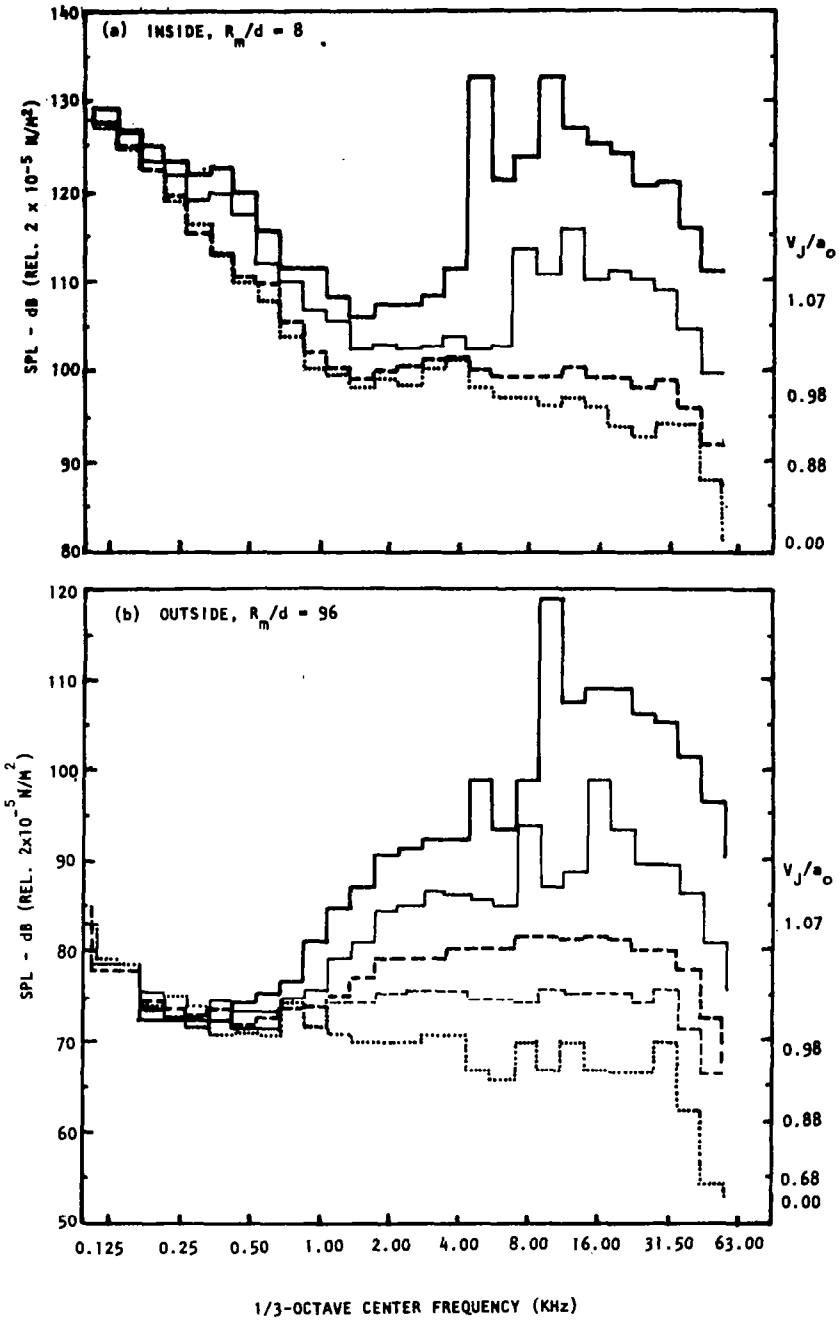

Figure 7.8 Typical spectra measured (a) inside and (b) outside the free-jet flow. $\theta_m = 90°$, $V_T/a_o = 0.26$, unheated model jet.

the mid- and high-frequency parts of the spectra are controlled by the noise from the model jet.

It is important to keep the above observations in mind when we discuss the validation of the transformation procedure in Section 7.3. All data with unacceptable signal-to-noise ratio have been discarded for this purpose.

It should be noted that in Figures 7.8(a) and 7.8(b), the spectra at the two highest jet velocities, i.e. $V_J/a_o = 0.98$ and 1.07, contain shock noise since the jet was operated at supercritical pressure ratios at these velocities. The shock noise contribution consists of the screech component as well as the broadband component. Although it is possible to suppress the screech component by installing a small metal projection at the nozzle lip, it was decided not to do so, since the introduction of any hardware in the vicinity of the nozzle exit will affect the free-jet flow, and hence the forward velocity simulation of the jet noise sources. The screech tones are normally much higher in level than the broadband shock noise, and if necessary, they can be removed visually during the data analysis.

7.3 EXPERIMENTAL RESULTS

It was pointed out earlier that the limited results (obtained mainly for $\theta_m = 90°$ and $V_T/a_o \doteq 0$) showed that a true inverse square law was essentially obeyed by the measurements acquired as close as three model-jet diameters. At other measurement angles and flow velocities, this may not be quite true in reality. To circumvent this possibility, the following philosophy was adopted in the data comparisons: *Whenever a comparison is made between measured data inside and outside the free jet, both corrected to IWT conditions, the corresponding comparison is also (first) made for the model jet operated alone with zero or minimum free-jet velocity.* The latter will reveal not only any deviations from a true inverse square law, but also any inaccuracies in the system frequency response corrections (e.g. microphone pressure response correction, nose cone free-field correction as a function of incidence angle, etc.) that may be present. These deviations can be expected to exist also in the comparisons where both the model jet and the free jet are operated together. For a fixed model-jet velocity, if the order of the deviations for the $V_T/a_o \doteq 0$ case is similar to the order of deviations for other V_T/a_o values, then it can be justifiably concluded that the transformation procedure has been essentially validated.

Typical comparisons of data measured inside and outside the free jet, corrected to IWT conditions, are shown in Figures 7.9 and 7.10 for unheated jet. Pairs of spectra for $V_J/a_o = 0.88$ and $V_T/a_o = 0.00$, 0.09, 0.18 and 0.26 are presented for the emission angle θ_T of 50° in Figure 7.9 and 90° in Figure 7.10. At $\theta_T = 50°$, the spectra agree very well. At $\theta_T = 90°$, even at zero tunnel velocity [see Figure 7.10(a)], there are small deviations between the two spectra. We believe that these differences are due to an inaccuracy in the gain settings of the two microphones (one with the nose cone and one

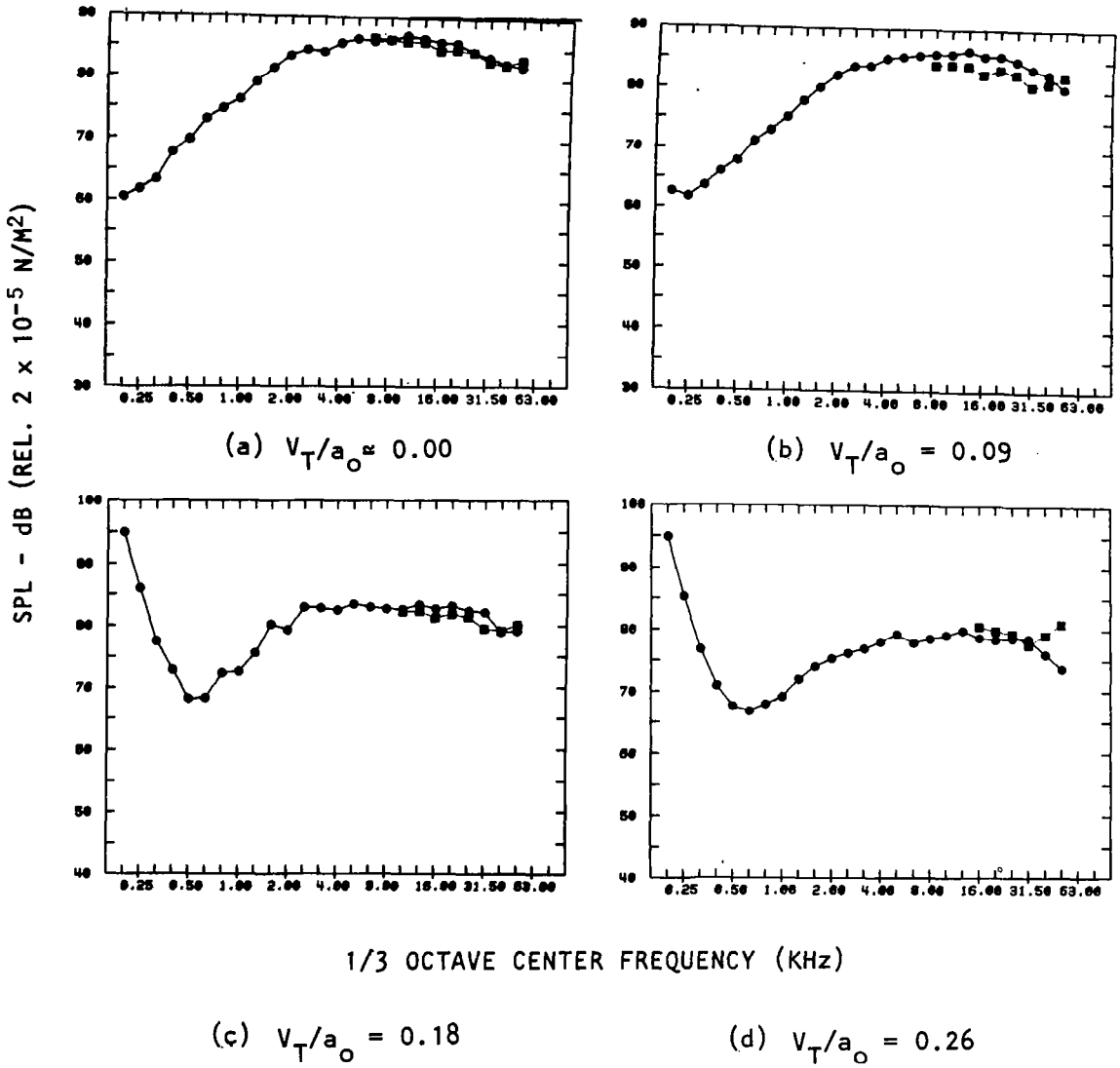

(a) $V_T/a_o \simeq 0.00$

(b) $V_T/a_o = 0.09$

(c) $V_T/a_o = 0.18$

(d) $V_T/a_o = 0.26$

Figure 7.9 Comparison of data measured inside (⊡) and outside (⊙) the free jet corrected to ideal wind tunnel conditions. *(Emission angle and distance (100d) refer to estimated source location.)* $\theta_T = 50^\circ$, $V_J/a_o = 0.88$ (unheated).

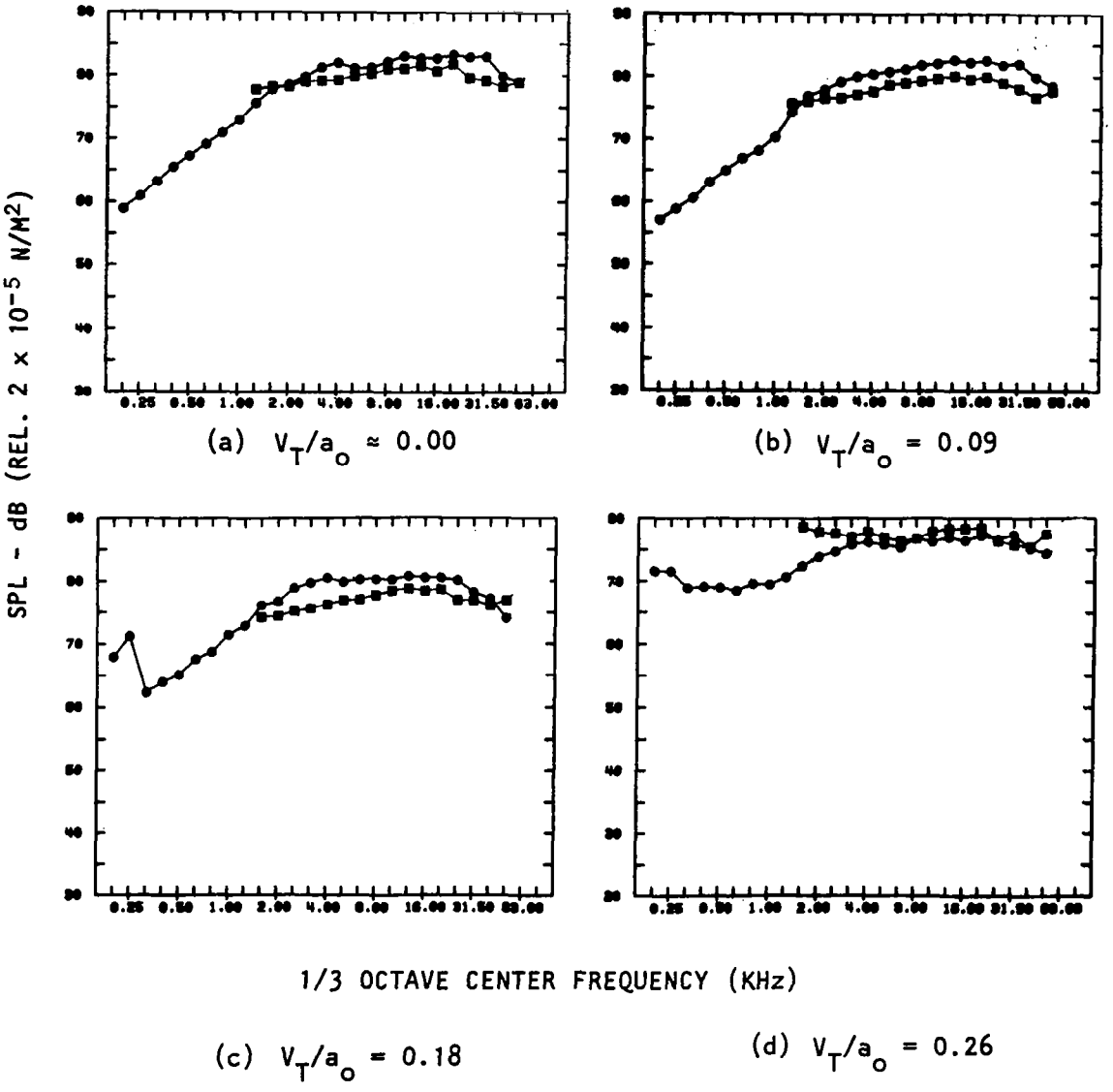

Figure 7.10 Comparison of data measured inside (□) and outside (O) the free jet corrected to ideal wind tunnel conditions. *(Emission angle and distance (100d) refer to estimated source location.)* $\theta_T = 90°$, $V_J/a_o = 0.88$ (unheated).

without the nose cone) used separately for the two measurements, and not due to a deviation from the true inverse square law. This statement is supported by the results from another test, where it was found that if only one microphone is used to measure the spectra inside and outside the flow in sequence, the true inverse square law is obeyed quite accurately (for example, see Figures 7.4 and 7.5). The deviations between the spectra measured inside and outside the flow are similar at all free-jet velocities. Based upon these arguments, it can be said that the results at $V_T/a_o = 0.09$ and 0.18 essentially validate the data transformation procedure. At the highest velocity, $V_T/a_o = 0.26$, the agreement between the two spectra is not always as good due to the flow-noise contamination, especially at the lower frequencies.

Due to inadequate signal-to-noise ratio in the forward arc, where the jet mixing noise for a given jet velocity is much lower than in the rear arc, forward arc data for subcritical conditions are not presented here. Some data for supercritical conditions are presented for rear arc as well as forward arc measurements in Figure 7.11 ($\theta_T = 50°$), 7.12 ($\theta_T = 90°$) and 7.13 ($\theta_T = 110°$) for an unheated jet operated at $V_J/a_o = 0.98$. It should be noted that the data presented in these figures are for shock-containing flows. The parts of spectra corresponding to jet mixing noise (i.e. the lower frequencies) appear to have been transformed within the measurement accuracies. In these comparisons, the undesirable contamination from flow noise appears to be significant only for the $\theta_T = 50°$ case (Figure 7.11).

7.4 DISCUSSION AND CONCLUSIONS

In the comparisons shown above, it should be noted that the estimated IWT spectra corresponding to the inflow measurements have a cut-off point at some low frequency, which is a function of the emission angle and the free-jet velocity. In reality, sound pressure levels were obtained at frequencies lower than this cut-off frequency, but when the inflow data were transformed to the IWT conditions, the transformation process required inflow measurements at angles much smaller than $\theta_m = 30°$, which was the limit of the present measurements. In the present calculations, the source location as a function of frequency has been taken into account. Thus, the lower the frequency, the farther downstream the sources of noise are located. If one were to calculate the source location corresponding to the frequencies for which no data appear in Figures 7.9 through 7.13, and then to determine the ray angle ψ_T (for a given emission angle θ_T and free-jet Mach number V_T/a_o centered at the source, one would find that the ray will pass through points outside the limit of the angular range ($\theta_m = 30°$ to 120°) of measurement. For this reason, it was not possible to compare the inside and outside data, transformed to IWT conditions, at frequencies lower than these cut-off frequencies.

Based on the results presented and the comments made in this section, the following conclusions can be drawn:

(1) At the zero (or minimum) free-jet velocity, the data measured inside and outside the free jet and subsequently transformed to the IWT conditions

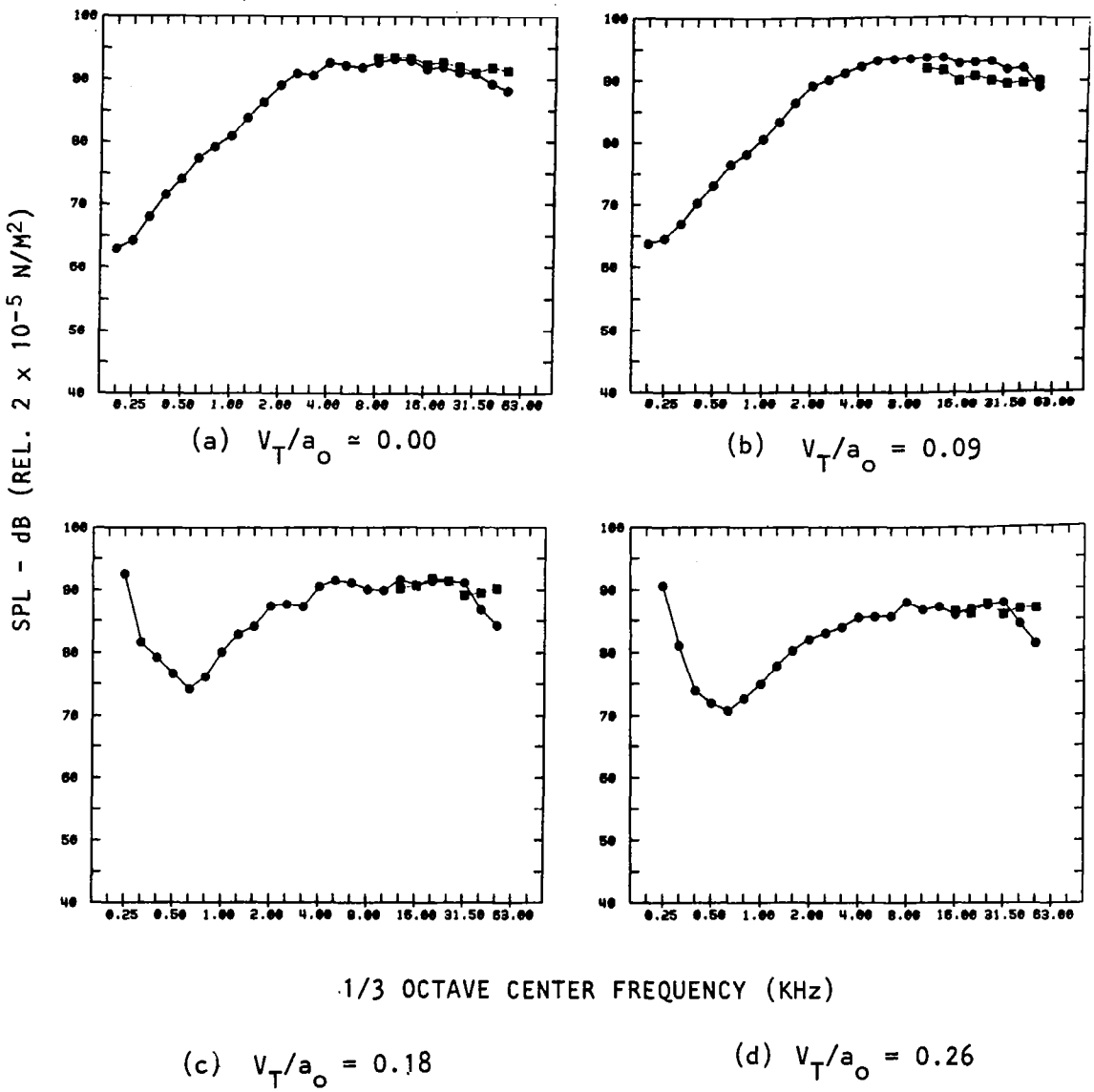

Figure 7.11 Comparison of data measured inside (□) and outside (○) the free jet corrected to ideal wind tunnel conditions. *(Emission angle and distance (100d) refer to estimated source location.)* $\theta_T = 50°$, $V_j/a_o = 0.98$ (unheated).

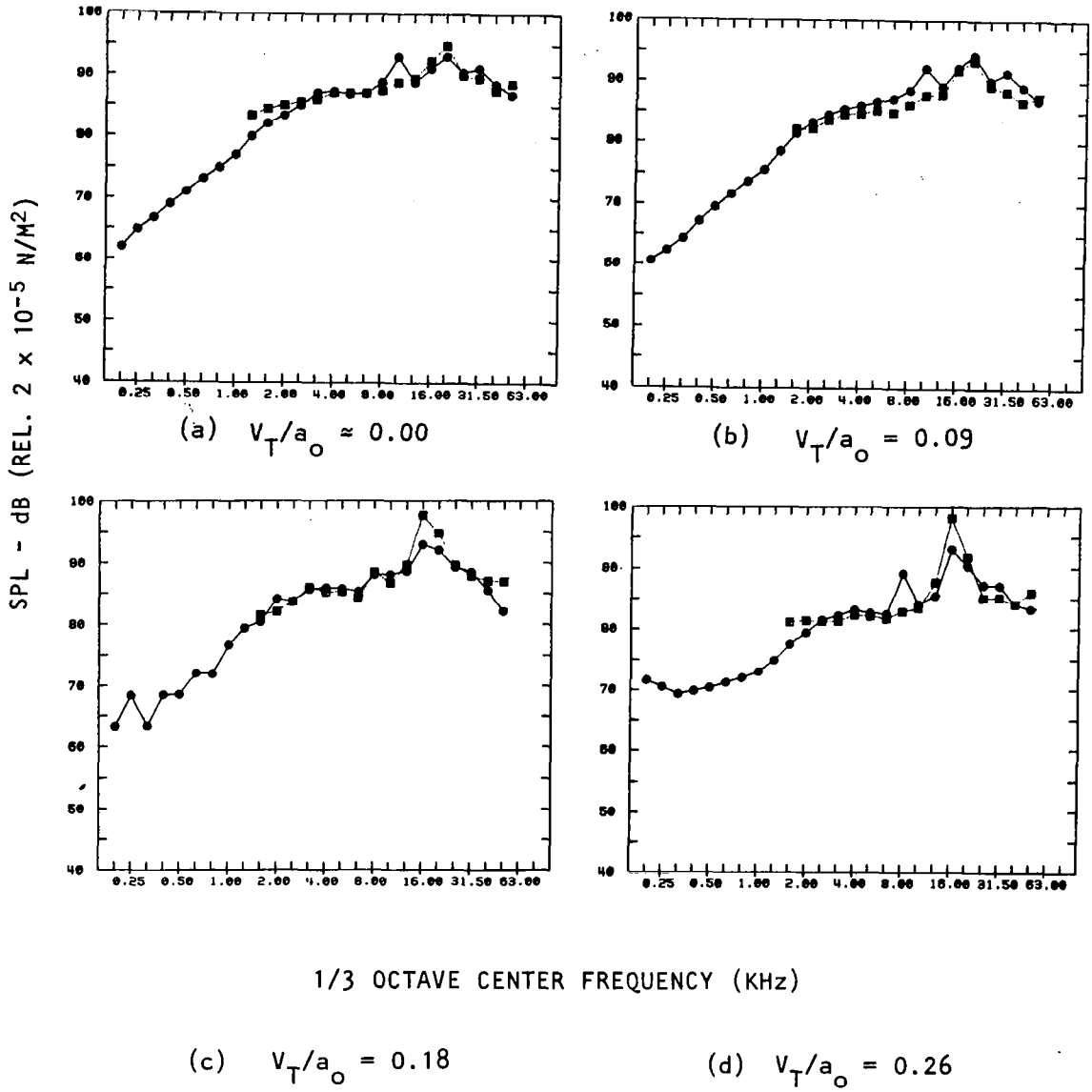

Figure 7.12 Comparison of data measured inside (□) and outside (O) the free jet corrected to ideal wind tunnel conditions. *(Emission angle and distance (100d) refer to estimated source location.)* $\theta_T = 90°$, $V_j/a_o = 0.98$ (unheated).

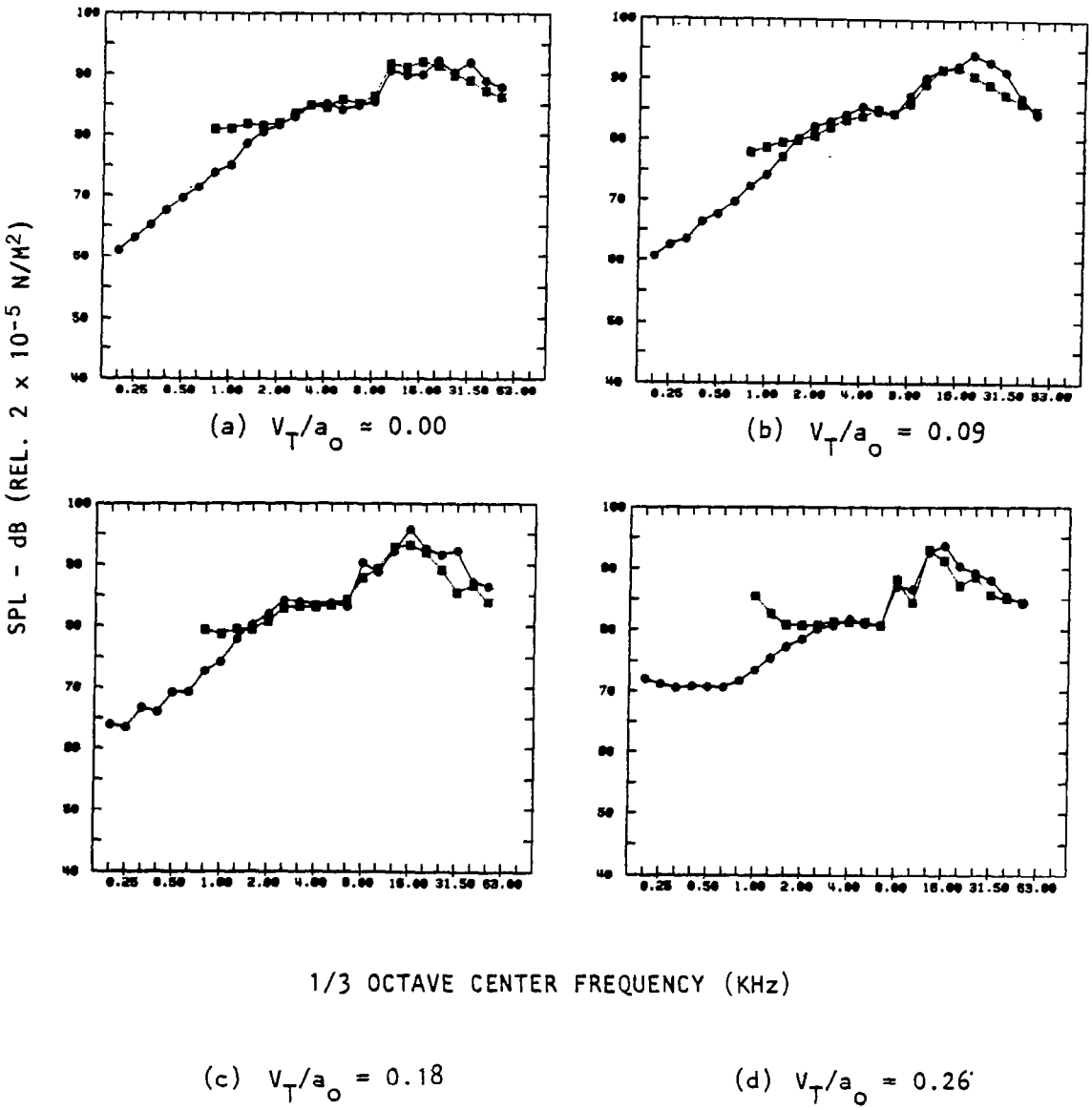

Figure 7.13 Comparison of data measured inside (□) and outside (○) the free jet corrected to ideal wind tunnel conditions. *(Emission angle and distance (100d) refer to estimated source location.)* $\theta_T = 110°$, $V_j/a_o = 0.98$ (unheated).

compare within the measurement accuracy for most cases. This demonstrates that the jet mixing noise source locations utilized in the transformation procedure are realistic, and that the results follow a true inverse square law dependence even at small distance from the model jet.

(2) For model jets operated at subcritical conditions, a good agreement is obtained between the data measured inside and outside the free jet at all but the highest free-jet velocity. This confirms the validity of the transformation procedure over a wide range of frequencies, angles and free-jet velocities.

(3) For model jets operated at supercritical conditions, the transformation procedure is verified primarily at the low frequencies where mixing noise dominates both in the rear arc and in the forward arc. In addition, even the high frequency parts of the spectra agree well in the rear arc, where the shock noise contribution, relative to the mixing noise contribution, is minimum.

(4) The results presented for the subcritical conditions are actually sufficient to show that the transformation procedure, designed to convert data measured in a free-jet flight simulation experiment to the corresponding ideal wind tunnel condition, has been largely verified.

8. EFFECTS OF SIMULATED FORWARD FLIGHT ON JET NOISE, SHOCK NOISE AND INTERNAL NOISE

8.1 OBJECTIVES

The experiments that will be described in this section are designed to study the effects of forward velocity on turbulent mixing noise, shock-associated noise and internal noise from unheated and heated jets operated in the inflight simulation mode. Typical data from these experiments were used in Section 7 to establish the validity and accuracy of the transformation procedure, which enables the conversion of measured data obtained in a free-jet facility to the corresponding ideal wind tunnel conditions. The main objective in the present section is to establish whether or not the presence of internal noise and shock-associated noise can account for the observed anomalies (discussed in Section 1) between flight data and free-jet data projected to flight case.

To achieve this objective, inflight simulation experiments were conducted in the Lockheed anechoic free-jet facility. Measurements outside the free-jet flow were conducted using unheated and heated model jets, operated at subcritical as well as supercritical pressure ratios. A specially designed noise generator, described in Section 3.3, was used to study flight effects on internal noise.

The measured data were transformed to the ideal wind tunnel conditions. The transformation procedure was described in Section 6. In essence, this procedure takes proper account of source distribution effects in a jet flow, and the refraction of sound caused by the free-jet shear layer. The correction procedure incorporates all these effects in a realistic manner, and using the measured results at fixed measurement angles, θ_m, it yields estimated results at constant emission angles, θ_T, for an observer moving with the nozzle (i.e. the ideal wind tunnel case).

The effects of forward velocity on jet mixing noise and shock-associated noise are discussed in Section 8.3. Also presented in the same section are some comments regarding the source location corrections for shock noise and internal noise. The experimental results dealing with jet noise in the presence of internal noise are presented and scaled in Section 8.4.

8.2 TEST PROGRAM

The test programs for the results presented in Section 7 and those to be discussed in the present section were identical. Since the test program and the necessary calibrations (e.g. acoustic cleanliness of the jet rig, background noise and data quality, etc.) have already been described in detail in Section 7, they will not be repeated here.

8.3 EXPERIMENTAL RESULTS WITHOUT INTERNAL NOISE

8.3.1 Effect of Source Location Corrections

Strictly speaking, in transforming any spectrum obtained in a free-jet flight simulation experiment to the corresponding IWT conditions, appropriate source location corrections *must* be applied, regardless of whether the noise source under examination is jet mixing noise, shock noise, or internal noise. In the case of jet mixing noise, sufficient source location information (as a function of frequency) is available, at least for the static case. For internal noise, however, one can perhaps assume that all frequencies are emitted at the nozzle exit plane location. In the case of shock noise, little quantitative information is available which gives source location *explicitly* as a function of frequency. It is, however, known that shock noise is generated on an aggregate at the shock locations, which are normally located close to the jet exit (compared to the large source location distances for the mixing noise component at low frequencies). One could thus argue that, in principle, the shock noise and the internal noise components can be assumed to be located at the nozzle exit plane for data transformation purposes. This would be a reasonably valid assumption if the particular spectrum in question is dominated by shock noise and/or internal noise at *all* frequencies. But in practice, and as is the case in the present work, shock noise and internal noise sources are dominant only at the higher frequencies while the low frequencies are dominated by turbulent mixing noise. Therefore, if one needs to study the effects of tunnel velocity on the total noise spectrum containing both turbulent mixing noise and shock or internal noise, one should, in principle, conduct the data transformation in two parts: low frequencies (jet mixing noise) *with* source location corrections, and high frequencies (shock noise or internal noise) *without* source location corrections. This will increase the complexity of the problem significantly, especially if one wanted to compute the OASPL's for these cases. The reason is that with source location corrections applied, the shock noise or internal noise contribution to the OASPL will be in error, whereas without source location corrections, the contribution from jet mixing noise will produce errors in the computation of OASPL's. It was, therefore, decided to examine the order of magnitude of these errors for data containing shock noise and internal noise. Computations were performed to obtain 1/3-octave spectra with and without source location corrections. Typical results for measurements conducted outside the free-jet flow are shown in Figures 8.1(a), 8.1(b) and 8.1(c) for a shock-containing jet operated at $V_J/a_o = 1.07$ ($\xi = 2.5$). Data for emission angles $\theta_T = 50°$ (rear arc), 90° and 110° (forward arc) are shown for tunnel Mach number $V_T/a_o = 0.09$. It is quite clear from these figures that the regions of spectra, normally associated with shock noise (*in this case*, beyond 5 KHz) are not influenced by the source location corrections.

It is emphasized, however, that this is not to imply that source location corrections are not important. Applying source location corrections is equivalent to applying distance (*between source and observer*) corrections. In the above example, the measurements were made at a reasonably large distance from the nozzle ($R_m/d = 96$) and hence from the sources. At small measurement distances, the source location corrections can be very important. This is illustrated in Figures 8.1(d), 8.1(e) and 8.1(f), where the effects of source location corrections are examined for data measured *inside* the free-jet flow.

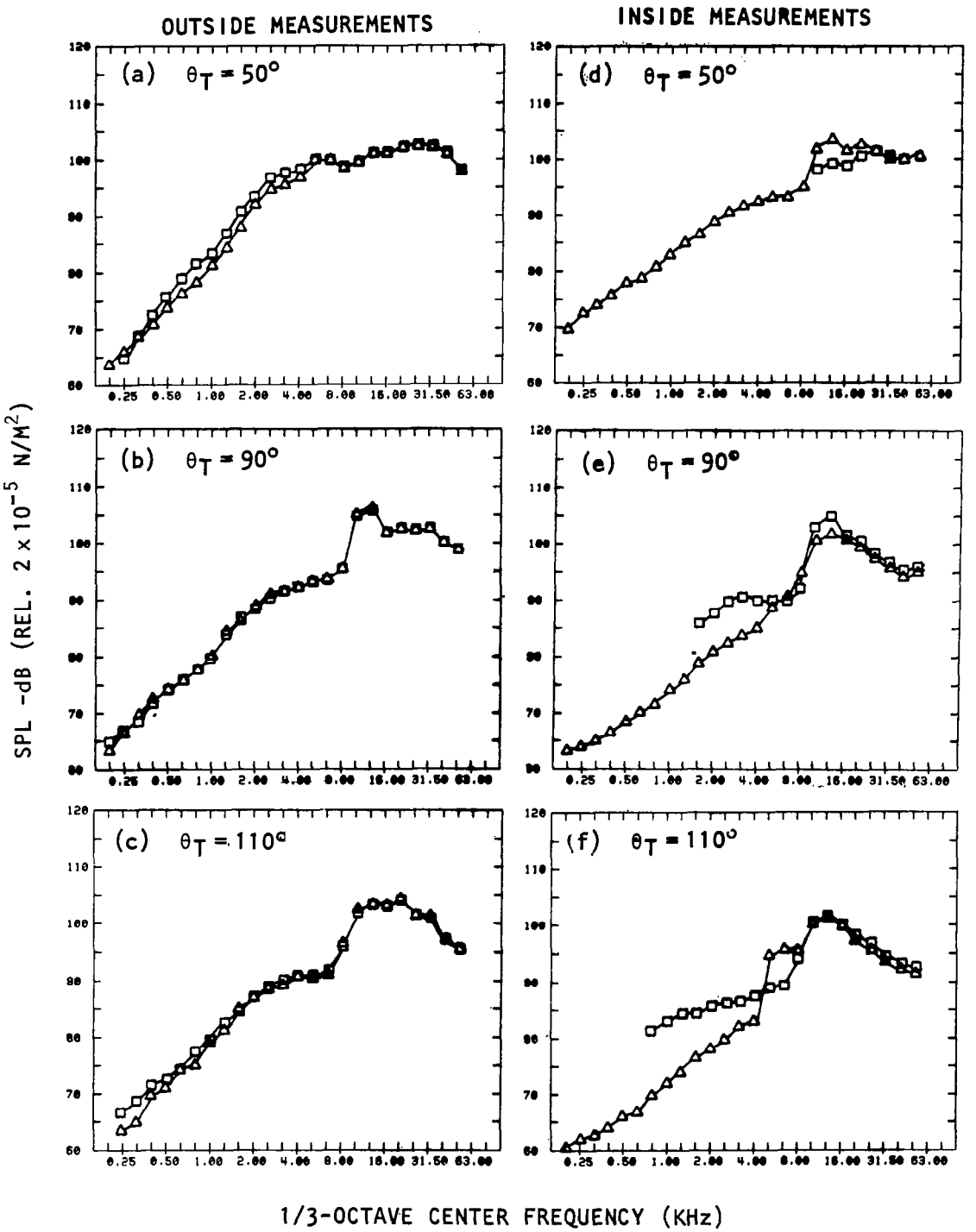

Figure 8.1 Effect of source location corrections on data transformed to IWT conditions. —□—, with source location corrections; —△— without source location corrections. $V_J/a_o = 1.07$, $p_R/p_o = 2.5$ (unheated), $V_T/a_o = 0.09$.

The jet conditions in these figures are identical to those in Figures 8.1(a) through 8.1(c). The effects of source location corrections are much more pronounced in this case, especially at the lower frequencies. This is to be expected since for small measurement distances, the distance between the observer and the nozzle exit (used for data transformation *without* source location corrections) can be considerably different from the true distance between the observer and a low frequency source (used for data transformation *with* source location corrections) located farther downstream of the nozzle exit. Based upon the same arguments, the high-frequency noise in this case is not affected much because these noise sources are located close to the nozzle exit.

Returning now to the free-jet data, it was found that the source location corrections were not important in the regions of spectra dominated by internal noise, as was the case with the shock noise data discussed above. The evidence is presented in Figures 8.2(a) and 8.2(b) for a typical internal noise data point.

Based on the above discussions, it was decided to apply source location corrections (i.e. source location corrections applicable to mixing noise) to all data, irrespective of whether it contained shock noise and/or internal noise. By doing so, the effect of forward velocity on all three noise sources is expected to be correctly interpreted.

8.3.2 Spectral Results

Subcritical Conditions. Typical 1/3-octave SPL spectra for unheated ($V_J/a_o = 0.88$) and heated ($V_J/a_o = 1.25$, $T_R = 870K$) jets are shown in Figures 8.3 and 8.4, respectively, as a function of tunnel Mach number. Spectra for minimum tunnel velocity, and $V_T/a_o = 0.09$, 0.18 and 0.26 are presented for emission angles of $\theta_T = 50°$, 90° and 110°.

The general features exhibited by these spectra at constant emission angles are qualitatively similar to those noted in our previous work (ref. 8.1). With progressive increase in tunnel velocity, the noise levels are reduced at all angles. Note that at the two highest tunnel Mach numbers, i.e. $V_T/a_o = 0.18$ and 0.26, the spectra at the low frequency end ($f \lesssim 1$ KHz) are contaminated in some cases by the free-jet noise. The reductions in noise levels with tunnel velocity are scaled on a relative velocity basis in subsection 8.3.4, where the results with significant contamination have been discarded.

Supercritical Conditions. Typical results for supercritical conditions showing the effect of tunnel Mach number are presented in Figure 8.5. One-third octave spectra at $\theta_T = 50°$, 90° and 110° are presented for a heated jet ($T_R = 870K$) operated at the pressure ratio of 3.86 ($V_J/a_o \doteq 2.25$). In the rear arc [$\theta_T = 50°$, Figure 8.5(a)], the effect of tunnel velocity is similar to that observed previously for the subcritical conditions. This is to be expected since, at this angle, the spectrum is dominated by turbulent mixing noise. In contrast, at $\theta_T = 90°$ and 110°, the static spectrum ($V_T/a_o \doteq 0$) is dominated by shock noise at high frequencies and by mixing noise at low

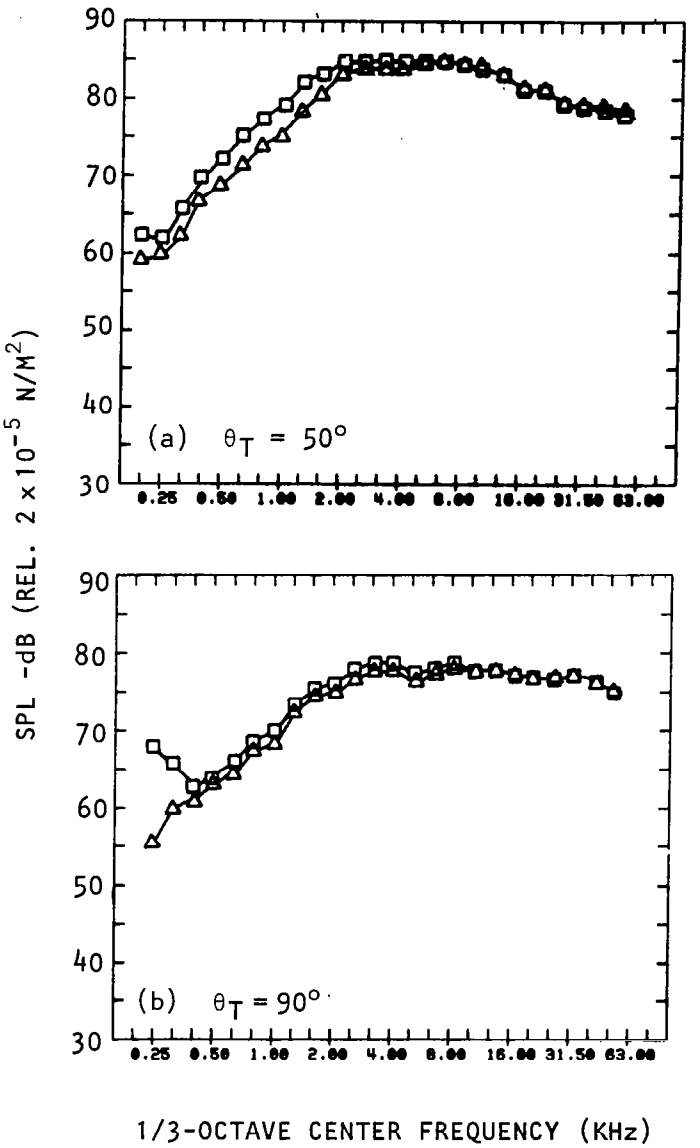

Figure 8.2 Effect of source location corrections on data transformed to IWT conditions. —□—, with source location corrections; —△—, without source location corrections. $V_J/a_o = 0.88$ (internal noise source and jet operated together), $T_R = 520K$, $V_T/a_o = 0.09$.

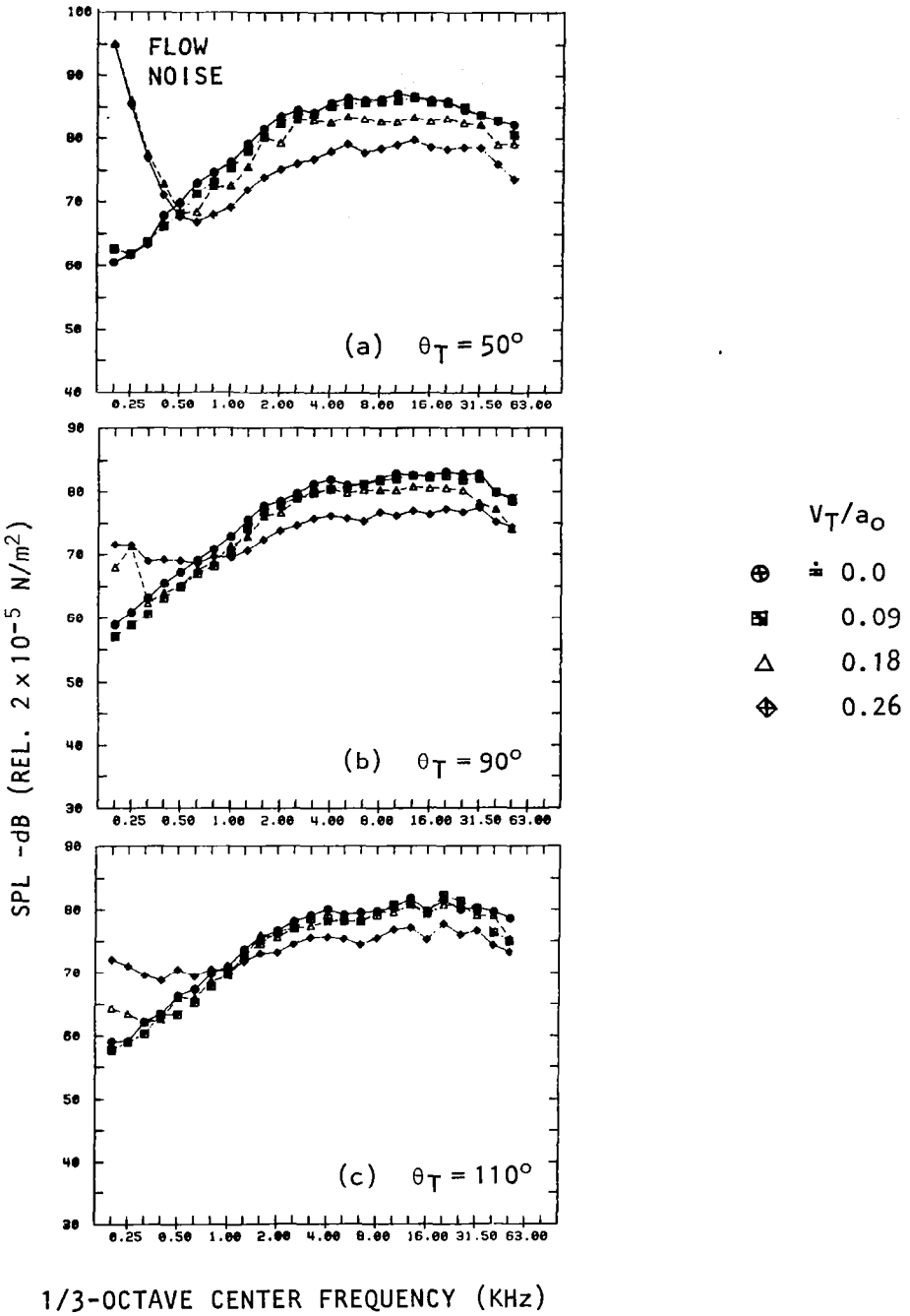

Figure 8.3 Effect of tunnel Mach number on free-jet data transformed to ideal wind tunnel conditions. *(Emission angle and distance (100 d) refer to estimated source location.)* $V_J/a_o = 0.88$ (unheated).

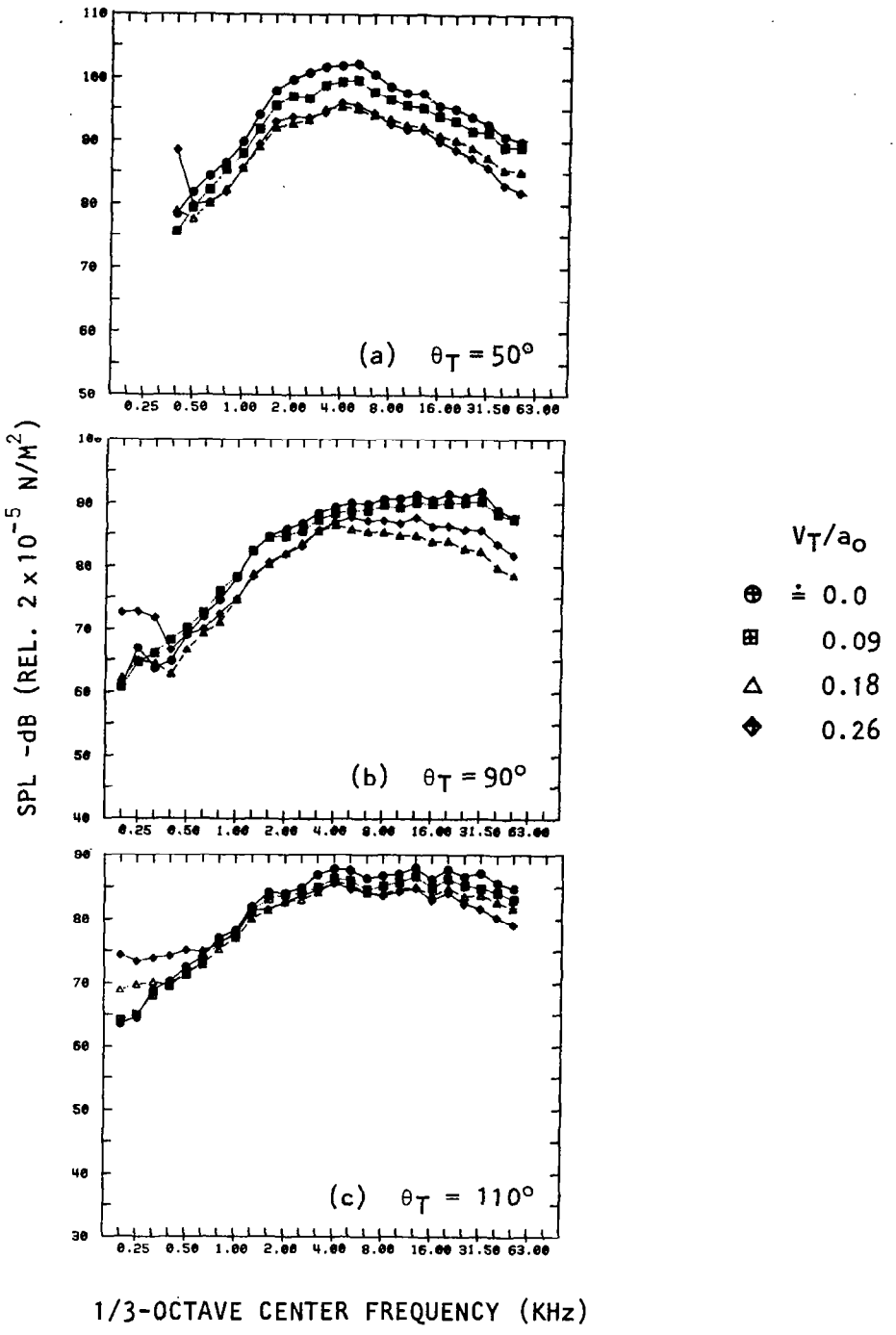

Figure 8.4 Effect of tunnel Mach number on free-jet data transformed to ideal wind tunnel conditions. (*Emission angle and distance (100d) refer to estimated source location).* V_J/a_o = 1.25 (heated), 870K.

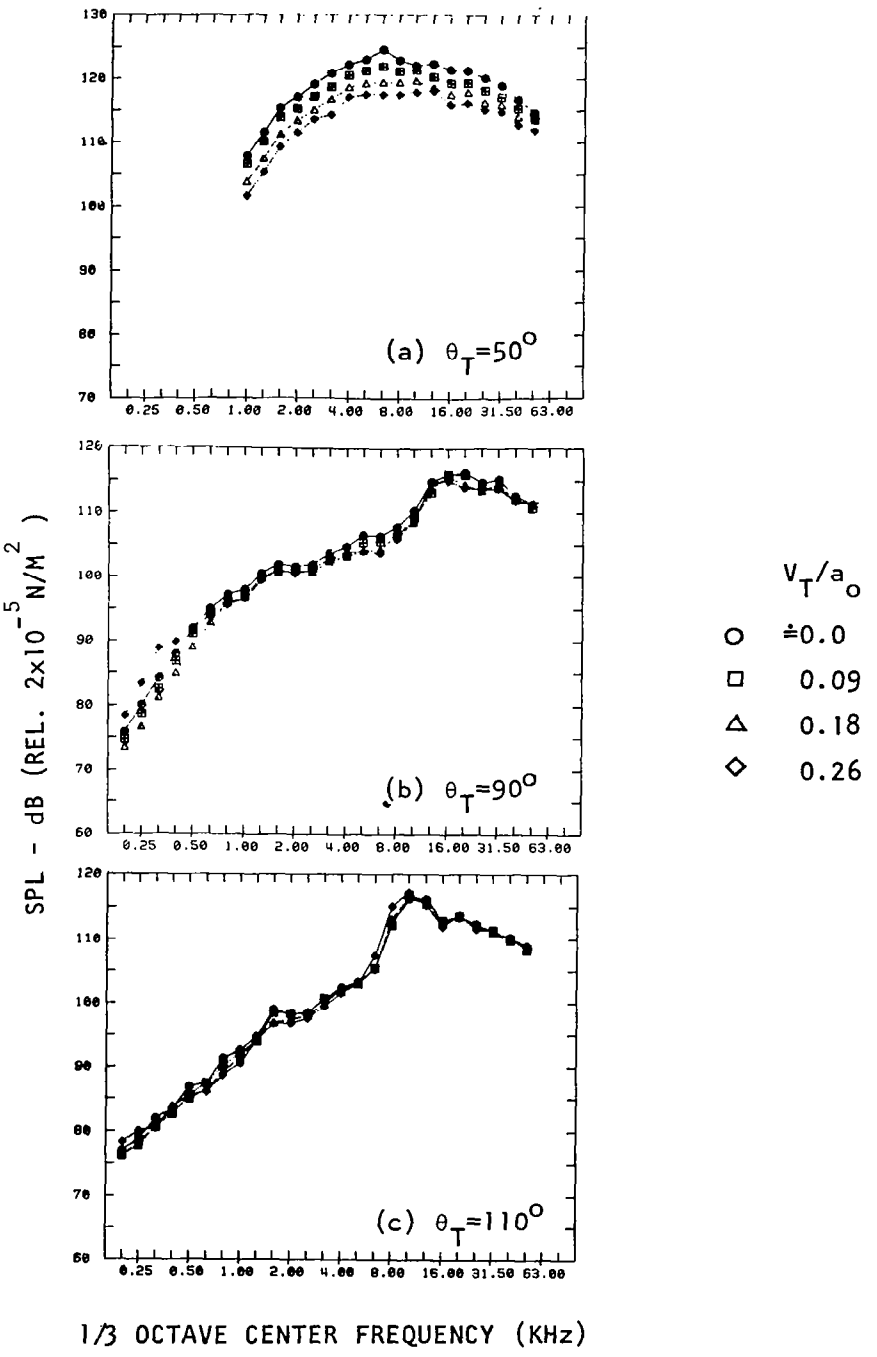

Figure 8.5 Effect of tunnel Mach number on free-jet data transformed to ideal wind tunnel conditions. *(Emission angle and distance (100 d) refer to estimated source location.)* $V_J/a_o = 2.25$ (heated); $T_R = 870K$; $p_R/p_o = 3.86$.

frequencies. At these two angles, there is a small but consistent reduction in noise with tunnel velocity at the low frequencies, whereas at the high frequencies, the noise levels remain relatively unchanged (within measurement accuracy) as the tunnel velocity is increased. The changes in shock noise levels with tunnel velocity will be examined quantitatively in Section 8.4.3.

8.3.3 Overall SPL Results

The overall sound pressure levels were obtained by summing the levels in various one-third octave bands. The summation was carried out over the frequency range from 1 KHz to 40 KHz to avoid flow noise at frequencies below 1 KHz and possible instrumentation noise at frequencies above 40 KHz. The omission of frequencies higher than 40 KHz was necessary only for data at a few subcritical conditions.

The effect of tunnel velocity on the directivity of overall SPL's of the heated jet ($T_R = 870K$) at four pressure ratios (one subcritical and three supercritical) is shown in Figure 8.6. For the sake of clarity, the results at the two intermediate tunnel velocities ($V_T/a_o = 0.09$ and 0.18) are not included here. These results will, however, be included in the quantitative analysis which is discussed in the later parts of this section. For the subcritical jet operating condition [Figure 8.6(a)], a reduction in OASPL with tunnel velocity is obtained at all emission angles. The magnitudes of the reductions increase as the observer moves from the forward arc to the rear arc. This behavior is consistent with that noted in our previous work on flight effects on shock-free jets (ref. 8.1).

When the flight effects shown in Figure 8.6 are examined in a systematic manner as a function of increasing jet pressure ratio, several interesting features are revealed. These features, and the inferences drawn from the observed effects are explained as follows. At the subcritical condition [Figure 8.6(a)], the sound field consists of pure jet mixing noise, and hence a reduction with tunnel velocity is obtained at all angles. As the jet becomes supercritical, the shock noise component is dominant at angles close to $\theta_T = 90°$ and in the forward arc, while the jet mixing noise component is dominant in the rear arc. Thus, with increasing tunnel velocity, as the mixing noise component reduces in level at all angles, the shock noise component becomes more prominent in the forward arc, and this leads to smaller noise reductions at large angles to the jet exhaust. In fact, at the two highest pressure ratios, a careful inspection of the forward arc data points in Figures 8.6(c) and 8.6(d) shows that there is a tendency for the noise levels in the forward arc to increase with tunnel Mach number. In Section 8.4.3, it will be shown that these observed changes in shock noise levels with forward velocity can be attributed directly to the propagation effects which are always present when a stationary sound source is surrounded by a moving fluid (e.g. in a wind tunnel) or when a sound source is convected in a stationary medium. Furthermore, if the strength (i.e. radiated sound power) of the shock noise sources (or internal noise sources) remains constant, then its static directivity will be modified by four powers of the Doppler factor, D_T, in the flight case.

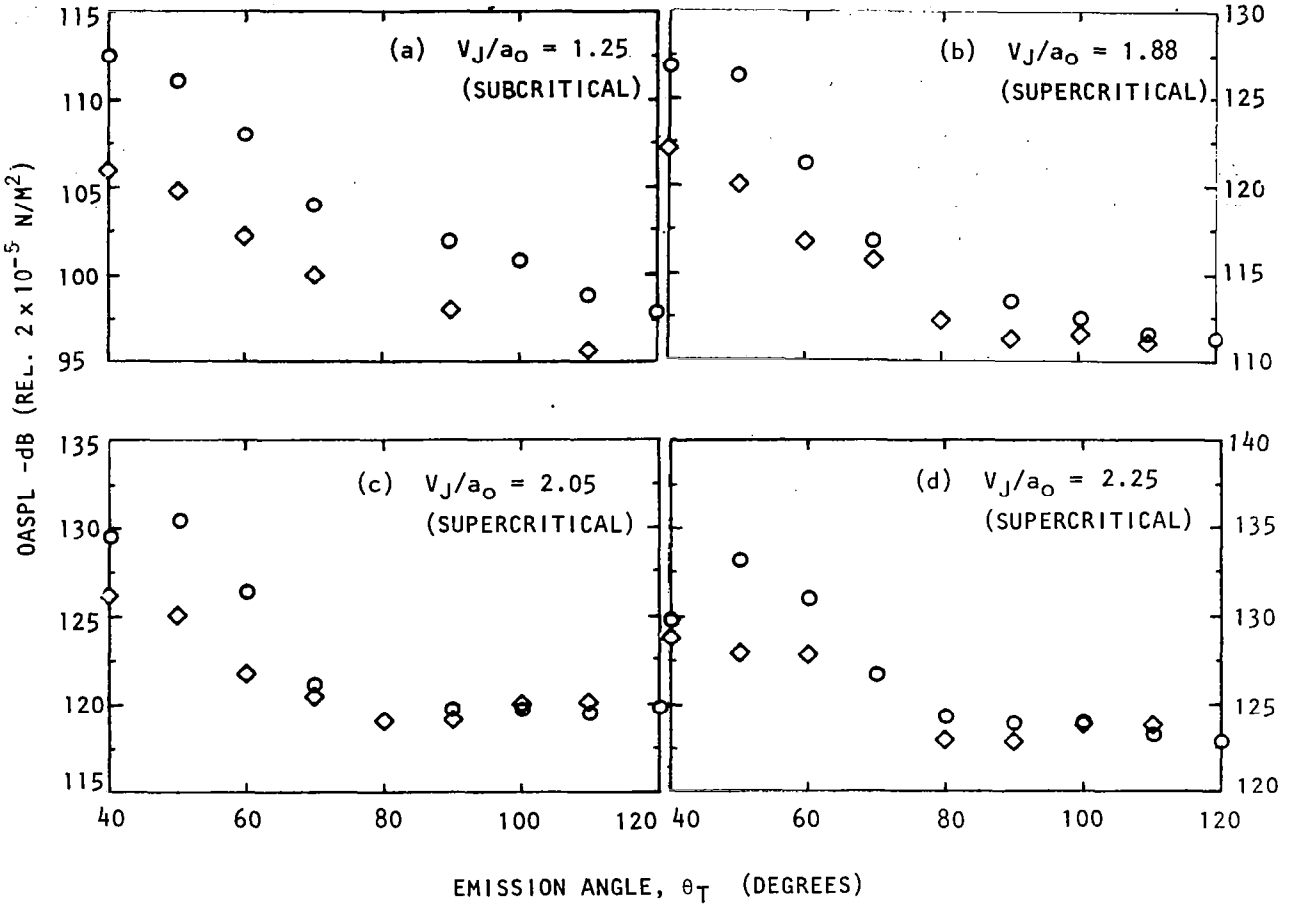

Figure 8.6 Effect of tunnel velocity on the directivity of overall SPL's of heated jet (T_R = 870K). V_T/a_o: O , 0.00, ◇, 0.26. P_R/P_o: (a) 1.43, (b) 2.30, (c) 2.80, (d) 3.86.

Similar results were obtained for unheated jets, and these are shown in Figure 8.7. Here, not only do the results follow the trends discussed above for the heated jet, but a large increase in noise in the forward arc is obtained at the highest pressure ratio [Figure 8.7(c)]. Once again, this observation is entirely consistent with the fact that for a fixed (supercritical) nozzle pressure ratio, the shock noise component is *relatively* stronger for an unheated jet than for a heated jet.

In Figures 8.6 and 8.7, the OASPL's at $\theta_T = 120°$ for the flight case are not available. The reason for this is that in the transformation of free-jet data to IWT conditions, the high-frequency SPL's at this emission angle could not be calculated because these calculations required free-jet data at measurement angles (θ_m) greater than 120°, which were not acquired in the experimental program.

8.3.4 Relative Velocity Scaling of Shock-Free Data

In order to provide a quantitative description of the reductions in OASPL at all emission angles considered, the shock-free results were correlated on the relative velocity ($V_{REL} = V_J - V_T$) basis, as described below.

The overall intensity of turbulent mixing noise at an emission angle, θ_T, can be written to scale according to

$$I(\theta_T) \propto V_{REL}^m \quad V_J^n , \tag{8-1}$$

where the exponents m and n are functions of θ_T. The corresponding OASPL is, therefore, given by

$$OASPL(\theta_T) \propto 10 \log_{10} [V_{REL}^m \quad V_J^n]. \tag{8-2}$$

From the above scaling relationship, the reduction in OASPL from minimum tunnel velocity (V_{To}) to any other tunnel velocity (V_T) can be written as

$$\Delta OASPL(\theta_T) = 10 \log_{10} \left\{ \frac{V_J - V_{To}}{V_J - V_T} \right\}^m . \tag{8-3}$$

The relative velocity exponent m is simply the slope of a line which correlates values of measured ΔOASPL as a function of the velocity parameter $10 \log_{10}[(V_J - V_{To})/V_{REL}]$.

The measured reductions in OASPL at various emission angles for the heated jet are plotted against this velocity parameter in Figure 8.8, and the relative velocity exponent line is drawn through the experimental points at each emission angle, θ_T. The magnitude of the scatter is well within the bounds of the experimental accuracy. Those data points whose spectra displayed inadequate signal-to-noise ratio are not included in this figure.

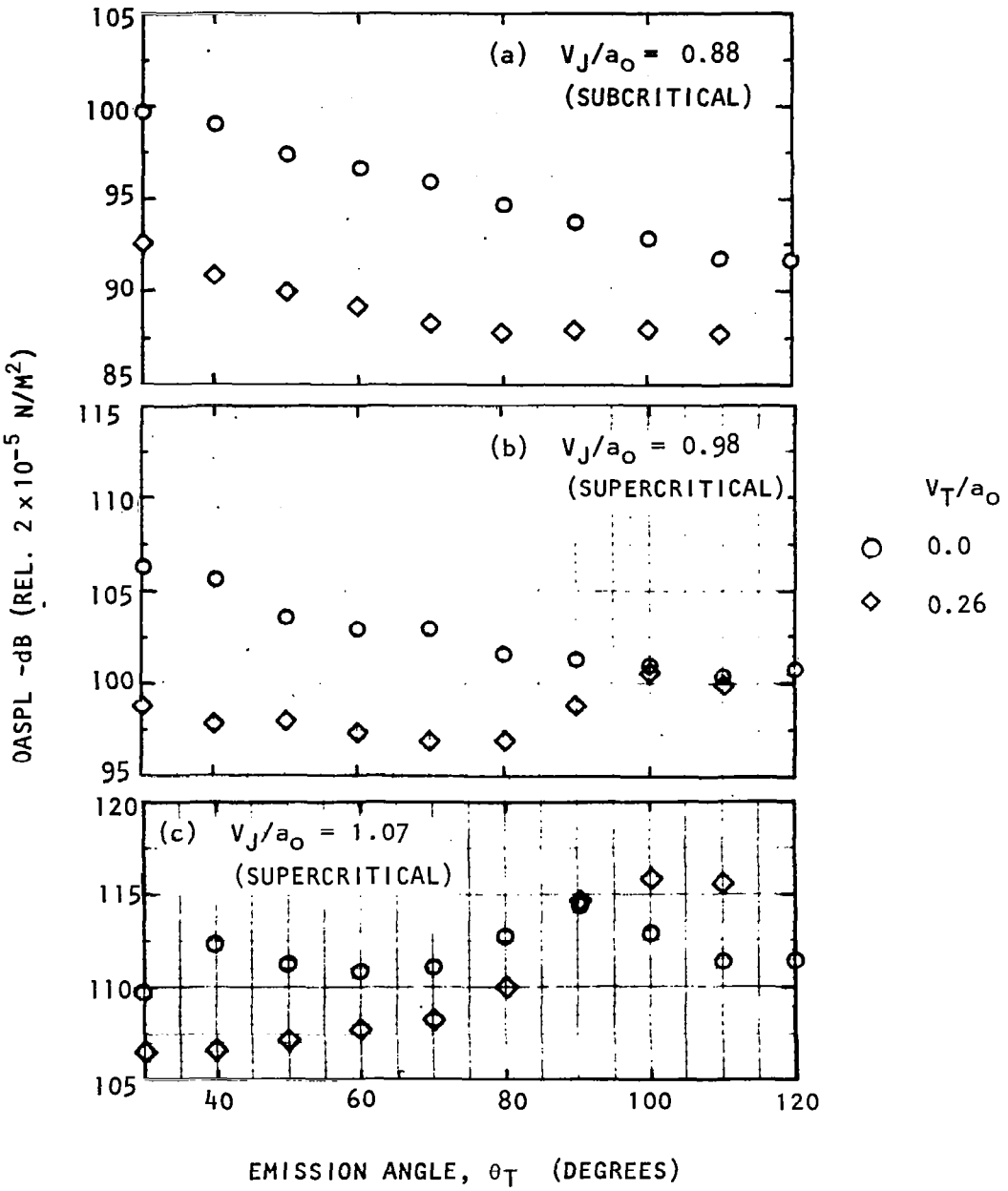

Figure 8.7 Effect of tunnel velocity on the directivity of overall SPL's of unheated jet. p_R/p_o: (a) 1.8, (b), 2.1, (c) 2.5.

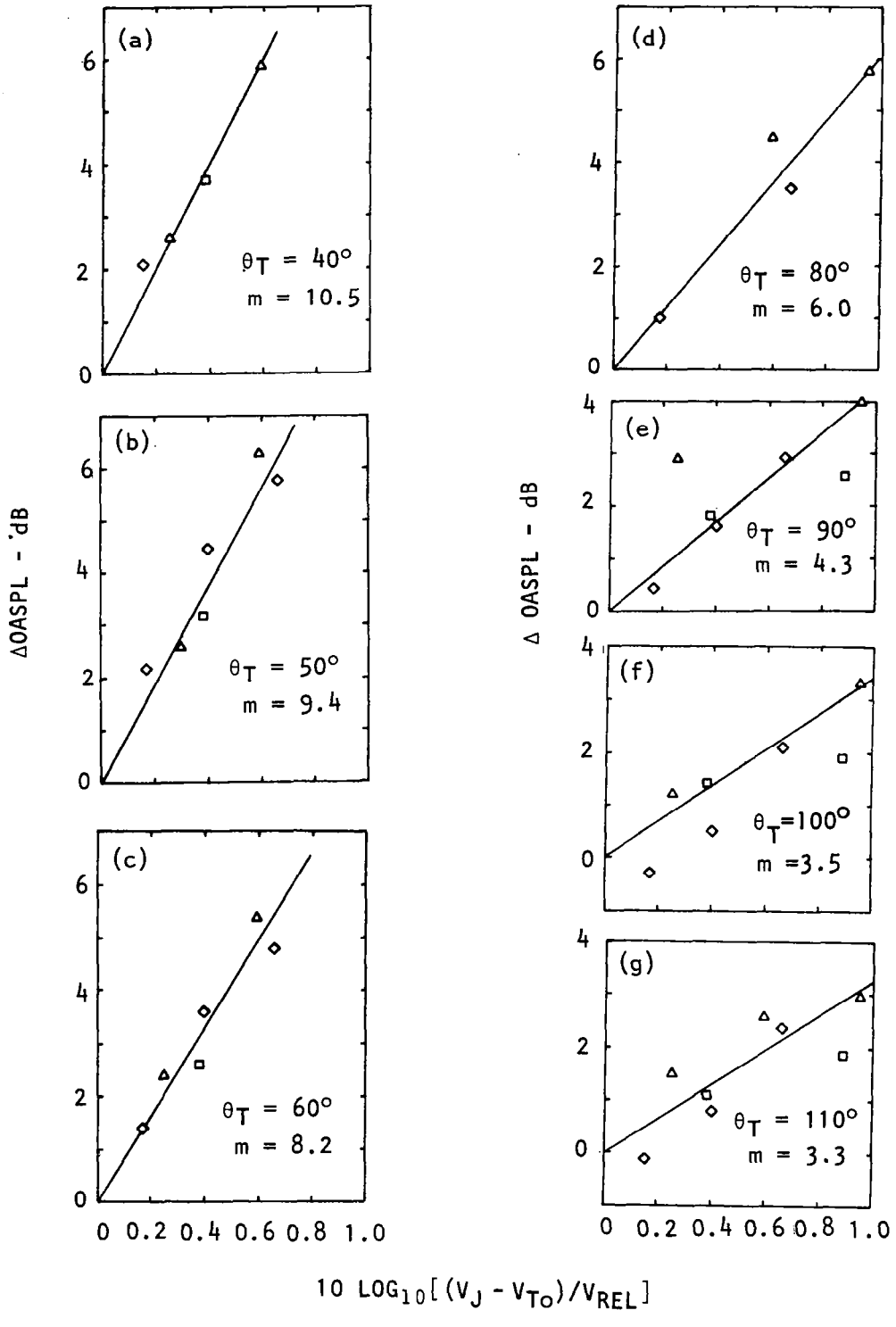

Figure 8.8 Relative velocity scaling of OASPL reductions at various emission angles for shock-free heated jets (T_R = 870K). V_J/a_o: □ , 0.89; △ , 1.25; ◇ , 1.70.

Finally, the variation of relative velocity exponent m with emission angle θ_T is presented in Figure 8.9. Also shown in this figure are the exponent values obtained in our previous work using unheated jets (ref. 8.1), the Pratt and Whitney data for heated jets (ref. 8.2), the Rolls-Royce full-scale flight data (ref. 8.3), and the Douglas full-scale flight data (ref. 8.6). The P&W data and the present results for heated jets agree quite well with each other and also with the Douglas flight data. An important observation that can be made from this figure is that shock-free heated jets provide a higher exponent (i.e., *higher noise reductions with forward velocity*) than shock-free unheated jets in the rear arc.

The comparison of relative velocity exponents derived from free-jet simulation experiments with the envelope of exponents obtained from full-scale flight experiments of Rolls-Royce is rather discouraging. At low angles to the jet exhaust, it appears that flight simulation experiments are in "reasonable" agreement with the actual flight results. At larger angles, however, the reductions in noise levels with forward motion observed in the model simulation experiments are larger than those measured in the flight tests. At $\theta_T = 90°$, there is little or no change in the aircraft flight noise levels, whereas the free-jet experiments indicate significant noise reductions which scale on approximately 4 to 5 powers of the relative velocity (for heated jets).

The discrepancy between the inflight simulation results and the actual flight results thus still remains to be resolved. It is readily admitted that there are subtle differences in the two sets of experiments: in the flight simulation tests, there is no relative motion between the source and the observer, whereas in the flyover tests, the noise source is being convected relative to a stationary observer. However, further considerations also show that none of the features associated with source motion (for example, eddy convection velocity effects, source acceleration effects, etc.) will affect the results at 90° to the direction of motion. The flight simulation results presented here *are* guaranteed to be dominated by pure jet mixing noise. On the other hand, the full-scale flight results cannot be *guaranteed* to be free from engine internal noise or other noise sources. The role played by such non-jet mixing noise sources, if significantly present, is demonstrated in Section 8.4, where the effects of forward velocity on jet noise in the presence of internal noise is examined and compared with the same full-scale flight data considered above.

8.4 EXPERIMENTAL RESULTS WITH INTERNAL NOISE

8.4.1 Spectral Results

Typical one-third octave SPL spectra showing the effects of tunnel velocity on jet noise contaminated with internal noise are presented in Figure 8.10 for an unheated jet and in Figure 8.11 for a heated jet. It is reminded that in each case the free-jet data have been transformed to the ideal wind tunnel conditions, and are expressed for the emission distance of 100 model-jet diameters. The results are shown at the emission angles of 50°, 90° and 110°, at $V_J/a_o = 0.49$ for the unheated jet and $V_J/a_o = 0.93$ for

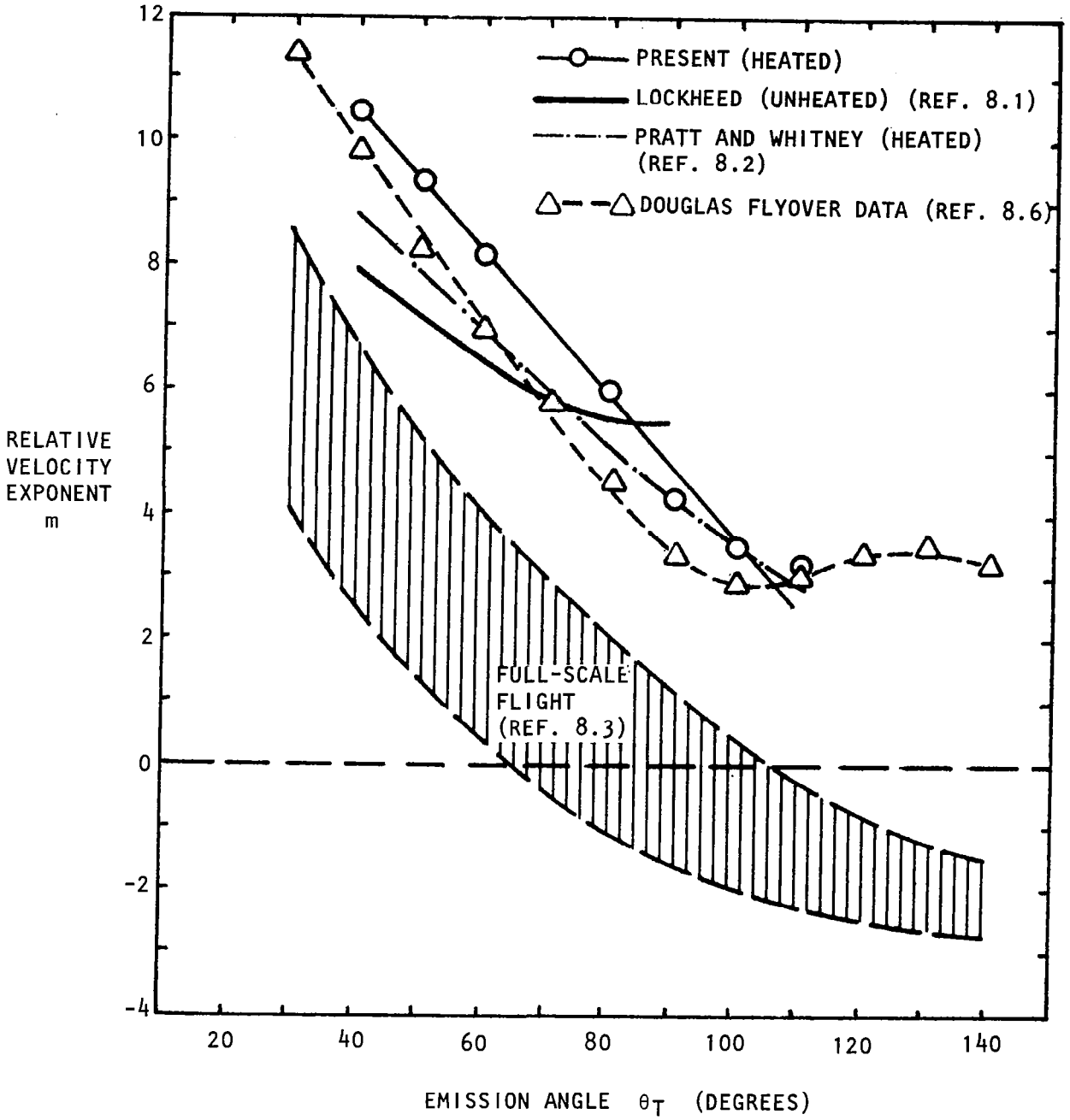

Figure 8.9 Variation of relative velocity exponent with emission angle.

the heated jet. As before, the free-jet velocities are given by V_T/a_o = minimum, 0.09, 0.18, and 0.26.

These results are drastically different from the results presented earlier for pure jet mixing noise, especially at $\theta_T = 90°$ and 110°. The internal noise contribution is dominant mainly at frequencies higher than about 5 KHz, as described in Section 3.4. Figures 8.10 and 8.11 show that in the rear arc ($\theta_T = 50°$), the noise levels decrease with forward velocity at all frequencies where the signal-to-noise ratio is adequate. At $\theta_T = 90°$, there is very little change at $V_T/a_o = 0.09$, while for the higher tunnel Mach numbers, the SPL's show a slight increase instead of the reductions noted previously for pure jet mixing noise. In the forward arc [Figures 8.10(c) and 8.11(c)], the noise levels increase significantly with forward velocity. Finally, at all angles, the low-frequency parts of the spectra at the two highest Mach numbers are contaminated by free-jet noise. However, this is of no real concern, since the low-frequency part essentially consists of the jet mixing noise component, which has already been investigated earlier.

The effect of tunnel velocity on internal noise thus appears to reduce the noise in the rear arc and increase the noise in the forward arc. The OASPL results corresponding to the spectral results discussed above are presented in the next subsection.

8.4.2 Overall SPL Results

Typical directivities of overall SPL's showing the effects of tunnel velocity on jet noise contaminated with internal noise are presented in Figure 8.12 for an unheated jet operated at three jet velocities, i.e., $V_J/a_o = 0.49$, 0.67 and 0.88. For the sake of clarity, data for the minimum and the maximum tunnel velocities only are shown. As pointed out in Section 3.3, the contribution of internal noise to the overall SPL, although *significant* at each jet velocity, is maximum at the lowest jet velocity and minimum at the highest jet velocity.

At $V_J/a_o = 0.49$ [Figure 8.12(a)], the internal noise contribution *relative* to the jet mixing noise contribution is highest. For this condition, a significant noise reduction with forward velocity is obtained in the rear arc, there is little change at $\theta_T = 90°$, and a significant noise increase is obtained in the forward arc. As the jet velocity is increased to $V_J/a_o = 0.67$ [see Figure 8.12(b)], the reductions in the rear arc are increased while the noise levels at $\theta_T = 90°$ and in the forward arc show very little change. At the highest jet velocity $V_J/a_o = 0.88$ [Figure 8.12(c)], reductions in noise levels are obtained at all emission angles, showing that at this condition, the OASPL's are primarily controlled by the jet mixing noise contribution.

The results shown in Figure 8.12 were for unheated jets. Similar results were obtained for heated jets, and these are shown in Figures 8.13(a), 8.13(b) and 8.13(c) for $V_J/a_o = 0.89$, 0.93 and 1.32, respectively. These results also show that when the internal noise contribution is comparable to or higher than the jet mixing noise contribution, reduction in noise levels are obtained in

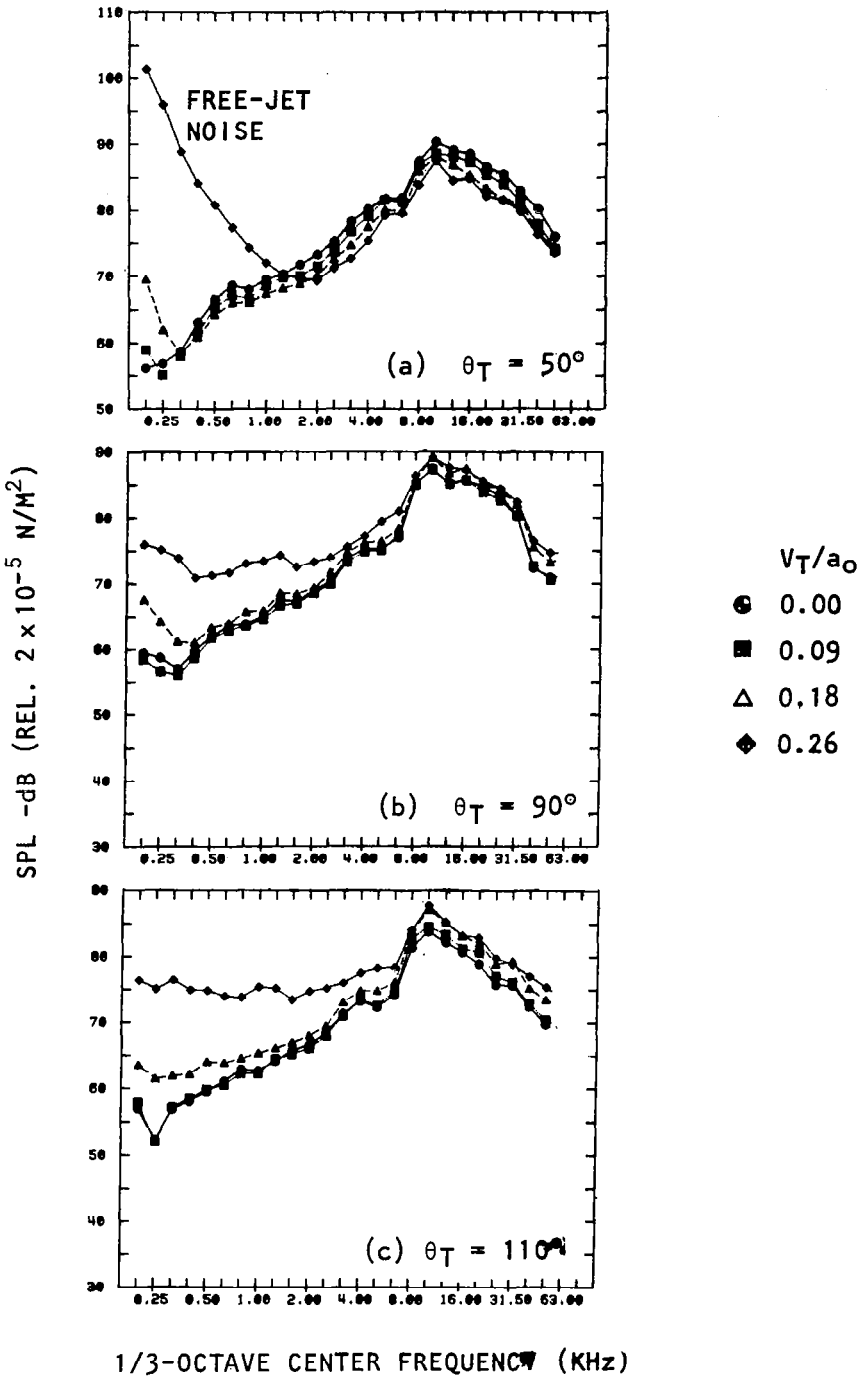

Figure 8.10 Effect of tunnel Mach number on free-jet data (for jet noise with internal noise) transformed to ideal-wind-tunnel conditions. V_J/a_o = 0.49 (unheated).

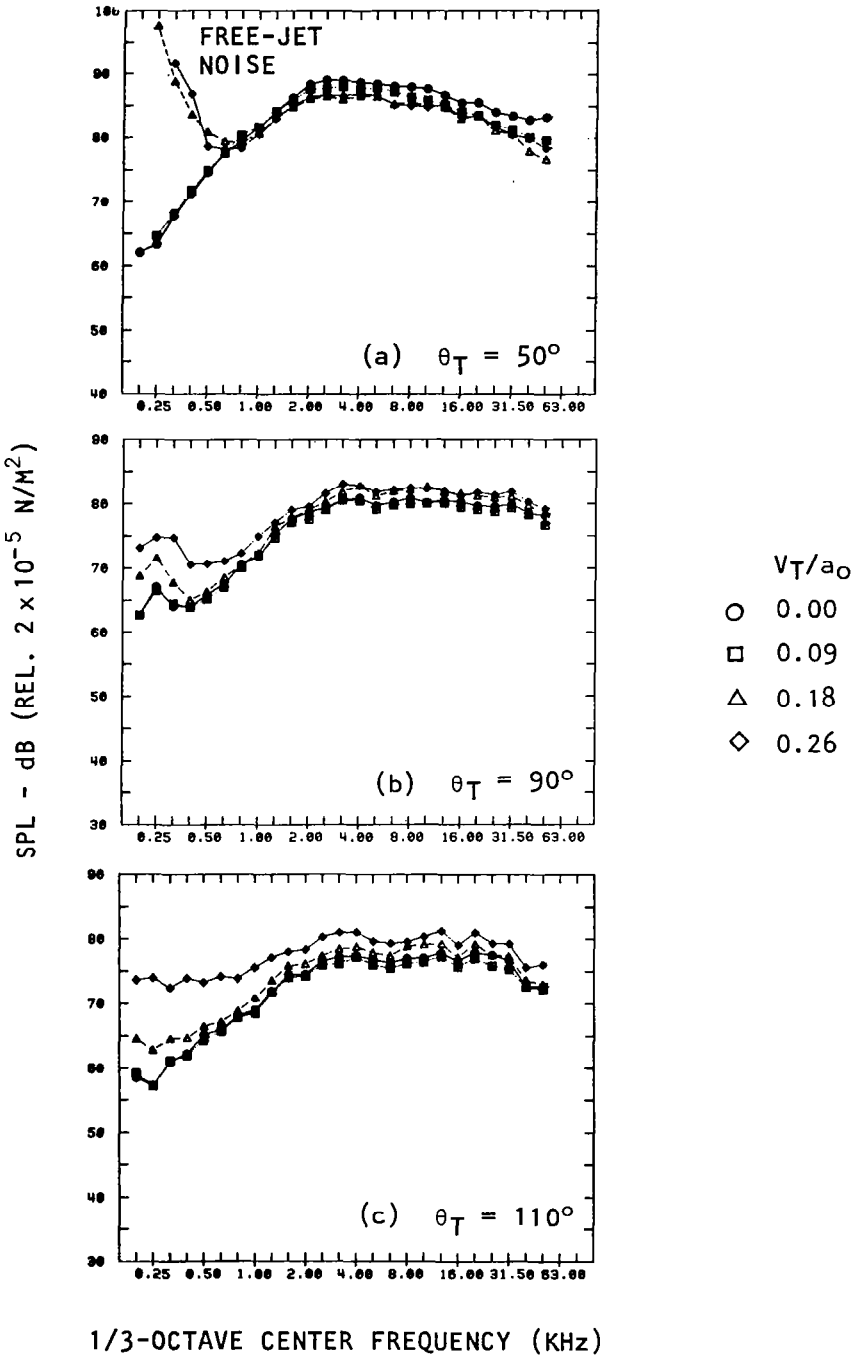

Figure 8.11 Effect of tunnel Mach number on free-jet data (for jet noise with internal noise) transformed to ideal-wind-tunnel conditions. V_J/a_o = 0.93 (heated), T_R = 533K.

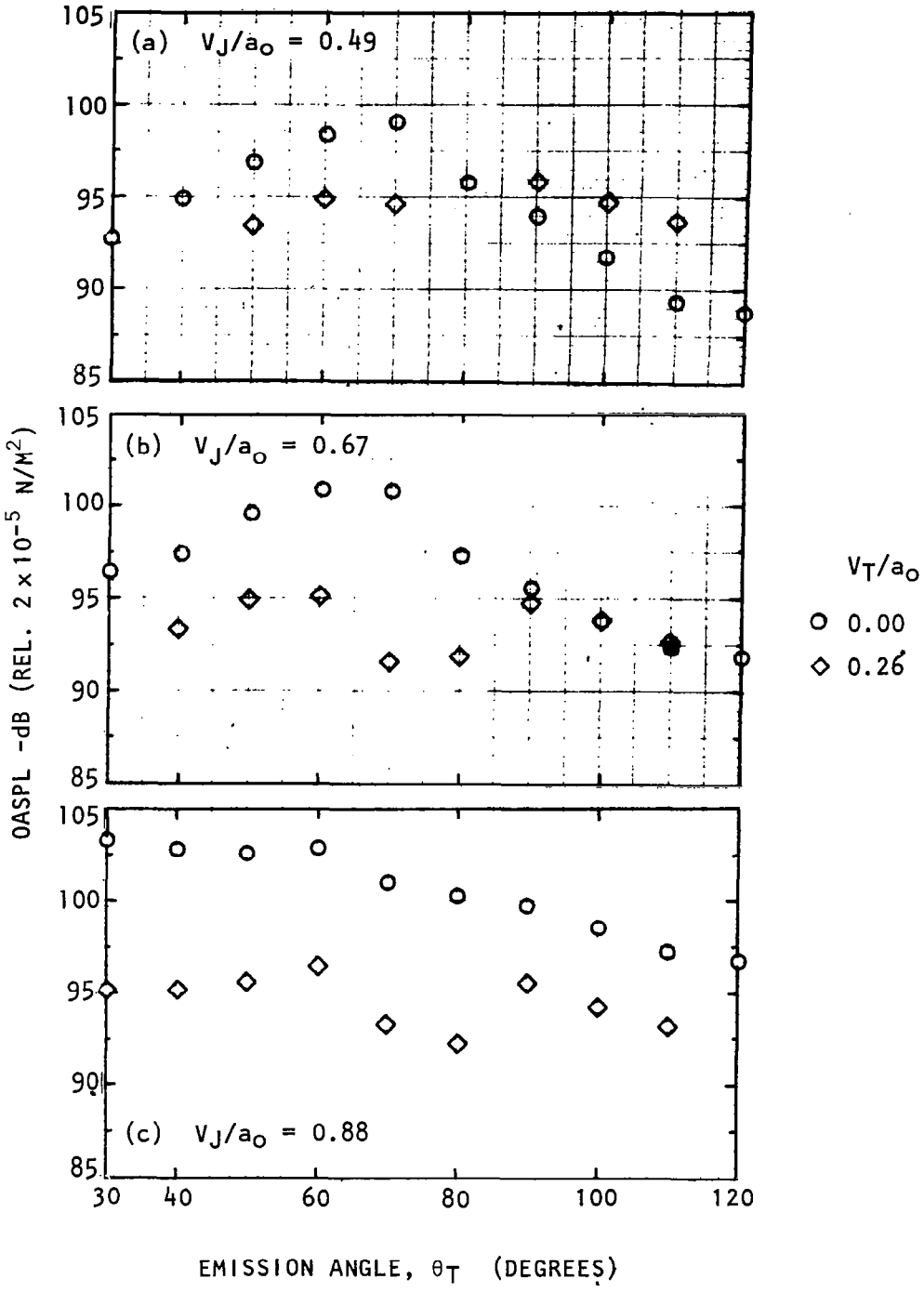

Figure 8.12 Effect of tunnel velocity on the directivity of overall SPL's for unheated jet with internal noise.

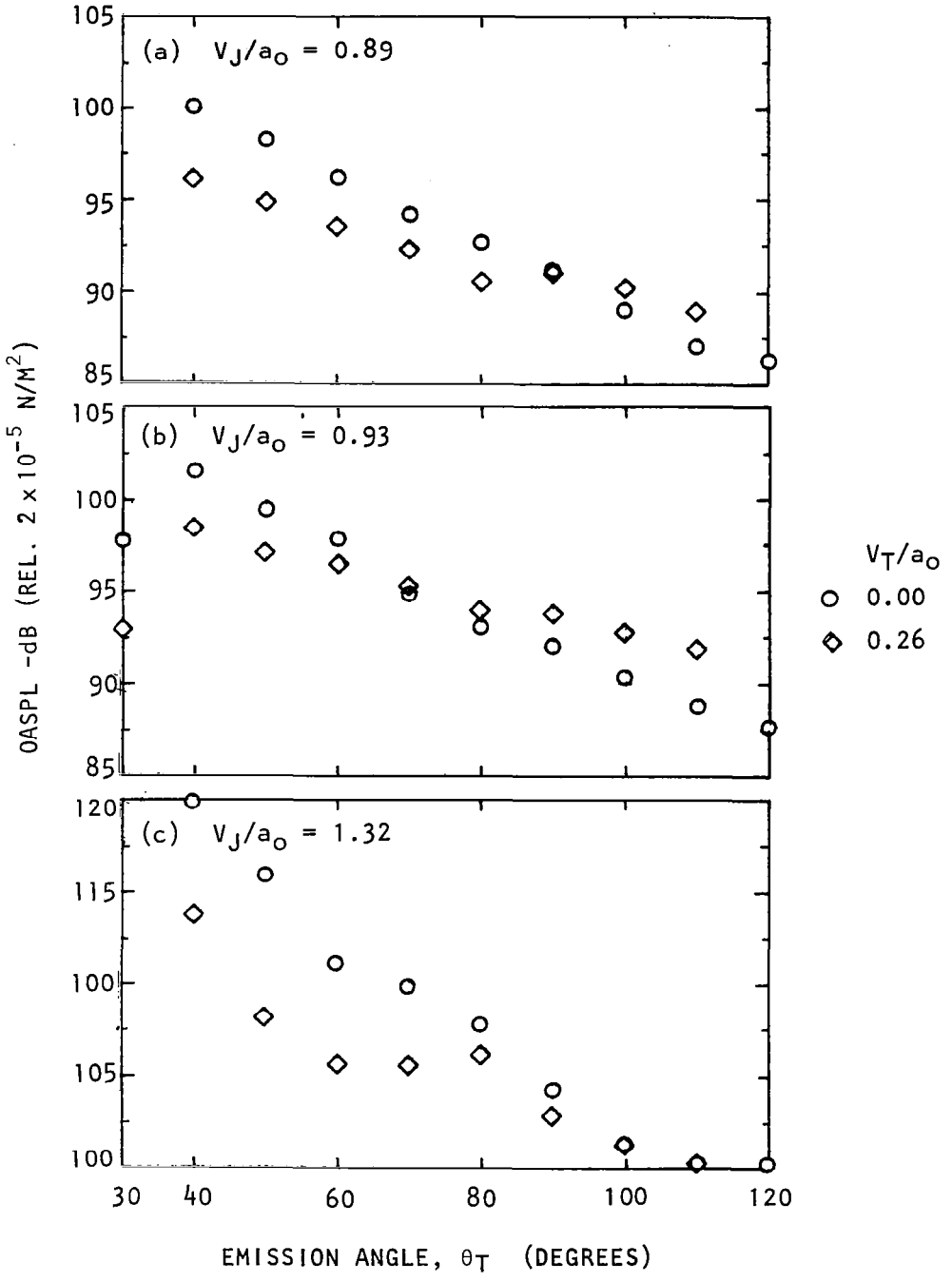

Figure 8.13 Effect of tunnel velocity on the directivity of overall SPL's for heated jet (T_R = 533K) with internal noise.

the rear arc, there is little change around $\theta_T = 90°$, and noise levels increase in the forward arc.

The features discussed above appear to be qualitatively consistent with the results from the full-scale flight experiments, which were shown in terms of the relative velocity exponent in Figure 8.9. In order to see if the present simulation results with internal noise agree quantitatively with the full-scale flight results, the OASPL changes with forward velocity obtained in the present experiments were scaled on the relative velocity basis, as was done previously for pure jet mixing noise results. The OASPL changes at various emission angles are plotted against the relative velocity parameter, $10 \log_{10}[(V_J - V_{TO})/V_{REL}]$, in Figure 8.14. Unlike the results presented previously for jet noise *without* internal noise (Figure 8.8), the present results (i.e. jet noise *with* internal noise) do not display a *single* exponent value. Instead, the present results exhibit a *range* of exponent values (m) at each emission angle θ_T. The *upper limit* of m is normally associated with "high jet velocity/low tunnel velocity" conditions, where the contribution from jet mixing noise *relative* to the contribution from internal noise is maximum. Conversely, the *lower limit* of m is normally associated with "low jet velocity/high tunnel velocity" conditions, where the contribution from internal noise *relative* to the contribution from jet mixing noise is maximum. Thus, the exponent value in general varies between the two limits (at a given emission angle) depending upon the relative contributions from mixing noise and internal noise.

The ranges of exponent values obtained in this manner at all emission angles are superimposed on the exponent values obtained from full-scale aircraft flight data of Rolls-Royce (ref. 8.3), Douglas (ref. 8.6) and SNECMA (ref. 8.7) in Figure 8.15. The agreement between the present simulation results and the Douglas flight data is very good. This figure demonstrates that if the jet mixing noise data are contaminated with internal noise, one could indeed obtain relative velocity exponents that fall within the envelope of the Rolls-Royce and SNECMA full-scale flight data. As shown in Figure 8.15, the exponent values decrease as the degree of contamination from internal noise increases. It is interesting to note that the lower limiting value (obtained from the present experiments) of the exponent m at each emission angle θ_T is very close to the lower limit of the envelope of exponent values obtained from full-scale flight data of reference 8.3.

If it is assumed that there are no other explanations for the flight effects anomalies, it is tempting to conclude from the above comparisons that the full-scale flight data which do not agree with the flight simulation data may have been contaminated with internal noise. Although the internal noise may have been masked by jet mixing noise in the static case, it may well have influenced the changes in noise levels with forward velocity due to decreased contribution from mixing noise in flight. Of course, the significance of internal noise and shock noise in producing the anomalies between full-scale flight data and flight-simulation data has been recognized and/or hypothesized in the past by several investigators, and the results of the present study serve to demonstrate these effects in a systematic and comprehensive manner.

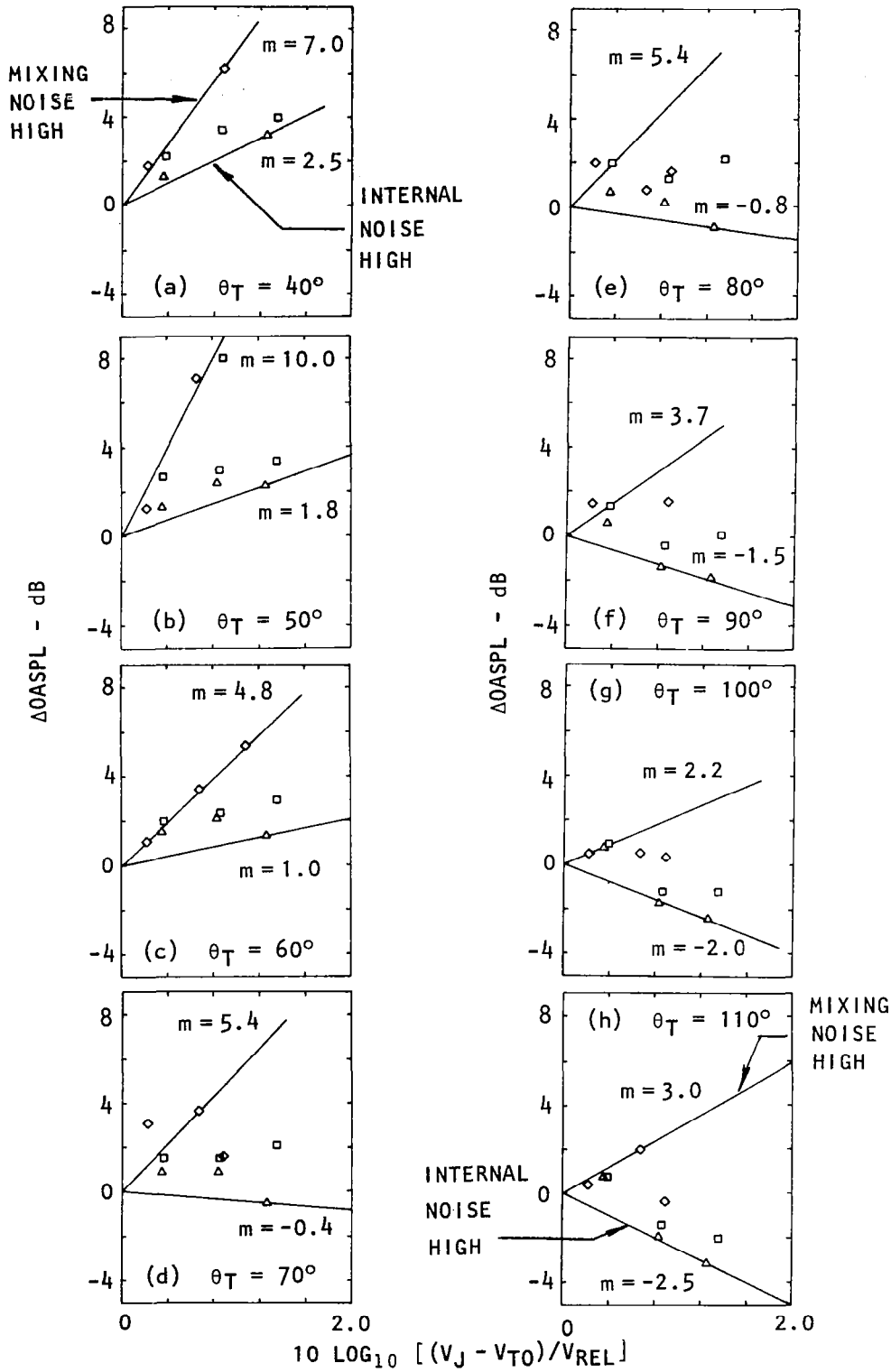

Figure 8.14 Relative velocity scaling of OASPL reductions at various emission angles for heated jets ($T_R \doteq 533K$) with internal noise. V_J/a_o: ◇ , 1.32; △ , 0.93; □ , 0.89.

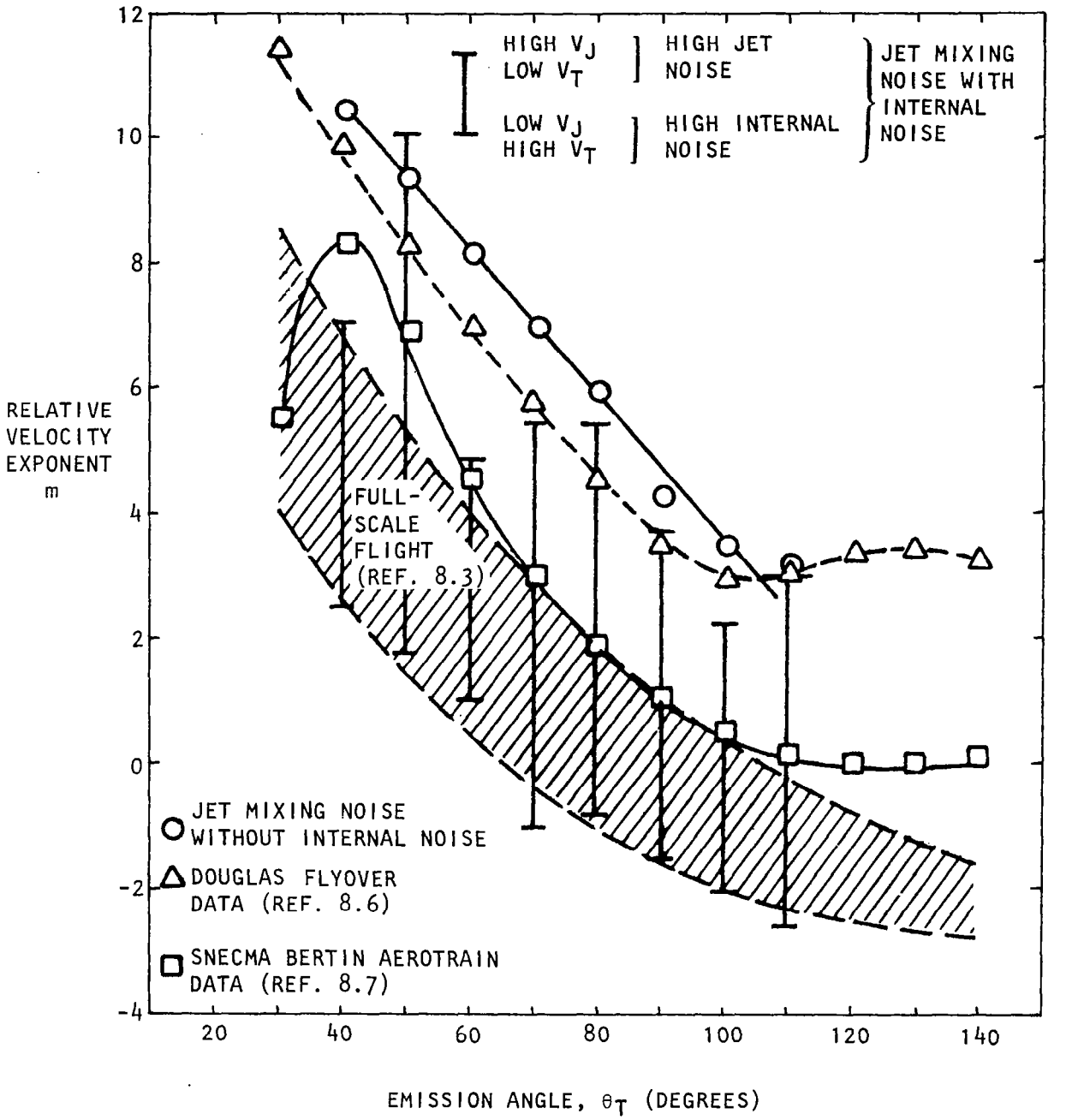

Figure 8.15 Variation of relative velocity exponent with emission angle with and without internal noise.

8.4.3 Scaling of Internal Noise

Figure 8.16 presents a composite picture of how jet noise data from the present experiments behave as a function of emission angle, θ_T, feee-jet velocity, V_T, and the relative velocity factor $10 \log_{10}[(V_J - V_{TO})/V_{REL}]$ when "contaminated" with internal noise; here the data are plotted in the form of ΔOASPL *versus* V_T and the above relative velocity factor (at each emission angle) for $V_J/a_o = 0.89$. In Figure 8.17, results are given in the same form for a slightly higher primary-jet velocity, $V_J/a_o = 0.93$. In both cases, at the lowest free-jet velocity (~30 m/s) a reduction in noise level (i.e. positive ΔOASPL) is obtained at every emission angle – the expected result for jet *mixing noise* – but as the free jet velocity is increased, a consistent trend of increase in noise is seen at angles greater than 90° (Figure 8.16) or 70° (Figure 8.17). This trend, which leads to negative ΔOASPL's in the forward arc, is too consistent to be fortuitous or to be the result of experimental error, and therefore efforts were made to investigate possible explanations for this. As might be expected, the main reason for the trend appears to be the so-called "convective amplification" of internal noise radiation by the free-jet flow, that is by forward motion as discussed in detail below.

Discussion. In most of the work described in this report, we are concerned with the relation between the power spectral density (psd) of the sound pressure at a point outside the free jet, P_o, and the corresponding psd value inside the free jet, P_T, of outward-going waves from the source region. The psd's P_o, P_T are defined (and measured) on a common ray path for which the wavenormal angles inside and outside the free jet are related (at the same frequency) by the equivalent of Snell's law.

$$\frac{a_T}{\cos\theta_T} + V_T = \frac{a_o}{\cos\theta_o} \qquad (8\text{-}4)$$

At a given frequency, this is the same as holding the axial wavenumber (k_x) constant, which is actually the more basic relation: it follows directly from using an *axially uniform* parallel flow model of the real free-jet flow field at any given axial location.

Provided the measurements are taken inside and outside the free-jet on the constant-k_x ray path, the *actual directivity* of the source, be it an experimental point source or a model jet, is of no consequence (as long as internal reflection effects are insignificant) when we consider the *transformation of free-jet flight simulation data*, it requires only a simple calculation to determine, θ_m, the angle of the microphone outside the free jet which receives radiation that is emitted at the required wavenormal angle θ_T (equal to the flyover emission time angle). Again, the actual directional characteristics of the source are unimportant.

Analysis of Forward Motion Effects on Internal Noise and Shock-Associated Noise. It is when we need to *analyze* estimated ideal wind tunnel data to determine the *change* in directivity of jet mixing noise, internal noise, shock-associated noise, etc., with forward velocity (V_T), that a

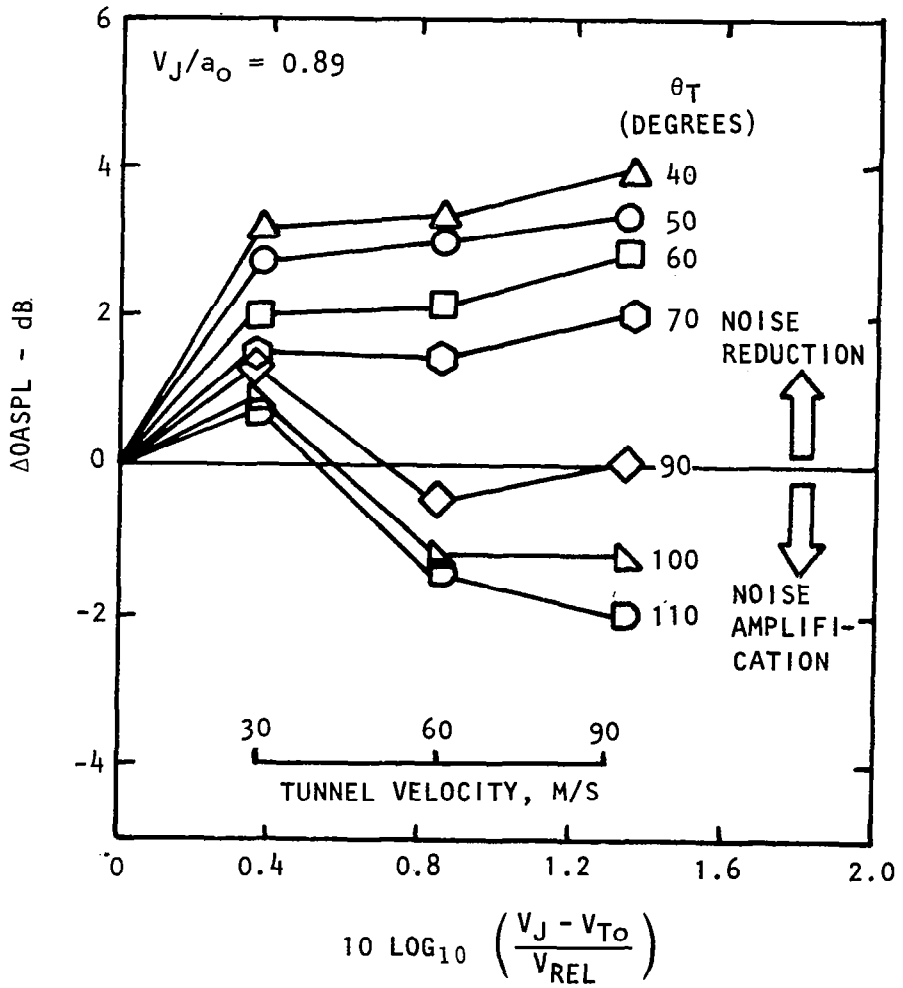

Figure 8.16 Relative velocity scaling of OASPL reductions at various emission angles for a heated jet ($V_J/a_o = 0.89$, $T_R = 533K$) with internal noise.

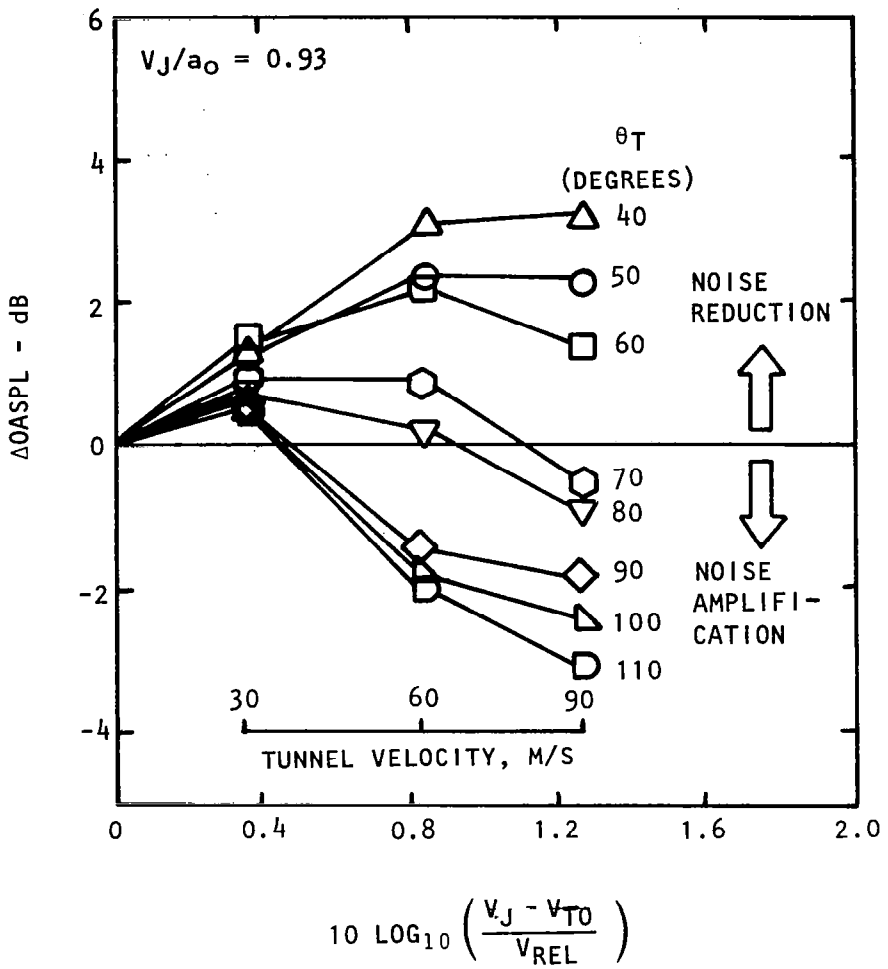

Figure 8.17 Relative velocity scaling of OASPL reductions at various emission angles for a heated jet ($V_J/a_o = 0.93$, T_R = 533K) with internal noise.

slightly different approach is required although the same principles are still employed. In particular, for reasons discussed below, k_x is held constant (or phase speed if the frequency is held constant) as V_T is varied, i.e.

$$\frac{\omega}{k_x} = \frac{a_T}{\cos\theta_T} + V_T = \text{const.} \tag{8-5}$$

To justify this, consider the case of internal noise radiation with the primary-jet shear layer modeled as an axially uniform, parallel sheared flow; then k_x is constant across the *primary* shear layer or

$$\frac{a_T}{\cos\theta_T} + V_T = \frac{a_J}{\cos\theta_J} + V_J \tag{8-6}$$

Here V_J is the primary nozzle exit velocity and θ_J is the wavenormal angle of internal noise wave-fronts propagating away from the nozzle exit toward the primary-jet shear layer (see Figure 8.18). The angle θ_J can be interpreted as the directivity angle of the internal noise radiation within the potential core of the primary jet. Clearly, if θ_T is adjusted so that the left-hand side of equation (8-6) is held constant (as V_T is varied) and the jet exit conditions V_J, a_J are held fixed, then θ_J remains constant and then any change in the radiated sound pressure can be attributed solely to forward velocity (V_T) effects and not to changes resulting from, in effect, refraction of the source directivity pattern.

In principle the constant in equation (8-5) and hence the required θ_T values can be evaluated by specifying certain values, θ_{To}, in the static case, i.e. θ_T is calculated from

$$\frac{a_T}{\cos\theta_T} + V_T = \frac{a_o}{\cos\theta_{To}} \tag{8-7}$$

For example, in the measured data presented below, θ_{To}, is varied between 40° and 120° in steps of 10°; the corresponding wavenormal angles, θ_T, at the highest free-jet velocity considered ($V_T = 0.26a_T$) as calculated from equation (8-7) are given in Table 8.1, assuming $a_T = a_o$. Except at the two smallest angles the wavenormal angle does not have to be changed significantly in order to hold the phase speed constant. Hence, in the analysis of the measured data presented below, this effect is ignored and θ_T is set to equal to θ_{To}.

Actually jet *mixing* noise would be analyzed in a different way, involving Doppler-shifted frequencies (although k_x is still held constant) and is not discussed further here; measurements have been analyzed on the basis of OASPL directivity changes with V_T in reference 8.1 and a theoretical investigation based on Lilley equation solutions was described in the same reference.

The question considered here is: what is the expected effect of V_T on internal or shock-associated noise radiation from the model primary jet? In

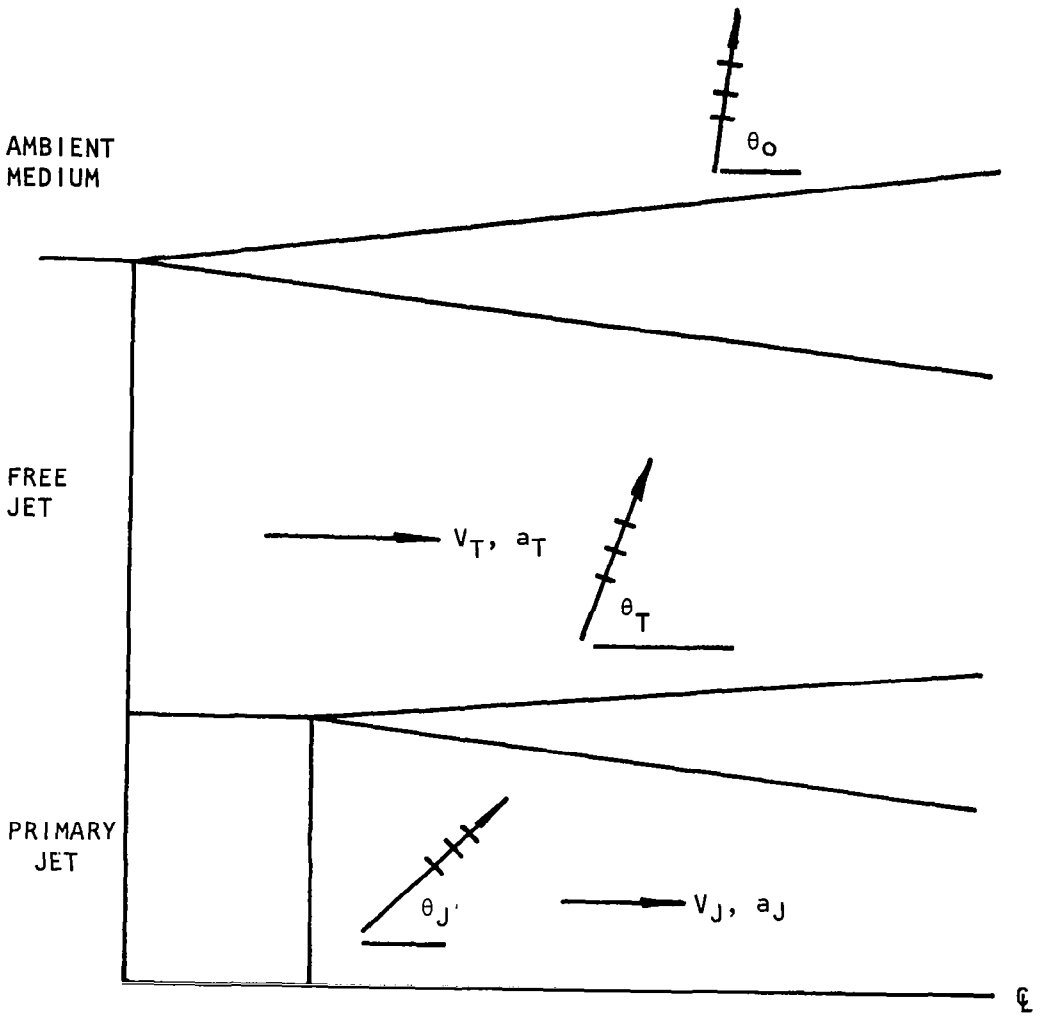

Figure 8.18 Wavenormal directions linked by constant phase speed condition in primary jet, free jet and outside free jet.

Table 8.1 Equal phase-speed wavenormal angles at free-jet velocities zero and $0.26a_T$

$V_T = 0$ θ_{To} (degrees)	$V_T = 0.26a_T$ θ_T (degrees)
40	17.7
50	39.5
60	54.9
70	68.0
80	79.5
90	90.0
100	99.6
110	108.3
120	116.3

order to answer this question we postulate that the internal noise radiates the *same acoustic power* into the (axisymmetric) ray tube or solid angle containing waves of a given axial wavenumber *independently of* V_T. This leads to the following relationship between the pressure psd in the static case (P_{To}) and the pressure psd in the forward motion case (P_T):

$$\underbrace{R_{rT}^2 \frac{P_T}{\rho_T} \{1 + \frac{V_T}{a_T} \cos\theta_T\}^4}_{\text{(forward motion)}} = \underbrace{R_{rTo}^2 \frac{P_{To}}{\rho_o}}_{\text{(static)}} \tag{8-8}$$

where subscript "o" refers to static conditions. The effect of forward motion on the pressure psd at the same wavenormal distance ($R_{rT} = R_{rTo}$) and ambient density ($\rho_T = \rho_o$) is therefore given by

$$\frac{P_T}{P_{To}} = \frac{1}{(1 + V_T \cos\theta_T / a_T)^4} \tag{8-9}$$

This result has been used previously to correlate *simulated* static-to-flight data (e.g. refs. 8.4, 8.5) and actual static-to-flight data dominated by internal noise and/or shock-associated noise (e.g. ref. 8.6). Here we have derived the result from theoretical considerations which do *not* involve specification of the source type (monopole, dipole etc.). Instead, we have utilized the relationship between sound *power* in a solid angle containing waves of fixed axial wavenumber and sound *pressure* in a uniformly moving fluid together with the hypothesis that the power radiated from internal noise and shock-associated noise sources into that solid angle is unaffected by forward motion at constant jet-exit conditions.

The significance of this hypothesis can be brought out more clearly by returning to the free-jet problem where measurements are taken outside the free jet (P_o) and corrected to ideal-wind-tunnel conditions (P_T) with the *calibration factor*, which in this case is the high-frequency or GA calibration factor C_{F_∞}:

$$P_T = \frac{R_{ra}\ R_{ro}}{R_{rT}^2} \cdot C_{F_\infty} \cdot P_o$$

$$= \frac{R_{ra}\ R_{ro}}{R_{rT}^2} \cdot \frac{\rho_T}{\rho_o(1 + V_T\cos\theta_T/a_T)^4} \cdot P_o \qquad (8\text{-}10)$$

Dividing equation (8-8) by equation (8-10) gives

$$R_{rTo}^2\ P_{To} = R_{ra}\ R_{ro}\ P_o\ . \qquad (8\text{-}11)$$

We find that apart from distance corrections there would be *no* effect of V_T on the variation of P_o (measured *outside* the free jet) from the static value, P_{To}, if the constant-k_x sound power hypothesis applies to the sources under consideration. Equations (8-4) and (8-7) show that P_o is measured on the ray path with a refraction angle, θ_o, which does not vary with V_T; here, in the ambient medium, the sound intensity and hence the sound power in the ray-tube are directly proportional to the psd, P_o. Thus, if k_x and the sound power radiated into the solid angle containing waves of that wavenumber remain constant and energy is conserved in the transmission process across the shear layer, the psd outside the free jet must be invariant with V_T as as indicated by equation (8-11).

To test the constant sound power hypothesis directly, one would ideally plot the ratio of the normalized free jet psd and static psd $R_{ra}R_{ro}P_o/R_{rTo}^2\ P_{To}$ versus V_T at constant values of θ_o and if the present hypothesis is correct, $R_{ra}R_{ro}P_o/R_{rTo}^2P_{To}$ would be independent of V_T for every θ_o value. However, our data analysis program were designed to produce ideal wind-tunnel data at specified values of θ_T rather than θ_o. Thus, the results presented below are in terms of ideal-wind-tunnel data *versus* θ_T instead of data measured outside the free jet *versus* θ_o. For these results equation (8-9) is the expected dependence on θ_T and V_T; the data, in general, follow that result quite closely. However, the significance of this is not that data agree with the $(1 + V_T\cos\theta_T/a_T)^{-4}$ result since P_T has been obtained from P_o with equation (8-10) *which involves the same factor*. That is, four powers of Doppler factor have been applied to the measured data, P_o, in order to estimate P_T. The significance of the results given in Figures 8.19 and 8.20 is that *deviations* of the measured data from the theoretical result (solid line) are reasonably small, indicating that the constant sound power hypothesis proposed above applies to these noise sources.

The results presented in Figures 8.19 and 8.20 refer respectively to conditions where *internal* noise and *shock-associated* noise are dominant – at

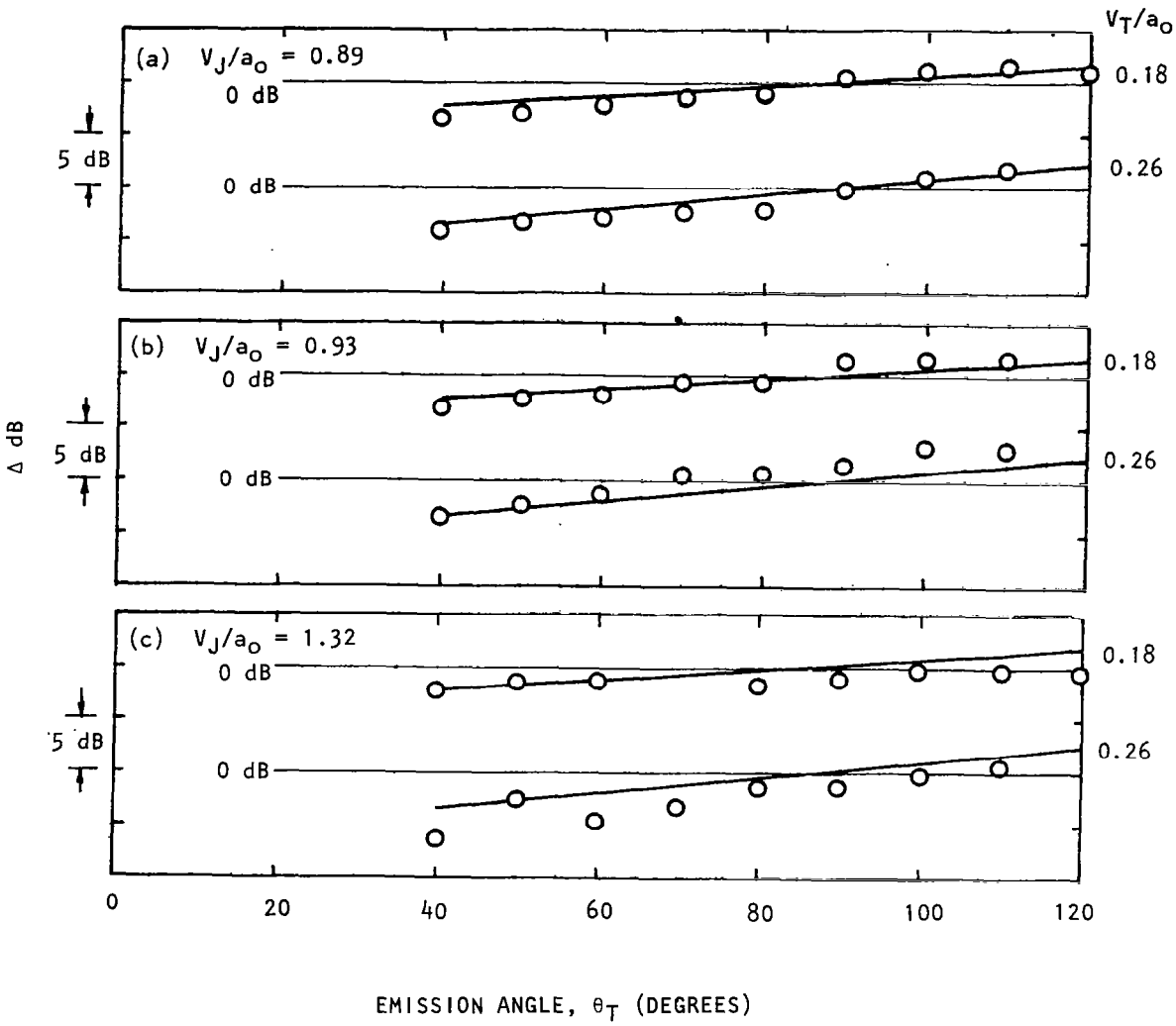

Figure 8.19 Measured ΔdB versus theoretical prediction for internal noise data. O , Experiment; —— $10 \log_{10} (D_T/D_{To})^4$ (Heated jet, T_R = 533K)

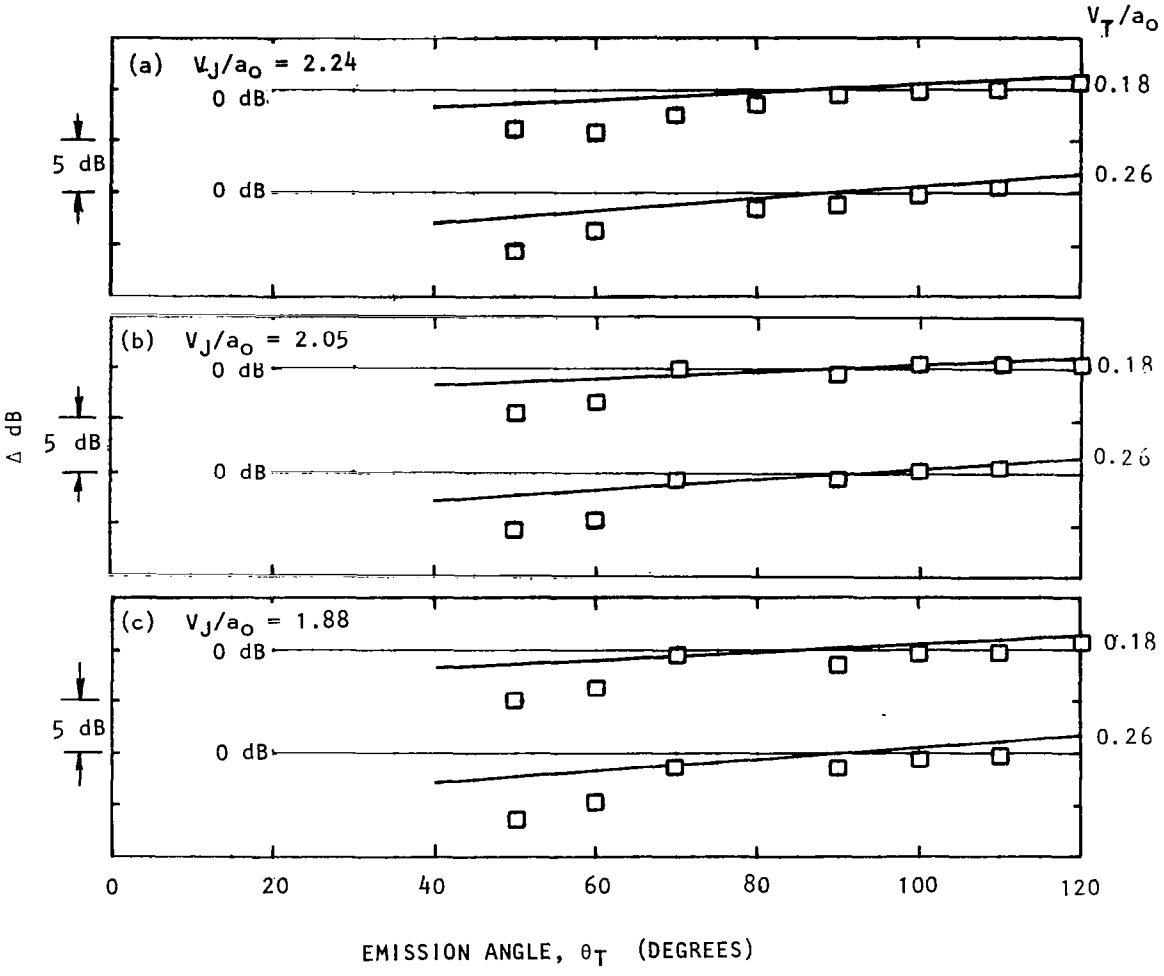

Figure 8.20 Measured ΔdB versus theoretical prediction for shock noise data. □ , Experiment; ——— 10 $\log_{10}$ $(D_T/D_{To})^4$ (Heated jet, T_R = 870K)

the simulated flight conditions indicated ($V_T/a_o = 0.18$ and 0.26) - but in Figure 8.20 mixing noise takes over from shock-associated in the rear arc ($\theta_T < 90°$). The theoretical line shown is actually four powers of a Doppler factor ratio, one of the factors being evaluated at the *minimum* free-jet velocity, V_{To}, at which the "static" data were acquired. This modified result can be obtained from a very straightforward extension of the theory presented above, viz.

$$\Delta dB = 10 \log_{10} \left\{ \frac{1 + M_{To}\cos\theta_T}{1 + M_T\cos\theta_T} \right\}^4 .$$

Here ΔdB is the difference between the overall SPL at a given tunnel Mach number, M_T, and that at the minimum tunnel Mach number, M_{To}.

For *prediction purposes* then, the above theoretical considerations taken together with the experimental results indicate that if the sound power emitted by internal noise or shock-associated noise as defined above does not alter with forward velocity (as seems to be the case here), then the flight noise levels are related to the static noise levels by

$$SPL_{flight} = SPL_{static} + 10 \log_{10} \left\{ \frac{1}{(1 + M_T\cos\theta_T)^4} \right\} \qquad (8\text{-}12)$$

and this result is *independent of the source type.*

8.5 CONCLUSIONS

The effects of forward motion on the noise from shock-free and shock-containing jets were examined by testing a model-scale convergent nozzle at unheated and heated conditions in the Lockheed anechoic free-jet facility. The experiments were conducted first in the absence of any internal noise, and later with an internal noise generator which injected broadband sound upstream of the nozzle. The data measured outside the free-jet flow were transformed to ideal wind tunnel conditions using the transformation procedure described in Section 6. The major conclusions are as follows:

(1) At subcritical jet operating conditions in the absence of internal noise (i.e. for pure jet mixing noise), the effect of forward motion is to provide a noise reduction at all angles and all frequencies for both unheated and heated jets. The relative velocity exponents for heated jets were higher than those for unheated jets in the rear arc.

(2) For shock-containing jets with no contamination from internal noise, the effect of forward velocity is essentially to provide a noise reduction in the rear arc and a noise increase in the forward arc, with little change at 90°.

(3) In the case of jet noise contaminated with internal noise, the effect of forward motion is similar to that for the supercritical jet (i.e.

noise reduction in the rear arc, noise increase in the forward arc, and little change at 90°.)

(4) When jet noise is contaminated with internal noise, the relative velocity exponent is reduced at all emission angles. The exact value of the exponent (at a particular emission angle) depends upon the degree of contamination. The envelope of the exponent values obtained in the present study encompasses the envelope of exponents published in the past using full-scale flight data.

(5) For prediction purposes, the OASPL's for shock noise and internal noise under static conditions are modified in flight by four powers of the Doppler factor. However, it has been shown that this result is a pure propagation effect, and it applies to any source type (i.e. monopole, dipole, etc.) provided that for any given axial wavenumber of the source excitation, the acoustic power radiated into the solid angle enclosing the far-field observer remains constant with forward velocity.

9. CONCLUSIONS

The three major objectives of the present investigation were:

(1) To obtain a thorough theoretical and experimental understanding of the effects of the free-jet shear layer on the transmission of sound from a model jet placed within the free jet to the far-field receiver located outside the free-jet flow, and hence, to evaluate the validity and accuracy of the free-jet flight simulation technique for forward velocity effects on jet noise.

(2) To provide transformation charts and a systematic computational procedure for converting measurements obtained from a free-jet simulation to the corresponding results from a wind tunnel simulation, and, finally, to the flight case.

(3) To experimentally establish the effects of simulated forward flight on engine internal noise source and shock-associated noise from model scale unheated and heated jets, and hence, to illustrate the role played by these non-jet mixing noise sources in producing the currently observed anomalies between flight data and free-jet simulation data projected to the flight case.

A summary of the work conducted to achieve these objectives and the main conclusions are as follows:

9.1 FREE-JET FLIGHT SIMULATION TECHNIQUE

The validity and accuracy of the free-jet flight simulation technique for forward velocity effects on jet noise was examined both theoretically and experimentally. In the experimental work, which was conducted in the Lockheed anechoic free-jet facility, the major emphasis was to verify (and if necessary modify) various aspects of a theoretical transformation procedure, developed in our previous work. The theoretical work was concentrated on assessing the validity of the high-frequency or geometric acoustics amplitude calibration factor (derived in our previous work) by detailed comparisons with the numerical solutions to the Lilley equation. Subsequent to these two items of work, the validity of the *complete* data transformation procedure was examined experimentally.

(1) Experimental Verification of Major Components of Transformation Procedure

(a) Redirection or refraction of sound by the mean sheared flow: A cross-correlation technique used to measure (indirectly) the refraction of waves transmitted across the free-jet shear layer confirmed that Snell's law holds to a good approximation over a wide range of incident wavenormal angles and free-jet velocities.

(b) Internal reflection of sound by the sheared flow: Internal reflection was found to be insignificant for the majority of data analyzed. Significant reflection was detected only in the total internal reflection regime.

(c) Transmission of sound through the mean sheared flow (coherent transmission): The relationships between sound pressure amplitudes inside and outside the free-jet flow were measured (using coherence analysis) on a *common ray path* emanating from a point source placed within the potential core of the free jet. These results confirm that the theoretical amplitude and distance calibration factors are valid within measurement accuracy and that the sound transmission across the shear layer can be adequately described by a geometric acoustics energy-conserving process.

(d) Transmission of sound through the unsteady sheared flow (turbulence absorption): The absorption of sound by turbulence in the free-jet shear layer, if present, is insignificant over the ranges of parameters of practical interest.

(e) Transmission of sound through the unsteady sheared flow (turbulence scattering): Frequency broadening of transmitted discrete tones was detected only when the ratio of shear layer thickness to sound wavelength, δ/λ, was about 10 or higher. Discrete tones with $\delta/\lambda \lesssim 10$ measured outside the free jet can be transformed to ideal-wind-tunnel conditions through the use of distance and amplitude calibration factors also used for broadband noise. For broadband noise sources, turbulence scattering effects pose no real problem.

Thus, the verification experiments have confirmed the validity of the important *individual components* of the calibration procedure.

(2) Theoretical Assessment of Amplitude Calibration Factor

The theoretical work was concentrated on the amplitude calibration factor, C_F, since this plays a key role in the data transformation procedure. In our previous work, this calibration factor was obtained from high-frequency (or geometric acoustics) analytic solutions to the Lilley equation when the typical free-jet shear layer thickness is large compared with the wavelength of sound. In the present work, the validity of this calibration factor was assessed by solving the Lilley equation numerically, using realistic models of the primary-jet and the free-jet mean flow fields and of the noise source itself, particularly for jet mixing noise.

Over the frequency range considered, the geometric-acoustics based calibration factor ($C_{F\infty}$) for the monopole source was found to be within ±1/2 dB of the numerical factor (C_F). Moreover, the magnitudes of the dipole and quadrupole calibration factor deviations were similar if not even less significant. This strongly suggests that any higher-order multipole source models that might be required to model internal noise or shock-associated noise will also have these negligible deviations of C_F from $C_{F\infty}$.

For most practical cases, model-scale jet noise data (consisting of jet mixing noise and/or internal noise and/or shock-associated noise) obtained in a free-jet flight simulation facility can be converted or calibrated to ideal-wind-tunnel conditions using the simple high-frequency amplitude calibration factor C_{F_∞} with a remarkable degree of accuracy.

(3) Experimental Verification of Complete Transformation Procedure

In order to assess the validity of the transformation procedure in its entirety, jet noise experiments were conducted first with the free-jet facility used in the conventional manner, with the microphones placed entirely outside the free-jet flow. Subsequently, the facility was used as a wind tunnel for which the measurements were conducted inside the potential core of the free jet. The test matrices for both sets of experiments were kept identical. Both sets of data (i.e., the free-jet data and the wind-tunnel data) were transformed to (common) ideal-wind-tunnel conditions, and the corresponding pairs of spectra were compared on an absolute basis. Good agreement was obtained between the two sets of measurements over a wide range of frequencies, angles and free-jet velocities. Thus, the *total* transformation procedure has been largely verified experimentally.

An important conclusion obtained during the course of these verification experiments using a model jet is concerned with jet noise characteristics at small measurement distances from the nozzle. In the past, jet noise measurements at small distances from the nozzle have been observed to depart from the usual inverse-square law dependence, and this behavior has been normally attributed to the so-called "near-field" effects. In the present work, however, it was found that, even for small measurement distances of the order of 8 model-jet diameters, these departures from inverse-square law dependence can be largely explained by properly accounting for source location (as a function of frequency) and directivity effects for jet mixing noise sources. Indeed with realistic source location and directivity corrections, jet mixing noise at small distances from the nozzle can be predicted quite accurately using an existing Lockheed prediction method.

9.2 TRANSFORMATION CHARTS AND COMPUTATIONAL PROCEDURE

In order to convert flight simulation data measured in a free-jet facility to the corresponding data that one would obtain from a wind tunnel simulation, and finally, in a flight situation, a self-contained transformation procedure has been provided. The procedure has been presented in two complementary parts. In the first part, a basic breakdown of the various components of the transformation procedure was given. To supplement the mathematical relationships, corresponding transformation charts were presented where possible. In the second part, a comprehensive computer program was presented and described in detail in the form of a user's guide.

9.3 EFFECTS OF SIMULATED FORWARD FLIGHT ON JET NOISE, SHOCK NOISE AND INTERNAL NOISE

The effects of forward motion on the noise from shock-free and shock-containing jets have been examined by testing a model-scale convergent nozzle at unheated and heated conditions in the Lockheed anechoic free-jet facility. The experiments were conducted first in the absence of any internal noise, and later with an internal noise generator which injected broadband sound upstream of the nozzle. The free-jet data were transformed to ideal-wind-tunnel conditions. The major conclusions are as follows:

(1) At subcritical jet operating conditions in the absence of internal noise (i.e., for pure jet mixing noise), the effect of forward motion is to provide a noise reduction at all angles and frequencies for both unheated and heated jets. The relative velocity exponents for heated jets were higher than those for unheated jets in the rear arc.

(2) For shock-containing jets with no contamination from internal noise, the effect of forward velocity is essentially to provide a noise reduction in the rear arc and a noise increase in the forward arc, with little change at 90°.

(3) In the case of jet noise contaminated with internal noise, the effect of forward motion is similar to that for the supercritical jet, i.e., noise reduction in the rear arc, noise increase in the forward arc, and little change at 90°.

(4) When jet noise is contaminated with internal noise, the relative velocity exponent is reduced at all emission angles. The exact value of the exponent (at a particular emission angle) depends upon the degree of contamination. The envelope of exponent values obtained in the present investigation encompasses the envelope of exponents published in the past using full-scale flight data.

(5) The present experiments have *illustrated* that the existing anomalies between full-scale flight data and model-scale flight simulation data could well be due to the contamination of flight data by internal noise. Although the internal noise may have been masked by jet mixing noise in the static case, it may well have influenced the changes in noise levels with forward velocity due to decreased contribution from mixing noise in flight. Of course the significance of internal noise and shock noise in producing the anomalies between flight data and flight simulation data has been recognized and/or hypothesized in the past, and the results of the present study serve to illustrate these effects in a systematic and comprehensive manner.

(6) For prediction purposes, the OASPL's for shock noise and internal noise under static conditions are modified in flight by four powers of the Doppler factor. However, it has been shown that this result is a pure propagation effect, and it applies to any source type (i.e. monopole, dipole, etc.) provided that for any given axial wavenumber of the source excitation, the acoustic power radiated into the solid angle enclosing the far-field observer remains constant with forward velocity.

APPENDIX 4A
SNELL'S LAW AND MINIMUM TRAVEL TIME

In stationary or moving non-uniform fluids a sound ray propagates between any two observation points along a path such that the travel time is a *minimum*. This result has been derived only quite recently from the theory of geometric acoustics by Ugincius (ref. 4.1) for ray paths in *moving fluids*. The flow model adopted in the recommended calibration procedure for the purposes of describing changes in ray geometry (angles and distances) - but not ray amplitude changes - is the cylindrical vortex sheet containing a *uniform* flow. Sound propagation across a vortex sheet does not immediately fall into the category of geometric acoustics propagation (slowly varying mean flow velocities on the wavelength scale). Thus, it is of interest to confirm that Snell's law, which applies to wavenormal refraction across an axially uniform shear layer of arbitrary thickness, *does* correspond to a minimum-travel-time ray path when used with the vortex-sheet flow model.

The ray path from a point A on the centerline of the cylindrical vortex sheet to a point B outside the flow is made up of two straight-line segments, as shown in the sketch on the next page.

The travel time between point A and the lipline intercept, I, is the distance travelled relative to the flow by the wavefronts $r_T/\sin\theta_T$ divided by the wave velocity relative to the flow, a_T; outside the flow the travel time is $(R_m\sin\theta_m - r_T)/a_o$ so that the total travel time is given by

$$\tau = \frac{(r_T/\sin\theta_T)}{a_T} + \frac{(R_m\sin\theta_m - r_T)}{a_o} \qquad (4A\text{-}1)$$

The wavenormal angle, θ_T, is related to the ray angle, ψ_T, according to the velocity triangle shown in the sketch, viz.

$$\cot\psi_T = \frac{V_T + a_T\cos\theta_T}{a_T\sin\theta_T} \qquad (4A\text{-}2)$$

and in order for the ray to pass through the point B (polar coordinates R_m, θ_m centered on A) we must have

$$R_m\cos\theta_m = r_T\cot\psi_T + (R_m\sin\theta_m - r_T)\cot\theta_o \qquad (4A\text{-}3)$$

Nothing has been assumed about the relation between θ_T and θ_o, other than the geometrical constraint given by equation (4A-3).

Eliminating $\cot\psi_T$ between equations (4A-2) and (4A-3) gives

$$R_m \cos\theta_m = r_T \left\{ \frac{V_T + a_T \cos\theta_T}{a_T \sin\theta_T} \right\} + (R_m \sin\theta_m - r_T) \cot\theta_o \tag{4A-4}$$

and differentiating the result gives

$$\frac{d\theta_T}{d\theta_o} = - \frac{(R_m \sin\theta_m - r_T)}{r_T} \left\{ \frac{\sin\theta_T}{\sin\theta_o} \right\}^2 \frac{a_T}{a_T + V_T \cos\theta_T}, \tag{4A-5}$$

which when substituted into the derivative of equation (4A-1) with respect to θ_o gives

$$\frac{d\tau}{d\theta_o} = \frac{(R_m \sin\theta_m - r_T)}{\sin^2\theta_o} \left\{ \frac{\cos\theta_o}{a_o} - \frac{\cos\theta_T}{a_T + V_T \cos\theta_T} \right\}. \tag{4A-6}$$

When Snell's law is assumed, i.e.,

$$\frac{a_o}{\cos\theta_o} = \frac{a_T}{\cos\theta_T} + V_T \tag{4A-7}$$

then equation (4A-6) reduces to

$$\frac{d\tau}{d\theta_o} = 0$$

confirming that Snell's law and minimum travel time are equivalent in the present vortex-sheet flow model.

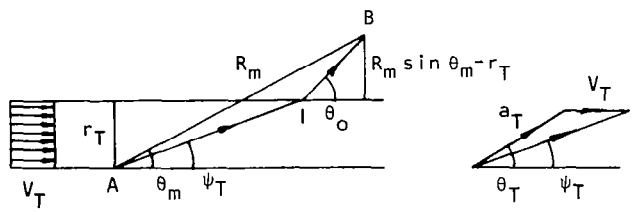

APPENDIX 4B
EXPERIMENTAL DETERMINATION OF AMPLITUDE CALIBRATION FACTOR

The calibration factor defined in Section 2.3 can be determined in principle (apart from distance corrections) simply by measuring the mean-square pressures $\overline{p_C^2}$ and $\overline{p_B^2}$ (in frequency bands) or auto-power spectral densities $G_{CC}(f)$ and $G_{BB}(f)$, by microphone C inside the flow and microphone B outside the flow, respectively. These measurements must refer *only* to the acoustic pressure signal radiated by the noise source at point A (see Figure 3.16). In other words, according to the definition of the amplitude calibration factor, the quantities of interest are the amplitude of the incident (or outward-going) pressure wave at microphone C and the amplitude of the transmitted pressure wave at microphone B.

In reality, the total signal sensed by microphone C contains contributions from the reflected wave as well as other extraneous noise sources, namely, free-jet flow noise and turbulent pressure fluctuations at the microphone. Similarly, microphone B also measures the unwanted extraneous noise source contributions. The reflected wave contribution at microphone C and the extraneous noise contributions at microphones C and B must therefore be removed in order to obtain a true measurement of the calibration factor. Fortunately, in the tests conducted to date (see section 4.3), internal reflections have *not* been detected at any of the points C, corresponding to the different ray angles, except for ray angle of $\psi_T = 140°$ and $V_T/a_T \geq 0.18$ where Snell's law predicts total internal reflection and, therefore, amplitude calibration factors could not be determined anyway. The other extraneous noise contributions at microphones C and B can therefore be removed by using coherence analysis. Thus, provided the signal at reference microphone A is entirely dominated by acoustic pressure fluctuations from the point sound source, the spectral density of the incident (or outward-going) wave at microphone C is given by $\gamma_{AC}^2(f)\ G_{CC}(f)$, and similarly, the spectral density of the transmitted wave at microphone B is given by $\gamma_{AB}^2(f)\ G_{BB}(f)$, where $\gamma^2(f)$ is the coherence function.

The required ratio of these coherent components can be conveniently expressed as

$$\frac{\gamma_{AC}^2(f)\ G_{CC}(f)}{\gamma_{AB}^2(f)\ G_{BB}(f)} = \frac{|G_{AC}(f)|^2}{|G_{AB}(f)|^2} \tag{4B-1}$$

by using the coherence function definition

$$\gamma_{xy}^2 = \frac{|G_{xy}|^2}{G_{xx}\ G_{yy}}\ , \tag{4B-2}$$

where G_{xy} is the cross-power spectral density.

Thus, the mean-square pressures (in frequency bands) of the incident wave at microphone C and the transmitted wave at microphone B, required to determine the calibration factor (apart from distance corrections), are obtained in practice by measuring and squaring the magnitudes of the cross-power spectral densities $|G_{AC}(f)|$ and $|G_{AB}(f)|$.

APPENDIX 4C
SAMPLE CALCULATION OF AMPLITUDE CALIBRATION FACTORS

Given:

$$M_T = V_T/a_T = 0.264$$

$$a_T/a_o = 0.993$$

$$a_o = 344.370 \text{ m/s}$$

$$\psi_T = 22.020^\circ$$

$$\theta_m = 30^\circ$$

$$R_m = 1.477 \text{ m}$$

$$R_T = 0.454 \text{ m}$$

$$r_T = 0.356 \text{ m}$$

Calculated:

$$R_{rT}/R_T = \{M_T\cos\psi_T + (1 - M_T^2\sin^2\psi_T)^{\frac{1}{2}}\}^{-1} = 0.806$$

$$R_{rT} = 0.366 \text{ m}$$

$$\tan\theta_o = (R_m\sin\theta_m - r_T)/(R_m\cos\theta_m - r_T\cot\psi_T) = 0.957$$

$$\theta_o = 43.748^\circ$$

$$R_{ro} = R_m\sin\theta_m/\sin\theta_o = 1.068 \text{ m}$$

$$\cos\theta_T = \cos\psi_T(1 - M_T^2\sin^2\psi_T)^{\frac{1}{2}} - M_T\sin^2\psi_T = 0.885$$

$$\theta_T = 27.71^\circ$$

$$D_T = (1 + M_T\cos\theta_T)^{-1} = 0.810$$

$$R_{ra} = \frac{1}{\sin\theta_o}\left[R_m\sin\theta_m + r_T\left\{\left(\frac{\sin\theta_o}{D_T\sin\theta_T}\right)^3\left(\frac{a_T}{a_o}\right) - 1\right\}\right] = 3.710 \text{ m}$$

Distance Calibration Factor:

$$R_{rT}^2/R_{ro}R_{ra} = 0.0338$$

$$10 \log_{10}(R_{rT}^2/R_{ro}R_{ra}) = -29.41 \text{ dB}$$

Measured Amplitude Calibration Factor:

$$C_{F_m} = \left\{ 20 \log_{10} \frac{|G_{AC}(f)|}{|G_{AB}(f)|} - 29.41 \right\} \text{dB}$$

Calculated Amplitude Calibration Factor:

$$C_F = 10 \log_{10} \{D_T^4(\rho_T/\rho_o)\}$$

$$= 10 \log_{10} \{D_T^4/(a_T/a_o)^2\} = -3.593 \text{ dB}$$

APPENDIX 6A

DISTANCE AND ANGLE CORRECTIONS FOR THE FLIGHT CASE

In the data transformation procedure, when the Doppler frequency shift is applied to the wind-tunnel data, we obtain the flight data $SPL_F(R,\theta_T)$. As shown in Figure 6A.1, for a *fixed frequency* f, these flight data are obtained at various emission angles θ_T *relative to source position S* on an arc of radius R *centered at S*. In order to predict the corresponding flight data $SPL_F(R_n,\theta_{Tn})$ at various emission angles θ_{Tn} *relative to nozzle exit position N* on an arc of radius R_n *centered at N*, two corrections are required: a distance correction which relates distances R and SO, and an angle correction which gives θ_{Tn} in terms of θ_T.

Angle Correction

The angle correction depends on whether R_n is greater than, equal to, or smaller than the source location distance x_s'. The three cases are discussed below:

(1) $R_n > x_s'$ (Figure 6A.1):

In this case, for every value of θ_T, there is a corresponding value of θ_{Tn} which is given by

$$\theta_{Tn} = \theta_T - \sin^{-1}(x_s' \sin\theta_T/R_n). \tag{6A-1}$$

(2) $R_n = x_s'$ (Figure 6A.2):

In this case, the data $SPL_F(R,\theta_T)$ for $\theta_T < 90°$ cannot be used. At $\theta_T = 90°$, $\theta_{Tn} = 0°$ and the observer (O) and source (S) positions coincide. Therefore, data at $\theta_T = 90°$ also cannot be used. For $\theta_T > 90°$, a value of θ_{Tn} corresponding to a value of θ_T is obtained. The relationship between the two angles is

$$\theta_{Tn} = \theta_T - (180° - \theta_T). \tag{6A-2}$$

(3) $R_n < x_s'$ (Figure 6A.3):

This situation gives a very interesting result. As shown in Figure 6A.3, the data $SPL_F(R,\theta_T)$ for $\theta_T < \{180° - \sin^{-1}(R_n/x_s')\}$ cannot be used in this case. For $\theta_T \equiv \{180° - \sin^{-1}(R_n/x_s')\}$, one value of θ_{Tn} is obtained, and this is given by

$$\theta_{Tn} = \cos^{-1}(R_n/x_s'). \tag{6A-3}$$

For $\theta_T > \{180° - \sin^{-1}(R_n/x_s')\}$, two corresponding values of θ_{Tn}, given by

$$\left.\begin{aligned} \theta_{Tn2} &= \theta_T - \sin^{-1}(x_s' \sin\theta_T/R_n) \\ \theta_{Tn1} &= 2\theta_T - 180° - \theta_{Tn2} \end{aligned}\right\} \qquad (6A\text{-}4)$$

are obtained.

Distance Correction

For all three cases discussed above, the source-to-observer distance SO is given by the cosine rule as

$$SO^2 = R_n^2 + x_s'^2 + 2R_n x_s' \cos\theta_{Tn}, \qquad (6A\text{-}5)$$

and the distance correction in decibels is

$$C_{R_n}(dB) = 10 \log_{10} (R^2/SO^2). \qquad (6A\text{-}6)$$

Using the above corrections, the required inflight SPL's can be obtained from

$$SPL_F(R_n,\theta_{Tn}) = SPL_F(R,\theta_T) + C_{R_n}(dB). \qquad (6A\text{-}7)$$

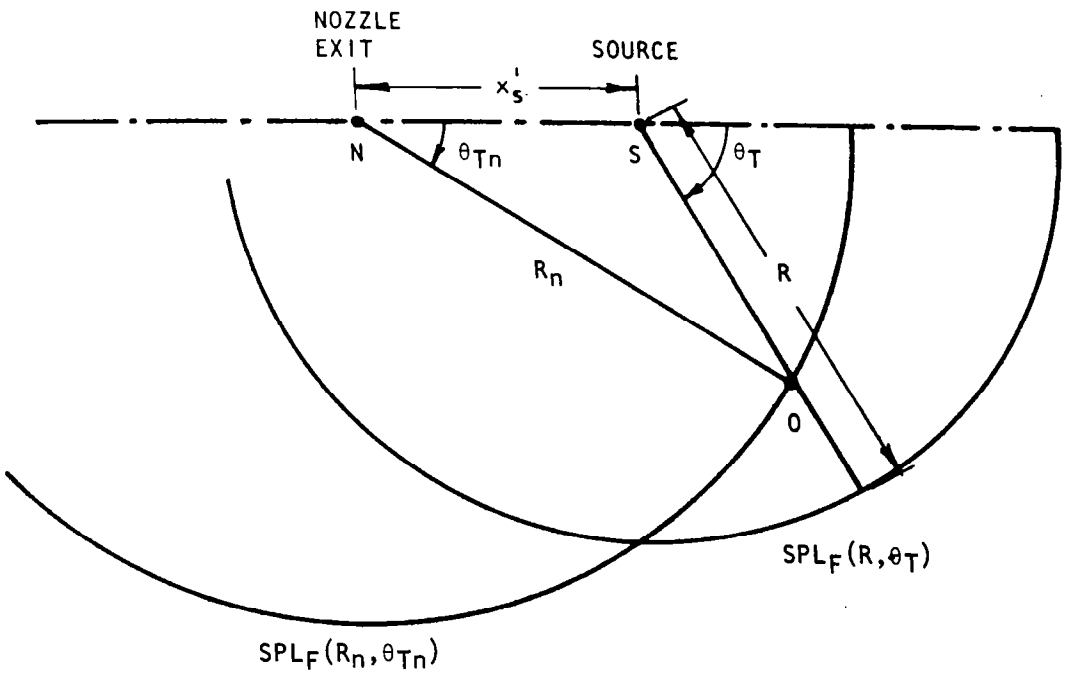

Figure 6A.1 Geometry for $R_n > x_s'$.

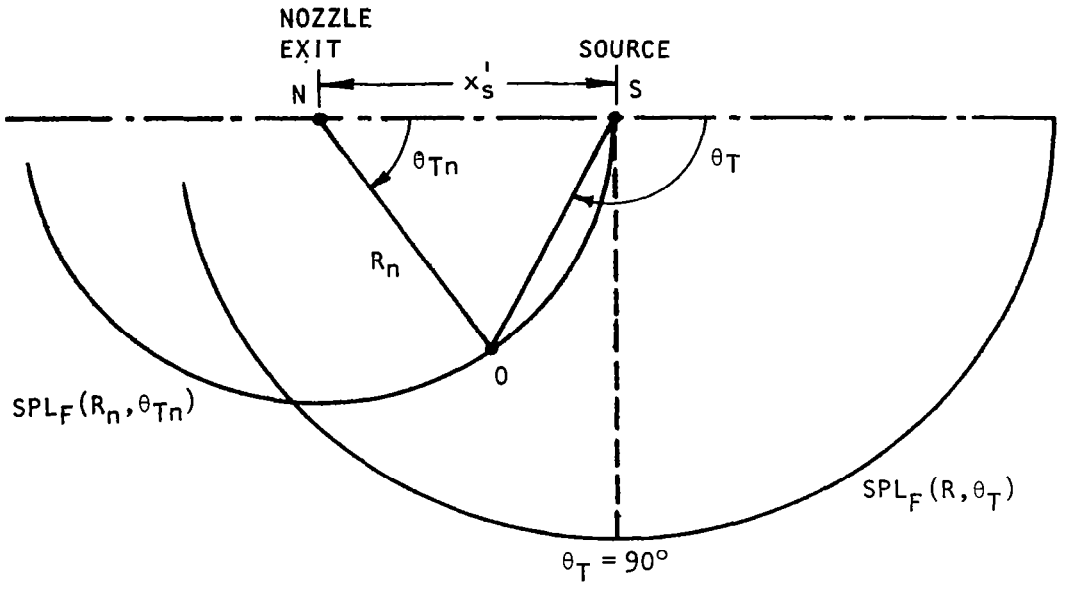

Figure 6A.2 Geometry for $R_n = x_s'$.

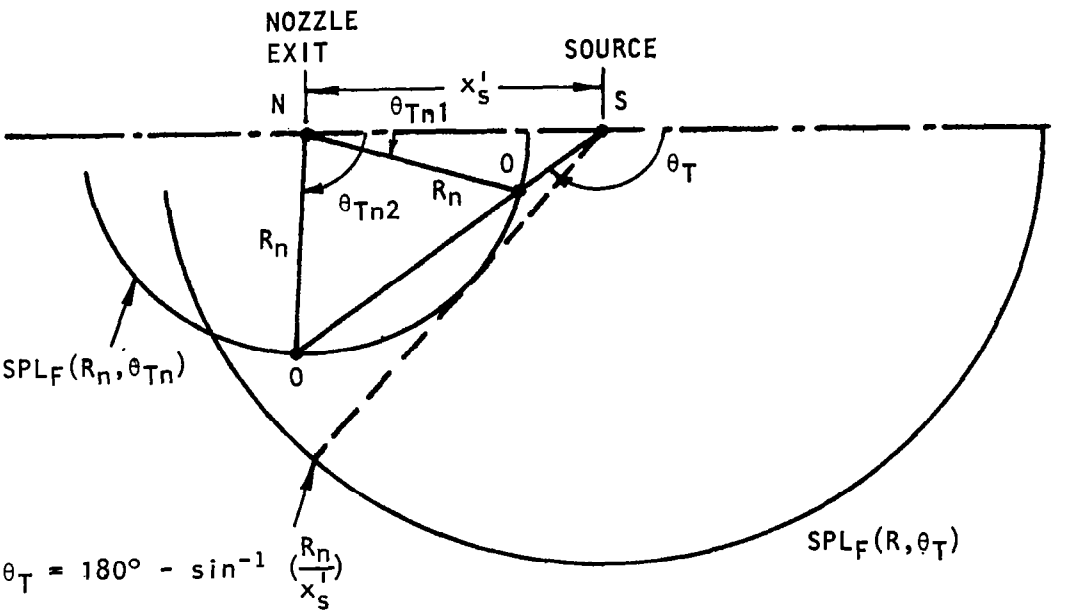

Figure 6A.3 Geometry for $R_n < x_s'$.

APPENDIX 7A

TRANSFORMATION OF INFLOW MEASUREMENTS TO IWT CONDITIONS

The purpose of this transformation procedure is to obtain the SPL (for a given frequency f) at some desired emission angle θ_T and some desired emission distance R_{rT} (=100d in the present investigation) using measured SPL's obtained at several measurement angles, θ_m, along a linear microphone traverse located at a distance r_m (=8d in the present investigation) from the jet centerline.

The geometry of this problem is defined in Figure 7A.1. The transformation can be carried out in four steps:

(1) Determine the source location x_s' corresponding to frequency f.

(2) Using the tunnel Mach number (M_T) and the desired emission angle θ_T, calculate the ray angle ψ_T and hence the distance x where the ray starting from the source at S intersects the line of microphone traverse used in the measurements.

(3) Interpolate the SPL measurements at x_i and x_{i+1} to obtain SPL at x.

(4) Extrapolate the SPL at x to the desired emission distance R_{rT}.

The equations used in these steps are given below.

Source Location x_s'

$$x_s'/d = (0.057\ S_m + 0.021\ S_m^2)^{-\frac{1}{2}} \tag{7A-1}$$

where

$$S_m = SD_m \tag{7A-2}$$

$$S = fd/V_J \tag{7A-3}$$

$$D_m = \{(1 - M_c\cos\theta_T)^2 + \alpha^2 M_c^2\}^{\frac{1}{2}} \tag{7A-4}$$

$$M_c = 0.67\ V_J/a_o \quad \text{and} \quad \alpha = 0.3 \tag{7A-5}$$

Distance x

$$\cot\psi_T = (\cos\theta_T + M_T)/\sin\theta_T \tag{7A-6}$$

$$x/d = x_s'/d + (r_m/d)\cot\psi_T \tag{7A-7}$$

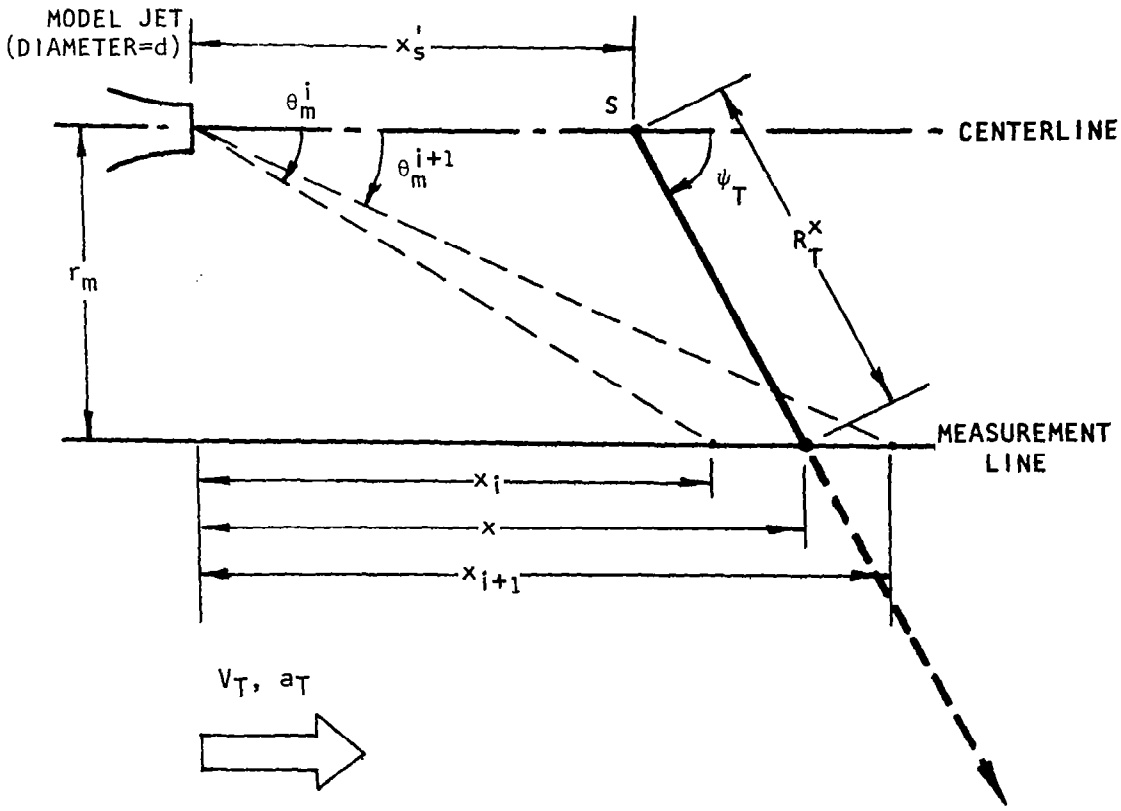

Figure 7A.1 Geometry for transformation of inflow measurements to IWT conditions.

Interpolation

$$x_i/d = (r_m/d) \cot \theta_m^i \tag{7A-8}$$

$$x_{i+1}/d = (r_m/d) \cot \theta_m^{i+1} \tag{7A-9}$$

Find i such that $x_i \leq x \leq x_{i+1}$ and calculate

$$h = (x - x_i)/(x_{i+1} - x_i) \tag{7A-10}$$

$$SPL_x = h\ SPL_{x_{i+1}} + (1 - h) SPL_{x_i} \tag{7A-11}$$

Extrapolation

$$(R_T^x/d)^2 = (r_m/d)^2 + (x/d - x_s'/d)^2 = \{(r_m/d)\mathrm{cosec}\psi_T\}^2 \tag{7A-12}$$

$$R_{rT}^x/d = (R_T^x/d) / \{M_T \cos\psi_T + (1 - M_T^2 \sin^2\psi_T)^{\frac{1}{2}}\} \tag{7A-13}$$

$$SPL_{R_{rT}} = SPL_x - 20 \log_{10} (R_{rT}/R_{rT}^x) \tag{7A-14}$$

APPENDIX
LIST OF SYMBOLS

$\bar{a}(r)$	speed of sound in parallel sheared flow
a	speed of sound in uniform flow region
C_F	amplitude calibration factor
C_{Fmo}	low-frequency, monopole calibration factor†
$C_{F\infty}$	high-frequency or geometric acoustics calibration factor
C_R	distance calibration factor
d	model-jet nozzle diameter
D	Doppler factor $(1 + V\cos\theta/a)^{-1}$
f	frequency
G_{xx}, G_{xy}	auto-, cross-power spectral density
H	height of aircraft flight path from microphone
k_o	acoustic wavenumber, ω/a_o
k_x	axial wavenumber
m	exponent of relative velocity
M	Mach number
M_A	aircraft Mach number
M_c	axial eddy convection Mach number
M_{To}	minimum tunnel Mach number
n	azimuthal mode number
OASPL	overall sound pressure level

†*In Section 5, C_{Fm} is the monopole calibration factor; elsewhere C_{Fm} is the* <u>*measured*</u> *amplitude calibration factor.*

p	acoustic pressure
p_o	ambient pressure in anechoic room
p_1	free-jet intake static pressure
p_R	reservoir or plenum static pressure
p_T	tunnel or free-jet test section static pressure
P	total pressure
P_R	reservoir or plenum total pressure
Q	volume source distribution
r	radial coordinate (cylindrical)
r_T	free-jet (or tunnel) nozzle radius
R	nondimensional radial coordinate, $k_o r$*
R_m	microphone or measurement radius
R_{xx}, R_{xy}	auto-, cross-correlation function
R_r	radiation (or wavenormal) distance, relative to uniform flow
R_ψ	distance between observer and aircraft engine at reception time
R_θ	distance between observer and aircraft engine at emission time
S	source strength
S_m	modified Strouhal number
S/N	signal-to-noise ratio
SPL	sound pressure level
t	time
T	temperature
$V(r)$	mean velocity in parallel sheared flow

In Section 5, $k_o r_T \equiv R_T$; elsewhere R_T is the distance along a ray path.

V_J	primary-jet exit velocity
V_r	ray speed
V_{REL}	relative velocity ($= V_J - V_T$)
V_T	tunnel or free-jet velocity
V_{T0}	minimum tunnel or free-jet velocity
x	axial distance or axial coordinate measured from the free-jet exit plane
x'	axial distance measured from primary-jet exit plane
γ^2	coherence function
δ	vorticity thickness of shear layer $\Delta V/\lvert dV/dr\rvert_{max}$
Δf	frequency analysis bandwidth
θ	polar angle of wavenormal direction (except θ_m), referred to *downstream* flow direction
θ_m	microphone or measurement angle referred to *downstream* flow direction
κ	nondimensional radial wavenumber defined by equation (5-3f)
λ	wavelength of sound
ξ	model-jet pressure ratio
$\bar{\rho}(r)$	mean density in parallel sheared flow
ρ	mean density in uniform flow region
τ	time delay
τ_{cd}	calculated time delay using diverging flow model
τ_{cv}	calculated time delay using vortex sheet model
τ_m	measured time delay
τ_{ref}	calculated time delay for internal reflection peak
ϕ	azimuthal coordinate
ϕ_{xy}	phase spectrum corresponding to cross-power spectral density G_{xy}

ψ	ray angle referred to *downstream* flow direction
ω	radian frequency

Subscripts

A,B,C,D	quantities pertaining to signals at microphones A (reference microphone), B (along transmitted ray), C (along incident ray), and D (along reflected ray)
d	dipole
F	flight
FJ	free jet
IWT	ideal wind tunnel
J	primary jet conditions
m	monopole
o	ambient conditions
par	partial profile
q	quadrupole
s	conditions at noise source location
T	free-jet exit or tunnel conditions

Superscripts

ν	temporal order of source distribution

Functions

$H_n^{(1)}$, $H_n^{(2)}$	Hankel functions of the first and second kind
J_n	Bessel function of the first kind
$W(z_1,z_2)$	Wronskian $z_1 z_2' - z_1' z_2$
δ	Dirac delta function

REFERENCES

1.1. Plumblee, H. E. (Editor): Effects of Forward Velocity on Turbulent Jet Mixing Noise. NASA CR-2702, 1976.

1.2. Tanna, H. K.; and Morris, P. J.: Inflight Simulation Experiments on Turbulent Jet Mixing Noise. AIAA Paper No. 76-554, 1976.

1.3. Cocking, B. J.; and Bryce, W. D.: Subsonic Jet Noise in Flight Based on Some Recent Wind Tunnel Results. AIAA Paper No. 75-462, 1975.

1.4. Cocking, B. J.: The Effect of Flight on Subsonic Jet Noise. AIAA Paper No. 76-555, 1976.

1.5. Packman, A. B.; Ng, K. W.; and Paterson, R. W.: Effect of Simulated Forward Flight on Subsonic Jet Exhaust Noise. AIAA Paper No. 75-869, 1975.

1.6. Strout, F. G.; and Atencio, A.: Flight Effects on JT8D Engine Jet Noise as Measured in the NASA Ames 40- by 80-foot Wind Tunnel. AIAA Paper No. 76-556, 1976.

1.7. Drevet, P.; Duponchel, J. P.; and Jacques, J. R.: Effect of Flight on the Noise from a Convergent Nozzle as Observed on the Bertin Aerotrain. AIAA Paper No. 76-557, 1976.

1.8. Bushell, K. W.: Measurement and Prediction of Jet Noise in Flight. AIAA Paper No. 75-461, 1975.

1.9. Low, J. K. C.: Effect of Forward Motion on Jet and Core Noise. AIAA Paper No. 77-1330, 1977.

1.10. Von Glahn, U.; and Goodykoontz, J.: Installation and Airspeed Effects on Jet Shock-Associated Noise. NASA TM X-71792, 1975.

1.11. Stone, J. R.: Flight Effects on Exhaust Noise for Turbojet and Turbofan Engines — Comparison of Experimental Data with Prediction. NASA TM X-73552, 1976.

1.12. Dowling, A.: Convective Amplification of Real Simple Sources. *J. Fluid Mech.*, vol. 74, 1976, pp. 529-546.

1.13. Bechert, D.; and Pfizenmaier, E.: On the Amplification of Broadband Jet Noise by Pure Tone Excitation. *Journal of Sound and Vibration*, vol. 43, 1975, pp. 581-587.

1.14. Moore, C. J.: The Role of Shear-Layer Instability Waves in Jet Exhaust Noise. *Journal of Fluid Mechanics*, vol. 80, 1977, pp. 321-367.

2.1. Plumblee, H. E. (Editor): Effects of Forward Velocity on Turbulent Jet Mixing Noise. NASA CR-2702, July 1976.

2.2. Candel, S. M.; Guedel, A.; and Julienne, A.: Radiation, Refraction and Scattering of Acoustic Waves in a Free Shear Flow. AIAA Paper No. 76-544, July 1976.

2.3. Amiet, R. K.: Correlation of Open Jet Wind Tunnel Measurements for Shear Layer Refraction. AIAA Paper No. 75-532, March 1975.

2.4. Jacques, J.: The Noise from Moving Aircraft; Some Relevant Models. Ph.D. Thesis, University of Cambridge, 1975.

3.1. Plumblee, H. E. (Editor): Effects of Forward Velocity on Turbulent Jet Mixing Noise. NASA CR-2702, 1976.

3.2. Burrin, R. H.; Dean, P. D.; and Tanna, H. K.: A New Anechoic Facility for Supersonic Hot Jet Noise Research at Lockheed-Georgia. In "The Generation and Radiation of Supersonic Jet Noise" (edited by H. E. Plumblee). AFAPL Technical Report AFAPL-TR-74-24, 1974.

4.1. Ugincius, P.: Ray Acoustics and Fermat's Principle in a Moving Inhomogeneous Medium. *Journal of the Acoustical Society of America*, vol. 51, 1972, pp. 1759-1763.

4.2. Plumblee, H. E. (Editor): Effects of Forward Velocity on Turbulent Jet Mixing Noise. NASA CR-2702, 1976.

4.3. Clapper, W. S. (Editor): High Velocity Jet Noise Source Location and Reduction. Task 4 – Development/Evaluation of Techniques for "Inflight" Investigation. FAA Report No. FAA-RD-76-79, vol. IV, 1977.

4.4. Candel, S. M.; Guedel, A.; and Julienne, A.: Radiation, Refraction and Scattering of Acoustic Waves in a Free Shear Flow. AIAA Paper No. 76-544, 1976.

4.5. Candel, S. M.; Julienne, A.; and Julliand, M.: Shielding and Scattering by a Jet Flow. AIAA Paper No. 76-545, 1976.

5.1 Candel, S.; Guedel, A.; and Julienne, A.: Refraction and Scattering of Sound in an Open Wind Tunnel Flow. ONERA T.P. No. 1975-79, 1975.

5.2. Amiet, R. K.: Correction of Open Jet Wind Tunnel Measurements for Shear Layer Refraction. AIAA Paper No. 75-532, 1975.

5.3. Jacques, J.: The Noise from Moving Aircraft; Some Relevant Models. Ph.D. Thesis, University of Cambridge, 1975.

5.4. Plumblee, H. E. (Editor): Effects of Forward Velocity on Turbulent Jet Mixing Noise. NASA CR-2702, 1976.

5.5. Morfey, C. L.; and Tester, B. J.: Noise Measurements in a Free-Jet Flight Simulation Facility: Shear Layer Refraction and Facility-to-Flight Corrections. *Journal of Sound and Vibration*, vol. 54, 1977, pp. 83-106.

5.6. Amiet, R. K.: Refraction of Sound by a Shear Layer. AIAA Paper No. 77-54, 1977.

5.7. Lilley, G. M.; Plumblee, H. E.; Strahle, W. C.; Ruo, S. Y.; and Doak, P. E.: Theory of Turbulence Generated Jet Noise, Noise Radiation from Upstream Sources, and Combustion Noise. Vol. IV, The Generation and Radiation of Supersonic Jet Noise. AFAPL-TR-72-53, 1972.

5.8. Tester, B. J.; and Morfey, C. L.: Developments in Jet Noise Modelling - Theoretical Predictions and Comparisons with Measured Data. *Journal of Sound and Vibration*, vol. 46, 1976, pp. 79-103.

5.9. Plumblee, H. E. (Editor): The Generation and Radiation of Supersonic Jet Noise, Vol. II, Studies of Jet Noise, Turbulence Structure and Laser Velocimetry. AFAPL-TR-76-65-Vol. II, 1976.

5.10. Schubert, L. K.: Numerical Study of Sound Refraction by a Jet Flow. I. Ray Acoustics. *Journal of the Acoustical Society of America*, vol. 51, 1972, pp. 439-446.

5.11. Blokhinstev, D. I.: Acoustics of a Non-homogeneous Moving Medium. NACA TM-1399, 1946.

5.12. Tester, B. J.; and Burrin, R. H.: On Sound Radiation from Sources in Parallel Sheared Jet Flows. AIAA Paper No. 74-57, 1974.

5.13. Grosche, F.-R.: Distributions of Sound Source Intensities in Subsonic and Supersonic Jets. AGARD CP-131, 1973 (see also AIAA Paper No. 73-989, 1973).

5.14. Laufer, J.; Kaplan, R. E.; and Chu, W. T.: On Noise Produced by Subsonic Jets. Proceedings of the Second Interagency Symposium on University Research in Transportation Noise, vol. 1, 1974, pp. 50-58.

5.15. Morfey, C. L.; Tester, B. J.; and Szewczyk, V. M.: New Scaling Laws for Hot and Cold Jet Mixing Noise Based on a High-Frequency Model. AIAA Paper No. 77-1287, 1977.

5.16. Morfey, C. L.; and Tester, B. J.: Noise Measurements in a Free-Jet Flight Simulation Facility: Shear Layer Refraction and Facility-to-Flight Corrections. AIAA Paper No. 76-531, 1976.

5.17. Tanna, H. K.; Dean, P. D.; and Burrin, R. H.: The Generation and Radiation of Supersonic Jet Noise. Vol. III, Turbulent Mixing Noise Data. AFAPL-TR-76-65-Vol. III, 1976.

5.18. Dash, R.: Analysis of Flight Effects on Noise Radiation from Jet Flow Using a Convecting Quadrupole Model. AIAA Paper No. 78-192, 1978.

5.19. Munt, R. M.: The Interaction of Sound with a Subsonic Jet Issuing From a Semi-Infinite Cylindrical Pipe. *Journal of Fluid Mechanics*, vol. 83, 1977, pp. 609-460.

6.1. Laufer, J.; Kaplan, R. E.; and Chu, W. T.: On Noise Produced by Subsonic Jets. Proceedings of the Second Interagency Symposium on University Research in Transportation Noise, vol. 1, 1974, pp. 50-58.

8.1. Plumblee, H. E. (Editor): Effects of Forward Velocity on Turbulent Jet Mixing Noise. NASA CR-2702, 1976.

8.2. Packman, A. B.; Ng, K. W.; and Paterson, R. W.: Effect of Simulated Forward Flight on Subsonic Jet Exhaust Noise. AIAA Paper No. 75-869, 1975.

8.3. Bushell, K. W.: Measurement and Prediction of Jet Noise in Flight. AIAA Paper No. 75-461, 1975.

8.4. Von Glahn, U.; and Goodykoontz, J.: Installation and Airspeed Effects on Jet Shock-Associated Noise. NASA TM X-71792, 1975.

8.5. Bryce, W. D.; and Pinker, R. A.: The Noise from Unheated Supersonic Jets in Simulated Flight. AIAA Paper No. 77-1327, 1977.

8.6. Low, J. K. C.: Effect of Forward Motion on Jet and Core Noise. AIAA Paper No. 77-1330, 1977.

8.7. Drevet, P.; Duponchel, J. P.; and Jacques, J. R.: Effects of Flight on the Noise from a Convergent Nozzle as Observed on the Bertin Aerotrain. AIAA Paper No. 76-557, 1976.

☆U.S. GOVERNMENT PRINTING OFFICE: 1978-635-004/27

1. Report No.	2. Government Accession No.	3. Recipient's Catalog No.
NASA CR-3056		

4. Title and Subtitle	5. Report Date
THE FREE JET AS A SIMULATOR OF FORWARD VELOCITY EFFECTS ON JET NOISE	October 1978
	6. Performing Organization Code
7. Author(s)	8. Performing Organization Report No.
K. K. Ahuja, B. J. Tester, and H. K. Tanna	LG78ER0065
	10. Work Unit No.
9. Performing Organization Name and Address	
Lockheed-Georgia Company Marietta, Georgia 30063	11. Contract or Grant No. NAS3-20050
	13. Type of Report and Period Covered
12. Sponsoring Agency Name and Address	Contractor Report
National Aeronautics and Space Administration Washington, D.C. 20546	14. Sponsoring Agency Code

15. Supplementary Notes

Final report. Project Manager, A. M. Karchmer, V/STOL and Noise Division, NASA Lewis Research Center, Cleveland, Ohio 44135.

16. Abstract

A thorough theoretical and experimental study of the effects of the free-jet shear layer on the transmission of sound from a model jet placed within the free jet to the far-field receiver located outside the free-jet flow was conducted. The validity and accuracy of the free-jet flight simulation technique for forward velocity effects on jet noise was evaluated. Transformation charts and a systematic computational procedure for converting measurements from a free-jet simulation to the corresponding results from a wind-tunnel simulation, and, finally, to the flight case were provided. The effects of simulated forward flight on jet mixing noise, internal noise and shock-associated noise from model-scale unheated and heated jets were established experimentally in a free-jet facility. It was illustrated that the existing anomalies between full-scale flight data and model-scale flight simulation data projected to the flight case could well be due to the contamination of flight data by engine internal noise.

17. Key Words (Suggested by Author(s))	18. Distribution Statement
Jet noise; Shock noise; Internal noise; Flight effects; Transformation; Free-jet simulation; Wind-tunnel simulation; Shear layer; Lilley equation; Reflection; Refraction; Transmission; Turbulence scattering; Turbulence absorption	Unclassified - unlimited STAR Category 71

19. Security Classif. (of this report)	20. Security Classif. (of this page)	21. No. of Pages	22. Price*
Unclassified	Unclassified	322	A14

* For sale by the National Technical Information Service, Springfield, Virginia 22161